COMPUTATIONAL BIOENGINEERING
OF THE
GASTROINTESTINAL TRACT

POH YONG CHENG

NATIONAL UNIVERSITY OF SINGAPORE

2012

COMPUTATIONAL BIOENGINEERING OF THE GASTROINTESTINAL TRACT

By POH YONG CHENG

B.Eng. in Bioengineering (1st Class Hons.), NUS

Thesis Supervisor:
Dr Martin Lindsay Buist

Advisory Committee Members:
Professor P.S. Thiagarajan
Dr Gerald Udolph
Dr Levent Yobas

A THESIS SUBMITTED FOR
THE DEGREE OF DOCTOR OF PHILOSOPHY

NUS GRADUATE SCHOOL FOR INTEGRATIVE
SCIENCES & ENGINEERING

NATIONAL UNIVERSITY OF SINGAPORE

May 2012

Acknowledgements

Firstly, I am heartily thankful and owe a great deal to my supervisor, Dr Martin Buist, who has been a very supportive, engaging, generous, patient and easy-going mentor during this challenging Ph.D. journey which began in 2008. I deeply appreciate the effective advice he had provided for my research and professional development, the flexibility he had given me to explore interests, and the extensive silent efforts devoted to helping us the best he could; all of these amidst his heavy work schedule and beyond. His all-in-one traits of selflessness, astuteness, calmness, far-sightedness, and resoluteness are inspiring. I have gained and learned much from Dr Martin in many ways, be it technical skills or otherwise. Thank you for everything, and I look forward to continue working together in the future, if possible.

Next, I am indebted to the NUS Graduate School (NGS) for Integrative Sciences and Engineering for providing the generous scholarship financial support, in terms of monthly stipend and educational allowance, that enabled me to get the books I require and to attend the beneficial international conferences and courses. I am also grateful to the administration folks in the NGS office, Ivy, Irene, Vivien, Rahayu and several others for their immense help which greatly smoothed this Ph.D. stint.

Professor P.S. Thiagarajan, Dr Gerald Udolph and Dr Levent Yobas were members of my thesis advisory committee; I would like to thank them for their

time, patience, and useful advice on scientific work and career development during our Ph.D. progress meetings over the years.

The Computational Bioengineering Laboratory is a place that I have spent a lot of my time in (naturally!), and it evokes fond memories. The members of the lab, past and present, had made a significant impact on my life. Dr Alberto Corrias, now a lecturer of NUS, has been a very helpful, understanding and supportive colleague. He has generously helped and provided research opportunities to me. Dr David Nickerson, now in Auckland Bioengineering Institute (ABI), similarly, has been very supportive during his stint here, and even when overseas in ABI. I am deeply thankful for his patience, guidance, teaching and advice on numerous occasions. Viveka, Aishwariya and May Ee were students in the lab, whom I have had the pleasure to befriend. During the past few years, we have had deep discussions regarding research and life, thank you for the support and encouragement when the going got tough. William Chung, also a lab-mate of several years, is like a big brother to us in the lab, always thoughtful and ready to sincerely help us the best he could; I would remember the good times such as the run sessions we had, including those with Alberto, in training for the Standard Chartered Marathon. My students, Swe Swe Thet Paing, Jeremy Lye, Kenneth Tan and Nicholas Cheng (now a PhD student in this lab), it has been a pleasure to work with you in our research projects and I am also very thankful for your help and support. Li Liang and Jing Wui are relatively new students to the lab, and it has also been a great pleasure to have befriended and worked with you.

ii

Ariel Tan, Soneela, Pradeepa, Bramasta, Ali Hasnain, Matthew Pan, George, Jingling and Jian Hao.

I am also grateful for the support of friends beyond NUS, good friends such as Ken and Ben from Singapore Polytechnic, whom I had the honour to work with, for a small start-up, which gained me good experience beyond research. Additional thanks for your counsel and encouragement when I faced difficulties with academic pursuits. My apologies to everyone else, here in Singapore, or overseas, whom I have been unable to name, and have supported me in one way or another during this Ph.D.; I offer you my sincerest regards.

Last, but not the least, to my parents, my deepest gratitude for your selfless and unwavering support, sacrifice and encouragement. I will remain forever indebted to you and I hope that as I develop professionally, I can provide you a much better life than during those tough years of raising me and my brother up.

To my parents
C.K. Poh
K.H. Ng

Table of Contents

Summary

Recent evidence has suggested that the presence of ion channel mutations in the interstitial cells of Cajal (ICC) and the smooth muscle cells (SMC) may cause gastrointestinal (GI) motility disorders. Specifically, the R76C mutation of a sodium channel interacting protein, telethonin and the G298S mutation of the sodium channel were found in patients presenting with idiopathic intestinal pseudo-obstruction and irritable bowel syndrome, respectively. However, the genotype to phenotype link remains unclear. How, if at all, do these mutations disrupt GI organ electromechanics and lead to motility disorders?

Multi-scale computational modelling is an attractive approach that works synergistically with experimental and clinical efforts, towards the elucidation of disorder etiology and in treatment development. Here, the hypothesis that the rare and missense mutations of R76C and G298S are pathogenic factors for GI motility disorders was investigated through the development of multi-scale computational models.

Computer models describing the electrophysiology of wild-type, R76C and G298S sodium channels were developed and validated. Eleven models were selected for higher spatial scale investigations. At the single cell scale, a novel, biophysical single cell model of the human small intestine SMC electrophysiology was developed, which together with existing well-established gastric models of ICC and SMC electrophysiology, were used to integrate and investigate the sodium channel models. At the multi-cellular

scale, two influential features of tissue electrophysiology were described to create a realistic one dimensional gastric model. An extended bidomain method was developed to integrate the presence of multiple intercommunicating ICC and SMC from the single cell descriptions, while the electrical slow wave entrainment and propagation mechanisms, essential for healthy electrical behaviour, were incorporated. Eventually, a one dimensional model simulating a strip of gastric wall was implemented to investigate the effects of the mutations.

From the *in silico* experiments, the R76C mutation caused a gain-of-function effect as reflected in the increased sodium current entry in all the single cell models of the ICC and SMC as well as in the ICC and SMC present in the gastric strip model. Consequently, the ICC and SMC electrophysiology were altered, with an increase in slow wave duration, resting voltage depolarization and an increase in slow wave frequency. The G298S mutation, in general, caused a loss-of-function effect where sodium current entry decreased in the single cell models and the gastric strip model. However, these changes did not translate into significant electrical slow wave changes. Therefore, neither mutation is definitively pathogenic, however the R76C mutation seems to offer a greater potential than the G298S mutation in causing GI motility disorders.

Future work should refine existing models with new ones developed, following new yet reliable experimental findings. GI organs are electromechanical, therefore the development of a multi-scale mechanical

framework, coupled to the existing multi-scale electrophysiology framework can reveal how electrical alterations from mutations are translated into mechanical disruptions to cause GI motility dysfunction.

List of Tables

List of Figures

Chapter 1
Introduction

"A journey of a thousand miles begin with a single step."
– Laozi, Chinese philosopher

1 Introduction

1.1 Motivation

Significant advances in our understanding of the gastrointestinal (GI) tract in health and disease have been achieved in recent times, however, much remains unknown with regards to the etiology of most functional GI disorders. A functional disorder is one that arises despite the absence of structural damage to an organ. In such cases, treatments target alleviation of symptoms instead of the underlying mechanisms of the disorder [1]. In some cases, the treatment causes undesirable side-effects. To complicate matters, GI disorders are typically heterogeneous and complex, meaning that a multitude of genetic and/or environmental factors are involved in the pathogenesis of the disorder. This poor understanding of etiology has contributed to the unwillingness of several pharmaceutical companies to develop GI drugs, despite an apparent huge and expanding demand [2]. More importantly, we are unable to improve the quality of life and reduce economic costs to the victims of these chronic GI disorders.

A series of comprehensive studies by Everhart and Rudhl on the burden of digestive diseases in the United States has estimated that GI diseases have affected about 72 million Americans, caused about 10% of all deaths and resulted in a staggering total cost of USD142 billion in 2004 alone [3-5]. In the Asia-Pacific region, the prevalence of irritable bowel syndrome is fast increasing, particularly in emerging economies, brought about by changes in

diet and lifestyle [6] (see Figure 1.1). In the local context (Singapore), Changi

General Hospital reported that irritable bowel syndrome affects 30% to 50%

of the local population, and that patients might suffer from "a great deal of

discomfort and distress" but schemes are available to help patients "control the

symptoms" of the GI disorder [7]. Given the increasing prevalence and

substantial adverse impacts of GI disorders, expediting our understanding of

GI tract in health and diseases is critical.
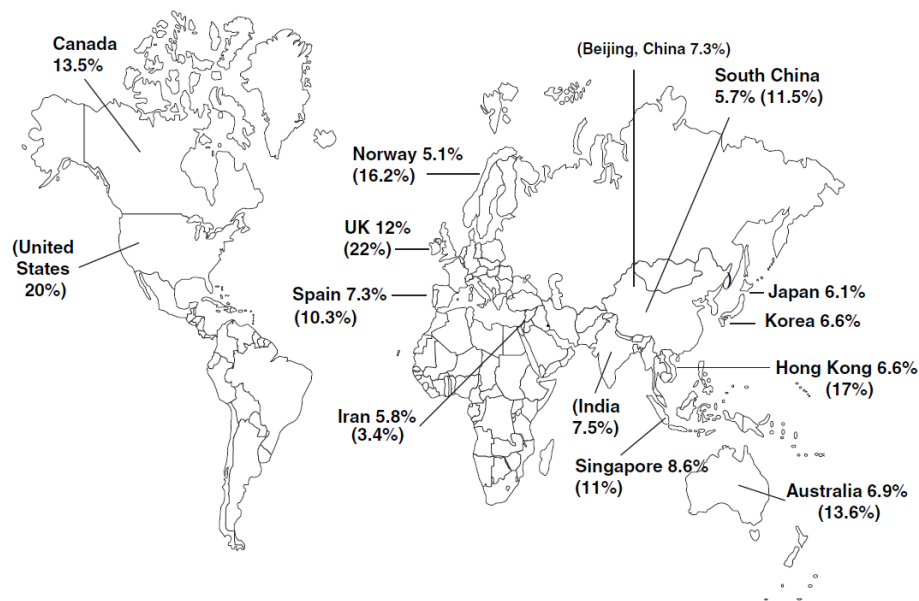
Figure 1.1. World map of prevalence of irritable bowel syndrome from 2000 to 2004 by Rome 2 criteria, while in parentheses are statistics by Manning criteria. Adapted from [6].

The key focus for us is idiopathic GI motility disorders of the stomach and

small intestine; such disorders include gastroparesis, delayed gastric emptying,

rapid gastric emptying, irritable bowel syndrome and intestinal pseudo-

obstruction, and are characterized by a mix of symptoms such as abdominal

pain, early satiety, nausea, constipation and diarrhoea. Idiopathic GI motility

disorders are usually diagnosed through a series of steps that includes looking

at medical history and performing indicative tests such as radionuclide transit

tests through imaging, ingestible measurement capsules and the examination of faecal bacteria growth. Should these tests indicate an absence of structural lesion but a presence of motility impairment, it is classified as a case of a functional disorder of GI motility with unknown causation.

Nonetheless, there are an increasing number of studies that correlate some of these idiopathic disorders with genetic variants such as ion channel mutations. Ion channelopathies are well known for other electrically active body systems such as in the nervous system where potassium channel mutations are known to cause episodic ataxia and in the cardiac system where sodium channel mutations are known to cause dysrhythmias [8, 9]. Similarly, it is possible that genetic mutations, specifically those of ion channels in the primary motility effectors of the smooth muscle cells (SMC) and the pacemaking interstitial cells of Cajal (ICC), are candidates for causing GI dysrhythmia and subsequently motility disorders in a subset of patients. Some prokinetic drugs are designed to alleviate GI motility disorder symptoms through actions on ion channels; examples include nifedipine, diltiazem, otilonium bromide which act on calcium channels, lidocaine, ranolazine which act on sodium channels, and glipizide, amiodarone which act on potassium channels, while lubiprostone acts on chloride channels [10]. However, these prokinetics drugs are likely prescribed to improve motility through "blind" actions on ion channels, since the underlying mechanisms of the motility disorders are not well-understood. Furthermore, due to the non-specific expression of these ion channels in other body systems, some of these drugs could impose adverse side-effects. Despite this, ion channels remain as promising targets for the treatment of GI motility

disorders because of benefits such as specific targeting of drugs on ion channel sub-types and their macro-complexes as well as the high throughput of ions across channels that increases drug efficacy [10, 11].

However, so far, there are no ion channel mutations of the ICC and SMC which are known to cause motility disorders. Early evidence suggests the SCN5A gene encoded sodium channel, which is found in the ICC and SMC, as a potential candidate for ion channelopathy of GI motility. Sodium channel mutations have been statistically correlated with GI symptoms [12, 13] while rare and missense mutations were identified in the blood of patients suffering from chronic intestinal motility disorders (see Table 1.1 for some of these sodium channel related mutations) [14, 15]. However, it remains unclear how these mutations contribute to GI motility disorders and further studies are challenged by limitations in experimental techniques applied to the GI tract. Computational modelling therefore represents a key tool to further our understanding of GI motility in health and disease.

Table 1.1. List of SCN5A related mutations associated with GI and cardiac symptoms, referred to by the references [14, 15] in the main text.

Mutation related to SCN5A	GI Symptoms	Cardiac Symptoms
R76C	Yes [14]	Not tested
G298S	Yes [15]	Yes [206]
G1743R	Not tested	Yes [13]
R1623Q	Not tested	Yes [13]
R1644H	Not tested	Yes [13]
E1784K	Not tested	Yes [13]

1.2   Approach

Computational modelling in biology and physiology in the recent years, has received strong attention. Multidisciplinary efforts have been invested to model, analyze and predict complex biological and physiological mechanisms with reasonably good success. However, several major challenges exist, one is the so-called "grand challenge" of multi-scale computational modelling that involves integrating interdependencies across several observation scales, while maintaining computational efficiency. Research work into multi-scale computational modelling promises to help us better understand disease mechanisms, establish diagnostic biomarkers, personalize and optimize treatment, and to develop new therapeutic options.

The International Union of Physiological Sciences (IUPS) Physiome Project, set up some 10 years ago, is one such project aimed at multi-scale modelling [16]. It is a worldwide public effort that includes the construction of a computational framework to understand human physiology which involves the development of integrative models across several scales. These scales consists of gene expression to cell to organism, modelled in a number of aspects such as gene regulatory networks, protein pathways, integrative cellular function and multi-cellular structure-function relationships in a tissue or whole organ.

One major theme of the IUPS Physiome Project is the digestive and GI system, also known as the GIome [17], and this is the main theme that this PhD thesis falls under. The aim is to model GI motility to understand its healthy and diseased states with an eye towards improving GI healthcare. The cardiac

computational modelling field is much more mature and has observed successes in the elucidation of ion channelopathy etiology and drug development. This contrasts the relatively nascent field of GI computational modelling. Nonetheless, progress has accelerated in recent years due to a steep increase in our understanding of GI tract physiology.

Developing computer models of multiple spatial scales are required in this research. Here, the approach to such multi-scale modelling would necessarily be a pragmatic one, i.e., a "middle-out" approach where models are built and refined from any scale with good availability of information [18]. These models are then integrated to the multi-scale framework as shown in Figure 1.2. For example, one can begin with improving an existing multi-cellular description, followed by modelling ion channels, building a single cell model, and then (re-)investigating the effects of ion channel variants at different levels of this multi-scale GI framework.
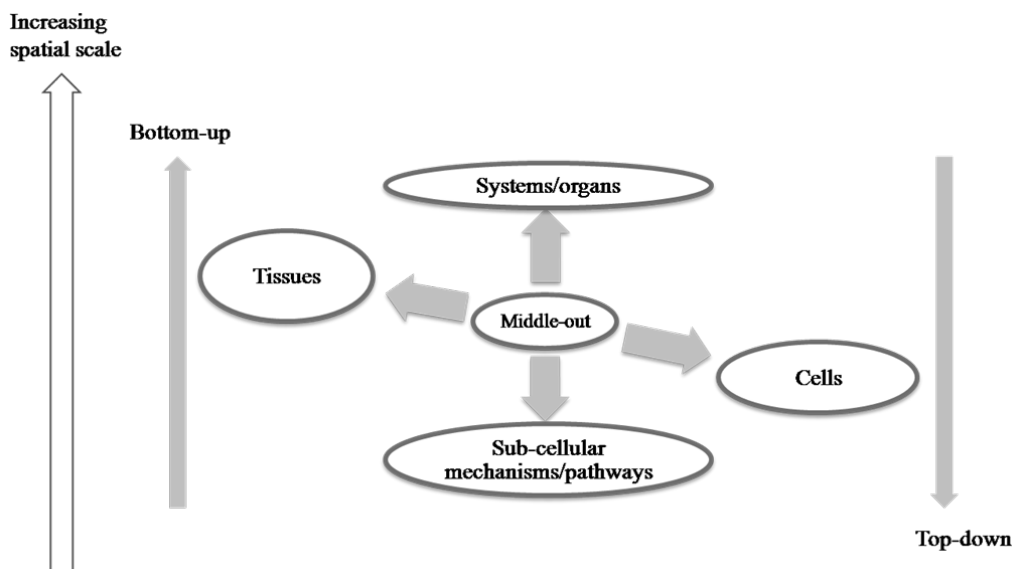
Figure 1.2. Pragmatic approach for multi-scale modelling. Instead of pursuing a top-down (from systems to sub-cellular mechanism) or bottom-up (in the reverse hierarchy), the pragmatic approach of middle-out [18] is chosen. This means models are built and refined at

any scale, depending on the availability of information and resources; efforts should be made to iteratively refine and integrate models from these different scales into a systemic framework.

At each spatial scale, model construction is guided by an ideal outline shown in Figure 1.3. An adequate model is formulated with a suitable level of structural complexity and granularity, while a chosen set of parameters is parameterized against training data. The model output is then checked against validation data and subjected to sensitivity and robustness testing, if necessary. These will provide information useful for decisions in modelling design, and for providing feedback on the training data. This can be repeated from time to time to improve the model as further data and findings appear. Modelling can additionally be viewed to be in an iterative relationship with clinical and experimental studies where progress in any of these three major research thrusts can assist each other's development. For instance, modelling can provide insights to guide experimental design whose results can in turn help to refine or discriminate existing models.
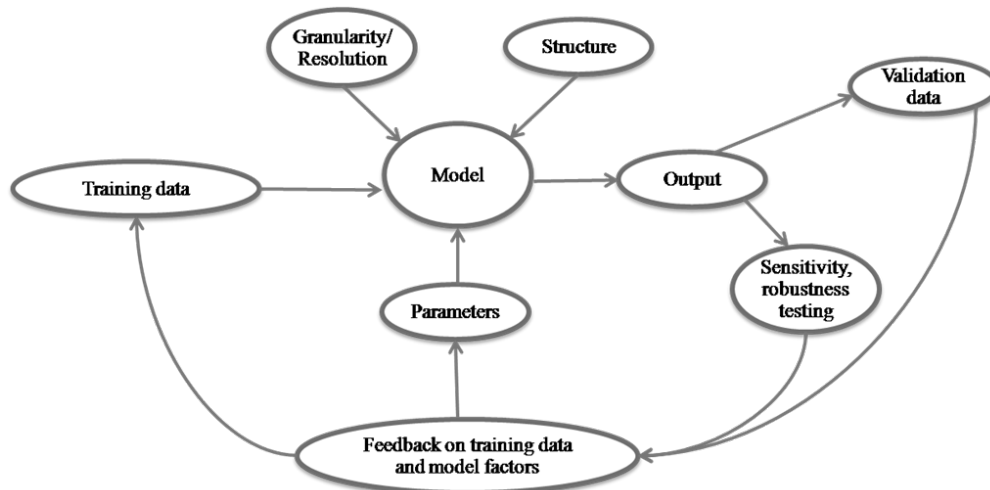
Figure 1.3. An ideal outline for creating an adequate model at any spatial scale.

1.3 Hypothesis and objectives

Against the above background, the motivation in this thesis is to examine the primary hypothesis that *ion channel mutations, particularly the mutations of SCN5A, contribute to GI motility disorders*. The following objectives were therefore defined:

(1) Development of novel computer models describing the wild-type (normal) and mutation affected ion channels, as well as other ion channel variants that arise from alternative splicing and polymorphism.

(2) Development of a novel and biophysically based human jejunal smooth muscle cell model.

(3) Development of novel multi-cellular models that describe:

(a) An extended bidomain framework of multiple cell types

(b) The incorporation of tissue heterogeneities

(4) Integration of the ion channel models into existing and newly developed single cell and multi-cellular models, and then to investigate the mutations' contribution towards GI motility disorders.

1.4 Organization of thesis

This thesis is organized into six chapters to address the hypothesis and objectives that were identified. An outline of the subsequent chapters is given below.

Chapter 2 - Background

The first part of this chapter provides an introduction to the biology and physiology of GI motility, particularly for the stomach and small intestine. The existing GI models across the spatial scales are then reviewed.

Chapter 3 – Ion channel modelling

At the sub-cellular level, the focus is on modelling ion channel electrophysiology. The theoretical methods and experimental information useful for ion channel modelling are discussed. This includes two major formalisms, i.e., the Hodgkin-Huxley formalism and the multi-state Markov formalism. The traditional Hodgkin-Huxley formalism was first examined by modelling the human sodium channels in wild-type and mutation affected states (i.e., a R76C mutation). This formalism was found to be inadequate in describing channel kinetics. Subsequently, the Markov formalism was applied to create models that were able to describe channel kinetics well. The same Markov modelling methodology was then applied to model human sodium channels for four common polymorphic-splice variants under wild-type state and a G298S mutation state, resulting in a basic set of eight sodium channel models. With these models, the mutations were computationally investigated in existing biophysically based single cell models of the stomach. Additionally, the interest in examining an alternative ion channel mutation led to the modelling and investigation of a potassium channel mutation, I177N, which is also discussed in this chapter.

Chapter 4 - Single cell modelling

Existing single cell models of GI electrophysiology do not include a human intestinal smooth muscle model, while recent experimental data are coming from the human small intestine, and early evidence suggests sodium channelopathies of intestinal motility disorders. Therefore, a novel biophysically based human jejunal SMC model of the small intestine was developed with the details discussed in this chapter. Subsequently, the sodium channel models that were developed in Chapter 3 were integrated into the human jejunal SMC model to evaluate the consequences of these mutations.

Chapter 5 - Multi-cellular modelling
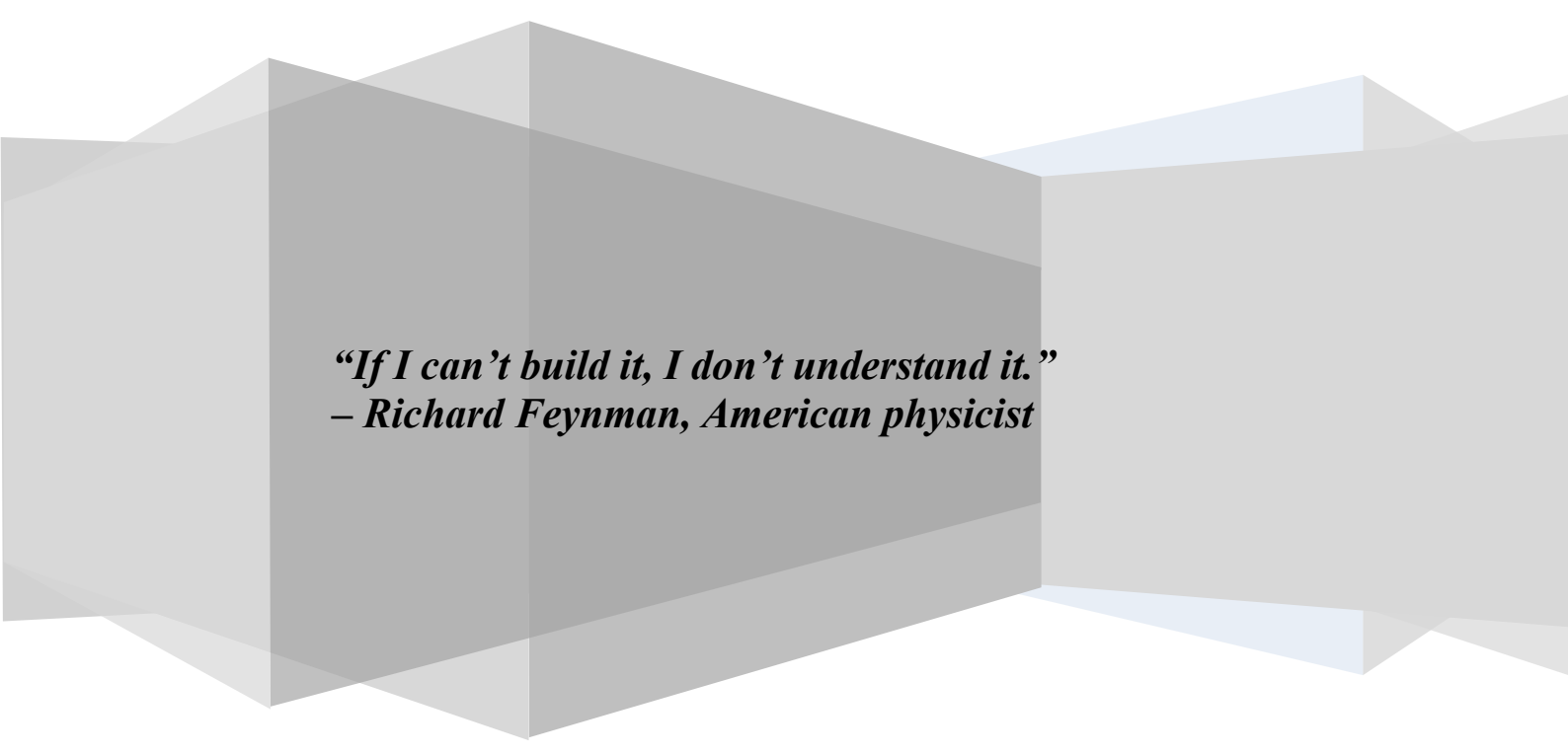
In integrative multi-scale modelling, one aim is to appropriately integrate cellular descriptions into a multi-cellular framework such as a tissue or organ model where there is intercellular communication and where tissue heterogeneities are incorporated. Given the complexity of the GI wall tissue, the traditional bidomain framework is unsuitable in accounting for the multitude of cell types and their distribution, in GI electrophysiology. Therefore, an extended bidomain framework for including multiple cell types was developed. The development and validation of the extended bidomain framework as well as the incorporation of tissue heterogeneities are presented in this chapter. This is followed by an examination of the effects of ion channel mutations in the multi-cellular model developed here.

Chapter 6 – Conclusions

This chapter summarizes the research work presented in this thesis and recommends future work to advance the current development and findings.

Chapter 2
Background

"If I can't build it, I don't understand it."
– Richard Feynman, American physicist

2 Background

2.1 Gastrointestinal tract physiology

2.1.1 Overview

The gastrointestinal (GI) tract, also known as the digestive tract or alimentary canal, comprises a series of connected organs that perform a range of functions that include ingestion of food, digestion of contents through mechanical and biochemical actions, absorption of nutrients, electrolytes and water, and excretion of waste products. The GI tract also acts as a component of the immune system, protecting the human body against attacks from pathogenic microorganisms and toxic materials that can enter the GI tract via what we eat [19-22]. These functions are executed and assisted by the main and accessory organs of the human GI tract as shown in Figure 2.1. In the proximal to distal direction, we have the tongue, jaw and teeth followed by the oesophagus that delivers the swallowed contents to the stomach, which then releases the processed materials to the small intestine through to the large intestine, before the eventual waste materials are stored in the rectum for excretion through the anus. The accessory organs of parotid gland, liver, gallbladder and pancreas provide supportive functions such as secretion of digestive agents and metabolism of absorbed nutrients. The *stomach* and the *small intestine*, and in particular their *motility* function, are the focus of this work.
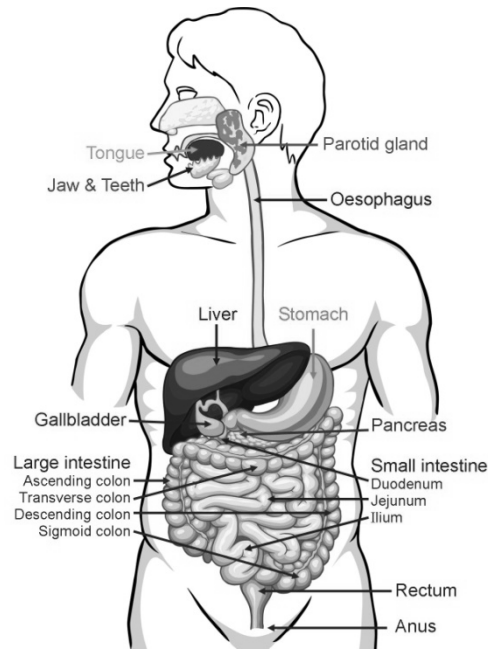
Figure 2.1. Anatomy of the human GI tract. Adapted from [23].

2.1.2   Stomach

The stomach is located between the oesophagus and the small intestine. It is a hollow muscular organ that can be divided into three key regions of the fundus, the corpus and the antrum. The fundus, located at the proximal end of the stomach, acts as a storage space for incoming food through adaptive relaxation. The corpus and the antrum, which are located in the mid region and distal region of the stomach respectively, are the areas in which significant phasic motility occurs. They are electrically active with rhythmic electrical slow waves at a frequency of 3 cycles per minute (cpm), as illustrated in Figure 2.2. The propagation of these slow waves from the initiation site at the corpus to the antrum coordinates peristalsis. Rings of contraction are formed at the corpus and travel towards the antrum. A contraction ring takes approximately 20 s to move from the initiation site at the corpus to the distal antrum. At the extremities of the stomach are sphincters that connect to the adjacent organs, i.e., the lower oesophageal sphincter at the proximal end connects to the

oesophagus, and the pyloric sphincter at the distal end connects to the duodenum of the small intestine. Particularly, if the pyloric sphincter is closed when the stomach contracts, retrograde propulsion of the gastric contents occurs, resulting in mixing and breaking down of food. The amount of contents that gets transported into the duodenum of the small intestine depends on the extent of pylorus opening. The pylorus also acts as an electrical barrier that prevents the electrical slow waves from the duodenum from interfering with stomach motility and vice versa [19-22, 24].
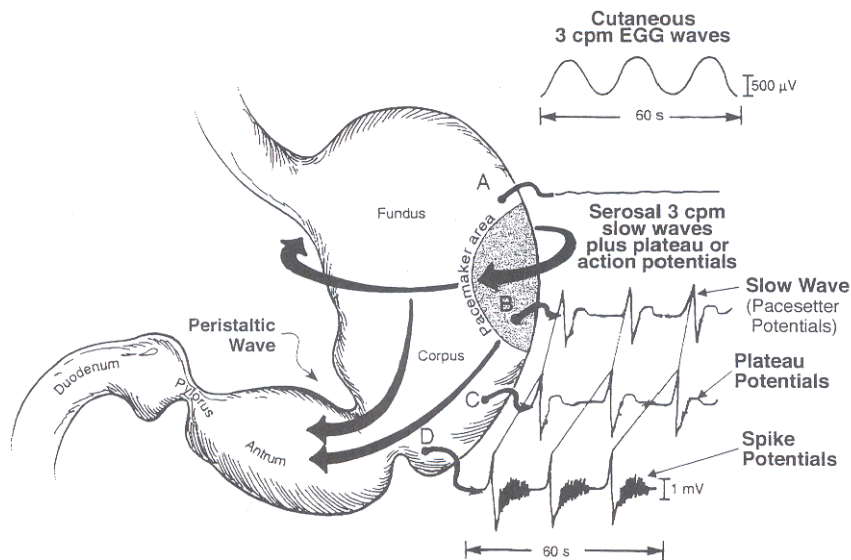
Figure 2.2. Electrical recordings and peristaltic waves from the stomach. Electrical slow waves of 3 cycles per min of varying morphology can be recorded from the corpus to antrum of the human stomach. The fundus is known to be electrically quiescent and exhibits tonic contraction and relaxation to accommodate food. Peristaltic waves, in the form of contraction rings, are coordinated by electrical slow waves and propagate towards the antrum. Spike potentials on slow waves are an indication of stronger smooth muscle contraction in the stomach wall. Adapted from [24].

2.1.3 Small intestine

The small intestine, which is located between the stomach and the large intestine, can be divided into three regions, i.e., the duodenum, the jejunum and the ileum (see Figure 2.3). The small intestine is where most of the

digestion and nutrient absorption take place. Two main types of motility are present in the small intestine. The first type is segmentation, where the small intestine is organized into several non-propagating compartments of contractions. This facilitates chyme turn-over and mixing with digestive secretions. The second type is peristalsis which facilitates the transport of digesta down the GI tract, akin to that in the stomach. Notably, the jejunum forms about 40% of the small intestine, and thus provides a significant surface area for digestion and absorption. Motility in the small intestine is also driven by intrinsic electromechanical activity of its cells. However, the coordination of electrical and mechanical activities is not as well understood compared to the stomach [25].
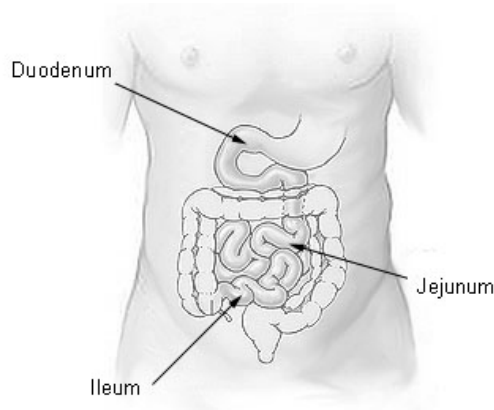
Figure 2.3. The human small intestine. It is divided into three regions, the duodenum, jejunum and ileum. Adapted from [26].

2.1.4 Motility

Motility results from rhythmic relaxation and contraction of the GI walls. It is an important activity that enables the GI tract to perform transportation, mixing and excretion of materials. Motility occurs in the GI walls due to the electrical and mechanical (i.e., electromechanical) activities of relevant cells

that are present within. Extrinsic factors, such as neural signalling, hormones and the immune system modulate motility [27]. Figure 2.4 shows an anatomical outline of a general section through the GI wall, containing cells responsible for motility. The innermost layer is the mucosa that forms the immediate wall of the lumen and is responsible for secretion and absorption. The muscularis muscosae is a thin layer of smooth muscle that supports secretion of digestive agents from the mucosal glands, while the submucosa plexus contains a network of neurons that forms part of the enteric nervous system. Next, the submucosa is where blood and lymphatic vessels run through. These vessels are essential for the transport of nutrients and substances, to and away from the GI wall. The submucosa is followed by the circular smooth muscle layer where circumferential muscular contractions occur. Then, there is the myenteric plexus which also contains a network of neurons that form the enteric nervous system. Both the submucosa and myenteric plexi provide the major nerve supply to GI tract and mediate motor control and sensory control. The longitudinal muscle layer is where longitudinal muscular contractions occur; this layer is thinner relative to the circular muscle layer. The smooth muscle cells in both the circular and longitudinal layers are electrically excitable and can transduce electrical signals into contractions through calcium linked actomyosin cross-bridging activity. In addition, both muscle layers receive signalling input from the enteric neurons. Finally, the outermost layer is the serosa which is a thin layer of connective tissue (about 0.1-0.2 microns, [28]) containing serous cells that secrete lubricating fluids to protect its organs from frictional damage [17, 29-34].
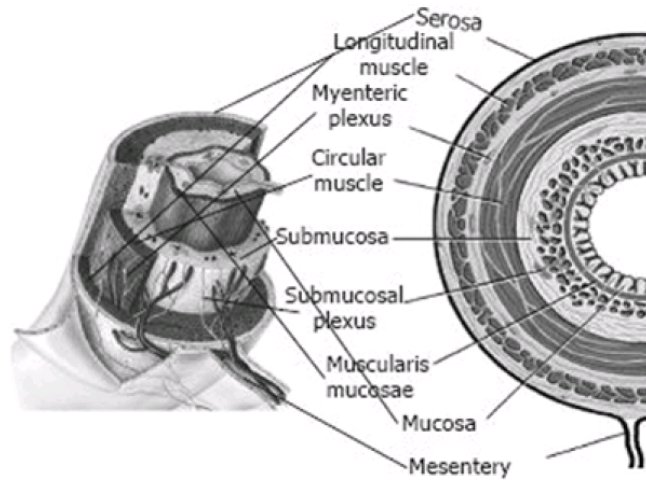
Figure 2.4. General structure of the human GI wall. Adapted from [35]

It was previously thought that the GI circular and longitudinal smooth muscles were electrically self-exciting and that this led to their contractions. First discovered by Cajal in 1893 [36], the interstitial cells of Cajal (ICC) were later found to be the electrical pacemaker cells responsible for the excitation and, therefore, mechanical actions of the electrically excitable but passive GI smooth muscle cells [37]. A variety of ICC sub-types were found to locate in different layers of the GI wall, as shown in Figure 2.5 [38]. Briefly, the ICC of the myenteric plexus, ICC-MY (also known as ICC-MP), are generally accepted as the primary pacemaker cells in the stomach and small intestine, while ICC of the submucosa plexus, ICC-SMP, are accepted as the primary pacemaker cells in the colon [39, 40]. The circular muscle layer ICC, ICC-CM, and the longitudinal muscle layer ICC, ICC-LM, serve the role of active regeneration of slow waves that are conducted into these layers from the primary pacemaker ICC-MY [41, 42]. ICC-CM and ICC-LM are considered as intramuscular ICC (ICC-IM), and these, together with the deep muscular plexus ICC, ICC-DMP, are suggested to mediate enteric neuronal signalling

[43]. Not much is known about the functional roles of the other ICC sub-types except for their identification in the respective anatomical locations within the GI wall.
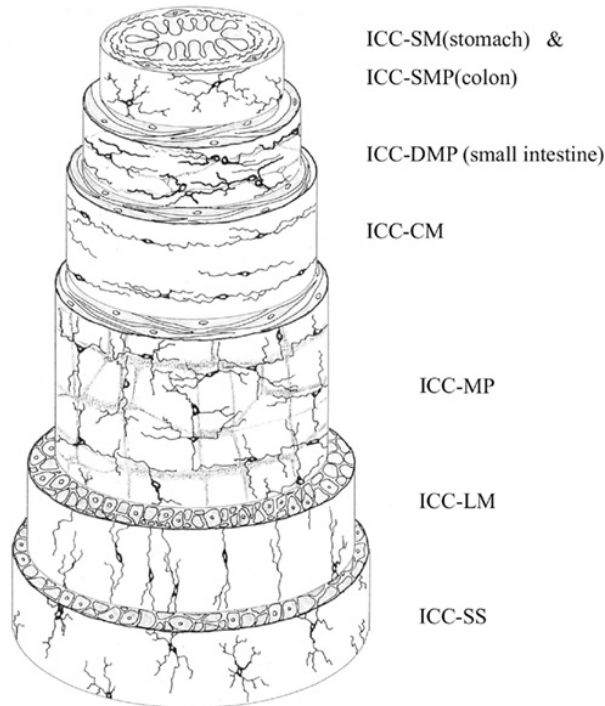
Figure 2.5. A variety of interstitial cells of Cajal (ICC) is present in different layers of the GI tract. ICC-SM is found at submucosa-circular muscle interface of stomach pylorus. Similarly, ICC-SMP is found at the interface of submucosa plexus and circular muscle of the colon. ICC-DMP are in the deep muscular plexus of the small intestine. ICC-CM and ICC-LM are the ICC located within the circular and longitudinal muscle layers respectively. ICC-MP is the ICC network found in the myenteric plexus between the circular and longitudinal smooth muscle layers. ICC-SS are the ICC found in the subserosal tissue space. Adapted from [38].

2.1.5 Cellular electrophysiology of key motility cells

The key cell types in the stomach and the small intestine that are involved in GI motility are the smooth muscle cells (SMC) from the circular muscle layer and the ICC-MY. The circular smooth muscle layer, found in both the stomach and small intestine, is the thickest muscle layer in the GI wall, and is therefore a main effector of motility. Adjacent to the circular smooth muscle layer, is the myenteric plexus layer, in which the pacemaking ICC-MY are found. The

ICC-MY form a network within the myenteric plexus. This network is well-established to initiate and coordinate electrical slow waves that excite the circular smooth muscle layer [44-46]. On the other hand, lesions on the ICC-MY and its network are known to cause GI motility disorders [47-50]. Given the critical function of the ICC-MY as well as of the circular SMC, these are deemed to be the key cell types involved in motility. Here, the research focus is on describing the electrophysiological characteristics of these key cell types in the stomach and the small intestine. The electrophysiology of these cells is important in determining the smooth muscle mechanical activity and hence motility.

Stomach

The ICC-MY excite the largely passive SMC; direct evidence of electrical coupling between the ICC-MY and SMC was provided by Hirst et al [51]. Figure 2.6 shows that the ICC electrical slow waves dictate the SMC electrical slow wave morphology and frequency. However, the SMC slow waves are of lower amplitude than the ICC slow waves due to the degree of electrical coupling through gap junction proteins, the low ICC-to-SMC ratio and the intrinsic excitability of the SMC.

In the stomach of large mammals such as dogs and humans, a dominant slow wave frequency of about 3 cpm is typically recorded from an intact stomach. However, studies have shown that isolated cells (or tissues) exhibit a gradient of decreasing intrinsic frequency from the corpus to the antrum (for example, canine recordings as shown in Figure 2.7) [52, 53]. The variation in intrinsic

frequency arises due to cellular variations in pacemaking properties of the ICC in the ICC-MY network, and this frequency gradient is central to the healthy performance of gastric motility [54, 55]. Typically, the fastest pacemaking ICC appear in the corpus and entrain other slower ICC in the ICC-MY network through a putative voltage-to-calcium transduction mechanism, mediated by calcium ion channels [56].
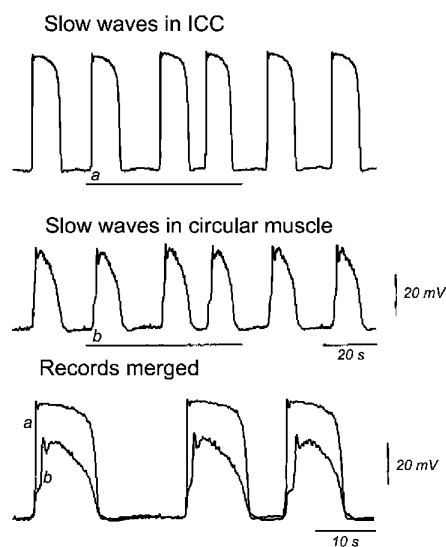
Figure 2.6. Slow waves recorded from the guinea pig gastric ICC and SMC. Adapted from [51].

This entrainment feature is responsible for the initiation of electrical slow waves and contraction rings from the corpus and for organizing their aboral propagation towards the antrum. Without the frequency gradient, the entire corpus and antrum will activate and contract at the same time, and normal peristalsis will not be possible. Therefore, any lesion on the ICC network, a disruption of the frequency gradient or a malfunction of the entrainment mechanism can lead to gastric motility disorders. There is increasing evidence that ICC and its network impairment, such as those that arise from

complications of diabetes, can cause gastric dysmotility (for example, gastroparesis) [47, 57, 58]. Extrinsic factors such as neuronal or paracrine
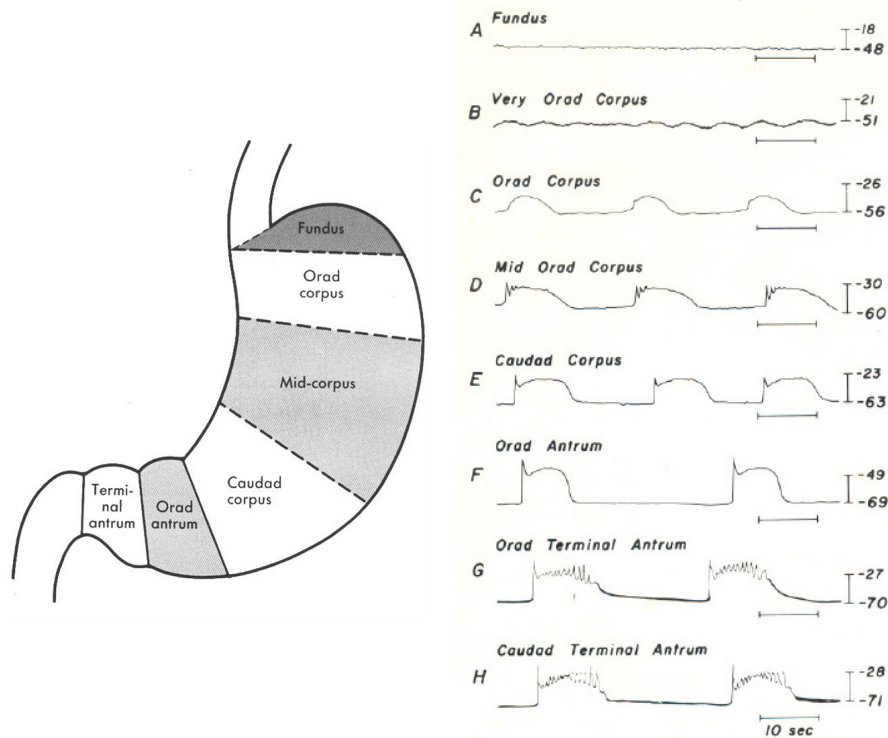
Figure 2.7. Intrinsic slow waves of the canine stomach. Note the decrease in frequency and polarization of resting membrane potential from the corpus down to the antrum. Adapted from [53].

signalling can also disrupt frequency regulation. Prostaglandin, a paracrine substance, was found to exert chronotropic effects through studies of tachygastria (hypermotility) in animals and humans [59, 60]. A chronotropic agent can also cause the antral ICC to pace at a higher frequency than the corpus ICC. This can result in functional uncoupling in the form of retrograde slow wave propagation that causes hypomotility and reduces stomach emptying [61].

Small intestine

The ICC-MY and SMC electrophysiology of the small intestine is similar to the gastric counterparts. However, one salient difference is the intrinsic frequency of the electrical slow waves. In the stomach, the typical entrained frequency is at 3 cpm, whereas much higher frequencies have been recorded in the small intestine. It was noted in canine and feline small intestines that intrinsic slow wave frequencies start at around 14 cpm at the duodenum and decreases to around 10 cpm at the ileum [62, 63]. Human recordings are limited with recent measurements indicating 8 cpm in the human small intestine (location unspecified) [64] and 6 cpm in the human jejunum [45]. These human results were recorded from waste tissue of morbidly obese patients who had undergone gastric bypass surgery.

Additionally, the propagation pattern of small intestine slow waves is unclear, however initial evidence suggests the presence of a single pacemaking site in the duodenum near the pylorus junction as opposed to the alternative belief of multiple active pacemaking sites along the small intestine. The apparent gradient of decreasing slow wave frequency from the duodenum to the ileum putatively arises due to the occasional blockage of slow wave propagation along the small intestine [65, 66]. Such a frequency gradient has been suggested to facilitate high intensity mixing in the proximal small intestine for effective nutrient absorption due to its higher frequencies while slower frequencies at the distal region facilitates the processing of more slowly digested substances such as fats and bile before entry to the large intestine [67].

2.1.6 Sub-cellular mechanisms

Moving down the spatial scale, the contribution of sub-cellular mechanisms to cellular electrophysiological behaviour is examined here. The membranes of excitable cells contain a variety of transmembrane proteins that confers membrane electrical excitability. These include ion channels that can be gated by different factors such as membrane voltage, ligands, and mechanical forces. Upon activation, these channels open and conduct specific ions across the cell membrane with characteristic kinetics, thereby changing the distribution of the intracellular and extracellular concentrations of ionic species and hence their respective electrochemical gradients. Key ionic species include sodium, calcium, potassium and chloride ions. Other transmembrane proteins that regulate ionic flow include pumps and exchangers.

A dynamic potential difference (also known as membrane voltage) arises in the cell due to the transmembrane exchange of ions, the ionic concentrations in the immediate extracellular and intracellular spaces of the cellular membrane, as well as the cell membrane's capacitive properties. The distribution of intracellular and extracellular concentrations of an ionic species produces what is known as Nernst potential [68]. Should the membrane voltage differ from the Nernst potential, then this potential difference creates a driving force that pushes this species of ions through the ion selective channels that are open. This in turn shapes cellular membrane voltage/potential. Intracellular mechanisms such as buffering proteins and organelles regulate ion sequestration and release, which will also influence free ionic concentrations, the Nernst potential and ultimately the membrane voltage.

The ICC and SMC contain the following general types of ion channels: Calcium-selective conductances, sodium-selective conductances, potassium-selective conductances, calcium-activated potassium conductances, chloride-selective conductances, and non-selective cationic conductances. The specific types of ion channels that are present in a cell depend on the spatial location in the stomach, small intestine and the animal species. Each type or sub-type of ion channel type exhibits different kinetics in regulating ionic flow; their functional roles are typically different but they act in a concerted fashion to engender normal slow waves in the ICC and SMC. Farrugia (1999) provides a comprehensive review of the ionic conductances in both the GI SMC and ICC [69], Vogalis (2000) has a review on GI potassium channels [70] while a number of other review papers that discuss ionic conductances for ICC electrophysiology can be found in [71-73].

Since ion channels play critical roles in the electrophysiology of the ICC or SMC, ion channel variations and changes in their expression level can alter electrical behaviour, and in turn affect mechanical behaviour. Such alterations can propagate across the spatial scales and eventually cause adverse changes to motility at the level of the whole organ. Ion channel variations include those that arise from alternative splicing, polymorphisms and genetic mutations, and can confer differentiated kinetic behaviour. As for ion channel expression, it determines the number of viable ion channels in a cell that would influence the magnitude of an ionic current that shapes membrane voltage.

Specifically, alternative splicing refers to the selective removal of mRNA exons that result in translated proteins of the same type, but of different sizes and possibly with different properties. For polymorphisms and genetic mutations, these refer to changes in the genetic sequence that can translate to a change in amino acid residue of the protein. Alternative splicing, polymorphisms and genetic mutations can therefore result in functional consequences for a protein. Splice and polymorphic variants are found in healthy subjects but may increase or decrease disease susceptibility. For instance, a novel splice variant of the ANO-1 CaCC, found in a patient with diabetic gastroparesis and not in healthy subjects, is a putative pathophysiological factor that confers disease susceptibility [42]. Genetic mutations, typically associated with diseased subjects, may serve as a substantial factor underlying disease etiology, and can be assisted by alternative splicing and polymorphisms present in the same ion channel protein. For instance, the kinetic behaviour of sodium channels in its most common background form of Q1077del splice variant is more strongly affected by the G298S genetic mutation, relative to its other common backgrounds [12]. So far, no ion channel variants of the ICC and SMC are known to cause GI motility disorders but there are initial evidence implicating sodium channel mutations in intestinal motility disorders [14, 15].

2.2 Multi-scale modelling of the gastrointestinal tract

Multi-scale mathematical and computational modelling is ideally suited to succinctly represent and integrate the tremendous volume of experimental data arising across the multiple scales. These models can be applied to understand

how different parts and activities of the various spatial scales interact in the complete picture. Multi-scale modelling of the GI electrophysiology has existed for some time and this section discusses the existing notable models of the ICC and SMC, across the spatial scales of single cell, multi-cells as well as the human torso.

2.2.1 Single cell models

Hodgkin-Huxley model

The cellular electrophysiology of most single cell models of the ICC and SMC used a governing equation of membrane potential which described a cell as a simple parallel conductance electrical circuit. This approach follows the Nobel prize winning seminal work of Hodgkin and Huxley in 1952, where a model of giant squid axon electrophysiology was created (see Figure 2.8) [74]. The governing equation is given by:

$$\frac{dV_m}{dt} = -\frac{I_{ion} + I_{Stim}}{C_m},$$
(2.1)

where V_m is the membrane potential, I_{ion} is the sum of ionic currents that contribute to cellular electrophysiology, I_{Stim} is a stimulus current that, if present, is delivered by an external source such as a neighbouring cell or an electrode, and C_m is the membrane capacitance. The choice of I_{ion} depends on the ionic currents carried by ion channels, pumps, exchangers and any other sub-cellular mechanisms that may contribute to cellular electrophysiology. There are a number of mathematical approaches to model the various I_{ion} including the traditional Hodgkin-Huxley gating-variable approach, the

multi-state Markov approach, as well as the less common Poisson Nernst

Planck approach [75, 76].
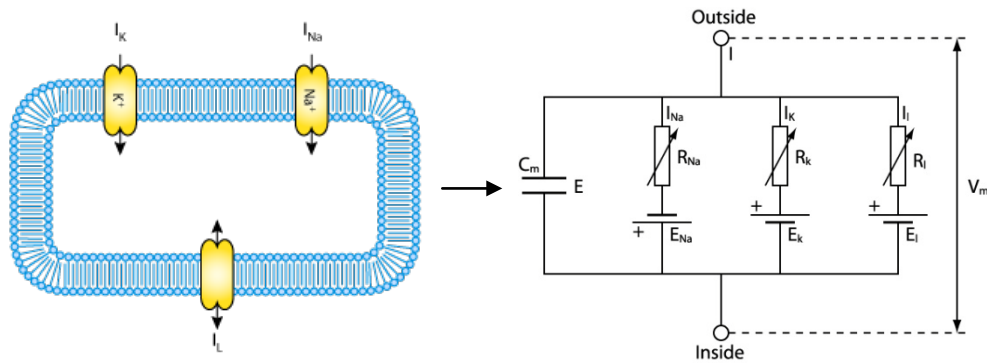
Figure 2.8. The Hodgkin-Huxley parallel conductance electrical circuit (right) is the gold-standard for modelling electrophysiology of a single cell (left). C_m refers to the cell capacitance, reflecting the ability of a cell membrane to store charges on either sides of the membrane, V_m refers to the (trans-)membrane potential with the intracellular potential as the reference point, E_x refers to the Nernst potential of the various ions, and R_x refers to the variable resistances (or equivalently, conductances) of the ion channels.

As an illustration, Figure 2.8 shows the parallel conductance circuit that

Hodgkin and Huxley have used to model the giant squid axon cell model

electrophysiology. The membrane potential (or voltage) is defined to be the

difference of potential inside a cell, minus the potential outside of a cell. Three

types of currents, i.e., the sodium current, potassium current, and non-selective

leakage current (I_{Na}, I_K, and I_l respectively) were sufficient to describe the

axon membrane potential. Each of these ionic current is described by an

Ohmic equation:

$$I_X = \frac{1}{R_X}(V_m - E_X),$$
(2.2)

where a particular ionic current, I_X, is given by the multiplication of the

inverse of a variable resistance, R_X and the potential difference between the

membrane potential, V_m, and the Nernst potential, E_X. The inverse of R_X is also commonly and equivalently described in terms of a conductance, G_X:

$$I_X = G_X(V_m - E_X). \tag{2.3}$$

In turn, G_X is typically a product of the channel's maximum conductance in a cell, $\overline{G_X}$ and the probability of a single channel in the open state to conduct ions, P_O:

$$G_X = \overline{G_X} P_O. \tag{2.4}$$

P_O is time variant and dependent on V_m which regulates the ion channels' open probability. $\overline{G_X}$ is assumed constant in the model, but in the biological context it may vary due to altered expression, localization and degradation of the ion channels.

The Nernst potential, E_X, is an electrochemical property of an ionic species, that arises from the distribution of intracellular and extracellular ionic concentrations of this ion. It can be described by:

$$E_X = \frac{RT}{z_X F} ln \frac{[X]_o}{[X]_i}, \tag{2.5}$$

where R, T, F are the ideal gas constant, temperature, and Faraday's constant respectively, X refers to the ion type, z_X is the valence of X, $[X]_i$ and $[X]_o$ refer to the ionic concentration of X in the intracellular and extracellular spaces respectively.

2.2.2 SMC models

Early models

Following Hodgkin and Huxley's landmark model in 1952, the development of Hodgkin-Huxley type single cell models of the GI tract appeared later, in the 1990s. These models contain greater cellular complexity such as in the number of influential ionic currents that shape membrane potential. These models include:

(1) Lang & Rattray's 1992 Hodgkin-Huxley type smooth muscle model that contains four ionic currents, namely, I_{Ca}, the calcium current, I_{Kdel}, the delayed rectifier potassium current, I_{leak}, the leakage current, and I_{KCa}, the calcium activated potassium current which together were able to describe self-excitatory smooth muscle slow waves that matched experimental observations from several regions of the GI tract (with appropriate variation of the free parameters) [77]. The governing equation for V_m, the smooth muscle cell membrane potential that has C_m as the cell capacitance, is therefore:

$$\frac{dV_m}{dt} = -\frac{1}{C_m}(I_{Ca} + I_{Kdel} + I_{leak} + I_{KCa}). \tag{2.6}$$

(2) Skinner et al's 1993 Hodgkin-Huxley type smooth muscle model described four ionic currents, namely, I_{Na}, the sodium current, I_K, the potassium current, I_{KCa}, the calcium activated potassium current, and I_{Ca}, the calcium current [78]. In addition, thermodynamically based equations were used to

describe I_{NaK}, the sodium-potassium pump, I_{CaP}, the calcium pump, and I_{NaCa}, the sodium-calcium exchanger. Both pumps contain a variable, dependent on an oscillatory ATP concentration, which drives the rhythmic slow waves reproduced by this model. The governing equation for V_m, the smooth muscle cell membrane potential that has C_m as the cell capacitance, is therefore:

$$\frac{dV_m}{dt} = -\frac{1}{C_m}(I_{Na} + I_K + I_{KCa} + I_{Ca} + I_{NaK} + I_{CaP} + I_{NaCa}). \qquad (2.7)$$

(3) Miftakhov et al's 1996 and 1999 small intestinal smooth muscle models, also based on Hodgkin-Huxley formalism, describe smooth muscle electrical activity based on I_{Ca}^{f}, the fast calcium current, I_{Ca}^{s}, the slow calcium current, I_K, the potassium current, I_{KCa}, the calcium activated potassium current, and I_{Cl}, the chloride current [79-81]. The governing equation for V_m, the smooth muscle cell membrane potential that has C_m as the cell capacitance and α as a numeric constant, is therefore:

$$\frac{dV_m}{dt} = -\frac{\alpha}{C_m}\left(I_K + I_{KCa} + I_{Ca}^{f} + I_{Ca}^{s} + I_{Cl}\right). \qquad (2.8)$$

Miftakhov et al's models also included elaborate descriptions of electrical stimuli provided by the enteric nervous system to the smooth muscles. These models were able to replicate rhythmic electrical slow waves, as well as spikes/action potentials that appear on the slow wave plateau which are responsible for stronger contractions in the intestinal smooth muscles.

However, one common salient issue with the above models is the assumption that GI smooth muscles are self-excitatory. This was because the establishment and acceptance of ICC as the pacemaker cells exciting the smooth muscles post-dated these early models. Therefore, these models are rather limited in their potential applications, such as in the investigation of consequences of ion channel variants.

Corrias and Buist's SMC model

In 2007, Corrias and Buist constructed a biophysically based single cell electrophysiology model of the canine gastric SMC [82], underpinned by Hodgkin-Huxley type ionic current descriptions. Figure 2.9 shows a schematic of the Corrias and Buist SMC model, with the following governing equation:

$$\frac{dV_m}{dt} = -\frac{1}{C_m}\big(I_{CaL} + I_{LVA} + I_{Na} + I_{BK} + I_{Kr} + I_{Ka} + I_{bK}$$

$$+ I_{NSCC} + I_{Ca}^{homeo} + I_{Stim}\big),$$

(2.9)

where C_m is the cell membrane capacitance, V_m is the membrane voltage which is dependent on the following critical ionic currents: I_{CaL} is the L-type calcium current, I_{LVA} is the low voltage-activated calcium current, I_{Na} is the voltage-dependent sodium current, I_{BK} is the big conductance calcium-activated potassium current, I_{Kr} is the delayed rectifier potassium current, I_{Ka} is the A-type potassium current, I_{bK} is the background leakage potassium current, I_{NSCC} is the relatively passive non-selective cationic current, and due to the lack of experimental data, I_{Ca}^{homeo}, is a phenomenological description

of calcium handling by mechanisms such as sarcoplasmic reticulum regulation and sodium-calcium exchanger. I_{Ca}^{homeo} is required to achieve intracellular calcium homeostasis. To excite the electrically passive SMC, the ICC stimulation is supplied through the term I_{Stim}:

$$I_{Stim} = G_{couple}(V_m - V_{ICC}),$$

(2.10)

where G_{couple} is the coupling conductance between ICC and SMC, V_m is the SMC membrane potential, and V_{ICC} is the ICC membrane potential. In the original paper, the ICC stimulus is a prescribed waveform resembling experimental observations, with a resting membrane potential of -70 mV, amplitude of 60 mV, and a coupling conductance of 1.1 nS. A noteworthy point is that the SMC model has to be parameterized to ensure reasonable electrical excitability. In the physiological situation, the density of ICC to density of SMC is said to be low (for example, less than 10% ICC and more than 90% SMC in gastric tissue [83]), therefore the SMC should not demand too much energy from ICC for its stimulation; ICC in turn requires considerable energy for self-excitation, evidenced by the high density of ICC mitochondria. This was considered in the model through the use of a suitably low coupling conductance.

Figure 2.10 shows the SMC model predicted slow waves that are in good agreement to the canine gastric SMC recordings. The model was further validated through additional computational tests. Being biophysically based and robust, the model is amenable for further integrative studies such as the

investigation of mutation of its constituent ionic conductances, and in multi-cellular studies. However, one limitation of the model is that the ionic current descriptions were constructed from more than one animal species, with the global membrane voltage being able to match the canine slow wave recordings. Therefore, as new data appear, an update to make it an animal specific model may be performed.
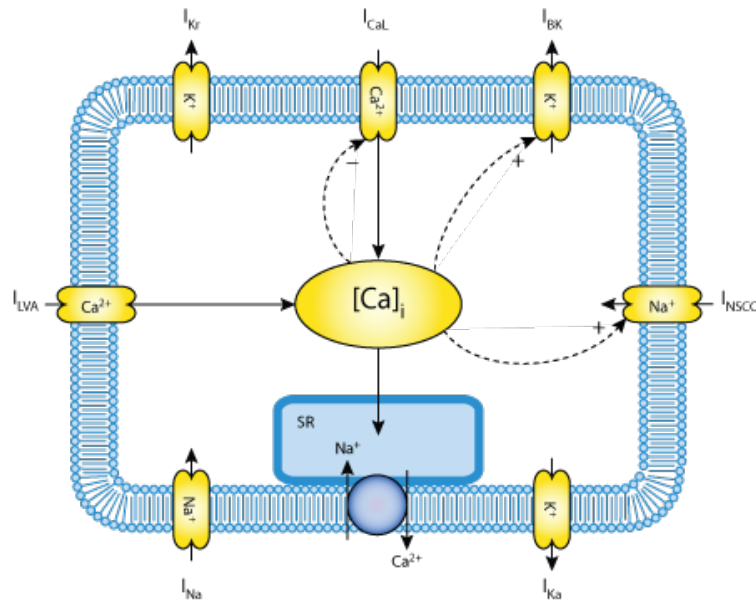
Figure 2.9. Biophysically based canine gastric single SMC model of electrophysiology by Corrias and Buist [82]. Adapted from CellML repository [84].
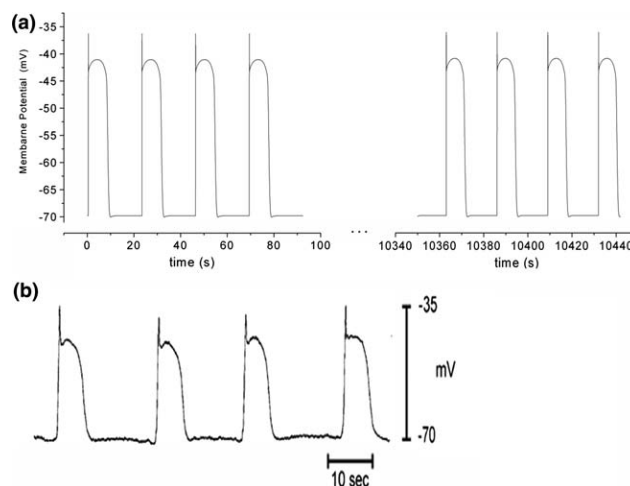
Figure 2.10. Corrias and Buist SMC slow waves. (a) shows the simulated SMC slow waves which are in good agreement with slow waves experimentally recorded from the canine gastric smooth muscle tissue in (b). Adapted from [82].

2.2.3 ICC models

The ICC, unlike the SMC, exhibits spontaneous pacemaking ability. A biophysically based ICC model would therefore have to describe the pacemaker mechanism. To facilitate the discussion of the models, a brief discussion on the current understanding of ICC pacemaking mechanism is provided here.

The pacemaker mechanism is an object of much debate with two prevailing hypotheses. One is the non-selective cationic conductance (NSCC) hypothesis that posits the endoplasmic reticulum, mitochondria and a partial plasma membrane space containing the NSCC, together, constitute a pacemaker unit as shown in Figure 2.11; several pacemaker units within a ICC are spontaneously active and summate to elicit spontaneous ICC slow waves [85]. Specifically, the cytosolic subspace in this pacemaker unit is where calcium handling/cycling occurs at a particular frequency. The endoplasmic reticulum releases calcium through IP3 receptor mediated channels, while the mitochondrion uptakes calcium through its uniporters at a faster rate (than calcium release from endoplasmic reticulum), thus causing a marked reduction of the subspace calcium. This then activates the calcium inhibited NSCC which leads to an influx of calcium ions that depolarizes the cellular membrane voltage. Additional auxiliary calcium regulatory mechanisms include the endoplasmic reticulum calcium ATPase that pumps cytosolic calcium into the endoplasmic reticulum, and the mitochondrion's sodium-calcium exchanger that releases calcium into the cytosolic subspace of the pacemaker unit. The pacemaker units within an ICC and between ICC,

coordinate the calcium-cycling-to-voltage activity through putative transducers in the form of ICC membrane voltage-dependent calcium channels; this enables a synchronized or entrained calcium-cycling frequency and slow wave frequency.
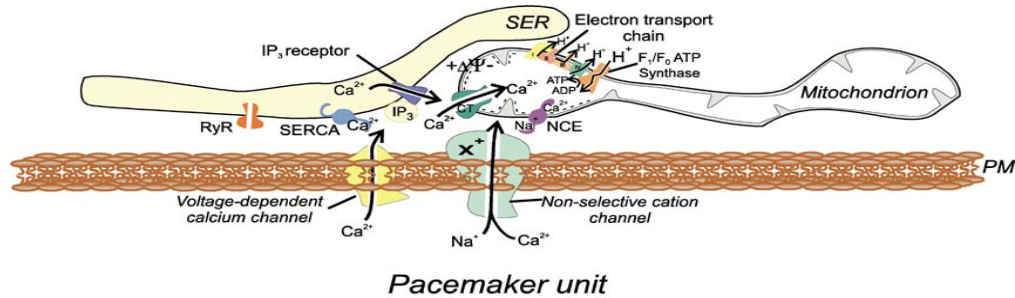
Figure 2.11. ICC pacemaker unit from the non-selective cationic channel (NSCC) pacemaking hypothesis. The pacemaker unit comprises a (sarco-)endoplasmic reticulum (SER), mitochondrion and a non-selective cationic channel. Coordinated calcium handling by the SER, the mitochondrion, and the NSCC results in spontaneous pacemaking in the ICC. The voltage-dependent calcium channels carry voltage information to regulate the frequency of calcium handling in the PU, and hence the whole cell slow wave frequency. Adapted from [85].

The other major competing hypothesis is that of a calcium-activated chloride conductance (CaCC) as the pacemaking conductance. CaCC of the GI tissue has been observed for a long time, but it was not until recently that a molecular identity for the CaCC was established to be encoded by the ANO-1 gene [86-89]. Inhibition of ANO-1 CaCC in ICC was found to inhibit slow waves in a number of studies [64, 90]. Subsequently, ANO-1 CaCC was demonstrated to be a reliable biomarker to identify GI ICC [91]. Moreover, altered expression of ANO-1 CaCC has been linked to diabetic gastroparesis [58]. These provided strong support that CaCC is indeed responsible for ICC pacemaking and is a good challenge to the NSCC hypothesis.

Aliev et al's phenomenological model

In 2000, Aliev et al proposed a simple description of an ICC-driven SMC [92]. The model described electrical activity in the intestine based on two linear ordinary differential equations derived from the works of Fitzhugh and Nagumo [93, 94]. The equations are:

$$\frac{du}{dt} = ku(u - a)(1 - u) - v, \tag{2.11}$$

$$\frac{dv}{dt} = \epsilon(\gamma(u - \beta) - v), \tag{2.12}$$

where u is the normalized transmembrane potential of the ICC or SMC, v is a recovery variable, k is rate constant, a is normalized threshold potential, ϵ is an excitability parameter, γ and β are rate constants used to shift equilibrium to achieve excitability in the SMC, and oscillatoriness in the ICC. All the dependent variables were tuned to replicate intestinal slow wave behaviour. The equations were applied to a dual cable one dimensional framework, where one cable represents a layer of coupled ICC, and the other cable represents a layer of coupled SMC. The simplicity of the descriptions allowed better computational efficiency and was used in a number of initial studies for anatomically realistic multi-dimensional models of the stomach and small intestine [95-100]. However, Aliev et al's model is phenomenological with no explicit representation of influential ionic currents (unlike the biophysically based Hodgkin-Huxley models), nor is there a physical correspondence for its parameters. This created limitations such as its inapplicability to study ion channel variants (for example, mutations) and computational instability in simulations with long period of slow wave activity.

Youm et al's intestinal ICC model

Following Aliev et al's phenomenological model that describes the ICC electrical activity, Youm et al constructed the first biophysically based single cell ICC model for the murine small intestine, published in 2006. Figure 2.12 shows the model schematic while the governing equation of the membrane voltage is given by:

$$\frac{dV_m}{dt} = -\frac{1}{C_m}(I_{CaL} + I_{AI} + I_{VDDR} + I_{KI} + I_{NaCa} + I_{PMCA} + I_{NaK}), \qquad (2.13)$$

where there are four types of ion channels that carry I_{CaL}, the L-type calcium current, I_{AI}, the inward autonomous current which supposedly carries potassium, calcium and sodium ions, I_{VDDR}, the voltage dependent dihydropyridine resistant current, and I_{KI}, which is the inward potassium current. One exchanger and two pumps that regulate ionic homeostasis in the cytosol were also included, these are I_{NaCa}, the sodium-calcium exchanger, I_{PMCA}, the plasma membrane calcium ATPase pump, and I_{NaK}, the sodium-potassium pump. Spontaneous slow wave generation is driven by I_{AI}, which is a current constructed based on murine small intestine recordings. I_{AI}, and hence the ICC slow wave are regulated by intracellular calcium which in turn is dependent on the membrane ion channels and exchangers that carry calcium ions, as well as the endoplasmic reticulum mediated calcium regulation. Experimental evidence suggested IP3-mediated release of calcium from the endoplasmic reticulum as a critical regulator of the intracellular calcium. In the model, an endoplasmic reticulum component that describes IP3-mediated

release of calcium, I_{IP3R}, a calcium leak current, I_{leak}, and a calcium uptake current, I_{up}, were included to provide for the necessary calcium regulation.

Figure 2.13 shows the slow waves predicted by Youm et al's model.
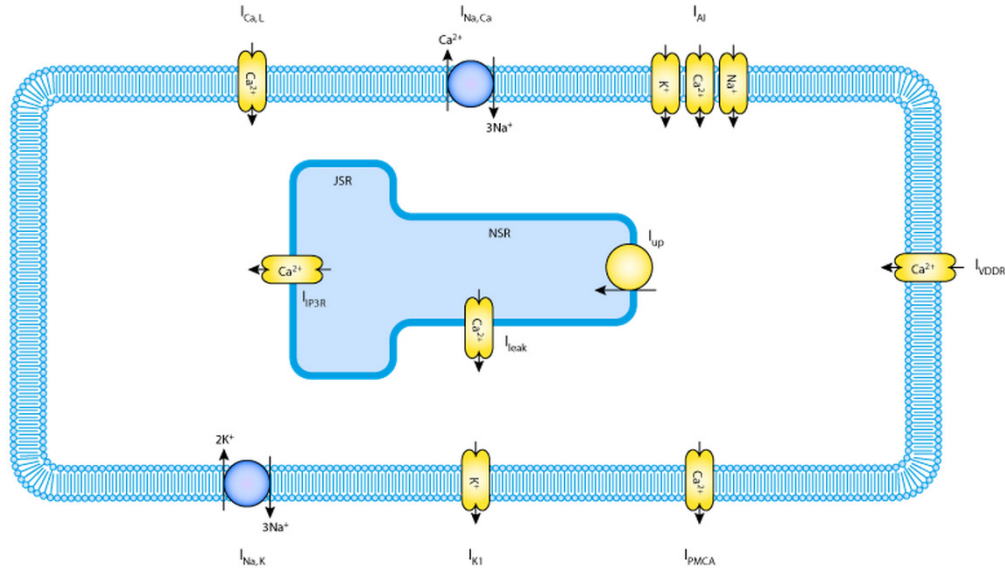
Figure 2.12. Biophysically based intestinal ICC single cell model of electrophysiology by Youm et al [101]. Adapted from CellML repository [84].

Youm et al's model was a good step forward in providing a biophysically based description of the intestinal ICC electrophysiology. The simplicity of the model reduces the computational cost of using the single cell model in higher spatial scale modelling. However, recent experimental findings limit the potential applications of this model. Firstly, studies have demonstrated that the mitochondrion is an important element in regulating intracellular calcium ions, and therefore in the generation of slow waves. Several studies have shown that in the presence of mitochondrial uncouplers, ICC failed to produce slow waves [102, 103]. Secondly, the model lacks critical ion channels that are present in the ICC, which includes the calcium activated potassium channels [104], ether-a-go-go channels [105] and sodium channels [106]. The absence

of these ion channel descriptions hinders investigation of channelopathies, for example, sodium channelopathy that was associated with intestinal disorders [14, 107]. Lastly, the model captures neither of the two prevailing hypotheses of pacemaker mechanism.
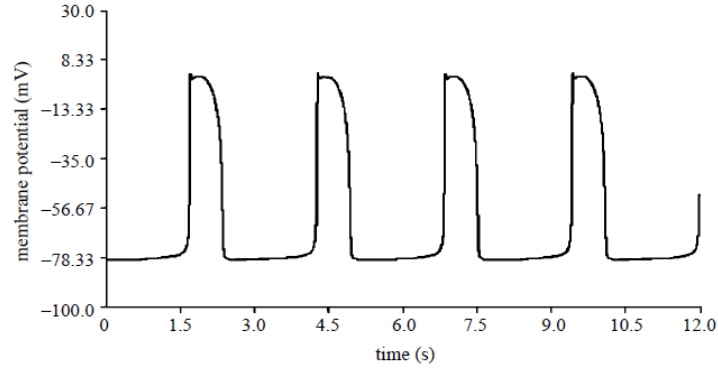
Figure 2.13. Simulated ICC slow waves from Youm et al's ICC model, with a relatively high frequency of 22.86 cpm. Adapted from [101].

Corrias and Buist's ICC-MY model

In 2008, Corrias and Buist constructed a biophysically based single cell electrophysiology model of the guinea-pig gastric ICC which is underpinned by Hodgkin-Huxley based ionic current descriptions [108]. Figure 2.14 shows a schematic of the Corrias and Buist ICC model, with the following governing equation:

$$\frac{dV_m}{dt} = -\frac{1}{C_m}(I_{CaL} + I_{VDDR} + I_{Na} + I_{ERG} + I_{Kv11} + I_{BK} +$$

$$I_{CaCl} + I_{NSCC} + I_{bK} + 2FV_{cyto}J_{Ca-ext}),$$

(2.14)

where the essential ionic currents include I_{CaL}, the L-type calcium current, I_{VDDR}, the voltage-dependent dihydropyridine-resistant calcium current, I_{Na}, the voltage-dependent sodium current, I_{ERG}, the ether-a-go-go voltage-

dependent potassium current, I_{Kv11}, the $K_v1.1$ gene encoded voltage-dependent potassium channels carrying the current, I_{BK}, the big conductance calcium-activated potassium current, I_{CaCl}, the calcium-activated chloride channels, I_{NSCC}, the non-selective cationic conductance carrying the current, I_{bK}, the background leakage potassium current, and the calcium extrusion mechanism whose calcium current is given by $2FV_{cyto}J_{Ca-ext}$, in which F is Faraday's constant, V_{cyto} is the cytoplasmic volume of the ICC, and J_{Ca-ext} is the calcium efflux (in concentration per unit time).
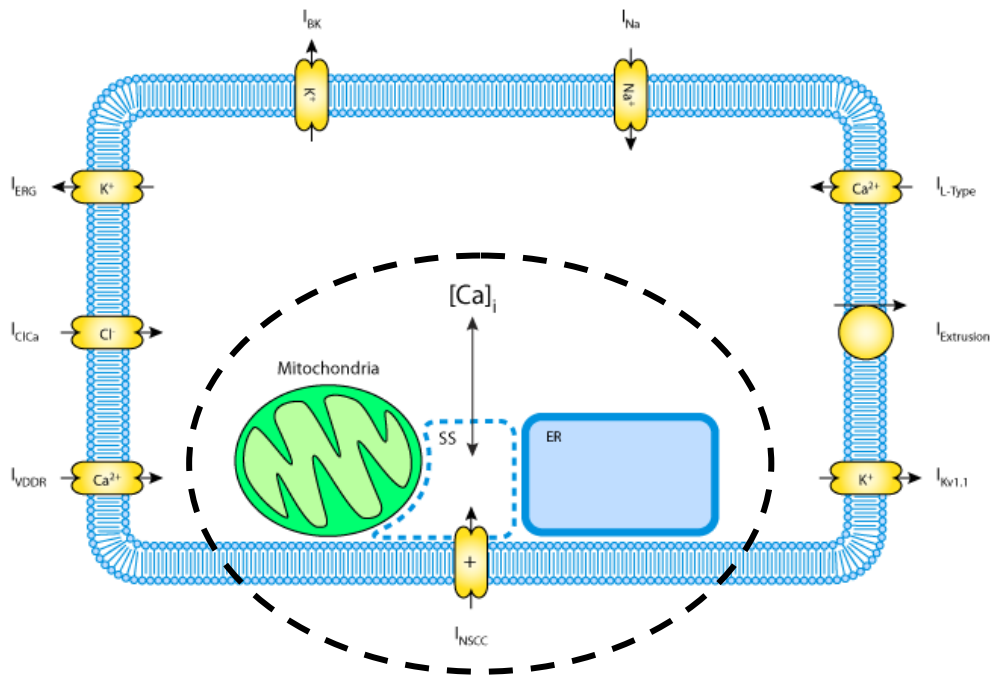
Figure 2.14. Biophysically based guinea-pig gastric ICC single cell model of electrophysiology by Corrias and Buist [108]. Adapted from CellML repository [84].

The ICC model was made self-excitatory by describing the NSCC pacemaking mechanism through the use of a sub-membrane space (SS) in the pacemaker unit that is formed by the mitochondria, endoplasmic reticulum (ER), and the

NSCC (encircled in dashed line in Figure 2.14). The governing equation for the pacemaker unit describes calcium-handling derived from Fall and Keizer [109] and assumes the following form:

$$\frac{d[Ca^{2+}]_{SS}}{dt} = -J_{UNI} + J_{NaCa} - J_{SERCA} + J_{ER} - J_{leak},\qquad(2.15)$$

where mitochondria calcium handling involves J_{UNI}, the calcium uptake by its uniporter, and J_{NaCa}, the calcium release by its sodium-calcium exchanger; ER handling involves J_{ER}, the calcium release by its IP3 receptor mediated channels, and J_{SERCA}, the calcium uptake by its calcium pump; J_{leak} represents the calcium leakage between the cytosolic space and SS.

In the pacemaker unit, the frequency of calcium-handling follows a frequency close to the typical frequency of gastric slow waves at 3 cpm which in turn drives the whole cell electrophysiology to reproduce realistic slow waves of 3 cpm. Figure 2.15 shows the simulated ICC slow waves in good agreement against experimental observation from the guinea-pig antral ICC.
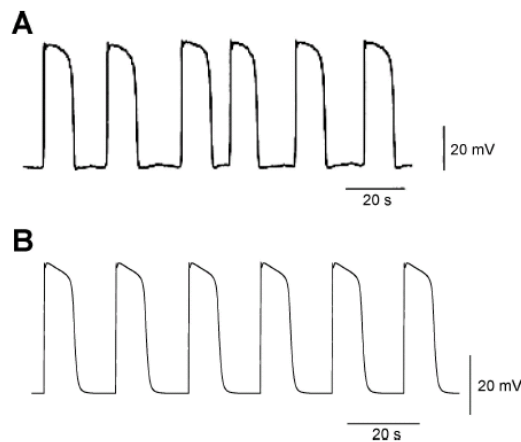
Figure 2.15. Corrias and Buist ICC slow waves. *A* shows the antral ICC from the guinea-pig stomach while *B* shows the simulated gastric ICC slow waves from the Corrias and Buist

model. A good agreement between simulation and experimental data was observed. Adapted from [108].

The ICC model was well-validated and contained the essential ionic currents and sub-cellular components to describe cellular electrophysiology, including ion channels that the Youm et al's model lacked. For instance, the inclusion of a sodium channel description in the ICC model provides for the investigation of the consequences of its mutations on cellular electrophysiology. The biophysically based model also makes it suitable for multi-cellular studies, which can overcome the limitations inherent in Aliev et al's phenomenological model.

Despite being robust and biophysically based, there is space to improve the ICC model. For instance, the constituent descriptions of ionic currents and sub-cellular mechanisms were constructed from experimental data arising from different animal species. The global behaviour of predicted ICC slow wave potentials matched the slow wave recordings from the guinea pig. In the case of calcium homeostasis, a phenomenological description was employed since experimental data was lacking. Therefore, as more findings appear in the literature, corresponding updates can be made, such as to work towards an animal or human specific model. As mentioned earlier in this section, the NSCC pacemaking hypothesis is now challenged by new evidence that suggest CaCC as the pacemaking conductance. Therefore, the ICC model could serve as a platform to develop and integrate the new CaCC pacemaking mechanism, to evaluate these two competing hypotheses, and to elucidate any additional roles that the CaCC may play in ICC electrophysiology.

Additionally, as these single cell models would be integrated into computationally demanding multi-cellular models such as a tissue block or whole organ, the computational efficiency of the constituent cellular models ought to be maximized. The original ICC model used an extensive description of intracellular calcium dynamics from Fall and Keizer's model to describe calcium handling in the pacemaker unit; this increased the computational cost significantly. Therefore, the description of this component of the ICC model could be simplified to contain only the essentials for pacemaker unit calcium handling (as has been practised, for example by Du et al [110]).

Faville et al's intestinal ICC model

Faville et al's intestinal ICC model is made up of two components, a bulk cytoplasm cell model [111] and a pacemaker unit (PU) model [112], as shown in Figure 2.16. Here, the governing equation of the ICC membrane voltage is given by:

$$\frac{dV_m}{dt} = -\frac{1}{C_m}\left(I_{Ca(T)} + I_{Ca(Ext)} + I_L + I_{K(KB)} + I_{K(v1.1)} + I_{K(ERG)} + \sum_{i=1}^{n} I_{PU} \right), \quad (2.16)$$

where $I_{Ca(T)}$ is the T-type calcium current, $I_{Ca(Ext)}$ is the calcium extrusion pump, I_L is the small leak current, $I_{K(KB)}$ is the background potassium current, $I_{K(v1.1)}$ is the voltage dependent potassium current and $I_{K(ERG)}$ is the ether-a-go-go potassium current. These ionic currents constitute the bulk cytoplasmic component of the overall ICC model. The PU component is represented by I_{PU} which refers to the sum of currents from one pacemaker

unit that contribute towards membrane potential, while n refers to the total number of pacemaker units, to be defined by the user.

A single pacemaker unit is made up of four components, i.e., the endoplasmic reticulum (ER), the mitochondrion, a "subspace 2" for ionic exchange between the ER and mitochondrion, and another "subspace 1" that is shared by the ER, mitochondrion, "subspace 2" and the plasma membrane. The PU produces unitary potentials, V_{PU}, that are shaped by the ionic currents in the PU, which is given by the following governing equation:

$$\frac{dV_{PU}}{dt} = -\frac{1}{C_m}(I_{Ca} + I_{Na} + I_{NSCC-Ca} + I_{NSCC-Na} + I_{PM} + I_{NaP}), \qquad (2.17)$$

where I_{Ca} is the calcium current, I_{Na} is the sodium current, $I_{NSCC-Ca}$ is the non-selective cationic current for calcium ions, $I_{NSCC-Na}$ is the non-selective cationic current for sodium ions, I_{PM} is the plasma membrane calcium pump and I_{NaP} is the sodium pump. These ionic currents are dependent on both membrane potential as well as the intracellular calcium in subspace 1. The intracellular calcium in subspace 1 is regulated by the interplay of mechanisms involving subspace 2, the ER and the mitochondrion. Specifically, the ER releases IP3 mediated calcium through J_{IPR} and uptakes calcium through an endoplasmic reticulum calcium ATPase pump, J_{SERCA}; while the mitochondrion releases calcium through a sodium-calcium exchanger, J_{NCX} and uptakes calcium through its uniporter, J_{MCU}. The calcium flux between

subspace 1 and subspace 2 is mediated by J_{S1S2} while the calcium flux

between subspace 2 and the bulk cytoplasm is mediated by the calcium flux,

J_{S2Cy}. The pacemaking mechanism in the PU is based on the NSCC

hypothesis (i.e., through the I_{NSCC} currents). The unitary potentials from each

of the PU contribute towards ICC membrane voltage through the term I_{PU}.

Figure 2.17 shows the predicted slow waves for ten PU (i.e., n=10), which

were found to resemble murine slow waves [111].
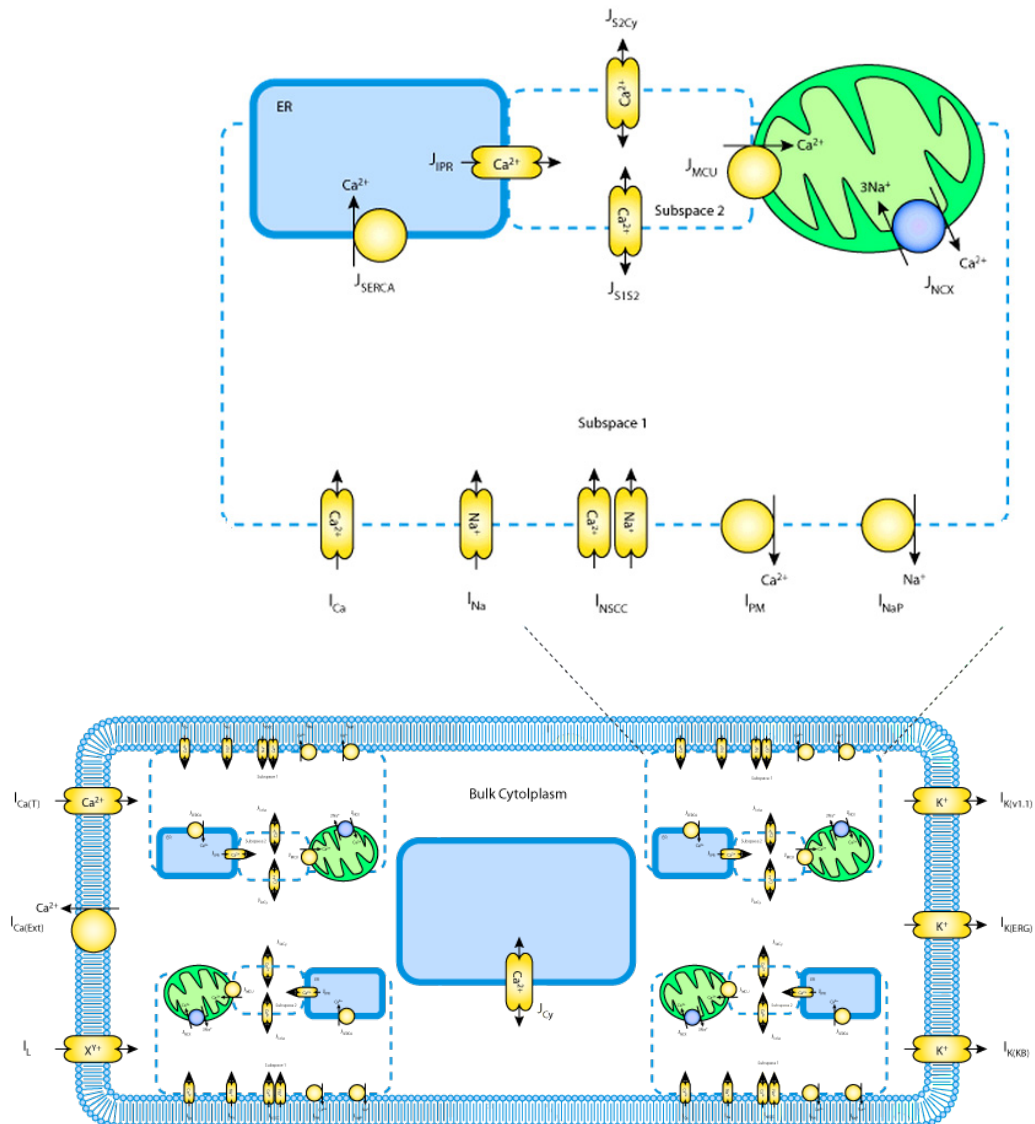
Figure 2.16. Faville et al's ICC model [111] is made up of two main components: One is the bulk cytoplasm cell model that describes ionic currents in the plasma membrane, and a

cytoplasmic calcium flux, J_{CY}. The second component, the pacemaker unit, is shown in the blow-up; each pacemaker unit contains four compartments of endoplasmic reticulum (ER), mitochondrion, subspace 1 and subspace 2. The number of pacemaker units in the ICC model is user-defined. Adapted from CellML repository [84].
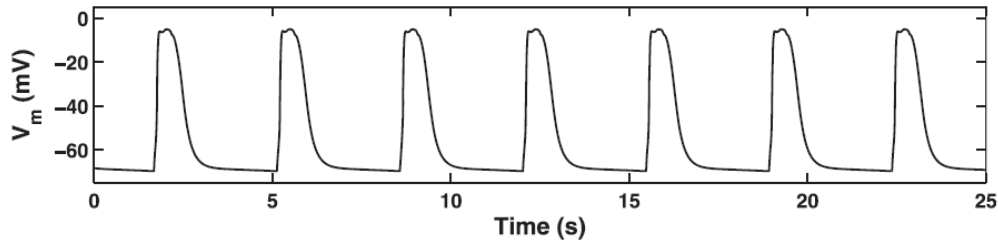
Figure 2.17. Simulated ICC slow waves, with a frequency of 17.4 cpm, from Faville et al's model where the number of PU was set to 10. Adapted from [111].

Faville et al has constructed a biophysically detailed ICC model that incorporated multiple PUs. The PUs summate to contribute towards ICC slow waves, in agreement with some literature findings [85]. However, the bulk cytoplasm component lacks essential ionic currents that are found to exist in the ICC, these are the L-type calcium channels, calcium activated chloride channels [104] and voltage activated sodium channels [106]. The pacemaking mechanism in this model uses the NSCC hypothesis, which is now challenged by the CaCC hypothesis. Lastly, given the complexity of the ICC model, a heavy computational cost is expected, relative to the Youm et al's and Corrias and Buist's ICC models.

All in all, the later single cell models are biophysically-based and constructed using the Hodgkin-Huxley parallel conductance circuit approach to describe cellular electrophysiology (Eq. 2.1). ICC models specific to the stomach and small intestine are available, but their usability relies on what actually is the pacemaker mechanism, and this merits further investigation. To the best of our knowledge, a biophysically based SMC model is available for the stomach,

but not for the small intestine. There are also no known human ICC or SMC models.

2.2.4 Multi-cellular models

Multi-cellular models refer to the modelling of electrophysiology in a state where multiple cells are effectively coupled and can span several spatial dimensions from a one-dimensional cable of connected cells to a three-dimensional whole organ.

The earliest multi-cellular models appeared in the late 1960s to the 1970s, which were models based on relaxation oscillators coupled to each other. Basically, sets of simple ordinary differential equations were developed whose solutions exhibited oscillatory behaviour that replicated the rhythmic slow waves observed in the GI musculature. These equations that described an oscillator were derived from Van der Pol's 1926 theoretical framework describing self-sustaining oscillations [113]. A number of oscillators could be coupled to represent multi-cellular electrical coupling in the GI tissue and this was practised in a number of early studies [114-116]. These early models/framework are outdated as more experimental findings appear [117], with the major limitations being their inability to accurately reproduce realistic slow waves and that their descriptions are phenomenological with smooth muscles as self-pacing.

Sperelakis and Daniel's 2004 paper modelled SMC in a two-dimensional planar framework with the aim of studying the role of gap junction communication in the activation of intestinal smooth muscle cells by the ICC

[118]. Figure 2.18 shows the layout of this planar framework, where 25 SMC were connected in a five-by-five network, with a single ICC as the pacemaker that was connected to a SMC located at position E5. It was claimed that no gap junctions were incorporated in the model. Instead, the SMC and ICC were connected by resistance junctions, with the electric fields providing the excitation that transmits through the intercellular junctional clefts. However, some discrepancies casted the reliability of the study into doubt. The ICC membrane potentials reported in the paper had breached physiological values by over 30 mV, while the use of resistive elements to connect cells was exactly the approach used to model the presence of gap junction connections in well established studies [119].
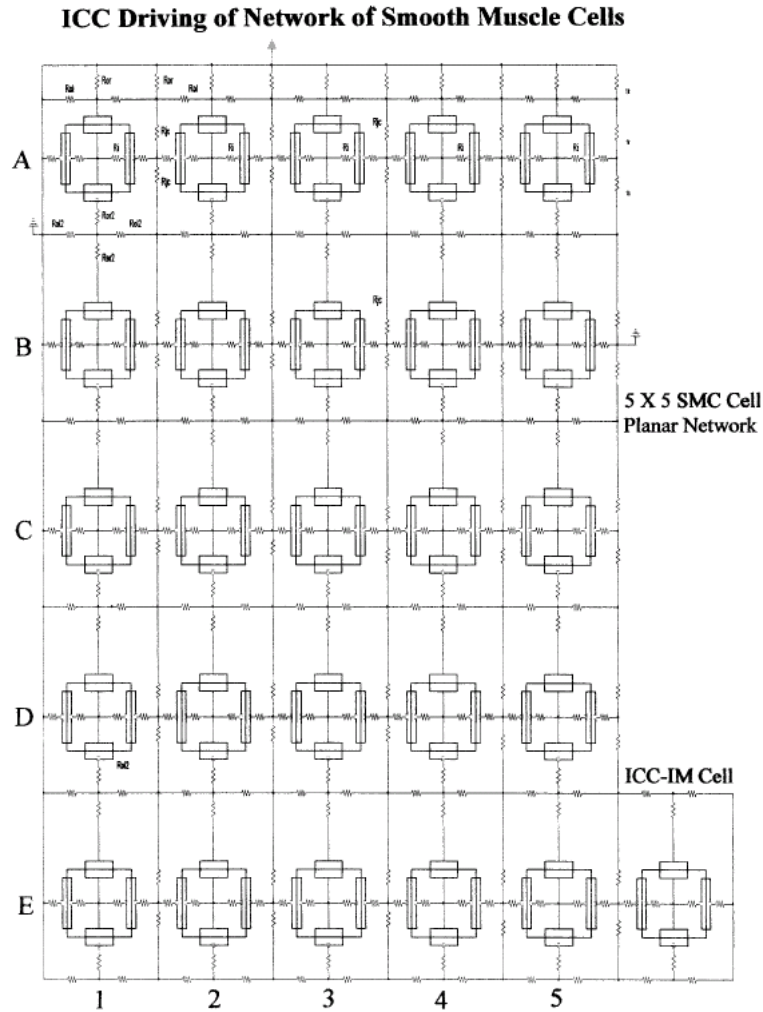
Figure 2.18. Sperelakis and Daniel's multi-cellular model. 25 SMC are arranged in a five by five network, to be excited by a single ICC that is connected to the SMC at position E5. Resistive elements are used to connect the cells, and intercellular communication is facilitated through the transmission of electric field excitation. Adapted from [118].

In a 2005 paper by Edwards and Hirst, a one dimensional transmural cable model that described the electrical propagation across the stomach wall, as shown in Figure 2.19, was presented. In it, there was an explicit representation of the longitudinal muscle, ICC-MY and the circular muscle [120]. This was achieved through three parallel conductance circuits connected in series by coupling conductances, g_{IC} and g_{IL}. This model was able to successfully reproduce slow wave behaviour from the different layers of the guinea-pig stomach, but leaned towards a phenomenological type of model since the

underlying cellular components do not describe specific ion channels necessary for electrophysiology.
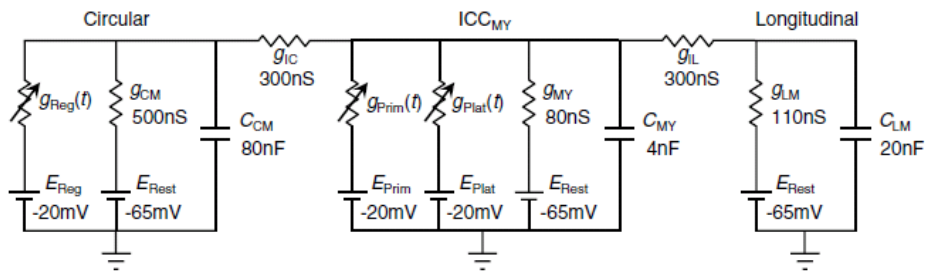
Figure 2.19. Edwards and Hirst's transmural cable model. The model represents a transmural cross-section of the stomach wall, and therefore consists of the essential components of the ICC-MY network, sandwiched by the circular muscle layer and the longitudinal muscle layer. The components are connected by two fixed conductances, while each component is made up of the phenomenological elements of resistors, capacitances and reversal potentials. Adapted from [120].

In the 2000s, a number of studies authored by researchers from the Auckland Bioengineering Institute (ABI) and the National University of Singapore (NUS) modelled multi-cellular electrical activity of the stomach and small intestine through the use of continuum based modelling [96, 98-100, 121]. Continuum modelling refers to the description of a tissue or organ structure as a continuum with spatially averaged properties, i.e., the connected or coupled SMC and ICC are reasonably represented as a syncytium. This continuum approach was widely practised in the modelling of cardiac electrical activity through the use of bidomain equations [122, 123]. Due to the unavailability of biophysically based single cell GI models during then, the multi-cellular studies by these researchers implemented Aliev et al's phenomenological cellular description [92] in the bidomain framework, and they were able to describe the electrical activity in the stomach and small intestine with good success. Figure 2.20 shows a realistic simulated human small intestine electrical activity from their work [99]. However, a number of limitations can

result since these models do not contain biophysically based cellular descriptions. For instance, the continuum models may not function properly should biophysical single cell models be integrated (in place of the Aliev et al's model) while the investigation of ion channel variants cannot be performed due to the lack of their explicit representation. The next limitation is that the traditional bidomain framework, which has historically worked well for cardiac tissue modelling, may not be ideally suited for the GI tissue. This is because the latter's musculature is complicated and can involve at least two cell types (i.e., the ICC and SMC) in the simulation studies, whereas the bidomain framework is known to work well for only one cell type as demonstrated in the cardiac simulation studies.
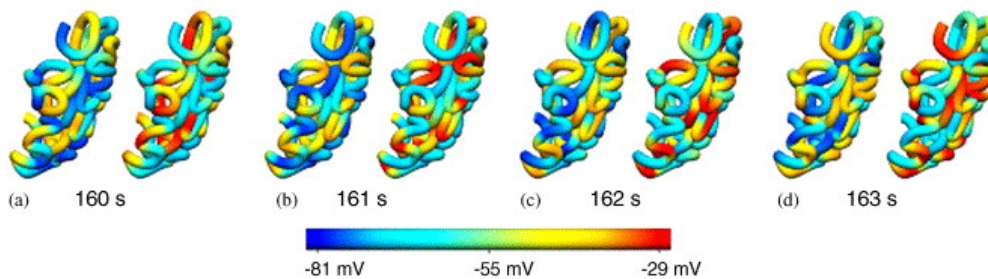
Figure 2.20. Simulated membrane potentials from the human small intestine model. Left panel of each pair of results corresponds to the SMC potentials, while the right panel corresponds to the ICC potentials. The ICC potentials are more depolarized than the SMC potentials. Also note that the potentials generally travel in the aboral direction over time. Adapted from [99].

In 2010, Du et al furthered the work by predecessors by integrating an adapted version of the Corrias and Buist ICC model into the traditional bidomain framework, to construct a two dimensional murine tissue model of ICC [110]. As mentioned earlier, a gradient of slow wave frequencies is observable in the stomach and small intestine. To create this gradient in his model, the Corrias and Buist ICC model was modified to include an additional description of a voltage-dependent and IP3-induced calcium release mechanism in the

pacemaker unit. This calcium release mechanism was based on an earlier work by Imitiaz et al [124].

In the one dimensional demonstration, seemingly stable entrainment was obtained with this new feature. Uncoupling or no entrainment was observed when the intracellular and extracellular conductivities were tuned to zero. The implementation was further extended into a two-dimensional tissue block, derived from the images of murine jejunal ICC-MY network. Figure 2.21 shows a successful implementation where simulated ICC slow waves initiated from the upper left hand corner and propagated radially until the whole tissue block was activated at about -25 mV.

However, one critical limitation of this modelling approach lies in the pacemaker unit. The entrainment mechanism was derived from Imitiaz et al [124] that described voltage mediated synthesis of IP3 in driving oscillatory calcium release from the ER. However, the mitochondrion was suggested to be a critical player in slow wave generation which was not included in the work of Imitiaz et al [102, 103]. Next, the pacemaking mechanism description of Imitiaz et al, which was adopted as an entrainment mechanism in the ICC model, operates on the premise that the membrane voltage drives the synthesis of IP3. Although this is possible, strong evidence suggests a voltage dependent dihydropyridine resistant calcium conductance as the entrainment mechanism [45]. Furthermore, the ICC pacemaking ability may actually be driven by ANO-1 CaCC [90]. Nonetheless, this work is commendable for its efforts in integrating a biophysically based ICC description into a bidomain tissue model

based on a realistic murine jejunum ICC-MY structure, as well as its application to demonstrate how ICC-MY impairment may cause dysrhythmia and dysmotility.
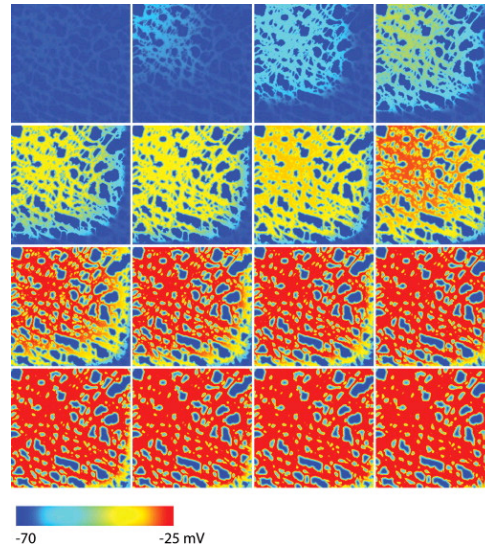
Figure 2.21. Simulated slow wave propagation in a two dimensional tissue block of murine jejunal ICC-MY network. Adapted from [110].

2.2.5 Torso models

The underlying electrical slow wave activities of the stomach and small intestine are measurable at the torso surface as an electrogram or magnetogram. Electrode based devices and magnetometers (for example, the Superconducting Quantum Interference Device, or SQUID) can record these far-field bioelectromagnetic signals non-invasively and can potentially assist clinicians in diagnosis and treatment. Examples include electrogastrography and magnetogastrography for the stomach [125, 126], electroenterography and magnetoenterography for the small intestine [127, 128]. A key issue that has prevented the reliability and widespread use of these measurement techniques/devices is the poor interpretability of the complex and noisy signals. Torso models, based on the aforementioned multi-scale models, can help in this regard. For instance, an ion channelopathy modelled at the protein channel

level, can be integrated into a multi-cellular framework through cellular descriptions, and then coupled to a torso model which could predict morphologic changes in electrography or magnetography recordings unique to that mutation.

Torso modelling to simulate the bioelectric and biomagnetic far-field signals for the stomach and the small intestine has been demonstrated by the same ABI and NUS researchers who reported the application of traditional bidomain framework to create the stomach and small intestine models [96, 98-100, 121]. The bidomain framework described in the previous section was implemented in anatomically realistic models of the stomach and small intestine derived from imaging (for example, from the visible human male project database [129]). The whole organ bidomain framework was solved, and its extracellular potentials over the organ geometry were used to create equivalent dipole sources necessary for solving the torso model equations. The torso volume, excluding the electrically active organ (i.e., the stomach or small intestine) was assumed to be a passive tissue conductor of the active organ's extracellular potentials. The torso volume potentials are described by the generalized Laplace equation:

$$\nabla \cdot (\sigma_o \nabla \varphi_o) = 0, \tag{2.18}$$

where subscript o denotes the region outside of the electrically active organ, σ_o is the tissue conductivity, and φ_o is the tissue potential. The extracellular potentials of the organ that were solved are coupled to this equation through the continuity of potentials and currents. An electric field distribution that

pervades the passive torso volume, including the torso (skin) surface potentials, or electrography, can then be computed.

To calculate the corresponding magnetic field, one of the Maxwell's quasi-static equations, in which the magnetic field is uncoupled from the electric field, is used:

$$\nabla \times \boldsymbol{B} = \mu_0 \boldsymbol{J}, \tag{2.19}$$

where $\boldsymbol{B}$ is the magnetic field, μ_0 is the permittivity of free space and $\boldsymbol{J}$ is the electric current density which is contributed by two components:

$$\boldsymbol{J} = \boldsymbol{J}^i - \sigma \nabla \varphi, \tag{2.20}$$

where $\boldsymbol{J}^i$ is the contribution from primary current sources (dipoles from the active organ) and $\sigma \nabla \varphi$ is the contribution from the secondary volume current that arises from the conductivity of the passive torso volume. This series of equations can be solved using finite element and boundary element methods [130, 131]. The resultant simulated electrical and magnetic activities, analogous to that measurable with torso surface electrodes and magnetic sensors respectively, have been validated [96, 98-100, 121]. Figure 2.22 shows an example of the simulated electrical and magnetic activities for the human stomach. The small intestine, due to its convoluted structure, presents an added challenge to torso modelling [132].
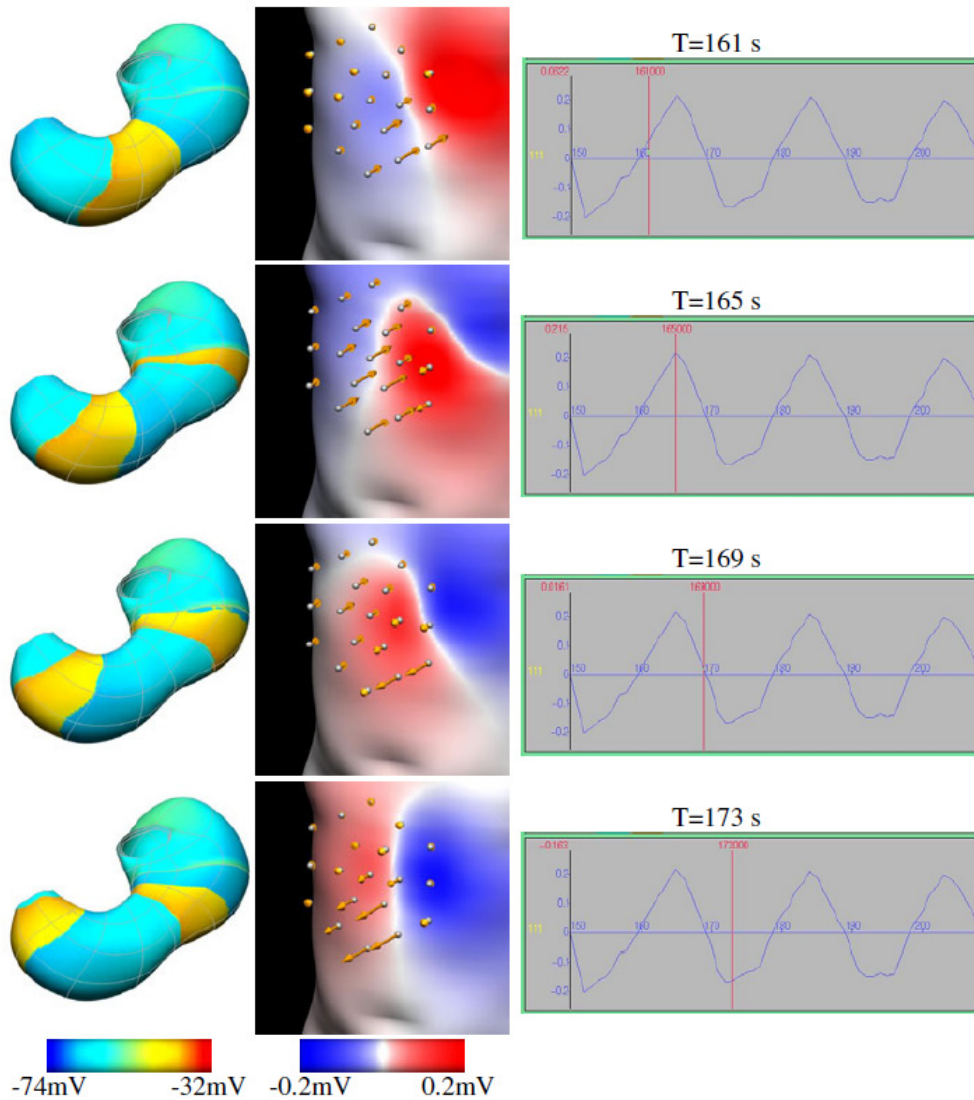
Figure 2.22. Simulated electrical and magnetic activities for a human stomach. Left panel shows slow wave propagation in the stomach. Middle panel shows the corresponding electrical potential distribution on the abdominal surface, and magnetic field gradients in arrows. Note that the skin surface potentials are much weaker than that of the stomach. Right panel shows a corresponding simulated unipolar electrode recording. Adapted from [121].

GI conditions can arise due to abnormal electrophysiological behaviour and these are difficult to diagnose without surgical intervention to obtain electrical recordings. Therefore, electrography and magnetography are appealing in their non-invasiveness. In particular, magnetography provides an added advantage of finer recordings, since the magnetic field is less attenuated by tissue volume than are the electrical signals on the skin surface [133].

This section has provided an overview on torso modelling, and several challenges are inherent in this pursuit. A good multi-scale framework from the sub-cellular to whole organ electrophysiology is critical to its development. A torso model also serves as an important part of a mature GI framework, to actualize clinical applications; for example, in the use of electrography and magnetography for diagnostic purposes.
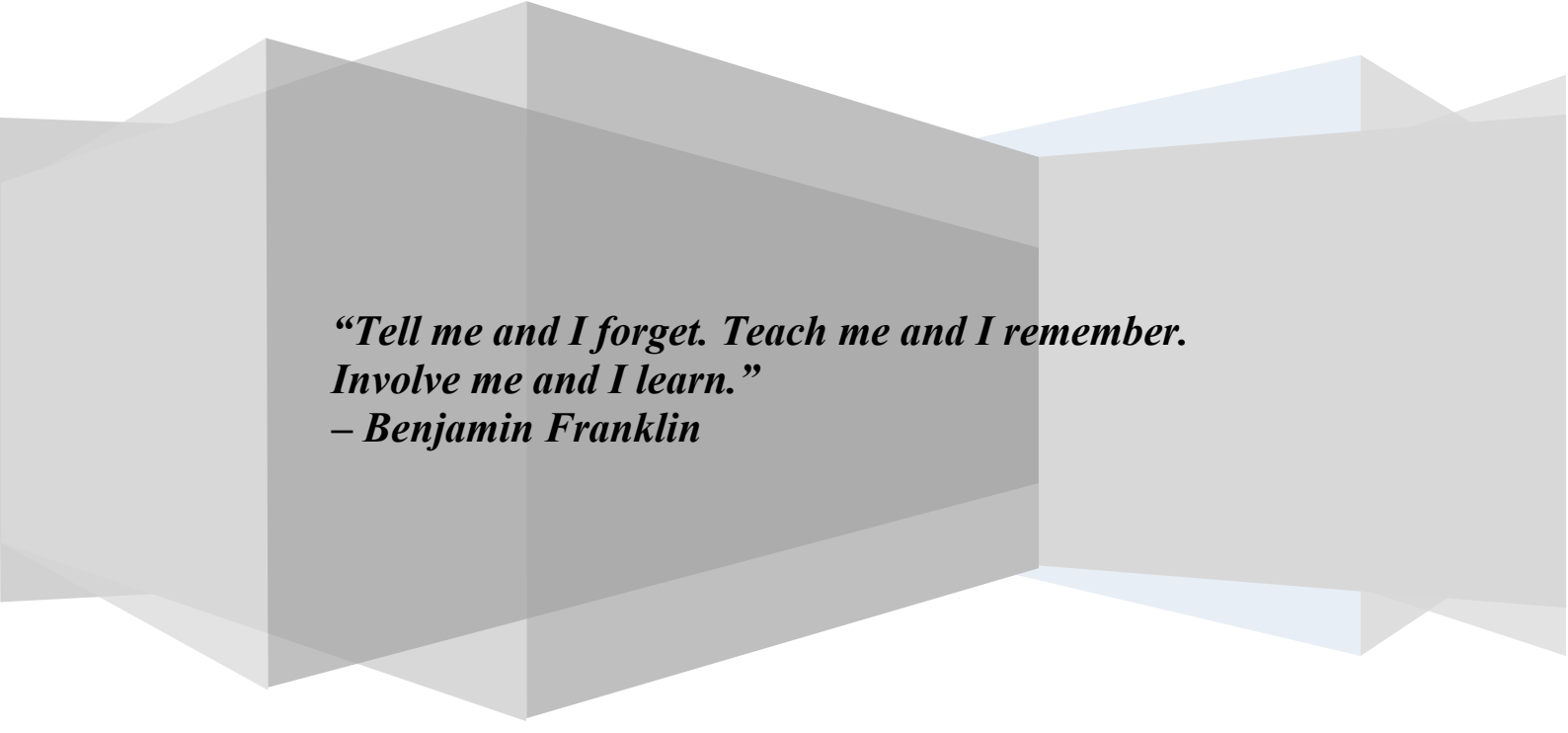
2.3   Chapter summary

The motility function of the stomach and small intestine is of interest in this thesis work. Motility in these organs is required for digestive functions such as mixing, nutrients absorption and transport of the ingested contents. The GI wall consists of the ICC-MY and SMC which are key cell types involved in motility. The ICC-MY are the electrical pacemakers that interact with the relatively passive SMC to produce coordinated motility behaviour. In the healthy stomach, electrical slow waves originate from the corpus and propagate aborally, with a dominant frequency of 3 cpm while the small intestine has its pacemaking site in the proximal duodenum during the quiescent state, with higher slow wave frequencies that range from 6 cpm to 14 cpm. The ICC-MY and SMC are excitable due to their sub-cellular mechanisms such as membrane ion channels, exchangers and pumps that regulate intracellular ionic concentrations and membrane voltage. Given the critical role of ion channels in cellular electrophysiology, its variation such as a mutation is capable of contributing to, or causing, motility disorder. Initial evidence suggests sodium channelopathy in motility disorders. However, the

genotype to phenotype link is unclear. Multiple spatial scale modelling is an important approach to bridge the gap. Suitable ion channel models describing wild-type and mutation states can be developed. The existing guinea-pig gastric ICC model and the canine gastric SMC model are suitable biophysically based models in which the ion channel models can be integrated to investigate the consequences of its mutation. No human small intestine ICC or SMC model was found in the existing literature. The single cell models, that contain the ion channel models of interest, can be examined at the multi-cellular level. The traditional bidomain framework serves as a basis to model inter-communicating cells in a tissue or organ and with which to examine electrical behaviour. The existing bidomain descriptions can be improved or extended to better describe GI electrophysiology. For instance, the two key cell types of ICC-MY and SMC as well as any slow wave frequency gradient in a GI organ can be incorporated. Torso modelling represents the highest spatial scale of modelling that future studies, beyond this thesis, can look into. To demonstrate awareness, the torso modelling approach was described. Dipoles can be computed from the solution to the bidomain equations that describe whole organ electrophysiology. A torso model then uses the dipole results to solve for the electric or magnetic field at the body surface. A channelopathy may result in a unique electrogram or magnetogram useful for diagnostics.

Chapter 3
Ion channel modelling

"Tell me and I forget. Teach me and I remember.
Involve me and I learn."
– Benjamin Franklin

3   Ion channel modelling

This chapter first describes the general methods used to model ion channel electrophysiology, followed by the application of some of these methods to model ion channels and their variants. The effects of the ion channel variants, particularly the mutations, were then investigated in existing single cell models of the gastric ICC and SMC.

3.1   Hodgkin-Huxley formalism

Hodgkin and Huxley in their Nobel prize winning work presented the first membrane excitability model of squid giant axon action potentials, with which they were able to reproduce realistic action potentials underpinned by two currents carried by voltage-dependent ion channels of sodium and potassium [74]. They used a series of voltage clamp experiments to characterize the kinetics of these voltage-dependent ion channels and devised mathematical methods to model the ion channel kinetics. A parallel conductance electrical circuit integrated with the kinetic models of ion channels was used to describe axon membrane excitability. The model was successful in accounting for the main properties of the action potentials and hence provided convincing evidence that their methods were feasible. To date, the Hodgkin-Huxley formalism remains widely-used and is considered a classical formalism.

The Hodgkin-Huxley formalism of modelling ion channels basically hypothesizes that an assembly of several independent gating particles exists in

the cellular membrane that mediate the flow of ions. Each gating particle bears

a net electronic charge which can be modulated by membrane voltage to reside

in either the open or closed state.

Figure 3.1 shows the gating particle model, where there are two states, C

refers to the closed state probability and O refers to the open state probability,

$\alpha(V_m)$ and $\beta(V_m)$ are, respectively, the closed to open rate transition variable

and the open to closed rate transition variable that are dependent on membrane

voltage, V_m. Note that C is equivalent to 1-O.

$$\alpha(V_m)$$
$$C \underset{\beta(V_m)}{\overset{}{\rightleftharpoons}} O$$
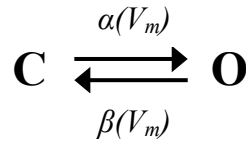
Figure 3.1. A Hodgkin-Huxley two-state gating particle model. The gating particle can either be in the open state, O, or in the closed state, C (probability of open and closed states sum up to 1). The forward and backward transitions are given by α and β respectively and are functions of membrane voltage, V_m.

The corresponding first-order kinetic equation of the gating particle is then

given by Eq. 3.1. As for the description of rate transition equations, α and β,

Hodgkin and Huxley used a variety of empirical functions that followed the

general forms shown in Eqs. 3.2 to 3.3, where A, B, and C are the parameters

whose values are determined by fitting against the appropriate experimental

data:

$$\frac{dO}{dt} = \alpha(1 - O) - \beta O, \tag{3.1}$$

$$\alpha \ or \ \beta = A exp\left(\frac{V_m - B}{C}\right), \tag{3.2}$$

$$\alpha \ or \ \beta = \frac{A}{\pm 1 + exp\left(\frac{V_m - B}{C}\right)}. \tag{3.3}$$

The analytical solution to Eq. 3.1 is given by:

$$O = \frac{\alpha}{\alpha + \beta} + Dexp\frac{-t}{\left(\frac{1}{\alpha + \beta}\right)},$$

(3.4)

where D is an arbitrary constant. In this equation, the term $\frac{1}{\alpha+\beta}$ is a time

constant which can be replaced with τ_O while the term $\frac{\alpha}{\alpha+\beta}$ is the steady-state

value of the open state which can be denoted by O_∞ since as $t\to\infty$, $O\to O_\infty$.

Also, with the initial condition of $O=O_O$ at $t=0$, D then becomes $O_O - O_\infty$

thus giving the following re-expressed equations:

$$O = O_\infty + (O_O - O_\infty)exp\frac{-t}{\tau_O},$$

(3.5)

$$\frac{dO}{dt} = \frac{O_\infty - O}{\tau_O},$$

(3.6)

$$\tau_O = \frac{1}{\alpha + \beta},$$

(3.7)

$$O_\infty = \frac{\alpha}{\alpha + \beta}.$$

(3.8)

Alternatively, the steady-state value, O_∞ can be described by a biophysical

function, i.e., the Boltzmann equation. The Boltzmann equation of statistical

mechanics describes the statistical distribution of a particle under a certain

temperature and electrical field during equilibrium. The relative probability of

a particle in state 2 over state 1 is given by:

$$\frac{P_2}{P_1} = \frac{exp\left(\frac{-u_2}{k_BT}\right)}{exp\left(\frac{-u_1}{k_BT}\right)}$$

$$= exp\left(\frac{-(u_2 - u_1)}{k_BT}\right),$$

(3.9)

where u refers to the single particle energy at a particular state, k_B is the Boltzmann constant, T is the temperature. The equation can be extended to a more chemical form of concentrations and molar energies:

LHS of Eq. 3.9:

$$\frac{P_2}{P_1} = \frac{\frac{Particles\ in\ 2}{volume * total\ particles}}{\frac{Particles\ in\ 1}{volume * total\ particles}}$$

$$= \frac{\frac{C_2}{total\ particles}}{\frac{C_1}{total\ particles}}$$

$$= \frac{[P_2]}{[P_1]}, \tag{3.10}$$

RHS of Eq. 3.9:

$$exp\left(\frac{-(u_2 - u_1)}{k_B T}\right) = exp\left(\frac{-N_A(u_2 - u_1)}{N_A k_B T}\right)$$

$$= exp\left(\frac{-(U_2 - U_1)}{N_A \frac{R}{N_A} T}\right)$$

$$= exp\left(\frac{-(U_2 - U_1)}{RT}\right); \tag{3.11}$$

equating LHS to RHS gives the following:

$$\frac{[P_2]}{[P_1]} = exp\left(\frac{-(U_2 - U_1)}{RT}\right), \tag{3.12}$$

where $[P]$ is the concentration of particle P at particular state, U is the molar energy at that state, R is the ideal gas constant and N_A is Avogadro constant.

With the above as a basis, consider the gross kinetics of the transition between channel opening and closing: $C \longleftrightarrow O$. Starting with Eq. 3.9, let state 2 be the open state, O, and state 1 be the closed state, C. The change in energies

$(u_2 - u_1)$ can be broken down into two components: (1) ω, the energy required for conformational change that is independent of membrane potential, and (2) $z_g q_e V_m$, the energy due to membrane potential (V_m), required to move the gating charges (z_g), that results in channel opening to conduct a gating current (q_e is the elementary charge). These give:

$$\frac{O}{C} = exp\left(\frac{-(\omega - z_g q_e V_m)}{k_B T}\right), \tag{3.13}$$

Eq. 3.13 is used to derive open probability at equilibrium or steady-state:

$$\frac{C}{O} + 1 = exp\left(\frac{(\omega - z_g q_e V_m)}{k_B T}\right) + 1, \tag{3.14}$$

$$\frac{O}{O + C} = \frac{1}{exp\left(\frac{(\omega - z_g q_e V_m)}{k_B T}\right) + 1}, \tag{3.15}$$

where $\frac{O}{O+C}$ is effectively the steady-state open probability, O_∞.

Simplifying Eq. 3.15 gives the following general form of:

$$O_\infty = \frac{1}{exp\left(-\frac{z_g q_e}{k_B T}\left(V_m - \frac{\omega}{z_g q_e}\right)\right) + 1}$$

$$= \frac{1}{exp\left(-\frac{\left(V_m - \frac{\omega}{z_g q_e}\right)}{\frac{k_B T}{z_g q_e}}\right) + 1}$$

$$= \frac{1}{1 + exp\left(-\frac{(V_m - V_0)}{K}\right)}, \tag{3.16}$$

which is the form of Boltzmann equation commonly used to fit against steady-state gating values, where V_0 and K are constants to be determined from experimental data.

3.1.1 Hodgkin-Huxley ionic current

An ion channel can comprise a number of independent gating variables (of the same or different type) and is permeable to ionic flow when all its gates are opened. For example, in the Hodgkin-Huxley 1952 paper, the sodium channel was modelled to contain three identical activation gating particles, m, and one inactivation gating particle, h, therefore giving the following equations to solve for the sodium current that flows through the sodium channels:

$$\frac{dm}{dt} = \beta_m(1 - m) - \alpha_m m, \tag{3.17}$$

$$\frac{dh}{dt} = \beta_h(1 - h) - \alpha_h h, \tag{3.18}$$

$$I_{Na} = G_{Na}m^3h(V_m - E_{Na}), \tag{3.19}$$

where Eqs. 3.17 and 3.18 solve for the open probability of each type of gating particle, which in turn gives the effective open probability, m^3h, of a sodium channel. This then solves for the sodium current, I_{Na}, for a given maximum sodium channel conductance, G_{Na}, and a driving force due to the difference of the membrane voltage, V_m, and the sodium Nernst potential, E_{Na}.

3.2 Thermodynamic formalism

The classical Hodgkin-Huxley approach uses empirical functions of voltage to define the rate transition equations (Eqs. 3.2 and 3.3). Biophysically based equations such as the Boltzmann equation can also be used (Eq. 3.16). This section describes another biophysical approach to define rate transition equations based on thermodynamics. To illustrate, Figure 3.2 shows two

coupled states that hypothetically correspond to two states of an ion channel

protein, where I refers to the initial state and F refers to the final state, and

their forward and backward rate transitions are denoted by $r_f(V_m)$ and $r_b(V_m)$

respectively.

$$I \underset{r_b(V_m)}{\overset{r_f(V_m)}{\rightleftharpoons}} F$$
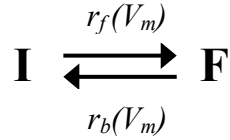
Figure 3.2. Thermodynamics to describe rate transition between two states of an ion channel. I refers to the initial state while F refers to the final state. Thermodynamically, the rate of the forward transition, $r_f(V_m)$, and backward transition, $r_b(V_m)$, depend exponentially on the free energy barrier between the two states and hence can be described by $r(V_m) = r_0 exp\left(-\frac{\Delta G(V_m)}{RT}\right)$.

According to the theory of reaction rates, a rate transition $r(V_m)$ depends

exponentially on the free energy barrier between two states [134, 135]:

$$r(V_m) = r_0 exp\left(-\frac{\Delta G(V_m)}{RT}\right), \tag{3.20}$$

$$\Delta G(V_m) = G^*(V_m) - G_0(V_m), \tag{3.21}$$

where r_0 is a constant, $\Delta G(V_m)$ is the free energy barrier dependent on

membrane voltage, V_m, R is the ideal gas constant and T is the temperature.

$\Delta G(V_m)$ is defined to be the difference between the free energy of the

activated state, $G^*(V_m)$, and the free energy of the initial state, $G_0(V_m)$. Note

that the smaller the energy barrier between two states, the faster the transition

between them.

Applying a Taylor series expansion to Eqs. 3.20 and 3.21, the following

general non-linear thermodynamic rate transition equation was achieved:

$$r(V_m) = r_0 exp\left(-\frac{\left(A^* + B^* V_m + C^* V_m^2 + \cdots\right) - \left(A_0 + B_0 V_m + C_0 V_m^2 + \cdots\right)}{RT}\right)$$

$$= r_0 exp\left(-\frac{\left(A + B V_m + C V_m^2 + \cdots\right)}{RT}\right),$$

(3.22)

where the rate transition equation is now expressed in both linear $(A + BV_m)$ and non-linear components $(CV_m^2 + \cdots)$ of free energy where A, B, C,… are parameter values to be determined from experimental data. The thermodynamic significance of the free energy components was proposed: (1) The constant linear term, A, corresponds to the free energy component independent of membrane voltage, (2) the linear term, BV_m, describes the interaction between the membrane voltage electrical field and the isolated charges and rigid dipoles of the ion channel state [136-139], (3) while the non-linear components, $CV_m^2 + \cdots$, describe the effects of electronic polarization and pressure induced by an electrical field or mechanical constraints on charge movement (due to the ion channel protein structure) [136-138]. These are true for both the initial state (subscript 0) and for the activated state (superscript *).

Through the above approach, the forward and backward rate transition equations for the pair of state transitions in Figure 3.2 can be described by:

$$r_f(V_m) = r_f^0 exp\left(-\frac{\left(a_1 + b_1 V_m + c_1 V_m^2 + \cdots\right)}{RT}\right),$$

(3.23)

$$r_b(V_m) = r_b^0 exp\left(-\frac{\left(a_2 + b_2 V_m + c_2 V_m^2 + \cdots\right)}{RT}\right),$$

(3.24)

where the superscript *0* denotes the initial state of a single transition. Note that $a_1, b_1, c_1, ...$ and $a_2, b_2, c_2, ...$ are not necessarily inter-related even though the same two states are involved in these two transitions.

Should the membrane voltage be relatively small, then the general non-linear thermodynamic rate transition equation in Eq. 3.22 can be simplified to the following general linear thermodynamic form:

$$r(V_m) = r_0 exp \left(-\frac{(a + bV_m)}{RT} \right),$$

(3.25)

in which there are three parameter values to determine per rate equation, i.e., r_0, *a* and *b*. A smaller number of parameters will give a higher computational efficiency. For further information in using thermodynamic rate transitions, the reader is referred to the work of Willms et al [140].

3.3 Multi-state Markov formalism

The Hodgkin-Huxley formalism has its limitations. For example, the Hodgkin-Huxley sodium channel model assumes that the activation and inactivation gating particles are independent, and this may conflict with experimental findings that demonstrated these processes are dependent [141-144]. The multi-state Markov formalism offers an alternative approach to describe ion channel behaviour. Markov models typically follow a topology with multiple states, where each state can correspond to a protein conformational state of the ion channel (a good review is by Sakmann and Neher [145]).

The topology of a general Markov model for an ion channel is shown in Figure 3.3. Any ion channel can exist in three main types of states, namely the closed state type (superscript C), the open state type (superscript O) and the inactivated state type (superscript I). Within each state type, an ion channel can further exist in several states as denoted by the subscripts i, j and k. Transitions can take place between states of the same type and between different state types, as indicated by the bidirectional arrows in Figure 3.3. The selection of an appropriate topology for a particular ion channel can rely on experimental observations such as ion channel protein structures, macroscopic voltage clamp recordings and microscopic single channel recordings, if available. For example, some potassium channels are known not to exhibit inactivation behaviour, and therefore the I-type cluster of inactivation states can be removed from the general topology.
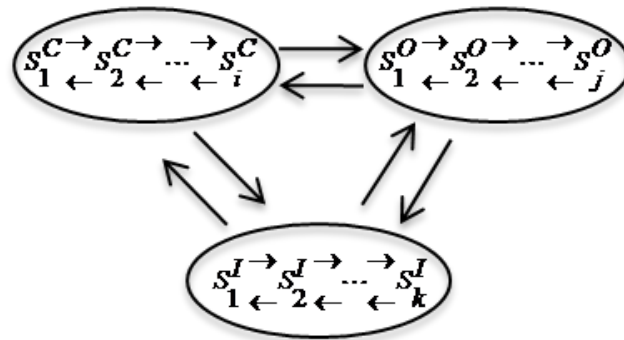
Figure 3.3. General Markov model topology. An ion channel can exist in one of the three main types of states, i.e., closed state (superscript C), open state (superscript O), and inactivation state (superscript I). For each of the three main state types, the ion channel can further exist in sub-states denoted by subscripts i, j, and k. State transitions can exist between states of each type, and between different state types (as indicated by the bidirectional arrows connecting the states).

In Markov models, it is assumed that the transition probability between states depends only on the present state and not the historical values. Each pair of transition states from a Markov model could be described by Figure 3.4 where S_i and S_f refer to the initial state and final state respectively, and each of these

states assumes a probability value at each time point, i.e., $P(S_i,t)$ and $P(S_f,t)$.

The transition probability from one state to the another is described by $P(S_i \rightarrow S_f)$ for the forward transition and $P(S_f \rightarrow S_i)$ for the backward transition.

This interpretation is extensible to all transition pairs within a Markov model, and gives rise to the following governing equation for the time derivative of any state (probability) in a Markov model:

$$\frac{dP(S_i,t)}{dt} = \sum_{f=1}^{n} P(S_f,t) P(S_f \rightarrow S_i) - \sum_{f=1}^{n} P(S_i,t) P(S_i \rightarrow S_f), \qquad (3.26)$$

where $P(S_i,t)$ is the state variable whose probability is solved for in the equation, f refer to each state that is directly coupled to the state S_i, n is the total number of states for f, the left term in the right hand side of the equation represents all transitions going into S_i, while the right term (in the right hand side of the equation) represents all transitions going away from S_i.

$$S_i \underset{P(S_f \rightarrow S_i)}{\overset{P(S_i \rightarrow S_f)}{\rightleftharpoons}} S_f$$
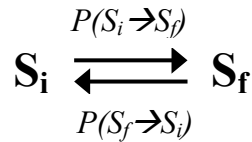
Figure 3.4. A pair of state transitions from a Markov model. S_i and S_f refer to the initial state and final state of this transition pair respectively, and each of these two states possesses a probability value at each point in time, i.e., $P(S_i,t)$ and $P(S_f,t)$. The rate of (probability) transition from one state to another is then described by $P(S_i \rightarrow S_f)$ for the forward transition and $P(S_f \rightarrow S_i)$ for the backward transition.

Eq. 3.26 describes the state probability of a single ion channel (i.e., a stochastic Markov model) due to the explicit representation of time in the state variable. Eq. 3.26 can, however, be extrapolated to the macroscopic scale which describes the state probabilities of a population of an ion channel type and predicts continuous macroscopic currents. The research in this thesis deals

with macroscopic currents, and therefore Eq. 3.26 was adjusted to the following representation:

$$\frac{dS_i}{dt} = \sum_{f=1}^{n} S_f r_{fi} - \sum_{f=1}^{n} S_i r_{if},$$ (3.27)

where S_i refers to the fraction of ion channels in state i, and S_f refers to the fraction of ion channels in state f (i.e., state probability), while r_{fi} and r_{if} refer to the rate variables (instead of transition probabilities) of the backward ($S_f \rightarrow S_i$) and forward ($S_i \rightarrow S_f$) transitions respectively. As before, these rate variables can depend on voltage and/or other factors that regulate the ion channel state transitions (for example, ligands such as acetylcholine or calcium ions). Therefore, the thermodynamic equations described earlier in section 3.2 can be utilized in a multi-state Markov model for voltage dependent transitions.

Some ion channels obey microscopic reversibility when they reach thermodynamic equilibrium. Microscopic reversibility can be implemented in Markov modelling of such ion channels [146]. Appendix 1 shows a simple illustration of how microscopic reversibility may be applied. It helps to reduce the number of parameters, depending on the nature of closed loop reactions in the model topology. Recommended methods to test if an ion channel type obeys microscopic reversibility require single channel recordings [147]. However, such experimental data was not available for the modelling work in this thesis. The Markov modelling approach discussed earlier is of a stationary nature, in which the rate transitions between states are not dependent on time. Stationary models have been successfully used to describe

macroscopic ionic currents and to study channelopathies. Recently, a non-stationary approach to create Markov models was proposed [148, 149]. This approach relies, ideally, on both macroscopic data as well as microscopic data from single channel recordings. It aims to provide a unique description of ion channel activity based on microscopic statistical properties of single channels. These non-stationary models are defined in only two states, i.e., closed and open states, without a biophysical representation of the ion channel. The approach also requires the ion channel gating to satisfy certain single channel properties.

Finally, it is generally accepted that multi-state Markov models are able to better describe ion channel kinetics. However, the tradeoff comes from the greater model complexity that leads to issues such as a greater challenge in estimating parameter values from experimental data, an increase in computational load due to more variables, and a greater difficulty in relating the multiple time constants with the experimentally derived time constants [150].

3.4   Ligand gated ion channels

Ion channels can exist in different states, the transition between states can depend on membrane voltage, as well as ligands. If an ion channel is activated by ligands such as calcium ions, the Hill equation is one way to model this behaviour. For an equilibrium reaction of an n number of ligands, L, to an ion channel or receptor, R:

$$nL + R \xleftrightarrow{} L_nR, \tag{3.28}$$

its dissociation constant, K_D, expressed in terms of concentrations is:

$$K_D = \frac{[L]^n[R]}{[L_nR]}. \tag{3.29}$$

Its Hill equation is then defined to be the fraction of ligand bound receptors, θ, as given by:

$$\theta = \frac{[L_nR]}{[R]_{total}}. \tag{3.30}$$

where $[R]_{total}$ refers to the total concentration of receptors available in the system.

Mass balance for $[R]$ gives:

$$[R]_{total} = [L_nR] + [R], \tag{3.31}$$

which is rearranged to:

$$[R] = [R]_{total} - [L_nR], \tag{3.32}$$

Eq. 3.32 is then substituted into K_D of Eq. 3.29:

$$K_D = \frac{[L]^n([R]_{total} - [L_nR])}{[L_nR]}. \tag{3.33}$$

Further rearrangement of Eq. 3.33 gives the final form of the Hill Equation:

$$\frac{[L_nR]}{[R]_{total}} = \frac{1}{\frac{K_D}{[L]^n} + 1}, \tag{3.34}$$

$$\theta = \frac{1}{\frac{K_D}{[L]^n} + 1}, \tag{3.35}$$

where n is the Hill coefficient. An n value bigger than 1 indicates positive cooperativity, i.e., binding of ligand promotes subsequent ligand binding, while a value smaller than 1 indicates negative cooperativity, i.e., binding of ligand inhibits subsequent ligand binding. In ion channel modelling parlance,

θ refers to the steady-state open probability that is dependent on the ligand concentration, $[L]$.

3.5   Gastrointestinal sodium channels

The general methods for modelling ion channels were discussed in the preceding section; here, the GI sodium channels are introduced, which will be followed by a discussion on sodium channel modelling. A voltage-gated sodium (Na) channel is a transmembrane protein that conducts sodium ions into a cell and is commonly referred to as $Na_v1.x$, where v denotes voltage sensitivity (or dependency), '1' refers to the sodium channel family, and x denotes the sub-family the sodium channel belongs to. The alpha subunit of a sodium channel is pore-forming and functional. It is made up of four repeat domains, each having six segments, with intracellular and extracellular linkers connecting the segments and domains. The distribution of amino acid residues of differing characteristics and the structure of the tertiary protein endow the alpha subunit with voltage-sensitivity and ion-selectivity. Sodium channels are also known to inactivate due to the intracellular linkers and the C-terminus domain of the alpha subunit. Endogenous auxiliary proteins such as beta subunits do interact with the sodium channel alpha subunit (forming macro-molecular complexes) and are capable of altering channel properties such as voltage sensitivity and mechanosensitivity [151, 152]. There are at least nine known members of the sodium channel alpha subunit family, and they include neuronal sodium channels whose alpha subunit is encoded by the SCN1A/SCN2A/SCN3A genes, the skeletal muscle sodium channel encoded by the SCN4A gene, and cardiac muscle sodium channel encoded by SCN5A.

In these excitable cell types, the sodium channels play a critical role, i.e., the sodium current carried by these channels are responsible for the rapid upstroke phase of the electrical action potential in these cells, as well as for refractoriness (due to channel inactivation) [153].

In the gastrointestinal tract, SCN5A encoded alpha subunit was discovered in the key motility cell types of ICC-MY [106] and the circular SMC [154, 155] from the human jejunum. The gastrointestinal SCN5A sodium channels were found to be near identical to the cardiac SCN5A sodium channels in terms of its amino acid homology [155], are voltage sensitive, tetrodotoxin resistant, and were also found to be mechanosensitive [156-159]. From the experiments on tissue samples, it was suggested that the SCN5A sodium current plays an essential role in the control of intestinal motor function through its influence on electrical slow waves such as on the resting membrane potential, rate of rise of upstroke and frequency (but not a driver of the upstroke, unlike in the cardiac cells) [106].

Cardiac SCN5A mutations are known to cause diseases such as Brugada syndrome and LQT syndrome [160, 161], while neuronal sodium channel mutations are known to cause diseases such as epilepsy [9] and pain hypersensitivity [162]. Interestingly, in a 2006 epidemiological study, patients with cardiac SCN5A mutations were correlated with GI symptoms, particularly abdominal pain [13]. The identity of the mutations, except for one loss-of-function mutation, was not revealed. The same study also showed the absence of a link with the most common potassium channelopathy (encoded

by KCNH2 and also expressed in the gastrointestinal tract). This suggested that the GI complaints were specific to SCN5A. A separate study indicated a similar result, where patients with gain-of-function cardiac SCN5A mutation (causing LQT syndrome) were also correlated with abdominal pain [163]. Even more recently, SCN5A related mutations were found in patients with intestinal motility disorders. Patients with idiopathic intestinal motility disorder had blood samples taken for molecular screening for rare and missense mutations on the SCN5A and related genes. Two rare missense mutations were identified and transfected into HEK-293 cells for voltage clamp studies, which revealed that these mutations were able to alter channel kinetics under the biological conditions of the HEK-293 cells. Specifically, a R76C mutation of the SCN5A sodium channel interacting protein, telethonin, appeared to induce a gain-of-function change in the sodium channel kinetics, and could possibly alter its mechanosensitivity. This is a novel, rare and missense mutation found in one patient with idiopathic intestinal pseudo-obstruction [14]. The other is a rare and missense G298S mutation of the SCN5A gene, found in a patient with irritable bowel syndrome [15]. This mutation was examined in HEK-293 cells in four different but common SCN5A backgrounds (unlike the R76C study) that arise from alternative splicing (Q1077/Q1077del) and a naturally occurring polymorphism (H558/H558R). The voltage-clamp findings indicate that these four backgrounds (or so-called sodium channel variants) affect sodium channel behaviour in the wild-type and mutated states. For the G298S mutation, its major influence on sodium channel appeared to be a loss-of-function effect.

Although the R76C and G298S mutations were discovered in patients with idiopathic intestinal disorders, and were found to cause a change in sodium channel behaviour in HEK-293 cells, this does not automatically mean that the mutation is responsible for the disease. The use of further experimental techniques to examine these SCN5A mutations is challenging. In terms of using cultured cells of ICC-MY and SMC, their phenotype and their phenotype maintenance might not sufficiently or consistently replicate their native counterparts to properly investigate these mutations. As for animal models, the SCN5A channels are currently found to be negligibly (or not) expressed in smaller mammals such as the mouse and guinea pig [164]. Multi-scale computational modelling is an alternative that can potentially address this genotype-phenotype gap. Suitable ion channel models describing the aforementioned sodium channel variants can be developed and then integrated into higher spatial scale models to predict and understand their consequences.

The subsequent sections of this chapter will, firstly, describe the use of the traditional Hodgkin-Huxley formalism to model wild-type and R76C affected sodium channels as studied in the aforementioned R76C study by Mazzone et al [14]. A multi-state Markov formalism was subsequently used to model the same channels for its better accuracy in representing channel kinetics. This is followed by the modelling of polymorphic-splice variants of wild-type and G298S sodium channels from the study by Saito et al [15]. The consequences of these sodium channel variants were also examined through their integration into single cell models of gastric ICC and SMC.

3.6 Modelling sodium channels using a Hodgkin-Huxley formalism

3.6.1 Experimental data

Three groups of experimental data from Mazzone et al [14], labeled according to what was transfected into the HEK-293 cell expression system, were used to develop the sodium channel models, i.e., SCN5A (with the SCN5A gene only), TCAP (with the SCN5A gene and wild-type telethonin gene, TCAP) and R76C (with the SCN5A gene and R76C TCAP gene). They comprised detailed I_{Na} versus time data over a range of clamping voltages with seven cells for each of the three groups (a sample is shown in Figure 3.5), as well as gross kinetic data such as peak current versus clamping voltage, time to peak, fast and slow inactivation time constant values. These data were processed and appropriately used to parameterize the sodium channel models.
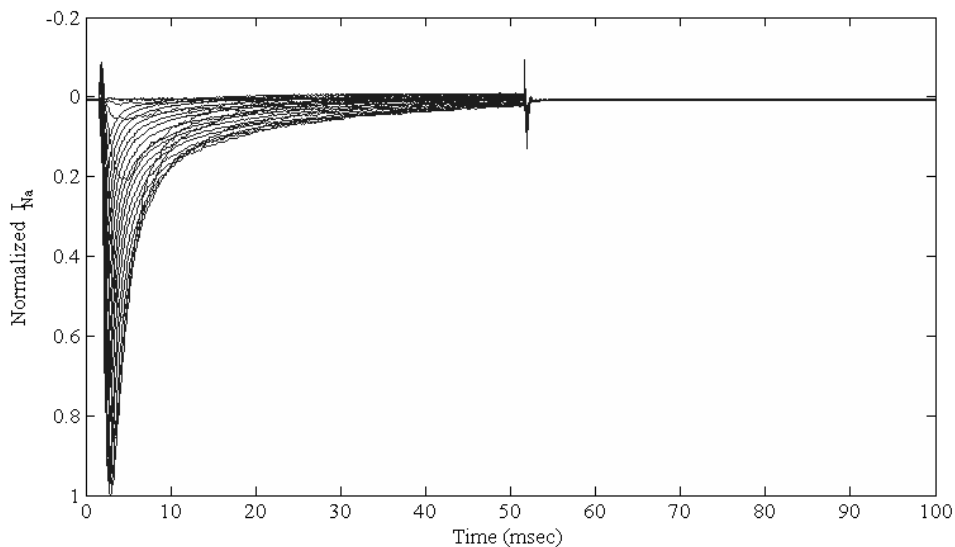
Figure 3.5. A sample of the experimental data from one of the seven cells of the SCN5A group (file number, 07119000.abf). The normalized sodium current time traces, for all 24 clamping voltages, were overlaid.

The Hodgkin-Huxley formalism was applied to construct the sodium channel model using experimental data from the R76C study by Mazzone et al [14].

The sodium channel was defined to follow the conventional configuration of three activation gates, *m*, and one inactivation gate, *h*, which gives the following form of sodium current equation, I_{Na} (see Figure 3.6 for explanation):

$$I_{Na} = G_{Na}m^3 h(V_m - E_{Na}), \tag{3.36}$$

where the remaining symbols follow their usual meaning. Key to completing the description of a sodium channel model is the mathematical descriptions that solve for *m* and *h*. Three Hodgkin-Huxley sodium channel models corresponding to the wild-type sodium channel (SCN5A model), the sodium channel under wild-type telethonin augmentation (TCAP model), and the sodium channel under R76C telethonin augmentation (R76C model) were constructed.
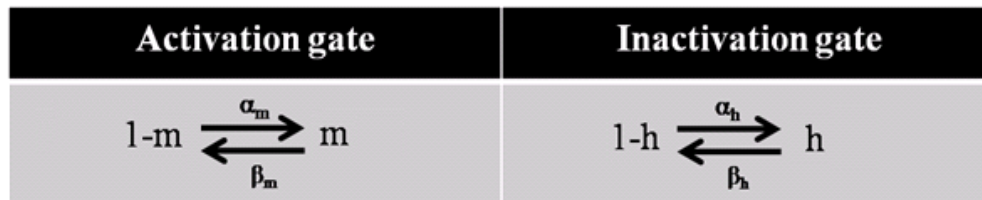
Figure 3.6. The sodium channel, here, is defined to contain two types of gates, i.e., the activation and inactivation gates. The activation gate's open probability is given by *m* and the close probability is given by *1-m*, while for the inactivation gate, the open probability is given by *h* and the close probability is given by *1-h*. α is a voltage dependent rate constant that controls the forward transition from closed to open state of a gate while *β* is the voltage dependent rate constant that controls the backward transition from open to closed state of a gate. When all gates of a channel are open, ions are able to flow through it under a potential difference driving force.

3.6.2   Voltage clamp protocol

Two voltage clamp protocols from the study of Mazzone et al [14] were used in the simulation protocol to develop the sodium channel models. One is an activation protocol designed to study the activation properties of the sodium

channels. As shown in Figure 3.7, the cell is held at a holding voltage of -100 mV before stepping to a clamping voltage for 50 ms. This is repeated with a start-to-start time of 1 s, and for a range of clamping voltages starting from -80 mV to 35 mV with an interval size of 5 mV. The inactivation protocol is more complicated, and designed to study the channels' inactivation properties. As shown in Figure 3.8, the holding voltage is -100 mV, and the clamping voltage duration is 3 s (to ensure that the channels are steadily inactivated). A voltage of -110 mV that lasts 0.1/0.2 ms is required after 3 s of voltage clamping to normalize transients, before ending off at a voltage of -40 mV. This protocol is designed to sense the extent of inactivation through the amount of activation of the inactivated sodium currents measured at the terminal voltage of -40 mV. This is repeated for a range of clamping voltages from -130 mV to -60 mV with an interval size of 5 mV and with a start-to-start time of 4 s.
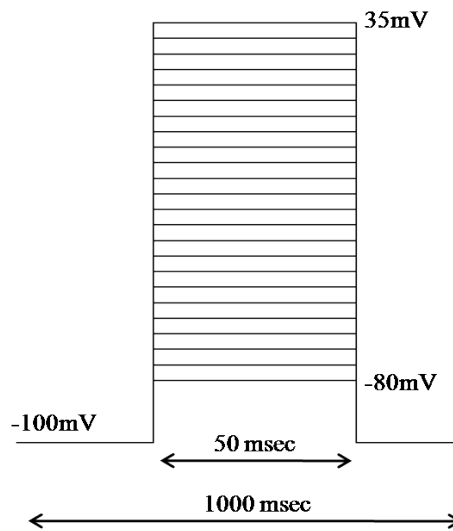
Figure 3.7. Activation voltage clamp protocol. Holding voltage is at -100 mV, clamping voltage is from -80 mV to 35 mV at step size of 5 mV. The clamping duration is 50 ms, while the start to start time is 1 s.
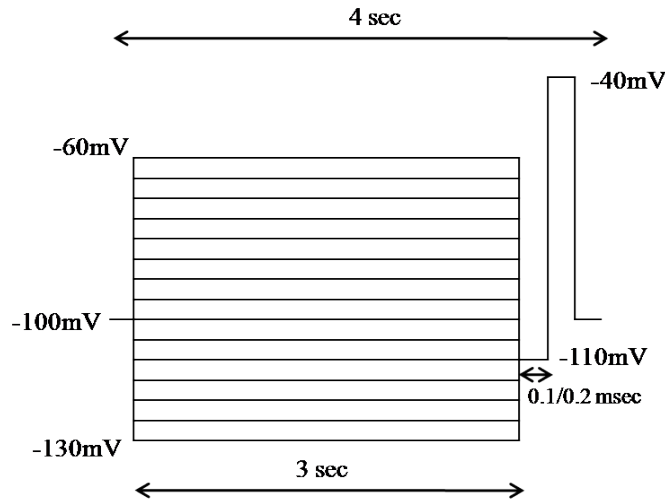
Figure 3.8. Inactivation voltage clamp protocol. Holding voltage is at -100 mV, clamping voltage is from -130 mV to -60 mV at step size of 5 mV with a clamping duration of 3 s. Subsequently, the cell is subjected to 0.1 or 0.2 ms of -110 mV voltage to normalize transients, before ending off with a voltage of 40 mV. The start to start time is 4 s.

3.6.3 Data for model parameterization

To parameterize the Hodgkin-Huxley sodium channel models (or formulations), four types of gross kinetic data are required. These are the activation gate's steady-state values, m_∞, and time constant values, τ_m; and the inactivation gate's steady- state values, h_∞, and time constant values, τ_h.

The gross kinetic data of m_∞, τ_m and τ_h were obtained by fitting an analytical solution of I_{Na} in Eq. 3.36 against the detailed experimental data of I_{Na} versus time measured under the activation protocol, while h_∞ values were derived from the peak currents measured under the inactivation protocol. Solving the differential equations of the gating variables, m and h, of the form shown in Eq. 3.6, gives the following analytical solution of I_{Na}:

$$I_{Na} = G_{Na} \left(m_\infty - (m_\infty - m_0) \, exp \left(-\frac{t}{\tau_m} \right) \right)^3 \left(h_\infty - (h_\infty - h_0) \, exp \left(-\frac{t}{\tau_h} \right) \right) (V_m - E_{Na}),$$

$$(3.37)$$

where m_0 and h_0 refer to the initial values of the m and h gates respectively, with all other symbols carrying the same meaning as before. Eq. 3.37 can be simplified by assuming that a depolarization from the holding voltage to any clamping voltage is significantly large such that m_0 is much smaller than m_∞, while h_∞ is approximately zero at sufficiently large voltages. The simplified analytical solution is therefore:

$$I_{Na} = G_{Na} m_\infty{}^3 h_0 \left(1 - exp \left(-\frac{t}{\tau_m} \right) \right)^3 exp \left(-\frac{t}{\tau_h} \right) (V_m - E_{Na}). \qquad (3.38)$$

With Eq. 3.38 as a basis, a freely available program, Stimfit [165], was used to fit for the values of m_∞, τ_m and τ_h against the I_{Na} versus time experimental data from the activation protocol. This was repeated for all three cases of SCN5A, TCAP and R76C.

The last variable of h_∞ was first examined through the chain-rule differentiation of Eq. 3.36:

$$\frac{dI_{Na}}{dt} = \frac{\partial I_{Na}}{\partial m} \frac{dm}{dt} + \frac{\partial I_{Na}}{\partial h} \frac{dh}{dt}. \qquad (3.39)$$

The gradient at peak current is zero, therefore the time derivative term of I_{Na} becomes zero at this point. Under the inactivation protocol, the sodium channels are under voltage clamp long enough for the m gates to reactivate, and become steadily open at a constant value (say m_{const}) until the peak current time point, measured at the terminal voltage of -40 mV. Therefore, it

can be assumed that $\frac{dm}{dt} = 0$. This leaves $\frac{\partial I_{Na}}{\partial h} \frac{dh}{dt} = 0$ at the peak current time point, i.e., $\frac{\partial I_{Na}}{\partial h} = 0$ or $\frac{dh}{dt} = 0$. It is known that $\frac{dh}{dt} = \frac{h_\infty - h}{\tau_h}$, and taking $\frac{dh}{dt} = 0$, one gets $h = h_\infty$ at the peak current:

$$I_{Na}^{Peak} = G_{Na} m_{const}^3 h_\infty (V_m - E_{Na}), \tag{3.40}$$

where I_{Na}^{Peak} is the peak sodium current measured at each of the clamping voltages, V_m, under the inactivation protocol. The maximal (or biggest) I_{Na}^{Peak} at voltage, V^{Max}, is then given by I_{Na}^{Max} with the assumption that $h_\infty = 1$:

$$I_{Na}^{Max} = G_{Na} m_{const}^3 1 \left(V^{Max} - E_{Na} \right). \tag{3.41}$$

The I_{Na}^{Peak} in Eq. 3.40 was normalized with I_{Na}^{Max} in Eq. 3.41 to get the equation of h_∞:

$$\frac{I_{Na}^{Peak}}{I_{Na}^{Max}} = \frac{G_{Na} m_{const}^3 h_\infty (V_m - E_{Na})}{G_{Na} m_{const}^3 1 (V^{Max} - E_{Na})}, \tag{3.42}$$

$$h_\infty = \frac{\left(\frac{I_{Na}^{Peak}}{I_{Na}^{Max}} \right)}{\left(\frac{V_m - E_{Na}}{V^{Max} - E_{Na}} \right)}. \tag{3.43}$$

The parameter values in the right hand term of Eq. 3.43 can be easily obtained from experimental data to compute the h_∞ value for each voltage, V_m. Therefore, with the above equations, one can derive m_∞, τ_m, h_∞ and τ_h values from experimental data to parameterize a Hodgkin-Huxley formulation.

3.6.4 General forms of the four formulation sets

Four sets of Hodgkin-Huxley type formulations that use the rate constants and/or the steady-state and time constant values to describe the m and h gates were identified. These four sets of formulations are described below in Tables 3.1 to 3.4. The parameter values of these formulations were subsequently fitted against experimental data, and their goodness-of-fit compared. The best set of formulation was selected to represent the m and h gates of the sodium channel model.

Table 3.1. Formulation 1. The variables are the steady-state and time constant values of the activation and inactivation gates. *A, B, C, D, E, a, b, c, d, e* are parameters whose values were fitted to experimental data.

Variables	Equations
m_∞	$\dfrac{1}{1 + exp\left(-\dfrac{(V_m - A)}{B}\right)}$
τ_m	$C + D exp(-EV_m)$
h_∞	$\dfrac{1}{\left(1 + exp\left(-\dfrac{(V_m - a)}{b}\right)\right)^2}$
τ_h	$c + d exp(-eV_m)$

Table 3.2. Formulation 2. It is identical to formulation 1, except that the parameter values of m_∞ were fitted to normalized m_∞ data.

Variables	Equations
m_∞	$\dfrac{1}{1 + exp\left(-\dfrac{(V_m - A)}{B}\right)}$
τ_m	$C + D exp(-EV_m)$
h_∞	$\dfrac{1}{\left(1 + exp\left(-\dfrac{(V_m - a)}{b}\right)\right)^2}$
τ_h	$c + d exp(-eV_m)$

Table 3.3. Formulation 3. The variables are the rate values of the forward and backward transitions of opening and closing of the activation and inactivation gates. *A, B, C, D, E, a, b, c, d* are parameters whose values were fitted to experimental data. Since the experimental data are in steady-state values and time constant values, therefore their equivalent forward and backward rate values were obtained by using Eqs. 3.7 and 3.8.

Variables	Equations
α_m	$A\,exp\left(\dfrac{V_m}{B}\right)$
β_m	$\dfrac{-C\,(V_m + D)}{exp\left(-\dfrac{V_m + D}{E}\right) - 1}$
α_h	$\dfrac{1}{exp\left(-\dfrac{V_m - a}{b}\right) + 1}$
β_h	$c\,exp\left(\dfrac{V_m}{d}\right)$

Table 3.4. Formulation 4. Here, the inactivation gating is described by the steady-state and time constant variables (following Table 3.1 or Table 3.2) while the activation gating is described by the forward-backward transition rate variables (following Table 3.3). *A, B, C, D, E, a, b, c, d, e* are parameters whose values were fitted to the appropriate experimental data.

Variables	Equations
α_m	$A\,exp\left(\dfrac{V_m}{B}\right)$
β_m	$\dfrac{-C\,(V_m + D)}{exp\left(-\dfrac{V_m + D}{E}\right) - 1}$
h_∞	$\dfrac{1}{\left(1 + exp\left(-\dfrac{(V_m - a)}{b}\right)\right)^2}$
τ_h	$c + d\,exp(-eV_m)$

3.6.5   Parameterization and selection of the formulation sets

The parameter values of each of the four sets of formulations were computed through the use of Microsoft Excel's add-on 'Solver'. Three sets of values were obtained for each of the three groups of cells, SCN5A, TCAP and R76C, as shown in Tables 3.5 to 3.8.

Table 3.5. Formulation 1 with the corresponding parameter values for each of the three cases of SCN5A, TCAP and R76C.

Equations			
m_∞	$\dfrac{1}{1 + exp\left(-\dfrac{(V_m - A)}{B}\right)}$		
τ_m	$C + Dexp(-EV_m)$		
h_∞	$\dfrac{1}{\left(1 + exp\left(-\dfrac{(V_m - a)}{b}\right)\right)^2}$		
τ_h	$c + dexp(-eV_m)$		
Parameter values			
	SCN5A	TCAP	R76C
A	59.78	62.35	63.05
B	5.406	5.414	4.972
C	0.07329	0.06113	0.06161
D	0.1048	0.06312	0.09190
E	0.02592	0.03351	0.03061
a	-86.53	-85.04	-86.5
b	-6.5	-7.2	-6.5
c	1.325	1.386	0.9329
d	0.08901	0.03494	0.03381
e	0.07587	0.08742	0.09200

Table 3.6. Formulation 2 with the corresponding parameter values for each of the three cases of SCN5A, TCAP and R76C.

Equations			
m_∞	$\dfrac{1}{1 + exp\left(-\dfrac{(V_m - A)}{B}\right)}$		
τ_m	$C + Dexp(-EV_m)$		
h_∞	$\dfrac{1}{\left(1 + exp\left(-\dfrac{(V_m - a)}{b}\right)\right)^2}$		
τ_h	$c + dexp(-eV_m)$		
Parameter values			
	SCN5A	TCAP	R76C
A	55.35	56.81	56.55
B	7.631	8.756	9.070
C	0.07329	0.06113	0.06161
D	0.1048	0.06312	0.09190
E	0.02592	0.03351	0.03061
a	-86.53	-85.04	-86.5
b	-6.5	-7.2	-6.5
c	1.325	1.386	0.9329
d	0.08901	0.03494	0.03381
e	0.07587	0.08742	0.09200

Table 3.7. Formulation 3 with the corresponding parameter values for each of the three cases of SCN5A, TCAP and R76C.

Equations			
α_m	$A\,exp\left(\dfrac{V_m}{B}\right)$		
β_m	$\dfrac{-C(V_m + D)}{exp\left(-\dfrac{V_m + D}{E}\right) - 1}$		
α_h	$\dfrac{1}{exp\left(-\dfrac{V_m - a}{b}\right) + 1}$		
β_h	$c\,exp\left(\dfrac{V_m}{d}\right)$		
Parameter values			
	SCN5A	TCAP	R76C
A	0.1422	0.1669	0.3533
B	-33.20	-35.69	-105.9
C	0.08037	0.1018	0.09514
D	66.86	67.05	63.53
E	3.321	3.316	4.554
a	-13.966	-16.432	-31.768
b	20.805	21.152	11.092
c	3.38e-11	3.65e-11	3.09e-11
d	-4.402	-4.400	-4.401

Table 3.8. Formulation 4 with the corresponding parameter values for each of the three cases of SCN5A, TCAP and R76C.

Equations			
α_m	$A\,exp\left(\dfrac{V_m}{B}\right)$		
β_m	$\dfrac{-C(V_m + D)}{exp\left(-\dfrac{V_m + D}{E}\right) - 1}$		
h_∞	$\dfrac{1}{\left(1 + exp\left(-\dfrac{(V_m - a)}{b}\right)\right)^2}$		
τ_h	$c + dexp(-eV_m)$		
Parameter values			
	SCN5A	TCAP	R76C
A	0.1422	0.1669	0.3533
B	-33.20	-35.69	-105.9
C	0.08037	0.1018	0.09514
D	66.86	67.05	63.53
E	3.321	3.316	4.554
a	-86.53	-85.04	-86.5
b	-6.5	-7.2	-6.5
c	1.325	1.386	0.9329
d	0.08901	0.03494	0.03381
e	0.07587	0.08742	0.09200

The fully defined formulations for SCN5A, TCAP and R76C, as shown in Tables 3.5 to 3.8, were then used together with the sodium current equation of Eq. 3.36 (with G_{Na} defined to be 1), to perform simulations to solve the models for normalized sodium currents under the activation and inactivation protocols (as shown in Figures 3.7 and 3.8). The results were processed according to the methods under section 3.6.3 to obtain the gross kinetic data of m_∞, h_∞, τ_m, and τ_h. The gross kinetic values derived from the predicted data was then compared against the experimental data, both graphically (see Figures 3.9 to 3.11) and quantitatively through the calculation of the mean squared error. Table 3.9 shows the mean squared error with the shaded boxes indicating the formulation that gives the least error for each metric (m_∞, h_∞, τ_m, τ_h) while the total sum of mean squared error gives the sum of all error over all three cases. Formulation 4 was deemed to be the best formulation since it provided the best fit to the most number of metrics, and gave a total sum of mean squared error that ranked second. This was followed by Formulation 2 and Formulation 1, while Formulation 3 has an error that is significantly larger than the rest. Formulation 4 was used in the subsequent work.
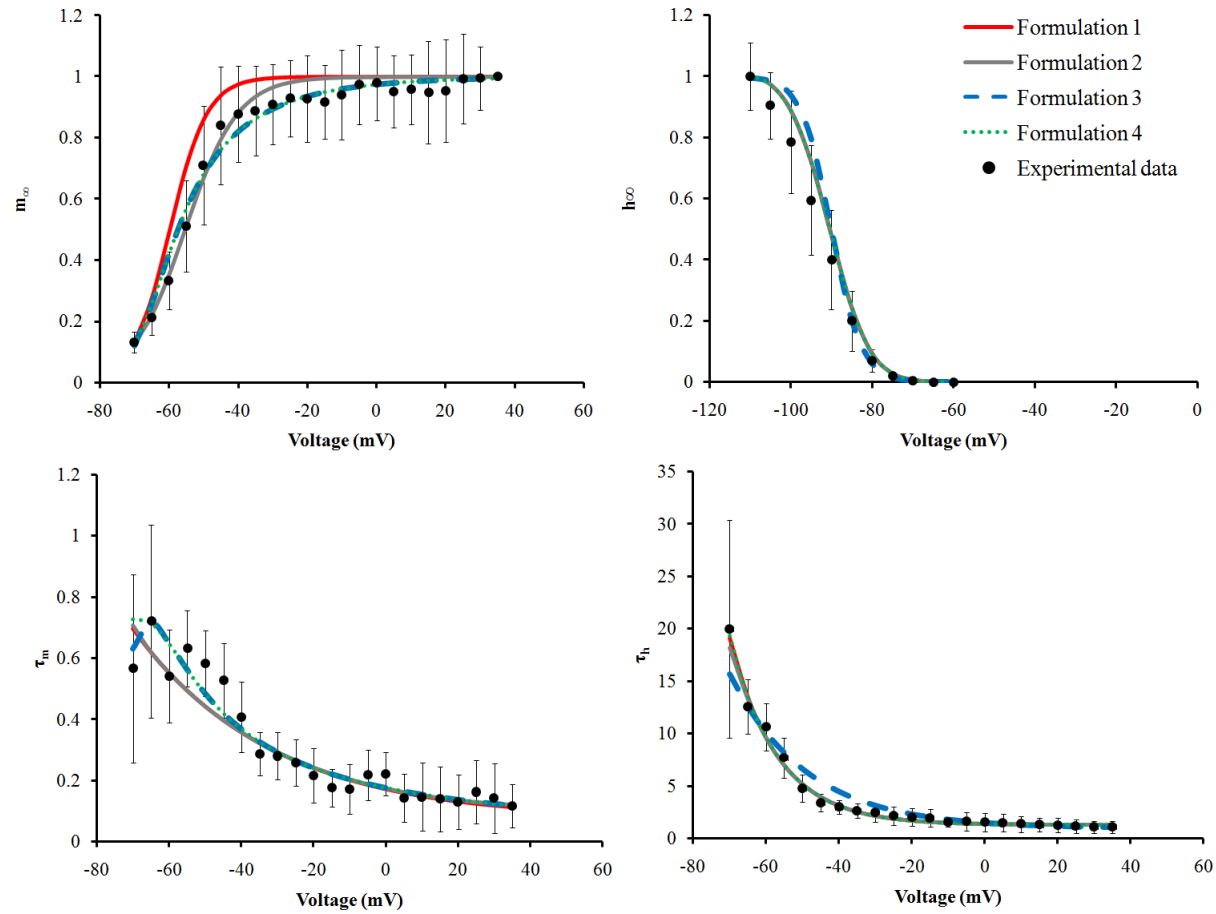
Figure 3.9. A comparison of fit between the predicted data for all four formulations against the corresponding experimental data, for the case of SCN5A. Error bars represent one standard deviation of the mean.
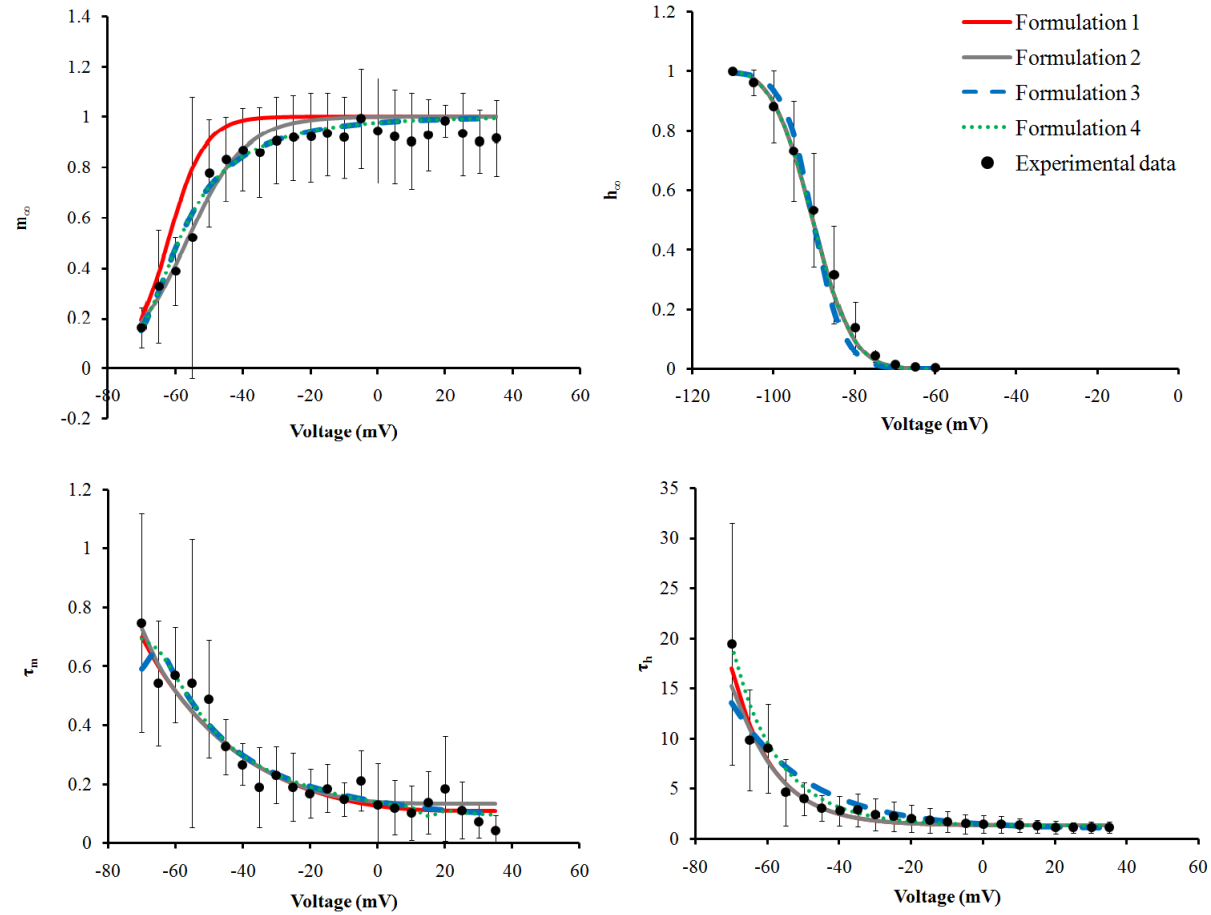
Figure 3.10. A comparison of fit between the predicted data for all four formulations against the corresponding experimental data, for the case of TCAP. Error bars represent one standard deviation of the mean.
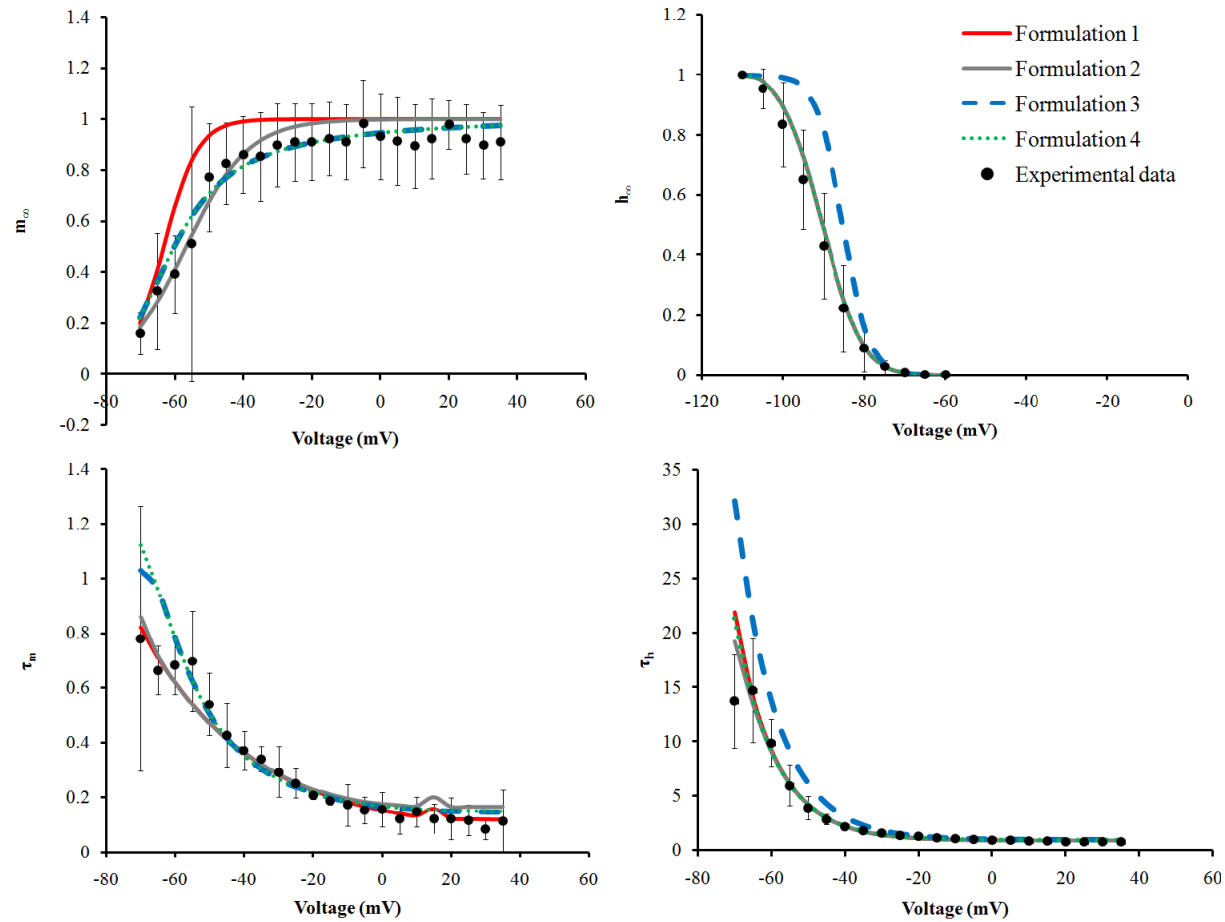
Figure 3.11. A comparison of fit between the predicted data for all four formulations against the corresponding experimental data, for the case of R76C. Error bars represent one standard deviation of the mean.

Table 3.9. Table of mean squared error when all formulations were compared against experimental data of m_∞, τ_m, h_∞ and τ_h.

		Mean Squared Error (MSE)			
		Formulation 1	Formulation 2	Formulation 3	Formulation 4
SCN5A	m_∞	0.0071215	0.0016202	0.0013657	0.0013657
	h_∞	0.0037373	0.0037588	0.0074872	0.0037293
	τ_m	0.0040450	0.0043586	0.0044878	0.0024316
	τ_h	0.19577	0.29737	1.4000	0.18332
	Sum of MSE	0.21067	0.30710	1.4133	0.19085
TCAP	m_∞	0.012193	0.0036454	0.0026760	0.0026760
	h_∞	0.000854	0.00083245	0.0028144	0.00086396
	τ_m	0.0024084	0.0024914	0.0032608	0.002328
	τ_h	0.57221	1.0677	2.3596	1.0032
	Sum of MSE	0.58767	1.0747	2.3684	1.0091
R76C	m_∞	0.016487	0.0044231	0.0027734	0.0027734
	h_∞	0.0012869	0.0013425	0.031066	0.0012994
	τ_m	0.0019381	0.0031637	0.0079992	0.010509
	τ_h	3.0921	1.5010	18.741	2.6909
	Sum of MSE	3.1118	1.5099	18.783	2.7055
Total sum of MSE		3.9101	2.8917	22.565	3.9055

To determine how Formulation 4 performs against the detailed experimental data of sodium current over time, the same voltage clamp activation protocol shown in Figure 3.7 was applied to the Hodgkin-Huxley model described by Formulation 4, for all three groups of SCN5A, TCAP and R76C. Figures 3.12 to 3.14 show the simulation results of normalized sodium current versus time plots for selected voltages from -70 mV to 30 mV, for SCN5A, TCAP and R76C respectively. A common misfit for all three groups was observed to be the inability of the Hodgkin-Huxley model in describing the inactivation of sodium current, even though the model was able to predict the peak sodium current at the right time points. Specifically, the Hodgkin-Huxley model appears to predict sodium currents that tend to inactivate faster than the experimental recordings. This discrepancy is worth attention because in

cellular electrophysiology, the extent of sodium channel inactivation affects the amount of current influx that could alter cellular membrane voltage. Therefore, the decision was made to evaluate the multi-state Markov formalism in developing models that can accurately describe sodium current, including its inactivation.
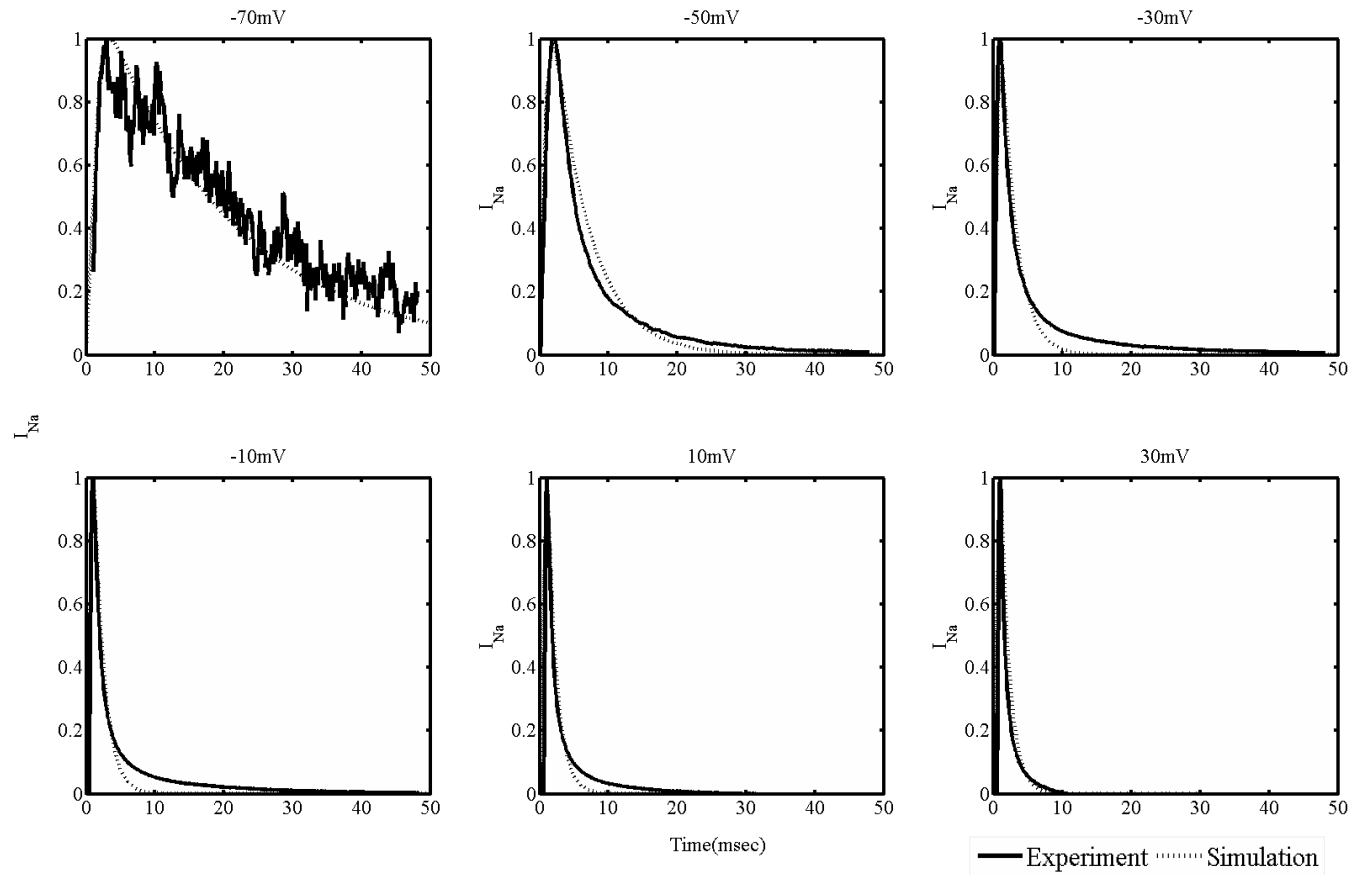
Figure 3.12. A comparison of the normalized sodium current over time between predicted data from formulation 4 and experimental data, for the SCN5A group. Each subplot corresponds to the sodium current produced under a selected clamping voltage used in the patch clamp experiments.
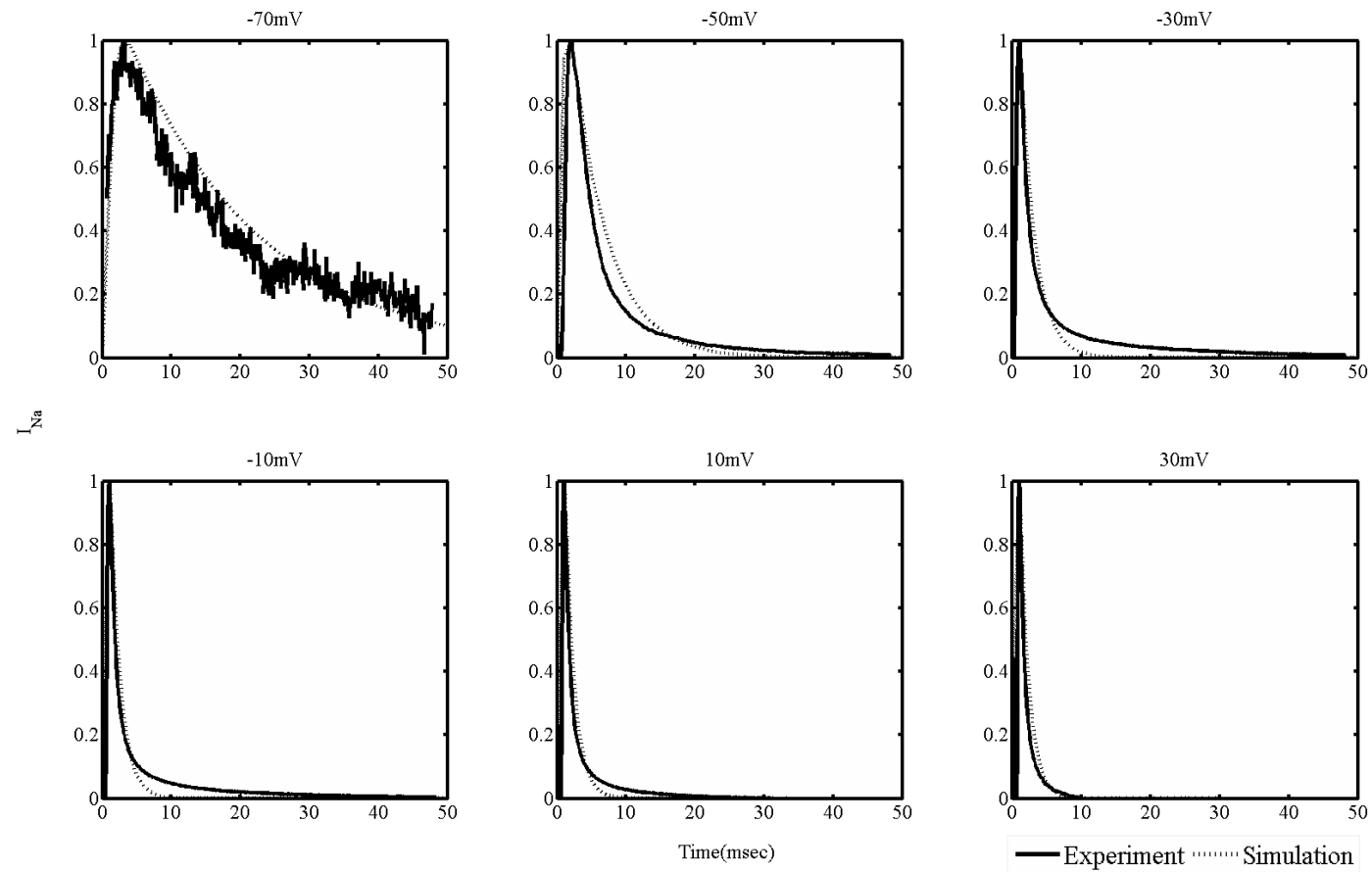
Figure 3.13. A comparison of the normalized sodium current over time between predicted data from formulation 4 and experimental data, for the TCAP group. Each subplot corresponds to the sodium current produced under a selected clamping voltage used in the patch clamp experiments.
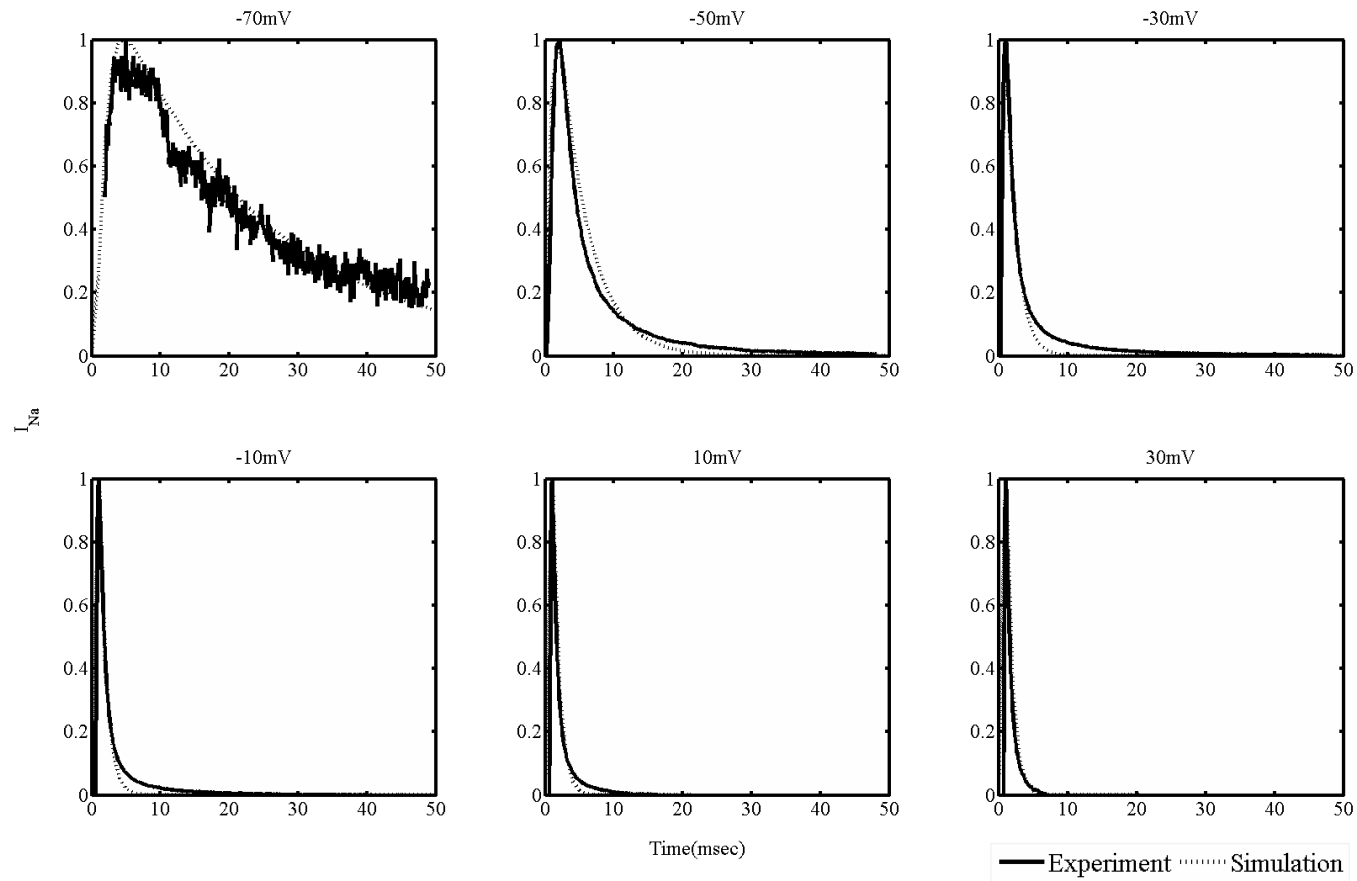
Figure 3.14. A comparison of the normalized sodium current over time between predicted data from formulation 4 and experimental data, for the R76C group. Each subplot corresponds to the sodium current produced under a selected clamping voltage used in the patch clamp experiments.

3.7 Modelling the sodium channels using the Markov formalism

3.7.1 Model topology

The Markov model topology used to create the sodium channel models is shown in Figure 3.15. This topology has been used previously to describe an existing cardiac sodium channel model and was selected since the protein structure homology is essentially identical between the cardiac and intestinal sodium channels [106, 166].
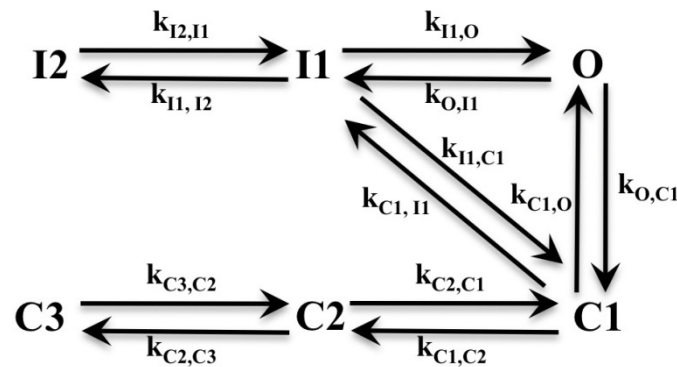
Figure 3.15. The six-state topology of the Markov sodium channel model. It consists of three closed states (*C1, C2, C3*), two inactivated states (*I1, I2*) and one open state (*O*). The transition rates, *k*, between states are voltage-dependent; their parameters are fitted to experimental data.

The model describes the sodium channel in terms of six states, three closed states (*C1, C2, C3*), two inactivated states (*I1, I2*) and one open state (*O*). These six states can correspond to the structure-function characteristics of the protein sodium channel, where the sequential activation of each of the four homologous domains parallelizes the transitions from *C3* to *C2* to *C1* to *O* states. It is known that the sodium channel exhibits two discernible types of inactivation due to the intracellular linkers and C-terminus domain, therefore these are represented by two inactivation states of *I1* and *I2*. A transition rate $k_{i,j}$, governs the transition between two states and is defined to depend on

membrane voltage, V_m. Following sections 3.2 and 3.3 that discussed the use of thermodynamic descriptions for the transition rates between states in a multi-state Markov model, a simplified linear form of Eq. 3.25, as proposed by Stevens [138] was tested:

$$k = A exp(B + CV_m),$$
(3.44)

while two nonlinear forms (with thermodynamic equations of Eq. 3.23 and 3.24 as a basis) as proposed by Destexhe and Huguenard [167] and Ozer [168] were also examined:

$$k = A exp\left(B + CV_m + DV_m^2 + EV_m^3 + \cdots\right),$$
(3.45)

$$k = A exp(B(V_m - V_C)^2) + D exp(E(V_m - V_F)^2) + \cdots,$$
(3.46)

where in the above Eqs. 3.44 to 3.46, *A, B, C, D, E, V_C* and *V_F* are unknown parameters whose values can be fitted to experimental data.

After experimenting with a number of different forms for the transition rate equations, the three parameter equation in Eq. 3.44 was selected as it was the simplest form that could adequately describe the data. As shown in Figure 3.15, there are 12 possible transitions and the resulting sodium channel model therefore would include 12 of such transition rate equations for a total of 36 unknown parameters to be determined. Following the general Markov model description, Eq. 3.27 was used to derive the system of first order differential equations that arises from Figure 3.15 and is given by:

$$\frac{dC1}{dt} = -\left(k_{C1,C2} + k_{C1,I1} + k_{C1,O}\right)C1 + k_{C2,C1}C2 + k_{I1,C1}I1 + k_{O,C1}O, \tag{3.47}$$

$$\frac{dC2}{dt} = -\left(k_{C2,C1} + k_{C2,C3}\right)C2 + k_{C1,C2}C1 + k_{C3,C2}C3, \tag{3.48}$$

$$\frac{dC3}{dt} = -k_{C3,C2}C3 + k_{C2,C3}C2, \tag{3.49}$$

$$\frac{dI1}{dt} = -\left(k_{I1,C1} + k_{I1,I2} + k_{I1,O}\right)I1 + k_{C1,I1}C1 + k_{I2,I1}I2 + k_{O,I1}O, \tag{3.50}$$

$$\frac{dI2}{dt} = -k_{I2,I1}I2 + k_{I1,I2}I1, \tag{3.51}$$

$$\frac{dO}{dt} = -\left(k_{O,C1} + k_{O,I1}\right)O + k_{C1,O}C1 + k_{I1,O}I1, \tag{3.52}$$

In a general Markov model, the sum of all open states gives the effective open probability that can be used to compute the ionic current through a population of channels. In this case, the sodium channel model has one open state, O, and its corresponding ionic current can be described by:

$$I_{Na} = G_{Na}O(V_m - E_{Na}). \tag{3.53}$$

3.7.2 Derivation of the open probability

The whole cell patch clamp experimental data from SCN5A, TCAP and R76C consists of sodium current recordings over time for each cell and for each clamping voltage. From the perspective of a sodium channel model, a current will only flow when the channel is in the open state, thus the sodium current time recordings must be reconciled with channel open probability over time, $P_O(t)$. Therefore, the whole cell sodium current is given by:

$$I_{Na}(t) = G_{Na} P_O(t)(V_m - E_{Na}). \tag{3.54}$$

$I_{Na}(t)$ can be normalized using a single value of a recorded peak sodium current, I_{Na}^{peak}, that occurs at a clamping voltage, V_m^{peak}, with an open probability, P_O^{peak}, such that $P_O^{peak}(V_m^{peak} - E_{Na})$ is at a peak value:

$$\frac{I_{Na}(t)}{I_{Na}^{peak}} = \frac{G_{Na} P_O(t)(V_m - E_{Na})}{G_{Na} P_O^{peak}(V_m^{peak} - E_{Na})}. \tag{3.55}$$

Assuming that the maximum sodium channel conductance, G_{Na}, remains unchanged, and with the rearrangement of Eq. 3.55, one can obtain from the whole cell patch clamp data:

$$P_O(t) = P_O^{peak} \frac{I_{Na}(t)}{I_{Na}^{peak}} \left(\frac{V_m^{peak} - E_{Na}}{V_m - E_{Na}} \right). \tag{3.56}$$

The advantage of this approach is that the maximum whole cell sodium conductance need not be determined as it is cancelled out. V_m^{peak} is the clamping voltage that produced the peak current corrected for series resistance. One might assume P_O^{peak} is 1.0, but this is physically impractical because it implies that all of the sodium channels in a cell are open simultaneously which is highly unlikely for a channel that exhibits inactivation. The P_O^{peak} value was estimated from experimental data by using the Hodgkin-Huxley analytical solution from Eq. 3.37:

$$I_{Na}^{peak}(t_{peak}) = G_{Na} m_\infty{}^3 h_0 \left(1 - exp\left(-\frac{t_{peak}}{\tau_m} \right) \right)^3 exp\left(-\frac{t_{peak}}{\tau_h} \right)(V_m - E_{Na}),$$

$$\tag{3.57}$$

where the recurring symbols follow their earlier meaning and t_{peak} refers to the time at which the selected I_{Na}^{peak} occurs. Eq. 3.57 is essentially the same as Eq. 3.54 when $I_{Na} = I_{Na}^{peak}$, therefore the open probability equation can be obtained:

$$P_O^{peak} = m_\infty^{\ 3} h_0 \left(1 - exp \left(-\frac{t_{peak}}{\tau_m} \right) \right)^3 exp \left(-\frac{t_{peak}}{\tau_h} \right). \tag{3.58}$$

Given the time, t_{peak}, at which I_{Na}^{peak} occurs, P_O^{peak} can be obtained. The values of m_∞, τ_m, τ_h for the selected I_{Na}^{peak} can be obtained from the kinetic data derived from Hodgkin-Huxley modelling of the sodium channel (i.e., Figures 3.9 to 3.11). Since the holding voltage of the patch clamp experiments was -100 mV, h_0 can assume the value of h_∞ at -100 mV which was earlier derived from the inactivation experimental data (also shown in Figures 3.9 to 3.11). The resulting P_O^{peak} can be inserted into Eq. 3.56 to calculate $P_O(t)$ from the experimental $I_{Na}(t)$ data.

3.7.3   Estimation of parameter values

Experimental data from Mazzone et al [14], corresponding to the three transfection groups of SCN5A, TCAP and R76C, were used to parameterize the Markov model. In each group, there were seven cells with each cell providing detailed $I_{Na}(t)$ data at 24 clamping voltages (-80 mV to 35 mV at intervals of 5 mV). After baseline corrections, the methodology described in the previous section was applied across each set of seven cells to obtain $P_O(t)$

for each clamping voltage. A simple averaging procedure was performed that yielded three sets of 24 traces of $P_O^{avg}(t)$ from which the unknown parameter values were determined.

To estimate the parameter values, the model described in Figure 3.15 was implemented in MATLAB and was subjected to the same voltage activation protocol that was used in the patch clamp experiments (see Figure 3.7). ODE15S, a MATLAB function was chosen to integrate the system of ordinary differential equations (Eqs. 3.47 to 3.52) during the fitting process [169]. Fminsearch, another MATLAB function, was used to minimize the objective function for parameterization. All of the clamping voltages were fitted simultaneously. The intention was to train the model to generalize the underlying behaviour trend of the sodium channels according to the physiological voltages that the clamping voltages cover. The objective function, F_{min}, was defined to be the sum of squared difference between the predicted open probability, $P_O^{model}(t)$, and the experimental data derived open probability, $P_O^{avg}(t)$, across all 24 traces:

$$F_{min} = \sum_{trace=1}^{24} \sum_{time} \left(P_O^{model} - P_O^{avg} \right)^2.$$

(3.59)

The quality of fit from the parameter estimation was quantified by calculating the percentage error between $P_O^{model}(t)$ and $P_O^{avg}(t)$ across all data points:

$$Percentage\ error, e = \frac{100\sqrt{\sum_{trace=1}^{24} \sum_{time} \left(P_O^{model} - P_O^{avg}\right)^2}}{\sum_{trace=1}^{24} \sum_{time} P_O^{avg}}.$$

(3.60)

A good initial guess greatly facilitated the convergence of the parameter estimation. A method to obtain the initial guess was developed based on a multi-state version of the traditional Hodgkin-Huxley gating formalism [170]. In this approach, each transition rate of the Markov model was specified as an integer multiple of the rates in a two-state gating format. The two-state rate constants can either be fitted to the patch clamp data or taken from an existing sodium channel model. Figure 3.16 illustrates the result of such an adaptation for the six-state model from Figure 3.15. To further illustrate, consider the transition of *C3→C2*, where $k_{C3,C2}$ is equivalent to $3\alpha_m^{HH}$ (here, α_m^{HH} is the opening rate of the Hodgkin-Huxley activation gate). The voltage-dependent equation of α_m^{HH} of the Hodgkin-Huxley sodium channel model as described in, for example, ten Tusscher et al [171] was used to calculate the value of $k_{C3,C2}$ for each of the 24 clamping voltages and then $k_{C3,C2} = A exp(B + C V_m)$ can be fitted to the results to obtain the initial guesses/estimates of the unknowns, *A, B* and *C*. This process was repeated to obtain good initial estimates for the remaining state transitions.
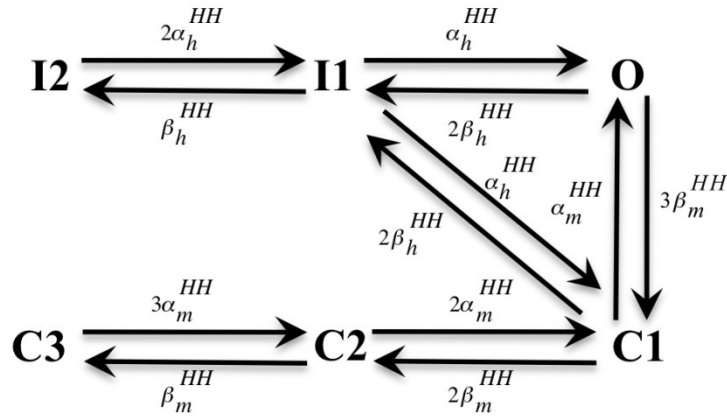
Figure 3.16. A multi-state Hodgkin-Huxley model, equivalent to the Markov sodium model in Figure 3.15 was used to obtain a good initial guess for the fitting procedure. The rate value of each transition is assigned as an integer multiple of the rate value of an activation or inactivation gate in a Hodgkin-Huxley sodium channel model.

3.7.4   Estimation of maximum sodium channel conductance

The use of expression systems such as HEK-293 cells are useful in examining channel kinetics, however they do not provide direct information on maximum whole cell sodium conductance (or ion channel density) in native cell populations such as in the human GI ICC and SMC. Furthermore, the existing literature does not explicitly contain the maximum sodium conductance in a human GI ICC or SMC. Their physiological values were therefore estimated using the SCN5A model in conjunction with published experimental data from the human jejunal ICC and SMC [106, 154]. The maximum sodium conductance, G_{Na}, for each cell type was derived such that the predicted maximum sodium current, I_{Na}^{max}, from the ICC and SMC models matched the corresponding native cell experimental data. From Strege et al [106], the mean maximal peak sodium current of -177.5 pA gave an estimated G_{Na} of 32.67 nS in the ICC and from Holm et al [154], the mean maximal peak sodium current of -142 pA gave an estimated G_{Na} of 24.17 nS.

3.7.5 Results of the fitting

The fitting procedure was applied to the experimental data from each of the transfection groups resulting in three sodium channel models. The optimized rate equation parameters for the SCN5A, TCAP and R76C models are shown below:

Table 3.10. Table of parameter values for SCN5A, TCAP and R76C models.

General rate equation	$Aexp(B + CV_m)$								
Model	SCN5A			TCAP			R76C		
State transition	A (ms^{-1})	B	C (mV^{-1})	A (ms^{-1})	B	C (mV^{-1})	A (ms^{-1})	B	C (mV^{-1})
O→I1	1.6164	0.30763	0.0060535	1.5031	0.36057	0.013723	1.7059	0.25972	0.010794
I1→I2	0.027735	0.051490	-0.046865	0.048229	0.026852	-0.00039991	0.093675	0.090650	-0.010767
C3→C2	0.00052548	-0.069102	0.0031945	4.2888e-06	0.25713	0.0098716	0.011545	-0.28925	-0.00039366
C2→C1	1.4496	-0.15660	0.058353	0.95831	0.29962	0.052254	1.0577	-0.38600	0.075900
C1→O	1.5329	0.0093193	0.041075	2.4093	-0.014853	0.039009	2.4818	0.010733	0.042291
I2→I1	0.0039239	2.6793	0.0061468	0.0011524	4.4643	0.061081	0.0021109	1.2968	0.0017296
C2→C3	0.55432	-0.099074	0.036441	0.67540	-0.078236	0.013469	0.68451	-0.17156	0.028433
C1→C2	3.1566	0.36352	0.077193	2.4647	0.61872	0.060615	2.8189	0.39519	0.072258
O→C1	2.3915	-13.335	-0.25289	2.5386	-9.4247	-0.17572	1.5057	-12.211	-0.22722
I1→C1	1.9046	-2.4840	0.020406	2.9223	-2.9928	-0.00095557	1.4574	-2.7369	0.0066217
C1→I1	0.00021688	-0.063438	0.0046683	0.00029607	-1.2366	0.0025689	0.0017829	-32.331	-0.0031479
I1→O	0.12052	-9.6028	0.083025	0.047343	-11.439	0.37114	0.41627	-10.725	0.26954

The quality of fit was quantified according to Eq. 3.60 and the errors for SCN5A, TCAP and R76C models were 0.245%, 0.108% and 0.106% respectively. As for a graphical comparison between model and experimental data, Figures 3.17 to 3.19 show the quality of fit for detailed data of normalized sodium current over time for a selected subset of clamping voltages for all three groups of SCN5A, TCAP and R76C, while the complete results can be found in Appendix 2.
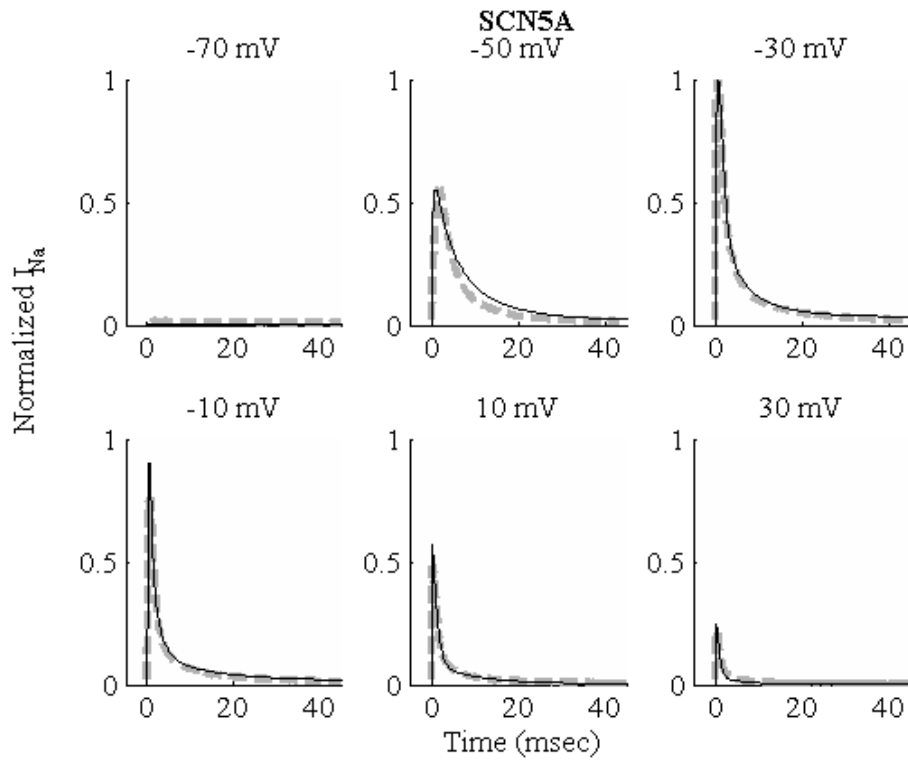
Figure 3.17. Comparison between model data and experimental data for SCN5A group. Solid line for model predicted data, dashed gray lines for average experimental data.
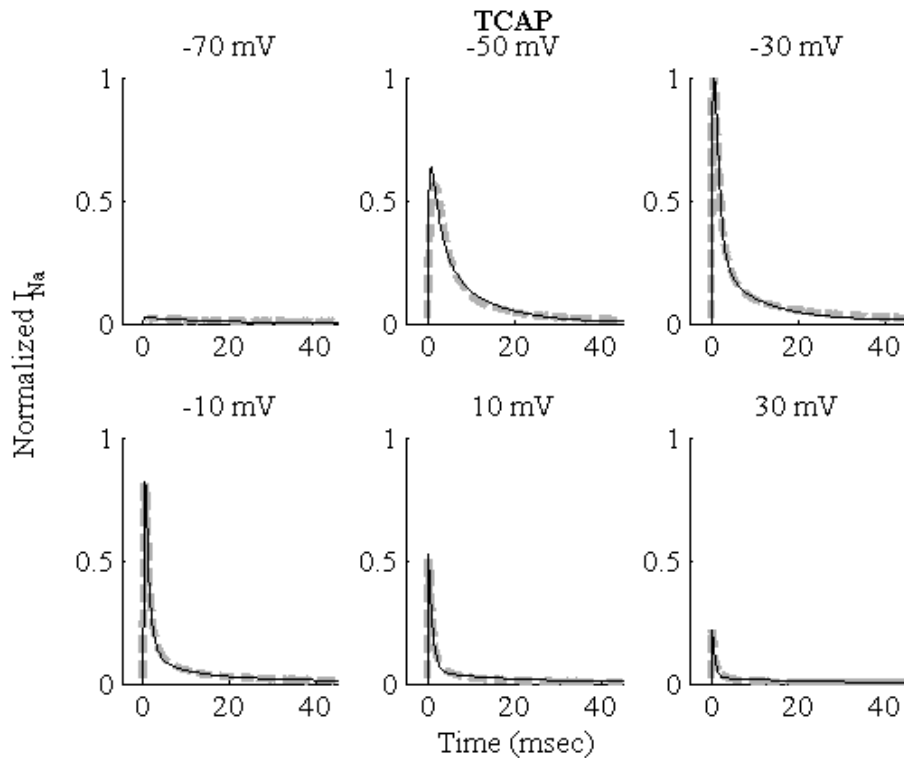
Figure 3.18. Comparison between model data and experimental data for TCAP group. Solid line for model predicted data, dashed gray lines for average experimental data.
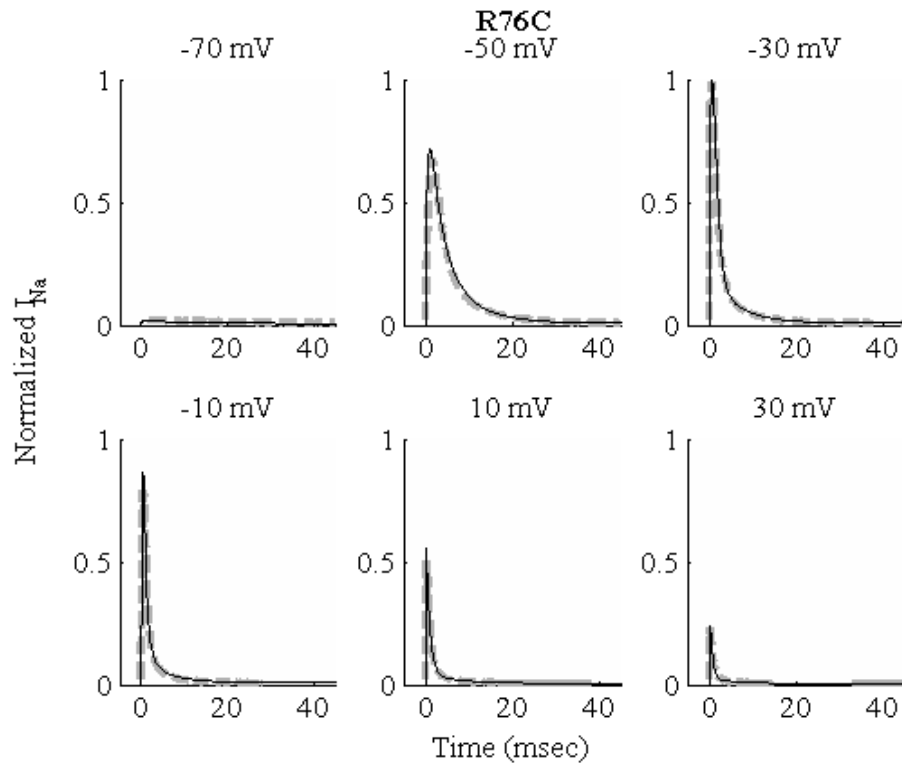
Figure 3.19. Comparison between model data and experimental data for R76C group. Solid line for model predicted data, dashed gray lines for average experimental data.

The sodium channel models were created primarily using whole cell patch clamp data from HEK-293 cells. To get an indication of the value of these models in describing native wild-type channel behaviour, each of the three models were compared against sodium currents from patch clamp recordings from native human jejunal ICC and SMC. Figure 3.20 shows that the SCN5A model has the best agreement to the experimental data for both ICC and SMC, followed by the TCAP model, and then the R76C model. Quantitatively, the differences with experimental data, calculated using Eq. 3.60, are: For the ICC, 0.130% (SCN5A), 0.134% (TCAP) and 0.174% (R76C), and for the SMC, 0.118% (SCN5A), 0.128% (TCAP) and 0.156% (R76C). Therefore, as expected, the sodium channel model without exogenous telethonin augmentation (SCN5A) best reproduces the wild-type channel behaviour in

the human ICC and SMC. Although the three models agree well with the experimental data from the HEK-293 transfection studies, some differences were noted with the native cells. One explanation could be the influence of currents from unblocked channels in the cells under patch clamp measurements.
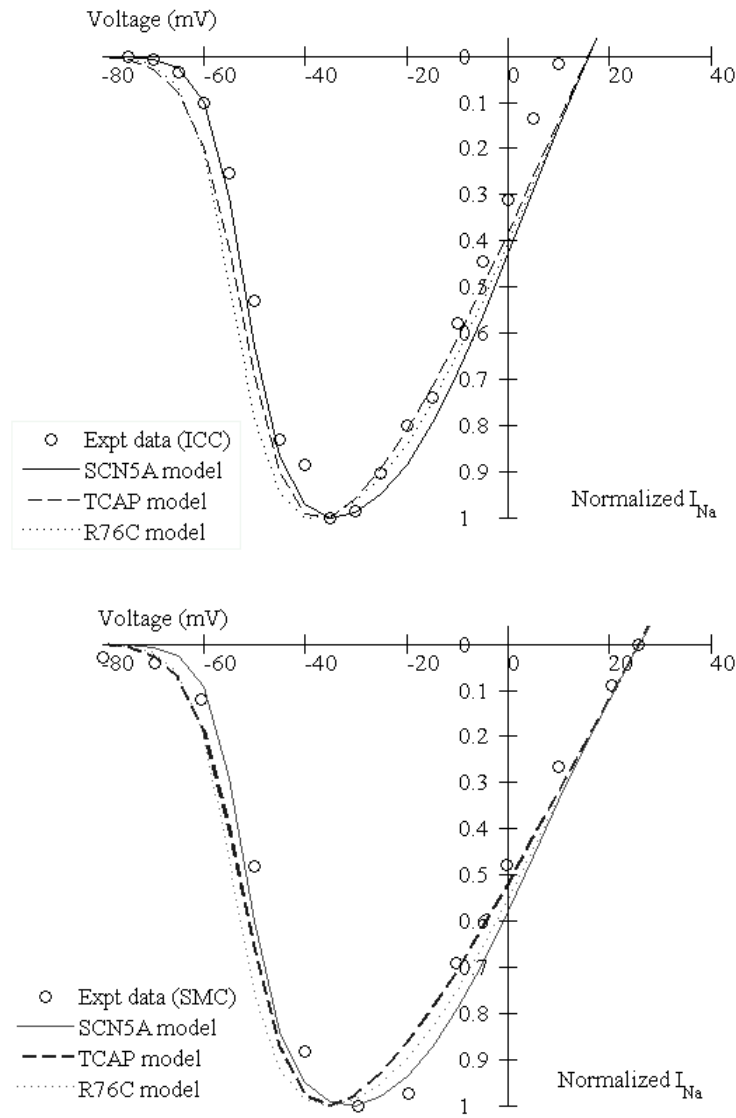
Figure 3.20. Normalized peak sodium current versus clamping voltage. Top panel compares model data against human jejunal ICC experimental data while bottom panel compares model data against human jejunal SMC experimental data.

To further validate the sodium channel models, a voltage clamp protocol resembling that of a GI single slow wave was used (see Figure 3.21). The predicted response of all three models demonstrated key qualities of a sodium current that were consistent with experimental observations, i.e., a rapid initial inactivation at the 100 ms time point followed by a late reactivation at the 200 ms time point [172].
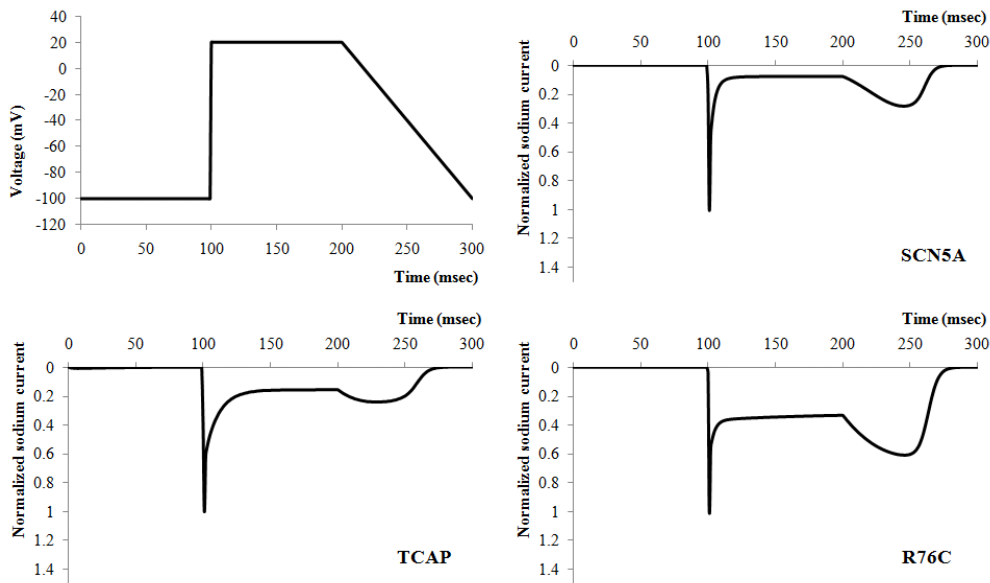
Figure 3.21. Slow wave like voltage clamp protocol results. Upper left corner shows the slow wave like voltage clamp protocol. The other figures show the response of the SCN5A, TCAP and R76C models to the voltage clamp protocol. Experimental recordings of the wild-type sodium current to the voltage clamp protocol also showed the presence of fast inactivation at the 100 ms time point, and a reactivation at the 200 ms time point [172].

3.7.6 Cellular consequences of the R76C mutation

The SCN5A and R76C models were integrated into existing models of ICC and SMC electrophysiology to evaluate the cellular consequences of the R76C mutation. Specifically, the gastric ICC model describing guinea-pig slow waves [108] and gastric SMC model describing canine slow waves [82] were chosen (as introduced in Chapter 2, Sections 2.2.2 and 2.2.3). These gastric models each contain an existing description of the sodium channel which was

constructed based on limited experimental data that was available at that time. In each cell type, the existing channel description was therefore replaced by the Markov models developed here, together with the appropriate cell type's maximum whole-cell conductance. In addition, in integrating the sodium channel models (here, or later) to the single cell models (and other higher scale models in this thesis work) which are at a standard body temperature of 37°C, a temperature coefficient, Q10, with a value of 2.45 was applied for the sodium channel models [82, 108].

HEK-293 cells express native TCAP, therefore the SCN5A model actually describes sodium channel behaviour in the presence of endogenous TCAP. Patch clamp simulation results indicated that the SCN5A model presented similar kinetics to TCAP, agreeing with observations made in Mazzone et al's experimental study [14] (i.e., steady-state values, time to peak values in Figure 4 and the fast and slow inactivation time constants in Figure 5 of [14]). Given that the SCN5A model matched better with human jejunal data than TCAP (see Figure 3.20), the SCN5A and R76C models were used in each cell type to perform simulations of 300 s of electrical activity. Figure 3.22 shows the simulation results of the membrane potentials; the upper panel shows that the R76C mutation has caused a slight increase in plateau phase duration of the ICC membrane potential by about 750 ms while the lower panel shows the R76C mutation has caused a slight depolarization of the resting phase potential in the SMC by about 0.940 mV. Near identical simulation results were obtained when R76C is compared against TCAP, instead of SCN5A in the ICC and SMC models. Figure 3.23 shows the corresponding sodium

current behaviour where the presence of mutation resulted in a greater influx of sodium currents in both the ICC and SMC. These results indicate that although the sodium channels are not the initiator of slow waves as they are in other cells, the presence of the R76C mutation is sufficient to cause notable changes in cellular electrophysiology.
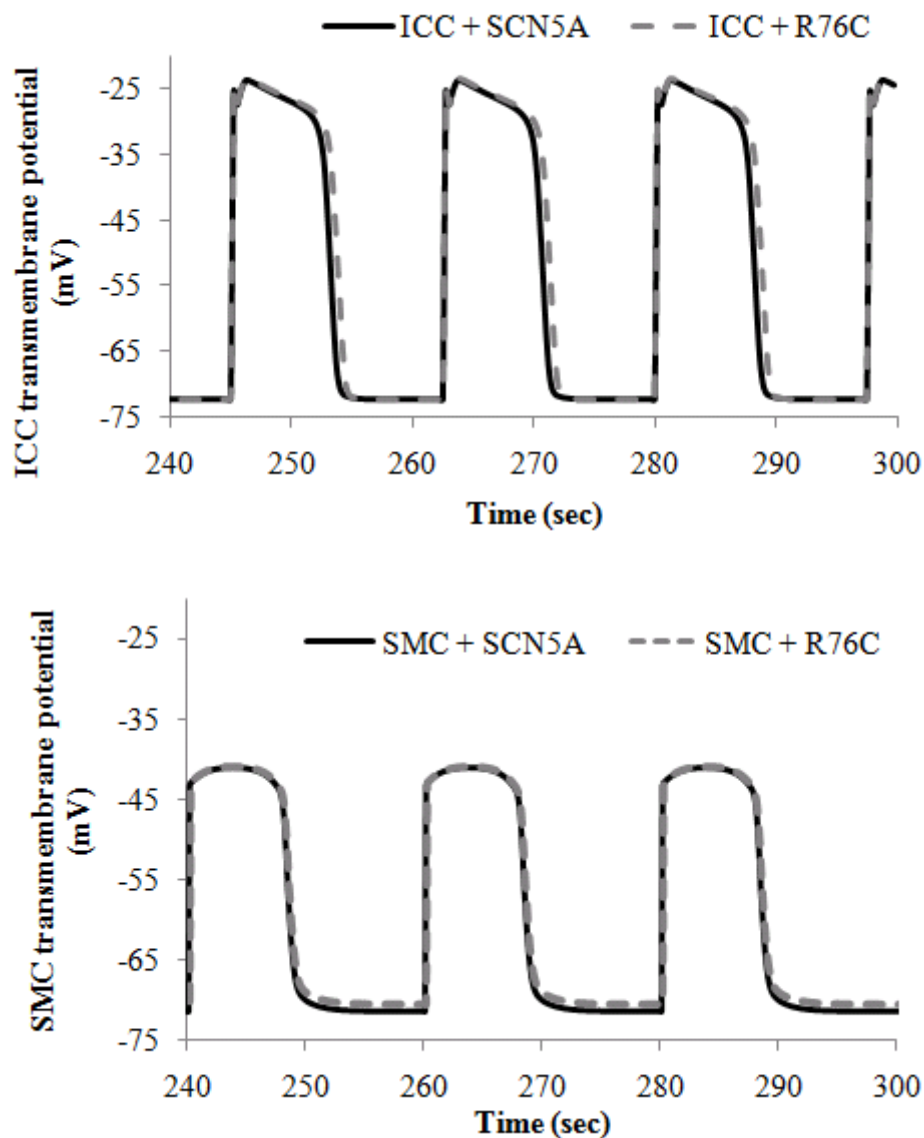
Figure 3.22. Slow wave simulation results. Upper panel shows the effect of the R76C mutation in the ICC membrane potential; lower panel shows the effect of the R76C mutation in the SMC membrane potential.
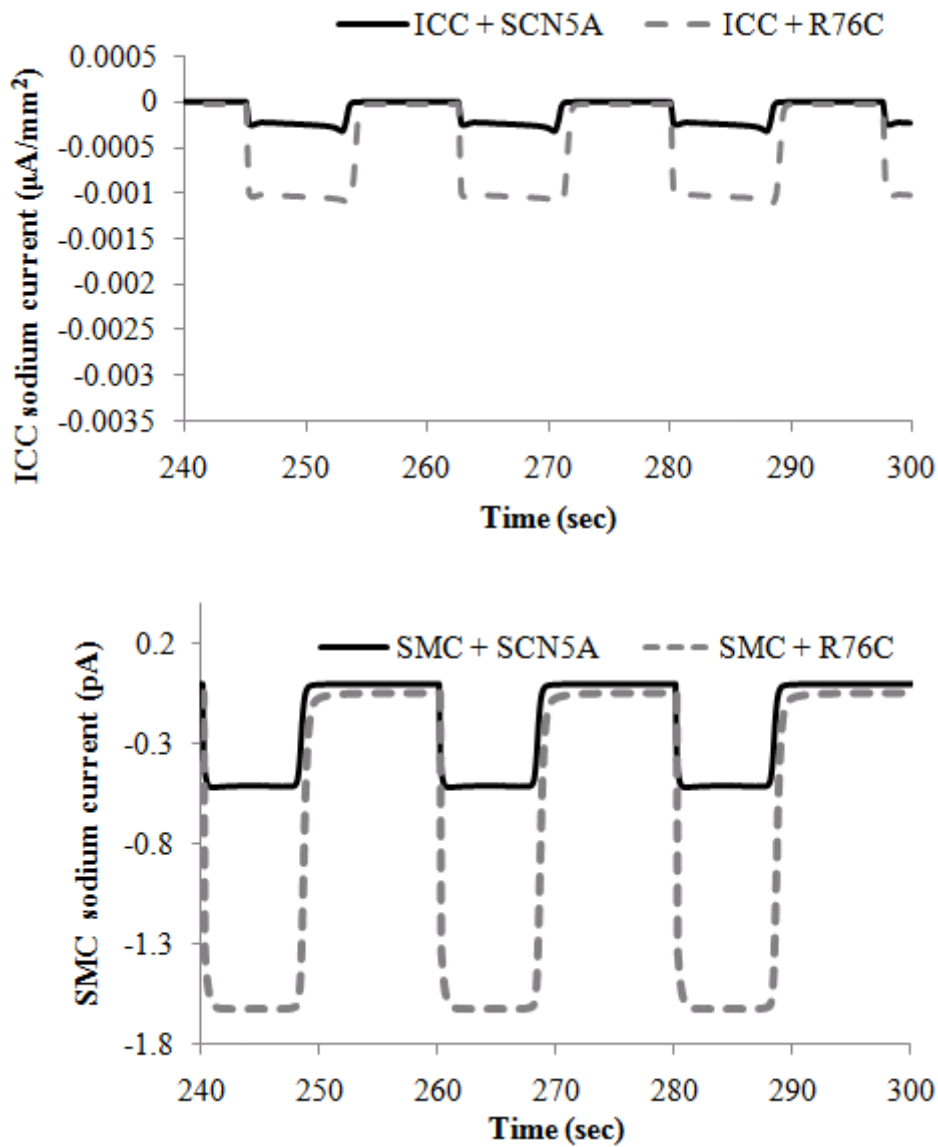
Figure 3.23. Sodium current simulation results. Upper panel shows the ICC sodium currents while lower panel shows the SMC sodium currents.

3.7.7 Discussion

In Section 3.6, it was demonstrated that the Hodgkin-Huxley formalism was not able to adequately describe the time course of channel inactivation (see Figures 3.12 to 3.14), therefore the Markov formalism was then used to construct the sodium channel models. It was shown that the Markov models of SCN5A, TCAP and R76C were indeed able to describe time course behaviour

of sodium channels adequately, which included channel inactivation (see Figures 3.17 to 3.19 and Appendix 2). The apparent increase in computational cost incurred from the more complex Markov model over a Hodgkin-Huxley model is reducible by using the implicit Euler method (over forward Euler method) with, for example, LU decomposition and back substitution to solve the resulting linear system. In addition, it is worth noting that the three-parameter rate equation shown in Eq. 3.44 can be simplified to a two-parameter form of $k = A'exp(CV_m)$. The two-parameter form can be considered to improve computational efficiency in higher spatial scale investigations and in the parameterization procedure. For convenience, the parameter values of the simplified rate equations corresponding to Table 3.10 can be found in Appendix 5.

The sodium channel kinetics were assumed to be identical in both the ICC and SMC, since identical alpha subunits of the sodium channel exist in both cell types. Furthermore, it was inferred from native channel data that the ICC and SMC sodium channels behave in a similar manner [106, 154]. Therefore, any of the three channel models can be integrated into either the ICC or SMC model. However, should it be established that telethonin expression in ICC is absent, then it is only a simple matter of only including the Markov sodium channel models for study in the SMC model and not the ICC model.

Sodium channel activation and inactivation kinetics with and without the R76C mutation were analyzed by simulating the patch clamp protocol described by Mazzone et al [14]. The results agree with those noted

experimentally. The resting membrane voltage range, within which steady-state sodium current was expected to flow, was enlarged (also known as the window current). The time to reach peak current was slightly decreased, while the fast time constant of inactivation was also decreased. These macroscopic observations were further examined in terms of the state transitions in the Markov models over the physiological range of membrane potentials, i.e., from -70 mV to -20 mV. For the transition between any pair of connected states i and j, the steady-state value of state i was described by $k_{i,j}/(k_{i,j}+k_{j,i})$ and the characteristic time constant given by $1/(k_{i,j}+k_{j,i})$. The results are shown in Figures 3.24 and 3.25. It was found that near the resting membrane potential, the mutation caused an increase in steady-state value of O which brought about a net shift in the opening direction, resulting in more channels that reside in the open state. In turn, this may explain the observation of an enlargement of the window current. Upon depolarization, the time constant for the transition pair of O and $I1$ became significantly smaller in the presence of mutation which could exert a net influence in causing a reduction in the time until peak current as well as a decrease in fast inactivation due to the faster kinetics brought about by a smaller time constant.

From the whole cell simulations, changes in the transmembrane potential profile of the gastric ICC and SMC were observed upon the inclusion of the R76C mutation. The duration of the ICC plateau phase was increased slightly, which was a consequence of a net increase in sodium current amplitude when compared to the wild-type channel. It appears that the R76C mutation's effect on increasing open probability overcame its effect on causing smaller fast time

constant of inactivation values which may have otherwise resulted in plateau shortening. An expanded window current near the resting membrane potential, as observed by Mazzone et al [14], suggested that the resting membrane potential may increase with an increased inward current. Indeed this agrees with the model predictions in the SMC where the resting membrane potential was depolarized. This was also consistent and reflected in the predicted SMC sodium current which saw the mutation increasing the sodium current during the resting phase. In the self-exciting single ICC model, the frequency of the slow waves was unchanged in the presence of the mutation, and this implies that the alteration of the sodium current was not sufficient to significantly change intracellular calcium handling which would be necessary to elicit a frequency change. The single SMC model received a prescribed ICC stimulus input of fixed frequency, and therefore unable to experience a change in its slow wave frequency.

Although the same sodium channel formulations were included in both the ICC and SMC models, significant differences were observed when comparing the effects of the same mutation on resting potential. The expansion of window current near the resting potential indicates an expected increase in the inward sodium current and hence a depolarization. However, the extent of this depolarization depends on the magnitude of the whole cell sodium channel conductance relative to the conductances of the other channel types. Here, the proportion of the whole cell conductance contributed by the sodium channels in the ICC at the resting membrane potential was substantially smaller than in the SMC. Hence, upon the inclusion of the R76C model, the effects on the

SMC resting membrane potential were substantially larger than those observed in the ICC. These aside, it was noted that the consequences of the R76C mutation in ICC and SMC are consistent with it being a gain-of-function mutation as determined from the HEK-293 patch clamp studies.

Additionally, the observed effects of the Markov sodium channel models in the simulated single cell membrane potential of ICC and SMC are contingent on the assumption that the whole cell sodium conductance remains unchanged in the presence of telethonin and/or its mutation. Future studies that confirm any effects on the whole cell sodium conductance such as through an alteration of SCN5A expression level and single sodium channel conductance would aid in the interpretation of the current findings.
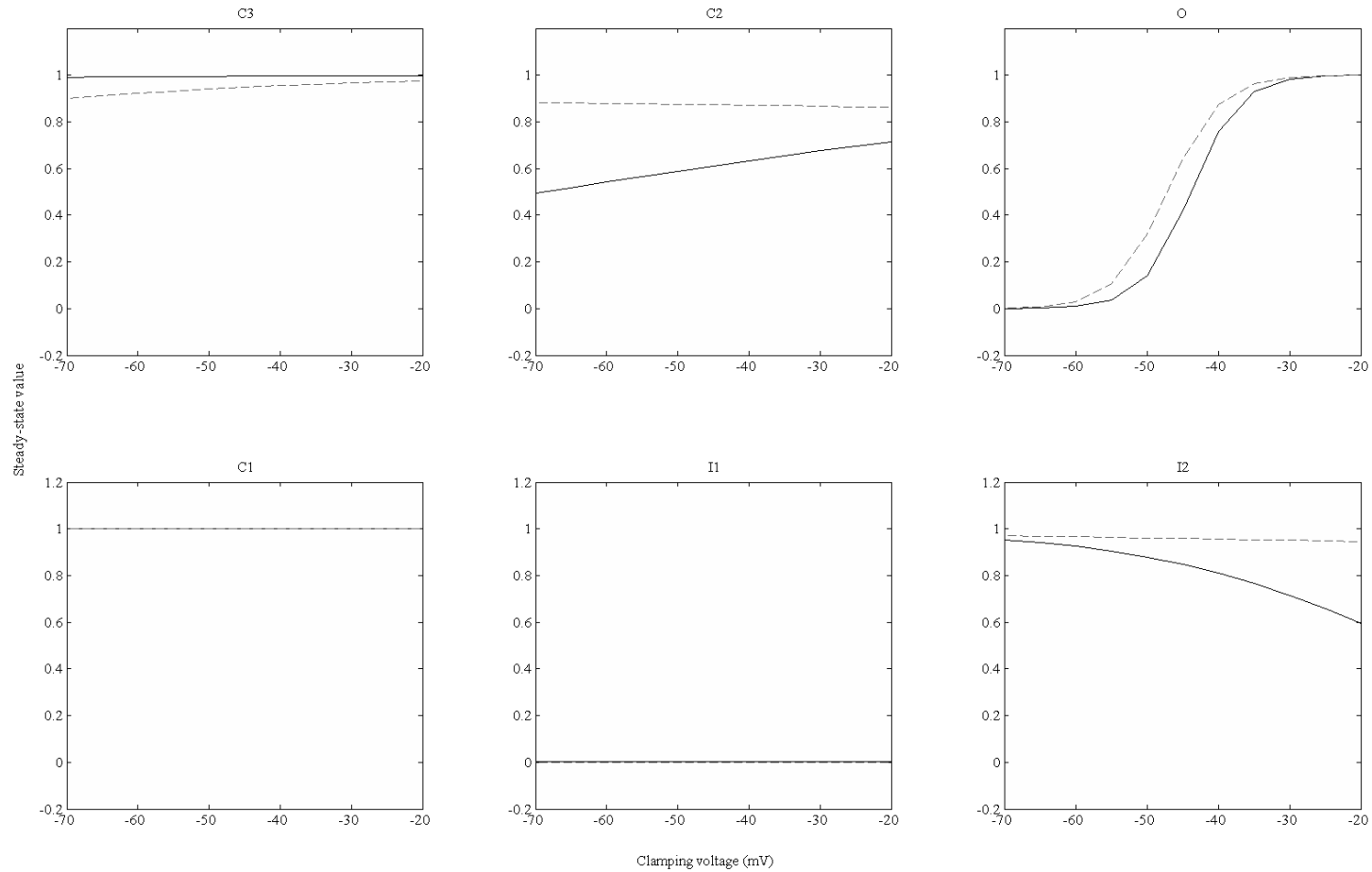
Figure 3.24. Steady-state values of all six states of the Markov sodium channel model. Solid line refers to the SCN5A model, while dashed line refers to the R76C model.
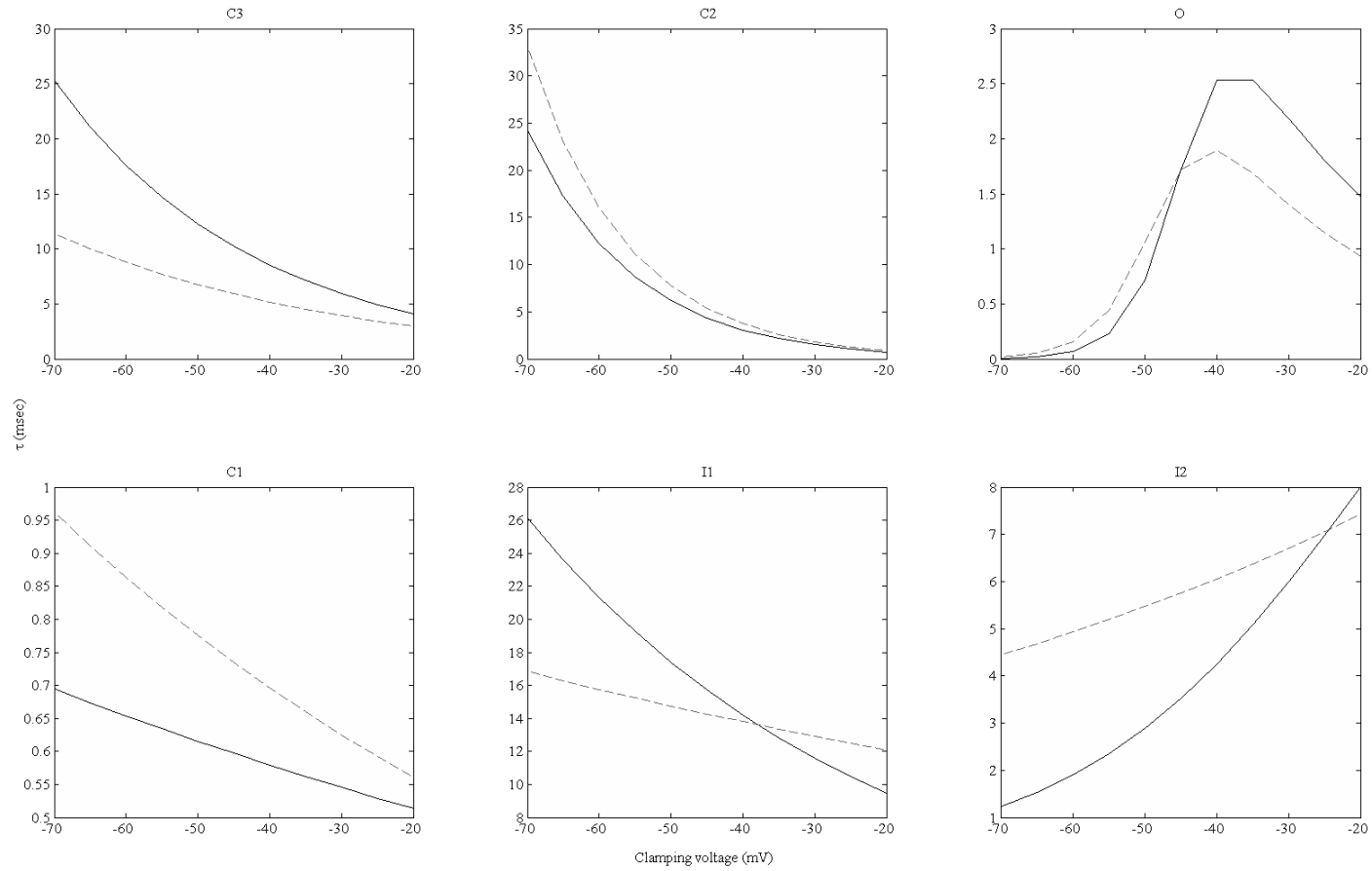
Figure 3.25. Time constant values, τ, of all six states of the Markov sodium channel model. Solid line refers to the SCN5A model, while dashed line refers to the R76C model.

3.8 Modelling polymorphic-splice variants and G298S mutation

The preceding section discussed the modelling and investigation of the R76C mutation that caused a gain-of-function in the SCN5A sodium channels. Here, the modelling and investigation of a loss-of-function mutation in SCN5A itself will be discussed. As previously mentioned, G298S is a rare and missense mutation discovered in a patient with idiopathic irritable bowel syndrome (IBS) in a study by Saito et al [15]. It was determined that the patient was heterozygous for a common polymorphism, H558R, however it was not known if the G298S mutation resided on the H558 and/or H558R allele. Including the common alternative splicing of SCN5A transcripts, i.e., Q1077/Q1077del, four common backgrounds are possible: H558/Q1077del, H558R/Q1077del, H558/Q1077 and H558R/Q1077. Table 3.11 shows the estimated frequencies of each background in the population [173].

Table 3.11. Estimated frequencies of the four common SCN5A sodium channel backgrounds in the population.

Polymorphism	Alternative splicing	Estimated frequencies in population
H558	Q1077del	45%
H558R	Q1077del	20%
H558	Q1077	25%
H558R	Q1077	10%

The transfection experiments in HEK-293 expression systems were consequently performed in eight groups, that is, four common backgrounds in the G298 (wild-type) state and another four common backgrounds that carried the G298S mutation created by site-directed mutagenesis. For each of the eight groups, a number of transfected HEK-293 cells were used to record sodium currents using the whole cell patch clamp approach, which followed the same

activation protocol that was used in Mazzone et al's study on the R76C mutation (see Figure 3.7) [14]. For ease of referencing, the eight groups of HEK-293 cells have been assigned the following names as shown in Table 3.12.

Table 3.12. Table of assigned names for each of the eight groups of HEK-293 cells used in the voltage clamp experiments.

Assigned group name	SCN5A channel variants		
	Polymorphism	Alternative splicing	G298 (wild-type) or G298S (mutation)
V1_WT	H558	Q1077del	G298
V1_MT	H558	Q1077del	G298S
V2_WT	H558R	Q1077del	G298
V2_MT	H558R	Q1077del	G298S
V3_WT	H558	Q1077	G298
V3_MT	H558	Q1077	G298S
V4_WT	H558R	Q1077	G298
V4_MT	H558R	Q1077	G298S

In the HEK-293 experiments, the G298S mutation was found to cause a loss-of-function effect on the sodium channels in all four backgrounds. The notable changes were a decrease in peak currents and an increase in time to peak for a subset of the range of clamping voltages that were used. Further experiments revealed that the single channel conductance was not changed by mutation, but a change in the maximum whole cell conductance was not ruled out. Perfusion patch clamp on the HEK-293 cells showed that mechanosensitivity of the sodium channels was reduced by the mutation (10 ml/min of bath solution for 60 s).

A Markov formalism using the same methodology as put forth in section 3.7 was used to create eight sodium channel models corresponding to each of the

eight groups of sodium channel variants. The same model topology with six states was used (see Figure 3.15). The experimental data in the aforementioned G298S study [15] was obtained from Mayo Clinic collaborators, and was sufficient to be divided into training data and validation data. Table 3.13 shows the breakdown of experimental data that was provided, i.e., the number of cells for each of the eight groups under five different holding voltages (-100 mV to -60 mV at an increment of 10 mV). The number of cells for the perfusion studies (at -100 mV of holding voltage) was also provided. The experimental data from each cell recorded sodium current over time for a total of 24 clamping voltages (from -80 mV to 35 mV with a voltage step size of 5 mV). Upon inspection of the experimental data, it was determined that the quality of data for holding voltages of -70 mV and -60 mV was poor due to the low signal-to-noise ratio. This was a consequence of the smaller currents that were recorded at more depolarized holding voltages. Moreover, the same data, from the holding voltages of -70 mV and -60 mV, was used in Saito et al's paper to compare the peak currents only, and was not used to analyze the kinetic parameters of time to peak and inactivation time constants [15]. Therefore, the decision was made to use the experimental data from the holding voltages of -100 mV, -90 mV and -80 mV where the experimental data from -100 mV and -90 mV was applied to train the parameter values, while the experimental data from -80 mV was used for validating the predictions of the sodium channel models.

Table 3.13. The number of cells for the experimental data provided by Mayo Clinic.

Group	Number of cells							
	Holding voltage (no perfusion)					Perfusion (-100mV of holding voltage)		
	-100 mV	-90 mV	-80 mV	-70 mV	-60 mV	before	during	after
V1_WT	29	22	30	23	23	27	27	27
V1_MT	16	20	21	14	14	20	20	20
V2_WT	9	9	9	9	9	9	9	9
V2_MT	13	17	17	6	6	16	16	16
V3_WT	10	10	10	10	10	10	10	10
V3_MT	8	7	12	5	5	12	12	12
V4_WT	10	9	9	9	9	9	9	8
V4_MT	6	10	10	5	5	10	10	10

3.8.1 Results of the Markov sodium channel models

The same fitting procedure used to create the SCN5A, TCAP and R76C models was again applied to determine the parameter values using the training data. The quality of fit between the model predicted data and training data was quantified using Eq 3.60. For the holding voltage of -100 mV, the error range was between 0.5071% to 1.1396%, while the error range of the holding voltage of -90 mV was between 0.5227% to 1.1559% (Tables 3.14 and 3.15). Figures 3.26 and 3.27 show a sample of the graphical comparison between model and experimental data for the most common background at the holding voltage of -100 mV while Figures 3.28 and 3.29 show a sample of the same comparison for the holding voltage of -90 mV. The full results for both holding voltages are found in Appendices 3, 4, 6 and 7. From these comparisons, all eight models of V1_WT, V1_MT, V2_WT, V2_MT, V3_WT, V3_MT, V4_WT and V4_MT were well fitted to the experimental training data. Their corresponding parameter values are given in Tables 3.16 to 3.19. As mentioned in Section 3.7.7, the transition rate equations can be

simplified to a two-parameter form, for which the parameter values for all of the G298S models can be found in Appendix 9.

Table 3.14. Table of fitting error for holding voltage of -100 mV.

Holding voltage of -100 mV	
Group	% Error
V1_WT	0.69377
V1_MT	0.62208
V2_WT	0.70608
V2_MT	0.72843
V3_WT	1.0610
V3_MT	0.85971
V4_WT	0.50715
V4_MT	1.1396

Table 3.15. Table of fitting error for holding voltage of -90 mV.

Holding voltage of -90 mV	
Group	% Error
V1_WT	0.570388
V1_MT	0.65179
V2_WT	0.72637
V2_MT	0.69124
V3_WT	1.1559
V3_MT	0.93977
V4_WT	0.52273
V4_MT	1.0917
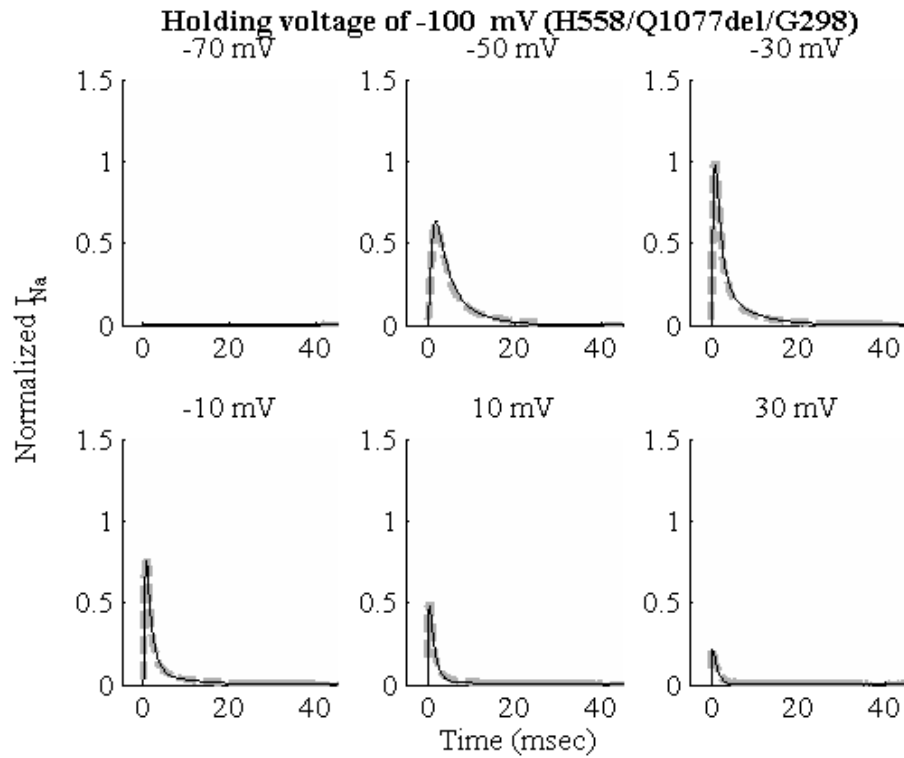
Figure 3.26. A comparison between V1_WT model predicted data (solid lines) and the corresponding training data (dashed lines) at holding voltage of -100 mV.
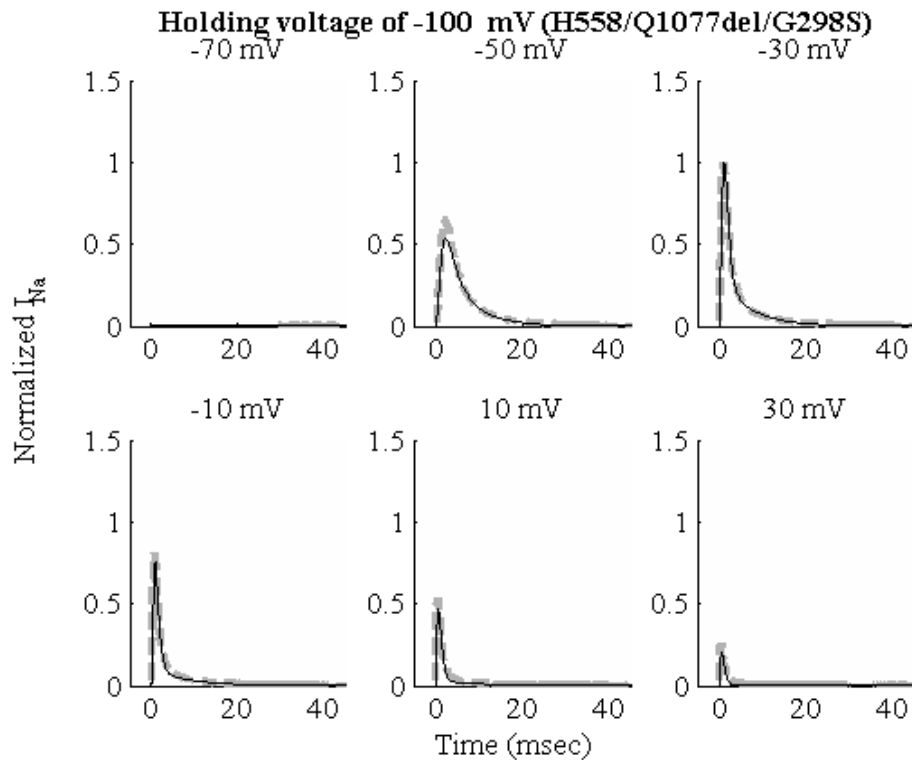
Figure 3.27. A comparison between V1_MT model predicted data (solid lines) and the corresponding training data (dashed lines) at holding voltage of -100 mV.
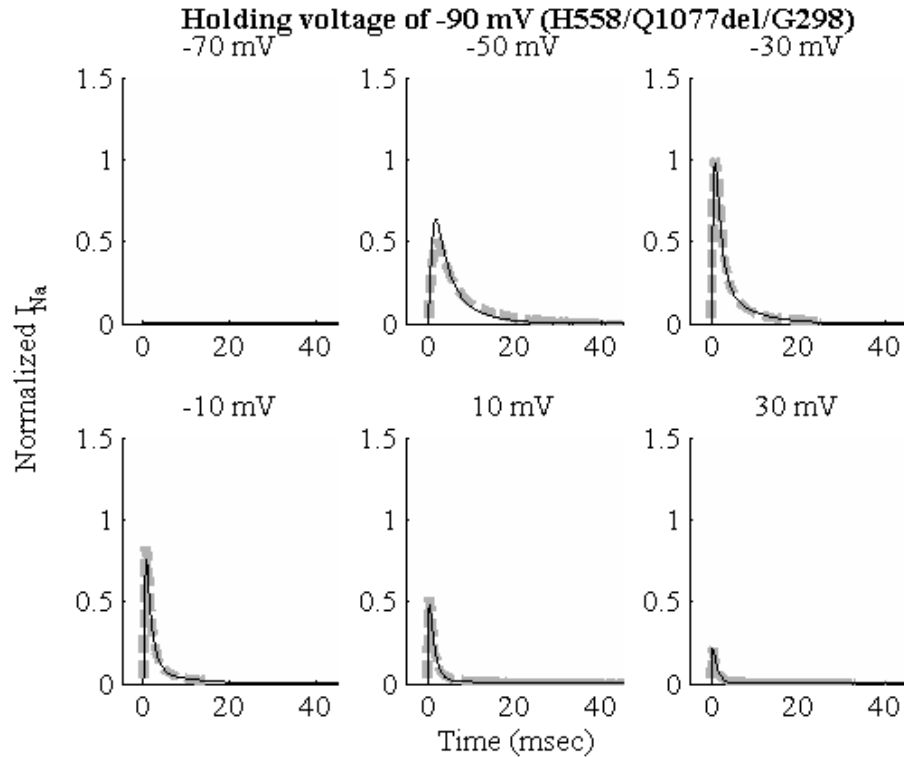
Figure 3.28. A comparison between V1_WT model predicted data (solid lines) and the corresponding training data (dashed lines) at holding voltage of -90 mV.
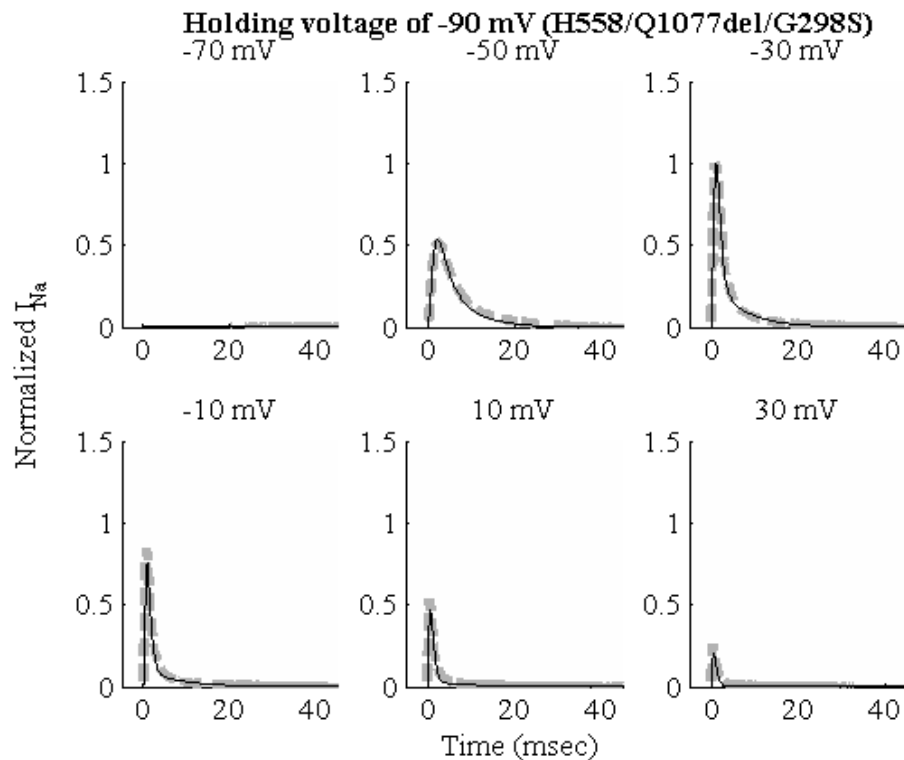
Figure 3.29. A comparison between V1_MT model predicted data (solid lines) and the corresponding training data (dashed lines) at holding voltage of -90 mV.

Table 3.16. Table of parameter values for V1_WT (H558/Q1077del/G298) and V1_MT (H558/Q1077del/G298S) models.

General rate equation	$Aexp(B + CV_m)$					
Model	**V1_WT**			**V1_MT**		
State transition	**A (ms^{-1})**	**B**	**C (mV^{-1})**	**A (ms^{-1})**	**B**	**C (mV^{-1})**
O→I1	0.036687	3.4265	0.014105	0.031603	3.6945	0.013251
I1→I2	0.48967	4.1594	-0.00147	0.20522	0.19431	8.25E-05
C3→C2	0.16336	-0.25374	1.35E-05	0.40111	-1.3898	6.71E-07
C2→C1	1.9098	1.03012	0.009075	1.2666	0.63593	0.012529
C1→O	1.6082	1.2926	0.027162	0.15202	8.8928	0.15577
I2→I1	4.81E-08	0.16182	-0.19518	9.08E-07	1.3507	-0.07881
C2→C3	0.003925	-0.01698	-0.03231	0.011512	-0.15544	-0.00944
C1→C2	0.30529	-5.497	-0.12304	0.001446	0.68823	-0.09343
O→C1	0.000276	-0.25465	-0.18870	5.32E-05	0.14220	-0.15874
I1→C1	0.14825	1.6128	-0.00232	0.063163	0.000863	0.002923
C1→I1	0.3965	-0.9776	-0.00217	0.026344	1.8257	-0.00109
I1→O	6.15E-08	-1.8516	0.21914	5.04E-08	-0.16421	-0.10859

Table 3.17. Table of parameter values for V2_WT (H558R/Q1077del/G298) and V2_MT (H558R/Q1077del/G298S) models.

General rate equation	$Aexp(B + CV_m)$					
Model	**V2_WT**			**V2_MT**		
State transition	**A (ms^{-1})**	**B**	**C (mV^{-1})**	**A (ms^{-1})**	**B**	**C (mV^{-1})**
O→I1	2.0449	-0.39552	0.019379	1.5990	-0.25874	0.013426
I1→I2	0.19991	-0.15856	-0.00024	0.65879	-1.1944	0.005872
C3→C2	0.65340	3.7882	-0.00029	0.001369	17.975	-0.05534
C2→C1	0.43400	3.5372	0.038026	1.2835	2.4612	0.059176
C1→O	1.1336	1.6813	0.014891	0.003716	7.0674	0.00391
I2→I1	2.75E-09	3.0226	-0.10784	1.11E-06	3.9328	0.041269
C2→C3	41.0241	-0.15853	0.10401	0.002079	17.664	0.056623
C1→C2	0.17463	-0.00398	-0.08117	0.033643	-1.2428	-0.05566
O→C1	1.71E-06	-0.08985	-0.24795	2.09E-05	0.59890	-0.22839
I1→C1	0.025078	0.81180	0.000115	0.018812	0.97575	0.001762
C1→I1	0.079915	0.61268	-0.03967	0.019384	-0.29525	-0.04812
I1→O	2.37E-08	0.45067	0.000219	3.13E-08	0.41019	-0.00099

Table 3.18. Table of parameter values for V3_WT (H558/Q1077/G298) and V3_MT (H558/Q1077/G298S) models.

General rate equation	$Aexp(B + CV_m)$					
Model	**V3_WT**			**V3_MT**		
State transition	**A (ms^{-1})**	**B**	**C (mV^{-1})**	**A (ms^{-1})**	**B**	**C (mV^{-1})**
O→I1	1.0509	-0.00188	0.013052	0.011	4.5396	0.003512
I1→I2	0.16014	1.52E-05	7.28E-05	6.5172	0.83560	0.0751
C3→C2	2.24E-05	0.23347	0.011129	0.29188	18.894	0.018823
C2→C1	39.163	3.1225	0.00193	0.10035	3.6565	-0.00096
C1→O	3.3076	0.16137	0.029006	9.0263	0.004581	0.037862
I2→I1	0.000171	-0.00542	0.001704	0.001941	2.1773	0.076449
C2→C3	2.7201	0.29930	-0.08035	0.11062	0.000483	0.008181
C1→C2	6.0014	3.6398	0.11515	0.14561	-0.49537	-0.10116
O→C1	0.000472	-11.815	-0.3522	0.0001	-5.8355	-0.26534
I1→C1	0.11804	-0.603	-0.00267	0.59724	-6.57E-05	-0.00184
C1→I1	0.062142	-201.50	0.003774	0.034989	-0.73327	-0.09776
I1→O	3.5451	-111.31	-0.04346	0.024731	-0.6599	0.088102

Table 3.19. Table of parameter values for V4_WT (H558R/Q1077/G298) and V4_MT (H558R/Q1077/G298S) models.

General rate equation	$Aexp(B + CV_m)$					
Model	V4_WT			V4_MT		
State transition	A (ms^{-1})	B	C (mV^{-1})	A (ms^{-1})	B	C (mV^{-1})
O→I1	1.6045	-0.4034	0.016644	0.67157	0.36888	0.010451
I1→I2	0.14322	-0.09503	-0.00027	1.2060	3.6722	0.07498
C3→C2	0.68867	2.5953	-0.00028	0.039218	1.2313	1.37E-05
C2→C1	0.041242	6.6360	0.073074	4.2345	0.32816	0.02748
C1→O	1.4307	1.2250	0.005846	10.820	0.57825	0.079874
I2→I1	1.45E-09	6.4684	-0.09772	4.97E-05	-0.16724	-0.05031
C2→C3	36.432	-0.12012	0.12543	0.00134	0.83136	-0.03935
C1→C2	0.070957	-0.00802	-0.08102	0.88776	-0.67163	0.000154
O→C1	1.32E-06	0.060388	-0.23442	1.42E-05	-1.6516	-0.23273
I1→C1	0.021741	1.0796	5.52E-05	0.000701	-0.00196	0.20869
C1→I1	0.077563	-0.11975	-0.07212	0.051036	0.87166	0.000195
I1→O	2.87E-08	1.0721	7.24E-05	3.36E-05	-0.10936	-0.1016

Further tests were performed to validate these eight models. Table 3.20 shows the errors, for each model, between the predicted data and the validation data measured with the holding voltage of -80 mV. The error range was from 0.5838% to 1.5250%. Figures 3.30 and 3.31 show a sample of the graphical comparison between model data and validation data for the most common background at the holding voltage of -80 mV; the full results are found in Appendices 8 and 10. Additionally, as is the case for the R76C work, a slow wave like voltage clamp protocol (the same as that shown in Figure 3.21) was applied to each of the eight models. As shown in Figure 3.32, the models exhibited the expected behaviour of a rapid spike like inactivation at the 100 ms time point, followed by a small reactivation at around the 200 ms time point.

Table 3.20. Table of error for holding voltage of -80 mV.

Holding voltage of -80 mV	
Group	% Error
V1_WT	0.86434
V1_MT	1.0574
V2_WT	0.99495
V2_MT	1.0017
V3_WT	1.52503
V3_MT	1.2960
V4_WT	0.58381
V4_MT	1.4706
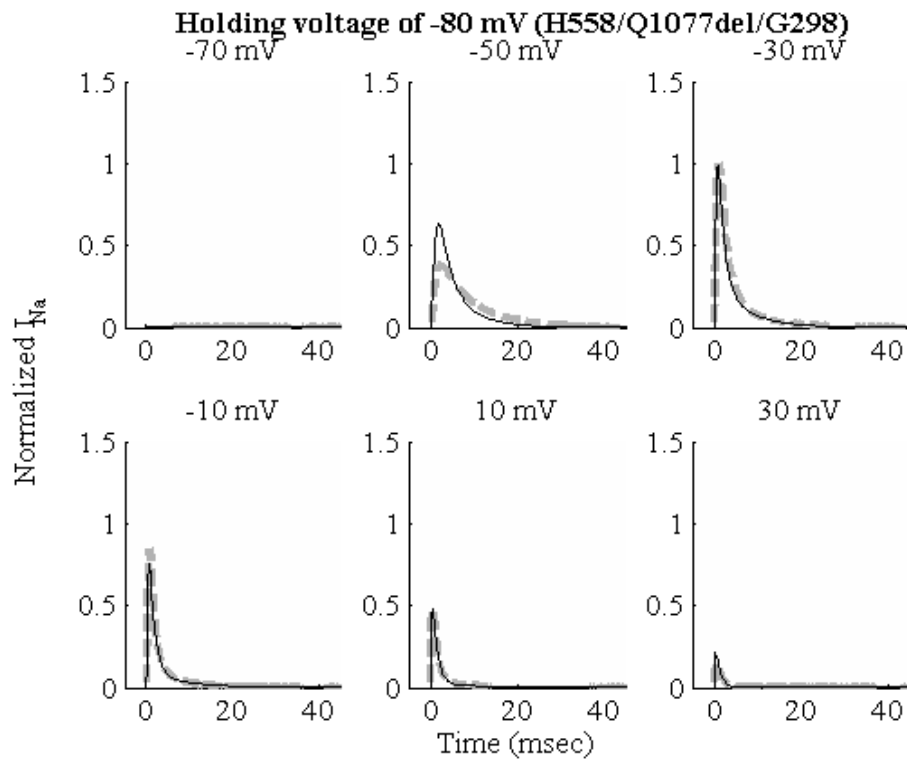
Figure 3.30. A comparison between V1_WT model predicted data (solid lines) and the corresponding training data (dashed lines) at holding voltage of -80 mV.
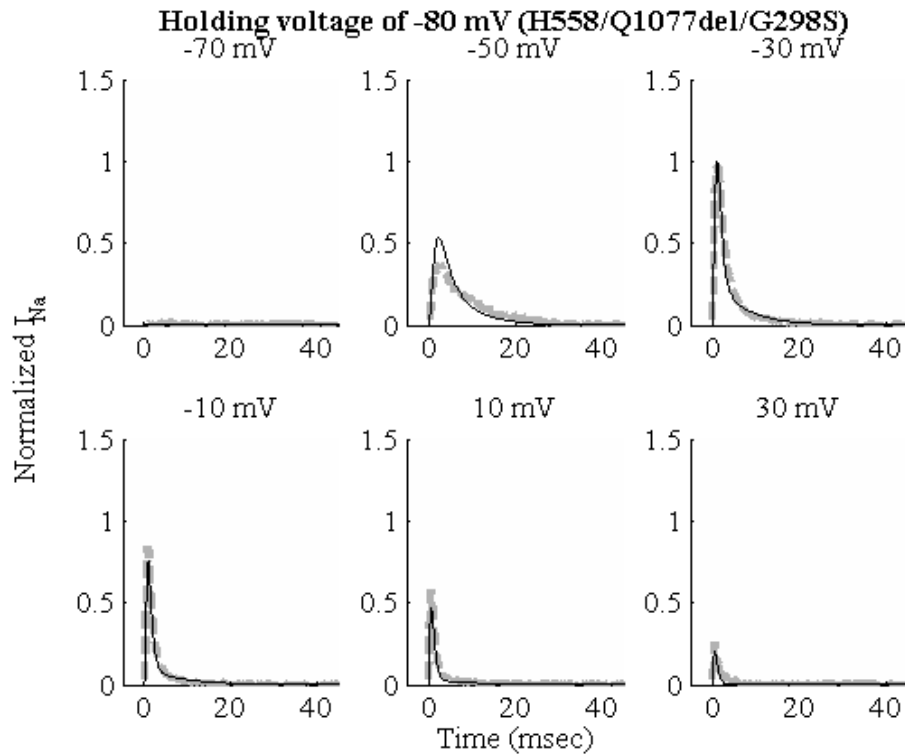
Figure 3.31. A comparison between V1_MT model predicted data (solid lines) and the corresponding training data (dashed lines) at holding voltage of -80 mV.

As mentioned previously, the SCN5A sodium channels have been found in human jejunal ICC and SMC. However, the sodium channel background in these human samples is unknown. The experimental samples were taken from the surgical waste of different patients and could possibly belong to any of the four common backgrounds (Table 3.11) or a mix in the case of averaged data [106, 154]. Nevertheless, from the reported peak current versus voltage (I-V) results in Saito et al's G298S study, the normalized I-V behaviour is not expected to differ significantly from the equivalent I-V behaviour from the human ICC and SMC [15, 106, 154]. Therefore, the same human I-V results used to compare against the earlier SCN5A, TCAP and R76C models were used here to compare against the simulated I-V results from the eight sodium channel models (under identical voltage clamp conditions).
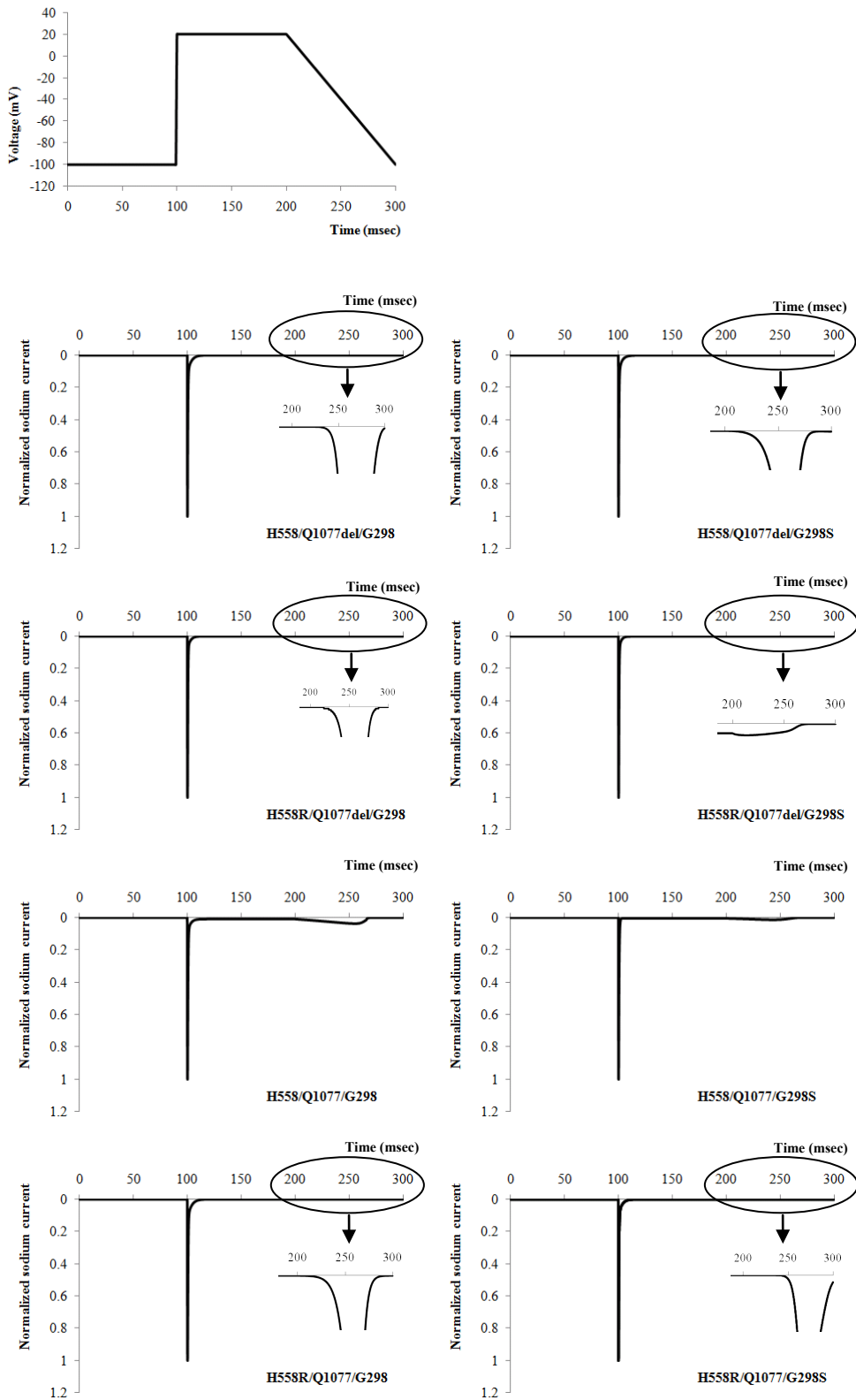
Figure 3.32. Slow wave like voltage clamp protocol results. Top panel shows the slow wave like voltage clamp protocol applied to check the response from each of the eight sodium channel models. Their results were printed in the lower panels which agreed with experimental observations that the sodium current exhibited a spike-like rapid inactivation at the 100 ms time point, followed by a miniscule reactivation at around the 200 ms time point [172]. Inset for some subplots shows a magnification of the reactivation.

Figures 3.33 and 3.34 show the comparison between the predicted I-V from each of the eight models against the ICC and SMC experimental data respectively. The results indicated that the predicted normalized I-V were in general agreement with the human experimental data over the given voltage range. It is noteworthy that the V3_MT (or H558/Q1077/G298S) model presented a significant depolarizing shift in peak voltage, relative to its wild-type result (V3_WT), for both the ICC and SMC. This implied that, where the peak current is concerned, the mutation will cause a greater influx of current relative to the wild-type. This might appear to contra-indicate the loss-of-function effect the G298S mutation is reported to confer. Nonetheless, the plausibility of altered expression of H558R/Q1077del SCN5A has not been ruled out. In another words, this apparent gain-of-function effect in peak currents can be reversed into a loss-of-function effect through a sufficiently reduced population of active H558R/Q1077del/G298S channels.
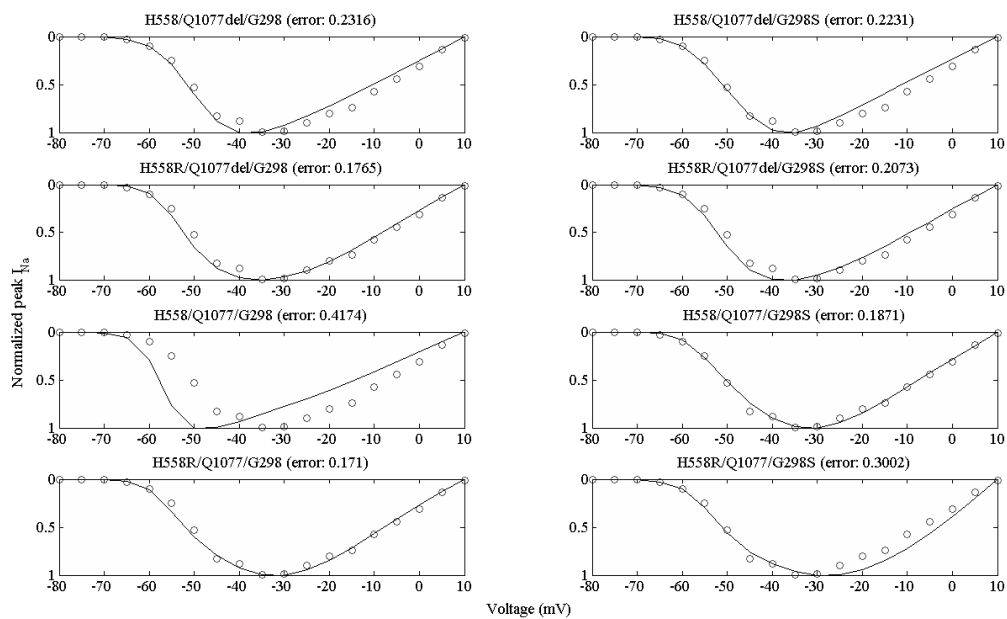
Figure 3.33. ICC I-V plots. In each of the eight subplots, the same human ICC experimental I-V data (in circles) were compared against equivalent simulated I-V data (solid lines) from each of the eight models. The corresponding error index between experimental and model data is printed for each subplot.
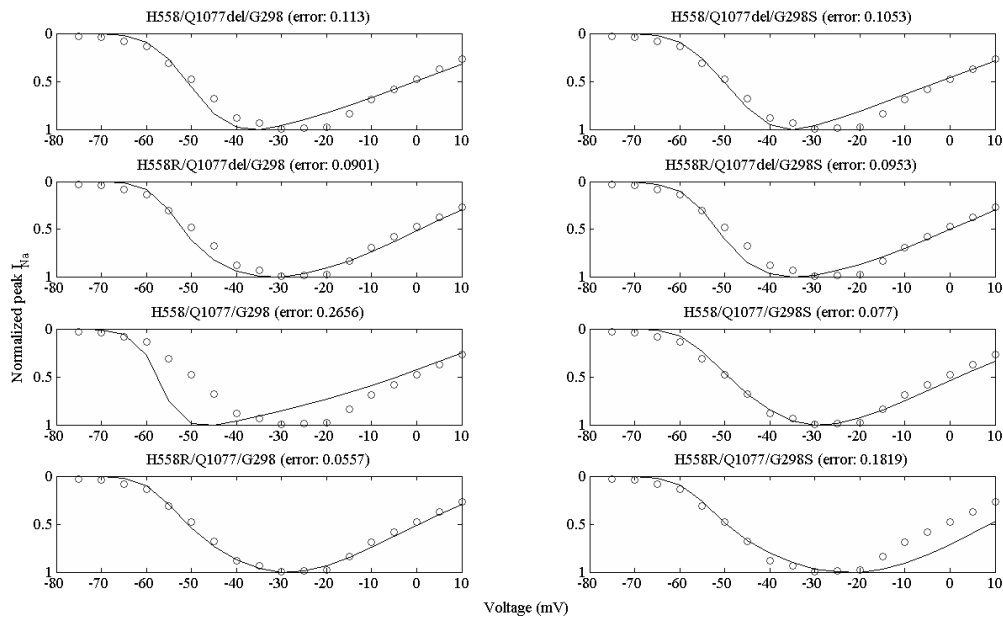
Figure 3.34. SMC I-V plots. In each of the eight subplots, the same human SMC experimental I-V data (in circles) were compared against equivalent simulated I-V data (solid lines) from each of the eight models. The corresponding error index between experimental and model data is printed for each subplot.

3.8.2 Estimation of maximum sodium channel conductance

As mentioned earlier, the use of expression systems, such as HEK-293 cells, are useful in examining channel kinetics, however they do not provide direct information on maximum whole cell sodium conductance (or ion channel density) in native cell populations such as in the human GI ICC and SMC. Alternative splicing, polymorphisms, and genetic mutations may also affect the effective density of sodium channels in a cell [173, 174]. Saito et al suggested that even though the sodium single channel conductance was not found to be significantly altered by the G298S mutation, they believed that the number of available channels may have decreased through an unknown mechanism [15].

Previously in the R76C work, the maximum sodium conductance in the native cells of ICC and SMC were derived from the SCN5A model such that the maximum sodium current experimentally measured in the human jejunal ICC and SMC was reproduced by the SCN5A model under the same conditions. The estimated maximum conductance is therefore also dependent on the set of HEK-293 experimental data from which the SCN5A model was constructed. For the G298S work, the experimental data belonged to a different study, hence the estimated maximum sodium channel conductances can be and were indeed different from what was reported earlier for the R76C work.

For the native cells, the background of the sodium currents reported for the human jejunal ICC and SMC are unknown and may correspond to a mix of polymorphic-splice backgrounds. Therefore, the four wild-type sodium channel models cannot be matched to the experimental results according to their backgrounds to obtain the appropriate maximum conductances. Nonetheless, it will be interesting to check the implied maximum conductances. The same mean maximal peak sodium current of -177.5 pA in the single ICC (Strege et al, [106]) and -142 pA in the single SMC (Holm et al, [154]) were used to estimate the maximum conductances. Table 3.21 shows the estimated maximum sodium channel conductance values, G_{max}^{ICC} and G_{max}^{SMC}, for each of the four backgrounds in the human ICC and SMC.

Due to the uncertainty in the effects of the polymorphism, alternative splicing and mutation in affecting maximum conductances, the averaged values of the

maximum sodium channel conductances in the ICC and SMC were used to facilitate subsequent computational studies in higher spatial scale models.

Table 3.21. Table of maximum sodium channel conductance values for the human ICC and SMC.

Background	G_{max}^{ICC} (nS)	G_{max}^{SMC} (nS)
H558/Q1077del	10.279	7.6557
H558R/Q1077del	9.4437	6.9994
H558/Q1077	7.6235	5.7398
H558R/Q1077	11.079	8.1949
Average	9.6062	7.1475

3.8.3 The cellular consequences of the polymorphic-splice backgrounds and G298S mutation

As before, the existing gastric ICC [108] and SMC [82] models of electrophysiology were used to evaluate the cellular consequences of the sodium channel variants that arise from the four common backgrounds and the G298S mutation. Each of the two cellular models contains a prior description of the sodium channel which was constructed with limited data. Therefore, the sodium channel description was replaced with the Markov models developed here and the respective averaged whole cell sodium channel maximum conductance values, reported in Table 3.21, were used.

The eight Markov sodium channel models were integrated separately in the ICC and SMC models. Initially, only homozygous situations were considered, i.e., each cellular model did not contain a mix of the eight sodium channel model. Although, biologically, heterozygous situations such as 50% wild-type and 50% G298S of a particular background (or any other feasible

combination) is possible, the homozygous results would provide information on the necessity to examine the heterozygous situations.

Figures 3.36 to 3.38 contain the ICC simulation results for the eight sodium channel models from all four backgrounds. The upper panels compare the ICC membrane potential in the presence of G298S mutation while the lower panels compare the ICC wild-type and G298S sodium currents. It was observed that the G298S mutation caused a general reduction in sodium current for the H558/Q1077del and H558R/Q1077 backgrounds while there is an apparent increase in sodium current due to the mutation for the H558R/Q1077del and H558/Q1077 backgrounds. Despite the mutation causing a change in the sodium currents, this was not sufficient to cause a significant change in membrane potential in the ICC model for all of the backgrounds.

Figures 3.39 to 3.42 contain the simulation results from the SMC for the eight sodium channel models from all four backgrounds. Again, the upper panels compare the SMC membrane potentials, with and without the influence of the G298S mutation while the lower panels compare the SMC wild-type and G298S sodium currents. It was observed that the G298S mutation has, in general, caused a reduction in sodium current for the H558/Q1077del, H558R/Q1077del and H558R/Q1077 backgrounds, while there was an increase in sodium current for the H558/Q1077 background. Similarly, despite these changes in sodium currents, the SMC membrane potential was not significantly perturbed. This was with the exception of the H558/Q1077del background where a noticeable hyperpolarization of the SMC resting

membrane potential was observed, which was consistent with the decrease in resting phase sodium current due to the mutation. Coincidentally, the H558/Q1077del is the most common background with 45% prevalence in the human population.

In the above homozygous situations that were explored in the ICC and SMC, the backgrounds and mutations do not appear to have a significant effect on ICC and SMC electrophysiology. Therefore, by inference, the numerous possible heterozygous situations should result in a similar outcome for ICC and SMC electrophysiology. Thus, these heterozygous situations were not examined.

The G298S mutation was characterized to be a loss-of-function mutation in the HEK-293 experiments, which appear to contradict the mixed effects in the ICC and SMC. This can be explained by the uncertainty in the maximum sodium channel conductance in the single ICC and SMC cells. In these simulations, the maximum sodium conductance in the ICC and SMC were assumed to be the same across all backgrounds. It is possible that in the actual biological situation, the mutation could reduce the maximum whole cell conductance of the sodium channels to an extent that reverses the gain in sodium current to produce a net current smaller than that of its wild-type counterpart. Similarly, the number of active sodium channels may be up-/down- regulated differently depending on the sodium channel background. The regulation pattern in the native cells may also differ from the HEK-293 cells. Additionally, over-compensation from homeostatic regulation may be

another mechanism that explains the paradoxical gain-of-function and loss-of-function phenotypes predicted by the G298/G298S SCN5A models. Homeostatic regulation in general is a mechanism where a biological cell senses and attempts to compensate for phenotypical changes, such as those arising from genetic mutation, through the regulation of protein expression [175]. In some cases, homeostatic regulation over-compensates and causes a paradoxical reversal of function [176]. All these might explain the lack of influence of the mutation on ICC and SMC electrophysiology. Also, should the wild-type maximum conductances turn out to be much higher than what was determined and used in the current simulation studies, the sodium currents may then exert significant influence on GI cellular electrophysiology.

The lack of influence of the G298S mutation might also be attributed to the lacking aspects of the cellular models that were used; for instance, the gastric models do not track all the ionic concentration changes over time. The sodium and potassium ions are artificially kept in homeostasis resulting in constant Nernst potentials. It might well also be the case that the sodium channels do not contribute to the motility and its disorders. Finally, studies have shown that the $Na_v1.5$ sodium channel is present in the human jejunal ICC and SMC, but to date, no studies have confirmed the presence or absence of the same sodium channels in the human stomach. Furthermore, the R76C mutation was associated with intestinal pseudo-obstruction while the G298S mutation was associated with irritable bowel syndrome; these are motility disorders of the intestines. The consequences of these mutations might be more pronounced in the jejunal cells of the small intestine as opposed to the gastric cells.

Therefore, jejunal cell models would be useful to gain additional insights. The development of a human jejunum smooth muscle cell model and the results of investigating the sodium channel mutations in the new cell model, are described in the next chapter.
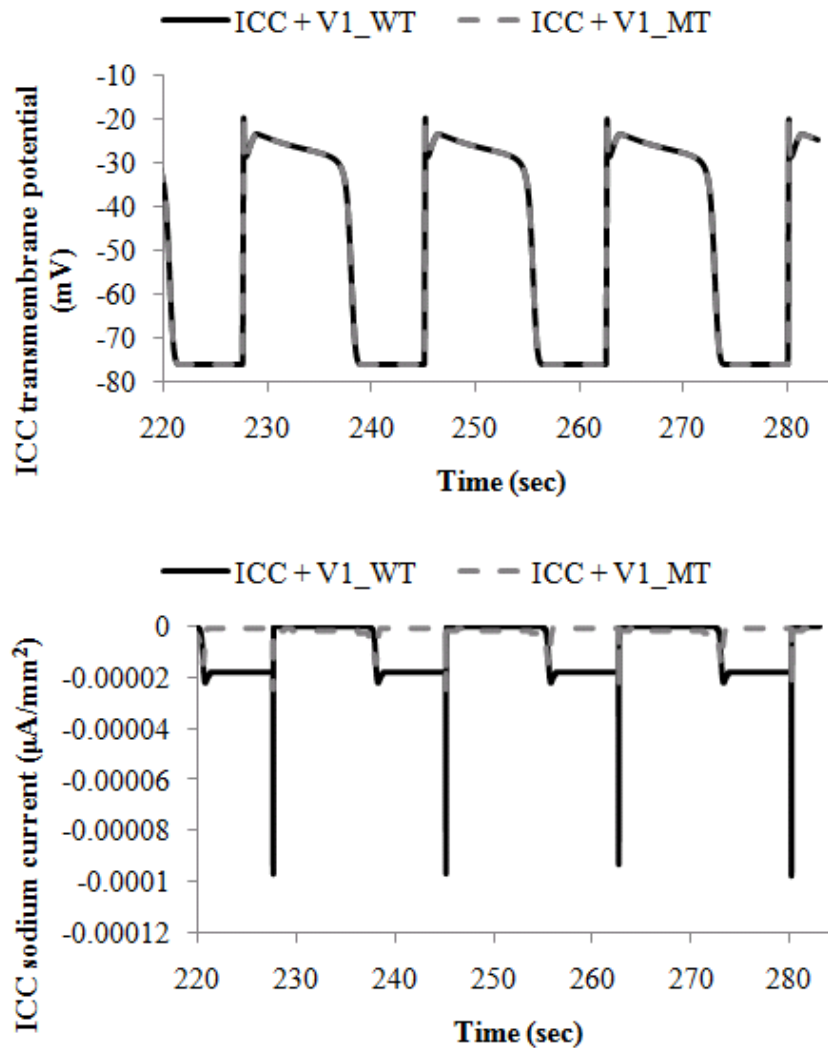
Figure 3.35. ICC membrane potential and sodium current for the H558/Q1077del background. The G298S mutation reduced the sodium current but was unable to significantly alter the ICC membrane potential. Results in black solid line correspond to the presence of wild-type sodium channels in the ICC, while grey dashed line correspond to G298S sodium channels in the ICC.
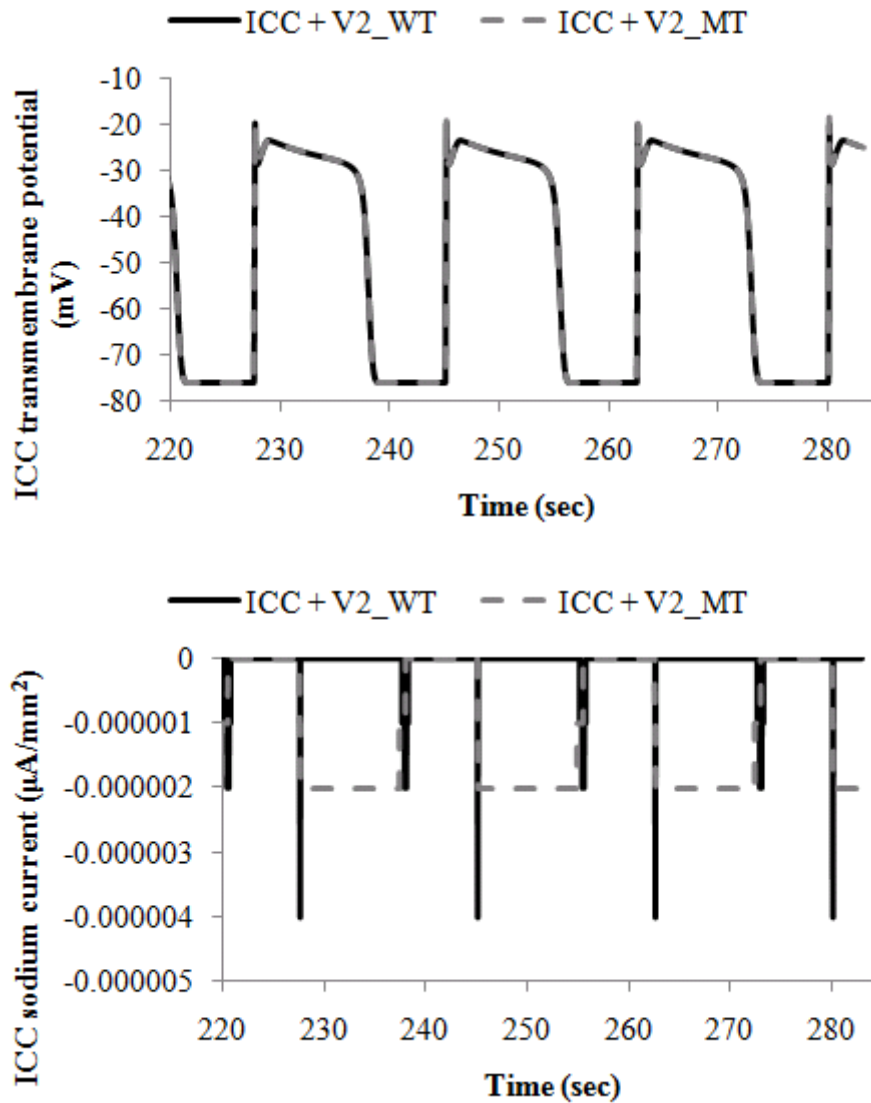
Figure 3.36. ICC membrane potential and sodium current for the H558R/Q1077del background. The G298S mutation increased the sodium current but was unable to significantly alter the ICC membrane potential. Results in black solid line correspond to the presence of wild-type sodium channels in the ICC, while grey dashed line correspond to G298S sodium channels in the ICC.
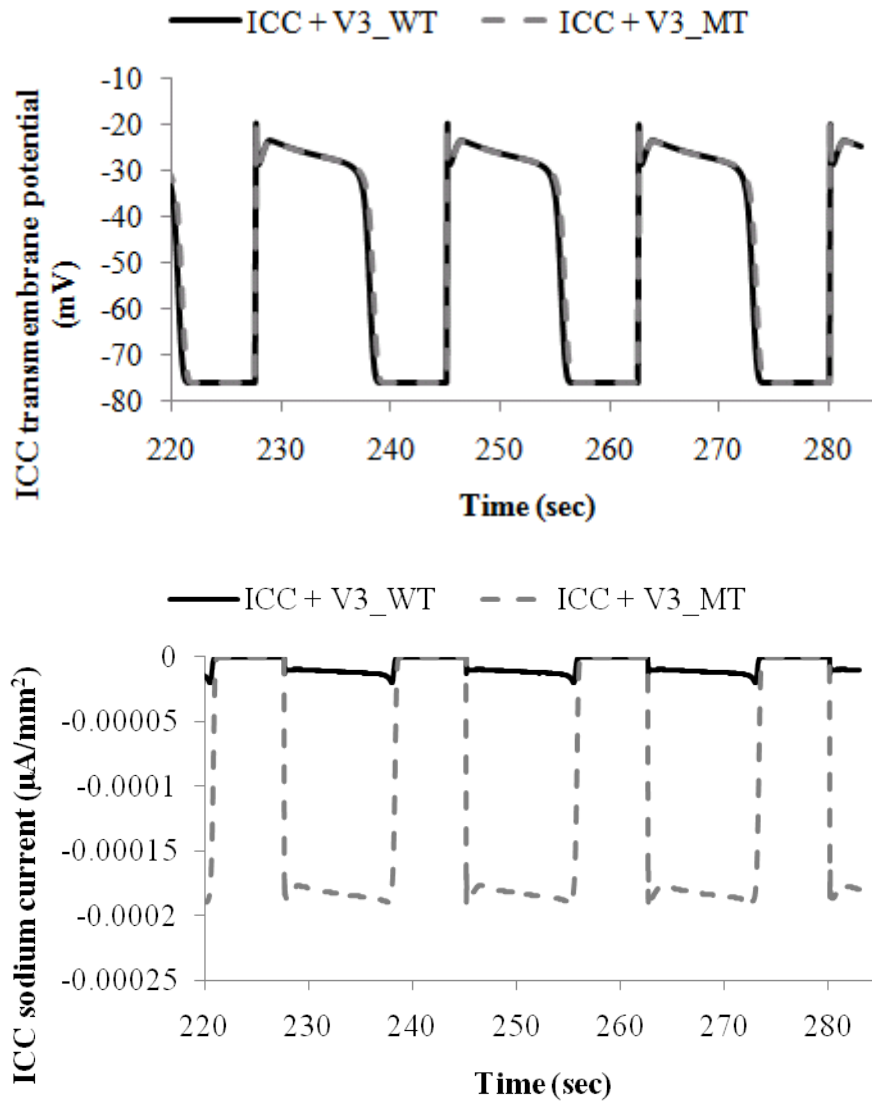
Figure 3.37. ICC membrane potential and sodium current for the H558/Q1077 background. The G298S mutation increased the sodium current and was able to very slightly prolong ICC membrane potential plateau duration. Results in black solid line correspond to the presence of wild-type sodium channels in the ICC, while grey dashed line correspond to G298S sodium channels in the ICC.
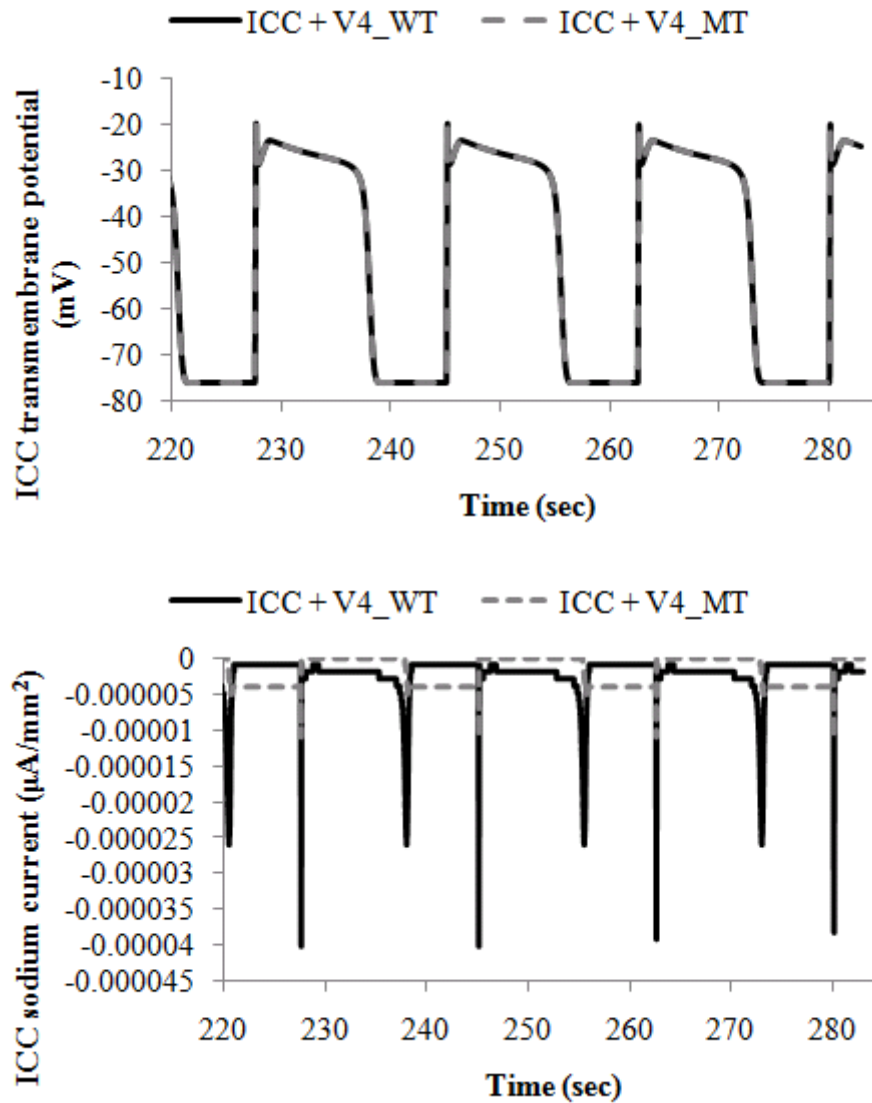
Figure 3.38. ICC membrane potential and sodium current for the H558R/Q1077 background. The G298S mutation reduced the sodium current but was unable to significantly alter the ICC membrane potential. Results in black solid line correspond to the presence of wild-type sodium channels in the ICC, while grey dashed line correspond to G298S sodium channels in the ICC.
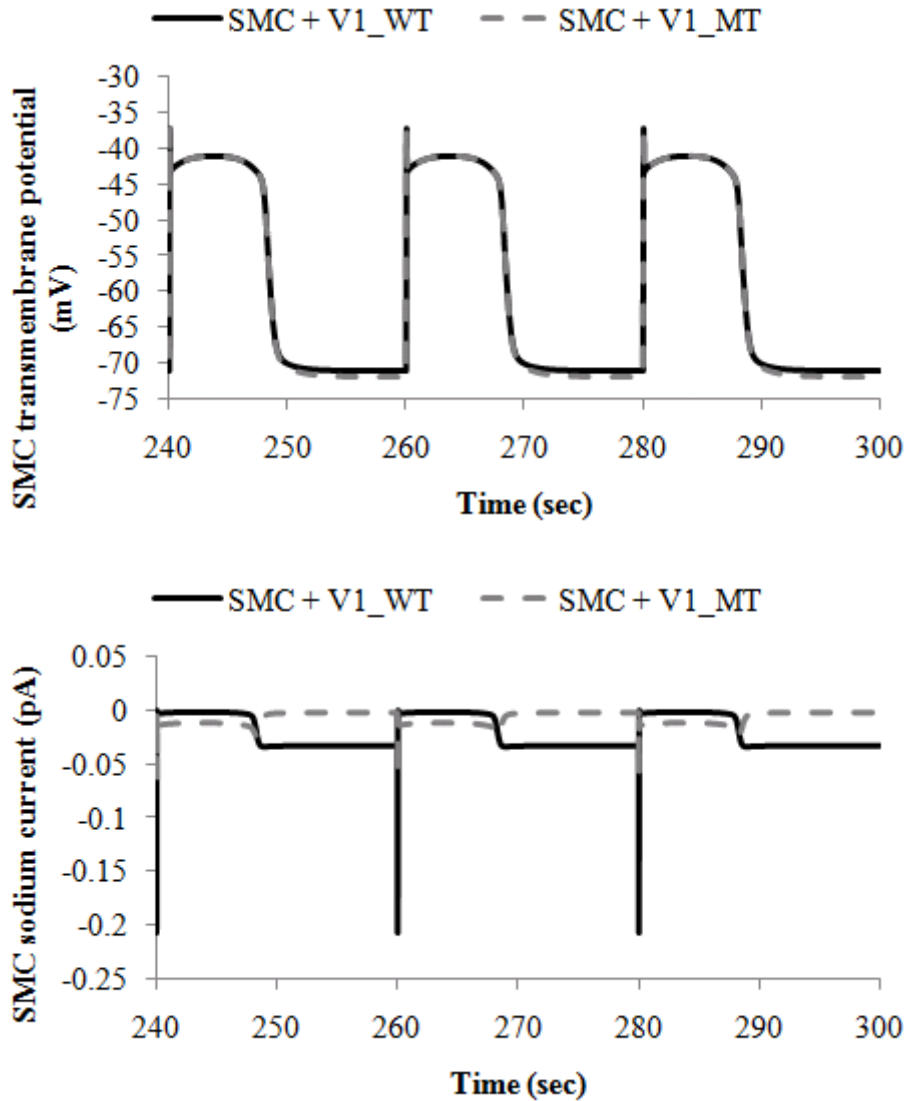
Figure 3.39. SMC membrane potential and sodium current for the H558/Q1077del background. The G298S mutation reduced the sodium current and slightly hyperpolarized the SMC resting membrane potential. Results in black solid line correspond to the presence of wild-type sodium channels in the SMC, while grey dashed line correspond to G298S sodium channels in the SMC.
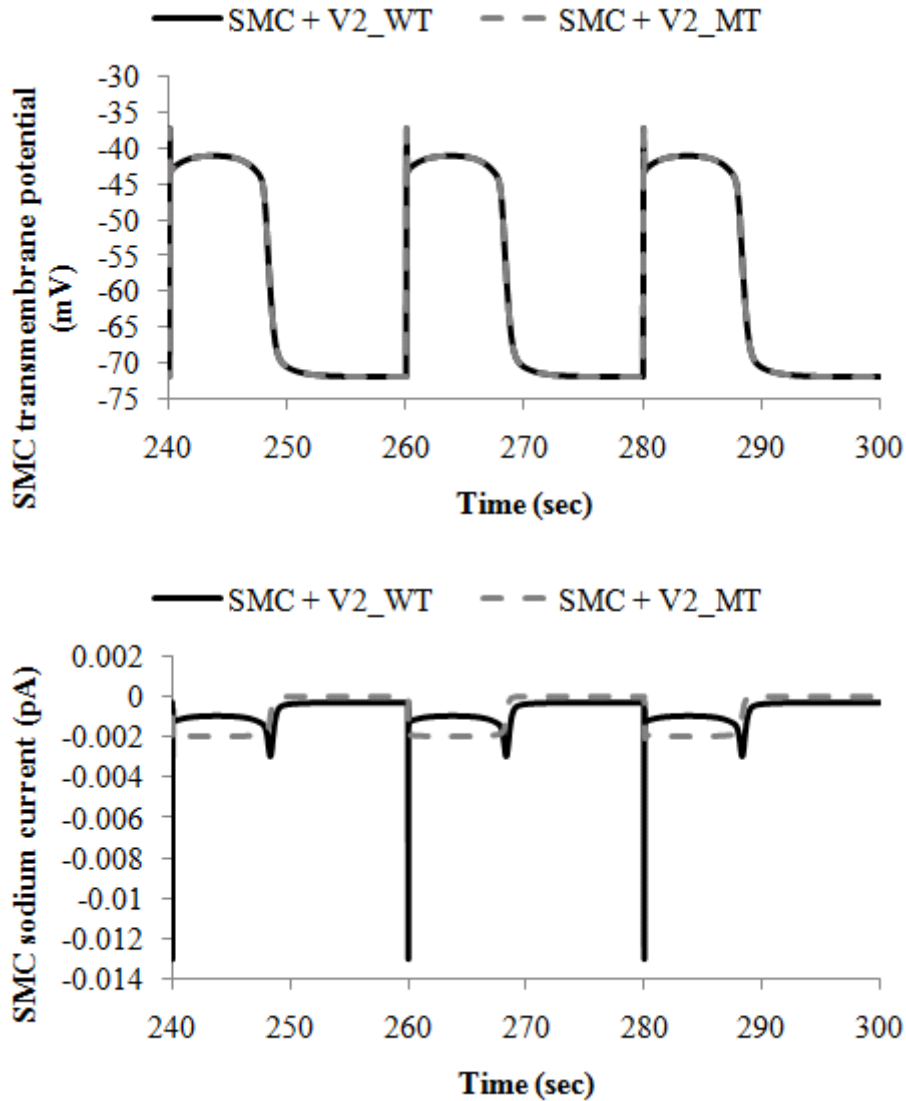
Figure 3.40. SMC membrane potential and sodium current for the H558R/Q1077del background. The G298S mutation reduced the peak sodium current but was unable to significantly alter the SMC membrane potential. Results in black solid line correspond to the presence of wild-type sodium channels in the SMC, while grey dashed line correspond to G298S sodium channels in the SMC.
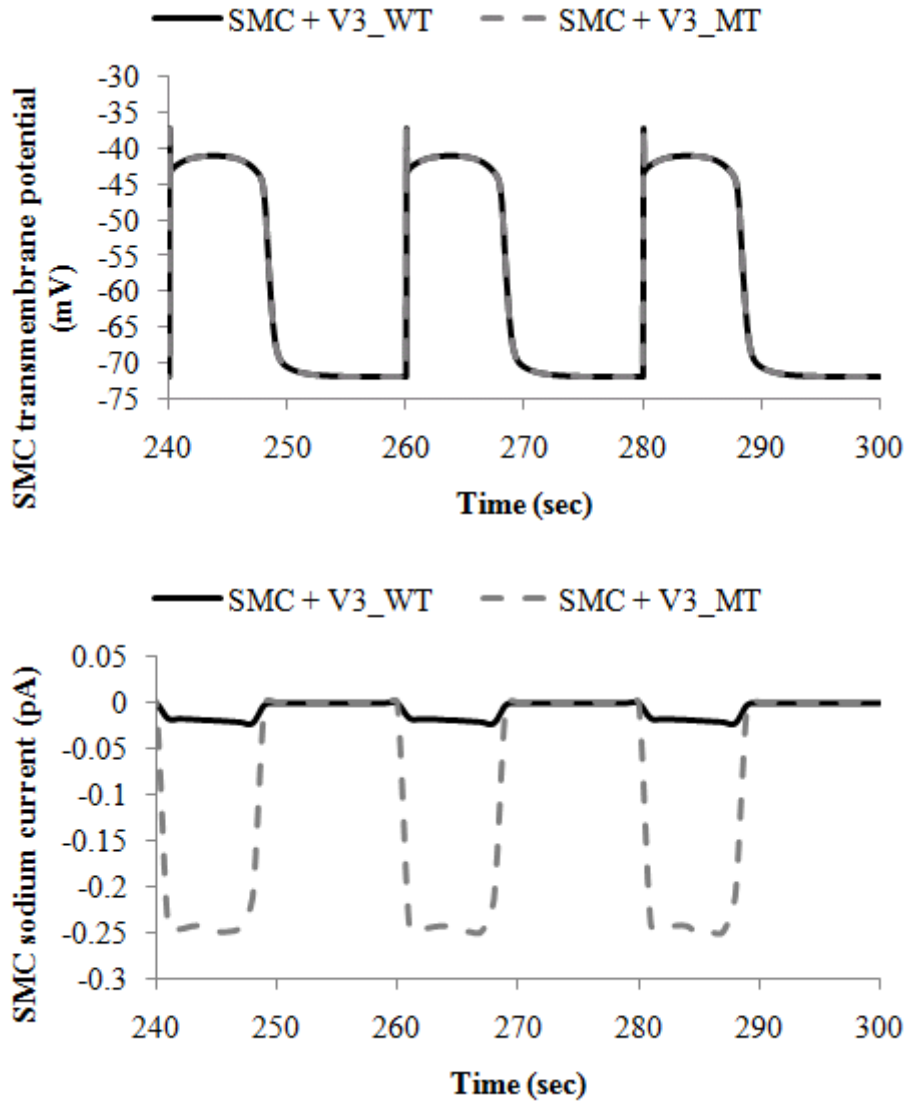
Figure 3.41. SMC membrane potential and sodium current for the H558/Q1077 background. The G298S mutation reduced the sodium current but was unable to significantly alter the SMC membrane potential. Results in black solid line correspond to the presence of wild-type sodium channels in the SMC, while grey dashed line correspond to G298S sodium channels in the SMC.
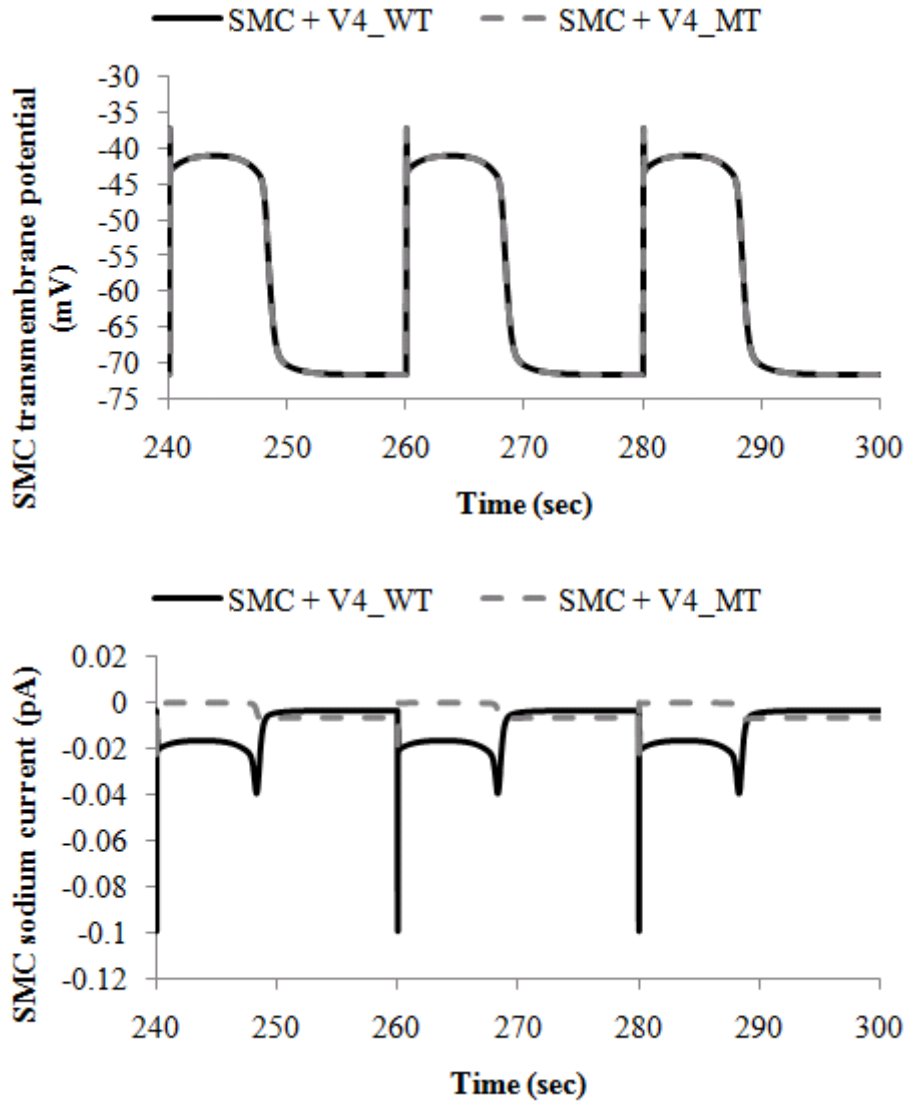
Figure 3.42. SMC membrane potential and sodium current for the H558R/Q1077 background. The G298S mutation reduced the sodium current but was unable to significantly alter the SMC membrane potential. Results in black solid line correspond to the presence of wild-type sodium channels in the SMC, while grey dashed line correspond to G298S sodium channels in the SMC.

3.8.4   Further discussion

Steady-state values and time constants

One additional set of results were obtained from each of the eight sodium channel models, i.e., the steady-state values and characteristic time constants for each pair of connected states. To recapitulate, for a state i of a pair of connected states, i and j, its steady-state value is described by $k_{i,j}/(k_{i,j}+k_{j,i})$ and the characteristic time constant is given by $1/(k_{i,j}+k_{j,i})$ (where j is the state that i is connected to). These results are shown in Appendices 11 and 12. Briefly, the results indicated that the presence of G298S mutation tends to alter the steady-state values of the *C2, I1* and *O* states of the sodium channels, across the various backgrounds, such that there is a net reduction in open probability. This is with the exception of the H558/Q1077 background where the near zero steady-state values of *C3* suggested that more channels are available to open which resulted in a gain-of-function effect as observed in the earlier cellular results. For the time constants, the G298S mutation seemed to slow the kinetics of the sodium channels because in all backgrounds, except H558/Q1077, the time constants for several pairs of connected states were increased. For the H558/Q1077 background, *C2* and *C1* were the only pair of transition states with an increase in time constants while all other transition pairs exhibited a general decrease in time constants. However, these differences in time constants due to mutation did not seem to significantly change the sodium time course behaviour in each background, under the activation voltage clamp. The G298S mutation is located in the extracellular linker of the 5th and 6th segments of domain I of the sodium channel alpha

subunit, and the results so far support this linker as having functional importance in influencing state transitions to sodium channel opening.

Perfusion/mechanosensitivity considerations

The same experimental study by Saito et al examined the effect of G298S mutation on the mechanosensitivity of sodium channels [15]. Mechanical stimulation was applied through a perfusion of bath solution at 10 ml/min. Whole cell patch clamp recordings were measured before, during and after perfusion. It was reported that perfusion significantly increased the peak sodium currents and that the G298S mutation was capable of altering the mechanosensitivity of the sodium channels in only the H558/Q1077del background (i.e., the perfusion induced increase in peak currents were significantly reduced by the mutation). An earlier mechanosensitivity study by Morris and Juranka [157] further characterized the SCN5A sodium channel kinetics as being able to accelerate reversibly with stretch.

As detailed experimental data on Saito et al's perfusion measurements were available (Table 3.13), the perfusion induced changes in sodium currents in all four backgrounds, with and without G298S mutation, were quantified. Perfusion/mechanical stimulation is known to consistently alter the sodium currents and can be quantified using two metrics, an amplitude scaling factor and a time scaling factor, as shown below:

$$I_{Na}^{mec} = A_{sf} I_{Na} \left(\frac{t}{T_{sf}} \right), \tag{3.61}$$

where I_{Na}^{mec} is the sodium current measured under mechanical stimulation, I_{Na}

is the baseline sodium current which is a function of time t; A_{sf} is the

amplitude scaling factor while T_{sf} is the time scaling factor. The baseline

sodium current can be mapped to the mechanically stimulated sodium current

through these two scaling factors. Table 3.22 shows the averaged values of the

amplitude and time scaling factors for each of the eight sodium channel

variants (derived from the before-and-during perfusion data, and the after-and-

during perfusion data). Note that the values of the scaling factors are

independent of the clamping voltage. The results in Table 3.22 were re-

expressed graphically in Figure 3.43 to aid analysis.

Table 3.22. Scaling factors for the mechanically stimulated sodium channels.

Sodium channel variant number	Sodium channel variant	Average amplitude scaling factor, A_{sf}	Average time scaling factor, T_{sf}
1	V1_WT	1.5905	0.81755
2	V1_MT	1.4293	0.85976
3	V2_WT	1.3557	0.80684
4	V2_MT	1.3997	0.82005
5	V3_WT	1.2407	0.86214
6	V3_MT	1.6506	0.87174
7	V4_WT	1.2523	0.82643
8	V4_MT	1.5424	0.83956

It was observed from Table 3.22 and Figure 3.43, that the time scaling factor

appeared relatively constant with values that indicated accelerated kinetics,

under perfusion, for all eight variants. Greater fluctuation in the amplitude

scaling factors was observed. The amplitude scaling factor was reduced in the

presence of mutation for the most common H558/Q1077del background.

However, for all the remaining three backgrounds, the amplitude scaling factor

was higher in the presence of mutation. This implies that the mutation was

only able to reduce the mechanosensitivity of the sodium channels in the most

common background of H558/Q1077del, while appearing to provide resistance against a reduction in mechanosensitivity in the other three backgrounds. The initial experimental findings by Saito et al also determined that the G298S mutation reduced mechanosensitivity only in the most common background of H558/Q1077del [15].
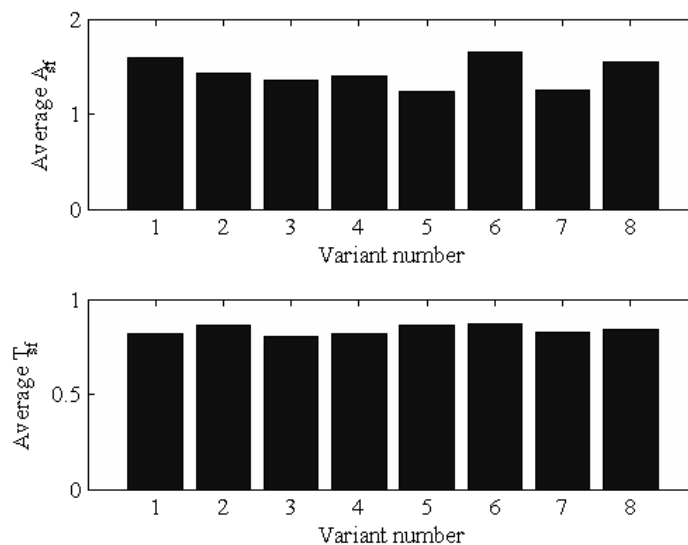
Figure 3.43. The average amplitude and time constant scaling factors for WT and G298S states of each of the four backgrounds were compared graphically. Refer to Table 3.22 for more details.

In terms of experimental data analysis, here, the peak sodium current from all 24 clamping voltages were identified from the HEK-293 cells, before, during and after perfusion. The amplitude scaling factor for each cell was derived by dividing the maximal peak sodium current from the mechanically activated sodium channels, with the corresponding peak sodium current from either before or after perfusion. Subsequently, with the amplitude scaling factors, optimization was performed to parameterize the time scaling factors for each HEK-293 cell. The amplitude and time scaling factor results were checked by comparing the scaled sodium current time traces (for both the before and after

perfusion results) against the corresponding mechanically activated sodium currents, for all 24 clamping voltages. The scaling factors for each cell were averaged as shown in Table 3.22 and Figure 3.43. It would be interesting for future studies to examine how the functional effects of the G298S mutation are conferred to the sodium channels of the various common backgrounds under stretch conditions.

The amplitude and time constant scaling factors reported here are useful to derive a set of parameter values for each of the eight Markov sodium channel models. In turn, these models can be used to examine the effects of G298S mutation on cellular electrophysiology under perfusion or mechanical activation. Briefly, to derive the parameter values, the '*A*' parameter of each exponential rate equation (i.e., Eq. 3.44) is to be divided by the time constant scaling factor, while the maximum sodium channel conductance is multiplied by the amplitude scaling factor. Because the time scaling factor values are smaller than one, perfusion or mechanical stimulation should accelerate the activation and inactivation of the sodium current in all backgrounds, mutation or not. This, alone, implies that the sodium current will be reduced, which is not expected to significantly alter cellular electrophysiology of the ICC and SMC. As for the amplitude scaling factors that were increased in the presence of the mutation, the resulting mechanically modulated sodium current should become larger compared to unperturbed conditions, and hence possess a greater potential in altering cellular electrophysiology. Mechanosensitivity altered by mutation may therefore possibly contribute to GI motility disorders.

3.9   Modelling $K_v 1.1$ potassium channel and its mutation

A variety of voltage gated potassium channels, which are found in the GI ICC and SMC, typically constitutes a significant efflux of potassium ions that modulates cellular excitability. However, there are no known experimental studies on potassium channel mutations as a cause for GI motility disorders. Nevertheless, gastrointestinal motility disorders are heterogeneous and complex, multiple factors can serve a subset of patients. It is therefore possible that a potassium channel mutation in the GI ICC and/or SMC may contribute to GI disorders. Hence, there is an interest here to examine the impact of a known potassium channelopathy of another body system, in the context of the GI tract. A missense mutation, I177N of the $K_v 1.1$ voltage-gated potassium channel, known to cause episodic ataxia by affecting the central and peripheral nervous system, was chosen for this study [177]. $K_v 1.1$ channels are known to exist in the GI ICC but not the SMC [178].

The $K_v 1.1$ channel is a quaternary protein comprising four identical protein subunits. Figure 3.44 shows a protein subunit with the predicted location of the I177N mutation; four such subunits form a mutated $K_v 1.1$ channel. Segment 4, S4, of a $K_v 1.1$ subunit is the membrane voltage sensor which can interact with other subunit segments, and lead to a variety of conformational states depending on the membrane voltage.
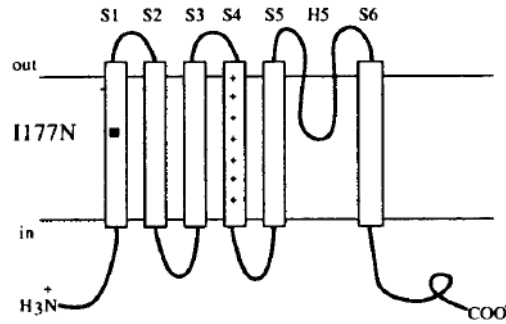
Figure 3.44. A $K_v1.1$ subunit that consists of six transmembrane segments. The I177N mutation is putatively located in segment 1 of the subunit. Four such subunits can assemble to form a quaternary $K_v1.1$ protein channel capable of conducting potassium ions. Picture is adapted from Imbrici et al [177].

The activation and deactivation of the S4 voltage sensor from each subunit in a channel was defined to follow the Hodgkin-Huxley kinetics. This means a $K_v1.1$ channel can exist in sequential states of four deactivated S4 segments to three, two, one and zero deactivated S4 segments. The corresponding rate transition values, in this forward direction, are therefore defined by applying the appropriate integer multiple on a basal rate transition value; this is likewise for the backward direction where four activated S4 segments deactivate sequentially. Additionally, the $K_v1.1$ tetramer is thought to behave cooperatively, that is, the tetramer can exist in a closed-oriented un-relaxed state or in open-oriented relaxed state, the transition between a closed-oriented state to its corresponding open-oriented state depends on the number of activated S4 segments. The more activated S4 segments there are, the faster the transition from the closed-oriented state to the open-oriented state (i.e., a relatively larger value of rate transition). Similarly, the more deactivated S4 segments there are, the faster the transition from the open-oriented state to the closed-oriented state. Because of these behaviours, the Monod-Wyman-Changeux topology and kinetics as discussed in McCormack et al's work were

adopted [179]. Figure 3.45 shows the simplified topology diagram for the $K_v1.1$ channel. Basically, it contains an upper tier of closed-oriented un-relaxed states and a lower tier of open-oriented relaxed states. It is only when the channel is in the O state that it conducts potassium ions. The horizontal rate transitions follow Hodgkin-Huxley kinetics while the vertical rate transitions follow cooperative behaviour. These are incorporated by applying the appropriate multiplier values on the common rate transition equations.
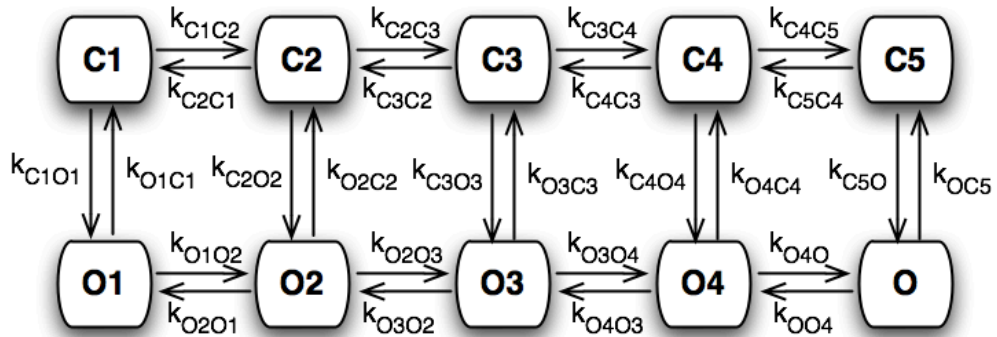
Figure 3.45. The model topology chosen for $K_v1.1$ channel. Upper tier states are closed-oriented un-relaxed states while lower tier states are open-oriented relaxed states. Here, O is defined to be the state that the channel conducts potassium ions. The channel kinetics, i.e., the forward/backward and upward/downward transition rates follow the Hodgkin-Huxley behaviour and cooperative behaviour, respectively. The rate equations are found in Eqs. 3.62 to 3.94.

The equations that define the $K_v1.1$ model are found in Eqs. 3.62 to 3.94; I_{Kv11} describes the total $K_v1.1$ current computed from the maximum conductance, G_{Kv11}, the open probability, $O,$ and the potential difference comprising membrane voltage, V_m, and potassium reversal potential, E_K. α, β, δ and γ are common rate equations to be expressed with the appropriate multiplier in accordance to the prescription of the Hodgkin-Huxley and cooperative mechanisms. k_B is the Boltzmann constant and T is the

temperature that the $K_v1.1$ channels operate under. $p1$ to $p7$ are parameter values to be to be fitted to experimental data. Since the $K_v1.1$ model was used to describe both the wild-type and I177N homomeric channels, therefore two sets of parameter values were obtained. The experimental data, recorded from human $K_v1.1$ expressed in Xenopus Oocytes, which was presented in Figures 2 and 3 of Imbrici et al's paper were digitized and utilized to parameterize the wild-type and mutation models [177].

$$I_{Kv11} = G_{Kv11}O(V_m - E_K), \tag{3.62}$$

$$\propto = p1 exp\frac{p2V_m}{k_BT}, \tag{3.63}$$

$$\beta = p3 exp\frac{p4V_m}{k_BT}, \tag{3.64}$$

$$\delta = p5, \tag{3.65}$$

$$\gamma = p6, \tag{3.66}$$

$$\varphi = p7, \tag{3.67}$$

$$k_B = 8.617e - 5, \tag{3.68}$$

$$k_{C1C2} = 4 \propto, \tag{3.69}$$

$$k_{C2C3} = 3 \propto, \tag{3.70}$$

$$k_{C3C4} = 2 \propto, \tag{3.71}$$

$$k_{C4C5} = \propto, \tag{3.72}$$

$$k_{C2C1} = \beta, \tag{3.73}$$

$$k_{C3C2} = 2\beta, \tag{3.74}$$

$$k_{C4C3} = 3\beta, \tag{3.75}$$

$$k_{C5C4} = 4\beta, \tag{3.76}$$

$$k_{O1O2} = 4\varphi \propto, \tag{3.77}$$

$$k_{O2O3} = 3\varphi \propto, \tag{3.78}$$

$$k_{O3O4} = 2\varphi \propto, \tag{3.79}$$

$$k_{C4O} = \varphi \propto, \tag{3.80}$$

$$k_{O2O1} = \frac{\beta}{\varphi}, \tag{3.81}$$

$$k_{O3O2} = \frac{2\beta}{\varphi}, \tag{3.82}$$

$$k_{O4O3} = \frac{3\beta}{\varphi}, \tag{3.83}$$

$$k_{OO4} = \frac{4\beta}{\varphi}, \tag{3.84}$$

$$k_{C1O1} = \frac{\gamma}{\varphi^4}, \tag{3.85}$$

$$k_{C2O2} = \frac{\gamma}{\varphi^3}, \tag{3.86}$$

$$k_{C3O3} = \frac{\gamma}{\varphi^2}, \tag{3.87}$$

$$k_{C4O4} = \frac{\gamma}{\varphi}, \tag{3.88}$$

$$k_{C5O} = \gamma, \tag{3.89}$$

$$k_{O1C1} = \delta\varphi^4, \tag{3.90}$$

$$k_{O2C2} = \delta\varphi^3, \tag{3.91}$$

$$k_{O3C3} = \delta\varphi^2, \tag{3.92}$$

$$k_{O4C4} = \delta\varphi, \tag{3.93}$$

$$k_{OC5} = \delta. \tag{3.94}$$

Table 3.23 shows the parameter values that define the equations for the wild-type and I177N K_v1.1 models, while Figures 3.46 and 3.47 contain the results of the model predictions compared against experimental data for the wild-type and mutation models respectively [177]. As the K_v1.1 channels were found to be present in the GI ICC and not the SMC, the K_v1.1 models were investigated in the Corrias and Buist single cell model of GI ICC [108].

Table 3.23. Parameter values of the wild-type and I177N K_v1.1 models.

Parameter	Wild-type model	I177N model
p1	0.2271	0.0259
p2	0.0010	0.0025
p3	0.0295	0.0428
p4	-0.0008	-1.6261e-4
p5	0.2158	1.4533e-5

p6	0.0368	0.8798
p7	12.0000	12.0000
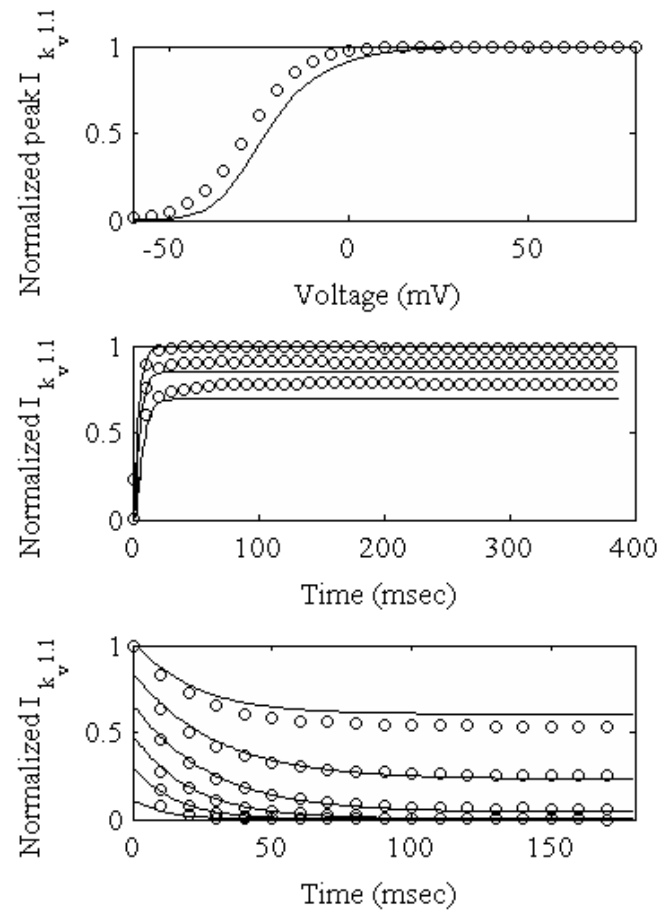
Figure 3.46. Validation results for the wild-type $K_v1.1$ model; solid lines refer to model predicted results while circles refer to experimental results. Top panel compares the results for normalized peak tail $K_v1.1$ currents against clamping voltage. Middle panel compares the activation time course for the $K_v1.1$ currents normalized against the peak current for the clamping voltages of 20 mV (lowest trace), 40 mV and 60 mV (highest trace). Bottom panel compares the deactivation time course for the $K_v1.1$ currents normalized against the peak current for the clamping voltages of -20 mV to -70 mV (interval of 10 mV); in the results, the higher the $K_v1.1$ trace, the more depolarized its corresponding clamping voltage is (for example, the top trace is for -20 mV and the bottom most trace is for -70 mV).

Figure 3.48 shows the simulation results of the ICC membrane potential for three different configurations of the $K_v1.1$ models in the ICC model. These are 100% wild-type $K_v1.1$ channels which represent wild-type homozygosity, 100% I177N $K_v1.1$ channels which represent mutation homozygosity, as well

as 50% wild-type-50% I177N channels which represent heterozygosity. The

simulation results of the ICC membrane voltage are consistent with the I177N
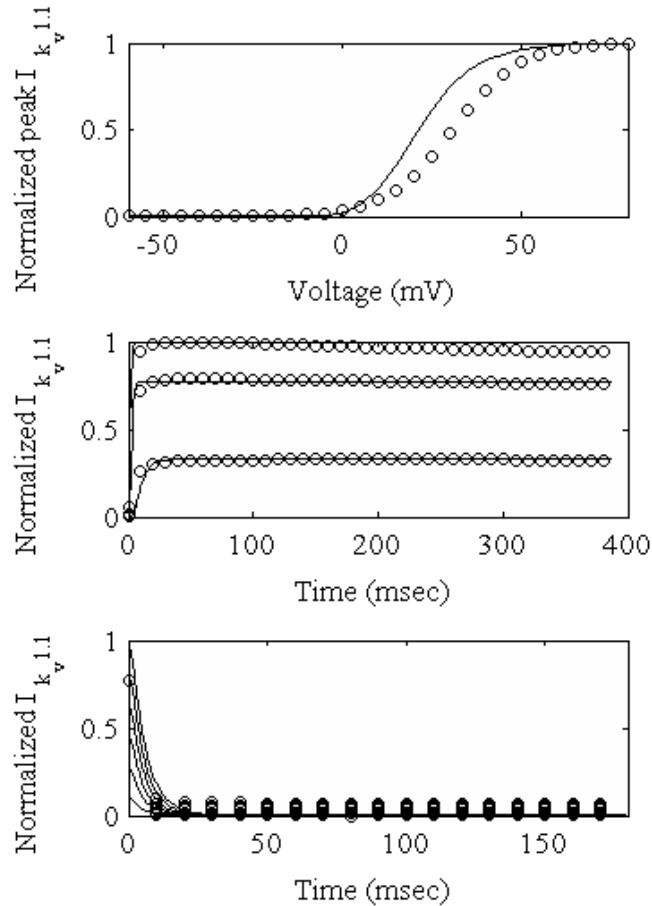
Figure 3.47. Validation results for the I177N mutated $K_v1.1$ model; solid lines refer to model predicted results while circles refer to experimental results. Top panel compares the results for normalized peak tail $K_v1.1$ currents against clamping voltage. Middle panel compares the activation time course for the $K_v1.1$ currents normalized against the peak current for the clamping voltages of 20 mV (lowest trace), 40 mV and 60 mV (highest trace). Bottom panel compares the deactivation time course for the $K_v1.1$ currents normalized against the peak current for the clamping voltages of -20 mV to -70 mV (interval of 10 mV); in the results, the higher the $K_v1.1$ trace the more depolarized its corresponding clamping voltage is (for example, the top trace is for -20 mV and the bottom most trace is for -70 mV).

mutation being a loss-of-function mutation. In the presence of 50% mutation,

the membrane voltage was less polarized than the result for no mutation. At

100% mutation, the membrane voltage was depolarized to an almost steady

value. Therefore, in general, the greater the mutation population, the weaker

the $K_v1.1$ current, and thus, the more the ICC depolarizes. Figure 3.49 then shows the corresponding results of the $K_v1.1$ currents. At 100% wild-type, the $K_v1.1$ current was greater than the current at heterozygosity (for about 4 s after the start of each period of the $K_v1.1$ current), while the current at 100% mutation presented an almost flat morphology with values that were generally the smallest of all three configurations. The appearance of an apparently flat current for the case of 100% mutation could be attributed to the mutated $K_v1.1$ channel being highly inactive over the plateau voltages and the absence of wild-type channels to assist repolarization (unlike the heterozygous situation); the $K_v1.1$ current and thus the ICC voltage became fixated at an almost steady value.

The results of this work demonstrated that the I177N mutation, if present in the GI ICC, is capable of altering the membrane voltage dramatically. Since ICC depolarizes the passive SMC, it is expected that a drastic change in SMC membrane voltage will arise. In turn, this may result in adverse changes in mechanical activity of the GI smooth muscles that can lead to abnormal motility. In addition, although the aforementioned statistical study by Locke et al reported no correlation of the cardiac KCNH2-encoded potassium channel mutations with GI symptoms [13], it does not contradict the findings here since the $K_v1.1$ channels are encoded by the KCNA gene and there are no known mutations of the $K_v1.1$ channels that cause cardiac disease [180].
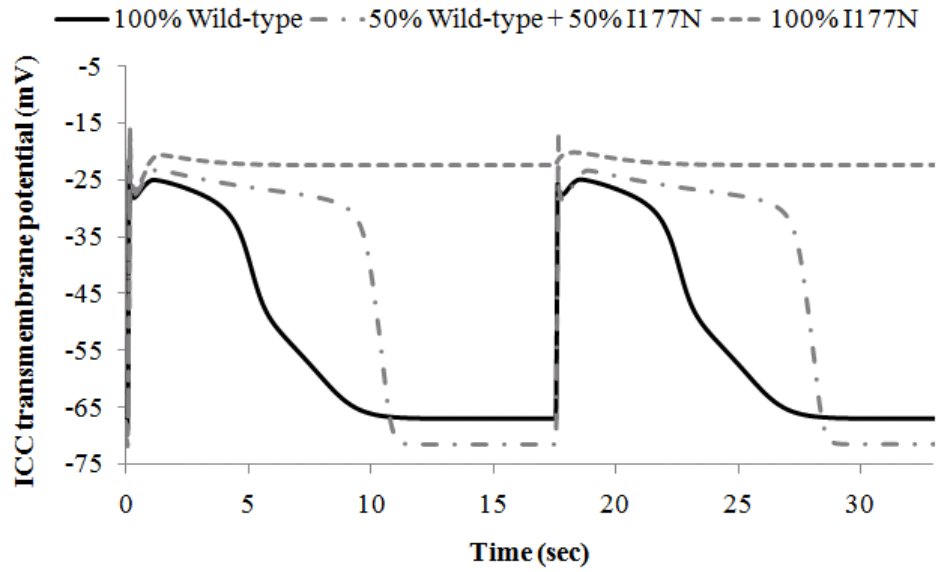
Figure 3.48. Simulation results for gastric ICC membrane voltage. The Markov models of wild-type and I177N $K_v1.1$ models were integrated into the ICC model with 100% wild-type channels, 100% mutated channels and 50% wild-type-50% mutated channels configurations.
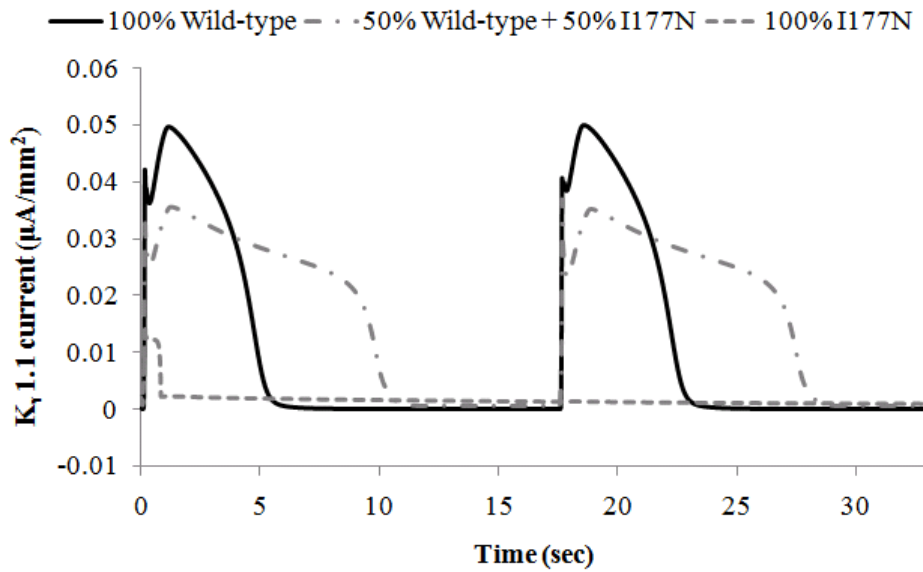
Figure 3.49. The corresponding simulation results of the gastric ICC $IK_v1.1$ currents are shown here.

3.10 Limitations and constraints in ion channel modelling

This chapter has described the various methods of modelling ion channel electrophysiology. The modelling and investigation of a number of sodium channel variants as well as a potassium channel mutation were examined. This last section of this chapter will discuss the limitations and constraints that were realized during the course of ion channel modelling.

Voltage clamp data

Experimental information is crucial to the development of computer models of ion channels. However, it is not always possible to have all the experimental data needed to construct the ideal model. The patch clamp techniques are a common approach to measure the electrical activity of a single ion channel, a cluster of a few ion channels or a population of channels in a single cell, under different clamping configurations and protocols. Typically, single ion channel recordings can yield valuable statistical information such as single channel conductance and channel open duration distribution which can in turn help in the design of an ion channel model topology (i.e., the number and types of main ion channel states) [181]. In the case of R76C modelling, single channel recording was not performed, thus it is not known if the R76C mutation affects single channel conductance which can potentially alter the influence of sodium currents on cellular electrophysiology [14]. For the G298S mutation, it was determined from single channel recordings that the single channel conductance remained unchanged in the presence of mutation, but detailed experimental data was not available [15].

In the case of macroscopic current measurements, such as in whole cell patch clamping, whole cell currents are typically recorded with a clamping protocol designed to characterize the ion channel kinetics. These provide detailed information in the form of a series of ionic current over time recording for each clamping voltage. These detailed current over time information are usually summarized in the form of key metrics such as steady-state or peak ionic current over voltages, characteristic time values such as time to peak or inactivation time constants. While these key metrics serve the good purpose of highlighting channel kinetics, the information may not be sufficient for model construction, such as in Markov modelling. In the case of sodium channel modelling (R76C and G298S), it was fortunate that detailed information were acquired, in stages, from Mayo Clinic collaborators and these were very useful to train parameter values and to validate the models. In the case of $K_v1.1$ channel modelling, detailed information was not available even though attempts were made to obtain the data from the authors.

The issue of detailed experimental data also brings about the question of how much data is sufficient for effective and efficient model construction. Ideally, the experimental data would be divided into two groups, one group to train the parameter values, and the other group to serve as data to validate model predictions. For the case of G298S modelling, voltage clamp experiments were carried out over a wide range of conditions, therefore providing enough data for parameter training and for validation. However it is not always the case where sufficient experiments were performed to give enough data for model construction, which was the case for the R76C study.

The ability of ion channel models to do a good job in describing experimental observations in both general metrics and detailed data, does not guarantee that the models are always able to extrapolate well into native conditions that are not covered by the conditions from which the training and validation data were measured. Two caveats are:

(1) The models are built on experimental data measured from standard voltage clamp conditions and therefore can make good predictions on the ion channel behaviour under the same or similar voltage clamp conditions. In the native environment, the presence of effects from a multitude of sub-cellular mechanisms leads to a more dynamic variation in membrane potential behaviour, the ion channel models may therefore not realistically reflect its in situ behaviour. Another consideration is that the experimental data used to construct the sodium channel models were recorded with holding voltages that were generally more negative than the gastrointestinal slow wave resting voltages (for example -90 mV and -100 mV). Despite this, such a choice of holding voltage in the activation voltage clamp protocol facilitates the steady inactivation of the sodium channels to properly characterize the channel activation kinetics. On the other hand, the use of more depolarized holding voltages nearer to the slow wave resting voltages following the same voltage clamping protocol, though closer to the physiological conditions, does not provide for steady channel inactivation. Furthermore, as observed from the G298S data, the signal-to-noise ratio is significantly greater at these depolarized holding voltages. Therefore, to examine channel properties using

a more depolarized holding voltage necessitates a re-design in the clamping protocol.

(2) There are a number of approaches to characterize ion channels with patch-clamping. Single cells can be dissected from its native tissue and, with appropriate conditions currents through specific type/s of ion channels can be measured. Depending on availability, native cells may come from human tissue in the form of surgical waste or from animal models. The desired cell type can also be cultured for patch clamp experiments. Alternatively, transfection of genes encoding ion channels can be performed on expression systems such as HEK-293 cells, Xenopus oocytes and CHO cells with voltage clamping subsequently performed on these cells to record the ionic currents. The choice is sometimes dependent on factors such as the availability of human tissue, presence of specific ion channel type in an animal cell, phenotype development and maintenance in dissociated or cultured cells. Differences can and do exist in the ion channel kinetics recorded from these different sources. If the aim is to model human ion channels to develop a human cellular model, then experimental data from HEK-293 cells transfected with the human ion channel may not necessarily reflect the actual behaviour in the native milieu of the human cell. Cellular differences such as regulation of ion channel expression and turnover, as well as the presence or absence of auxiliary protein subunits can lead to a phenotype unlike that in the native cell. For instance, beta subunits are known to modulate cardiac sodium channel behaviour but are not expressed in the HEK-293 cells that have been commonly used to measure sodium currents [182, 183].

Over the course of Markov modelling of ion channels, particularly for the sodium channels, it was realized that information such as open probability over time, single channel conductance and number of channels in a cell are critical towards developing a good ion channel model. Because the experimental data to construct the sodium channels were measured from HEK-293 cells, one inherent uncertainty is the density or maximum conductance of these channels in the HEK-293 cells versus the native environment (i.e., the ICC and SMC). Therefore, a Hodgkin-Huxley based method to derive open probability over time was developed. As for the single channel conductance of the sodium channels, take the example of R76C modelling, it is not known how telethonin (both wild-type and mutated states) affects single channel conductance. These result in uncertainties about the effective maximum conductance of an ion channel population, which can amplify or diminish the effects of mutations or other types of variants and can cause a change in the outcome of the simulation predictions. One approach to overcome this is through the use of fluctuation analysis [184-187] which requires experimental data that has recorded repeated measurements from the same cell under the same protocol. Fluctuation analysis taps on the statistical properties of noisy experimental data to mine specific properties of an ion channel type in a cell. The non-stationary fluctuation analysis as demonstrated by Sigworth [187] derived important information of single channel current, open probability over time and the total number of channels in the system. Unfortunately, such non-stationary fluctuation analysis was not possible for the experimental data provided for this research work, since measurements were not made

repeatedly on the same cells. No explicit demand for such recordings and/or the challenge of maintaining cellular viability under repeated measurements might explain the absence of such experimental data. The details of non-stationary fluctuation analysis are available in Appendix 13.

One should also be mindful of the experimental errors that can affect the quality of experimental data being recorded. Series resistance offered by electrode tip can create an apparent shift in clamping voltage which may go up to as big as 20 mV (imagine a horizontal translation of the I-V plot), this can affect voltage-dependency described by the models. Errors can also arise in the time domain due to the limitations of Bessel filtering of the electrical signals recorded by patch-clamping. For example, a 10 kHz filter can result in up to 0.5 ms of error. Such errors can be significant for fast currents such as sodium in which the peak sodium current occurs in a time scale of an order close to such an error. Cell viability can also affect the quality of data, and one indicator is the reversal potential, where a non-physiological accumulation of ions shifts the reversal potential unnaturally.

Biological considerations

From a biological point of view, several factors may contribute to ion channel physiology and potentiate or diminish a mutation's effect on an ion channel. The following aims to raise awareness of some situations, most of which were not possible to incorporate in the existing computational framework, which can affect ion channel phenotype.

(1) Regulation of ion channels

The number of ion channels is regulated by a number of mechanisms such as the expression, trafficking, localization, and the degradation of ion channels. The number of active channels in turn affects the ion channels' influence on cellular behaviour. Dys-regulation can therefore be pathogenic. Figure 3.50 provides an example of the regulation of cardiac sodium channels [188]. Ion channel variants (for example, mutations) can affect regulatory processes such as ion channel expression [189], trafficking [190] and can be responsible for secondary effects of long-term expression of mutants [191, 192]. Processes like these can affect the functional phenotype of GI ion channels.
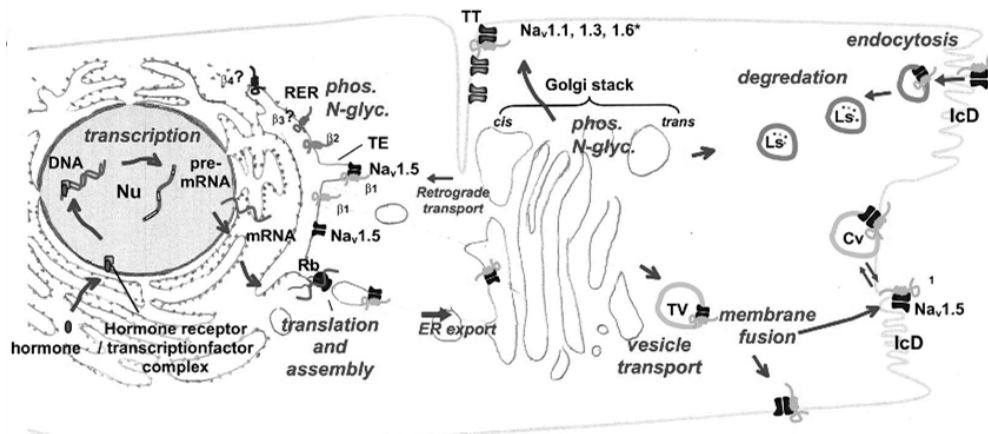
Figure 3.50. Regulation of the expression and trafficking of cardiac Na$_v$1.5 channels. Na$_v$1.1, Na$_v$1.3 and Na$_v$1.6 are found in mice and contribute to less than 5% of sodium currents. Abbreviations: β$_x$, beta subunits of sodium channels; C$_v$, caveolae; IcD, intercalated disk; Ls, lysosome; N-glyc, N-glycosylation; Nu, nucleus; phos, phosphorylation; RER, rough endoplasmic reticulum; TE, tubular element; TT, transverse tubule; TV, transport vesicle. Picture adapted from [188].

(2) Temperature

Gating defects due to mutations could be hidden or be less pronounced in the temperatures the experiments are performed under [193, 194]. To overcome this, voltage clamp experiments can be performed over the physiological (and even pathophysiological) temperature range of the human body where possible;

it is understandable that lower temperatures are sometimes used in experimental studies to reduce the rate of fast ion channels to aid measurement.

(3) Auxiliary elements

Auxiliary elements of ion channels are native/endogenous proteins that significantly augment the ion channel functions, but do not form the ion-carrying pore of a channel. Examples include beta, delta and gamma subunits that can affect channel gating properties as well as regulation such as turnover and localization [195]. For sodium channels, the alpha subunit is sufficient for function but these channels are known to be modulated by auxiliary proteins [196] such as telethonin [14], syntrophin [158], cytoskeleton [159] and beta subunits which are argued to be necessary for normal kinetics and voltage dependence of gating [197-199]. Auxiliary proteins are also known to alter voltage-gated potassium channels [200, 201] such as beta subunits [202, 203], and G proteins [204, 205]. Unfortunately, such auxiliary elements are not necessarily present in the expression systems used for voltage clamp experiments, therefore experimental design should consider the co-expression of auxiliary elements. The work of Wang et al is an example where the cardiac sodium beta-1 subunit was co-transfected with the cardiac sodium alpha subunit into a mammalian cell line (tsA201) for whole cell patch clamp functional characterization, since it was known that the cardiac beta subunits alter the functional characteristics of alpha subunits [206].

(4) Polymorphic-splice variants

Mutations aside, ion channel variations include polymorphisms and alternative splicing. These variants may confer differing biophysical properties on the same ion channels such as altered voltage and calcium sensitivities as well as in the regulation of their expression [15, 173, 207]. These variations also potentially provide resistance against mutagenic variations [208] or serve as susceptibility factors that may explain the physiological and pathophysiological states of the GI cells and organs. For example, a novel splice-variant of the ICC pacemaking calcium-activated chloride conductance found in diabetic samples may serve as a potential molecular drug target for diabetic gastroparesis [58, 209]. Additionally, ion channels and their variants may be expressed differentially across different GI organs and sometimes across different regions of the same organ. These variations and differences should be incorporated into the modelling framework, where necessary and possible, for more realistic predictions and applications [155].

3.11 Chapter summary

The R76C and G298S experimental studies [14, 15] characterized the electrical behaviour of the wild-type and mutation affected sodium channels in the HEK-293 cells. However, the effects of these sodium channel related mutations in the GI motility effector cells of ICC and SMC are unknown. This gap was bridged computationally by creating sodium channel models based on the HEK-293 cellular data from these experimental studies. This chapter has discussed the creation of various sodium channel models, and later, these models were integrated into the biophysical single cell models of the gastric

ICC and SMC to obtain insights on the cellular effects of these mutations. In creating the sodium channel models, the traditional Hodgkin-Huxley formalism was initially used to construct three sodium channel models of SCN5A, TCAP and R76C to investigate the cellular consequences of the R76C mutation of the sodium channel interacting protein, telethonin. Although the gross kinetics were well-matched with experimental data, the Hodgkin-Huxley formalism did not allow an adequate description of the inactivation behaviour of the sodium currents during voltage clamp simulations. Therefore the Markov formalism was employed where the sodium channel was described with a six-state topology. Subsequent investigations of the cellular consequences of the R76C mutation in gastric ICC and SMC electrophysiology showed that the R76C mutation was capable of gain-of-function influence on the electrical behaviour of these single cells. However, further work is required to confirm these findings. The same Markov modelling method was applied to model the SCN5A channel and its G298S mutation under four different backgrounds that arose from polymorphism and alternative splicing. Eight Markov models for the wild-type and G298S channels for each of the four backgrounds were constructed and validated against experimental data. Similarly, the G298S mutation models were examined in gastric ICC and SMC models, however the effect of mutation on the cellular electrophysiology was negligible. The $K_v1.1$ channels are known to contribute to GI ICC electrophysiology. To investigate the consequences of a loss of $K_v1.1$ function, models describing the wild-type and I177N mutation $K_v1.1$ channels were created. The results indicated a strong alteration of ICC electrophysiology due to the I177N mutation. All in all, the

simulation results here have shown that the mutations do affect gastric ICC and SMC membrane voltage, which existing experimental studies have not yet been able to demonstrate.

Chapter 4
Single cell modelling

"All models are wrong; some models are useful."
– George Box, statistician

4   Single cell modelling

SCN5A sodium channels have been experimentally identified in the circular smooth muscle of the jejunum in the human small intestine [154, 155]. The R76C and G298S mutations were also correlated with human intestinal disorders [14, 15]. Therefore, it would be pertinent to investigate the sodium channel models describing these two mutations in a human intestine cell model. However, no suitable biophysically based model of an intestinal SMC currently exists. Existing SMC models describe only stomach cells of animals [82, 108] while earlier SMC models by Miftakhov et al [210, 211] and Skinner et al [212] describe the SMC as being self-excitatory which are not consistent with recent findings that the ICC excites SMC. For the small intestine, the existing models are for the non-human ICC [111, 213, 214]. The following presents the development and validation of a novel biophysically based electrophysiological model of a human jejunal SMC (hJSMC). This is followed by an investigation of the consequences of the R76C and G298S mutations in the hJSMC model.

4.1   Model development

4.1.1   Governing Equation

The governing equation of the hJSMC model is based on the classical Hodgkin-Huxley approach that describes the cell membrane as a parallel conductance circuit. It is given by:

$$\frac{dV_m}{dt} = -\frac{I_{ion} + I_{Stim}}{C_m},$$
(4.1)

where V_m is the cellular membrane potential, t is the time, C_m is the cell membrane capacitance and I_{Stim} is an externally applied stimulus, usually provided by the ICC. C_m was chosen to be 50 pF, which is within the reported range of 39 to 65 pF for human jejunal myocytes [215-217]. I_{ion} is the sum of the ionic currents crossing the membrane and is given by:

$$I_{ion} = I_{CaL} + I_{CaT} + I_{Kv} + I_{BK} + I_{Na} + I_{NCX} + I_{NaK} + I_{NS},$$
(4.2)

where I_{CaL} and I_{CaT} are L-type and T-type calcium (Ca^{2+}) currents respectively, I_{Kv} is the voltage-dependent potassium (K^+) current, I_{BK} is the large conductance Ca^{2+} and voltage activated K^+ current, I_{Na} is the sodium (Na^+) current, I_{NaK} is the Na^+-K^+ pump, I_{NCX} is the Na^+-Ca^{2+} exchanger and I_{NS} is a non-selective leakage current. Figure 4.1 shows a schematic of the hJSMC model while the complete mathematical description of the model can be found in Appendix 14.
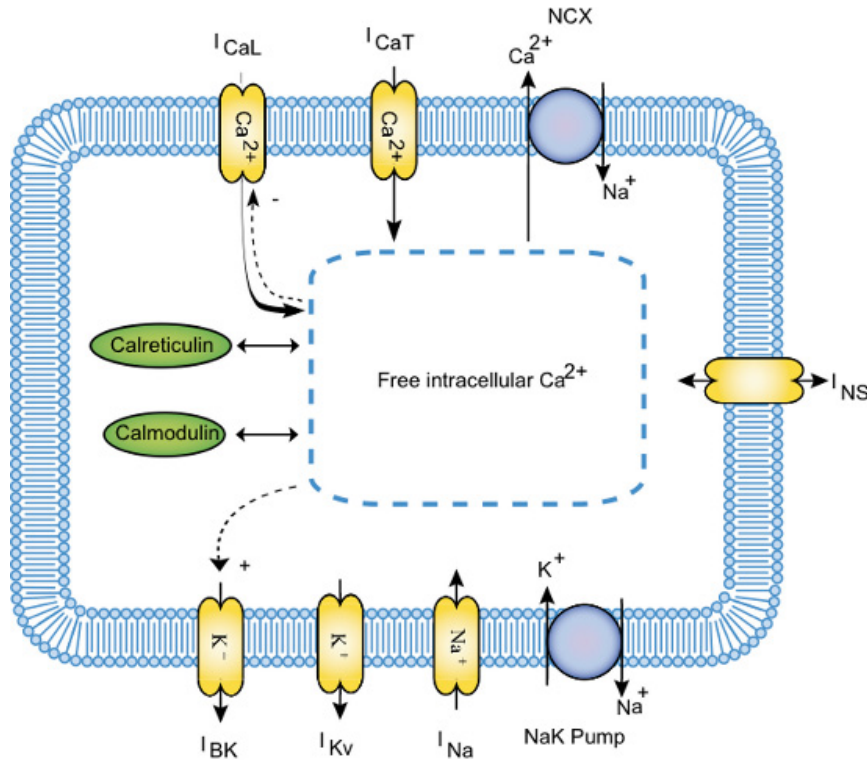
Figure 4.1. The hJSMC model schematic containing the ionic conductances and sub-cellular mechanisms that critically influence cellular potential of the hJSMC. See the text for a detailed description of the components.

4.1.2   Ionic current descriptions

The protein ion channels in the model are described by the traditional Hodgkin-Huxley method or the deterministic Markov method (see Chapter 3 for details). Here, it was determined that I_{CaL}, I_{BK} and I_{Na} were better described by the Markov method while I_{CaT}, I_{Kv} and I_{NS} were adequately described by the Hodgkin-Huxley method. Details for each of the ionic conductances and sub-cellular mechanisms are provided below.

4.1.3   L-type Ca^{2+} channels

I_{CaL} is carried by L-type Ca^{2+} channels which have been identified in human jejunal smooth muscle. These channels are considered the main pathway for

Ca^{2+} entry [218, 219]. A Markov formulation was chosen using a topology proposed by Faber et al as shown in Figure 4.2 [220].
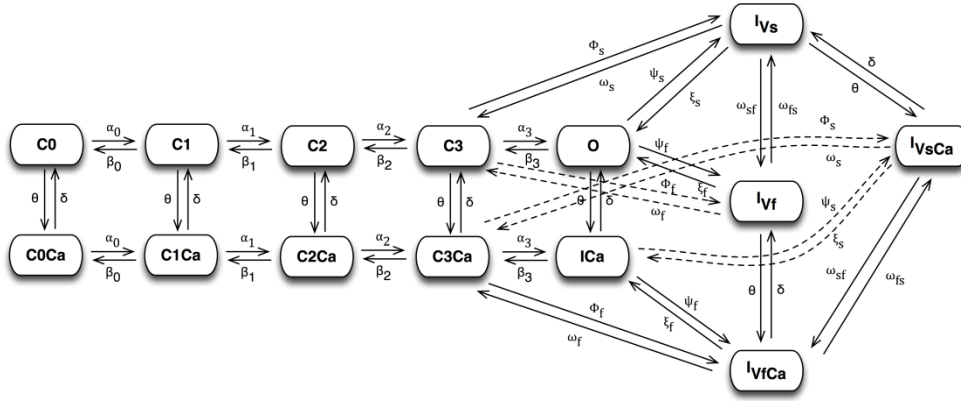
Figure 4.2. L-type Ca^{2+} channel model topology. Prefixes *C, I,* O denote closed, inactivated and open states respectively; suffixes *Ca, V, f,* s found in some of the states refer to calcium-bound, voltage-dependent, fast, and slow properties of these states, respectively. The topology was designed to best describe observed characteristics of the L-type Ca^{2+} channels.

The states and transitions were determined to incorporate experimentally characterized features of the L-type Ca^{2+} channels. The rate equations describing the state transitions depend on either V_m or $[Ca^{2+}]_i^{free}$. The kinetics of the human jejunal L-type channels were characterized through transfection of α$_{1C}$ and β$_2$ subunits into HEK-293 cells [221]. Here, the model parameters were fitted to replicate the experimental data of Lim et al [221] by imposing the same experimental conditions in the simulations. Voltage clamp was simulated with Ba^{2+} as the charge carrier, at an extracellular concentration of 10 mM. The presence of 2 mM EGTA in the pipette solution was simulated by switching off the Ca^{2+} dependency in the relevant transitions. The I_{CaL} equation is given by:

$$I_{CaL} = G_{CaL} P_O (V_m - E_{Ca}),$$

(4.3)

where G_{CaL} is the maximum conductance with a value of 1.44 nS, P_O is the open probability obtained by solving the Markov model, and E_{Ca} is the Nernst potential for Ca^{2+} ions. The predicted normalized current-voltage I-V plot was found to match well with experimental data as shown in Figure 4.3. Figure 4.4 shows the corresponding simulation result of L-type calcium current versus time plots for the clamping voltage range of -90 mV to 30 mV, which exhibited behaviour that agreed with experimental observations [221].
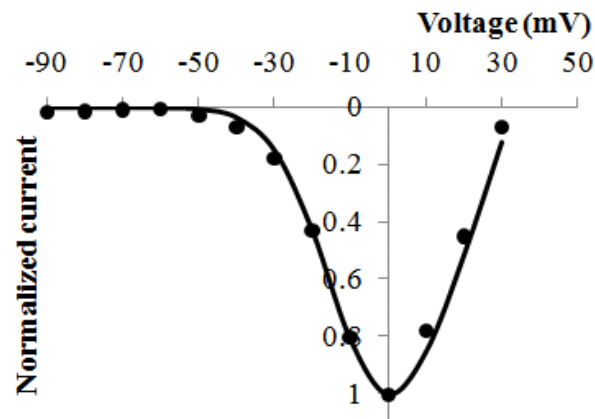
Figure 4.3. Normalized peak current versus voltage (I-V) plot for L-type calcium channels shows a good match between experimental data in dots (from Figure 1b of [221]) and simulated data in solid line.
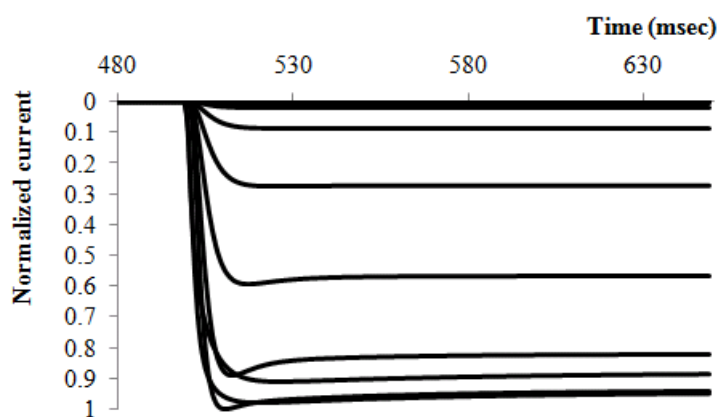
Figure 4.4. The predicted normalized current versus time plots for the L-type calcium channels for the clamping voltage range of -90 mV to 30 mV at a step size of 10 mV.

4.1.4   T-type Ca²⁺ channels

I_{CaT} are carried by low-voltage activated T-type Ca²⁺ channels which have been identified in the intestinal SMC and ICC from various species through functional differentiation of two distinct Ca²⁺ currents [222] and genetic expression studies [223]. Its expression in the human jejunum is less clear. Farrugia et al observed that nifedipine completely abolished inward currents in freshly isolated human jejunum cells which suggests that only L-type channels may be present. However, the possibility of "another Ca²⁺ channel type with low channel density and/or low open probability" was not excluded in the same study [217]. Therefore, the decision was to include T-type Ca²⁺ channels, albeit with a substantially lower whole cell conductance than for the L-type Ca²⁺ channels. The T-type currents were characterized by:

$$I_{CaT} = G_{CaT} d_{CaT} f_{CaT} (V_m - E_{Ca})$$

(4.4)

where G_{CaT} is the maximum conductance with a value of 0.0425 nS while d_{CaT} and f_{CaT} are the Hodgkin-Huxley activation and inactivation gating variables respectively. The parameters that characterize d_{CaT} and f_{CaT} were optimized to replicate the experimentally recorded kinetics in HEK-293 cells transfected with human Ca$_v$3.1 T-type Ca²⁺ channels [224]. The normalized I-V result agreed well with the experimental data as shown in Figure 4.5. Figure 4.6 shows the corresponding simulation result of T-type calcium current versus time plots for clamping voltage range of -90 mV to 30 mV which exhibited behaviour that also agreed with experimental observations [224].
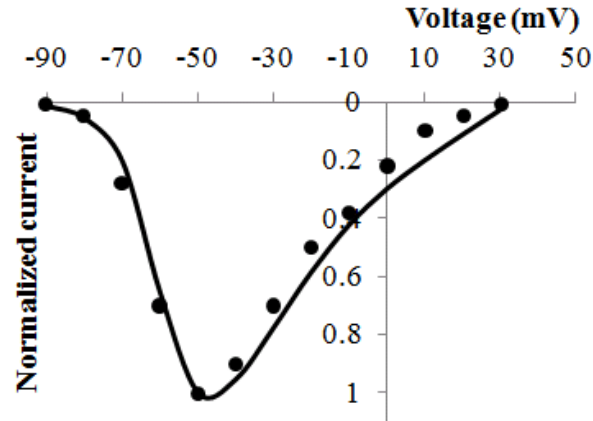
Figure 4.5. Normalized peak current versus voltage (I-V) plot for T-type calcium channels shows a good agreement between experimental data in dots (from Figure 1b of [224]) and model data in solid line.
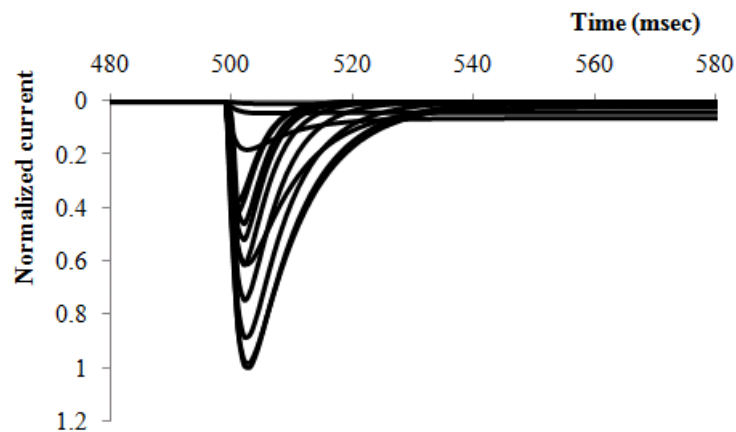
Figure 4.6. The predicted normalized current versus time plots for the T-type calcium channels for the clamping voltage range of -90 mV to 30 mV at a step size of 10 mV.

4.1.5   Voltage dependent K$^+$ channels

Voltage gated K$^+$ channels have been discovered and functionally characterized in many SMC along the GI tract (see [69] for review). The voltage dependent whole cell K$^+$ current was measured and characterized in freshly isolated human jejunal myocytes. In the model, such a current is described by the following equation:

$$I_{Kv} = G_{Kv} x_{Kv} y_{Kv} (V_m - E_K),$$

$$(4.5)$$

where G_{Kv} is the maximum conductance with a value of 1.0217 nS while x_{Kv} and y_{Kv} are the Hodgkin-Huxley activation and inactivation gates respectively, and E_K is the Nernst potential for K^+ ions. The model parameters were optimized in simulations that followed the same voltage clamp protocol used in the experiments performed by Farrugia et al on the human jejunum smooth muscle [225]. The model predictions agreed well with experimental data for the normalized I-V results over the physiological range of voltages as shown in Figure 4.7.
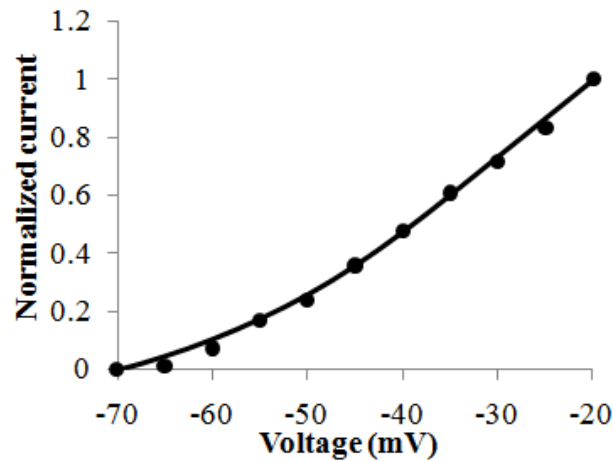
Figure 4.7. Normalized I-V plot of whole cell currents. A good agreement between model data (solid line) and experimental data (dots) from the human jejunal myocytes (from Figure 9 of [225]).

4.1.6 Ca^{2+} and voltage activated K^+ channels

The Ca^{2+} and voltage activated large conductance K^+ channels (BK) channels are found in the GI smooth muscles of several species [226-229, 234], and their high conservation across multiple species suggests the importance of such channels. Initial evidence of the presence of BK in human jejunal SMC is

found in the work of Strege et al [230]. To describe the kinetics of BK, a Markov description was adapted from Cox et al [231]. The model topology describes cooperative Ca^{2+} binding to each of the four alpha subunits of the BK homotetramer while transitions between a pair of closed and open states are voltage dependent (see Figure 4.8).
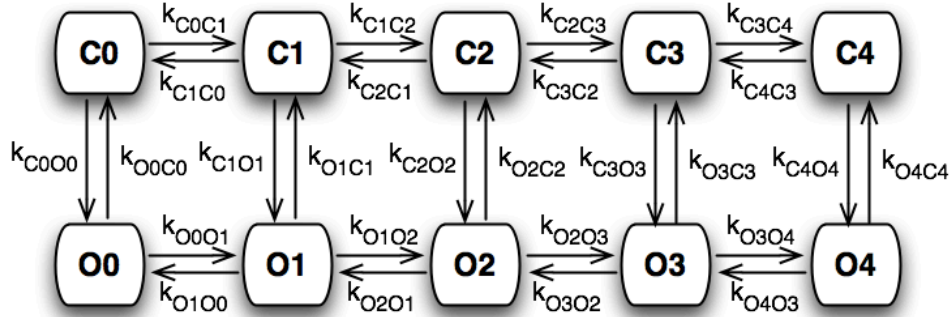
Figure 4.8. A10-state Markov model of homotetrameric BK channel. Upper tier states are various closed conformation states (with prefix *C*) while lower tier states are various open-oriented conformation states (with prefix *O*). In each tier, the horizontal transitions depend on $[Ca^{2+}]_i^{free}$, that reflects cooperative Ca^{2+} binding to each of the four alpha subunits of the BK homotetramer. The membrane voltage dependency is found in the vertical transitions between states. O4 is the conformation state that conducts ions across BK channels under a voltage driving force.

Due to the absence of human intestinal smooth muscle data, the model's parameter values were optimized against the human myometrium smooth muscle data over a voltage range of -70 mV to 60 mV, and over a physiological $[Ca^{2+}]_i^{free}$ range of 100 nM to 1000 nM [232, 233]. The I_{BK} equation is given by:

$$I_{BK} = G_{BK} P_O (V_m - E_K),\qquad(4.6)$$

where G_{BK} is the maximum conductance with a value of 80 nS. Figure 4.9 shows that the model was able to adequately describe experimentally recorded behaviour.

.
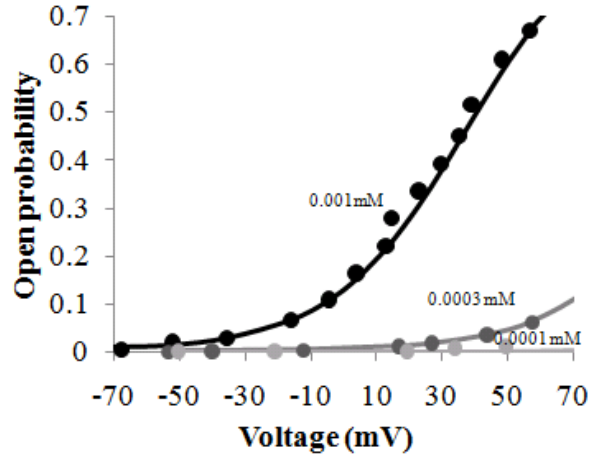
Figure 4.9. Open probability versus clamping voltage plots, across various $[Ca^{2+}]_i^{free}$, from 100 nM to 1000 nM. There is good agreement between experimental data in dots (from Figure 2b of [233]) and data from the BK model in solid lines.

4.1.7 Na$^+$ channels

As discussed in Chapter 3, I_{Na} is carried by the Na$_v$1.5 channels which are expressed in the human jejunal circular SMC [154, 159]. The sodium channel models that were developed in Chapter 3 were selectively integrated into the hJSMC model depending on the objectives. Figure 4.10 gives an example of the simulated wild-type sodium current versus time plots, from the R76C computational study in Chapter 3, which demonstrated realistic behaviour [154]. To investigate the consequences of R76C mutation, the wild-type model of SCN5A was selected and appropriately integrated into the hJSMC, the results of which served as a control to compare against the results of the R76C mutation in hJSMC. This is likewise for the wild-type models and the mutation models of the G298S work. The I_{Na} equation is given by:

$$I_{Na} = G_{Na} P_O (V_m - E_{Na}),$$
(4.7)

where G_{Na} is the maximum conductance with a value of 24.17 nS for the

R76C work and a value of 7.15 nS for the G298S work, and E_{Na} is the Nernst

potential for Na$^+$ ions.
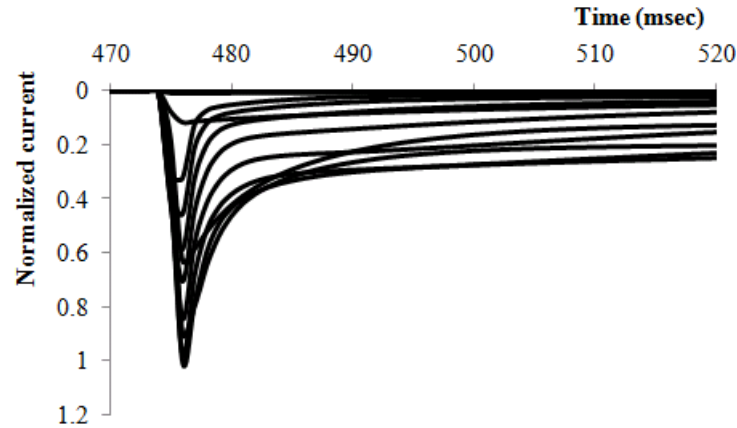
Figure 4.10. The simulated normalized current versus time plots for the wild-type sodium channels, from the R76C work, for the clamping voltage range of -80 mV to 30 mV at a step size of 10 mV.

4.1.8 Pumps and exchangers

Pumps and exchangers are widely known to regulate ionic homeostasis. The

Na$^+$-K$^+$ pump (NaK) is ubiquitous and essential for maintaining a high K$^+$

concentration and low Na$^+$ concentration in a cell but there is little information

for the gastrointestinal NaK pump except for early studies on the guinea-pig

taenia coli [235, 236]. The Na$^+$-Ca^{2+} exchanger, NCX serves to restore the

distribution of Ca^{2+} ionic concentrations across the cell membrane, by

removing Ca^{2+} from cells through the energy released from Na$^+$ influx along

its electrochemical gradient. NCX is also ubiquitous, but not much is known

for the intestinal NCX exchanger. Nonetheless, its presence was demonstrated

through staining in the murine jejunum smooth muscle [237]. Due to the lack

of quantitative data for NaK and NCX, the human cardiac descriptions from

ten Tusscher et al were implemented in the hJSMC model to solve for I_{NaK} and I_{NCX}. The maximum permeability was the only parameter adjusted in the I_{NaK} and I_{NCX} models to achieve homeostasis [171] since the lack of quantitative experimental data made it unsuitable to optimize other parameters of these models. Furthermore, in the original descriptions from the cardiac context, the maximum permeability parameters were also arbitrarily set and not directly supported by experimental findings.

4.1.9 Non-selective leak current

It was reported in single cell studies of the human jejunal smooth muscle that upon inhibition of the dominant outward currents, a non-selective linear leak current with 0 mV reversal potential was revealed. This leak current, I_{NS}, was defined to include both sodium (I_{NS_Na}) and potassium (I_{NS_K}) components. The total channel conductance was determined to be at least 45 fold smaller than the maximum conductance of I_{Kv}.

4.1.10 ICC stimulus current

The passive SMC are excited by the ICC pacemakers through protein gap junctions [238-241]. Here, in the absence of a suitable human ICC model, the ICC excitation is phenomenologically provided by I_{Stim}:

$$I_{Stim} = G_{couple}(V_m - V_m^{ICC}),$$

(4.8)

where G_{couple} represents the total gap junction coupling conductance between

ICC and SMC, while V_m^{ICC} is the membrane potential of the adjacent ICC

which was defined to be:

$$
V_m^{ICC} = \begin{cases} V_{rest}^{ICC} + V_{amp}^{ICC}\left(\dfrac{t}{f_2}\right) & for \quad 0 \le t < t_{peak}^{ICC} \\[2em] V_{rest}^{ICC} + V_{amp}^{ICC}\left(1 + \exp\left(\dfrac{-f_1}{2t_{slope}}\right)\right)\left(\dfrac{1}{1 + \exp\left(\dfrac{t - f_2 - 0.5f_1}{t_{slope}}\right)}\right) & for \quad t_{peak}^{ICC} \le t < t_{plateau}^{ICC} \end{cases}
$$

$$(4.9)$$

The waveform of V_m^{ICC} then appears as shown in Figure 4.11 where V_{rest}^{ICC} is

the ICC potential at the resting phase, V_{amp}^{ICC} is the amplitude of the slow wave

potential, V_{peak}^{ICC} is the peak potential. t_{peak}^{ICC} is the time duration for the upstroke

to take place, and $t_{plateau}^{ICC}$ is the time duration for the plateau phase. Together

they sum up to give the slow wave period, t_{period}.
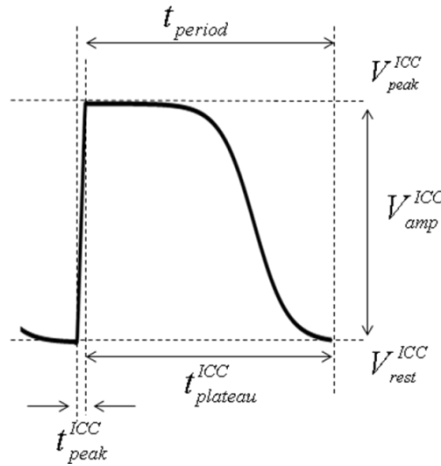
Figure 4.11. A single slow wave of ICC membrane potential, V_m^{ICC} where V_{rest}^{ICC} = -57 mV, V_{peak}^{ICC} =-23.5 mV, t_{peak}^{ICC} =300 ms and $t_{plateau}^{ICC}$ = 9700 ms. Refer to text for further explanation.

The frequency of slow wave activity was 6 cpm (or t_{period} = 10 s) based on experimental recordings from human jejunal myocytes at 6.03 ± 0.33 cpm [46].

4.1.11 Intracellular ionic concentrations

The intracellular concentration of each ionic species affects its Nernst potential which in turn affects the driving force for ionic currents. It is therefore relatively important to track these intracellular concentrations through the following equations:

$$\frac{d[Ca^{2+}]_i^{total}}{dt} = -\left(I_{CaL} + I_{CaT} - 2I_{NCX}\right)\frac{1}{z_{Ca}FV_{cell}}, \tag{4.10}$$

$$\frac{d[K^+]_i}{dt} = -\left(I_{Kv} + I_{BK} - I_{stim} - 2I_{NaK} + I_{NS\_K}\right)\frac{1}{z_K FV_{cell}} \tag{4.11}$$

$$\frac{d[Na^+]_i}{dt} = -\left(I_{Na} + 3I_{NaK} + 3I_{NCX} + I_{NS\_Na}\right)\frac{1}{z_{Na}FV_{cell}} \tag{4.12}$$

where the change in concentrations of each ionic species is a function of all related ionic currents carrying the respective ion type. Here, F is Faraday's constant, V_{cell} is the cell volume, z is the valence of an ion, subscript i refers to the intracellular space and superscript $total$ refers to the total intracellular calcium concentration.

4.1.12 Ca^{2+} buffering

Ca^{2+} buffering proteins exist in the myoplasmic space and bind to calcium ions, leaving a proportion of free unbound intracellular Ca^{2+} ions that can exert regulatory effects on Ca^{2+} sensitive ion channels, such as I_{CaL} and I_{BK},

and can influence the Ca^{2+} Nernst potential [218, 242]. The effects of two known Ca^{2+} buffering proteins were included in the hJSMC model. One is the ubiquitous calmodulin (CaM) expressed in all eukaryotic cells and the other is calreticulin (CRT) found in the cytosol of the jejunal smooth muscle tissue [237]. The equilibrium buffering equation that describes both buffering proteins was derived using the law of mass action and conservation of mass (derivation details can be found in Appendix 15):

$$\frac{d[Ca^{2+}]_i^{free}}{dt} = \frac{d[Ca^{2+}]_i^{total}}{dt} \div \left(1 + \frac{n_{CRT}[CRT]^{total} K_D^{CRT} \left([Ca^{2+}]_i^{free}\right)^{n_{CRT}-1}}{\left(\left([Ca^{2+}]_i^{free}\right)^{n_{CRT}} + K_D^{CRT}\right)^2} + \right.$$
$$\left. \frac{n_{CaM}[CaM]^{total} K_D^{CaM} \left([Ca^{2+}]_i^{free}\right)^{n_{CaM}-1}}{\left(\left([Ca^{2+}]_i^{free}\right)^{n_{CaM}} + K_D^{CaM}\right)^2} \right) ,$$

(4.13)

where $[Ca^{2+}]_i^{free}$ is the free intracellular calcium concentration, n is the hill coefficient, $[CRT]^{total}$, refers to the total buffering protein concentration for calreticulin, $[CaM]^{total}$, refers to the total buffering protein concentration for calmodulin and K_D is the dissociation constant; note that $\frac{d[Ca^{2+}]_i^{total}}{dt}$ from Eq. 4.10 is used in this equation to solve for $[Ca^{2+}]_i^{free}$.

4.1.13 Nernst potentials

The Nernst potential is dependent on intracellular and extracellular concentration of the ionic species. The intracellular concentrations were tracked according to Eqs. 4.10 to 4.13. The Nernst potential in turn affects the driving force that plays a role in determining the magnitude and direction of

ionic currents. Below shows the Nernst potential equations of calcium, potassium and sodium respectively:

$$E_{Ca} = \frac{RT}{z_{Ca}F} \log \frac{[Ca^{2+}]_o}{[Ca^{2+}]_i^{free}} , \tag{4.14}$$

$$E_{K} = \frac{RT}{z_{K}F} \log \frac{[K^{+}]_o}{[K^{+}]_i} , \tag{4.15}$$

$$E_{Na} = \frac{RT}{z_{Na}F} \log \frac{[Na^{+}]_o}{[Na^{+}]_i} . \tag{4.16}$$

4.2 Simulation Results

4.2.1 Slow waves and Ca²⁺ transients

The governing equation for hJSMC slow waves (Eq. 4.1) and its subsidiary equations were solved to obtain V_m over time. An implicit backward Euler method was necessary to solve the Markov descriptions, where the resulting linear system was solved using LU decomposition. For all other differential equations, an explicit forward Euler method was used. A single time step of 0.1 ms was sufficient for convergence and stability of the solution.

The model was able to predict slow waves that are in agreement with experimental recordings under the same conditions (compare Figure 4.12a with Figure 4.12b) [45]. The predicted peak amplitude is 23.88 mV and resting phase potential is -60.20 mV. Figure 4.12c shows the corresponding predicted $[Ca^{2+}]_i^{free}$ is 96 nM at rest and 256 nM at the plateau phase (i.e., an amplitude of 160 nM). Experimental $[Ca^{2+}]_i^{free}$ data for the human intestinal smooth muscle is limited; Bielefeldt et al reported a $[Ca^{2+}]_i^{free}$ value of about

60 nM under resting conditions for the cultured human intestinal smooth muscle cells [243], while Farrugia et al reported a resting $[Ca^{2+}]_i^{free}$ value of about 130 nM and a maximum increase of about 160 nM in $[Ca^{2+}]_i^{free}$ in the jejunal smooth muscle cell [217]. Therefore, the predicted $[Ca^{2+}]_i^{free}$ agrees well with these experimental observations. The stability of the hJSMC model was demonstrated through long term simulation of 30 minutes of electrical activity.
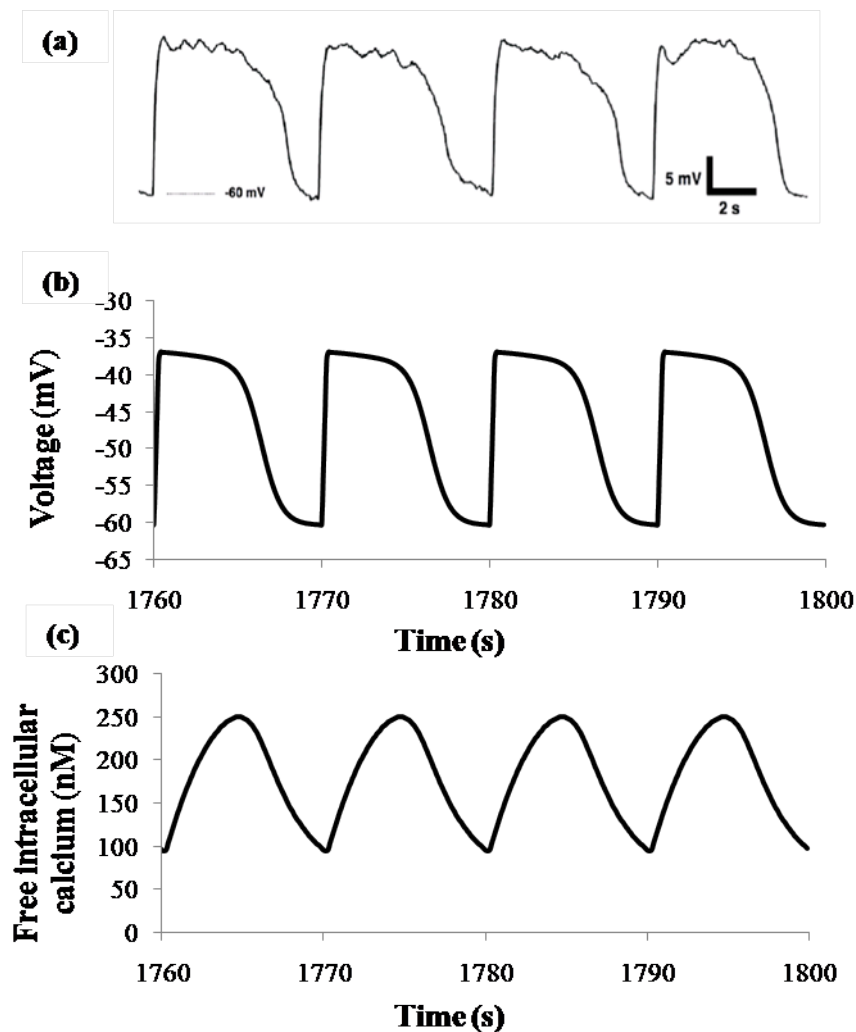
Figure 4.12. hJSMC results. (a) Experimentally recorded hJSMC slow waves, adapted from Lee et al [45]. (b) Simulated hJSMC slow waves after long term simulation of 30 minutes of electrical activity. (c) Predicted free intracellular calcium concentration.

The only other study known to record human intestinal slow waves was performed by Hwang et al [64] and exhibited different metrics from the earlier results by Lee et al [45]. The average frequency was higher at 7.5 cpm, and the amplitude was bigger at about 31 mV with a resting membrane potential of around -64 mV. These differences could arise due to tissue sample differences such as the location of the sample in the small intestine or the relative density of ICC to smooth muscle cells. The hJSMC model was able to replicate the slow waves from Hwang et al with some modification to the original ICC stimulus. The results are compared against the experimental recordings as shown in Figure 4.13.
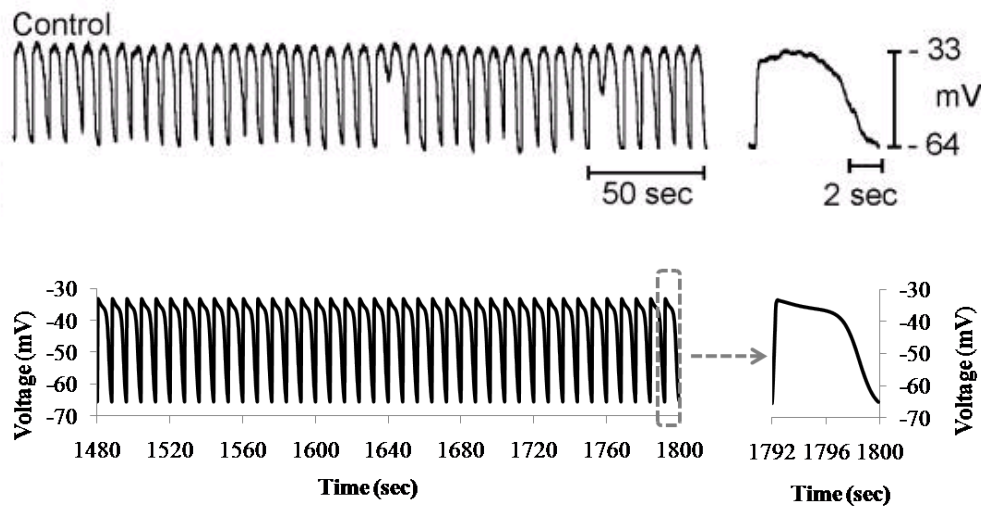
Figure 4.13. Simulated slow waves (lower panel) were able to match experimental results in the control traces of Figures 7A and 7B, reported in Hwang et al [64] (upper panel).

4.3   Altered conditions

The hJSMC model was subjected to further validation under altered conditions. Figure 4.14 shows the simulation results of whole cell current versus time traces for a hJSMC model subjected to activation voltage clamp from -80 mV to 20 mV with an increment size of 5 mV. Figure 4.14a shows

the results for a holding voltage of -70 mV while Figure 4.14b shows the results for a holding voltage of -20 mV. This was repeated with other holding voltages from 0 mV to -90 mV. For these results, it was observed that the steady-state behaviour of the whole cell currents is independent of holding voltage. Figures 4.14a and 4.14b also show that for a prolonged clamping period of 2000 ms there is negligible inactivation. These results matched the experimental observations on hJSMC [216].
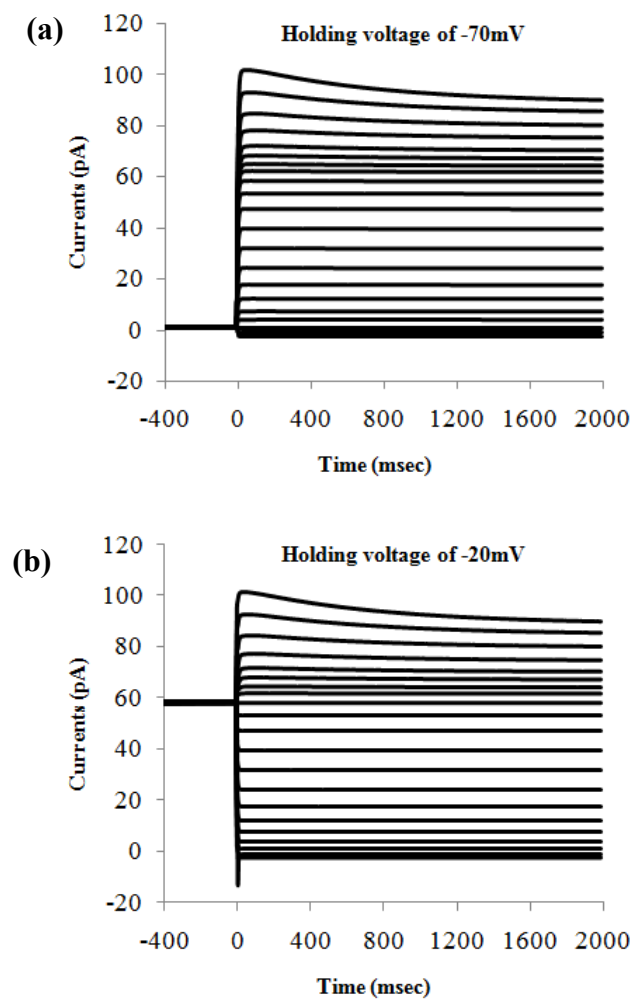
Figure 4.14. The whole cell current versus time traces from hJSMC subjected to voltage clamp with different holding voltages. (a) shows the results for original holding voltage of -70 mV. (b) shows the results for a holding voltage of -20 mV.

Experimentally, when isolated hJSMC was subjected to voltage clamp in Ca^{2+} free bath solution, negligible change to I-V behaviour was observed [216]. A

Ca^{2+} free bath environment was simulated in the hJSMC model by setting the extracellular and intracellular Ca^{2+} concentrations to 1e-7 mM. The simulation result in Figure 4.15 shows negligible change to I-V and this agrees with experimental observation.
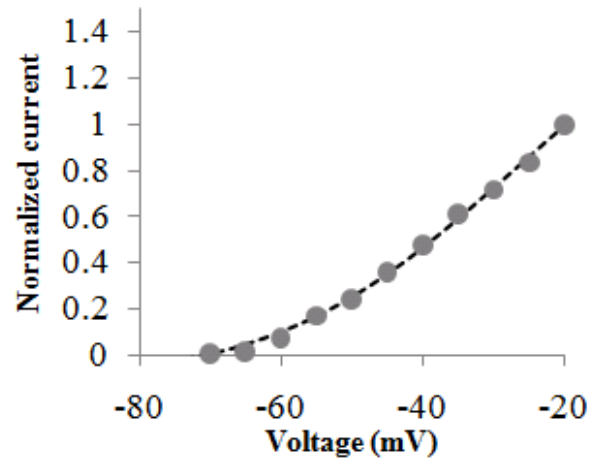
Figure 4.15. Predicted whole cell normalized I-V data from hJSMC model under the conditions where calcium concentrations were reduced to near zero to simulate the effect of calcium-free bath solution during voltage clamping. The dashed line is simulation data, while gray dots are experimental data under control conditions [216].

Under the condition where the prescribed ICC stimulation was switched off by setting G_{couple} to 0 nS, the hJSMC slow waves ceased with the V_m stabilizing at resting value of -73.1 mV as shown in Figure 4.16. This is in agreement with the hJSMC being an excitable but passive cell type, requiring stimulation from the pacemaking ICC. To simulate the experimental environment of an isolated hJSMC where there is an absence/reduction of carbon monoxide activation of the potassium channels and/or degradation of potassium channels, G_{Kv} was set to be 100 times smaller than its original value. The resulting stabilized resting potential gave a value of -37 mV. These values are within the recorded

range of initial potentials reported in Farrguia et al's work on isolated hJSMC, i.e., between 11 mV to 80 mV with an average of -41 mV [216].
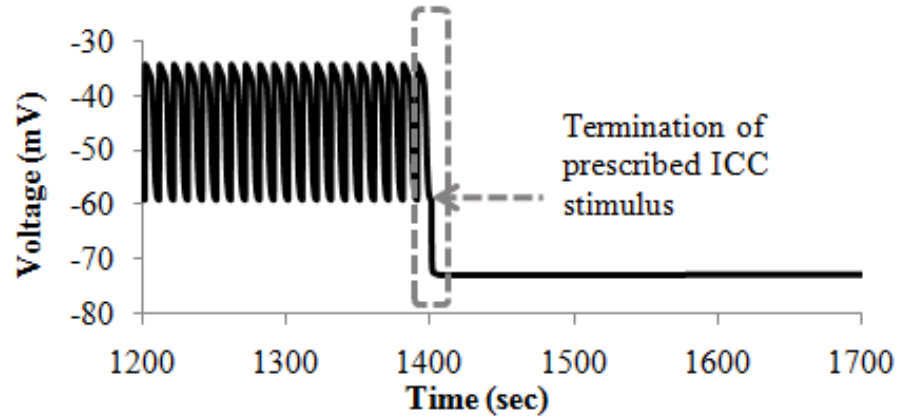
Figure 4.16. hJSMC response to termination of ICC stimulation. The coupling conductance between the ICC and hJSMC was set to zero at time point 1400 seconds. Correspondingly, the hJSMC slow waves ceased to a steady potential of about -73.1 mV.

Lee et al reported that the drug, 2-Aminoetoxydiphenyl borate (2-APB) was capable of inhibiting ICC slow waves. A concentration of 50 μM was able to reduce ICC frequency to about 4.90 cpm, increase time to peak by about 19.69% and reduce amplitude by about 32.90% [45]. This was simulated by implementing the same quantitative changes to the prescribed ICC stimulus. The resulting hJSMC voltage response is shown in Figure 4.17 which additionally demonstrated that the hJSMC model describes a cell that is passive whose excitation is dependent on the nature of the stimulation.
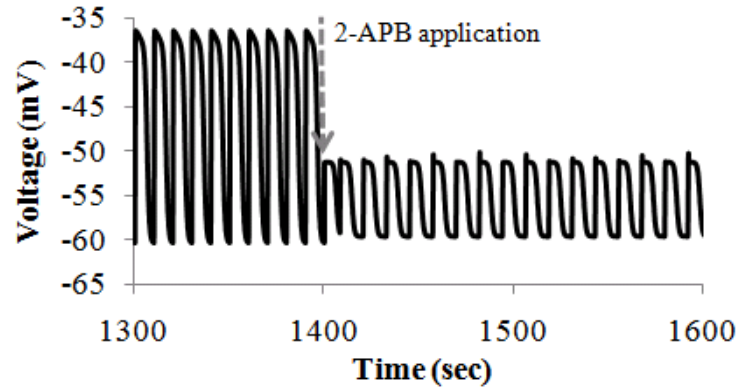
Figure 4.17. To simulate the effect of 2-APB, appropriate changes were made to the ICC stimulus, applied at a time point of 1400 seconds. Consequently, the hJSMC slow waves cycle at 4.9 times per minute, with a reduction in slow wave upstroke and plateau amplitude.

4.3.1 Contributions of ionic currents to hJSMC response

Two steps were taken to evaluate the contribution of the key ionic currents in the SMC slow waves. Firstly, the values of the corresponding currents at critical phases of a slow wave, i.e., the resting and plateau phases were normalized and plotted in Figure 4.18. Secondly, a sensitivity analysis was performed by separate adjustment of maximum channel conductance by ±50% with the original values serving as the control, as shown in Figure 4.19.

In both resting and plateau phases, the hJSMC model exhibited relatively strong outward currents through I_{Kv}, and this agrees with the experimental observation that the normal hJSMC exhibited strong outward potassium current that is a major determinant of the membrane potential [216]. This strong outward I_{Kv} is the main counter against the inward ICC stimulation current. The strong influence of I_{Kv} was further supported by the sensitivity analysis results in Figure 4.19a that demonstrated that a 50% increase in

maximum conductance of I_{Kv} significantly hyperpolarized membrane potentials and vice-versa for a 50% decrease in maximum conductance.

I_{BK} is another outward potassium current but here it plays a minor role in shaping membrane potential as demonstrated by the small amplitude of its size relative to I_{Kv} at both the resting and plateau phases (see Figure 4.18) as well as the very slight membrane potential changes upon ±50% of its maximum conductances (see Figure 4.19b). This is reasonable since I_{BK} has been found to be weakly voltage dependent over the physiological slow wave $[Ca^{2+}]_i^{free}$ range of between 96 nM to 256 nM predicted by the hJSMC model (see Figure 4.12). Greater electrical excitation of the hJSMC would result in greater $[Ca^{2+}]_i^{free}$ primarily through I_{CaL} and therefore greater contraction of the smooth muscle. Because of the sensitivity to calcium, I_{BK} would then act like a rheostat to regulate smooth muscle excitability and contractility under such circumstances.

I_{Na} is a relatively strong inward current at both the resting and plateau phases (see Figure 4.18). In the hJSMC model, the choice of maximum conductance for I_{Na} was based on a value determined from experimental I_{Na} in hJSMC [154, 244]. However, ±50% of the maximum conductance of I_{Na} did not seem to vary the membrane potential (see Figure 4.19c). This could be a consequence of an ICC driving force that is great enough to counteract any

I_{Na} influence on the hJSMC membrane potential. I_{Na} also exists in the ICC and can shape the ICC electrical slow waves [106], which in turn can affect the hJSMC slow waves.

The biggest inward current at the plateau phase is I_{CaL}. Its sensitivity analysis results in Figure 4.19d show that ±50% variation in maximum conductance for I_{CaL} changes membrane potential slightly at the plateau phase only. This is reasonable since I_{CaL} has been experimentally characterized to be relatively inactive over the range of the slow wave potentials (see Figure 4.3). Nonetheless, I_{CaL}, being the dominant Ca^{2+} current, was able to carry sufficient Ca^{2+} into the hJSMC essential for smooth muscle contractility [217, 245]. Figure 4.19e shows the corresponding $[Ca^{2+}]_i^{free}$ for ±50% variation in maximum conductance of I_{CaL} which demonstrated that a small change in membrane potential was able to lead to significant change in $[Ca^{2+}]_i^{free}$.
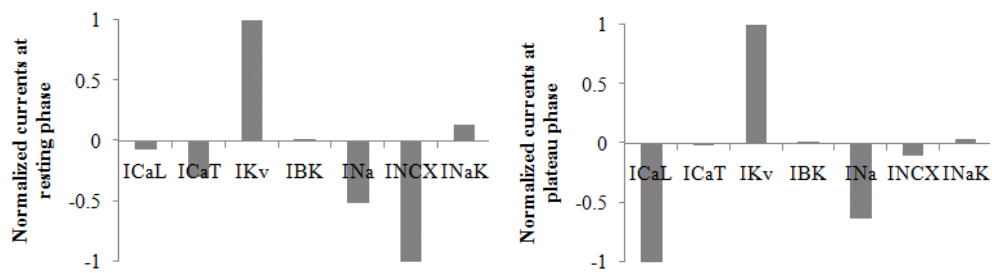
Figure 4.18. Ionic currents recorded from hJSMC simulation under control conditions. Left panel plot is for currents recorded from the resting phase, while right panel plot is for currents recorded from the plateau phase. Currents are normalized according to their directionality, i.e. negative value currents are normalized against the amplitude of the largest negative current at either the resting or plateau phase and vice versa.

4.4   Discussion of the hJSMC model

To the best of our knowledge, this is a first mathematical model that describes a human smooth muscle cell and in that of the small intestine. The key ionic currents were carefully selected, modelled and validated against experimental data. The overall hJSMC model was able to predict membrane potential behaviour that is in good agreement with experimental observations. These provided greater confidence in the choice of parameter values for the hJSMC model. The simulated $[Ca^{2+}]_i^{free}$ is within the expected range and the model was stable through long term simulation. The time-course of $[Ca^{2+}]_i^{free}$ was within physiological range, and it behaves in a manner consistent with what was captured in fluorescence imaging of Ca^{2+} transients in jejunal cells [45]. This would be useful for coupling this electrical model to a mechanical model of hJSMC as a realistic $[Ca^{2+}]_i^{free}$ is necessary for an appropriate trigger of pathways involved in cellular mechanics. Further validation was performed by subjecting the hJSMC model to voltage clamp simulations under a number of conditions. The corresponding simulation results, in terms of whole cell current versus time, and peak current versus clamping voltage, are consistent with that reported experimentally.
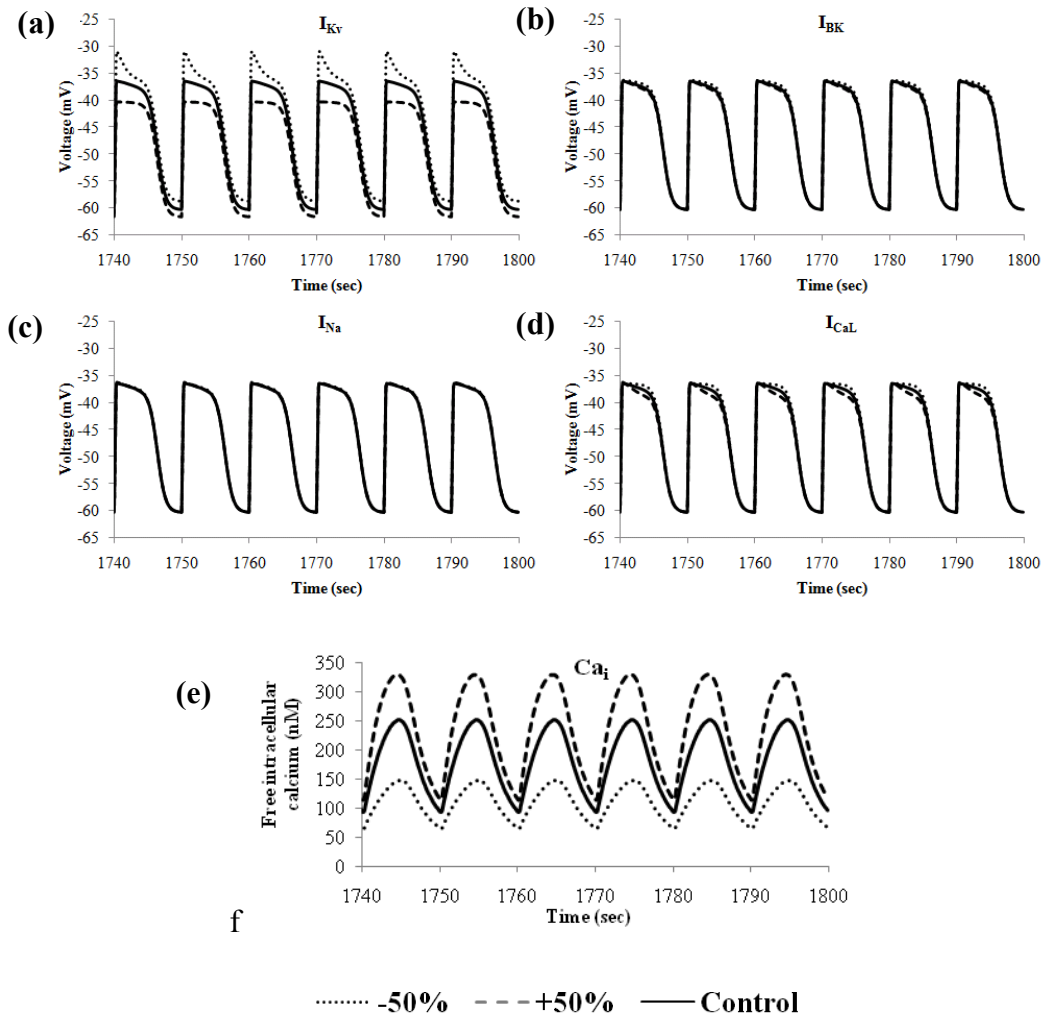
Figure 4.19. Sensitivity analysis by increasing/decreasing maximum channel conductance by 50% to evaluate the contributions of key ionic currents towards hJSMC membrane voltage. (e) shows the corresponding changes in $[Ca^{2+}]_i^{free}$ for the change in conductance in (d).

As some ionic currents were experimentally characterized in expression systems such as HEK-293 cells, it is impossible to draw conclusions on the correct value of the maximum conductance of these ionic currents from such experiments. The choice of maximum conductances in this model was therefore carefully selected to satisfy what is known about these ionic currents and the hJSMC slow waves from experimental studies. The model contains kinetic parameters derived from non-jejunal SMC data. The BK channels were parameterized from human myometrium smooth muscle data while the

homeostatic mechanisms describe human cardiac muscle kinetics. Therefore, as relevant human jejunal data appears, both the kinetic parameters as well as maximum conductance parameters in this model should be updated accordingly

Given the critical role of ICC in driving SMC excitation, the development of a suitable biophysically based human jejunal ICC model coupled to the hJSMC model would be beneficial to investigate the coupled state electrophysiology in affecting motility pattern. This pursuit is reliant on more experimental findings on human jejunal ICC. In this hJSMC model, a low coupling with the prescribed ICC stimulus, produced a peak ICC current that was at a relatively low value of -0.674 pA/pF. This aligns with the physiological situation where, despite the low ratio of ICC to SMC, the ICC were able to effectively excite the greater number of SMC in a tissue [83]. The hJSMC model is therefore expected to be amenable for higher scale studies such as when coupled to a biophysical ICC model or in multi-cellular modelling.

The hJSMC is an electromechanical cell that generates motility at the global level, with free intracellular calcium as a critical link between electrical and mechanical functions. Its calcium and sodium channels were found to be mechanosensitive [246, 247]. Therefore a mechanical extension to this model would be useful, for example, in the investigation of how mutation altered cellular electrics could translate into altered mechanics. This can be achieved through the incorporation of biological pathways associated with actomyosin active contraction and soft tissue mechanics of the hJSMC.

4.5   Investigation of the R76C and G298S mutations

The sodium channels that were presented in Chapter 3 were integrated into the hJSMC model. For the investigation of R76C mutation, 100% homozygosity was examined, i.e., the simulation results with 100% SCN5A versus 100% R76C were compared. Similarly, for the G298S investigation, simulation results for the 100% wild-type versus 100% G298S mutation were compared, for each of the four different common backgrounds.

Figure 4.20 shows the results for the investigation of the R76C mutation. The upper panel indicates that in the presence of R76C mutation, the membrane potential was slightly depolarized which was more obvious at the plateau phase of the slow waves. This is in correspondence to the sodium currents shown in the lower panel, where the R76C affected sodium current carried a greater influx of sodium currents than the wild-type current. This is consistent with the earlier observations that the R76C mutation exerts a gain-of-function effect.

However, even though the R76C mutation exerted a gain-of-function effect, the results differ from that of the gastric canine SMC (see Figures 3.22 and 3.23), where a depolarization in resting potential and not the peak potential was predicted. The gastric slow waves have more negative resting potentials, less depolarized peak potentials and slower frequency compared to the intestinal slow waves. These differences in cellular electrophysiological environment caused the sodium current response of the same wild-type and

R76C models to be different in the intestinal SMC models than in the gastric counterpart. This therefore caused a different change in membrane potential despite the incorporation of the same mutation.

Figures 4.21 to 4.24 show the results for investigating the G298S mutations in the four common backgrounds of H558/Q1077del, H558R/Q1077del, H558/Q1077, and H558R/Q1077. The upper panel of all the figures shows that the G298S mutation was incapable of causing any noticeable change to the hJSMC potential in all four backgrounds. This was even though the G298S sodium currents were different from their wild-type counterparts. In all backgrounds, except for H558/Q1077, the peak G298S sodium currents were smaller than the peak wild-type sodium currents, which is in agreement with G298S as a loss-of-function mutation. The increase in sodium current due to the G298S mutation in the H558/Q1077 background agreed with that observed in the gastric cell models. As before, the argument was the G298S mutation and/or the background of the sodium channel could affect the maximum sodium channel conductance in the cell, through expression pathways or otherwise, and can therefore reverse the apparent gain-of-function effect to a loss-of-function effect. In terms of the SMC membrane potential, in none of the backgrounds was the G298S mutation able to cause noticeable changes, unlike in the gastric SMC results where it was observed that the G298S mutation was able to slightly hyperpolarize the resting potentials in the most common background of H558/Q1077del (see Figure 3.39). Additionally, the corresponding predicted $[Ca^{2+}]_i^{free}$ were compared between wild-type and

G298S for all backgrounds; however there was no observable change in

$[Ca^{2+}]_i^{free}$ which is an indication that contraction may not be affected.
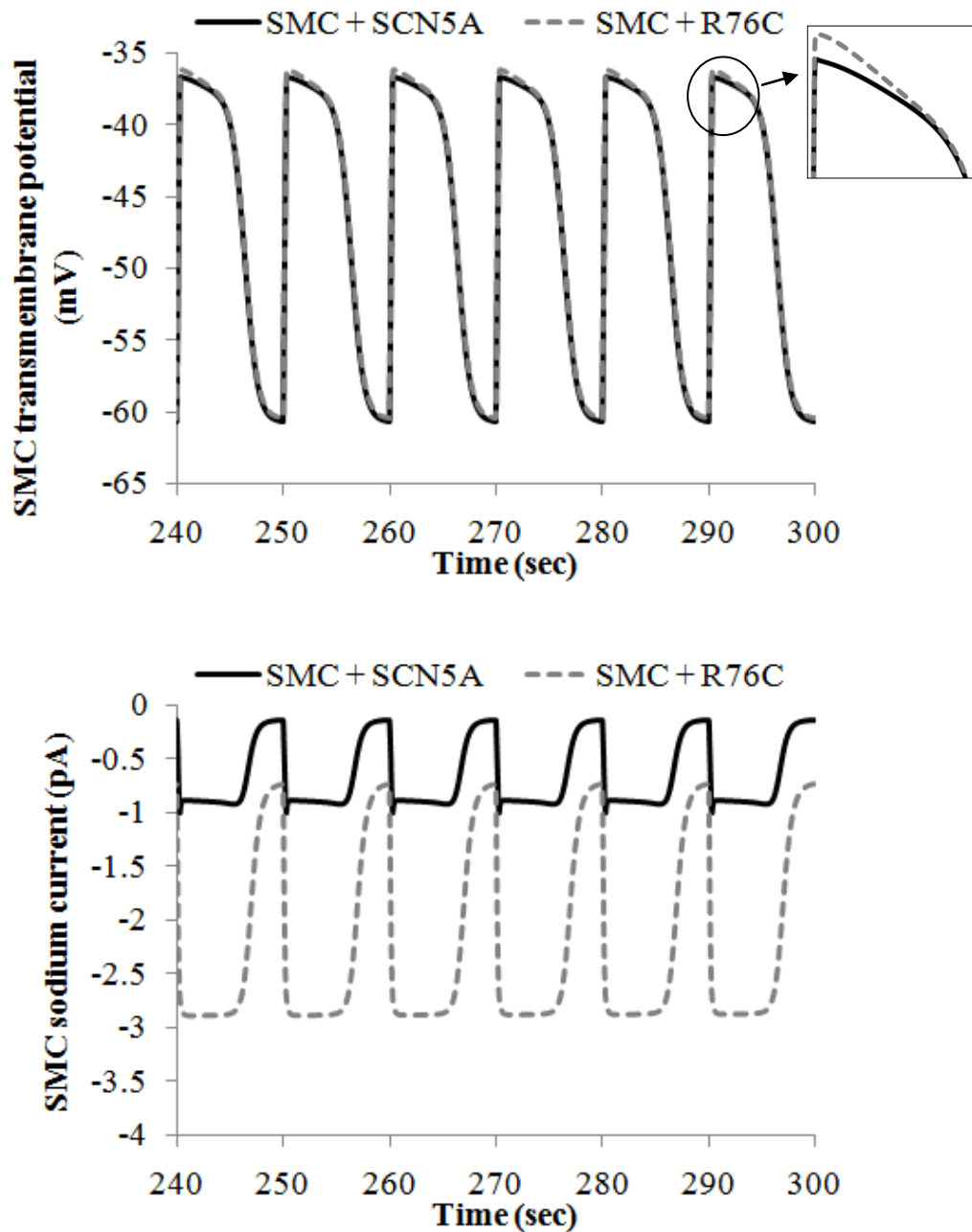
Figure 4.20. Results for the R76C mutation in hJSMC. Upper panel compares the wild-type membrane potential (black solid line) against membrane potential in the presence of R76C mutation (gray dashed line). Inset shows the enlargement of a slow wave plateau. Lower panel compares the wild-type and R76C sodium currents in the hJSMC model.

The lack of consequences of the mutations related to the sodium channels in the hJSMC can be explained by reasons similar to those mentioned in Chapter 3. The maximum conductance value affects the amount of sodium current and its contribution towards membrane potential. In the case of G298S, it is possible that due to mutation and/or ion channel background, the effective density of sodium channels may be up- or down- regulated. The contribution of sodium current also depends on the strength of other ionic currents that shape the membrane potential behaviour. Inter-species and inter-/intra-organ differences can result in the same ionic current having different extent of contribution towards shaping membrane potential. Here, the outward potassium currents were experimentally determined to be a strong influence, thus weakening the influence of other currents such as the sodium current. The hJSMC model was activated by a prescribed ICC stimulus and this constrained the SMC voltage behaviour; for instance, the frequency of the slow waves cannot change. Additionally, the mutations may act through sodium channels present in the ICC, and in turn affect SMC electrophysiology.
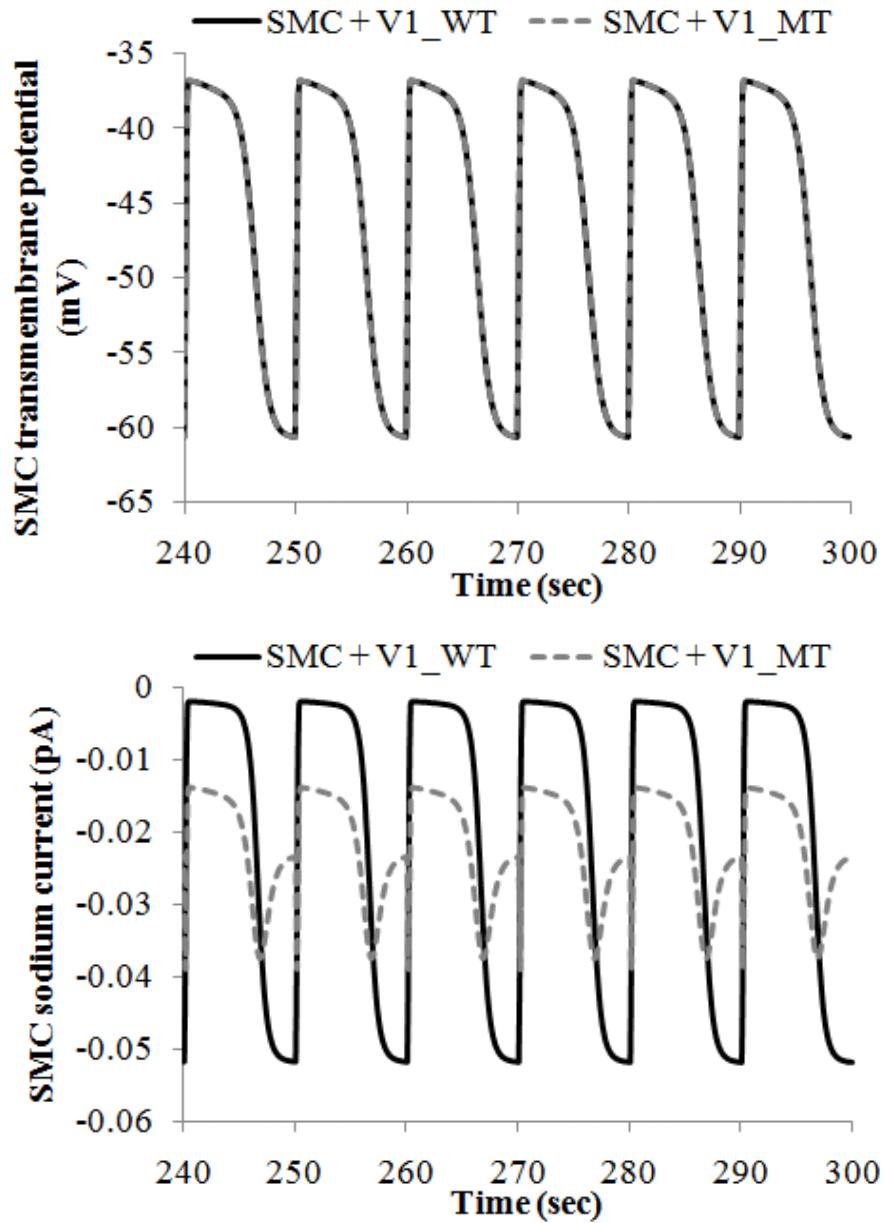
Figure 4.21. G298S mutation in hJSMC results for H558/Q1077del background. Upper panel compares the wild-type membrane potential (black solid line) against membrane potential in the presence of G298S mutation (gray dashed line). Lower panel compares the wild-type and G298S sodium currents in the hJSMC model.
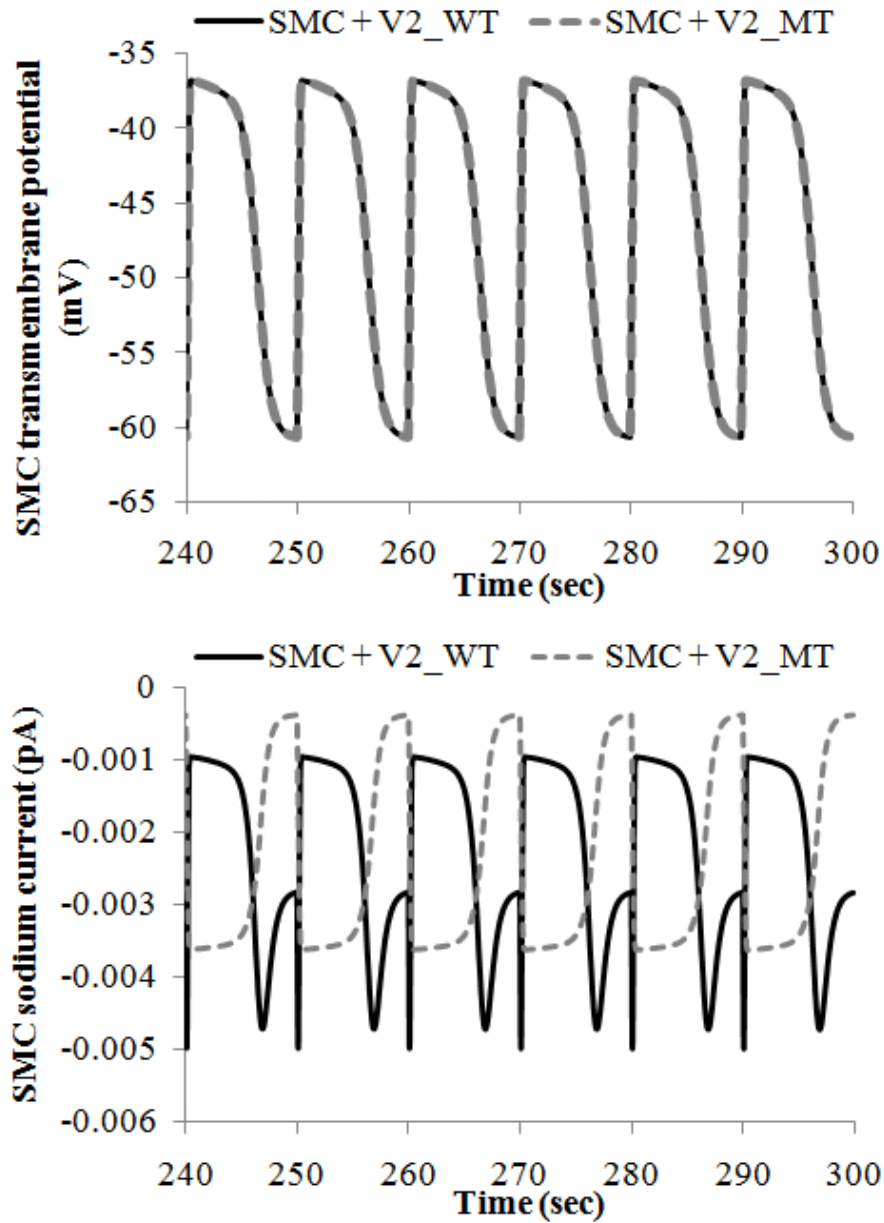
Figure 4.22. G298S mutation in hJSMC results for H558R/Q1077del background. Upper panel compares the wild-type membrane potential (black solid line) against membrane potential in the presence of G298S mutation (gray dashed line). Lower panel compares the wild-type and G298S sodium currents in the hJSMC model.
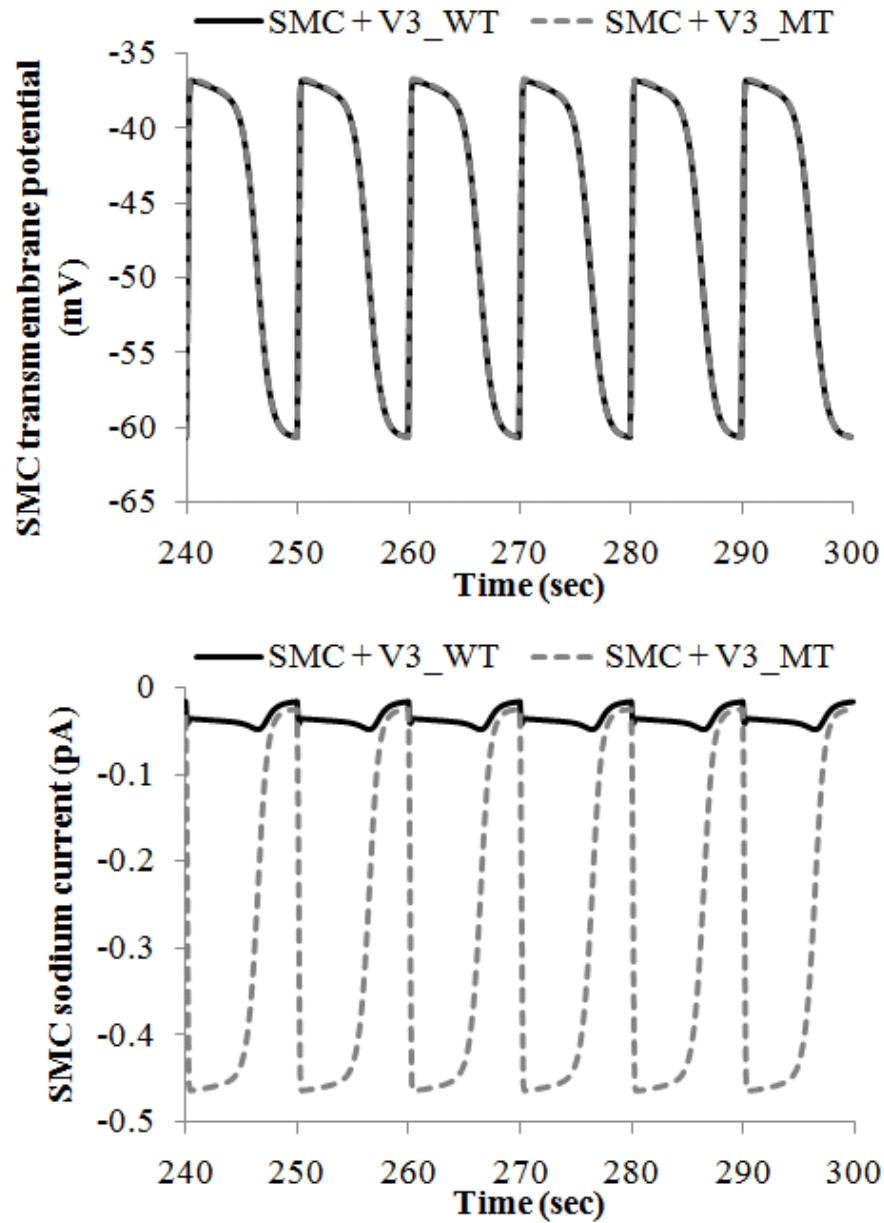
Figure 4.23. G298S mutation in hJSMC results for H558/Q1077 background. Upper panel compares the wild-type membrane potential (black solid line) against membrane potential in the presence of G298S mutation (gray dashed line). Lower panel compares the wild-type and G298S sodium currents in the hJSMC model.
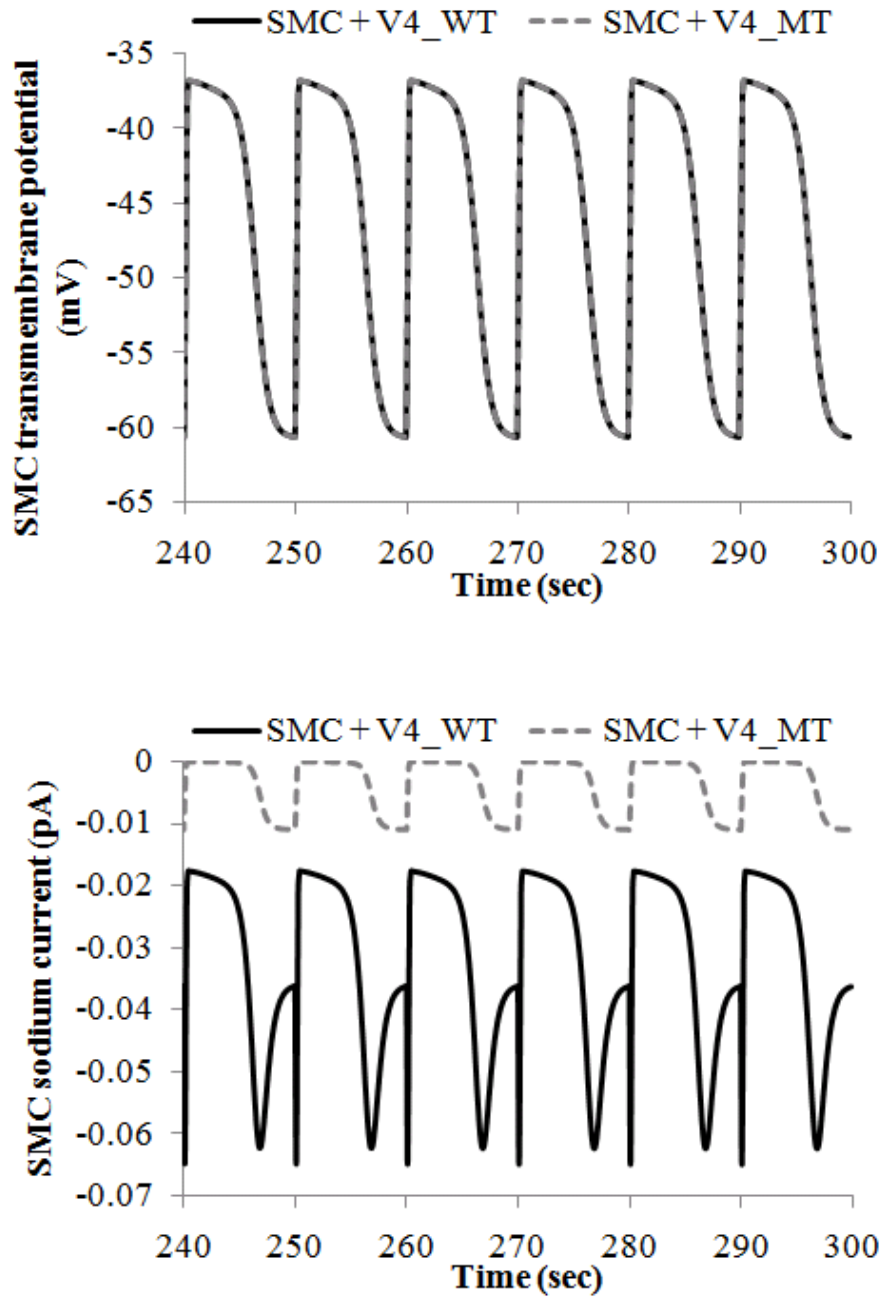
Figure 4.24. G298S mutation in hJSMC results for H558R/Q1077 background. Upper panel compares the wild-type membrane potential (black solid line) against membrane potential in the presence of G298S mutation (gray dashed line). Lower panel compares the wild-type and G298S sodium currents in the hJSMC model.

4.6   Chapter summary

A biophysically based electrophysiological model of the hJSMC was created and validated. This is a first human gastrointestinal cell model, and a first for the small intestine. Its electrophysiology was described by eight ionic currents including calcium, potassium, and sodium currents as well as an exchanger and a pump. The cell model predictions under normal and altered conditions agreed with experimental findings. These include the slow wave characteristics, intracellular calcium concentration and voltage clamp response. The R76C and G298S mutations were experimentally correlated with patients with intestinal motility disorders, but existing experimental studies have not been able to examine the consequences of these mutations in the human small intestinal smooth muscle [14, 15]. To overcome such a gap, the hJSMC model was subsequently used together with the sodium channel models developed in the preceding chapter to computationally investigate these mutations' effects on cellular electrophysiology. The R76C mutation was able to cause a small increase in the plateau potentials of the hJSMC slow waves while no noticeable change to the slow wave potentials was observed for the G298S mutation across all backgrounds. Any change in cellular electrical potential has the potential to alter the intracellular calcium level in the smooth muscle cell which can in turn lead to a change in cellular mechanical behaviour. Having examined the single cell scenario, the next chapter includes an investigation of the R76C and G298S mutations in a multi-cellular electrophysiological model of the stomach. This investigation might provide further insights into the consequences of mutations in a tissue construct where there is inter-cellular communication between ICC and SMC.

Chapter 5
Multi-cellular modelling

"The purpose of computing is insight, not numbers"
while "the purpose of computing numbers is not yet in
sight,"
– Richard Hamming, American mathematician

5 Multi-cellular modelling

The preceding two chapters have discussed modelling up to the spatial scale of a single cell. In the physiological situation, within a tissue or an organ, single cells can be organized into a multi-cellular syncytium, in which intercellular communication and spatial heterogeneities exist and affect behaviour.

5.1 Extended bidomain framework

5.1.1 Background

The traditional bidomain computational framework is one technique for multi-cellular modelling which is popularly applied in cardiac modelling. The bidomain approach describes the tissue or organ construct as a continuum with volume averaged properties. The control volume is divided into two domains, i.e., the intracellular domain of a single cell type separated by the cellular membranes from the extracellular space (see Figure 5.1).

The wall of GI organs where muscular activity occurs has a complex anatomy. It contains variants of the SMC and ICC as well as the enteric neuronal cells at various anatomical locations, which are all involved in generating motility. These SMC and ICC are connected to each other via gap junction proteins, and therefore form a continuum construct [38, 258]. Because of the anatomical complexity, the traditional bidomain equations that describe a single cell type in a tissue are therefore unable to realistically and effectively reflect the multiple cell types present in the GI wall. There were earlier attempts to model

the cellular heterogeneity in the GI wall which encountered limitations. Aliev et al's cable model solves the ICC and SMC domains separately in a monodomain format, i.e., without the effects of extracellular space communication, and without biophysically detailed cellular descriptions [213]. Large scale electrophysiological models of the stomach and small intestines were also developed [213, 248, 249], however these specified the ICC and SMC as separate discrete layers, unlike the more complex physiological situation where ICC are known to exist in several layers of the GI wall such as within the smooth muscle layers [38]. To address this gap, an attempt was made to extend the traditional bidomain framework to incorporate multiple cell types. The derivation to extend the bidomain framework, which follows Buist and Poh (2010) [250], is described in the next section.

5.1.2 Method

Traditional bidomain framework

Maxwell's equations that govern the electric fields and magnetic fields, as shown in Eqs. 5.1 to 5.4, are relevant for the development of the traditional bidomain framework where: E is the electric field intensity, B is the magnetic flux density, J is the electric flux density, ρ is the electric charge density, μ_0 is the permeability of free space, $\in_0$ is the permittivity of free space and t is time.

$$\nabla \bullet E = \frac{\rho}{\in_0}, \tag{5.1}$$

$$\nabla \times E = -\frac{\partial B}{\partial t}, \tag{5.2}$$

$$\nabla \bullet B = 0, \tag{5.3}$$

$$\nabla \times \boldsymbol{B} = \mu_0 \left(\boldsymbol{J} + \in_0 \frac{\partial \boldsymbol{E}}{\partial t} \right), \qquad (5.4)$$

In the GI environment, the electrical and magnetic fields occur at relatively low frequencies, therefore the time derivatives are assumed zero, resulting in quasi-static version of the Maxwell's equations which essentially uncouples the electric and magnetic fields:

$$\nabla \bullet \boldsymbol{E} = \frac{\rho}{\in_0}, \qquad (5.5)$$

$$\nabla \times \boldsymbol{E} = 0, \qquad (5.6)$$

$$\nabla \bullet \boldsymbol{B} = 0, \qquad (5.7)$$

$$\nabla \times \boldsymbol{B} = \mu_0 \boldsymbol{J}. \qquad (5.8)$$

Eq. 5.6 indicates that the curl of the electric field is zero in the GI physiological context; therefore $\boldsymbol{E}$ can be represented by the gradient of a scalar potential field, φ:

$$\boldsymbol{E} = -\nabla \varphi. \qquad (5.9)$$

Next, for any given control volume representing a multi-cellular construct, the continuity equation can be used to describe the transport of electrical charges across the boundaries. With charge conservation, the following form of continuity equation was obtained:

$$\nabla \bullet \boldsymbol{J} + \frac{\partial \rho}{\partial t} = 0. \qquad (5.10)$$

At equilibrium, there is no net current flux density, therefore the electric charge density in the control volume does not change with time, i.e., $\frac{\partial \rho}{\partial t} = 0$. The continuity equation is further reduced to:

$$\nabla \bullet \boldsymbol{J} = 0. \qquad (5.11)$$

J can be split into two components, one that is ohmic arising from tissue properties, J_o, and the other is an impressed current density from an external source, J_{imp}, i.e.,

$$J = J_o + J_{imp}. \tag{5.12}$$

J_o arises from tissue properties which can be expressed as a product of an electric field intensity, E, in the tissue, and the tissue conductivity, σ. By substituting E with Eq. 5.9, the final term in the following equation is obtained for J_o:

$$J_o = \sigma E$$

$$= -\sigma \nabla \varphi. \tag{5.13}$$

If the control volume is divided into two domains (i.e., a bidomain) of extracellular space and intracellular space, then J_o can be further subdivided into extracellular current density, J_e, and intracellular current density, J_i, with their respective conductivities and potentials given by σ_e, φ_e, σ_i and φ_i where subscripts e and i denote extracellular and intracellular spaces respectively. In the absence of an externally impressed current density, J_{imp} is zero, and Eq. 5.11 becomes the following:

$$\nabla \bullet J = \nabla \bullet J_o$$

$$= \nabla \bullet (J_e + J_i)$$

$$= \nabla \bullet (-\sigma_e \nabla \varphi_e - \sigma_i \nabla \varphi_i)$$

$$= 0. \tag{5.14}$$

Electric charges move from one domain to the other domain in the control volume across the membrane boundary through $\nabla \bullet J$. Here, the electric flux

density is defined to exit from the intracellular domain into the extracellular space, i.e.,

$$\nabla \bullet (\sigma_i \nabla \varphi_i) = A_m I_m, \tag{5.15}$$

$$\nabla \bullet (\sigma_e \nabla \varphi_e) = -A_m I_m, \tag{5.16}$$

where I_m refers to the electric current per unit area exiting the cellular membrane, and A_m refers to the membrane surface area to control volume ratio.

To link cellular electrical activity to a bidomain multi-cellular formulation, the term I_m is defined to be the sum of ionic currents crossing a cellular membrane, and thus assumes the following form:

$$I_m = C_m \frac{\partial V_m}{\partial t} + \sum I_{ion}, \tag{5.17}$$

where C_m is the membrane capacitance, V_m is the potential difference given by φ_i-φ_e and I_{ion} is the various ionic currents that cross the membrane. Combining Eqs. 5.15 to 5.17, the traditional bidomain equations are obtained:

$$\nabla \bullet (\sigma_i \nabla \varphi_i) = A_m \left(C_m \frac{\partial V_m}{\partial t} + \sum I_{ion} \right), \tag{5.18}$$

$$\nabla \bullet (\sigma_e \nabla \varphi_e) = -A_m \left(C_m \frac{\partial V_m}{\partial t} + \sum I_{ion} \right), \tag{5.19}$$

where Eqs 5.18 and 5.19 sum up to give:

$$\nabla \bullet (\sigma_e \nabla \varphi_e + \sigma_i \nabla \varphi_i) = 0. \tag{5.20}$$
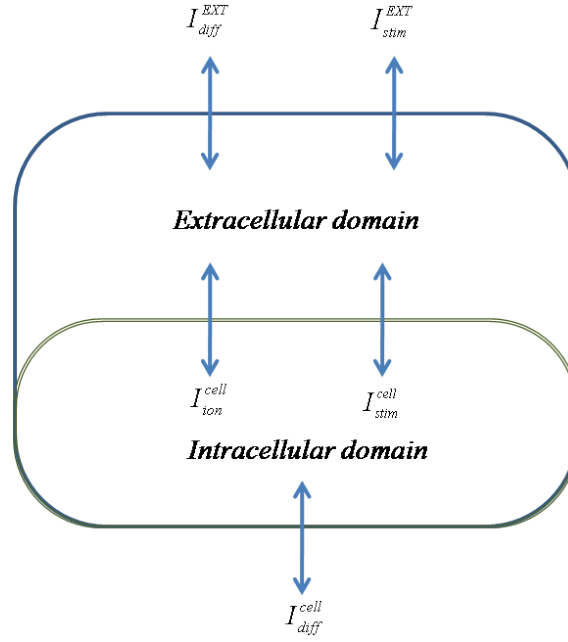
Figure 5.1. Schematic of the traditional bidomain framework. There are two domains, the extracellular domain and the intracellular domain, with different types of current fluxes. I_{diff}^{EXT} belongs to $\nabla \bullet (\sigma_e \nabla \varphi_e)$, I_{diff}^{cell} belongs to $\nabla \bullet (\sigma_i \nabla \varphi_i)$, I_{ion}^{cell} is equivalent to $A_m I_m$ while I_{stim}^{cell} and I_{stim}^{EXT} are any stimulus currents that may be injected into the extracellular and intracellular domains respectively.

Extending the bidomain framework to incorporate multiple cell types

The key to incorporate multiple cell types is through the distribution of membrane area of each cell type. In the case of having two cell types of the ICC and SMC, the total membrane area in the control volume is given by: (1) ICC membrane area in contact with extracellular space, (2) SMC membrane area in contact with the same extracellular space, and (3) the membrane area that connects the ICC and SMC. In the third scenario, the ICC and SMC are connected via protein gap junctions that are able to conduct ionic currents across these cells. Therefore, A_m can be re-expressed as:

$$A_m = \frac{A_{ICC} + A_{SMC} + A_{gap}}{V_{control}}$$

$$= A_m^{ICC} + A_m^{SMC} + A_m^{gap}, \tag{5.21}$$

where A_{ICC}, A_{SMC} and A_{gap} refer to the membrane area of the ICC, SMC, and the connected membrane area between ICC and SMC respectively, $V_{control}$ is the control volume, A_m^{ICC}, A_m^{SMC} and A_m^{gap} are the membrane area to control volume ratios for ICC, SMC and connected membrane area respectively. Eq. 5.21 can be generalized for n number of cell types and connected areas:

$$A_m = \frac{\sum_{i=1}^{n} A_i}{V_{control}} = \sum_{i=1}^{n} A_m^i. \tag{5.22}$$

Consequently, the traditional bidomain equations of Eqs. 5.18 and 5.19 are transformed into:

$$\nabla \bullet (\sigma_i \nabla \varphi_i) = A_m \left(C_m \frac{\partial V_m}{\partial t} + \sum I_{ion} \right)$$

$$= A_m^{ICC} \left(C_m^{ICC} \frac{\partial V_m^{ICC}}{\partial t} + \sum I_{ion}^{ICC} \right) +$$

$$A_m^{SMC} \left(C_m^{SMC} \frac{\partial V_m^{SMC}}{\partial t} + \sum I_{ion}^{SMC} \right)$$

$$= \nabla \bullet \left(\sigma_i^{ICC} \nabla \varphi_i^{ICC} + \sigma_i^{SMC} \nabla \varphi_i^{SMC} \right), \tag{5.23}$$

$$\nabla \bullet (\sigma_e \nabla \varphi_e) = - \left(\begin{array}{l} A_m^{ICC} \left(C_m^{ICC} \frac{\partial V_m^{ICC}}{\partial t} + \sum I_{ion}^{ICC} \right) + \\ A_m^{SMC} \left(C_m^{SMC} \frac{\partial V_m^{SMC}}{\partial t} + \sum I_{ion}^{SMC} \right) \end{array} \right). \tag{5.24}$$

For the connected membrane space where a local ionic current flows through the gap junctions between the ICC and SMC intracellular spaces, a simple linear relationship is assumed:

$$I_{gap} = g_{gap} \left(\varphi_i^{ICC} - \varphi_i^{SMC} \right), \tag{5.25}$$

where g_{gap} is the overall gap junction conductance, φ_i^{ICC} and φ_i^{SMC} are the intracellular potentials of the ICC and SMC respectively. The gap junction

current forms part of the membrane ionic currents, and is thus integrated into

the bidomain equations in the following manner:

$$\nabla \bullet (\sigma_i^{ICC} \nabla \varphi_i^{ICC}) = A_m^{ICC} \left(C_m^{ICC} \frac{\partial V_m^{ICC}}{\partial t} + \sum I_{ion}^{ICC} \right) + A_m^{gap} I_{gap},$$

(5.26)

$$\nabla \bullet (\sigma_i^{SMC} \nabla \varphi_i^{SMC}) = A_m^{SMC} \left(C_m^{SMC} \frac{\partial V_m^{SMC}}{\partial t} + \sum I_{ion}^{SMC} \right) - A_m^{gap} I_{gap},$$

(5.27)

while Eq. 5.20 is updated to:

$$\nabla \bullet (\sigma_e \nabla \varphi_e + \sigma_i^{ICC} \nabla \varphi_i^{ICC} + \sigma_i^{SMC} \nabla \varphi_i^{SMC}) = 0,$$

(5.28)

which together with Eqs. 5.26 and 5.27 constitute the key equations of the

extended bidomain framework.

Application of external stimulus to the extended bidomain framework

To apply external electrical stimulus to the control volume, useful for

bidomain studies, such as in the case of simulating an exogenous electrical

current injection from electrode/s (for example, from a pacemaking device),

the extended bidomain equations were adjusted to include external stimulus in

the following three possible ways:

(1) Stimulus I_{stim}^{ICC} injected into the ICC intracellular space,

$$\nabla \bullet \sigma_i^{ICC} \nabla \varphi_i^{ICC} = A_m^{ICC} \left(C_m^{ICC} \frac{\partial V_m^{ICC}}{\partial t} + \sum I_{ion}^{ICC} - I_{stim}^{ICC} \right) + A_m^{gap} I_{gap},$$

(5.29)

(2) Stimulus I_{stim}^{SMC} injected into the SMC intracellular space,

$$\nabla \bullet \sigma_i^{SMC} \nabla \varphi_i^{SMC} = A_m^{SMC} \left(C_m^{SMC} \frac{\partial V_m^{SMC}}{\partial t} + \sum I_{ion}^{SMC} - I_{stim}^{SMC} \right) - A_m^{gap} I_{gap}, \qquad (5.30)$$

(3) Stimulus I_{stim}^{EXT} injected into the shared extracellular space,

$$\nabla \bullet \left(\sigma_e \nabla \varphi_e + \sigma_i^{ICC} \nabla \varphi_i^{ICC} + \sigma_i^{SMC} \nabla \varphi_i^{SMC} \right) - I_{stim}^{EXT} = 0, \qquad (5.31)$$

Note that because the external stimulus changes the total energy of the whole control volume, therefore a stimulation should be applied such that long term stability is ensured (i.e., to ensure the conservation of charge in the continuity equation is observed). An example is the use of bipolar stimuli configuration or to bath the multi-cellular construct in interstitial fluid. A schematic of the extended bidomain framework is shown in Figure 5.2.
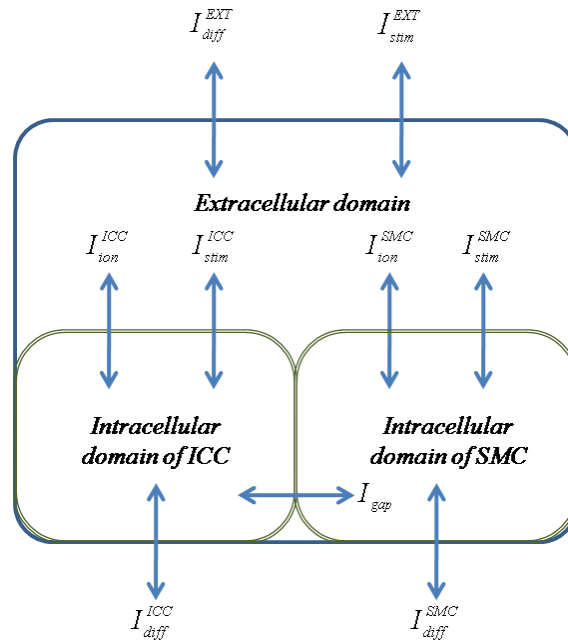
Figure 5.2. Schematic of the extended bidomain framework. The traditional bidomain framework was extended by dividing the intracellular domain into two sub-domains, one for the ICC and one for the SMC. Possible current fluxes are indicated by the arrows, where the new symbols carry the following meanings: I_{diff}^{ICC} belongs to $\nabla \bullet (\sigma_i^{ICC} \nabla \varphi_i^{ICC})$, I_{diff}^{SMC} belongs

to $\nabla \bullet (\sigma_i^{SMC} \nabla \varphi_i^{SMC})$, I_{ion}^{ICC} is equivalent to $A_m^{ICC} \left(C_m^{ICC} \frac{\partial V_m^{ICC}}{\partial t} + \sum I_{ion}^{ICC} \right)$ and I_{ion}^{SMC} is equivalent to $A_m^{SMC} \left(C_m^{SMC} \frac{\partial V_m^{SMC}}{\partial t} + \sum I_{ion}^{SMC} \right)$.

Implementation of the extended bidomain framework

The extended bidomain governing equations can be implemented in a format that facilitates solving the equations computationally:

Eqs. 5.29 and 5.30 were rearranged to have the $\frac{\partial V_m}{\partial t}$ term on the left hand side of the equations:

$$\frac{\partial V_m^{ICC}}{\partial t} = \frac{1}{C_m^{ICC}} \left(\frac{\nabla \bullet \sigma_i^{ICC} \nabla \varphi_i^{ICC}}{A_m^{ICC}} - \frac{A_m^{gap}}{A_m^{ICC}} I_{gap} - \sum I_{ion}^{ICC} + I_{stim}^{ICC} \right),$$

(5.32)

$$\frac{\partial V_m^{SMC}}{\partial t} = \frac{1}{C_m^{SMC}} \left(\frac{\nabla \bullet \sigma_i^{SMC} \nabla \varphi_i^{SMC}}{A_m^{SMC}} + \frac{A_m^{gap}}{A_m^{SMC}} I_{gap} - \sum I_{ion}^{SMC} + I_{stim}^{SMC} \right).$$

(5.33)

Linearity of the Laplacian operator was applied by adding and subtracting the $\nabla \cdot (\sigma_i \nabla \varphi_e)$ type terms in the diffusion equation of Eq. 5.31, resulting in:

$$\nabla \bullet \left(\sigma_e \nabla \varphi_e + \sigma_i^{ICC} \nabla \varphi_i^{ICC} + \sigma_i^{SMC} \nabla \varphi_i^{SMC} \right) - I_{stim}^{EXT} - \nabla \bullet (\sigma_i^{ICC} \nabla \varphi_e) -$$

$$\nabla \bullet (\sigma_i^{SMC} \nabla \varphi_e) + \nabla \bullet (\sigma_i^{ICC} \nabla \varphi_e) + \nabla \bullet (\sigma_i^{SMC} \nabla \varphi_e) = 0.$$

(5.34)

Simplifying Eq. 5.34 by substituting $V_m = \varphi_i - \varphi_e$ gives:

$$\nabla \bullet ((\sigma_e + \sigma_i^{ICC} + \sigma_i^{SMC}) \nabla \varphi_e) = I_{stim}^{EXT} - \nabla \bullet (\sigma_i^{ICC} \nabla V_m^{ICC}) - \nabla \bullet (\sigma_i^{SMC} \nabla V_m^{SMC}).$$

(5.35)

With the above form of the extended bidomain equations, i.e., Eqs. 5.32, 5.33 and 5.35, the following implementation was employed:

- The Corrias and Buist single cell models of gastric ICC and SMC electrical activity were integrated into the framework through the ICC and SMC ionic current terms [82, 108].

- The tissue geometry was defined to be a one dimensional 100 mm gastric strip.

- The space dimension was discretized using the central space finite difference method with a spatial resolution of 1 mm (Δx).

- The time dimension was discretized using the forward Euler method with a time step size of 0.1 ms (Δt).

- The resulting system of equations was solved using the biconjugate gradient stabilized method.

- Boundary conditions were imposed by: (1) setting the average of the extracellular field to be zero; (2) defining no flux boundary conditions, i.e., $\frac{\partial \varphi}{\partial n} = 0$, to compute the intracellular potentials for the boundary nodes.

- The following bidomain parameter values were used:

Table 5.1. Bidomain parameter values.

Parameter	Value	Units
σ_i^{ICC}	0.5	mS.mm^{-1}
σ_i^{SMC}	0.1	mS.mm^{-1}
σ_e	0.1	mS.mm^{-1}
C_m^{ICC}	0.01	μF.mm^{-1}
C_m^{SMC}	0.01	μF.mm^{-1}
A_m^{ICC}	100	mm^{-1}
A_m^{SMC}	100	mm^{-1}
A_m^{gap}	0.1	mm^{-1}

g_{gap}	0.2	mS.mm^{-2}

To solve the problem in the finite time central space (FTCS) method, the V_m^{ICC} and V_m^{SMC} at the next time point, $t + \Delta t$, are solved explicitly using Eqs. 5.32 and 5.33. Subsequently, V_m^{ICC} and V_m^{SMC} are used to solve Eq. 5.35 which gives φ_e at the new time point, $t + \Delta t$. Since V_m^{ICC}, V_m^{SMC} and φ_e are known for time $t + \Delta t$, therefore φ_i^{ICC} and φ_i^{SMC} at time $t + \Delta t$ can be computed and then placed back into Eqs. 5.32 and 5.33 to solve the next time iteration. This process is repeated until the completion of the required simulated time frame. The FTCS discretized form of Eqs. 5.32, 5.33 and 5.35 can be found in Appendix 16.

5.1.3   Results and Discussion

Without any external stimulus

Figure 5.3 shows the results of the simulations without any external stimulus. In (a) to (c), the spatiotemporal plots together with the corresponding electrical potential scale bars are shown for V_m^{ICC}, V_m^{SMC} and φ_e respectively. (d) shows a cross-section from the spatiotemporal plots at a distance of 50 mm (i.e., middle of the cable) where the typical physiological slow waves of V_m^{ICC} and V_m^{SMC} were observed [56, 251]. The appearance of φ_e depends on the nature of the boundary condition used. Here, the average of the extracellular potential field was set to zero. The simulated slow wave frequency was 2.9 cpm. The extended bidomain framework simulation results showed stable and realistic

electrical activity propagating across space and time. ICC are self-exciting and therefore no input is required to drive electrical activity in this cable model.

One interesting observation was made when g_{gap} (or equivalently A_m^{gap}) was increased. The amplitude of the ICC waveform decreased and became more triangular in shape until eventually the ICC pacemaking activity ceased. An increase in g_{gap} means an increase of electrical energy that is supplied to the SMC from the ICC. A high g_{gap} value places an energy demand that the ICC are unable to adequately provide, therefore leading to reduced or cessation of pacemaking activity. It has been proposed that in the thicker human GI wall, ICC in the myenteric plexus alone are not sufficient to sustain pacemaking activity through the relatively thick wall, and thus supportive elements such as intramuscular ICC are required [252].

(a)

(b)

(c)

(d)
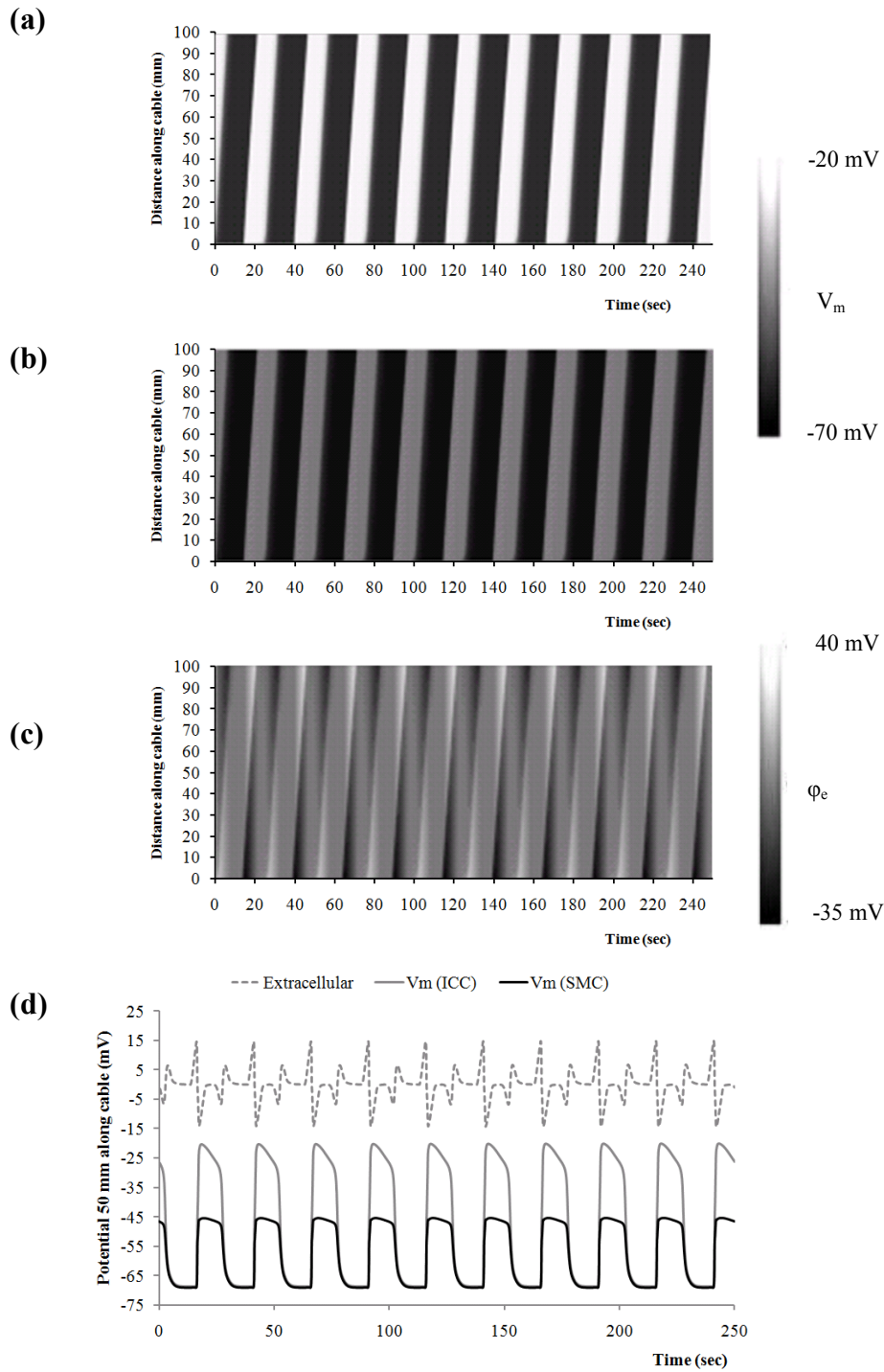
Figure 5.3. Extended bidomain results. (a) to (c) show the spatiotemporal plots of V_m^{ICC}, V_m^{SMC} and φ_e respectively. Distance 0 mm refers to the proximal end of the 100 mm cable geometry. There is stable propagation of electrical activity from 0 mm downwards to 100 mm, and across time. A single frequency of 2.9 cpm is observed. (d) shows a cross-section of the spatiotemporal plots at distance of 50 mm (middle of cable) for V_m^{ICC}, V_m^{SMC} and φ_e.

With external stimulus

The interest is to simulate intracellular electrode stimulation of the cells, therefore in the simulation studies, a periodic external stimulus with a duration of 200 ms and a frequency of 3.3 cpm was tested via I_{stim}^{ICC} and I_{stim}^{SMC} in a system with an intrinsic ICC pacing frequency of 2.9 cpm. Figure 5.4(a) shows the results for I_{stim}^{ICC} where stable entrainment with the stimulus frequency of 3.3 cpm was observed for both the ICC and SMC, while Figure 5.4(b) shows the results for I_{stim}^{SMC} where stable entrainment was also observed. The slightly gentler rate of rise in slow wave upstroke in (b) relative to (a), and to the original slow waves (in dashed lines) could have resulted from a reduced loading of the ICC by the SMC, because the injection of external energy into the SMC through I_{stim}^{SMC} helped the ICC in exciting the SMC.

(a)

(b)

-- - VmICC (2.9cpm) ——VmICC (3.3 cpm) ——VmSMC (3.3 cpm)
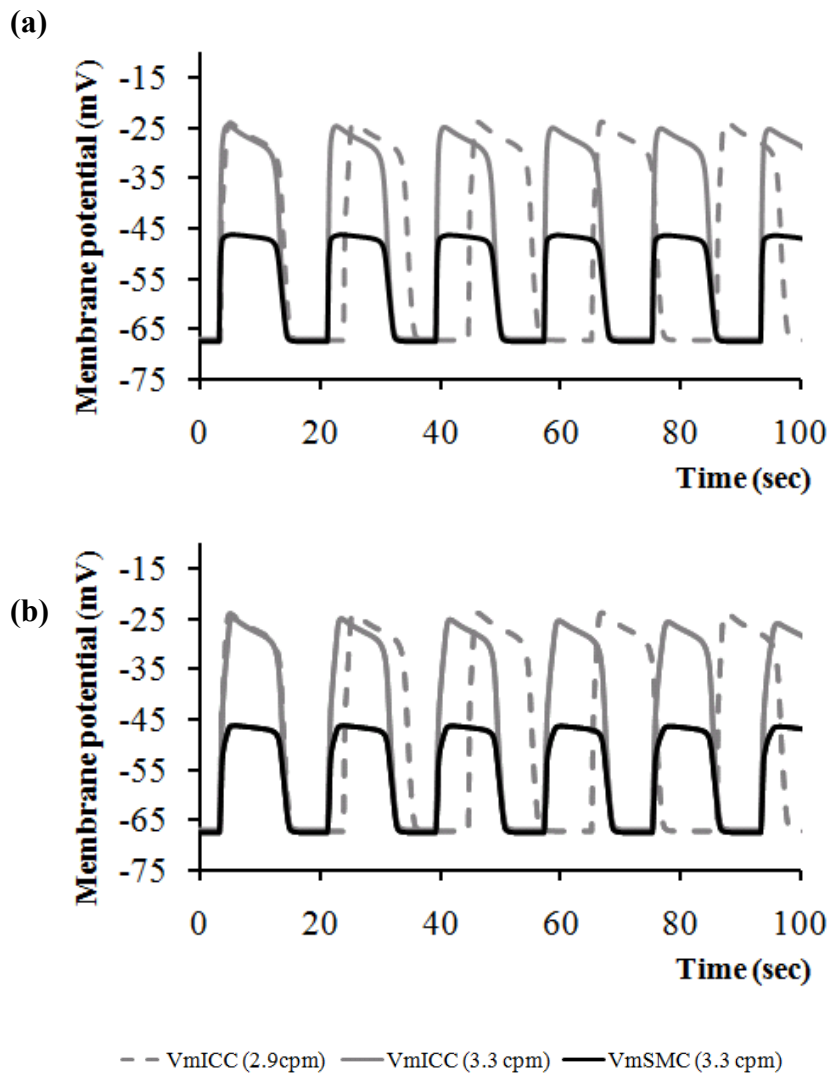
Figure 5.4. Simulation results for injection of stimulus current (I_{stim}) into the extended bidomain cable. Gray dashed lines show the unstimulated V_m^{ICC} with intrinsic frequency of 2.9 cpm. Gray solid lines show the stimulated V_m^{ICC} at 3.3cpm; similarly black solid lines show the stimulated V_m^{SMC} at 3.3cpm. (a) is the result for using I_{stim}^{ICC} while (b) is the result for using I_{stim}^{SMC} . Stable entrainment was observed for both cases.

Discussion

The extended bidomain framework was developed to incorporate multiple cell types in a tissue control volume. This concept was demonstrated here in a dual cell type, one dimensional cable model of a 100 mm gastric strip of ICC and SMC syncytium. The extended bidomain framework offers potential to be more generally applied.

For the GI tract, as mentioned in Chapter 2, a number of ICC and SMC variants with differing properties exist within the GI wall that contribute to motility. These include intramuscular ICC which are located within the smooth muscle layers. More recently, fibroblast like cells were suggested to be connected to the GI smooth muscles through protein gap junctions and act as a mediator for enteric neuronal transmission [253]. Therefore, these additional cell types can also be incorporated using the extended bidomain framework. The one dimensional framework can also be expanded into a two or three dimensional framework as in the case of a whole GI organ model.

Beyond the GI tract, the extended bidomain framework can be applied to other tissues where ICC-like cells exist or where multiple cell types are involved in tissue electrophysiology. These include the heart [254], myometrium [255, 256] and the pancreas [257]. In addition, fibroblast cells may play an important role in cardiac electrophysiology by interacting with the cardiocytes [258, 259], therefore the extended bidomain framework is applicable to investigate their roles in the heart [260].

An important element of the extended bidomain framework is the gap junction conductance that connects the ICC with the SMC, which was assumed here to be linearly dependent on a fixed maximum conductance and potential difference. However, these gap junctions formed by connexin proteins may exhibit more complex behaviour such as gating kinetics [261]. For the heart, gap junction abnormalities have been associated with cardiac propagation

issues that led to cardiac diseases [262]. Hence, this is a potentially worthwhile area to examine for GI organs.

Next, the extended bidomain framework describes inter-cellular communication and therefore slow wave conduction through the implementation of gap junction connections between cells, and the flow of conductivity-dependent electrical currents in the extracellular domain (alternatively termed "local circuit flow"). A possible limitation in this framework is the absence of a possible third mechanism of inter-cellular communication through the electric field at cell-to-cell junctional clefts. Previous studies have suggested that action potential propagation between cardiocytes is effectively due to electric field excitation at junctional clefts, i.e., a sufficiently negative potential that develops in a cleft provides for a supra-threshold depolarization in the post-junctional membrane [263]. Such a mechanism supports sequential activation of the cardiocytes. Simulation studies further suggested that gap junctions are essential but not key to activation in the cardiocytes. Hence, there is a possibility of a similar electric field mechanism in the gastrointestinal conduction system that may, to a certain extent, contribute to slow wave propagation. This is a noteworthy area to examine but is non-trivial to implement because the extended bidomain framework is based on continuum modelling whereby the multi-cellular model is not composed of a collection of discrete cells.

5.2 Modelling gastric slow wave propagation and entrainment

5.2.1 Background

To realistically model GI electrophysiology at the tissue or organ level, any critical or relevant factors that shape the macroscopic electrical activity need to be described. In the stomach, there are two such factors in the form of electrical gradients. These gradients are a result of spatially varying properties of heterogeneous gastric cells. This section discusses the methods and results for describing these gradients. Note that the derivations in this section follow the paper co-authored by the thesis author [264].

5.2.2 Frequency gradient and entrainment in the stomach

In the intact stomach, an ICC-MY network coordinates electrical propagation from the corpus to the antrum with a single frequency of 3 cpm. However, isolated smooth muscle tissue exhibits a gradient of decreasing frequency from the corpus to antrum, along the stomach's greater curvature [53, 265]. This is a result of ICC with higher intrinsic frequency, normally at the corpus region, that entrains the slower pacing ICC to produce a single frequency in the stomach [85, 265]. Therefore, suitable mechanisms are required to describe and integrate the frequency gradient and entrainment in the model.

Firstly, a mechanism for the ICC to generate different intrinsic frequencies is described. Under the NSCC hypothesis, the pacemaker unit (PU) in an ICC is made up of the endoplasmic reticulum (ER), mitochondria and plasma membrane ion channels, particularly the non-selective cationic channels

(NSCC). As discussed in Chapter 2, calcium ions are released from the ER through IP3-receptor mediated channels, followed by a stronger uptake of calcium by the mitochondria which results in a dip in PU calcium that activates the calcium inhibited NSCC. NSCC activation changes the membrane potential and sets up a slow wave frequency that follows the calcium cycling rate in the PU. There is some evidence to suggest, though not conclusively, that the IP3 concentration in the PU regulates the slow wave frequency in the murine stomach [266] and the small intestine [267]. An increase in the IP3 concentration increases the probability of calcium release from the ER which consequently causes a faster rate of calcium cycling, and hence a higher slow wave frequency. Here, to establish a ICC frequency gradient along the gastric cable, the IP3 concentration was therefore chosen as proxy via a linear IP3 concentration gradient with values of 645 nM at the proximal end of the cable, and 600 nM at the distal end to achieve a physiologically realistic entrained frequency of 3.1 cpm.

Next, an entrainment mechanism that allows the highest frequency ICC slow waves to synchronize the remaining ICC to follow the same frequency is described. Although calcium cycling in the PU sets the frequency, it is unlikely that a calcium signal from one ICC is able to directly coordinate another ICC's slow wave frequency. This is because calcium waves are known to travel much slower than electrical signals in the GI tissue. Therefore, a voltage based mechanism is more plausible and this is supported by experimental evidence that suggests a voltage-dependent, dihydropyridine-resistant (VDDR) conductance carrying calcium currents is involved in slow

wave entrainment [45, 268]. Firstly, the voltage signals from a faster frequency ICC is conducted to the slower ICC. Consequently, the VDDR channels in the slower ICC carry an increased influx of calcium into the cytosolic space as well as the enclosed PU space. The IP3 channels in the PU which are also calcium mediated therefore experience an increase in opening rate. In turn, calcium cycling in the PU is set at a higher frequency dictated by the pace-setting ICC [85].

The cable model here integrates the Corrias and Buist's single cell ICC model that contains a description of whole cell VDDR [108]. To model VDDR based entrainment, a fraction of the whole cell I_{VDDR}, d_{PU}, was directed into ICC PU space to form:

$$I_{VDDRPU} = G_{VDDR} d_{PU} d_{VDDR} f_{VDDR} (V_m^{ICC} - E_{CaPU}), \qquad (5.36)$$

where I_{VDDRPU} denotes the PU VDDR current, while G_{VDDR}, d_{VDDR} and f_{VDDR} represent the maximal whole cell conductance, activation gate and inactivation gate of the VDDR channels respectively. Their descriptions follow that of the original ICC model [108]. V_m^{ICC} refers to the ICC membrane potential, while E_{CaPU} is the Nernst potential of calcium within the PU. When an ICC is entrained by its neighbouring ICC, the electrical depolarization information is carried by I_{VDDRPU} which carries a current into the PU that phase-locks the calcium cycling to produce a frequency consistent with that of its neighbour. Here, d_{PU} is assigned 0.04 which was the smallest value that

produced entrainment. This also implies that the whole cell I_{VDDR} receives

$1 - d_{PU}$ (i.e., 0.96) of the original current, and is given by

$$I_{VDDR} = G_{VDDR}(1 - d_{PU})d_{VDDR}f_{VDDR}(V_m^{ICC} - E_{Ca}), \qquad (5.37)$$

where E_{Ca} refers to the Nernst potential of calcium in the bulk cytosolic

space, outside of the PU.

Under normal conditions, calcium cycling in the PU should observe

homeostasis as is the case in the whole cell calcium regulation, thus a calcium

homeostasis mechanism should be included for the PU. Due to the lack of

experimental findings, a phenomenological model of calcium extrusion,

I_{ExtPU}, was implemented to provide long term calcium homeostasis:

$$I_{ExtPU} = \frac{I_{ExtPU}^{max}}{\left(1 + exp\left(\frac{Ca_{PU} - Ca_{50}}{k}\right)\right)}, \qquad (5.38)$$

where I_{ExtPU}^{max} is the maximal calcium extrusion current with a value of

0.000315 mM/ms, Ca_{50} is the half concentration of calcium in PU at a value

of 100 nM, k is a slope factor set to be 15 nM and Ca_{PU} is the calcium

concentration in the PU.

With the additional mechanisms of I_{VDDRPU} and I_{ExtPU}, calcium cycling in

the PU is described by the following:

$$\frac{d[Ca^{2+}]_{PU}}{dt} = \left(I_{IP3} - I_{CaPump}\right)\frac{V_{ER}}{V_{PU}} + (I_{NaCa} - I_{uni})\frac{V_{mito}}{V_{PU}} - \left(\frac{I_{VDDRPU}}{zFV_{PU}} + I_{ExtPU}\right) - I_{leak}\frac{V_{cyt}}{V_{PU}},$$

(5.39)

where I_{IP3} is the calcium current efflux from the IP3 receptor dependent calcium channels of the ER, I_{CaPump} is the calcium current influx mediated by the calcium ATPase pump of the ER, V_{ER} refers to the volume fraction of the ER, I_{NaCa} refers to the calcium efflux from the mitochondria through its sodium-calcium exchanger, I_{uni} is the calcium current that imports calcium through the uniporter in the mitochondria while V_{mito} refers to the volume of the mitochondria, z is the calcium valence, F is Faraday's constant, I_{leak} is the leakage calcium current that flows from the cytosolic space into the PU subspace, V_{cyt} is volume fraction of the cytosol and V_{PU} is the volume fraction of the PU subspace. The descriptions and parameter values for these variables were derived from the original single cell ICC model, unless otherwise stated [108].

5.2.3   Resting membrane potential gradient in the stomach

Resting membrane potential (RMP) gradients exist in the stomach. In the canine stomach for instance, the RMP hyperpolarizes from the fundus to the antrum [53, 269]. Experimental evidence indicates that these RMP gradients may result from the regulation of outward potassium currents [270, 271]. The potassium channels are regulated by a wide variety of bio-agents such as gases

(for example, nitric oxide and hydrogen sulfide), inflammatory mediators, neurotransmitters and prostaglandins. However, quantitative data regarding the contribution of each of these factors towards RMP regulation is lacking. To overcome this limitation in the initial attempt to incorporate RMP gradients for a realistic multi-cellular model, carbon monoxide was selected as the proxy to modulate the potassium channels in the ICC and SMC cellular descriptions integrated in the cable construct. This choice was supported by findings that suggest carbon monoxide as key factor in regulation of potassium channels, and in the control of RMP [269, 271, 272].

Carbon monoxide is one of the endogenous gases found in human tissues and in the GI tract [269, 273]. ICC-MY in the GI tract has been proposed to be a source of production of carbon monoxide through the enzyme, heme-oxygenase-2 and its associated pathway [269, 274-276]. Murine experiments indicated that heme-oxgyenase-2 knock-outs do not exhibit a RMP gradient, thus supporting heme-oxygenase-2 produced carbon monoxide in modulating RMP [271] but the underlying mechanism of carbon monoxide action on RMP remains to be elucidated. Thus, carbon monoxide was assumed to be produced by ICC-MY with its concentration following the density of ICC-MY. In the stomach, ICC-MY is largely absent in the fundus but present in the corpus and antrum, therefore the ICC-MY density along the cable model was described by:

$$n_{ICCMY} = n_{SMC} \frac{\propto \gamma + (1 - \alpha)}{\left(1 + exp\left(\frac{\gamma - \gamma_{50}}{k}\right)\right)}, \tag{5.40}$$

where n_{SMC} is the number of SMC relative to each ICC, γ is the normalized coordinate with a range from 0 (representing proximal most end of stomach

cable) to 1 (representing the most distal end of the stomach cable), $\propto$ is 0.005,

γ_{50} is 0.5 and k is 0.01, thus giving the following profile:
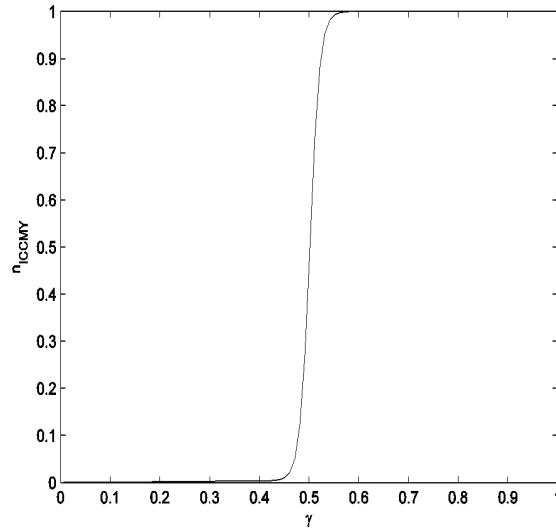
Figure 5.5. Distribution of relative ICC-MY density with n_{SMC} set to 1. $\gamma=0$ represents the proximal most end of the gastric cable model, while 1 represents the distal most end of the gastric cable model. The sharp transition, that starts somewhere at 0.45, demarcate the end of the fundus region and the beginning of the corpus, mimicking the physiological situation.

The carbon monoxide concentration, [*CO*], distribution commensurate with the ICC-MY density and was described by the following:

$$[CO] = 0.1 + \frac{0.4}{\left(1 + exp\left(\frac{\gamma - \gamma_{50}}{k}\right)\right)}, \tag{5.41}$$

where γ and k follow that of Eq. 5.40 and assumes the following profile:
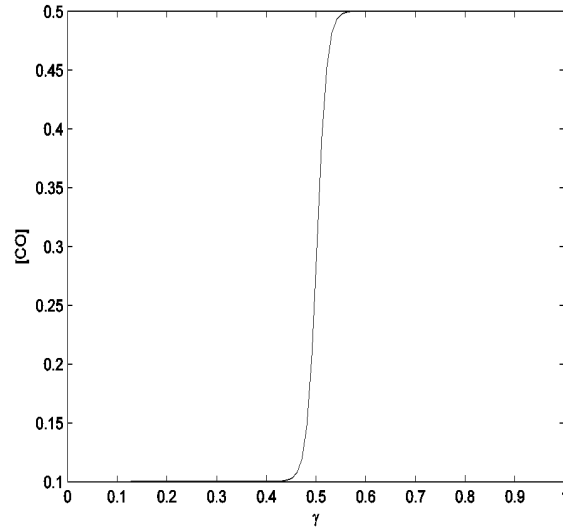
Figure 5.6. Distribution of carbon monoxide concentration. 0 represents the proximal most end of the gastric cable model, while 1 represents the distal most end of the gastric cable model.

The $[CO]$ profile described by Eq. 5.41 and Figure 5.6 was designed to follow experimental measurements of the canine stomach where $[CO]$ increases from around 0.1 nmol/mg in the fundus wet tissue to 0.5 nmol/mg of antrum wet tissue [271].

Carbon monoxide influences the potassium channels and here it was assumed that it acts on all potassium channels of the recipient SMC, i.e., the voltage-gated and calcium-dependent potassium channels. Carbon monoxide action on these channels was incorporated through an additional gating factor variable f_{CO} multiplied to all the potassium channel descriptions, i.e.,

$$f_{CO} = 2.475[CO] - 0.2375. \tag{5.42}$$

The parameter values in Eqs. 5.40 to 5.42 were selected to reproduce the RMP gradients experimentally recorded from canine tissue [53].

5.2.4 Gastric cable continuum model

In the attempt to demonstrate the feasibility of these approaches to describing the spatial variations, a simplified cable model was derived from the extended bidomain framework. Eqs. 5.26 and 5.27 were reduced to their one dimensional form, the linearity of the Laplacian operator was applied to both equations by adding and subtracting the term, $\sigma_i \frac{\partial^2 \varphi_e}{\partial x^2}$, and finally the extracellular potential was assumed to be constant, i.e., $\frac{\partial^2 \varphi_e}{\partial x^2} = 0$. These resulted in the following cable equations:

$$\sigma_i^{ICC} \frac{\partial^2 V_m^{ICC}}{\partial x^2} = A_m^{ICC} \left(C_m^{ICC} \frac{\partial V_m^{ICC}}{\partial t} + \sum I_{ion}^{ICC} \right) + A_m^{gap} I_{gap}$$

$$= A_m^{ICC} \left(C_m^{ICC} \frac{\partial V_m^{ICC}}{\partial t} + \sum I_{ion}^{ICC} + I_{couple} \right),$$

(5.43)

$$\sigma_i^{SMC} \frac{\partial^2 V_m^{SMC}}{\partial x^2} = A_m^{SMC} \left(C_m^{SMC} \frac{\partial V_m^{SMC}}{\partial t} + \sum I_{ion}^{SMC} \right) - A_m^{gap} I_{gap}$$

$$= A_m^{SMC} \left(C_m^{SMC} \frac{\partial V_m^{SMC}}{\partial t} + \sum I_{ion}^{SMC} - I_{couple} \right),$$

(5.44)

where the symbols carry the same meaning as in Eqs. 5.26 and 5.27, while the contribution of the gap junction current was replaced with I_{couple}. I_{couple} is effectively a form of I_{gap} (see Eq. 5.25) that incorporates the ICC-MY density, n_{ICCMY}, and assumes the following form:

$$I_{couple} = g_{couple} n_{ICCMY} \left(V_m^{ICC} - V_m^{SMC} \right),$$

(5.45)

In the absence of an explicit representation of the extracellular potentials, the ICC communicates with the SMC only through I_{couple}. The parameter values for Eqs. 5.43 to 5.45 used in this study are shown in Table 5.2.

Table 5.2. Cable model parameter values.

Parameter	Value	Units
σ_i^{ICC}	0.3	mS.mm^{-1}
σ_i^{SMC}	0.2	mS.mm^{-1}
C_m^{ICC}	0.01	µF.mm^{-1}
C_m^{SMC}	0.01	µF.mm^{-1}
A_m^{ICC}	100	mm^{-1}
A_m^{SMC}	100	mm^{-1}
A_m^{gap}	0.1	mm^{-1}
g_{couple}	0.005	mS.mm^{-2}

The cable model length was selected to be 337 mm which matched the length of the human stomach, from the proximal fundus to the terminal antrum along the stomach's greater curvature, as estimated from the data of the Visible Human Project [129]. An implicit forward time central space finite difference method was used to solve Eqs. 5.43 and 5.44, with a time step size of 0.1 ms and a grid size of 1 mm. The cellular descriptions of ICC and SMC electrophysiology by Corrias and Buist [82, 108] were integrated into the cable framework through the I_{ion} terms in Eqs. 5.43 and 5.44. These ionic currents were solved explicitly using the 4th order Runge-Kutta method.

5.2.5 Results and discussion

Testing the frequency gradient and slow wave entrainment

The entrainment mechanism was tested through an external stimulus injected into the ICC. Single cell ICC model was revised to include the entrainment mechanism from section 5.2.2 and defined to have an intrinsic frequency of 2.7 cpm. A periodic voltage stimulus of 10 mV in height, 200 ms in duration with 3.1 cpm frequency was injected into the ICC, which simulates the condition under which a faster pacing ICC entrains a slower ICC. The simulation results indicated that entrainment was achievable and remained stable during prolonged simulations. Figure 5.7 is a sample result of successful entrainment. The ICC membrane potential was initially following the intrinsic frequency of 2.7 cpm in the presence of the voltage stimulus (darker gray lines). The voltage stimulus took some time to cause entrainment at 3.1 cpm. The time point of a slow wave at which the stimulus was injected affects the speed of entrainment as the closer the stimulus was applied to the onset of a slow wave, the faster entrainment occurs. This was possibly due to the refractoriness of the ICC membrane potential whose retarding effect on the stimulus diminishes towards the end of a slow wave.
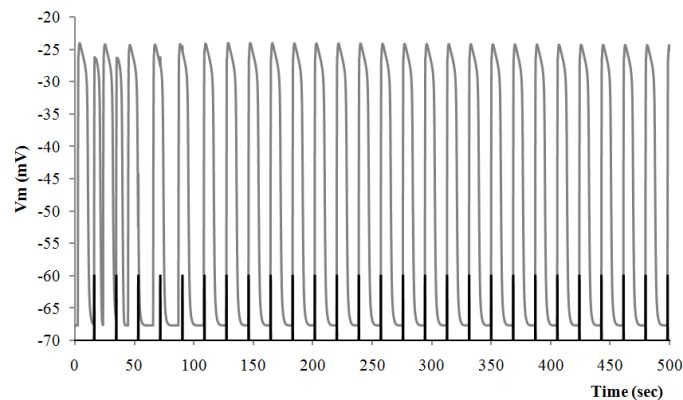
Figure 5.7. Single ICC model under periodic voltage stimulation. The intrinsic frequency of the ICC was 2.7 cpm, while the periodic stimulus has a frequency of 3.1 cpm as indicated by

the dark grey lines. Entrainment of the ICC occurred at about 125 s, in which the onset of the slow wave (in light grey) became aligned with the stimulus.

Following the earlier single ICC tests with a voltage stimulus, a logical next test was to use a model where one ICC with a higher intrinsic frequency is coupled to another ICC of a lower frequency. Firstly, the two cells were set at different frequencies through adjusting the IP3 concentration. Their overlaid slow waves are shown in the top panel of Figure 5.8. Next, the two cells were coupled with the gap junction current defined by Eq. 5.45 but without implementing the voltage-to-calcium entrainment mechanism. The results as shown in the middle panel of Figure 5.8 indicated the presence of intercellular communication but no entrainment, therefore resulting in erratic membrane potentials in both cells. The duration of the simulation was lengthened and the initial phase difference between the ICC was varied, but the absence of entrainment persisted. Subsequently, the proposed entrainment mechanism was implemented in the model and subjected to the same tests. Stable entrainment was successfully achieved as shown in the bottom panel of Figure 5.8.

The functional significance of proper entrainment lies in its contribution towards coordinated and timely propagation of slow waves from the corpus to the antrum. The absence of frequency gradient would elicit simultaneous depolarization, which is unrealistic, while ectopic pacemakers would disrupt slow wave propagation and affect contraction patterns, leading to abnormal motility. For instance, if ICC in the antrum pace at a frequency higher than the

ICC in the corpus, proper entrainment is affected leading to functional uncoupling in the form of dysmotility which may be harmful.
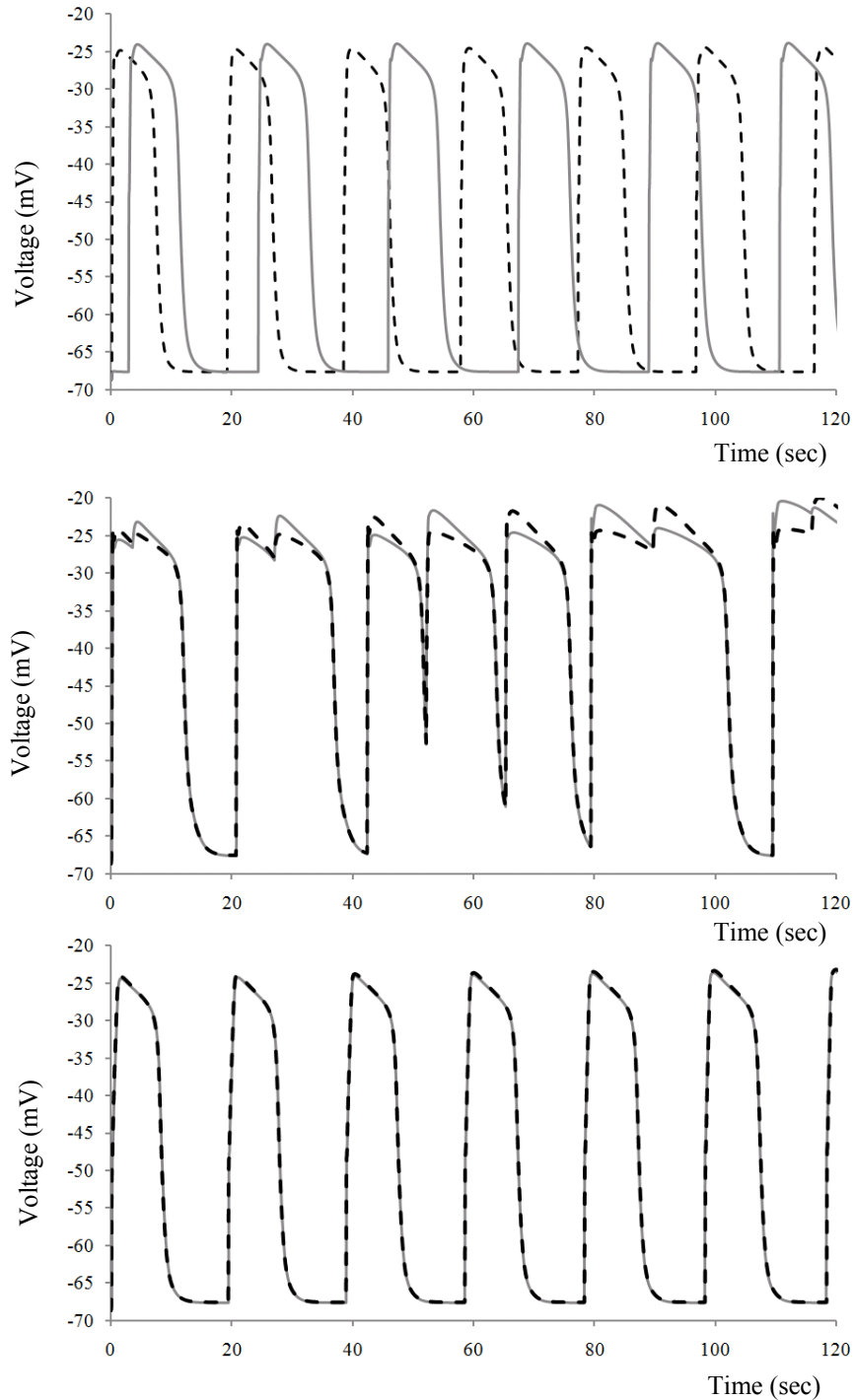
Figure 5.8. Testing entrainment using one cell of ICC coupled to another ICC. Top panel shows two uncoupled ICC at two frequencies of 3.2 cpm (gray solid line) and 3.0 cpm (black dashed line). Middle panel shows the two ICC in the coupled state but without implementing the entrainment mechanism; coupling causes persistent erratic slow wave behaviour under prolonged simulation. Bottom panel shows two coupled ICC with entrainment mechanism;

entrainment was successfully achieved with a frequency slightly lower than 3.2 cpm (of the faster pacing ICC).

RMP gradient and slow wave propagation

Carbon monoxide was used as a proxy to modulate SMC potassium channels to achieve a physiological RMP gradient in the cable model. Figure 5.9 shows the result of incorporating both the RMP gradient and entrainment mechanism through a spatiotemporal plot of the SMC membrane potential. It was observed that the resting membrane potential realistically changes from depolarized potentials to hyperpolarized potentials from the fundus to the antrum. The transition in resting potentials is less sharp than the ICC-MY density and carbon monoxide concentration, as shown in Figures 5.5 and 5.6. This contrast was attributed to sufficiently high tissue conductivities that smoothed the resting membrane potential variation. The lower panel of Figure 5.9 shows an orthogonal projection of the spatiotemporal plot which, as expected, demonstrated that the fundus is mostly electrically quiescent relative to the corpus and antrum region. The resting membrane potential stabilized at a hyperpolarized value at some point in the corpus through to the antrum.

The temporal electrical activity was extracted from the spatiotemporal dataset for the fundus, corpus and antrum giving the slow wave morphology shown in Figure 5.10. The RMP of the fundus, corpus and antrum were -42 mV, -60 mV and -68 mV, respectively, which are consistent with the experimental recordings of -40 mV in the guinea pig fundus [265] and -48 mV in the canine fundus, -60 mV for the mid orad corpus and -69 mV for the orad antrum [53].

Figure 5.10 also shows that fundus presents minute slow waves with a small
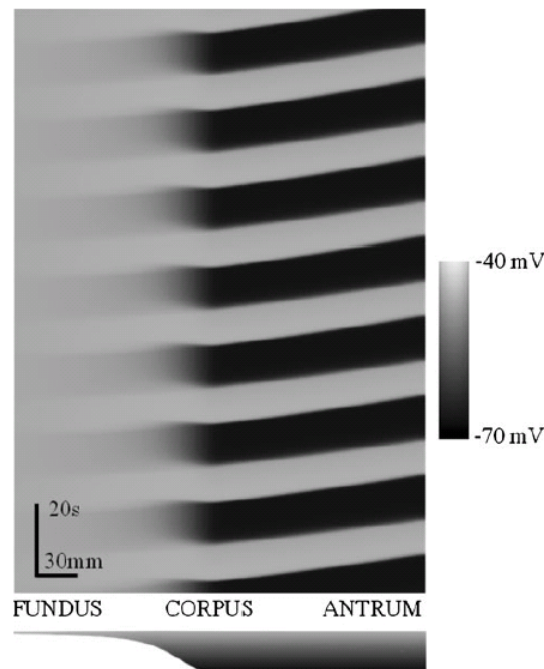
Figure 5.9. A spatiotemporal plot of simulated SMC electrical activity in the cable model, incorporated with frequency entrainment and RMP gradient. The fundus region is quiescent relative to the corpus and antrum, which is consistent with the physiological observation where slow waves appear to initiate from corpus and propagate aborally towards the antrum. Here, in the results, slow waves are produced at 3.1 cpm and stably propagate towards the antrum. The bottom panel shows an orthogonal projection of membrane potential across all time, from the fundus to the antrum where the fundus potentials are highly depolarized within a narrow range, while relatively sharp gradient of resting potential appeared for the transition into the proximal corpus region, and finally the resting potentials stabilized at a hyperpolarized value all the way to the end of the antrum in this cable.

amplitude of about 1 - 3 mV and the slow wave amplitude increases to a maximum of 27 mV in the distal antrum, close to a reported value of 30 mV from the guinea pig antrum [277]. Also noteworthy from Figure 5.10 is the phase difference between the slow waves from the various spatial locations that indicate an aboral propagation of slow waves. The simulation results suggest that the frequency gradient is an important factor in slow wave propagation while the tissue conductivities and RMP gradients contribute to a much lesser extent.
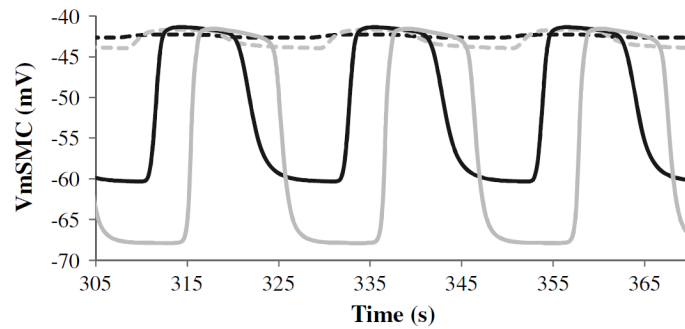
Figure 5.10. Simulated smooth muscle slow wave potentials at various spatial locations from the fundus to the antrum. With the most proximal end of the fundus as the reference point, dashed black line is at 3 mm, dashed grey line is at 67 mm, black solid line is at 135 mm and grey solid line is at 202 mm. As the distance increases from the fundus end, the slow waves become bigger in amplitude. The slow waves are also in the proper order, where the nearer the location is to the fundus, the earlier the start of the slow waves.

5.2.6 Limitations and recommendations

Transmural RMP gradient

The resting membrane potential gradient does not exist only in the longitudinal direction, but also across the GI wall, i.e., transmurally, in the stomach and small intestine of several animal species (such as murine, canine and humans). The transmural resting membrane potential was found to become depolarized towards to the inner circular smooth muscle (i.e., nearer to the lumen) since lesser carbon monoxide from the myenteric ICC gets diffused into a deeper smooth muscle layer [269, 278]. The physiological utility of resting membrane potential gradients is thought to allow graded contractile responses from the smooth muscles under different physiological conditions for effective motility control. Furthermore, the RMP gradient can influence electrical propagation from the outer to inner muscle layers. Therefore, it would be worthwhile to incorporate a transmural resting membrane potential gradient into the cable or higher spatial scale models,

towards creating more functionally realistic models and to better examine motility in health and disease.

Table 5.3 shows a list of transmural resting membrane potentials and carbon monoxide concentrations compiled from a number of papers for different animal species that, though limited, could assist a preliminary investigation of transmural resting membrane potential gradient in a multi-cellular framework. In the earlier discussion, carbon monoxide was used as a proxy to control resting membrane potential through a potassium current modulating factor that is a function of carbon monoxide concentration. The same approach can be applied to create a transmural resting membrane potential. This then requires a mathematical description of both the longitudinal and transmural spatial distribution of carbon monoxide concentration.

Table 5.3. Transmural resting membrane potential values and carbon monoxide concentration values, together with their references are provided here.

	Species	RMP outer circular muscle (mV)	RMP inner circular muscle (mV)	[CO] outer circular muscle (nmol/mg wet tissue)	[CO] inner circular muscle (nmol/mg wet tissue)
Fundus	canine	-47 [53]		0.2 [269, 278]	
	human	-47 [53, 279]			
Corpus/ antrum	canine	-60 [53]	-52 [53]	0.4(antrum) [269, 278]	0.24(antrum) [269, 278]
		-75 [280-282]	-64 [280-282]		
	human	-74 [279]	-62 [279]		
Jejunum	canine	-62 [53, 279, 283]	-50 [53, 279, 283]	1.44 [269, 278]	0.72 [269, 278]
	human	-69 [53, 279]	-59 [53, 279]		

Updating the pacemaking mechanism

The ICC cellular description is based on a NSCC pacemaking hypothesis, and as mentioned, recent evidence has suggested that a calcium-activated chloride conductance, encoded by the ANO-1 gene, is responsible for intrinsic pacemaking of the ICC. Therefore, it may be necessary to update the ICC model with a calcium-activated chloride mechanism and then re-evaluate the frequency and entrainment methods developed here [64, 90].

Re-parameterization

Experimental data is also lacking to parameterize the cable model, such as for the bidomain conductivities. Therefore, the parameter values here were determined so as to reproduce membrane potentials recorded from finite locations along the canine stomach reported in the work of Szurszewski [53]. With technological advances, a small number of recent studies have made high-resolution extracellular recordings of electrical activity over large surface of the canine stomach [284], porcine stomach [285] and human stomach [286] (versus finite location data from [53]), these promise a re-parameterization of the cable model parameter values (The interested reader can refer to Dinning et al [287] for a review of technical advances to monitor human motility patterns). Because these are extracellular potential recordings, the cable model requires an explicit representation of the extracellular potentials. An objective function can be set up for minimization against experimental data of these high resolution recordings to obtain the required parameter values. However, there are two caveats to be mindful of. The first is that, the increase in slow wave amplitudes from the fundus to the antrum could be a result of a more

polarized RMP due to polarizing bio-agents or higher amplitude electrical events stemming from the underlying cellular mechanisms (such as ionic currents), or both. Therefore, care should be taken to ensure the cellular models are realistic and up-to-date. For one, the appearance of ANO-1 calcium-activated chloride channel findings warrants an update. The second caveat is the potential contribution of intramuscular ICC, a significant variant of ICC, towards early activation of slow waves [284, 285, 288, 289]. The intramuscular ICC are interspersed between the smooth muscle cells [290] and are also found in high density in the gastric fundus which are devoid of ICC-MY [291].

Incorporation of other GI gases

Carbon monoxide aside, two other endogenous GI gases were later found to influence GI motility, i.e., hydrogen sulfide [292-294] and nitric oxide [295-297]. These gases affect the ion channels of GI smooth muscles and in turn alter electromechanical behaviour of these muscles. Hydrogen sulfide was found to activate human jejunal SCN5A encoded sodium channels by increasing peak currents and positively shifting steady-state activation [298]. Nitric oxide, a neurotransmitter produced by the enteric neurons, influences potassium channels in the GI smooth muscles [297, 299] and ICC [300]. Nitric oxide can also act as a co-factor with carbon monoxide in influencing human jejunal L-type calcium channels [221, 301]. Given the apparent importance of these gases in GI cellular activity and in GI motility, and as more experimental findings appear, it would be worthwhile to model their effects on ion channels

and subsequently their spatial distribution and influence at the tissue or organ level.

A jejunal cable model

The human jejunum smooth muscle cell model was earlier described. With the development of a suitable jejunal ICC cell model, a corresponding jejunal cable model can then be set up to better understand multi-cellular intestinal electrophysiology.

5.3   Investigation of the R76C telethonin mutation in a cable model

The effects of altered SCN5A function by the R76C telethonin mutation was investigated in single cell simulation studies in Chapter 3 and Chapter 4. One next step was to investigate the mutation in a multi-cellular setting where intercellular communication between the ICC and SMC was incorporated. The principles of creating an extended bidomain framework and for slow wave propagation and entrainment were applied to create a suitable one dimensional model to evaluate the consequences of mutation.

5.3.1   Method

The stomach fundus is known to be electrically quiescent while the slow waves are known to initiate in the corpus and propagate towards the antrum. The earlier Figure 5.9 shows that the RMP gradient stabilized at a relatively polarized and steady resting potential at some point in the corpus-to-antrum region. To efficiently study the effects of mutations on electrical behaviour in

gastric tissue, a cable with a physiological length of 180 mm was selected. This cable corresponds to a stretch of electrically active gastric strip, along the greater curvature, from the corpus, at the approximate slow wave initiation site, to the terminal antrum. Figure 5.11 shows the anatomical location of the 180 mm gastric cable, in the context of a whole stomach.
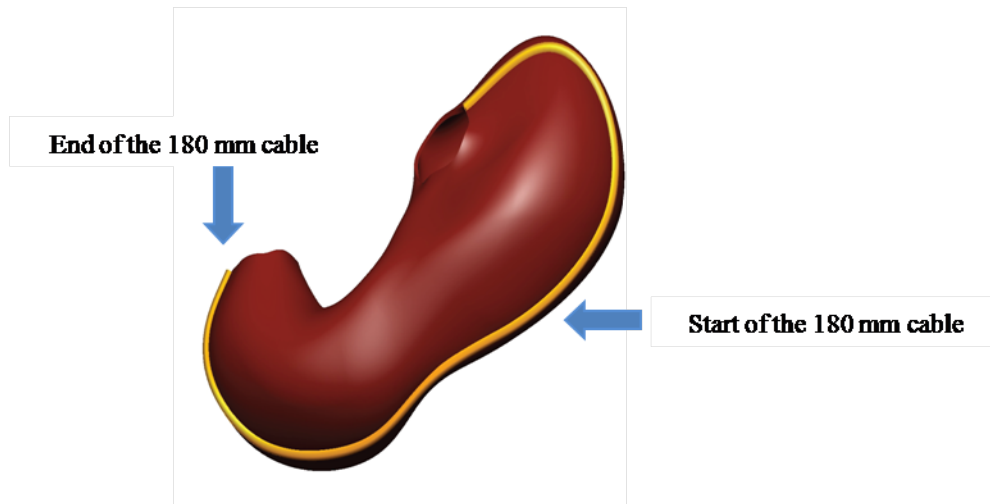
Figure 5.11. Picture of a human stomach. Yellow cable represents a gastric strip along the greater curvature. The blue arrow indicates the approximate position of the corpus that measures a distance of 180 mm to the terminal antrum, at the distal end of the gastric strip.

The approaches for the extended bidomain framework, and the entrainment mechanism that were discussed in the earlier sections of this chapter, were applied to create a similar continuum model with the chosen length of 180 mm. As before, the Corrias and Buist gastric ICC and SMC models were integrated into the continuum model. Due to the absence of a biophysically based human intestinal ICC model, the multi-cellular study of the small intestine was not performed.

Using the respective Markov sodium channel models developed in Chapter 3, the R76C mutation was investigated in a homozygous scenario, where the 180 mm cable model is separately integrated with 100% SCN5A channels and 100%

R76C affected sodium channels. It was assumed that telethonin exists in both the SMC as well as the ICC. The backward Euler Method was implemented for the Markov sodium channels, to be solved with LU decomposition, at the common time step size of 0.1 ms.

5.3.2 Results

The simulation results for the wild-type state, and the R76C mutation affected state are shown in Figure 5.12. Parts (a) and (b) show the spatiotemporal plot of the slow waves over the entire length of the 180 mm cable and over a steady-state time duration of 100 s. No noticeable impact on the slow wave propagation due to the R76C mutation was observed. The propagation speed of the slow waves, from the corpus to the antrum, was calculated to be 16.71 mm/s for the wild-type case, and 16.20 mm/s in the presence of the R76C mutation. Parts (c) and (e) show the ICC and SMC slow waves respectively, recorded at a location of 25 mm from the proximal end of the cable. It was observed that the R76C mutation resulted in a slight increase in frequency (dashed lines), relative to the wild-type result (solid lines). Parts (d) and (f) show the corresponding ICC and SMC sodium currents respectively, where the R76C sodium currents in both cases reflect a gain-of-function through the stronger inward currents brought about by the mutation. Part (g) shows the corresponding SMC intracellular calcium concentration which has a frequency consistent with the slow waves, but no change in the concentration values was observed. Note that the equivalent results for the location of 90 mm and 180 mm in the cable are provided in Appendix 17 and these results do not differ from those presented here.
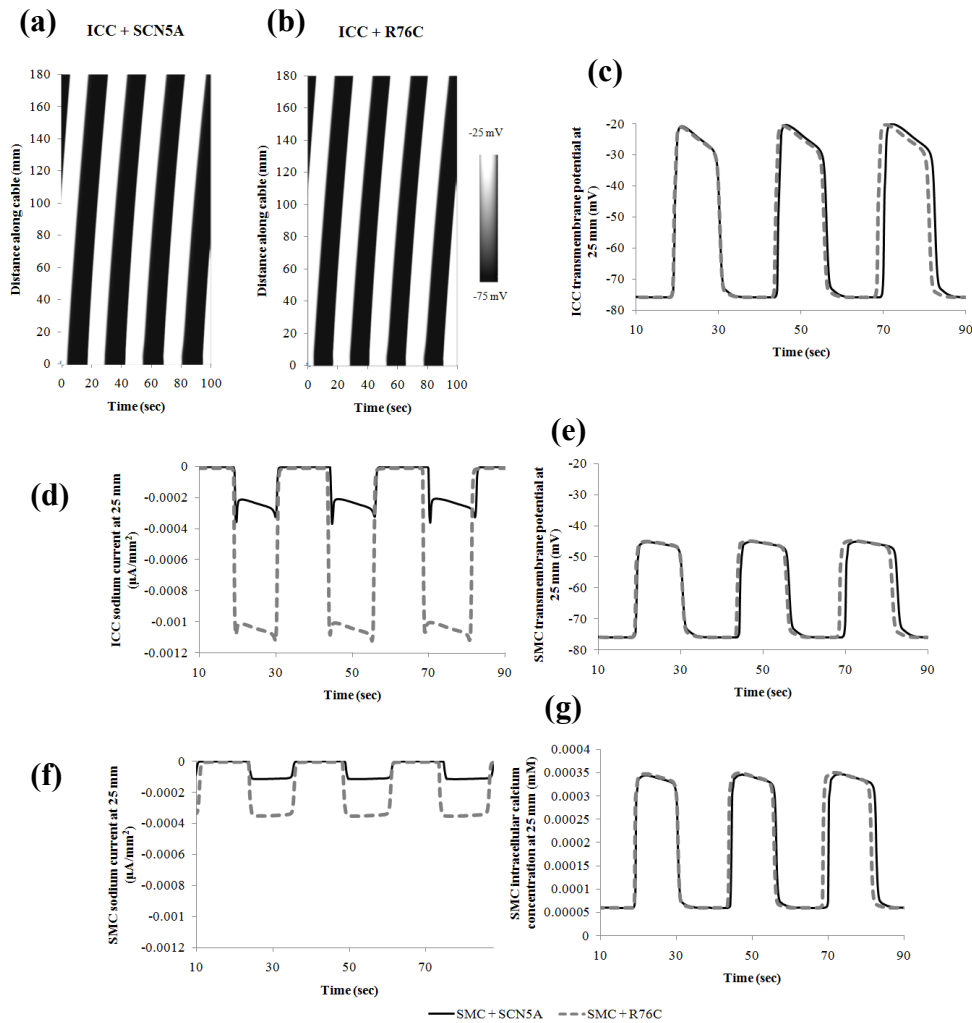
Figure 5.12. 180 mm cable model results for the R76C study. (a) and (b) are the spatiotemporal plots for ICC + SCN5A and ICC + R76C respectively. (c) and (e) are the ICC and SMC slow wave potentials respectively. (d) and (f) are the ICC and SMC sodium currents respectively. (g) is the SMC intracellular calcium concentration. Solid lines for wild-type results and dashed lines for R76C mutation results.

5.3.3   Discussion

The cable propagation speeds of 16.71 mm/s (wild-type) and 16.20 mm/s (R76C) correspond to propagation duration of 10.77 s and 11.11 s respectively, along the 180 mm cable. Therefore, the R76C mutation has resulted in a slightly slower propagation speed, and this may be consequential of the apparent increase in slow wave frequency that was observed in Figure 5.12(c).

One explanation for this is that at a faster frequency, slow wave excitation from a proximal node is delayed by the relatively greater refractoriness in the adjacent distal node at that time point. Consequently, the onset of slow wave in this distal node is delayed, therefore resulting in longer time duration for a slow wave to propagate over the same distance. Note that tissue conductivity was unchanged in the both the wild-type and R76C scenarios.

The ICC and SMC slow waves that were recorded at selected spatial points indicated a consistent slight increase in frequency. This contrasts with the single cell results where a slight lengthening of the ICC slow wave duration and depolarization of the SMC resting potential were observed. Therefore, in the multi-cellular environment where the ICC and SMC are interconnected, the pacemaking ICC appeared to have driven the SMC such that the SMC resting membrane potential was no longer depolarized by the R76C mutation, just like in the single ICC slow wave results. At steady-state in the multi-cellular setting, the increment in sodium current due to mutation seemed to have indirectly tuned the pacemaking mechanism, such that the slow waves were at a slightly higher pacing frequency. The ability of the R76C altered sodium current in increasing the ICC slow wave plateau duration, at the single cell level, is an indication of its potential to alter slow wave period, and hence frequency. The ICC slow wave frequency is driven by the pacemaking mechanism's frequency which in turn is reliant on the calcium cycling within. A change in ICC membrane potential due to the R76C altered sodium current could influence the regulation of ionic conductances that carry the calcium ions. Subsequently, the downstream calcium-dependent processes such as the

pacemaker mechanism could be affected, leading to altered frequency at steady state in the multi-cellular setting. The SMC slow waves, driven by the ICC excitation, follow the same frequencies.

Even though the R76C mutation induced observable changes in the cable model, it does not appear to be a significant adverse change against the wild-type/healthy state. The propagation speed and the slow wave frequency were only slightly changed, despite a relatively greater change in the sodium current influxes. Furthermore, the calcium concentration did not change, therefore implying that the contraction should not change in strength. Nonetheless, the R76C mutation might require additional conditions for greater impact on electrics. Furthermore, the cable model is built upon single cell ICC and SMC models of mixed animal species, of which the pacemaking mechanism is still of debate. A refinement of these single cell models would aid in the cable model studies. It is also known that electrics affect mechanics and vice versa, therefore the incorporation of mechanics is an important pursuit to further the findings here.

5.4   Investigation of the G298S mutation in a cable model

The G298S mutation of the sodium channel was investigated in the single cell models in Chapters 3 and 4. Here, the same mutation was investigated in a 180 mm cable model, in a similar manner to that of the R76C mutation in the previous section.

5.4.1   Method

The same 180 mm cable model used in the previous section to study the R76C mutation was employed here. The sodium channel models developed in Chapter 3 were used to investigate the G298S mutation in each of the four common polymorphic-splice backgrounds. From the earlier single cell results, homozygous scenarios should suffice for the investigation here, i.e., the cable model were separately integrated with 100% wild-type model and 100% G298S model, for each of the four common backgrounds.

5.4.2   Results

H558/Q1077del background

Figure 5.13 shows the wild-type G298 (V1_WT) and G298S mutation (V1_MT) simulation results for the most common background of H558/Q1077del. (a) and (b) show the spatiotemporal plots of the slow waves for the wild-type and mutation cases respectively, where no noticeable differences were observed between the two. The remaining results are the temporal plots for the slow waves taken at a location 25 mm from the proximal end of the cable model. (c) and (e) are the ICC and SMC slow waves respectively, where it was observed that the G298S mutation did not change the slow wave behaviour. (d) and (f) are the ICC and SMC sodium currents respectively, and here the G298S mutation has caused a general reduction in sodium current. Apparently, this reduction in sodium current was insufficient to elicit a change in the slow wave behaviour of the ICC and SMC. (g) shows the SMC intracellular calcium concentration, which did not change due to mutation, and therefore no change in contractile strength is expected.

H558R/Q1077del background

Figure 5.14 shows the wild-type G298 (V2_WT) and G298S mutation (V2_MT) simulation results for the background of H558R/Q1077del. As before, (a) and (b) are the spatiotemporal plots of the slow waves for the wild-type and mutation cases respectively, but no noticeable differences were observed. The other results are temporal plots for the slow waves, taken at a location of 25 mm from the proximal end of the cable model. Similarly, the mutation was not able to change the ICC and SMC slow waves and the SMC intracellular calcium concentration as shown in (c), (e) and (g) respectively. This was despite the mutation's ability to alter the sodium currents of the ICC and SMC, as shown in (d) and (f).

H558/Q1077 background

Figure 5.15 shows the wild-type G298 (V3_WT) and G298S mutation (V3_MT) simulation results for the background of H558/Q1077. As before, (a) and (b) are the slow wave spatiotemporal plots for the wild-type and mutation cases respectively, but again, no noticeable differences were observed. The other results correspond to temporal plots for slow waves at the same position of 25 mm on the cable model. The mutation was again unable to change the ICC and SMC slow waves and the SMC intracellular calcium concentration as shown in (c), (e) and (g) respectively, despite causing an increase in sodium current in both the ICC and SMC, as shown in (d) and (f). Note that, here the mutation has caused a clear increase in sodium current, consistent with the results from earlier single cellular studies that this background results in a distinct gain-of-function effect for the G298S mutation.

H558R/Q1077 background

Figure 5.16 shows the wild-type G298 (V4_WT) and G298S mutation (V4_MT) simulation results for the least common background of H558R/Q1077. As before, (a) and (b) are the slow wave spatiotemporal plots for slow waves at 25 mm. The mutation seems to have decreased the frequency of the ICC and SMC slow waves and the SMC intracellular calcium concentration slightly as shown in (c), (e) and (g) respectively. This was in the presence of a reduction in the sodium current in both the ICC and SMC as shown in (d) and (f). However, no change in the calcium concentration values was observed, an indication that no change in contraction strength is expected.

The equivalent results for all the four backgrounds at the locations of 90 mm and 180 mm in the cable are provided in Appendices 18 to 21. These results do not differ from those presented above. As for the propagation speed, the same value of 13.24 mm/s was computed for both the wild-type and G298S mutation in all four backgrounds.
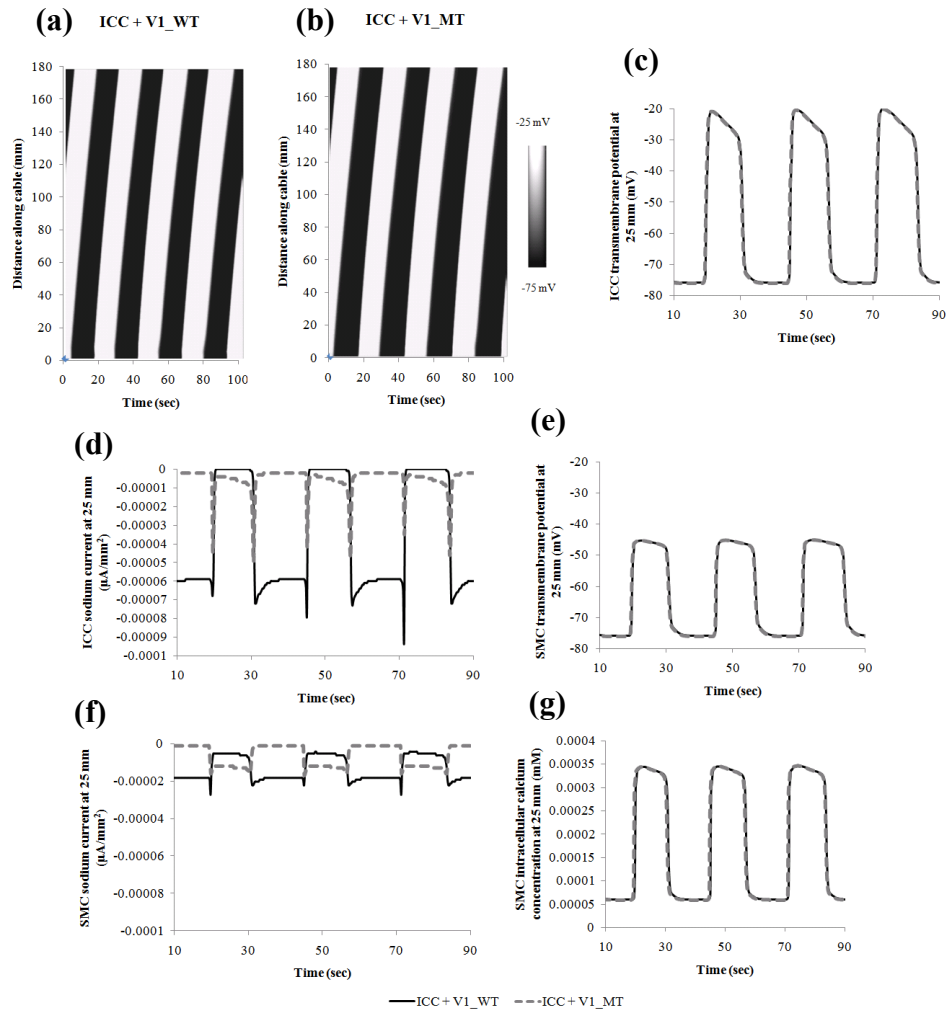
Figure 5.13. 180 mm cable model results for the H558/Q1077del background. (a) and (b) are the spatiotemporal plots for wild-type sodium channels and G298S sodium channels respectively. (c) and (e) are the ICC and SMC slow wave potentials respectively. (d) and (f) are the ICC and SMC sodium currents respectively. (g) is the SMC intracellular calcium concentration. Solid lines for wild-type results and dashed lines for G298S mutation results.
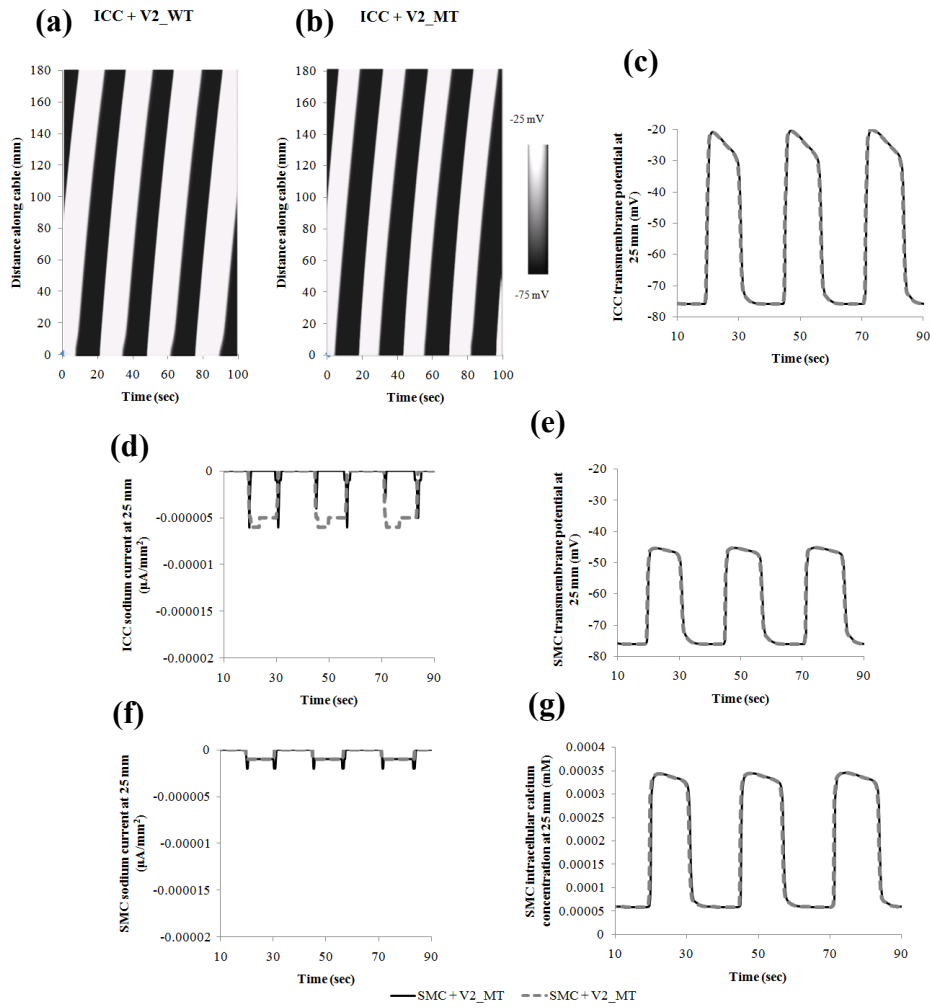
Figure 5.14. 180 mm cable model results for the H558R/Q1077del background. (a) and (b) are the spatiotemporal plots for wild-type sodium channels and G298S sodium channels respectively. (c) and (e) are the ICC and SMC slow wave potentials respectively. (d) and (f) are the ICC and SMC sodium currents respectively. (g) is the SMC intracellular calcium concentration. Solid lines for wild-type results and dashed lines for G298S mutation results.
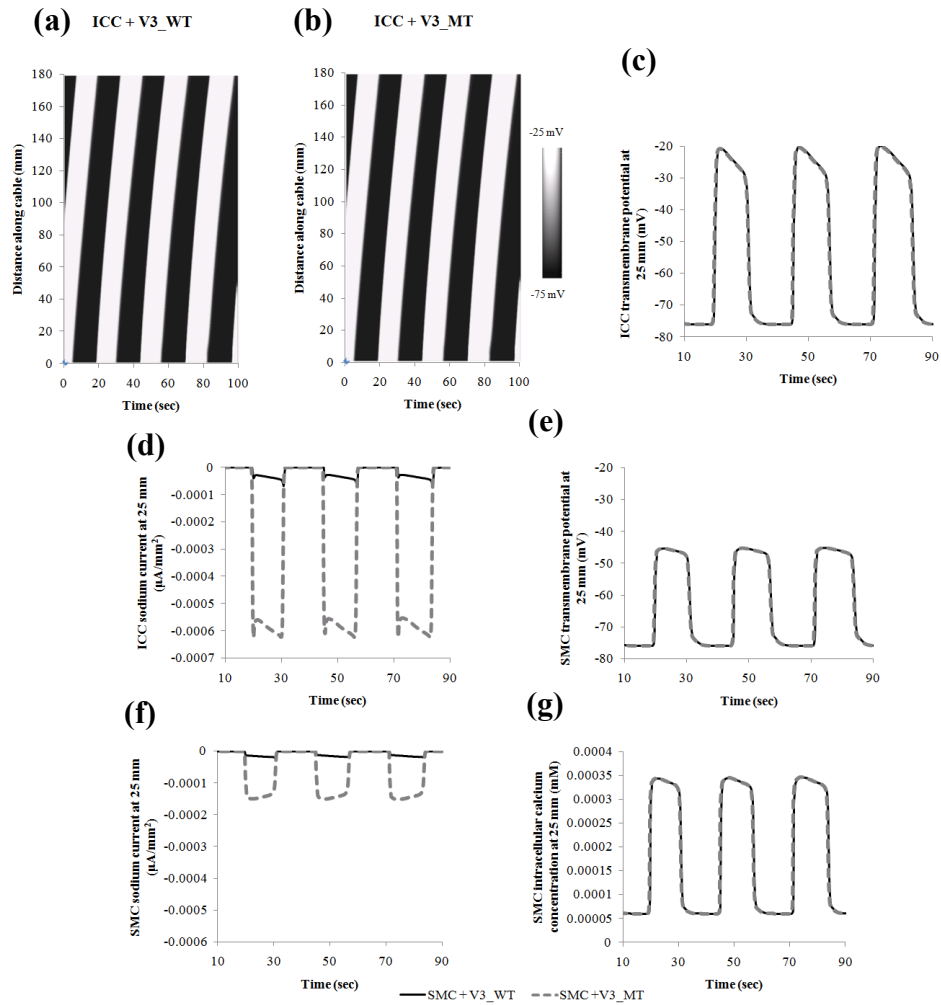
Figure 5.15. 180 mm cable model results for the H558/Q1077 background. (a) and (b) are the spatiotemporal plots for wild-type sodium channels and G298S sodium channels respectively. (c) and (e) are the ICC and SMC slow wave potentials respectively. (d) and (f) are the ICC and SMC sodium currents respectively. (g) is the SMC intracellular calcium concentration. Solid lines for wild-type results and dashed lines for G298S mutation results.
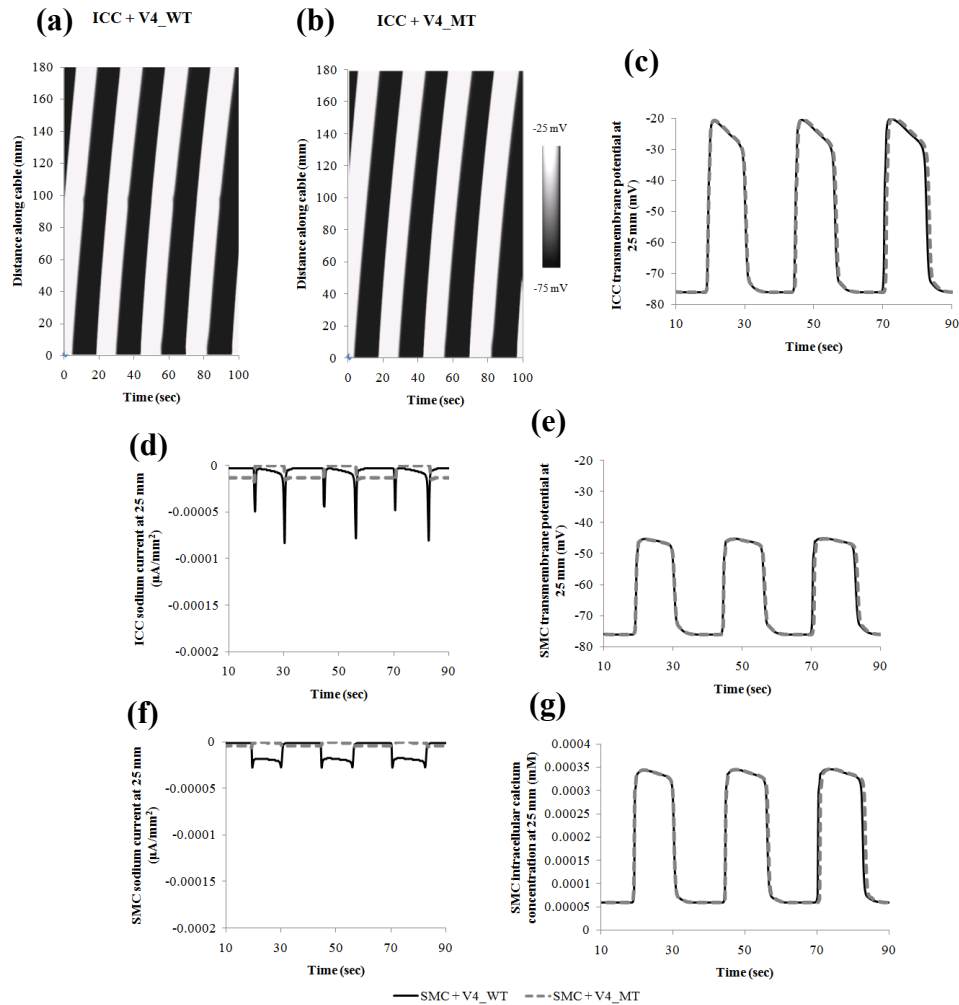
Figure 5.16. 180 mm cable model results for the H558R/Q1077 background. (a) and (b) are the spatiotemporal plots for wild-type sodium channels and G298S sodium channels respectively. (c) and (e) are the ICC and SMC slow wave potentials respectively. (d) and (f) are the ICC and SMC sodium currents respectively. (g) is the SMC intracellular calcium concentration. Solid lines for wild-type results and dashed lines for G298S mutation results.

5.4.3 Discussion

The results here are consistent with findings from the single cell studies, where almost negligible changes to the slow wave potentials were observed despite the G298S mutation causing a change in sodium currents in all four backgrounds. In all but the third background, the G298S mutation resulted in a net loss-of-function in sodium currents. A distinct and significant increase in sodium currents was observed for the third background of H558/Q1077; a

similar observation was made in the single cell studies. An interesting and new finding was that in the fourth background of H558R/Q1077, the mutation seemed to have elicited a slight decrease in frequency. A closer look at the sodium currents revealed that in the presence of the mutation, there are almost negligible sodium currents in the ICC and SMC that have caused this change. In another words, this suggests that the presence of sodium currents is necessary to maintain the slow wave frequency. As previously mentioned, the maximum sodium channel conductance is an uncertain parameter that can alter the effects of the mutations in these backgrounds. For instance, the third background of H558/Q1077 may, together with the mutation, reduce the maximum conductance through expression, trafficking, localization and/or degradation pathways in the biological situation. If so, instead of an increase in current, a loss in current may result. The uncertainty in the maximum conductance value also means that the existing values used in the model may have masked the pathogenic effects the mutation could have on the slow waves. Lastly, the propagation speed is relatively stable at 13.24 mm/s for all eight cases, mutation or not. This translates to travel duration of about 13.6 s. The absence of change in speed is expected, given that the slow wave potentials were not altered much by the mutation.

It appears that the G298S mutation is unable to cause an adverse electrophysiological change, despite its discovery in a patient with irritable bowel syndrome. However, its adverse influence potential may require additional conditions as well as with the use of physiological sodium channel maximum conductances. Experimental studies that clarify the effects of

H558/H558R polymorphism, Q1077/Q1077del alternative splicing, as well as the G298S mutation in altering the maximum conductance, particularly in the aspects of expression, trafficking and degradation, will help to improve the computational findings. As mentioned in the discussion for the R76C cable results, the gastric cable model is built upon single cell ICC and SMC models of mixed animal species, of which the pacemaking mechanism is still of debate. Therefore, a refinement of these models would help in the higher scale studies like this. The development of mechanical descriptions will also aid the findings here. The effects of mutation aside, it is hoped that the future work can additionally advance our understanding on whether the common sodium backgrounds are indeed unable to confer resistance or susceptibility to disease as the findings here seemed to indicate.

5.5   Chapter summary

The earlier sections of this chapter have demonstrated a successful proof-of-concept, through one dimensional 100 mm cable constructs, for (1) the extended bidomain framework for multiple cell types, and (2) the slow wave entrainment and propagation model through the incorporation of the entrainment mechanism, the frequency gradient, and the RMP gradient. Subsequently, the two concepts were applied to create a 180 mm cable model to study the mutations related to the sodium channels in the ICC and SMC. The R76C mutation was found to have a gain-of-function effect, and was able to slightly increase the slow wave frequency, but the change did not appear sufficient to cause disorder. The G298S mutation was found to have a primarily loss-of-function effect on the sodium currents, but did not translate to a significant change in slow wave behaviour. To try to obtain further insight, the one dimensional model can be scaled up to form a multi-dimensional tissue block to better examine how slow wave initiation and propagation characteristics over a greater volume of GI tissue may be affected by the mutations. Experimentally, such details require surgery to invasively record using multi-electrode arrays placed on the serosal surface of the stomach in live subjects [284-286]. Computationally, this is easier to investigate, and the multi-cellular framework can also serve to develop less invasive methods such as a multi-electrode device to record gastric electrical patterns from the skin surface instead.

Chapter 6
Conclusions

*"An expert is a man who has made all the mistakes,
which can be made, in a very narrow field."*
– Niels Bohr

6 Conclusions

The key hypothesis to investigate in this thesis was that *ion channel mutations, particularly the mutations of SCN5A, contribute to GI motility disorders*. This has been performed based on the objectives listed in Chapter 1, where computer models across the sub-cellular, single cell and multi-cellular spatial scales were developed and used. Specifically:

(1) Computer models describing the wild-type and mutation affected ion channels, including variants that arise from alternative splicing and polymorphism were developed.

(2) A biophysically based human jejunal smooth muscle cell model was developed.

(3) An extended bidomain model and an entrainment and propagation model were developed.

(4) Integrative investigation of the mutations in existing and newly developed single cell and multi-cellular models was performed.

All in all, in addressing the main hypothesis, significant modelling developments were made from the sub-cellular to the multi-cellular levels which were deemed to be valuable contributions to the multi-scale framework of GI motility. It is noteworthy that the descriptions here are necessarily

biased. The current GI models were constructed with appropriate granularity based on what are sufficient for the modelling objectives and the availability of experimental and clinical findings. As the famous systems biologist Denis Noble once said: "Models are partial representations. Their aim is explanation: To show which features of a system are necessary and sufficient to understand it" [18]. The computational cost would be too great to include all details, and possibly all resources in the universe would not be enough (as rationalized by Denis Noble in his book, The Music of Life [302]).

The models developed here, were applied to primarily investigate sodium channelopathies of GI motility from an electrophysiological perspective. A pacemaking ICC's electrical activity dictates the passive SMC's electrical response. Therefore, electrophysiological perturbations in the ICC and/or the SMC may cause a change in the SMC's intracellular calcium concentration through the calcium currents as well as any intracellular calcium regulatory mechanisms. The intracellular calcium concentration determines the extent of myosin light chain kinase activation and the subsequent smooth muscle contraction [303-305]. A suitable level of electrophysiological change can then cause an adverse change in contractility and motility. The results showed that the R76C mutation has a greater potential in altering electrophysiology than the G298S mutation. But it cannot yet be definitively concluded at this stage that these mutations are the primary cause of GI disorders.

6.1   Recommendations for future work

A number of factors may have masked the pathogenic potential of both mutations that future studies can help to clarify. Therefore the following key future works are suggested:

(1) Perform critical re-examination and updates for the existing gastric cell models against new findings that have appeared since the models were published; for instance, to relook the ICC pacemaking mechanism in the light of recent evidence that an ANO-1 encoded calcium-activated chloride channel serves as the pacemaking conductance [86, 89-91]. These are important towards a more realistic investigation of mutation consequences, and in the development of multi-cellular models.

(2) Investigate whether the sodium channel models can be further applied to mine useful biophysical statistics useful for understanding channelopathies. For instance, the application of appropriate statistical techniques to examine microscopic (single ion channel) properties using macroscopic descriptions that the sodium channel models describe.

(3) The development of a human intestinal ICC model is pertinent to examine the R76C and G298S mutations that were correlated with intestinal disorders. Further channelopathy investigations can then be performed by coupling the intestinal ICC model to the jejunal SMC model that was developed here. The extended bidomain framework approach can also be applied to integrate the intestinal ICC and SMC models into a multi-cellular model to study the

mutations. The mutations may well find greater impact in the intestinal ICC to cause altered contractility in the SMC of the small intestine.

(4) Develop a mechanical extension to the multi-scale electrical framework (for example, [306]), which can include descriptions of mechanosensitive ion channels [307-310] to single smooth muscle cell active contraction and soft tissue mechanics [311, 312], and to multi-cellular mechanical deformation. Motility is about both electrics and mechanics, a mechanical extension would reflect a more realistic physiological situation where electrics and mechanics interplay, in a duplex fashion, and thus eventually allow an examination of contractility and deformability in a GI tissue or organ [35].

(5) A model of the whole stomach electrophysiology (or even the whole small intestine) can be developed based on the multi-cellular approaches that were discussed earlier. Anatomical information from a suitable public database or patient specific imaging data can be used to create a realistic geometry of the organ model. A more realistic model like this benefits investigations but is limited by the availability of experimental and clinical data for its construction, as well as the high computational cost associated with a highly complex model. Nonetheless, a whole organ model can provide a clearer understanding of pathophysiology in the actual human organ and assist in diagnosis and treatment development. As mentioned in Chapter 2, a whole organ model will facilitate the development of torso (or diagnostic) models of electrography and magnetography that can correlate genotype disturbances at the sub-cellular level to unique electromagnetic signatures that can be non-invasively

measured at the body surface. This aids diagnosis for effective treatment. Multi-cellular models like these can also be applied to develop and optimize electrode-based GI pacemaking devices [313, 314].

(6) Peristalsis is a form of motility that moves the bolus in the GI tract during the post-prandial state; an impaired peristalsis results in motility disorders. Thus far, the focus was on the primary motility effector cells of the ICC-MY and the circular SMC. However, it is known that the enteric nervous system (ENS), present in the myenteric plexus, independently senses and provides extrinsic motor control on the ICC and SMC to elicit peristalsis through descending inhibition and ascending contraction. In addition, the longitudinal SMC layer which is the next thickest muscle layer to the circular smooth muscles, is also innervated by the ENS, activated by the ICC-MY and is said to functionally contribute to motility such as in peristalsis [315]. Therefore, given the significance of the ENS and the longitudinal SMC layer, it would be relevant to extend our computational studies into these areas to better understand motility in health and disease.

Finally, a grand goal of a comprehensive multi-scale computer framework of the GI system is to establish a workflow useful for decisions in personalized clinical diagnosis and treatment, where clinical measurements recorded from a patient, in several areas from general physiological data (for example, skin surface electrical recordings), to specific anatomical data and to experimental data from tissue samples, are used to customize multi-scale computer models. Analyses of the simulation predictions of these patient specific models can

provide more accurate diagnosis to select well targeted treatment strategy, and thereby improve the effectiveness of patient care (see Figure 6.1).
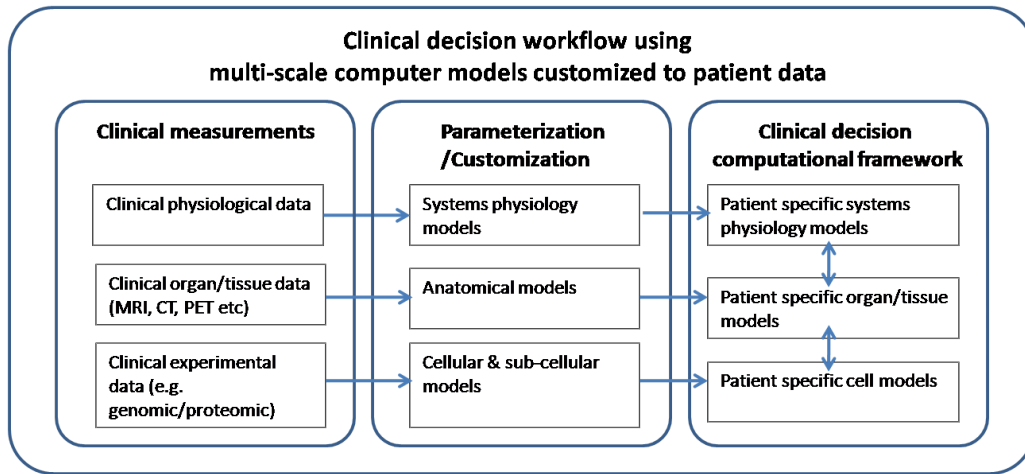
Figure 6.1. A clinical decision workflow that incorporates multi-scale computer models. Clinical data measured from a patient are used to parameterize the computer models. In turn, these patient specific models in the clinical computational framework will facilitate clinicians in making better decisions in their diagnoses and treatment strategies.

6.2 Computational notes

A number of computer languages, programs and tools were picked up and used during the PhD research, which can be found in Appendix 22. A sample implementation of the models presented in this thesis may be requested from the NUS Computational Bioengineering Laboratory or from the author through the following email address: poh.yongcheng@gmail.com.

6.3 Publications

- 2010: Buist M.L., Corrias A., **Poh, Y.C**. A Model of Slow Wave Propagation and Entrainment Along the Stomach. Annals of Biomedical Engineering. 2010 May 1. PMID: 20437204

- 2010: Buist M.L., and **Poh Y.C.** An Extended Bidomain Framework Incorporating Multiple Cell Types, Biophysical Journal. 2010 July 7. PMID: 20655828

- Du P., **Poh Y.C.**, Lim J., Gajendiran V., O'Grady G., Buist M.L., Pullan A., Cheng L. A Preliminary Model of Gastrointestinal Electromechanical Coupling. IEEE Trans Biomed Eng. 2011 August 30. PMID: 21878406

- 2011: **Poh Y.C.**, Beyder A., Strege P.R., Farrugia G., Buist M.L. Quantification of a Gastrointestinal Sodium Channelopathy. Journal of Theoretical Biology. 2011 September 6. PMID: 21959314

- 2011: **Poh Y.C.** and Buist M.L. A Computational Approach to Understanding Gastrointestinal Motility in Health and Disease. Conference Proceedings, IEEE Engineering in Medicine and Biology Society. 2011 August. PMID: 22254340

- 2012: **Poh Y.C.**, Corrias A., Cheng N., Buist M.L. A Quantitative Model of Human Jejunal Smooth Muscle Cell Electrophysiology. PLoS ONE. 2012 July 4. PMID: 22912702

- 2012: **Poh Y.C.**, Buist M.L. et al. Quantification and Characterization of G298S Variants in Gastrointestinal Pathophysiology. Manuscript in preparation.

6.4 Conference presentations, abstracts & proceedings

- **Poh Y.C.**, Corrias A., Buist M.L. Computational Investigation of Gastrointestinal Channelopathy in a Novel Cellular Model. NUS Bioengineering Showcase 2012, NUS, 10th May 2012, Singapore. *Won the Best Poster Award.*

- Buist M.L., Corrias A., **Poh Y.C.** Multi-scale Models of Gastrointestinal Electrophysiology. International Conference of Biomedical Engineering 2008, 3rd - 6th Dec 2008, Singapore

- Buist M.L., **Poh Y.C.** From Cell to Organ: A multi-scale challenge in GI electrophysiology. Poster Presentation at the Neurogastroenterology and Motility Conference 2009, 27th to 30th August 2009, Chicago, U.S.A.

- **Poh Y.C.**, Buist M.L. Computational modelling of the gastrointestinal tract. Bioengineering Seminar Series, Division of Bioengineering, NUS, 23rd October 2009, Singapore

- **Poh Y.C.**, Buist M.L. Linking Genotype to Phenotype in the Gastrointestinal Tract. Poster Presentation at the 3rd East Asian Pacific Student Workshop on Nano-Biomedical Engineering, NUS, 21st and 22nd December 2009, Singapore

- **Poh Y.C.**, Buist M.L. Linking Genotype to Phenotype in the Gastrointestinal Tract. Invited poster presentation at the 2nd NUS Graduate School (NGS) Symposium, 5th February 2010, Singapore

- **Poh Y.C.**, Buist M.L. Quantifying a Sodium Channelopathy in the Gastrointestinal Tract. Poster presentation at the 2010 Joint International Neurogastroenterology and Motility Meeting, 2010, Westin Copley Place Boston, 26th-29th August 2010, Massachusetts, U.S.A.

- **Poh Y.C.**, Buist M.L. Computational Investigation of a Sodium Channelopathy. Oral presentation at the 6th World Congress of Biomechanics (in conjunction with 14th ICBME, 5th APBiomech), 2010, 1st-6th August 2010, Singapore

- **Poh Y.C.**, Buist M.L. Cellular Consequences of a Genetic Defect in the Gastrointestinal Tract. Oral Presentation at the 4th East Asian Pacific Student Workshop on Nano-Biomedical Engineering, NUS, 15th and 16th December 2010, Singapore

- **Poh Y.C.**, Buist M.L. Electrophysiological consequence of genetic perturbation in gastrointestinal diseases - a computational investigation. Invited poster presentation at the 3rd NUS Graduate School (NGS) Symposium, 28th February 2011, Singapore

- Rachel Lees-Green, Arthur Beyder, Gianrico Farrugia, Gregory O'Grady, **Poh Y.C.**, Martin Buist, Andrew J. Pullan. Computational Modelling of the Human Sodium Channel: Mechanical Stretch Effects on the Electrical Function of Interstitial Cells of Cajal and Smooth Muscle Cells. Oral presentation at the Digestive Disease Week 2011, 7th-10th May 2011 Chicago, Illinois, U.S.A.

- **Poh Y.C.**, Buist M.L. Quantitative Study of Gastrointestinal Motility Channelopathy. Oral presentation at the Biomedical Engineering Society of Singapore 5th Scientific Meeting, NTU, 28th May 2011, Singapore

- **Poh Y.C.**, Buist M.L. Multi-scale Framework to Understand Gastrointestinal Motility Disorder. Oral presentation at the WACBE 5th World Congress of Biomedical Engineering, 18th-21st August 2011, Tainan, Taiwan

- **Poh Y.C.**, Buist M.L A Computational Approach to Understanding Gastrointestinal Motility in Health and Disease**.** Oral presentation at the 33rd IEEE Engineering in Medicine and Biology Conference, Boston Marriott Copley Place Hotel, 30th August - 3rd September 2011, Boston, Massachusetts, U.S.A.

- **Poh Y.C.**, M.L. Buist. Computational Investigation of Cellular Electrophysiology for Gastrointestinal Dysmotility**.** Poster presentation at the 3rd DUNES Scientific Symposium. DUKE-NUS Graduate Medical School, 7th October 2011, Singapore

- **Poh Y.C.**, M.L. Buist. Computational Electro-mechanics to Investigate Pathogenic Factors for Gastrointestinal Dysmotility**.** 5th Mechanobiology Conference. Shaw Alumni House, NUS, 9th-11th November 2011, Singapore

- **Poh Y.C.**, M.L. Buist. A Model of Intestinal Smooth Muscle Activity. 5th East Asian Pacific Student Workshop on Nano-Biomedical Engineering, National University of Singapore, 12th to 14th December 2011, Singapore

- **Poh Y.C.**, A. Corrias, M.L. Buist. A Channelopathy for Irritable Bowel Syndrome? 5th East Asian Pacific Student Workshop on Nano-Biomedical Engineering, National University of Singapore, 12th to 14th December 2011, Singapore

- **Poh Y.C.**, A. Corrias, M.L. Buist. A Computational Investigation of Gastrointestinal Channelopathy in a Novel Cellular Model, 4th NUS Graduate School of Integrative Sciences and Engineering Symposium. National University of Singapore, 16th January 2012, Singapore

6.5   Courses

- GEM4 Winter School. **Molecular and Cellular Biomechanics with a Special Focus on Pediatric Sciences and Medicine**. University of Texas at Austin, 4th to 14th January 2010. Financial support by NUS Graduate School. (**Poster presentation was made**). Austin, Texas, U.S.A.

- GEM4 Summer School. **Molecular and Cellular Biomechanics with a Special Focus on Mechanobiology**. National University of Singapore, 25th to 31th July 2010. Singapore

- **ANMS 5th Biennial Course on Gastrointestinal Motility and Neurogastroenterology in Clinical Practice, 2010**, Westin Copley Place Boston, Massachusetts, 26th August 2010. Boston, U.S.A.

- **Training Course for Teaching Assistants**, Centre for Development of Teaching and Learning, National University of Singapore, 22n-23rd September 2010. Singapore

- **Workshop on Electrical Fields at the Cell and Protein Scale.** 33rd IEEE Engineering in Medicine and Biology Conference, Boston Marriott Copley Place Hotel, Boston, Massachusetts. 31st August 2011. Boston, U.S.A.

- **Workshop on Biological Micro Electro Mechanical Systems (BioMEMS): Fundamentals and Applications.** 33rd IEEE Engineering in Medicine and Biology Conference, Boston Marriott Copley Place Hotel, Boston, Massachusetts. 2nd September 2011. Boston, U.S.A.

Chapter 7
Bibliography

The objective of medical education and biomedical research is "to heal the sick and to advance the science". – Charles H Mayo, one of Mayo Clinic's founding brothers

7 Bibliography

[1]   J.F. Kuemmerle, "Therapy of gastrointestinal motility disorders: moving in the right direction," *Gastroenterologist*, vol. 2, (no. 2), pp. 166-73, Jun 1994.

[2]   "FDA Announces Discontinued Marketing of GI Drug, Zelnorm, for Safety Reasons". USA Food and Drug Administration. 23rd March 2012.<http://www.fda.gov/NewsEvents/Newsroom/PressAnnou ncements/2007/ucm108879.htm>.

[3]   J.E. Everhart and C.E. Ruhl, "Burden of Digestive Diseases in the United States Part III: Liver, Biliary Tract, and Pancreas," *Gastroenterology*, vol. 136, (no. 4), pp. 1134-1144, Apr 2009.

[4]   J.E. Everhart and C.E. Ruhl, "Burden of Digestive Diseases in the United States Part II: Lower Gastrointestinal Diseases," *Gastroenterology*, vol. 136, (no. 3), pp. 741-754, Mar 2009.

[5]   J.E. Everhart and C.E. Ruhl, "Burden of Digestive Diseases in the United States Part I: Overall and Upper Gastrointestinal Diseases," *Gastroenterology*, vol. 136, (no. 2), pp. 376-386, Feb 2009.

[6]   K.A. Gwee, "Irritable bowel syndrome in developing countries--a disorder of civilization or colonization?," *Neurogastroenterol Motil*, vol. 17, (no. 3), pp. 317-24, Jun 2005.

[7]   Changi General Hospital,"The abc's of Health, Irritable Bowel Syndrome," CGH, SingHealth, Singapore, 2010.

[8]   M.J. Ackerman, "Cardiac channelopathies: it's in the genes," *Nat Med*, vol. 10, (no. 5), pp. 463-4, May 2004.

[9]   C.E. Clancy and R.S. Kass, "Theoretical investigation of the neuronal Na+ channel SCN1A: abnormal gating and epilepsy," *Biophysical journal*, vol. 86, (no. 4), pp. 2606-14, 2004.

[10]   G. Farrugia, "Ion channels as targets for treatment of gastrointestinal motility disorders," *European Review for Medical and Pharmacological Sciences*, vol. 12, pp. 135, 2008.

[11]   A. Beyder and G. Farrugia, "Targeting ion channels for the treatment of gastrointestinal motility disorders," *Therap Adv Gastroenterol*, vol. 5, (no. 1), pp. 5-21, Jan 2012.

[12]   B. Braak, T.K. Klooker, D. Scholvinck, N. Hofman, A. Wilde, and G.E. Boeckxstaens, "Abdominal symptoms in patients with long QT syndrome and a "gain of function" mutation in the Nav1.5 sodium channel," *Gastroenterology*, vol. 134, (no. 4), pp. A683-A683, Apr 2008.

[13]   G.R. Locke, M.J. Ackerman, A.R. Zinsmeister, P. Thapa, and G. Farrugia, "Gastrointestinal symptoms in families of patients with an SCN5A-encoded cardiac channelopathy: evidence of an intestinal channelopathy," *The American journal of gastroenterology*, vol. 101, (no. 6), pp. 1299-304, 2006.

[14]   A. Mazzone, P.R. Strege, D.J. Tester, C.E. Bernard, G. Faulkner, R. De Giorgio, J.C. Makielski, V. Stanghellini, S.J. Gibbons, M.J. Ackerman, and G. Farrugia, "A mutation in telethonin alters Nav1.5

function," *The Journal of biological chemistry*, vol. 283, (no. 24), pp. 16537-44, 2008.

[15] Y.A. Saito, P.R. Strege, D.J. Tester, G.R. Locke Iii, N.J. Talley, C.E. Bernard, J.L. Rae, J.C. Makielski, M.J. Ackerman, and G. Farrugia, "Sodium channel mutation in the irritable bowel syndrome: Evidence for an ion channelopathy," *American journal of physiology. Gastrointestinal and liver physiology*, 2008.

[16] IUPS Physiome Project. 23rd March 2012. <http://www.physiome.org.nz>

[17] H. Gregersen, "The Giome project," *Neurogastroenterol Motil*, vol. 18, (no. 5), pp. 401-2, May 2006.

[18] D. Noble, "The rise of computational biology," *Nat Rev Mol Cell Biol*, vol. 3, (no. 6), pp. 459-63, Jun 2002.

[19] L.R. Johnson, *Physiology of the gastrointestinal tract / editor-in-chief, Leonard R. Johnson ; associate editors, James Christensen ... [et al.]*, New York: : Raven Press, 1987.

[20] L.R. Johnson, *Physiology of the gastrointestinal tract*, New York: Raven Press, 1987.

[21] L.R. Johnson, *Physiology of the gastrointestinal tract*, Amsterdam ; Boston: Elsevier Academic Press, 2006.

[22] L.R. Johnson, *Physiology of the gastrointestinal tract*, Burlington, MA: Elsevier Academic Press, 2006.

[23] Jacqui Simcock. "Digestion: a monumental effort to nourish the body". Professional solutions for everyday health and wellbeing. 23rd March 2012. <http://www.healthandherbs.co.nz/Health-Library/The-Human-Body---Tell-me-about----/Digestion>

[24] K.L. Koch and R.M. Stern, *Handbook of electrogastrography*, New York: Oxford University Press, 2004.

[25] W.L. Hasler, "Small Intestinal Motility," in Physiology of the gastrointestinal tract 4th ed., Amsterdam ; Boston: Elsevier Academic Press, 2006, pp. 935-964.

[26] "Anatomy of the Gastrointestinal Tract". Los Altos Feeding Clinic. 23rd March 2012.<http://www.pediatricfeeding.org/gi_anatomy.html>

[27] J.D. Huizinga and W.J.E.P. Lammers, "Gut peristalsis is governed by a multitude of cooperating mechanisms," *American Journal of Physiology-Gastrointestinal and Liver Physiology*, vol. 296, (no. 1), pp. G1-G8, Jan 2009.

[28] H. Silberman and A.W. Silberman, *Principles and practice of surgical oncology : multidisciplinary approach to difficult problems*, Philadelphia: Wolters Kluwer/Lippincott Williams & Wilkins.

[29] H. Gregersen and G. Kassab, "Biomechanics of the gastrointestinal tract," *Neurogastroenterol Motil*, vol. 8, (no. 4), pp. 277-97, Dec 1996.

[30] A.J. Burns, "Disorders of interstitial cells of Cajal," *J Pediatr Gastroenterol Nutr*, vol. 45 Suppl 2, pp. S103-6, Dec 2007.

[31] K.M. Sanders, T. Ordog, and S.M. Ward, "Physiology and pathophysiology of the interstitial cells of Cajal: from bench to bedside. IV. Genetic and animal models of GI motility disorders caused by loss of interstitial cells of Cajal," *Am J Physiol Gastrointest Liver Physiol*, vol. 282, (no. 5), pp. G747-56, May 2002.

[32] A.M. Drewes, H. Gregersen, and L. Arendt-Nielsen, "Experimental pain in gastroenterology: a reappraisal of human studies," *Scand J Gastroenterol*, vol. 38, (no. 11), pp. 1115-30, Nov 2003.

[33] A.C. Guyton and J.E. Hall, *Textbook of medical physiology*, Philadelphia: Saunders, 2000.

[34] M. Takaki, "Gut pacemaker cells: the interstitial cells of Cajal (ICC)," *J Smooth Muscle Res*, vol. 39, (no. 5), pp. 137-61, Oct 2003.

[35] D.H. Liao, J.B. Zhao, and H. Gregersen, "Gastrointestinal tract modelling in health and disease," *World J Gastroenterol*, vol. 15, (no. 2), pp. 169-76, Jan 14 2009.

[36] S. Cajal, "sur les ganglions et plexus nerveux de l'in-testin.," *C.R. Soc Biol (Paris)* vol. 45, pp. 217-223, 1893.

[37] P. Langton, S.M. Ward, A. Carl, M.A. Norell, and K.M. Sanders, "Spontaneous electrical activity of interstitial cells of Cajal isolated from canine proximal colon," *Proc Natl Acad Sci U S A*, vol. 86, (no. 18), pp. 7280-4, Sep 1989.

[38] M. Hanani, G. Farrugia, and T. Komuro, "Intercellular coupling of interstitial cells of cajal in the digestive tract," *International Review of Cytology - a Survey of Cell Biology, Vol. 242*, vol. 242, pp. 249-+, 2005.

[39] G.M. Dick, I.D. Kong, and K.M. Sanders, "Effects of anion channel antagonists in canine colonic myocytes: comparative pharmacology of Cl-, Ca2+ and K+ currents," *British Journal of Pharmacology*, vol. 127, (no. 8), pp. 1819-1831, Aug 1999.

[40] S. Yoneda, H. Takano, M. Takaki, and H. Suzuki, "Properties of spontaneously active cells distributed in the submucosal layer of mouse proximal colon," *Journal of Physiology-London*, vol. 542, (no. 3), pp. 887-897, Aug 1 2002.

[41] E.J. Dickens, F.R. Edwards, and G.D.S. Hirst, "Selective knockout of intramuscular interstitial cells reveals their role in the generation of slow waves in mouse stomach," *Journal of Physiology-London*, vol. 531, (no. 3), pp. 827-833, Mar 15 2001.

[42] K. Horiguchi, G.S.A. Semple, K.M. Sanders, and S.M. Ward, "Distribution of pacemaker function through the tunica muscularis of the canine gastric antrum," *Journal of Physiology-London*, vol. 537, (no. 1), pp. 237-250, Nov 15 2001.

[43] H. Suzuki, S.M. Ward, Y.R. Bayguinov, F.R. Edwards, and G.D.S. Hirst, "Involvement of intramuscular interstitial cells in nitrergic inhibition in the mouse gastric antrum," *Journal of Physiology-London*, vol. 546, (no. 3), pp. 751-763, Feb 1 2003.

[44] G.D.S. Hirst, E.A.H. Beckett, K.M. Sanders, and S.M. Ward, "Regional variation in contribution of myenteric and intramuscular interstitial cells of Cajal to generation of slow waves in mouse gastric antrum," *Journal of Physiology-London*, vol. 540, (no. 3), pp. 1003-1012, May 1 2002.

[45] H.T. Lee, G.W. Hennig, N.W. Fleming, K.D. Keef, N.J. Spencer, S.M. Ward, K.M. Sanders, and T.K. Smith, "The mechanism and spread of pacemaker activity through myenteric interstitial cells of Cajal in human small intestine," *Gastroenterology*, vol. 132, (no. 5), pp. 1852-65, May 2007.

[46] T.K. Smith, H.T. Lee, G.W. Hennig, N.W. Fleming, K.D. Keef, N.J. Spencer, S.M. Ward, and K.M. Sanders, "The mechanism and spread of pacemaker activity through myenteric interstitial cells of Cajal in human small intestine," *Gastroenterology*, vol. 132, (no. 5), pp. 1852-1865, May 2007.

[47] E. Battaglia, G. Bassotti, G. Bellone, L. Dughera, A.M. Serra, L. Chiusa, A. Repici, P. Mioli, and G. Emanuelli, "Loss of interstitial cells of Cajal network in severe idiopathic gastroparesis," *World J Gastroenterol*, vol. 12, (no. 38), pp. 6172-7, Oct 14 2006.

[48] J.D. Huizinga, X.Y. Wang, J. Diamond, and L.W.C. Liu, "Loss of intramuscular and submuscular interstitial cells of Cajal and associated enteric nerves is related to decreased gastric emptying in streptozotocin-induced diabetes," *Neurogastroenterology and Motility*, vol. 21, (no. 10), Oct 2009.

[49] K.M. Sanders, T. Ordog, and S.M. Ward, "Physiology and Pathophysiology of the Interstitial Cells of Cajal: From Bench to Bedside IV. Genetic and animal models of GI motility disorders caused by loss of interstitial cells of Cajal," *American Journal of Physiology-Gastrointestinal and Liver Physiology*, vol. 282, (no. 5), pp. G747-G756, May 2002.

[50] S.M. Ward, I.Y. Chang, N.J. Glasgow, I. Takayama, K. Horiguchi, and K.M. Sanders, "Loss of interstitial cells of Cajal and development of electrical dysfunction in murine small bowel obstruction," *Journal of Physiology-London*, vol. 536, (no. 2), pp. 555-568, Oct 15 2001.

[51] H.M. Cousins, F.R. Edwards, H. Hickey, C.E. Hill, and G.D.S. Hirst, "Electrical coupling between the myenteric interstitial cells of Cajal and adjacent muscle layers in the guinea-pig gastric antrum," *Journal of Physiology-London*, vol. 550, (no. 3), pp. 829-844, Aug 1 2003.

[52] T.Y. Elsharkawy, K.G. Morgan, and J.H. Szurszewski, "Intracellular Electrical-Activity of Canine and Human Gastric Smooth-Muscle," *Journal of Physiology-London*, vol. 279, (no. Jun), pp. 291-307, 1978.

[53] J. Szurszewski, *Electrical basis for gastrointestinal motility. In: Physiology of the gastrointestinal tract / editor-in-chief, Leonard R. Johnson ; associate editors, James Christensen ... [et al.]*, New York: : Raven Press, 1987.

[54] T. Ordog, M. Baldo, R. Danko, and K.M. Sanders, "Plasticity of electrical pacemaking by interstitial cells of Cajal and gastric dysrhythmias in W/W mutant mice," *Gastroenterology*, vol. 123, (no. 6), pp. 2028-40, Dec 2002.

[55] T.Y. el-Sharkawy, K.G. Morgan, and J.H. Szurszewski, "Intracellular electrical activity of canine and human gastric smooth muscle," *J Physiol*, vol. 279, pp. 291-307, Jun 1978.

[56] S.M. Ward, R.E. Dixon, A. de Faoite, and K.M. Sanders, "Voltage-dependent calcium entry underlies propagation of slow waves in canine gastric antrum," *J Physiol*, vol. 561, (no. Pt 3), pp. 793-810, Dec 15 2004.

[57] M. Grover, G. Farrugia, M.S. Lurken, C.E. Bernard, M.S. Faussone-Pellegrini, T.C. Smyrk, H.P. Parkman, T.L. Abell, W.J. Snape, W.L. Hasler, A. Unalp-Arida, L. Nguyen, K.L. Koch, J. Calles, L. Lee, J. Tonascia, F.A. Hamilton, and P.J. Pasricha, "Cellular changes in

diabetic and idiopathic gastroparesis," *Gastroenterology*, vol. 140, (no. 5), pp. 1575-85 e8, May 2011.

[58] A. Mazzone, C.E. Bernard, P.R. Strege, A. Beyder, L.J. Galietta, P.J. Pasricha, J.L. Rae, H.P. Parkman, D.R. Linden, J.H. Szurszewski, T. Ordog, S.J. Gibbons, and G. Farrugia, "Altered expression of ano1 variants in human diabetic gastroparesis," *J Biol Chem*, vol. 286, (no. 15), pp. 13393-403, Apr 15 2011.

[59] C.H. Kim, F. Azpiroz, and J.R. Malagelada, "Characteristics of spontaneous and drug-induced gastric dysrhythmias in a chronic canine model," *Gastroenterology*, vol. 90, (no. 2), pp. 421-7, Feb 1986.

[60] K.M. Sanders, "Role of prostaglandins in regulating gastric motility," *Am J Physiol*, vol. 247, (no. 2 Pt 1), pp. G117-26, Aug 1984.

[61] C. Owyang and W.L. Hasler, "Physiology and pathophysiology of the interstitial cells of Cajal: from bench to bedside. VI. Pathogenesis and therapeutic approaches to human gastric dysrhythmias," *Am J Physiol Gastrointest Liver Physiol*, vol. 283, (no. 1), pp. G8-15, Jul 2002.

[62] N.E. Diamant and A. Bortoff, "Effects of transection on the intestinal slow-wave frequency gradient," *Am J Physiol*, vol. 216, (no. 4), pp. 734-43, Apr 1969.

[63] N.E. Diamant and A. Bortoff, "Nature of the intestinal low-wave frequency gradient," *Am J Physiol*, vol. 216, (no. 2), pp. 301-7, Feb 1969.

[64] S.J. Hwang, P.J. Blair, F.C. Britton, K.E. O'Driscoll, G. Hennig, Y.R. Bayguinov, J.R. Rock, B.D. Harfe, K.M. Sanders, and S.M. Ward, "Expression of anoctamin 1/TMEM16A by interstitial cells of Cajal is fundamental for slow wave activity in gastrointestinal muscles," *J Physiol*, vol. 587, (no. Pt 20), pp. 4887-904, Oct 15 2009.

[65] W.J. Lammers and B. Stephen, "Origin and propagation of individual slow waves along the intact feline small intestine," *Exp Physiol*, vol. 93, (no. 3), pp. 334-46, Mar 2008.

[66] W.J.E.P. Lammers and B. Stephen, "Origin and propagation of individual slow waves along the intact feline small intestine," *Experimental Physiology*, vol. 93, (no. 3), pp. 334-346, Mar 1 2008.

[67] T. Yamada and D.H. Alpers, *Textbook of gastroenterology*, Chichester, West Sussex ; Hoboken, NJ: Blackwell Pub., 2009.

[68] W. Nernst, "Zur Kinetik der in Losung befindlichen korper: Theorie der Diffusion. ," *Z. Phys. Chem.* , pp. 613-637, 1888.

[69] G. Farrugia, "Ionic conductances in gastrointestinal smooth muscles and interstitial cells of Cajal," *Annual Review of Physiology*, vol. 61, pp. 45-84, 1999.

[70] F. Vogalis, "Potassium channels in gastrointestinal smooth muscle," *Journal of Autonomic Pharmacology*, vol. 20, (no. 4), pp. 207-219, Aug 2000.

[71] S.D. Koh, S.M. Ward, T. Ordog, K.M. Sanders, and B. Horowitz, "Conductances responsible for slow wave generation and propagation in interstitial cells of Cajal," *Current Opinion in Pharmacology*, vol. 3, (no. 6), pp. 579-582, Dec 2003.

[72] K.M. Sanders, S.D. Koh, T. Ordog, and S.M. Ward, "Ionic conductances involved in generation and propagation of electrical slow

waves in phasic gastrointestinal muscles," *Neurogastroenterology and Motility*, vol. 16, pp. 100-105, Apr 2004.

[73] S.M. Ward, Y. Takeda, S.D. Koh, and K.A. Sanders, "Differential expression of ionic conductances in interstitial cells of Cajal in the murine gastric antrum," *Journal of Physiology-London*, vol. 586, (no. 3), pp. 859-873, Feb 1 2008.

[74] A.L. Hodgkin and A.F. Huxley, "A quantitative description of membrane current and its application to conduction and excitation in nerve," *The Journal of physiology*, vol. 117, (no. 4), pp. 500-44, 1952.

[75] D.S. Bolintineanu, A. Sayyed-Ahmad, H.T. Davis, and Y.N. Kaznessis, "Poisson-Nernst-Planck Models of Nonequilibrium Ion Electrodiffusion through a Protegrin Transmembrane Pore," *Plos Computational Biology*, vol. 5, (no. 1), Jan 2009.

[76] C.L. Gardner and J.R. Jones, "Electrodiffusion model simulation of the potassium channel," *J Theor Biol*, vol. 291C, pp. 10-13, Sep 19 2011.

[77] R.J. Lang, C. Rattraywood, and M.E. Holman, "A Simple Mathematical-Model of Spontaneous Electrical-Activity in a Single Smooth-Muscle Cell," *Japanese Journal of Pharmacology*, vol. 58, pp. P371-P371, 1992.

[78] F.K. Skinner, C.A. Ward, and B.L. Bardakjian, "Pump and exchanger mechanisms in a model of smooth muscle," *Biophys Chem*, vol. 45, (no. 3), pp. 253-72, Jan 1993.

[79] R.N. Miftakhov, G.R. Abdusheva, and J. Christensen, "Numerical simulation of motility patterns of the small bowel. II. Comparative pharmacological validation of a mathematical model," *Journal of theoretical biology*, vol. 200, (no. 3), pp. 261-290, Oct 7 1999.

[80] R.N. Miftakhov, G.R. Abdusheva, and J. Christensen, "Numerical simulation of motility patterns of the small bowel. 1. Formulation of a mathematical model," *Journal of theoretical biology*, vol. 197, (no. 1), pp. 89-112, Mar 7 1999.

[81] R.N. Miftakhov, G.R. Abdusheva, and D.L. Wingate, "Model predictions of myoelectrical activity of the small bowel," *Biol Cybern*, vol. 74, (no. 2), pp. 167-79, Feb 1996.

[82] A. Corrias and M.L. Buist, "A quantitative model of gastric smooth muscle cellular activation," *Annals of biomedical engineering*, vol. 35, (no. 9), pp. 1595-607, 2007.

[83] S.M. Ward and K.M. Sanders, "Response from sean m. Ward and kenton m. Sanders," *J Physiol*, vol. 590, (no. Pt 5), pp. 1301-2, Mar 1 2012.

[84] "CellML Model Repository". CellML. 23rd March 2012. <http://models.cellml.org/cellml>

[85] K.M. Sanders, S.D. Koh, and S.M. Ward, "Interstitial cells of Cajal as pacemakers in the gastrointestinal tract," *Annual Review of Physiology*, vol. 68, pp. 307-343, 2006.

[86] H.C. Hartzell, K. Yu, Q. Xiao, L.T. Chien, and Z. Qu, "Anoctamin/TMEM16 family members are Ca2+-activated Cl-channels," *J Physiol*, vol. 587, (no. Pt 10), pp. 2127-39, May 15 2009.

[87] Y.D. Yang, H. Cho, J.Y. Koo, M.H. Tak, Y. Cho, W.S. Shim, S.P. Park, J. Lee, B. Lee, B.M. Kim, R. Raouf, Y.K. Shin, and U. Oh,

"TMEM16A confers receptor-activated calcium-dependent chloride conductance," *Nature*, vol. 455, (no. 7217), pp. 1210-5, Oct 30 2008.

[88] L.Y. Jan, B.C. Schroeder, T. Cheng, and Y.N. Jan, "Expression cloning of TMEM16A as a calcium-activated chloride channel subunit," *Cell*, vol. 134, (no. 6), pp. 1019-1029, Sep 19 2008.

[89] L.J.V. Galietta, A. Caputo, E. Caci, L. Ferrera, N. Pedemonte, C. Barsanti, E. Sondo, U. Pfeffer, R. Ravazzolo, and O. Zegarra-Moran, "TMEM16A, a membrane protein associated with calcium-dependent chloride channel activity," *Science*, vol. 322, (no. 5901), pp. 590-594, Oct 24 2008.

[90] M.H. Zhu, T.W. Kim, S. Ro, W. Yan, S.M. Ward, S.D. Koh, and K.M. Sanders, "A Ca(2+)-activated Cl(-) conductance in interstitial cells of Cajal linked to slow wave currents and pacemaker activity," *J Physiol*, vol. 587, (no. Pt 20), pp. 4905-18, Oct 15 2009.

[91] G. Farrugia, P.J. Gomez-Pinilla, S.J. Gibbons, M.R. Bardsley, A. Lorincz, M.J. Pozo, P.J. Pasricha, M. Van de Rijn, R.B. West, M.G. Sarr, M.L. Kendrick, R.R. Cima, E.J. Dozois, D.W. Larson, and T. Ordog, "Ano1 is a selective marker of interstitial cells of Cajal in the human and mouse gastrointestinal tract," *American Journal of Physiology-Gastrointestinal and Liver Physiology*, vol. 296, (no. 6), pp. G1370-G1381, Jun 2009.

[92] R.R. Aliev, W. Richards, and J.P. Wikswo, "A simple nonlinear model of electrical activity in the intestine," *Journal of theoretical biology*, vol. 204, (no. 1), pp. 21-28, May 7 2000.

[93] R. Fitzhugh, "Impulses and Physiological States in Theoretical Models of Nerve Membrane," *Biophysical journal*, vol. 1, (no. 6), pp. 445-&, 1961.

[94] J. Nagumo, S. Arimoto, and S. Yoshizawa, "Active Pulse Transmission Line Simulating Nerve Axon," *Proceedings of the Institute of Radio Engineers*, vol. 50, (no. 10), pp. 2061-&, 1962.

[95] M.L. Buist, L.K. Cheng, K.M. Sanders, and A.J. Pullan, "Multiscale modelling of human gastric electric activity: can the electrogastrogram detect functional electrical uncoupling ?," *Experimental Physiology*, vol. 91, (no. 2), pp. 383-390, Mar 1 2006.

[96] L.K. Cheng, R. Komuro, T.M. Austin, M.L. Buist, and A.J. Pullan, "Anatomically realistic multiscale models of normal and abnormal gastrointestinal electrical activity," *World Journal of Gastroenterology*, vol. 13, (no. 9), pp. 1378-1383, Mar 7 2007.

[97] L.K. Cheng, G. O'Grady, P. Du, J.U. Egbuji, J.A. Windsor, and A.J. Pullan, "Gastrointestinal system," *Wiley Interdisciplinary Reviews-Systems Biology and Medicine*, vol. 2, (no. 1), pp. 65-79, Jan-Feb 2010.

[98] A. Pullan, L. Cheng, R. Yassi, and M. Buist, "Modelling gastrointestinal bioelectric activity," *Progress in Biophysics & Molecular Biology*, vol. 85, (no. 2-3), pp. 523-550, Jun-Jul 2004.

[99] A.S.H. Lin, M.L. Buist, N.P. Smith, and A.J. Pullan, "Modelling slow wave activity in the small intestine," *Journal of theoretical biology*, vol. 242, (no. 2), pp. 356-362, Sep 21 2006.

[100] A.S. Lin, A.L. Buist, L.K. Cheng, N.P. Smith, and A.J. Pullan, "Computational simulations of the human magneto-and

electroenterogram," *Annals of biomedical engineering*, vol. 34, (no. 8), pp. 1322-1331, Aug 2006.

[101] J.B. Youm, N. Kim, J. Han, E. Kim, H. Joo, C.H. Leem, G. Goto, A. Noma, and Y.E. Earm, "A mathematical model of pacemaker activity recorded from mouse small intestine," *Philos Transact A Math Phys Eng Sci*, vol. 364, (no. 1842), pp. 1135-54, May 15 2006.

[102] B.J. Kim, J.Y. Jun, I. So, and K.W. Kim, "Involvement of mitochondrial Na+-Ca2+ exchange in intestinal pacemaking activity," *World J Gastroenterol*, vol. 12, (no. 5), pp. 796-9, Feb 7 2006.

[103] S.M. Ward, T. Ordog, S.D. Koh, S.A. Baker, J.Y. Jun, G. Amberg, K. Monaghan, and K.M. Sanders, "Pacemaking in interstitial cells of Cajal depends upon calcium handling by endoplasmic reticulum and mitochondria," *J Physiol*, vol. 525 Pt 2, pp. 355-61, Jun 1 2000.

[104] W.J. Cho and E.E. Daniel, "Proteins of interstitial cells of Cajal and intestinal smooth muscle, colocalized with caveolin-1," *American Journal of Physiology-Gastrointestinal and Liver Physiology*, vol. 288, (no. 3), pp. G571-G585, Mar 2005.

[105] C.M. McKay, J. Ye, and J.D. Huizinga, "Characterization of depolarization-evoked ERG K+ currents in interstitial cells of Cajal," *Neurogastroenterology and Motility*, vol. 18, (no. 4), pp. 324-333, Apr 2006.

[106] P.R. Strege, Y. Ou, L. Sha, A. Rich, S.J. Gibbons, J.H. Szurszewski, M.G. Sarr, and G. Farrugia, "Sodium current in human intestinal interstitial cells of Cajal," *American journal of physiology. Gastrointestinal and liver physiology*, vol. 285, (no. 6), pp. G1111-21, 2003.

[107] Y.A. Saito, P.R. Strege, D.J. Tester, G.R. Locke, 3rd, N.J. Talley, C.E. Bernard, J.L. Rae, J.C. Makielski, M.J. Ackerman, and G. Farrugia, "Sodium channel mutation in irritable bowel syndrome: evidence for an ion channelopathy," *Am J Physiol Gastrointest Liver Physiol*, vol. 296, (no. 2), pp. G211-8, Feb 2009.

[108] A. Corrias and M.L. Buist, "Quantitative cellular description of gastric slow wave activity," *American journal of physiology. Gastrointestinal and liver physiology*, vol. 294, (no. 4), pp. G989-95, 2008.

[109] C.P. Fall and J.E. Keizer, "Mitochondrial modulation of intracellular Ca(2+) signaling," *J Theor Biol*, vol. 210, (no. 2), pp. 151-65, May 21 2001.

[110] P. Du, G. O'Grady, S.J. Gibbons, R. Yassi, R. Lees-Green, G. Farrugia, L.K. Cheng, and A.J. Pullan, "Tissue-specific mathematical models of slow wave entrainment in wild-type and 5-HT(2B) knockout mice with altered interstitial cells of Cajal networks," *Biophys J*, vol. 98, (no. 9), pp. 1772-81, May 19.

[111] R.A. Faville, A.J. Pullan, K.M. Sanders, S.D. Koh, C.M. Lloyd, and N.P. Smith, "Biophysically Based Mathematical Modeling of Interstitial Cells of Cajal Slow Wave Activity Generated from a Discrete Unitary Potential Basis," *Biophysical journal*, vol. 96, (no. 12), pp. 4834-4852, Jun 17 2009.

[112] R.A. Faville, A.J. Pullan, K.M. Sanders, and N.P. Smith, "A biophysically based mathematical model of unitary potential activity in

interstitial cells of Cajal," *Biophysical journal*, vol. 95, (no. 1), pp. 88-104, Jul 1 2008.

[113] B. van der Pol, "On "relaxation oscillations."," *Philosophical Magazine*, vol. 2, (no. 11), pp. 978-992, Nov 1926.

[114] T.S. Nelsen and J.C. Becker, "Simulation of the electrical and mechanical gradient of the small intestine," *Am J Physiol*, vol. 214, (no. 4), pp. 749-57, Apr 1968.

[115] S.K. Sarna, "Simulation of Slow-Wave Electrical Activity of Small Intestine," *American Journal of Physiology*, vol. 221, (no. 1), pp. 166-&, 1971.

[116] S.K. Sarna, Y.J. Kingma, and E.E. Daniel, "Effects of Partial Cuts on Gastric Electrical Control Activity and Its Computer Model," *American Journal of Physiology*, vol. 223, (no. 2), pp. 332-&, 1972.

[117] N.G. Publicover and K.M. Sanders, "Are relaxation oscillators an appropriate model of gastrointestinal electrical activity?," *Am J Physiol*, vol. 256, (no. 2 Pt 1), pp. G265-74, Feb 1989.

[118] N. Sperelakis and E.E. Daniel, "Activation of intestinal smooth muscle cells by interstitial cells of Cajal in simulation studies," *American Journal of Physiology-Gastrointestinal and Liver Physiology*, vol. 286, (no. 2), pp. G234-G243, Feb 2004.

[119] R. Vogel and R. Weingart, "The electrophysiology of gap junctions and gap junction channels and their mathematical modelling," *Biol Cell*, vol. 94, (no. 7-8), pp. 501-10, Nov 2002.

[120] F.R. Edwards and G.D.S. Hirst, "An electrical description of the generation of slow waves in the antrum of the guinea-pig," *Journal of Physiology-London*, vol. 564, (no. 1), pp. 213-232, Apr 1 2005.

[121] M.L. Buist, L.K. Cheng, R. Yassi, L.A. Bradshaw, W.O. Richards, and A.J. Pullan, "An anatomical model of the gastric system for producing bioelectric and biomagnetic fields," *Physiol Meas*, vol. 25, (no. 4), pp. 849-61, Aug 2004.

[122] R. Plonsey and R.C. Barr, "Mathematical modeling of electrical activity of the heart," *J Electrocardiol*, vol. 20, (no. 3), pp. 219-26, Jul 1987.

[123] M. Buist, G. Sands, P. Hunter, and A. Pullan, "A deformable finite element derived finite difference method for cardiac activation problems," *Ann Biomed Eng*, vol. 31, (no. 5), pp. 577-88, May 2003.

[124] M.S. Imtiaz, D.W. Smith, and D.F. van Helden, "A theoretical model of slow wave regulation using voltage-dependent synthesis of inositol 1,4,5-trisphosphate," *Biophys J*, vol. 83, (no. 4), pp. 1877-90, Oct 2002.

[125] L.A. Bradshaw, J.K. Ladipo, D.J. Staton, J.P. Wikswo, Jr., and W.O. Richards, "The human vector magnetogastrogram and magnetoenterogram," *IEEE Trans Biomed Eng*, vol. 46, (no. 8), pp. 959-70, Aug 1999.

[126] F.Y. Chang, "Electrogastrography: basic knowledge, recording, processing and its clinical applications," *J Gastroenterol Hepatol*, vol. 20, (no. 4), pp. 502-16, Apr 2005.

[127] W.O. Richards, L.A. Bradshaw, D.J. Staton, C.L. Garrard, F. Liu, S. Buchanan, and J.P. Wikswo, Jr., "Magnetoenterography (MENG):

noninvasive measurement of bioelectric activity in human small intestine," *Dig Dis Sci*, vol. 41, (no. 12), pp. 2293-301, Dec 1996.

[128] B.H. Brown, R.H. Smallwood, H.L. Duthie, and C.J. Stoddard, "Intestinal smooth muscle electrical potentials recorded from surface electrodes," *Med Biol Eng*, vol. 13, (no. 1), pp. 97-103, Jan 1975.

[129] V. Spitzer, M.J. Ackerman, A.L. Scherzinger, and D. Whitlock, "The visible human male: a technical report," *J Am Med Inform Assoc*, vol. 3, (no. 2), pp. 118-30, Mar-Apr 1996.

[130] C. Bradley and A. Pullan, "Application of the BEM in biopotential problems," *Engineering Analysis with Boundary Elements*, vol. 26, (no. 5), pp. 391-403, May 2002.

[131] C.P. Bradley, A.J. Pullan, and P.J. Hunter, "Geometric modeling of the human torso using cubic hermite elements," *Annals of biomedical engineering*, vol. 25, (no. 1), pp. 96-111, Jan-Feb 1997.

[132] T.M. Austin, L. Li, A.J. Pullan, and L.K. Cheng, "Effects of gastrointestinal tissue structure on computed dipole vectors," *Biomed Eng Online*, vol. 6, pp. 39, 2007.

[133] L.K. Cheng, G. O'Grady, P. Du, J.U. Egbuji, J.A. Windsor, and A.J. Pullan, "Gastrointestinal system," *Wiley Interdiscip Rev Syst Biol Med*, vol. 2, (no. 1), pp. 65-79, Jan-Feb 2010.

[134] H. Eyring, "The activated complex in chemical reactions," *Journal of Chemical Physics*, vol. 3, (no. 2), pp. 107-115, Feb 1935.

[135] F.H. Johnson, H. Eyring, and B.J. Stover, *The theory of rate processes in biology and medicine*, New York, 1974.

[136] O.S. Andersen and R.E. Koeppe, 2nd, "Molecular determinants of channel function," *Physiol Rev*, vol. 72, (no. 4 Suppl), pp. S89-158, Oct 1992.

[137] T.L. Hill and Y. Chen, "On the theory of ion transport across the nerve membrane. VI. Free energy and activation free energies of conformational change," *Proc Natl Acad Sci U S A*, vol. 69, (no. 7), pp. 1723-6, Jul 1972.

[138] C.F. Stevens, "Interactions between intrinsic membrane protein and electric field. An approach to studying nerve excitability," *Biophys J*, vol. 22, (no. 2), pp. 295-306, May 1978.

[139] R.W. Tsien and D. Noble, "A Transition State Theory Approach to Kinetics of Conductance Changes in Excitable Membranes," *Journal of Membrane Biology*, vol. 1, (no. 3), pp. 248-&, 1969.

[140] A.R. Willms, D.J. Baro, R.M. Harris-Warrick, and J. Guckenheimer, "An improved parameter estimation method for Hodgkin-Huxley models," *J Comput Neurosci*, vol. 6, (no. 2), pp. 145-68, Mar-Apr 1999.

[141] R.W. Aldrich, D.P. Corey, and C.F. Stevens, "A reinterpretation of mammalian sodium channel gating based on single channel recording," *Nature*, vol. 306, (no. 5942), pp. 436-41, Dec 1-7 1983.

[142] C.M. Armstrong, "Sodium channels and gating currents," *Physiol Rev*, vol. 61, (no. 3), pp. 644-83, Jul 1981.

[143] F. Bezanilla, "Gating of sodium and potassium channels," *J Membr Biol*, vol. 88, (no. 2), pp. 97-111, 1985.

[144] R.W. Aldrich, "Inactivation of voltage-gated delayed potassium current in molluscan neurons. A kinetic model," *Biophys J*, vol. 36, (no. 3), pp. 519-32, Dec 1981.

[145] B. Sakmann and E. Neher, *Single-channel recording*, New York: : Plenum Press, 1995.

[146] D. Colquhoun, K.A. Dowsland, M. Beato, and A.J.R. Plested, "How to impose microscopic: Reversibility in complex reaction mechanisms," *Biophysical journal*, vol. 86, (no. 6), pp. 3510-3518, Jun 2004.

[147] B.S. Rothberg and K.L. Magleby, "Testing for detailed balance (microscopic reversibility) in ion channel gating," *Biophysical journal*, vol. 80, (no. 6), pp. 3025-3026, Jun 2001.

[148] A. Nekouzadeh and Y. Rudy, "Statistical properties of ion channel records. Part I: relationship to the macroscopic current," *Math Biosci*, vol. 210, (no. 1), pp. 291-314, Nov 2007.

[149] A. Nekouzadeh and Y. Rudy, "Statistical properties of ion channel records. Part II: estimation from the macroscopic current," *Math Biosci*, vol. 210, (no. 1), pp. 315-34, Nov 2007.

[150] R.C. Cannon and G. D'Alessandro, "The ion channel inverse problem: Neuroinformatics meets biophysics," *Plos Computational Biology*, vol. 2, (no. 8), pp. 862-869, Aug 2006.

[151] W.A. Catterall, A.L. Goldin, S.G. Waxman, and P. International Union of, "International Union of Pharmacology. XXXIX. Compendium of voltage-gated ion channels: sodium channels," *Pharmacological reviews*, vol. 55, (no. 4), pp. 575-8, 2003.

[152] F.H. Yu and W.A. Catterall, "Overview of the voltage-gated sodium channel family," *Genome biology*, vol. 4, (no. 3), pp. 207, 2003.

[153] T.H. Bullock, R. Orkand, and A. Grinnell, *Introduction to nervous systems*, San Francisco: W.H. Freeman, 1977.

[154] A.N. Holm, A. Rich, S.M. Miller, P. Strege, Y. Ou, S. Gibbons, M.G. Sarr, J.H. Szurszewski, J.L. Rae, and G. Farrugia, "Sodium current in human jejunal circular smooth muscle cells," *Gastroenterology*, vol. 122, (no. 1), pp. 178-87, 2002.

[155] Y. Ou, S.J. Gibbons, S.M. Miller, P.R. Strege, A. Rich, M.A. Distad, M.J. Ackerman, J.L. Rae, J.H. Szurszewski, and G. Farrugia, "SCN5A is expressed in human jejunal circular smooth muscle cells," *Neurogastroenterology and motility : the official journal of the European Gastrointestinal Motility Society*, vol. 14, (no. 5), pp. 477-86, 2002.

[156] A. Beyder, J.L. Rae, C.E. Bernard, P.R. Strege, F. Sachs, and G. Farrugia, "Mechanosensitivity of Nav1.5, a voltage-sensitive sodium channel," *J Physiol*, Nov 1 2010.

[157] C.E. Morris and P.F. Juranka, "Nav channel mechanosensitivity: activation and inactivation accelerate reversibly with stretch," *Biophys J*, vol. 93, (no. 3), pp. 822-33, Aug 1 2007.

[158] Y. Ou, P. Strege, S.M. Miller, J. Makielski, M. Ackerman, S.J. Gibbons, and G. Farrugia, "Syntrophin gamma 2 regulates SCN5A gating by a PDZ domain-mediated interaction," *J Biol Chem*, vol. 278, (no. 3), pp. 1915-23, Jan 17 2003.

[159] P.R. Strege, A.N. Holm, A. Rich, S.M. Miller, Y. Ou, M.G. Sarr, and G. Farrugia, "Cytoskeletal modulation of sodium current in human

jejunal circular smooth muscle cells," *Am J Physiol Cell Physiol*, vol. 284, (no. 1), pp. C60-6, Jan 2003.

[160] E. Moric, E. Herbert, M. Trusz-Gluza, A. Filipecki, U. Mazurek, and T. Wilczok, "The implications of genetic mutations in the sodium channel gene (SCN5A)," *Europace : European pacing, arrhythmias, and cardiac electrophysiology : journal of the working groups on cardiac pacing, arrhythmias, and cardiac cellular electrophysiology of the European Society of Cardiology*, vol. 5, (no. 4), pp. 325-34, 2003.

[161] K. Ueda, C. Valdivia, A. Medeiros-Domingo, D.J. Tester, M. Vatta, G. Farrugia, M.J. Ackerman, and J.C. Makielski, "Syntrophin mutation associated with long QT syndrome through activation of the nNOS-SCN5A macromolecular complex," *Proceedings of the National Academy of Sciences of the United States of America*, vol. 105, (no. 27), pp. 9355-60, 2008.

[162] S.D. Dib-Hajj, T.R. Cummins, J.A. Black, and S.G. Waxman, "From genes to pain: Na v 1.7 and human pain disorders," *Trends in neurosciences*, vol. 30, (no. 11), pp. 555-63, 2007.

[163] B. Breg, K.K. Tamira, S. Dirk, H. Nynke, W. Arthur, and E.B. Guy, "W1337 Abdominal Symptoms in Patients with Long Qt Syndrome and a "Gain of Function" Mutation in the Nav1.5 Sodium Channel," *Gastroenterology*, vol. 134, (no. 4), pp. A-683, 2008.

[164] P.R. Strege, A. Mazzone, R.E. Kraichely, L. Sha, A.N. Holm, Y. Ou, I. Lim, S.J. Gibbons, M.G. Sarr, and G. Farrugia, "Species dependent expression of intestinal smooth muscle mechanosensitive sodium channels," *Neurogastroenterology and Motility*, vol. 19, (no. 2), pp. 135-143, Feb 2007.

[165] a.J.P. Schmidt-Hieber C, ""Stimfit." " in, [cited 9th January 2011] Accession no. Accession Number| Available rom Database Provider|.

[166] C.E. Clancy and Y. Rudy, "Linking a genetic defect to its cellular phenotype in a cardiac arrhythmia," *Nature*, vol. 400, (no. 6744), pp. 566-9, 1999.

[167] A. Destexhe and J.R. Huguenard, "Nonlinear thermodynamic models of voltage-dependent currents," *Journal of Computational Neuroscience*, vol. 9, (no. 3), pp. 259-270, Nov 2000.

[168] M. Ozer, "A comparative analysis of linear, nonlinear and improved nonlinear thermodynamic models of voltage-dependent ion channel kinetics," *Physica a-Statistical Mechanics and Its Applications*, vol. 379, (no. 2), pp. 579-586, Jun 15 2007.

[169] L.F. Shampine and M.W. Reichelt, "The MATLAB ODE suite," *Siam Journal on Scientific Computing*, vol. 18, (no. 1), pp. 1-22, Jan 1997.

[170] J.R. Balser, P.B. Bennett, and D.M. Roden, "Time-dependent outward current in guinea pig ventricular myocytes. Gating kinetics of the delayed rectifier," *J Gen Physiol*, vol. 96, (no. 4), pp. 835-63, Oct 1990.

[171] K.H. ten Tusscher, D. Noble, P.J. Noble, and A.V. Panfilov, "A model for human ventricular tissue," *Am J Physiol Heart Circ Physiol*, vol. 286, (no. 4), pp. H1573-89, Apr 2004.

[172] C.E. Clancy, M. Tateyama, H. Liu, X.H. Wehrens, and R.S. Kass, "Non-equilibrium gating in cardiac Na+ channels: an original

mechanism of arrhythmia," *Circulation*, vol. 107, (no. 17), pp. 2233-7, May 6 2003.

[173] J.C. Makielski, B. Ye, C.R. Valdivia, M.D. Pagel, J. Pu, D.J. Tester, and M.J. Ackerman, "A ubiquitous splice variant and a common polymorphism affect heterologous expression of recombinant human SCN5A heart sodium channels," *Circ Res*, vol. 93, (no. 9), pp. 821-8, Oct 31 2003.

[174] S. Poelzing, C. Forleo, M. Samodell, L. Dudash, S. Sorrentino, M. Anaclerio, R. Troccoli, M. Iacoviello, R. Romito, P. Guida, M. Chahine, M. Pitzalis, and I. Deschenes, "SCN5A polymorphism restores trafficking of a Brugada syndrome mutation on a separate gene," *Circulation*, vol. 114, (no. 5), pp. 368-76, Aug 1 2006.

[175] N. Desai and D.E. Clapham, "TRP channels and mice deficient in TRP channels," *Pflugers Arch*, vol. 451, (no. 1), pp. 11-8, Oct 2005.

[176] B. Rosati and D. McKinnon, "Regulation of ion channel expression," *Circ Res*, vol. 94, (no. 7), pp. 874-83, Apr 16 2004.

[177] P. Imbrici, A. Cusimano, M.C. D'Adamo, A. De Curtis, and M. Pessia, "Functional characterization of an episodic ataxia type-1 mutation occurring in the S1 segment of hKv1.1 channels," *Pflugers Arch*, vol. 446, (no. 3), pp. 373-9, Jun 2003.

[178] W.J. Hatton, H.S. Mason, A. Carl, P. Doherty, M.J. Latten, J.L. Kenyon, K.M. Sanders, and B. Horowitz, "Functional and molecular expression of a voltage-dependent K(+) channel (Kv1.1) in interstitial cells of Cajal," *J Physiol*, vol. 533, (no. Pt 2), pp. 315-27, Jun 1 2001.

[179] K. McCormack, W.J. Joiner, and S.H. Heinemann, "A characterization of the activating structural rearrangements in voltage-dependent Shaker K+ channels," *Neuron*, vol. 12, (no. 2), pp. 301-15, Feb 1994.

[180] http://www.iuphar-db.org/index.jsp, in, [cited 21st March 2012] Accession no. Accession Number| Available rom Database Provider|.

[181] J.N. Barrett, K.L. Magleby, and B.S. Pallotta, "Properties of single calcium-activated potassium channels in cultured rat muscle," *J Physiol*, vol. 331, pp. 211-30, Oct 1982.

[182] H. Watanabe, T.T. Koopmann, S. Le Scouarnec, T. Yang, C.R. Ingram, J.J. Schott, S. Demolombe, V. Probst, F. Anselme, D. Escande, A.C. Wiesfeld, A. Pfeufer, S. Kaab, H.E. Wichmann, C. Hasdemir, Y. Aizawa, A.A. Wilde, D.M. Roden, and C.R. Bezzina, "Sodium channel beta1 subunit mutations associated with Brugada syndrome and cardiac conduction disease in humans," *J Clin Invest*, vol. 118, (no. 6), pp. 2260-8, Jun 2008.

[183] B.H. Tan, K.N. Pundi, D.W. Van Norstrand, C.R. Valdivia, D.J. Tester, A. Medeiros-Domingo, J.C. Makielski, and M.J. Ackerman, "Sudden infant death syndrome-associated mutations in the sodium channel beta subunits," *Heart Rhythm*, vol. 7, (no. 6), pp. 771-8, Jun 2010.

[184] E. Neher and C.F. Stevens, "Conductance fluctuations and ionic pores in membranes," *Annu Rev Biophys Bioeng*, vol. 6, pp. 345-81, 1977.

[185] C.F. Stevens, "Inferences about membrane properties from electrical noise measurements," *Biophys J*, vol. 12, (no. 8), pp. 1028-47, Aug 1972.

[186] B. Neumcke and R. Stampfli, "Sodium currents and sodium-current fluctuations in rat myelinated nerve fibres," *J Physiol*, vol. 329, pp. 163-84, Aug 1982.

[187] F.J. Sigworth, "The variance of sodium current fluctuations at the node of Ranvier," *J Physiol*, vol. 307, pp. 97-129, Oct 1980.

[188] L.J. Herfst, M.B. Rook, and H.J. Jongsma, "Trafficking and functional expression of cardiac Na+ channels," *J Mol Cell Cardiol*, vol. 36, (no. 2), pp. 185-93, Feb 2004.

[189] B. Ye, C.R. Valdivia, M.J. Ackerman, and J.C. Makielski, "A common human SCN5A polymorphism modifies expression of an arrhythmia causing mutation," *Physiol Genomics*, vol. 12, (no. 3), pp. 187-93, Feb 6 2003.

[190] P.C. Viswanathan and J.R. Balser, "Inherited sodium channelopathies: a continuum of channel dysfunction," *Trends Cardiovasc Med*, vol. 14, (no. 1), pp. 28-35, Jan 2004.

[191] L. Wu, S.R. Archacki, T. Zhang, and Q.K. Wang, "Induction of high STAT1 expression in transgenic mice with LQTS and heart failure," *Biochem Biophys Res Commun*, vol. 358, (no. 2), pp. 449-54, Jun 29 2007.

[192] C.R. Bezzina, M.B. Rook, W.A. Groenewegen, L.J. Herfst, A.C. van der Wal, J. Lam, H.J. Jongsma, A.A. Wilde, and M.M. Mannens, "Compound heterozygosity for mutations (W156X and R225W) in SCN5A associated with severe cardiac conduction disturbances and degenerative changes in the conduction system," *Circ Res*, vol. 92, (no. 2), pp. 159-68, Feb 7 2003.

[193] T. Nagatomo, Z. Fan, B. Ye, G.S. Tonkovich, C.T. January, J.W. Kyle, and J.C. Makielski, "Temperature dependence of early and late currents in human cardiac wild-type and long Q-T DeltaKPQ Na+ channels," *Am J Physiol*, vol. 275, (no. 6 Pt 2), pp. H2016-24, Dec 1998.

[194] R. Dumaine, J.A. Towbin, P. Brugada, M. Vatta, D.V. Nesterenko, V.V. Nesterenko, J. Brugada, R. Brugada, and C. Antzelevitch, "Ionic mechanisms responsible for the electrocardiographic phenotype of the Brugada syndrome are temperature dependent," *Circ Res*, vol. 85, (no. 9), pp. 803-9, Oct 29 1999.

[195] U. Schulte, "Protein-protein interactions and subunit composition of ion channels," *CNS Neurol Disord Drug Targets*, vol. 7, (no. 2), pp. 172-86, Apr 2008.

[196] H. Abriel and R.S. Kass, "Regulation of the voltage-gated cardiac sodium channel Nav1.5 by interacting proteins," *Trends Cardiovasc Med*, vol. 15, (no. 1), pp. 35-40, Jan 2005.

[197] D.E. Patton, L.L. Isom, W.A. Catterall, and A.L. Goldin, "The adult rat brain beta 1 subunit modifies activation and inactivation gating of multiple sodium channel alpha subunits," *J Biol Chem*, vol. 269, (no. 26), pp. 17649-55, Jul 1 1994.

[198] L.L. Isom, K.S. De Jongh, D.E. Patton, B.F. Reber, J. Offord, H. Charbonneau, K. Walsh, A.L. Goldin, and W.A. Catterall, "Primary

structure and functional expression of the beta 1 subunit of the rat brain sodium channel," *Science*, vol. 256, (no. 5058), pp. 839-42, May 8 1992.

[199] L.L. Isom, D.S. Ragsdale, K.S. De Jongh, R.E. Westenbroek, B.F. Reber, T. Scheuer, and W.A. Catterall, "Structure and function of the beta 2 subunit of brain sodium channels, a transmembrane glycoprotein with a CAM motif," *Cell*, vol. 83, (no. 3), pp. 433-42, Nov 3 1995.

[200] I.B. Levitan, "Signaling protein complexes associated with neuronal ion channels," *Nat Neurosci*, vol. 9, (no. 3), pp. 305-10, Mar 2006.

[201] S. Dai, D.D. Hall, and J.W. Hell, "Supramolecular assemblies and localized regulation of voltage-gated ion channels," *Physiol Rev*, vol. 89, (no. 2), pp. 411-52, Apr 2009.

[202] Y.P. Torres, F.J. Morera, I. Carvacho, and R. Latorre, "A marriage of convenience: beta-subunits and voltage-dependent K+ channels," *J Biol Chem*, vol. 282, (no. 34), pp. 24485-9, Aug 24 2007.

[203] C. Franzini-Armstrong, "ER-mitochondria communication. How privileged?," *Physiology (Bethesda)*, vol. 22, pp. 261-8, Aug 2007.

[204] K.P. Currie, "G protein modulation of CaV2 voltage-gated calcium channels," *Channels (Austin)*, vol. 4, (no. 6), pp. 497-509, Nov-Dec 2010.

[205] A.C. Dolphin, "G protein modulation of voltage-gated calcium channels," *Pharmacol Rev*, vol. 55, (no. 4), pp. 607-27, Dec 2003.

[206] D.W. Wang, P.C. Viswanathan, J.R. Balser, A.L. George, Jr., and D.W. Benson, "Clinical, genetic, and biophysical characterization of SCN5A mutations associated with atrioventricular conduction block," *Circulation*, vol. 105, (no. 3), pp. 341-6, Jan 22 2002.

[207] T. Zimmer, C. Bollensdorff, V. Haufe, E. Birch-Hirschfeld, and K. Benndorf, "Mouse heart Na+ channels: primary structure and function of two isoforms and alternatively spliced variants," *Am J Physiol Heart Circ Physiol*, vol. 282, (no. 3), pp. H1007-17, Mar 2002.

[208] A.J. Ward and T.A. Cooper, "The pathobiology of splicing," *J Pathol*, vol. 220, (no. 2), pp. 152-63, Jan 2010.

[209] L.F. Lareau, R.E. Green, R.S. Bhatnagar, and S.E. Brenner, "The evolving roles of alternative splicing," *Curr Opin Struct Biol*, vol. 14, (no. 3), pp. 273-82, Jun 2004.

[210] R.N. Miftakhov and G.R. Abdusheva, "Numerical simulation of excitation-contraction coupling in a locus of the small bowel," *Biol Cybern*, vol. 74, (no. 5), pp. 455-67, May 1996.

[211] R.N. Miftakhov, G.R. Abdusheva, and J. Christensen, "Numerical simulation of motility patterns of the small bowel. 1. formulation of a mathematical model," *J Theor Biol*, vol. 197, (no. 1), pp. 89-112, Mar 7 1999.

[212] F.K. Skinner, C.A. Ward, and B.L. Bardakjian, "Pump and Exchanger Mechanisms in a Model of Smooth-Muscle," *Biophysical Chemistry*, vol. 45, (no. 3), pp. 253-272, Jan 1993.

[213] R.R. Aliev, W. Richards, and J.P. Wikswo, "A simple nonlinear model of electrical activity in the intestine," *J Theor Biol*, vol. 204, (no. 1), pp. 21-8, May 7 2000.

[214] Y.E. Earm, J.B. Youm, N. Kim, J. Han, E. Kim, H. Joo, C.H. Leem, G. Goto, and A. Noma, "A mathematical model of pacemaker activity

recorded from mouse small intestine," *Philosophical Transactions of the Royal Society a-Mathematical Physical and Engineering Sciences*, vol. 364, (no. 1842), pp. 1135-1154, May 15 2006.

[215] D.B. Duridanova, H.S. Gagov, D. Damyanov, and K.K. Boev, "Two components of potassium outward current in smooth muscle cells from the circular layer of human jejunum," *General Physiology and Biophysics*, vol. 16, (no. 1), pp. 49-58, Mar 1997.

[216] G. Farrugia, J.L. Rae, M.G. Sarr, and J.H. Szurszewski, "Potassium Current in Circular Smooth-Muscle of Human Jejunum Activated by Fenamates," *American Journal of Physiology*, vol. 265, (no. 5), pp. G873-G879, Nov 1993.

[217] G. Farrugia, A. Rich, J.L. Rae, M.G. Sarr, and J.H. Szurszewski, "Calcium Currents in Human and Canine Jejunal Circular Smooth-Muscle Cells," *Gastroenterology*, vol. 109, (no. 3), pp. 707-717, Sep 1995.

[218] A. Horowitz, C.B. Menice, R. Laporte, and K.G. Morgan, "Mechanisms of smooth muscle contraction," *Physiological Reviews*, vol. 76, (no. 4), pp. 967-1003, Oct 1996.

[219] G.L. Lyford, P.R. Strege, A. Shepard, Y. Ou, L. Ermilov, S.M. Miller, S.J. Gibbons, J.L. Rae, J.H. Szurszewski, and G. Farrugia, "alpha(1C) (Ca(V)1.2) L-type calcium channel mediates mechanosensitive calcium regulation," *Am J Physiol Cell Physiol*, vol. 283, (no. 3), pp. C1001-8, Sep 2002.

[220] G.M. Faber, J. Silva, L. Livshitz, and Y. Rudy, "Kinetic properties of the cardiac L-type Ca2+ channel and its role in myocyte electrophysiology: a theoretical investigation," *Biophys J*, vol. 92, (no. 5), pp. 1522-43, Mar 1 2007.

[221] I. Lim, S.J. Gibbons, G.L. Lyford, S.M. Miller, P.R. Strege, M.G. Sarr, S. Chatterjee, J.H. Szurszewski, V.H. Shah, and G. Farrugia, "Carbon monoxide activates human intestinal smooth muscle L-type Ca2+ channels through a nitric oxide-dependent mechanism," *Am J Physiol Gastrointest Liver Physiol*, vol. 288, (no. 1), pp. G7-14, Jan 2005.

[222] M. Yoshino, T. Someya, A. Nishio, and H. Yabu, "Whole-cell and unitary Ca channel currents in mammalian intestinal smooth muscle cells: evidence for the existence of two types of Ca channels," *Pflugers Arch*, vol. 411, (no. 2), pp. 229-31, Feb 1988.

[223] S.J. Gibbons, P.R. Strege, S. Lei, J.L. Roeder, A. Mazzone, Y.J. Ou, A. Rich, and G. Farrugia, "The alpha(1H) Ca2+channel subunit is expressed in mouse jejunal interstitial cells of Cajal and myocytes," *Journal of cellular and molecular medicine*, vol. 13, (no. 11-12), pp. 4422-4431, Nov-Dec 2009.

[224] G. Farrugia, P.R. Strege, L. Sha, A. Beyder, C.E. Bernard, E. Perez-Reyes, S. Evangelista, S.J. Gibbons, and J.H. Szurszewski, "T-type Ca(2+) channel modulation by otilonium bromide," *American Journal of Physiology-Gastrointestinal and Liver Physiology*, vol. 298, (no. 5), pp. G706-G713, May 2010.

[225] G. Farrugia, "Modulation of ionic currents in isolated canine and human jejunal circular smooth muscle cells by fluoxetine," *Gastroenterology*, vol. 110, (no. 5), pp. 1438-45, May 1996.

[226] C.D. Benham, T.B. Bolton, R.J. Lang, and T. Takewaki, "Calcium-Activated Potassium Channels in Single Smooth-Muscle Cells of Rabbit Jejunum and Guinea-Pig Mesenteric-Artery," *Journal of Physiology-London*, vol. 371, pp. 45-67, Feb 1986.

[227] A. Carl, H.K. Lee, and K.M. Sanders, "Regulation of ion channels in smooth muscles by calcium," *American Journal of Physiology-Cell Physiology*, vol. 271, (no. 1), pp. C9-C34, Jul 1996.

[228] R. Mitra and M. Morad, "Ca-2+ and Ca-2+-Activated K+ Currents in Mammalian Gastric Smooth-Muscle Cells," *Science*, vol. 229, (no. 4710), pp. 269-272, 1985.

[229] J.J. Singer and J.V. Walsh, "Characterization of Calcium-Activated Potassium Channels in Single Smooth-Muscle Cells Using the Patch-Clamp Technique," *Pflugers Archiv-European Journal of Physiology*, vol. 408, (no. 2), pp. 98-111, Feb 1987.

[230] P.R. Strege, S. Evangelista, G.L. Lyford, M.G. Sarr, and G. Farrugia, "Otilonium bromide inhibits calcium entry through L-type calcium channels in human intestinal smooth muscle," *Neurogastroenterology and Motility*, vol. 16, (no. 2), pp. 167-173, Apr 2004.

[231] D.H. Cox, J. Cui, and R.W. Aldrich, "Allosteric gating of a large conductance Ca-activated K+ channel," *Journal of General Physiology*, vol. 110, (no. 3), pp. 257-281, Sep 1997.

[232] P. Meera, M. Wallner, Z. Jiang, and L. Toro, "A calcium switch for the functional coupling between alpha (hslo) and beta subunits (K-v,K-ca beta) of maxi K channels (vol 382, pg 84, 1996)," *Febs Letters*, vol. 385, (no. 1-2), pp. 127-128, Apr 29 1996.

[233] P. Meera, M. Wallner, Z. Jiang, and L. Toro, "A calcium switch for the functional coupling between a (hslo) and beta subunits (K-v,K-Ca beta) of maxi K channels," *Febs Letters*, vol. 382, (no. 1-2), pp. 84-88, Mar 11 1996.

[234] A. Carl, H.K. Lee, and K.M. Sanders, "Regulation of ion channels in smooth muscles by calcium," *Am J Physiol*, vol. 271, (no. 1 Pt 1), pp. C9-34, Jul 1996.

[235] R. Casteels, G. Droogmans, and H. Hendrickx, "Electrogenic sodium pump in smooth muscle cells of the guinea-pig's taenia coli," *J Physiol*, vol. 217, (no. 2), pp. 297-313, Sep 1971.

[236] T. Magaribuchi, Y. Ito, and H. Kuriyama, "Activation of an electrogenic sodium pump in the smooth muscle cell membrane of guinea pig taenia coli during recovery after cold treatment," *Jpn J Physiol*, vol. 23, (no. 1), pp. 25-38, Feb 1973.

[237] W.J. Cho and E.E. Daniel, "Proteins of interstitial cells of Cajal and intestinal smooth muscle, colocalized with caveolin-1," *Am J Physiol Gastrointest Liver Physiol*, vol. 288, (no. 3), pp. G571-85, Mar 2005.

[238] J.D. Huizinga, L. Thuneberg, M. Kluppel, J. Malysz, H.B. Mikkelsen, and A. Bernstein, "W/Kit Gene Required for Interstitial-Cells of Cajal and for Intestinal Pacemaker Activity," *Nature*, vol. 373, (no. 6512), pp. 347-349, Jan 26 1995.

[239] T.K. Smith, J.B. Reed, and K.M. Sanders, "Origin and propagation of electrical slow waves in circular muscle of canine proximal colon," *Am J Physiol*, vol. 252, (no. 2 Pt 1), pp. C215-24, Feb 1987.

[240] S.M. Ward, A.J. Burns, S. Torihashi, and K.M. Sanders, "Mutation of the Protooncogene C-Kit Blocks Development of Interstitial-Cells and Electrical Rhythmicity in Murine Intestine," *Journal of Physiology-London*, vol. 480, pp. 91-97, Oct 1 1994.

[241] Y. Kito and H. Suzuki, "Properties of pacemaker potentials recorded from myenteric interstitial cells of Cajal distributed in the mouse small intestine," *J Physiol*, vol. 553, (no. Pt 3), pp. 803-18, Dec 15 2003.

[242] C.Y. Kao and M.E. Carsten, *Cellular aspects of smooth muscle function*, Cambridge ; New York: Cambridge University Press, 2005.

[243] K. Bielefeldt, C.A. Whiteis, R.V. Sharma, F.M. Abboud, and J.L. Conklin, "Reactive oxygen species and calcium homeostasis in cultured human intestinal smooth muscle cells," *Am J Physiol*, vol. 272, (no. 6 Pt 1), pp. G1439-50, Jun 1997.

[244] Y.C. Poh, A. Beyder, P.R. Strege, G. Farrugia, and M.L. Buist, "Quantification of gastrointestinal sodium channelopathy," *J Theor Biol*, vol. 293, pp. 41-8, Jan 21 2012.

[245] E.D. Evans and A.W. Mangel, "Depolarization-stimulated contractility of gastrointestinal smooth muscle in calcium-free solution: a review," *ISRN Gastroenterol*, vol. 2011, pp. 692528.

[246] A. Beyder, J.L. Rae, C. Bernard, P.R. Strege, F. Sachs, and G. Farrugia, "Mechanosensitivity of Nav1.5, a voltage-sensitive sodium channel," *J Physiol*, vol. 588, (no. Pt 24), pp. 4969-85, Dec 15 2010.

[247] G. Farrugia, A.N. Holm, A. Rich, M.G. Sarr, J.H. Szurszewski, and J.L. Rae, "A mechanosensitive calcium channel in human intestinal smooth muscle cells," *Gastroenterology*, vol. 117, (no. 4), pp. 900-5, Oct 1999.

[248] M.L. Buist, L.K. Cheng, K.M. Sanders, and A.J. Pullan, "Multiscale modelling of human gastric electric activity: can the electrogastrogram detect functional electrical uncoupling?," *Exp Physiol*, vol. 91, (no. 2), pp. 383-90, Mar 2006.

[249] A.S. Lin, M.L. Buist, N.P. Smith, and A.J. Pullan, "Modelling slow wave activity in the small intestine," *J Theor Biol*, vol. 242, (no. 2), pp. 356-62, Sep 21 2006.

[250] M.L. Buist and Y.C. Poh, "An extended bidomain framework incorporating multiple cell types," *Biophys J*, vol. 99, (no. 1), pp. 13-8, Jul 7 2010.

[251] G.D. Hirst and F.R. Edwards, "Generation of slow waves in the antral region of guinea-pig stomach--a stochastic process," *J Physiol*, vol. 535, (no. Pt 1), pp. 165-80, Aug 15 2001.

[252] G.D. Hirst, "An additional role for ICC in the control of gastrointestinal motility?," *J Physiol*, vol. 537, (no. Pt 1), pp. 1, Nov 15 2001.

[253] M. Kurahashi, H. Zheng, L. Dwyer, S.M. Ward, S. Don Koh, and K.M. Sanders, "A functional role for the 'fibroblast-like cells' in gastrointestinal smooth muscles," *J Physiol*, vol. 589, (no. Pt 3), pp. 697-710, Feb 1 2011.

[254] L.M. Popescu, M. Gherghiceanu, M.E. Hinescu, D. Cretoiu, L. Ceafalan, T. Regalia, A.C. Popescu, C. Ardeleanu, and E. Mandache, "Insights into the interstitium of ventricular myocardium: interstitial

Cajal-like cells (ICLC)," *J Cell Mol Med*, vol. 10, (no. 2), pp. 429-58, Apr-Jun 2006.

[255] D. Cretoiu, S.M. Ciontea, L.M. Popescu, L. Ceafalan, and C. Ardeleanu, "Interstitial Cajal-like cells (ICLC) as steroid hormone sensors in human myometrium: immunocytochemical approach," *J Cell Mol Med*, vol. 10, (no. 3), pp. 789-95, Jul-Sep 2006.

[256] S.M. Ciontea, E. Radu, T. Regalia, L. Ceafalan, D. Cretoiu, M. Gherghiceanu, R.I. Braga, M. Malincenco, L. Zagrean, M.E. Hinescu, and L.M. Popescu, "C-kit immunopositive interstitial cells (Cajal-type) in human myometrium," *J Cell Mol Med*, vol. 9, (no. 2), pp. 407-20, Apr-Jun 2005.

[257] L.M. Popescu, M.E. Hinescu, N. Ionescu, S.M. Ciontea, D. Cretoiu, and C. Ardelean, "Interstitial cells of Cajal in pancreas," *J Cell Mol Med*, vol. 9, (no. 1), pp. 169-90, Jan-Mar 2005.

[258] C. Vasquez, N. Benamer, and G.E. Morley, "The cardiac fibroblast: functional and electrophysiological considerations in healthy and diseased hearts," *J Cardiovasc Pharmacol*, vol. 57, (no. 4), pp. 380-8, Apr 2011.

[259] C. Vasquez, P. Mohandas, K.L. Louie, N. Benamer, A.C. Bapat, and G.E. Morley, "Enhanced fibroblast-myocyte interactions in response to cardiac injury," *Circ Res*, vol. 107, (no. 8), pp. 1011-20, Oct 15.

[260] N. Sperelakis, "An electric field mechanism for transmission of excitation between myocardial cells," *Circ Res*, vol. 91, (no. 11), pp. 985-7, Nov 29 2002.

[261] E.E. Daniel and Y.F. Wang, "Gap junctions in intestinal smooth muscle and interstitial cells of Cajal," *Microsc Res Tech*, vol. 47, (no. 5), pp. 309-20, Dec 1 1999.

[262] N.J. Severs, S.R. Coppen, E. Dupont, H.I. Yeh, Y.S. Ko, and T. Matsushita, "Gap junction alterations in human cardiac disease," *Cardiovasc Res*, vol. 62, (no. 2), pp. 368-77, May 1 2004.

[263] F.B. Sachse, A.P. Moreno, G. Seemann, and J.A. Abildskov, "A model of electrical conduction in cardiac tissue including fibroblasts," *Ann Biomed Eng*, vol. 37, (no. 5), pp. 874-89, May 2009.

[264] M.L. Buist, A. Corrias, and Y.C. Poh, "A model of slow wave propagation and entrainment along the stomach," *Ann Biomed Eng*, vol. 38, (no. 9), pp. 3022-30, Sep 2010.

[265] G.D. Hirst and F.R. Edwards, "Electrical events underlying organized myogenic contractions of the guinea pig stomach," *J Physiol*, vol. 576, (no. Pt 3), pp. 659-65, Nov 1 2006.

[266] T.W. Kim, S.D. Koh, T. Ordog, S.M. Ward, and K.M. Sanders, "Muscarinic regulation of pacemaker frequency in murine gastric interstitial cells of Cajal," *J Physiol*, vol. 546, (no. Pt 2), pp. 415-25, Jan 15 2003.

[267] J. Malysz, G. Donnelly, and J.D. Huizinga, "Regulation of slow wave frequency by IP(3)-sensitive calcium release in the murine small intestine," *Am J Physiol Gastrointest Liver Physiol*, vol. 280, (no. 3), pp. G439-48, Mar 2001.

[268] O. Bayguinov, S.M. Ward, J.L. Kenyon, and K.M. Sanders, "Voltage-gated Ca2+ currents are necessary for slow-wave propagation in the
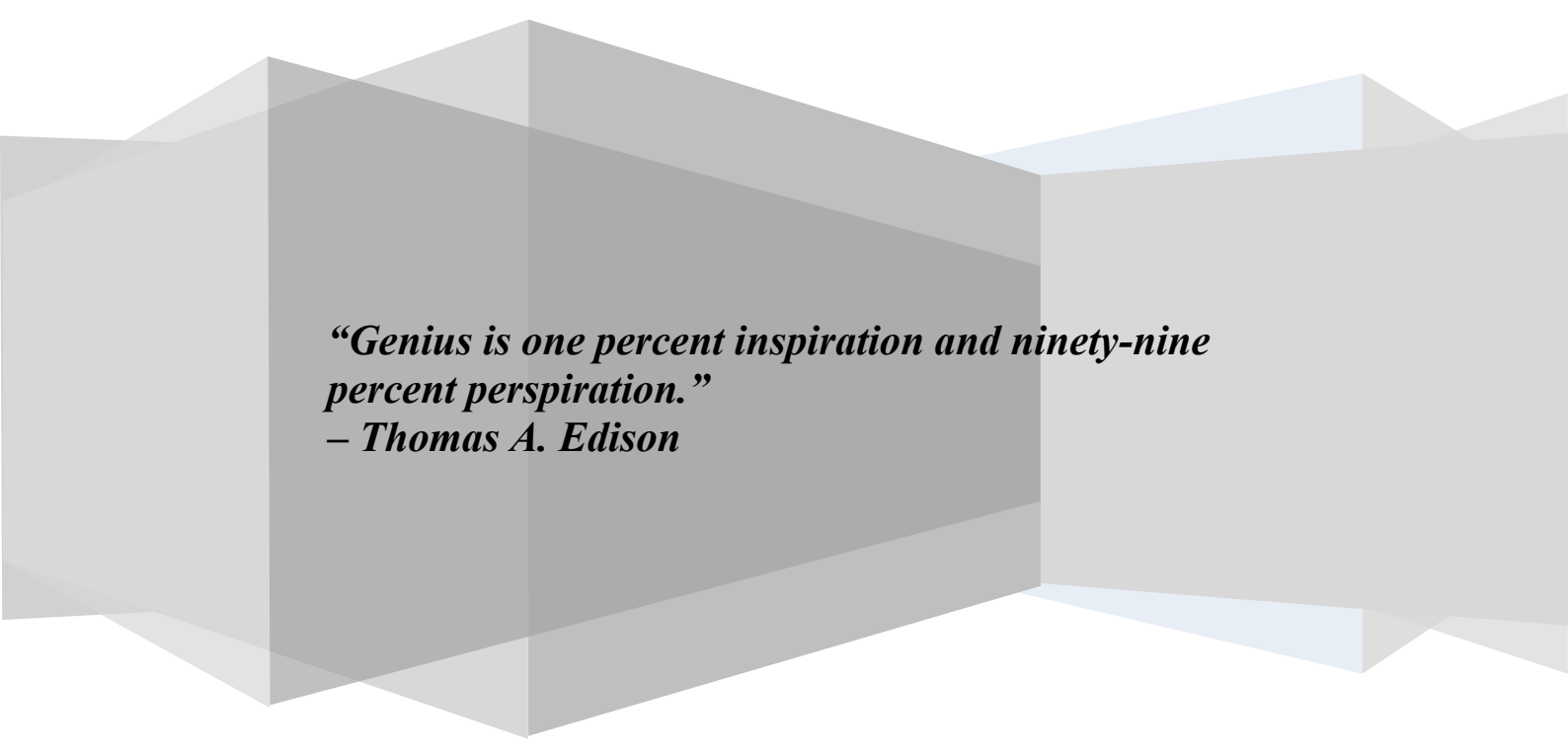
canine gastric antrum," *Am J Physiol Cell Physiol*, vol. 293, (no. 5), pp. C1645-59, Nov 2007.

[269]   J.H. Szurszewski and G. Farrugia, "Carbon monoxide is an endogenous hyperpolarizing factor in the gastrointestinal tract," *Neurogastroenterology and Motility*, vol. 16, pp. 81-85, Apr 2004.

[270]   G. Farrugia, W.A. Irons, J.L. Rae, M.G. Sarr, and J.H. Szurszewski, "Activation of whole cell currents in isolated human jejunal circular smooth muscle cells by carbon monoxide," *Am J Physiol*, vol. 264, (no. 6 Pt 1), pp. G1184-9, Jun 1993.

[271]   G. Farrugia, S. Lei, X. Lin, S.M. Miller, K.A. Nath, C.D. Ferris, M. Levitt, and J.H. Szurszewski, "A major role for carbon monoxide as an endogenous hyperpolarizing factor in the gastrointestinal tract," *Proceedings of the National Academy of Sciences of the United States of America*, vol. 100, (no. 14), pp. 8567-8570, Jul 8 2003.

[272]   G. Farrugia and S.J. Gibbons, "The role of carbon monoxide in the gastrointestinal tract," *Journal of Physiology-London*, vol. 556, (no. 2), pp. 325-336, Apr 15 2004.

[273]   W. Durante, F.K. Johnson, and R.A. Johnson, "Role of carbon monoxide in cardiovascular function," *J Cell Mol Med*, vol. 10, (no. 3), pp. 672-86, Jul-Sep 2006.

[274]   B. Kadinov, D. Itzev, H. Gagov, T. Christova, T.B. Bolton, and D. Duridanova, "Induction of heme oxygenase in guinea-pig stomach: roles in contraction and in single muscle cell ionic currents," *Acta Physiologica Scandinavica*, vol. 175, (no. 4), pp. 297-313, Aug 2002.

[275]   G. Farrugia, S.M. Miller, A. Rich, X. Liu, M.D. Maines, J.L. Rae, and J.H. Szurszewski, "Distribution of heme oxygenase and effects of exogenous carbon monoxide in canine jejunum," *Am J Physiol*, vol. 274, (no. 2 Pt 1), pp. G350-8, Feb 1998.

[276]   J.H. Szurszewski, S.M. Miller, G. Farrugia, P.F. Schmalz, L.G. Ermilov, and M.D. Maines, "Heme oxygenase 2 is present in interstitial cell networks of the mouse small intestine," *Gastroenterology*, vol. 114, (no. 2), pp. 239-244, Feb 1998.

[277]   F.R. Edwards and G.D. Hirst, "An electrical description of the generation of slow waves in the antrum of the guinea-pig," *J Physiol*, vol. 564, (no. Pt 1), pp. 213-32, Apr 1 2005.

[278]   G. Farrugia, S. Lei, X. Lin, S.M. Miller, K.A. Nath, C.D. Ferris, M. Levitt, and J.H. Szurszewski, "A major role for carbon monoxide as an endogenous hyperpolarizing factor in the gastrointestinal tract," *Proc Natl Acad Sci U S A*, vol. 100, (no. 14), pp. 8567-70, Jul 8 2003.

[279]   Y. Hara, M. Kubota, and J.H. Szurszewski, "Electrophysiology of Smooth-Muscle of the Small-Intestine of Some Mammals," *Journal of Physiology-London*, vol. 372, pp. 501-520, Mar 1986.

[280]   A.J. Bauer and K.M. Sanders, "Gradient in Excitation-Contraction Coupling in Canine Gastric Antral Circular Muscle," *Journal of Physiology-London*, vol. 369, (no. Dec), pp. 283-294, 1985.

[281]   A.J. Bauer and K.M. Sanders, "Passive and Active Membrane-Properties of Canine Gastric Antral Circular Muscles," *American Journal of Physiology*, vol. 251, (no. 2), pp. C268-C273, Aug 1986.

[282] A.J. Bauer, J.B. Reed, and K.M. Sanders, "Slow-Wave Heterogeneity within the Circular Muscle of the Canine Gastric Antrum," *Journal of Physiology-London*, vol. 366, (no. Sep), pp. 221-232, 1985.

[283] Y. Hara and J.H. Szurszewski, "Effect of potassium and acetylcholine on canine intestinal smooth muscle," *J Physiol*, vol. 372, pp. 521-37, Mar 1986.

[284] W.J. Lammers, L. Ver Donck, B. Stephen, D. Smets, and J.A. Schuurkes, "Origin and propagation of the slow wave in the canine stomach: the outlines of a gastric conduction system," *Am J Physiol Gastrointest Liver Physiol*, vol. 296, (no. 6), pp. G1200-10, Jun 2009.

[285] P. Du, G. O'Grady, J.U. Egbuji, W.J. Lammers, D. Budgett, P. Nielsen, J.A. Windsor, A.J. Pullan, and L.K. Cheng, "High-resolution mapping of in vivo gastrointestinal slow wave activity using flexible printed circuit board electrodes: methodology and validation," *Ann Biomed Eng*, vol. 37, (no. 4), pp. 839-46, Apr 2009.

[286] G. O'Grady, P. Du, L.K. Cheng, J.U. Egbuji, W.J. Lammers, J.A. Windsor, and A.J. Pullan, "Origin and propagation of human gastric slow-wave activity defined by high-resolution mapping," *Am J Physiol Gastrointest Liver Physiol*, vol. 299, (no. 3), pp. G585-92, Sep 2010.

[287] P.G. Dinning, J.W. Arkwright, H. Gregersen, G. O'Grady, and S.M. Scott, "Technical advances in monitoring human motility patterns," *Neurogastroenterology and Motility*, vol. 22, (no. 4), pp. 366-380, Apr 2010.

[288] H. Hashitani, A.P. Garcia-Londono, G.D. Hirst, and F.R. Edwards, "Atypical slow waves generated in gastric corpus provide dominant pacemaker activity in guinea pig stomach," *J Physiol*, vol. 569, (no. Pt 2), pp. 459-65, Dec 1 2005.

[289] G.D. Hirst, E.A. Beckett, K.M. Sanders, and S.M. Ward, "Regional variation in contribution of myenteric and intramuscular interstitial cells of Cajal to generation of slow waves in mouse gastric antrum," *J Physiol*, vol. 540, (no. Pt 3), pp. 1003-12, May 1 2002.

[290] T. Komuro, "Structure and organization of interstitial cells of Cajal in the gastrointestinal tract," *J Physiol*, vol. 576, (no. Pt 3), pp. 653-8, Nov 1 2006.

[291] C.J. Stratton, S.M. Ward, K. Horiguchi, and K.M. Sanders, "Immunocytochemical identification of interstitial cells of Cajal in the murine fundus using a live-labelling technique," *Neurogastroenterol Motil*, vol. 19, (no. 2), pp. 152-9, Feb 2007.

[292] D. Linden, L. Sha, A. Mazzone, G. Stoltz, C. Bernard, J. Furne, M. Levitt, G. Farrugia, and J. Szurszewski, "Intact mouse tissues endogenously produce hydrogen sulfide," *Neurogastroenterology and Motility*, vol. 19, pp. 21-21, Oct 2007.

[293] D.R. Linden, L. Sha, A. Mazzone, G.J. Stoltz, C.E. Bernard, J.K. Furne, M.D. Levitt, G. Farrugia, and J.H. Szurszewski, "Production of the gaseous signal molecule hydrogen sulfide in mouse tissues," *Journal of Neurochemistry*, vol. 106, (no. 4), pp. 1577-1585, Aug 2008.

[294] M.G. Sarr, M.S. Kasparek, and D.R. Linden, "Role of the gasotransmitter hydrogen sulfide in modulation of contractile function

in longitudinal muscle of rat jejunum," *Gastroenterology*, vol. 134, (no. 4), pp. A249-A249, Apr 2008.

[295] P. Prasad, "The role of nitric oxide in gastrointestinal health and disease," *Gastroenterology*, vol. 127, (no. 3), pp. 1014-1014, Sep 2004.

[296] V. Shah, G. Lyford, G. Gores, and G. Farrugia, "Nitric oxide in gastrointestinal health and disease," *Gastroenterology*, vol. 126, (no. 3), pp. 903-913, Mar 2004.

[297] N.J. Zyromski, J.A. Duenes, M.L. Kendrick, B.M. Balsiger, G. Farrugia, and M.G. Sarr, "Mechanism mediating nitric oxide-induced inhibition in human jejunal longitudinal smooth muscle," *Surgery*, vol. 130, (no. 3), pp. 489-496, Sep 2001.

[298] P.R. Strege, C.E. Bernard, R.E. Kraichely, A. Mazzone, L. Sha, A. Beyder, S.J. Gibbons, D.R. Linden, M.L. Kendrick, M.G. Sarr, J.H. Szurszewski, and G. Farrugia, "Hydrogen sulfide is a partially redox-independent activator of the human jejunum Na(+) channel, Na(v)1.5," *American Journal of Physiology-Gastrointestinal and Liver Physiology*, vol. 300, (no. 6), pp. G1105-G1114, Jun 2011.

[299] S.D. Koh, J.D. Campbell, A. Carl, and K.M. Sanders, "Nitric oxide activates multiple potassium channels in canine colonic smooth muscle," *Journal of Physiology-London*, vol. 489, (no. 3), pp. 735-743, Dec 15 1995.

[300] C.G. Park, Y.D. Kim, M.Y. Kim, J.S. Kim, S. Choi, C.H. Yeum, S.P. Parajuli, J.S. Park, H.S. Jeong, I. So, K.W. Kim, and J.Y. Jun, "Inhibition of pacemaker currents by nitric oxide via activation of ATP-sensitive K+ channels in cultured interstitial cells of Cajal from the mouse small intestine," *Naunyn-Schmiedebergs Archives of Pharmacology*, vol. 376, (no. 3), pp. 175-184, Nov 2007.

[301] L. Xue, G. Farrugia, S.M. Miller, C.D. Ferris, S.H. Snyder, and J.H. Szurszewski, "Carbon monoxide and nitric oxide as coneurotransmitters in the enteric nervous system: Evidence from genomic deletion of biosynthetic enzymes," *Proceedings of the National Academy of Sciences of the United States of America*, vol. 97, (no. 4), pp. 1851-1855, Feb 15 2000.

[302] D. Noble, *The music of life : biology beyond the genome*, Oxford ; New York: Oxford University Press, 2006.

[303] W.H. Guilford and D.M. Warshaw, "The molecular mechanics of smooth muscle myosin," *Comparative Biochemistry and Physiology B-Biochemistry & Molecular Biology*, vol. 119, (no. 3), pp. 451-458, Mar 1998.

[304] K.M. Sanders, "Regulation of smooth muscle excitation and contraction," *Neurogastroenterol Motil*, vol. 20 Suppl 1, pp. 39-53, May 2008.

[305] K.S. Murthy, "Signaling for contraction and relaxation in smooth muscle of the gut," *Annu Rev Physiol*, vol. 68, pp. 345-74, 2006.

[306] P. Du, Y.C. Poh, J.L. Lim, V. Gajendiran, G. Orgrady, M.L. Buist, A.J. Pullan, and L.K. Cheng, "A preliminary model of gastrointestinal electromechanical coupling," *IEEE Trans Biomed Eng*, vol. 58, (no. 12), pp. 3491-5, Dec 2011.

[307] A. Beyder, J.L. Rae, C. Bernard, P.R. Strege, F. Sachs, and G. Farrugia, "Mechanosensitivity of Na(v)1.5, a voltage-sensitive sodium channel," *Journal of Physiology-London*, vol. 588, (no. 24), pp. 4969-4985, Dec 15 2010.

[308] O.P. Hamill, "Twenty odd years of stretch-sensitive channels," *Pflugers Arch*, vol. 453, (no. 3), pp. 333-51, Dec 2006.

[309] R.E. Kraichely, P.R. Strege, M.G. Sarr, M.L. Kendrick, and G. Farrugia, "Lysophosphatidyl choline modulates mechanosensitive L-type Ca2+ current in circular smooth muscle cells from human jejunum," *Am J Physiol Gastrointest Liver Physiol*, vol. 296, (no. 4), pp. G833-9, Apr 2009.

[310] B. Martinac, "Mechanosensitive ion channels: molecules of mechanotransduction," *J Cell Sci*, vol. 117, (no. Pt 12), pp. 2449-60, May 15 2004.

[311] V. Gajendiran and M.L. Buist, "A quantitative description of the active force generation in gastrointestinal smooth muscle," *International Journal for Numerical Methods in Biomedical Engineering*, vol. 27 (no. 3), pp. 450-460, 2010.

[312] C.W. Chung and M.L. Buist, "A novel nonlinear viscoelastic solid model," *Nonlinear Analysis: Real World Applications*, vol. 13, (no. 3), pp. 1480-1488, 2012.

[313] Z.Y. Lin, R.W. McCallum, B.D. Schirmer, and J.D. Chen, "Effects of pacing parameters on entrainment of gastric slow waves in patients with gastroparesis," *Am J Physiol*, vol. 274, (no. 1 Pt 1), pp. G186-91, Jan 1998.

[314] J. Zhang and J.D. Chen, "Systematic review: applications and future of gastric electrical stimulation," *Aliment Pharmacol Ther*, vol. 24, (no. 7), pp. 991-1002, Oct 1 2006.

[315] J.D. Wood, "Integrative functions of the enteric nervous system," in Physiology of the gastrointestinal tract 4th ed., Amsterdam ; Boston: Elsevier Academic Press, 2006.

Appendices

"Genius is one percent inspiration and ninety-nine percent perspiration."
– Thomas A. Edison

Appendices

Appendix 1. Microscopic reversibility

Microscopic reversibility (MR) is achieved when a reaction reaches a steady-state where the degree of change in the forward direction equals to the degree of change in the backward direction, at steady-state amounts of the reactants. To illustrate, consider the following example of three state reaction system (see Figure A1.1).
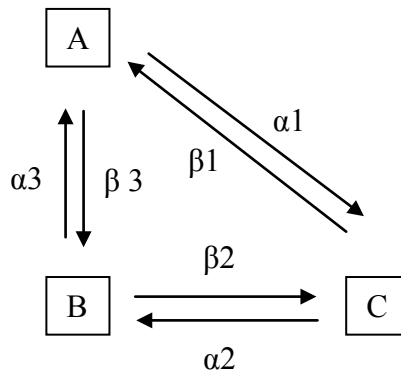
Figure A1.1. A closed loop, three state reaction system.

At equilibrium, three equations can be derived from the above reactions, i.e., Eqs. A1.1 to A1.3:

$$\alpha1A = \beta1C, \tag{A1.1}$$

$$\alpha2C = \beta2B, \tag{A1.2}$$

$$\alpha3B = \beta3A. \tag{A1.3}$$

Eq. A1.2 is divided by Eq. A1.3 to get:

$$\frac{\alpha2C}{\beta3A} = \frac{\beta2}{\alpha3}. \tag{A1.4}$$

Eq. A1.4 was rearranged to get:

$$\frac{C}{A} = \frac{\beta2\beta3}{\alpha2\alpha3}. \tag{A1.5}$$

Eq. A1.1 was rearranged to get:

$$\frac{C}{A} = \frac{\alpha 1}{\beta 1}.$$ (A1.6)

Eq. A1.5 is equivalent to Eq. A1.6:

$$\frac{\beta 2 \beta 3}{\alpha 2 \alpha 3} = \frac{\alpha 1}{\beta 1}.$$ (A1.7)

Rearrangement of Eq. A1.7 gives the MR relationship:

$$\alpha 1 \alpha 2 \alpha 3 = \beta 1 \beta 2 \beta 3.$$ (A1.8)

The MR relationship can be extended for closed loop reactions of more than three states. Take the following example of four state reaction system (Figure A1.2):
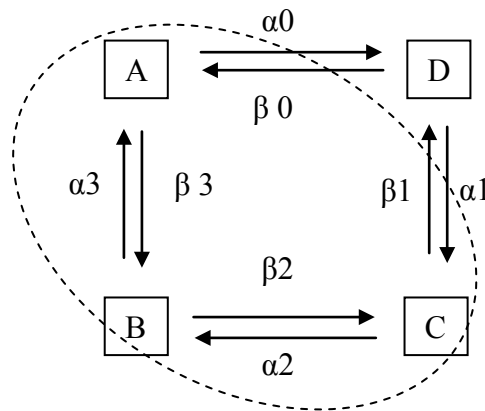
Figure A1.2. A closed loop, four state reaction system.

An additional state, D, has been introduced. Consider the equations of the transitions involving D, i.e., Eq. A1.9 and A1.10:

$$\alpha 0 A = \beta 0 D,$$ (A1.9)

$$\alpha 1 D = \beta 1 C.$$ (A1.10)

Eq. A1.10 is divided by Eq. A1.9 to get:

$$\frac{\beta 1 C}{\alpha 0 A} = \frac{\alpha 1}{\beta 0}. \tag{A1.11}$$

Eq. A1.11 was rearranged to get:

$$\frac{C}{A} = \frac{\alpha 0 \alpha 1}{\beta 0 \beta 1}. \tag{A1.12}$$

Eq. A1.12 was substituted into Eq. A1.5:

$$\frac{\alpha 0 \alpha 1}{\beta 0 \beta 1} = \frac{\beta 2 \beta 3}{\alpha 2 \alpha 3}. \tag{A1.13}$$

Eq. A1.13 was rearranged to get the MR relationship for four state reactions:

$$\alpha 0 \alpha 1 \alpha 2 \alpha 3 = \beta 0 \beta 1 \beta 2 \beta 3. \tag{A1.14}$$

By the same logic, the above relation can be extended to N states of closed loop reactions:

$$\alpha 0 \alpha 1 \alpha 2 \alpha 3 \ldots \alpha N = \beta 0 \beta 1 \beta 2 \beta 3 \ldots \beta N. \tag{A1.15}$$

Ion channels can exist in several states. The transition between states depends on the energy barrier and can be influenced by factors such as the membrane voltage changes. At equilibrium, transitions of ion channels involved in a closed loop should observe microscopic reversibility.

Appendix 2.   Complete sodium current results for SCN5A, TCAP & R76C

The complete results for the verification of the SCN5A, TACP & R76C sodium channel models are provided here, a subset of the results was shown in Chapter 3.
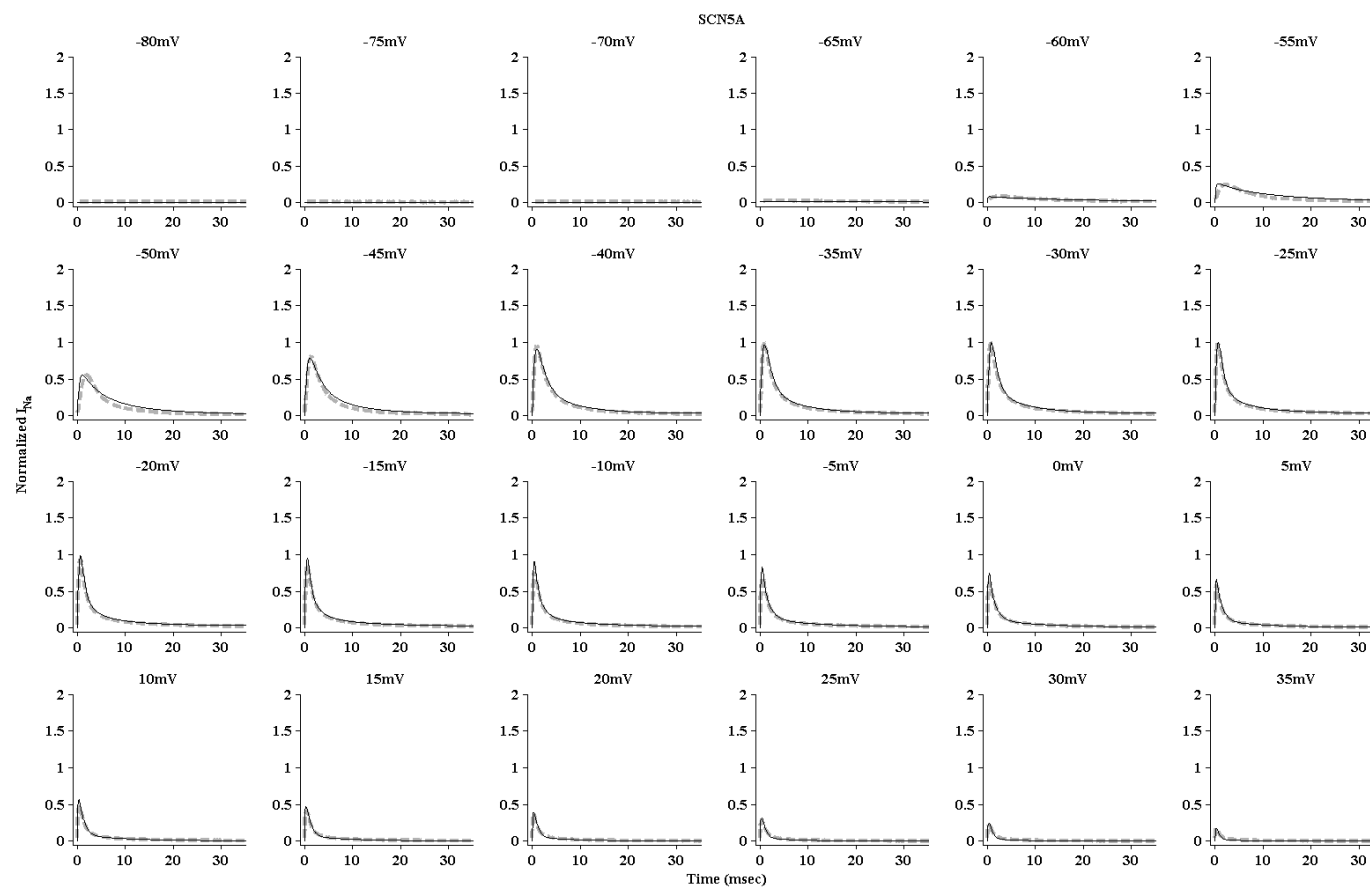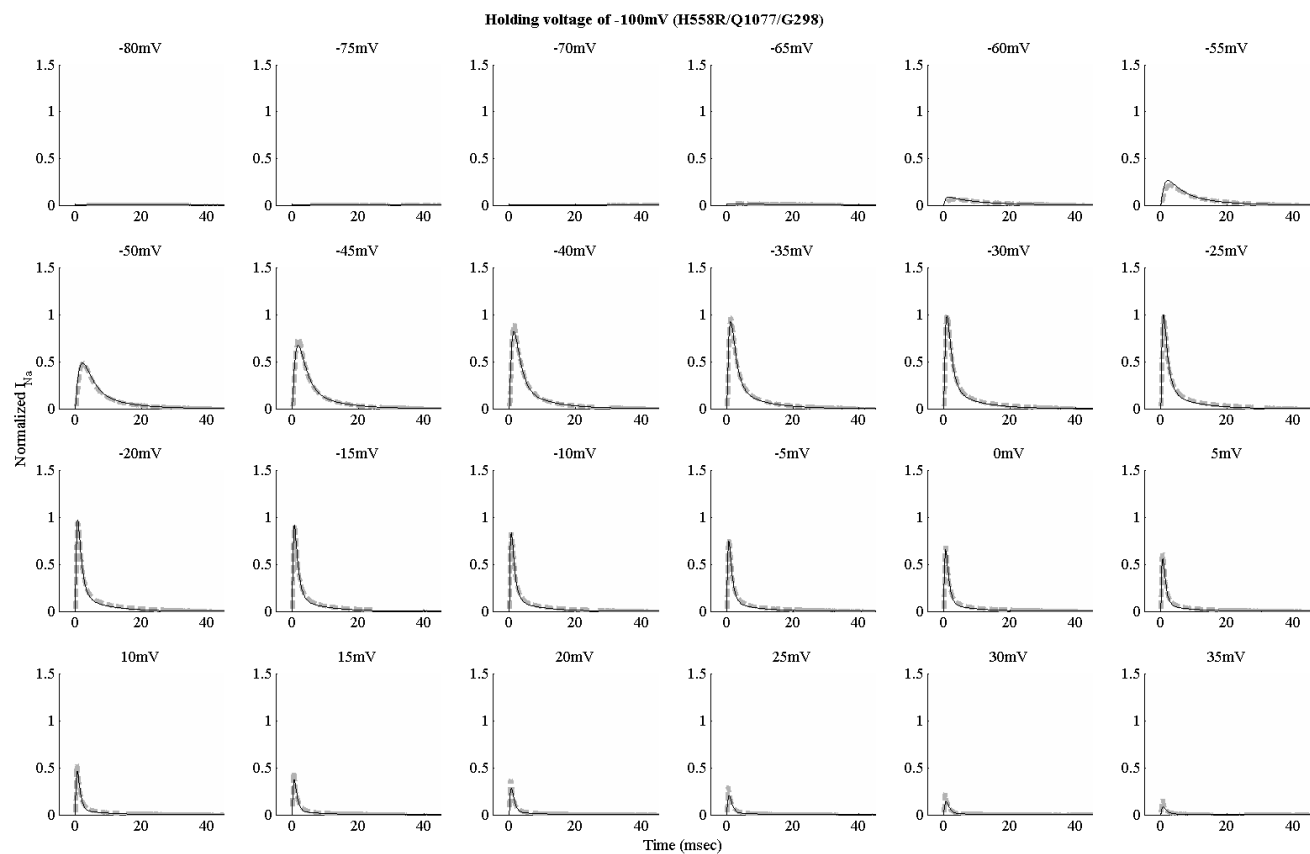
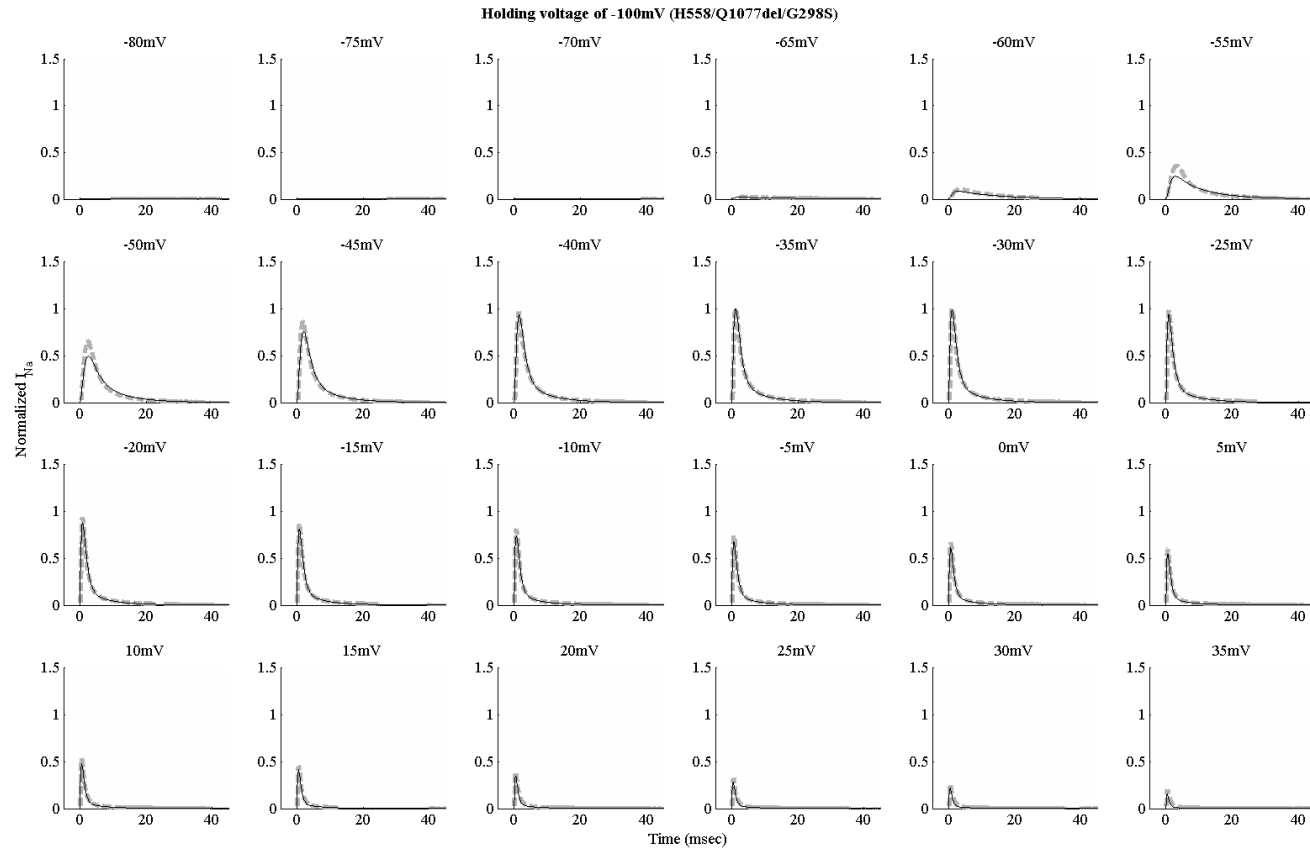Figure A2.1. Results for the SCN5A model. Each subplot represents the normalized sodium current versus time trace under a clamping voltage. A total of 24 clamping voltages were used, from -80 mV to 35 mV. Solid line represents model predicted data while dashed lines are for average experimental data.
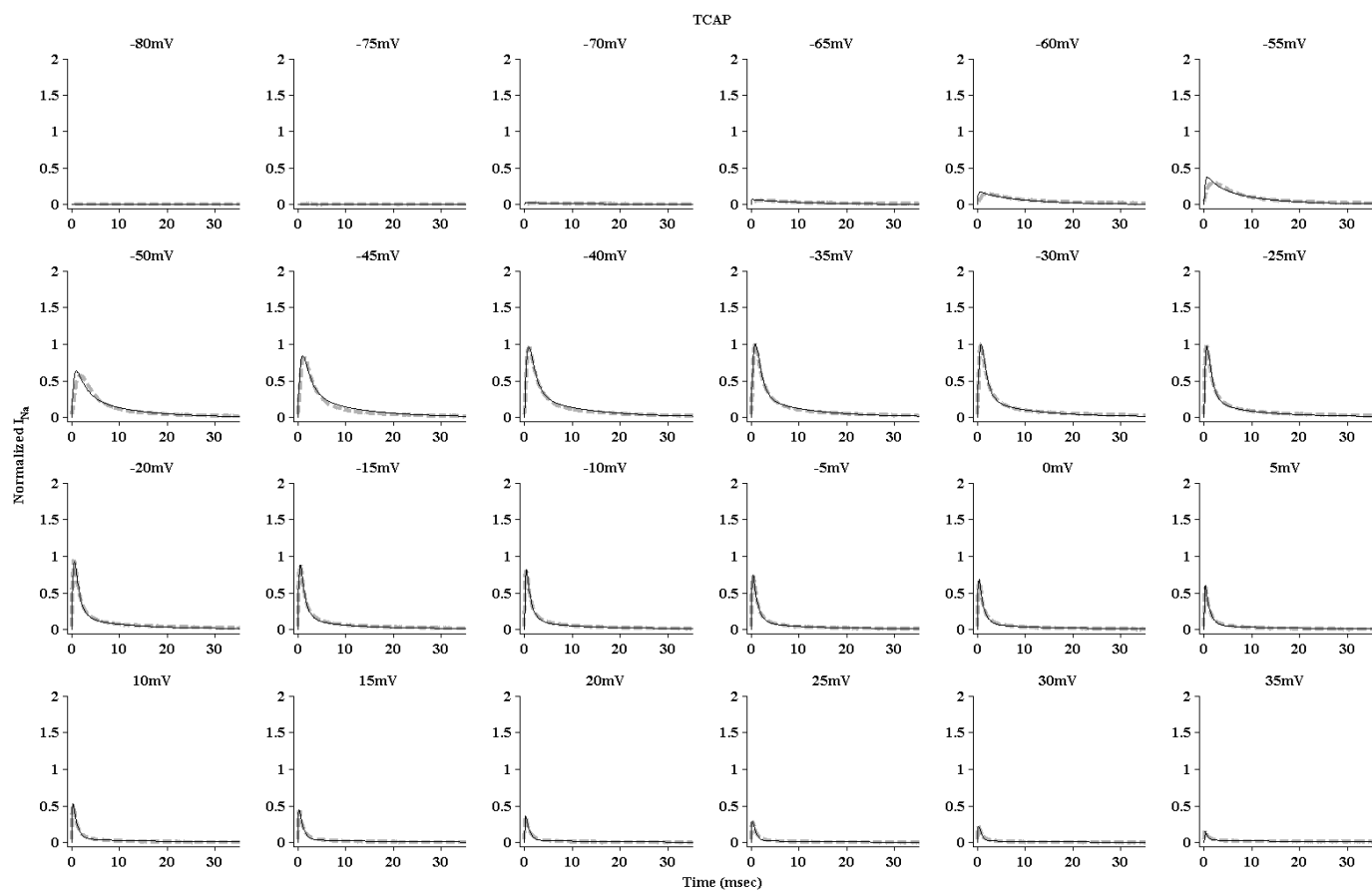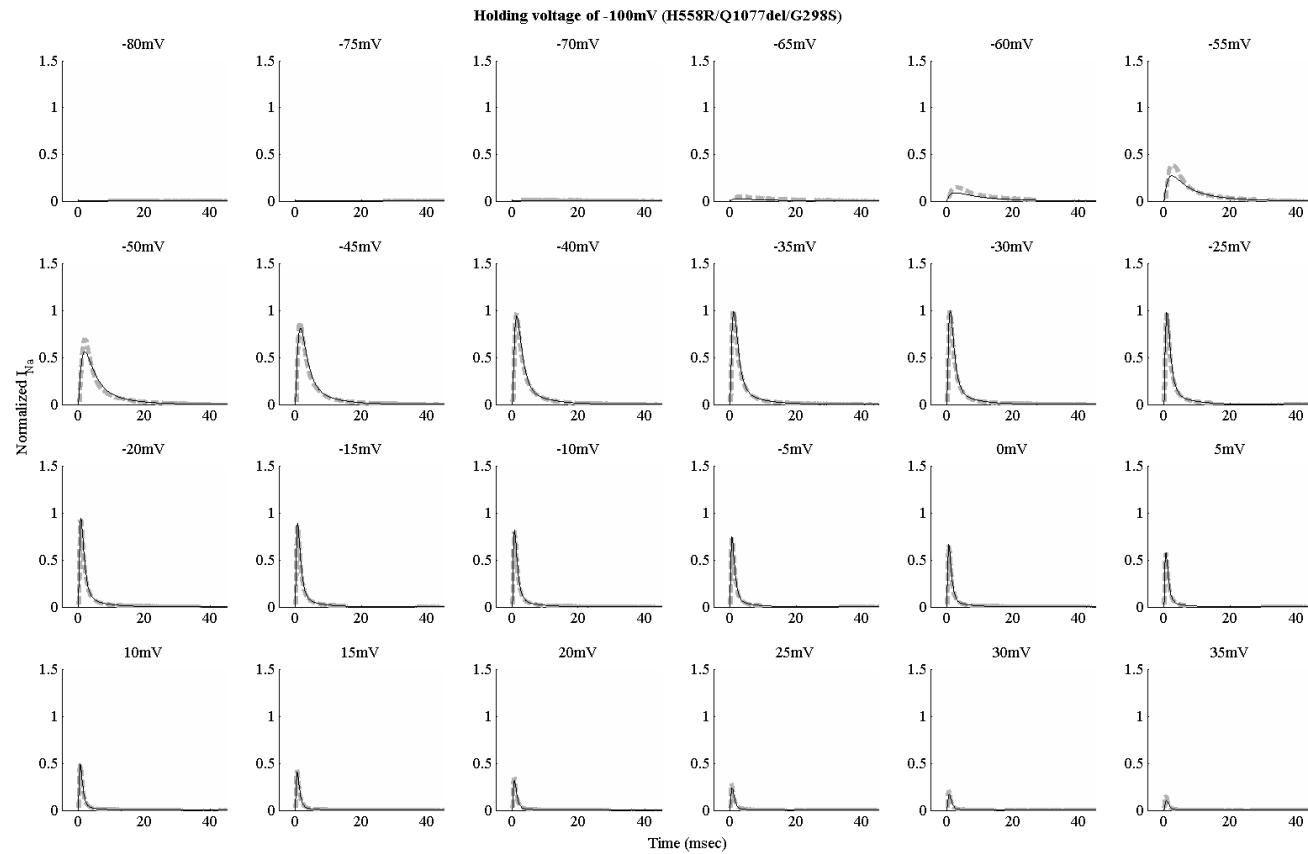
Figure A2.2. Results for the TCAP model. Each subplot represents the normalized sodium current versus time trace under a clamping voltage. A total of 24 clamping voltages were used, from -80 mV to 35 mV. Solid line represents model predicted data while dashed lines are for average experimental data.
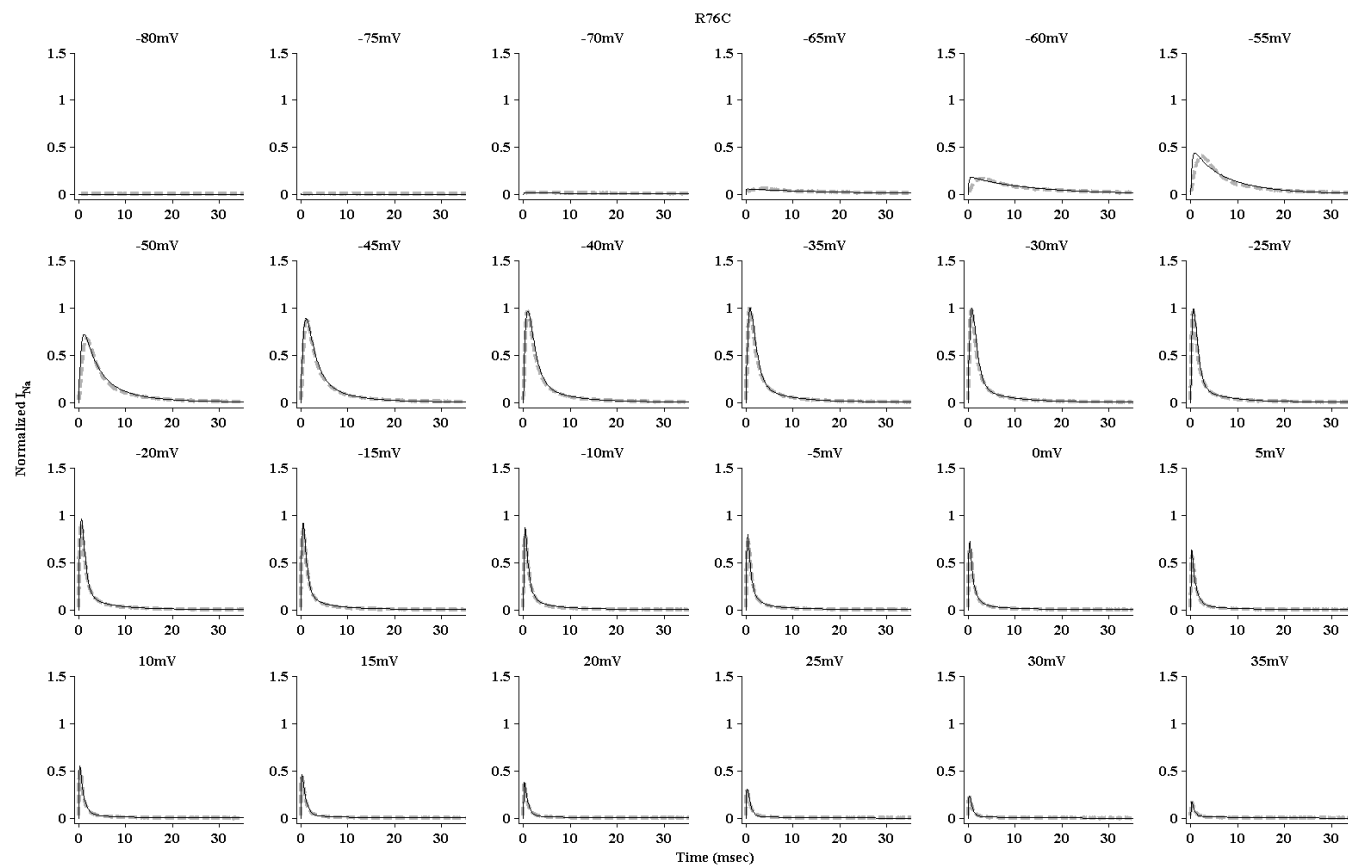
Figure A2.3. Results for the R76C model. Each subplot represents the normalized sodium current versus time trace under a clamping voltage. A total of 24 clamping voltages were used, from -80 mV to 35 mV. Solid line represents model predicted data while dashed lines are for average experimental data.

Appendix 3. Complete sodium current results for G298 models at -100 mV

The complete results for the verification of the G298 sodium channel models for all four backgrounds at -100 mV are provided here, a subset of the results was shown in Chapter 3.
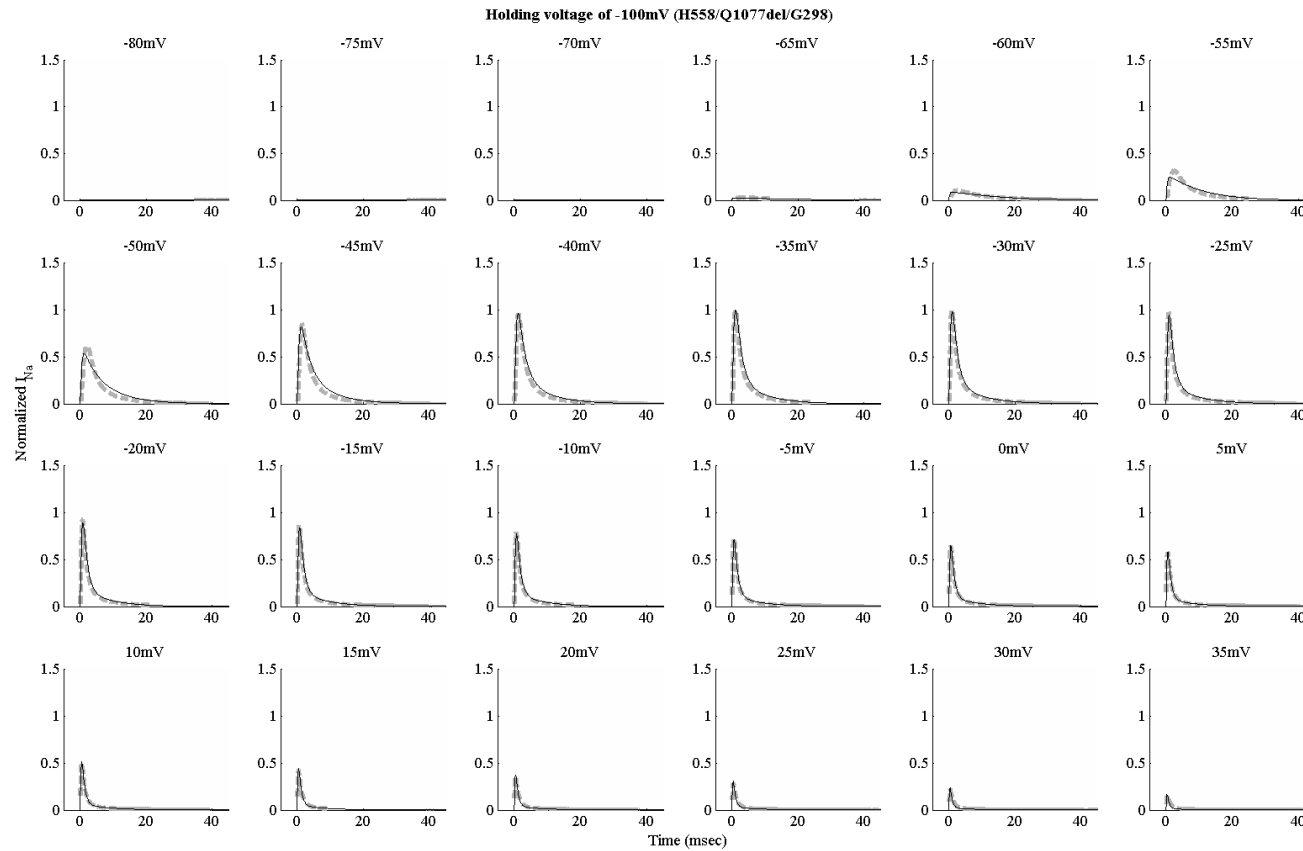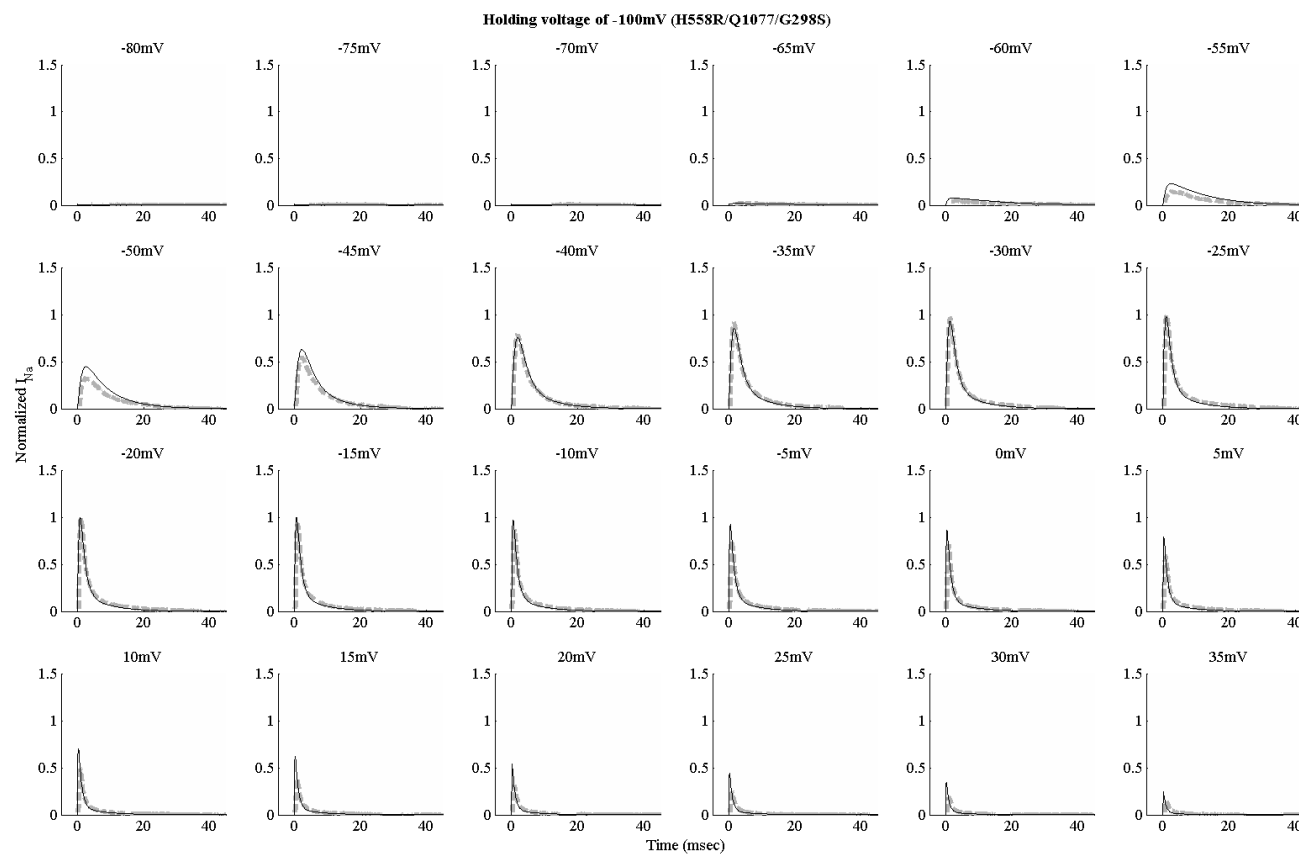
Figure A3.1. Results for the H558/Q1077del/G298 model. Each subplot represents the normalized sodium current versus time trace under a clamping voltage. A total of 24 clamping voltages were used, from -80 mV to 35 mV. Solid line represents model predicted data while dashed lines are for average experimental data.
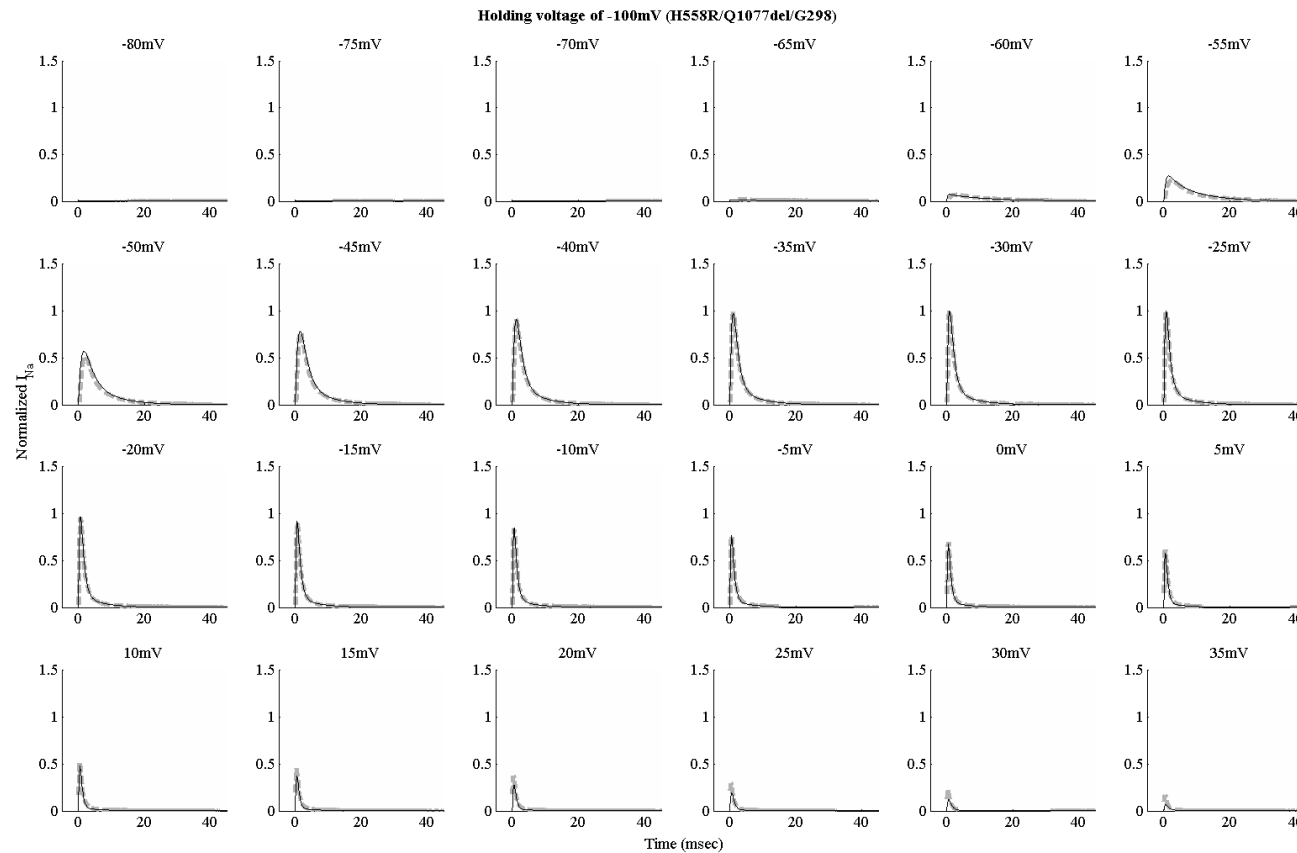
Figure A3.2. Results for the H558R/Q1077del/G298 model. Each subplot represents the normalized sodium current versus time trace under a clamping voltage. A total of 24 clamping voltages were used, from -80 mV to 35 mV. Solid line represents model predicted data while dashed lines are for average experimental data.
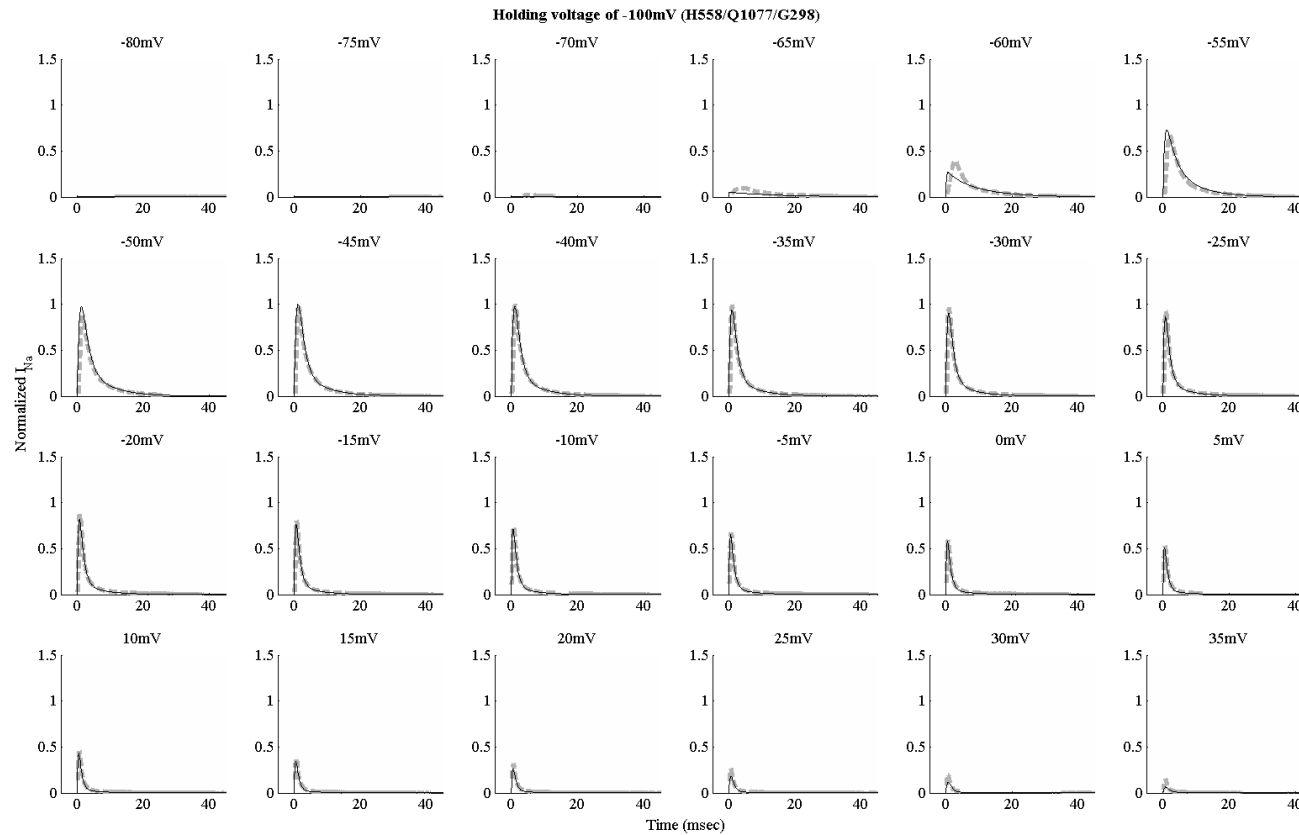
Figure A3.3. Results for the H558/Q1077/G298 model. Each subplot represents the normalized sodium current versus time trace under a clamping voltage. A total of 24 clamping voltages were used, from -80 mV to 35 mV. Solid line represents model predicted data while dashed lines are for average experimental data.

Figure A3.4. Results for the H558R/Q1077/G298 model. Each subplot represents the normalized sodium current versus time trace under a clamping voltage. A total of 24 clamping voltages were used, from -80 mV to 35 mV. Solid line represents model predicted data while dashed lines are for average experimental data.

Appendix 4.   Complete sodium current results for G298S models at -100 mV

The complete results for the verification of the G298S sodium channel models for all four backgrounds at -100 mV are provided here, a subset of the results was shown in Chapter 3.

Figure A4.1. Results for the H558/Q1077del/G298S model. Each subplot represents the normalized sodium current versus time trace under a clamping voltage. A total of 24 clamping voltages were used, from -80 mV to 35 mV. Solid line represents model predicted data while dashed lines are for average experimental data.

Figure A4.2. Results for the H558R/Q1077del/G298S model. Each subplot represents the normalized sodium current versus time trace under a clamping voltage. A total of 24 clamping voltages were used, from -80 mV to 35 mV. Solid line represents model predicted data while dashed lines are for average experimental data.
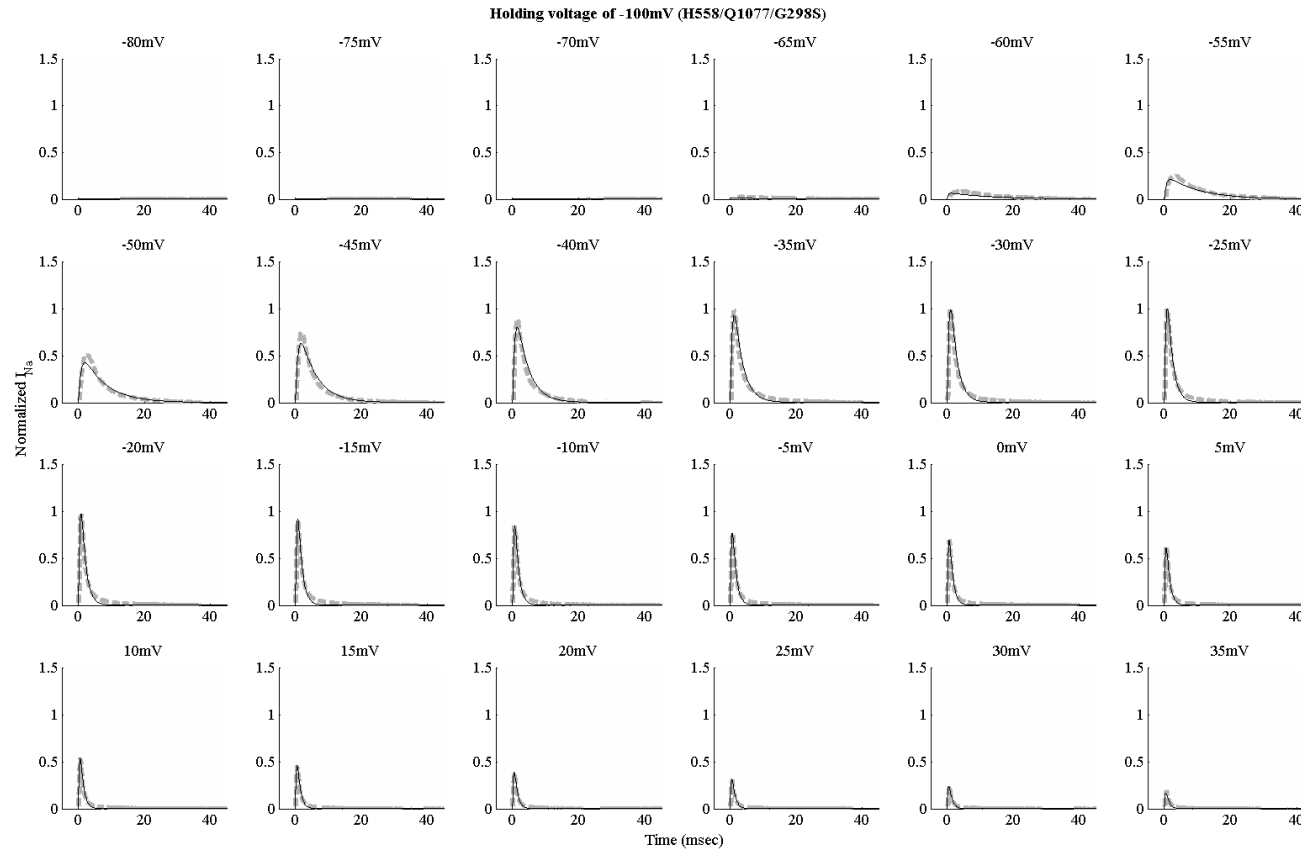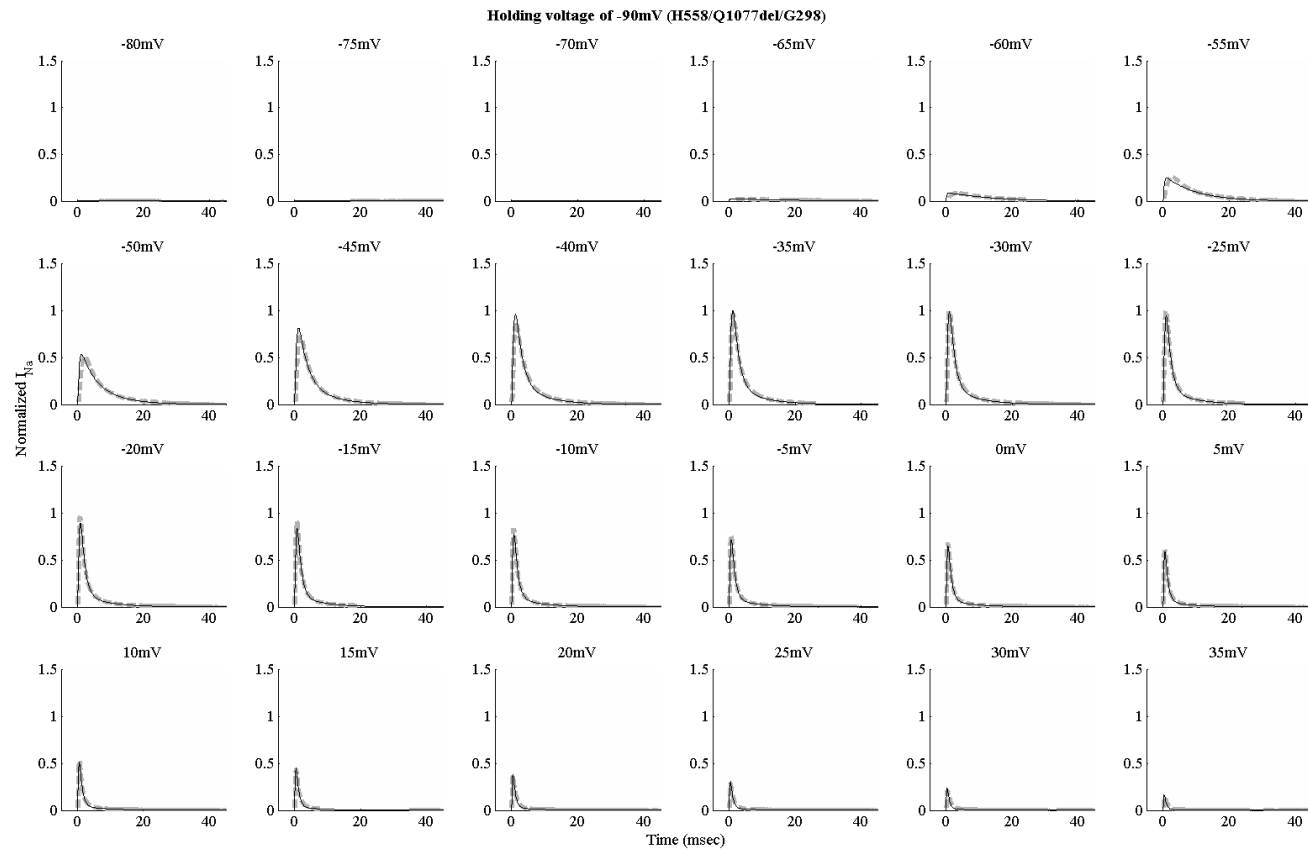
Figure A4.3. Results for the H558/Q1077/G298S model. Each subplot represents the normalized sodium current versus time trace under a clamping voltage. A total of 24 clamping voltages were used, from -80 mV to 35 mV. Solid line represents model predicted data while dashed lines are for average experimental data.

Figure A4.4. Results for the H558R/Q1077/G298S model. Each subplot represents the normalized sodium current versus time trace under a clamping voltage. A total of 24 clamping voltages were used, from -80 mV to 35 mV. Solid line represents model predicted data while dashed lines are for average experimental data.

Appendix 5.   Table of parameter values for the SCN5A, TCAP and R76C models

The original form of the rate equation, which is thermodynamically based, is given by $k = A exp(B + CV_m)$ and has three parameters of *A, B*, and *C*. In the event where the explicit representation of the three parameters does not matter, the simplified alternative form of $k = A'exp(CV_m)$ may be considered for implementation to improve computational efficiency such as for the parameterization procedure or in higher spatial scale investigations. For convenience, the parameter values of the simplified alternative form of the rate equations (corresponding to Table 3.10 in the main text) are provided here.

Table A5.1. Parameter values of the simplified rate equations for the SCN5A, TCAP and R76C models.

Model	SCN5A		TCAP		R76C	
Equation	$k_{i,j}$=A'exp(CV)					
State transition	A' (ms⁻¹)	C (mV⁻¹)	A' (ms⁻¹)	C (mV⁻¹)	A' (ms⁻¹)	C (mV⁻¹)
O→I1	2.1986234	0.0060535	2.1556658	0.013723	2.2118136	0.010794
I1→I2	0.0292005	-0.046865	0.0495416	-0.0003999	0.1025634	-0.010767
C3→C2	0.0004904	0.0031945	5.546E-06	0.0098716	0.0086452	-0.0003937
C2→C1	1.2394747	0.058353	1.2930917	0.052254	0.7189933	0.0759
C1→O	1.5472523	0.041075	2.3737791	0.039009	2.5085806	0.042291
I2→I1	0.0571904	0.0061468	0.1000977	0.061081	0.0077208	0.0017296
C2→C3	0.5020341	0.036441	0.6245736	0.013469	0.5765968	0.028433
C1→C2	4.5404017	0.077193	4.5758391	0.060615	4.1851257	0.072258
O→C1	3.867E-06	-0.25289	0.0002049	-0.17572	7.491E-06	-0.22722
I1→C1	0.1588606	0.020406	0.1465441	-0.0009556	0.094397	0.0066217
C1→I1	0.0002035	0.0046683	8.597E-05	0.0025689	1.622E-17	-0.0031479
I1→O	8.14E-06	0.083025	5.098E-07	0.37114	9.153E-06	0.26954

Appendix 6.   Complete sodium current results for G298 models at -90 mV

The complete results for the verification of the G298 sodium channel models

for all four backgrounds at -90 mV are provided here, a subset of the results
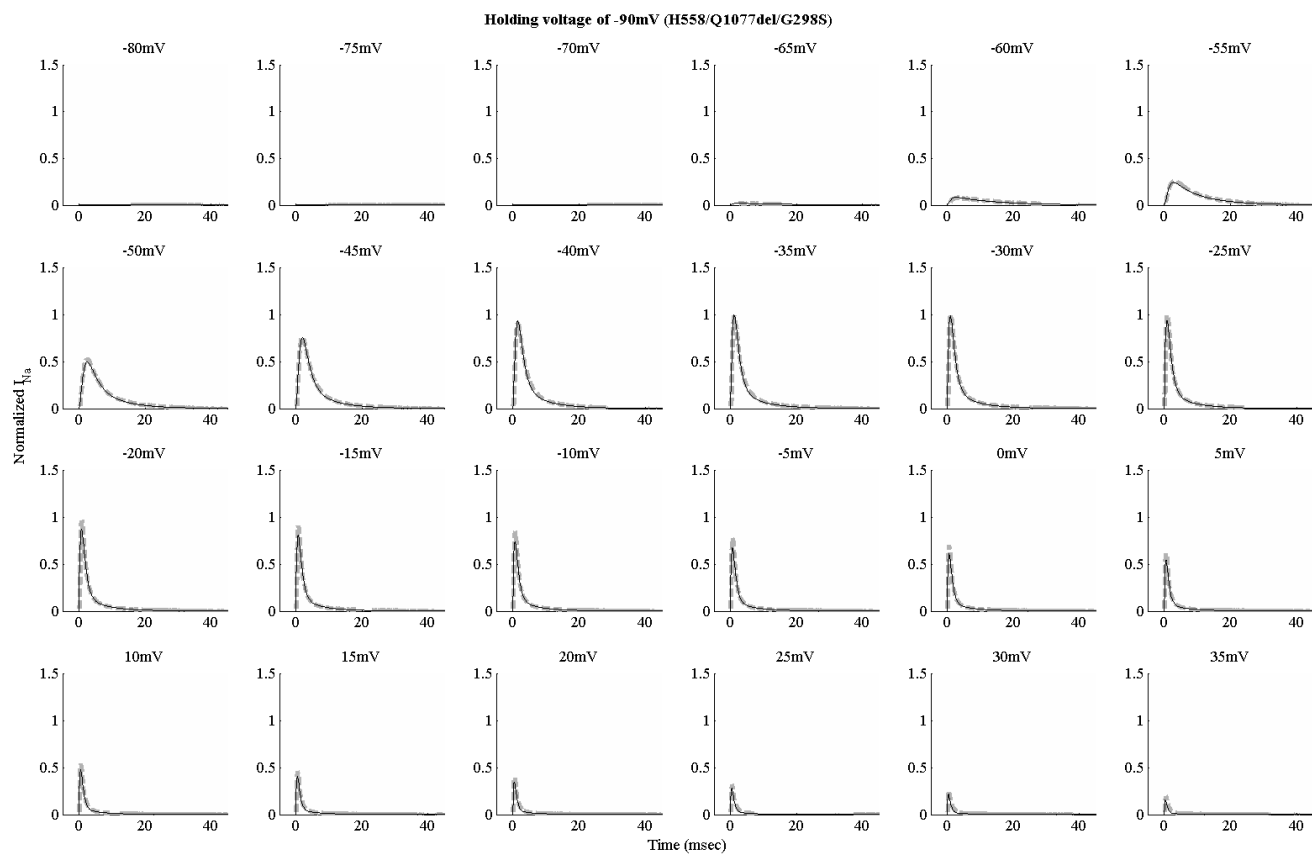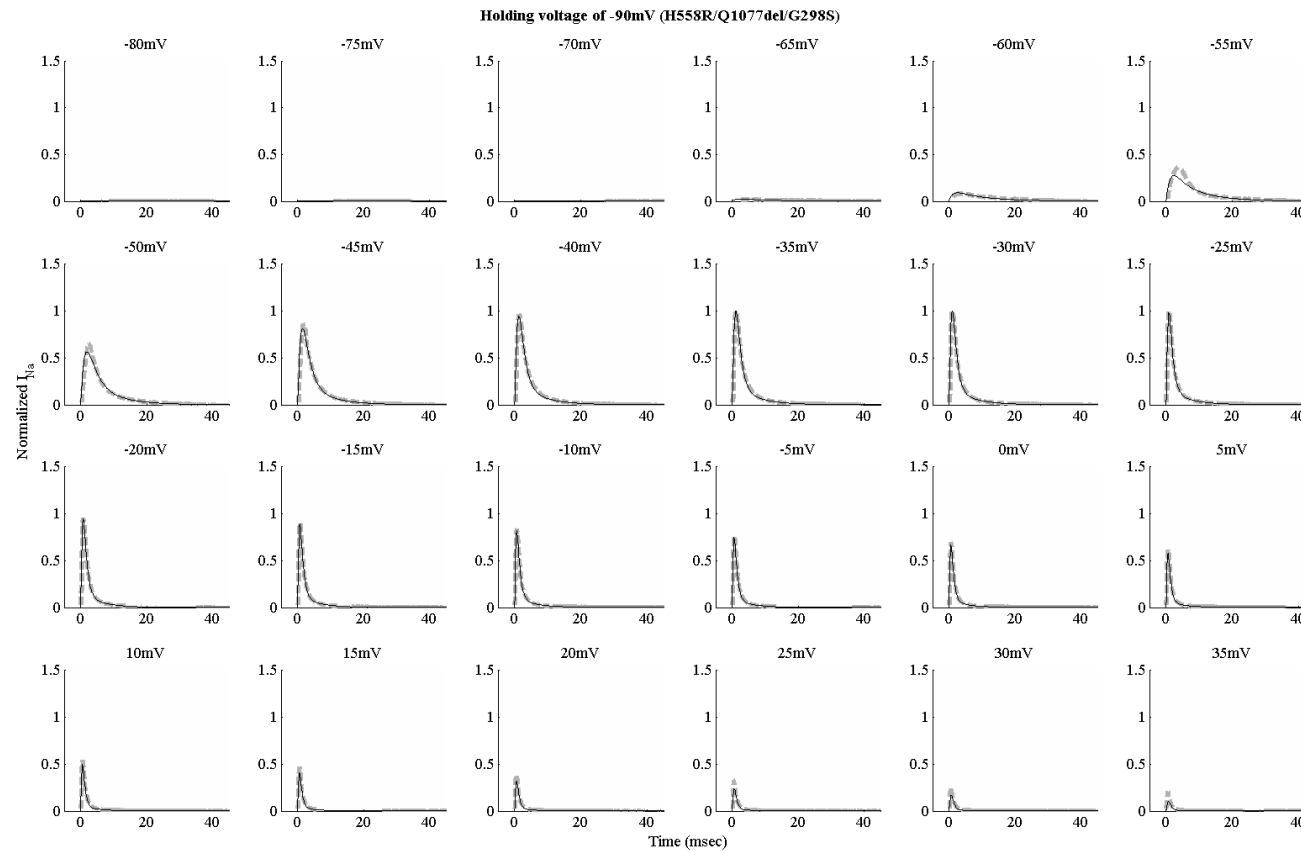
was shown in Chapter 3.

Figure A6.1. Results for the H558/Q1077del/G298 model. Each subplot represents the normalized sodium current versus time trace under a clamping voltage. A total of 24 clamping voltages were used, from -80 mV to 35 mV. Solid line represents model predicted data while dashed lines are for average experimental data.
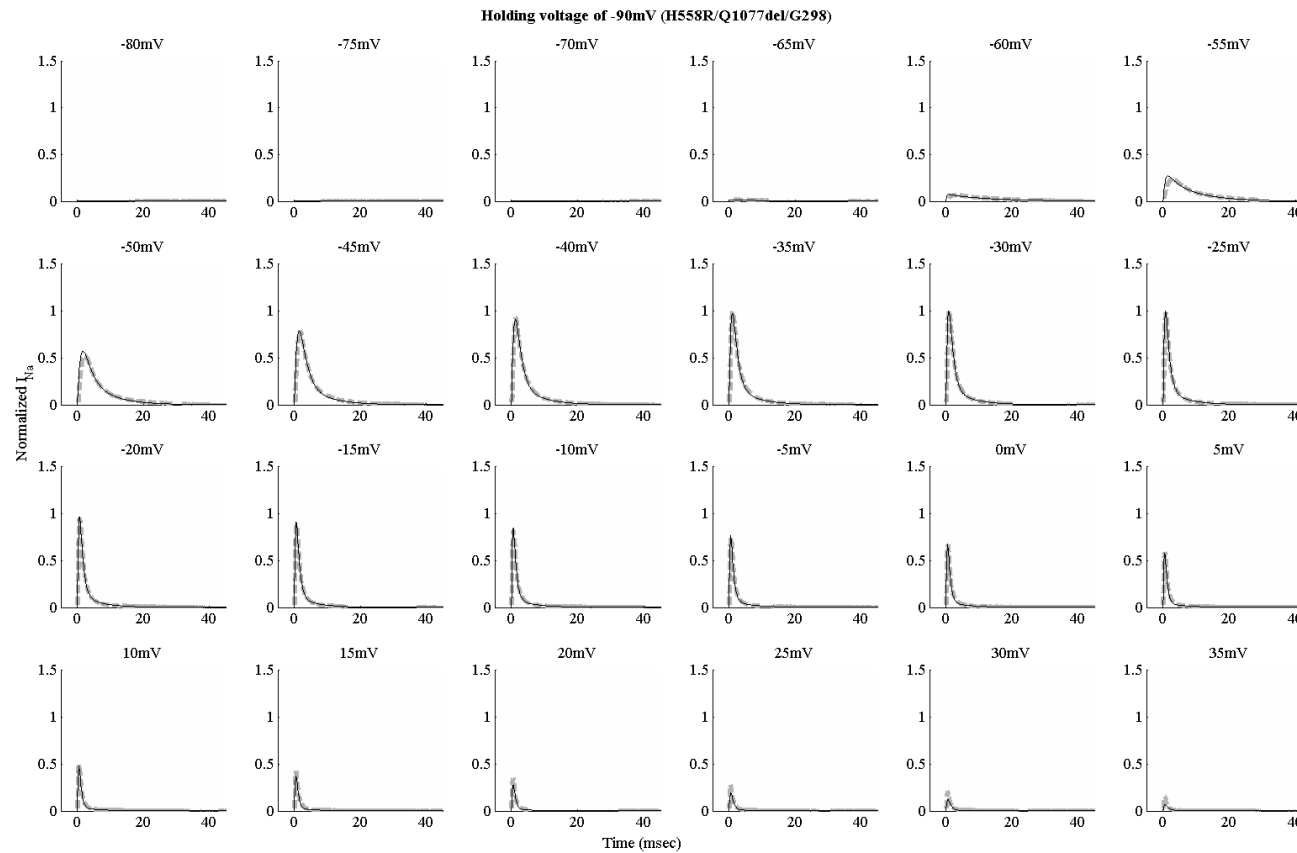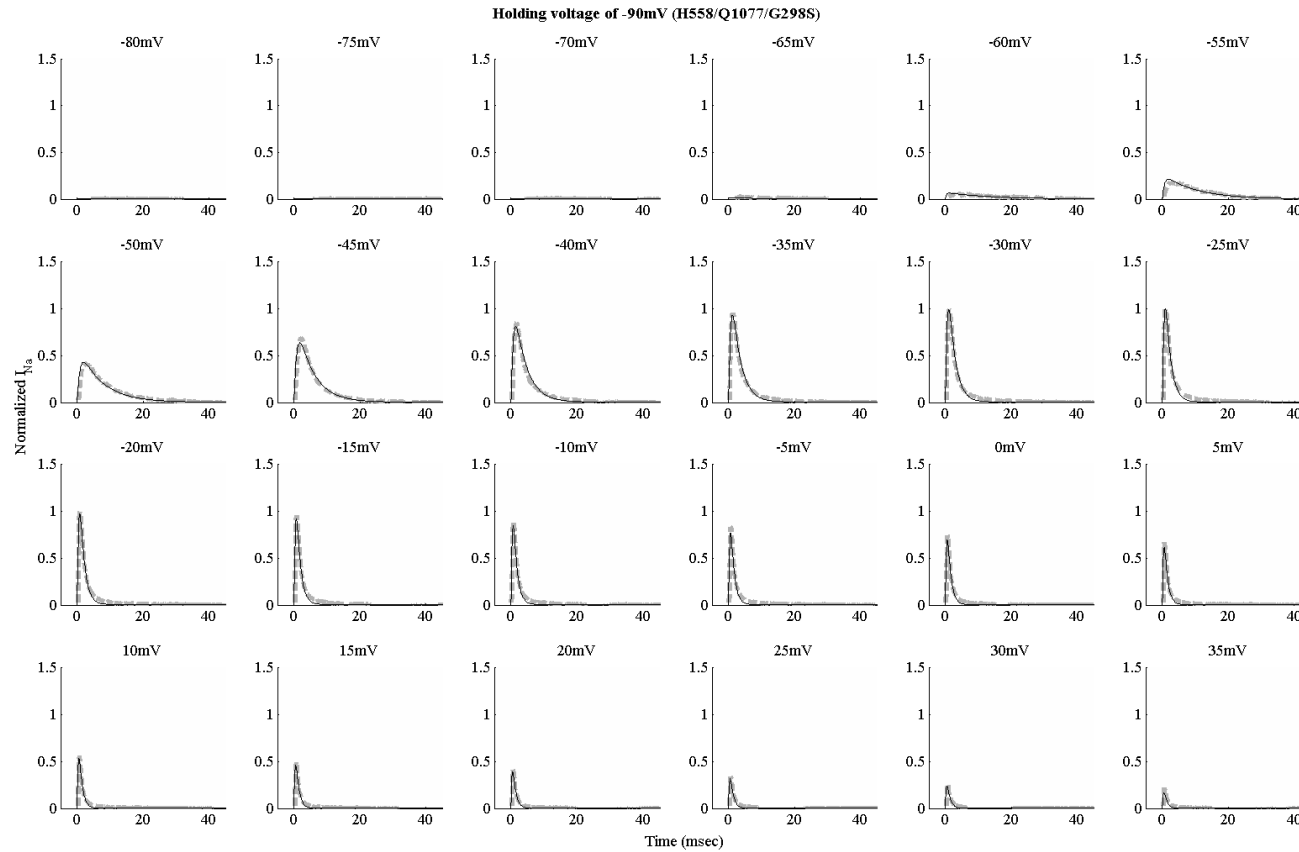
Figure A6.2. Results for the H558R/Q1077del/G298 model. Each subplot represents the normalized sodium current versus time trace under a clamping voltage. A total of 24 clamping voltages were used, from -80 mV to 35 mV. Solid line represents model predicted data while dashed lines are for average experimental data.
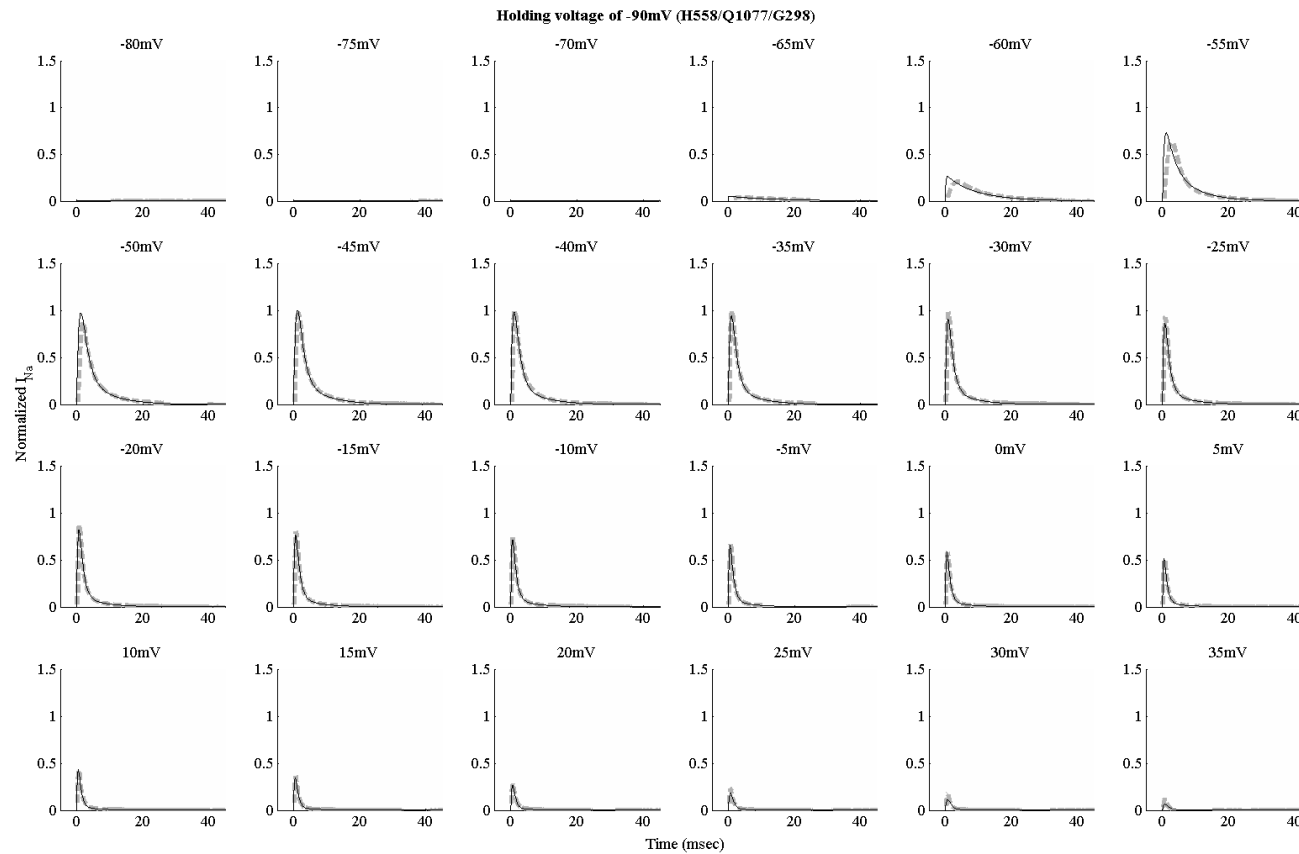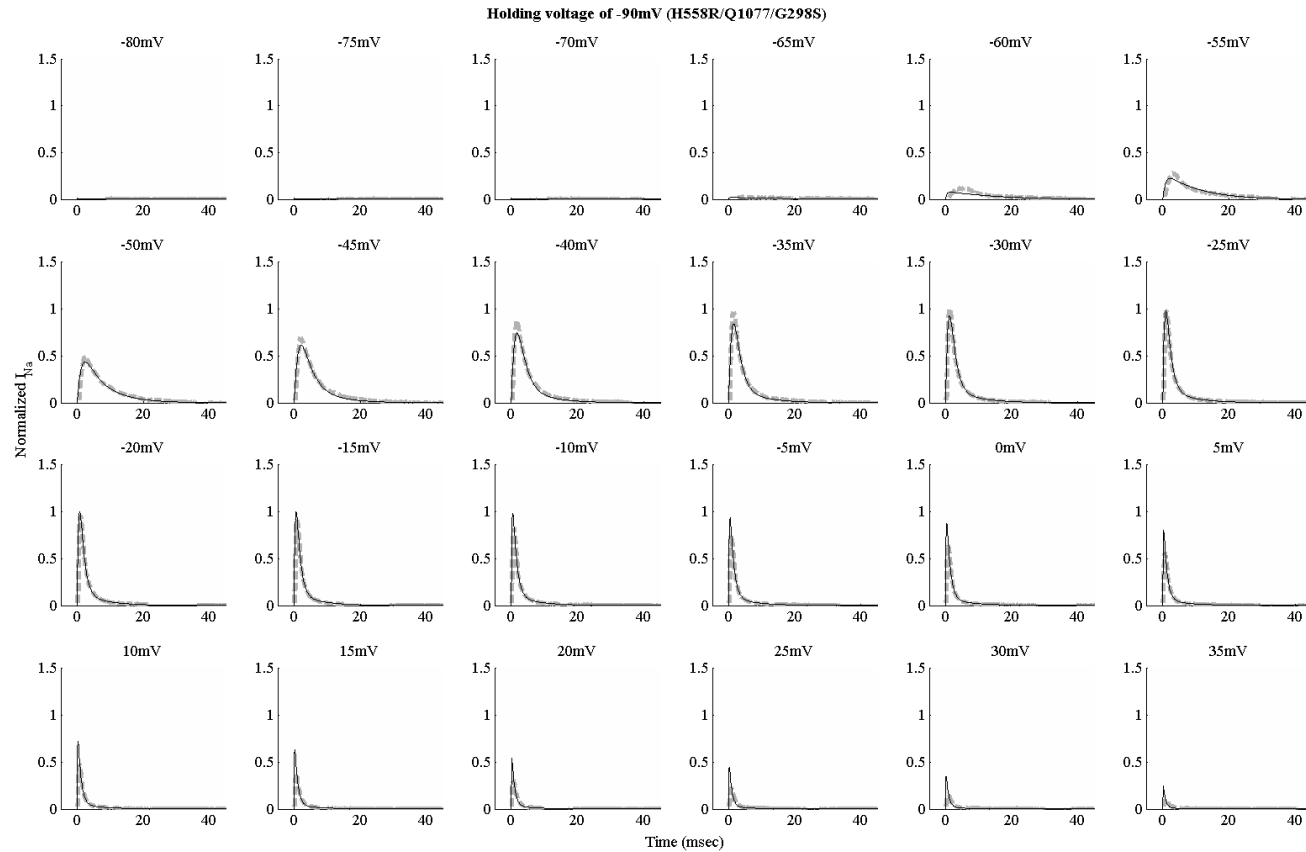
Figure A6.3. Results for the H558/Q1077/G298 model. Each subplot represents the normalized sodium current versus time trace under a clamping voltage. A total of 24 clamping voltages were used, from -80 mV to 35 mV. Solid line represents model predicted data while dashed lines are for average experimental data.
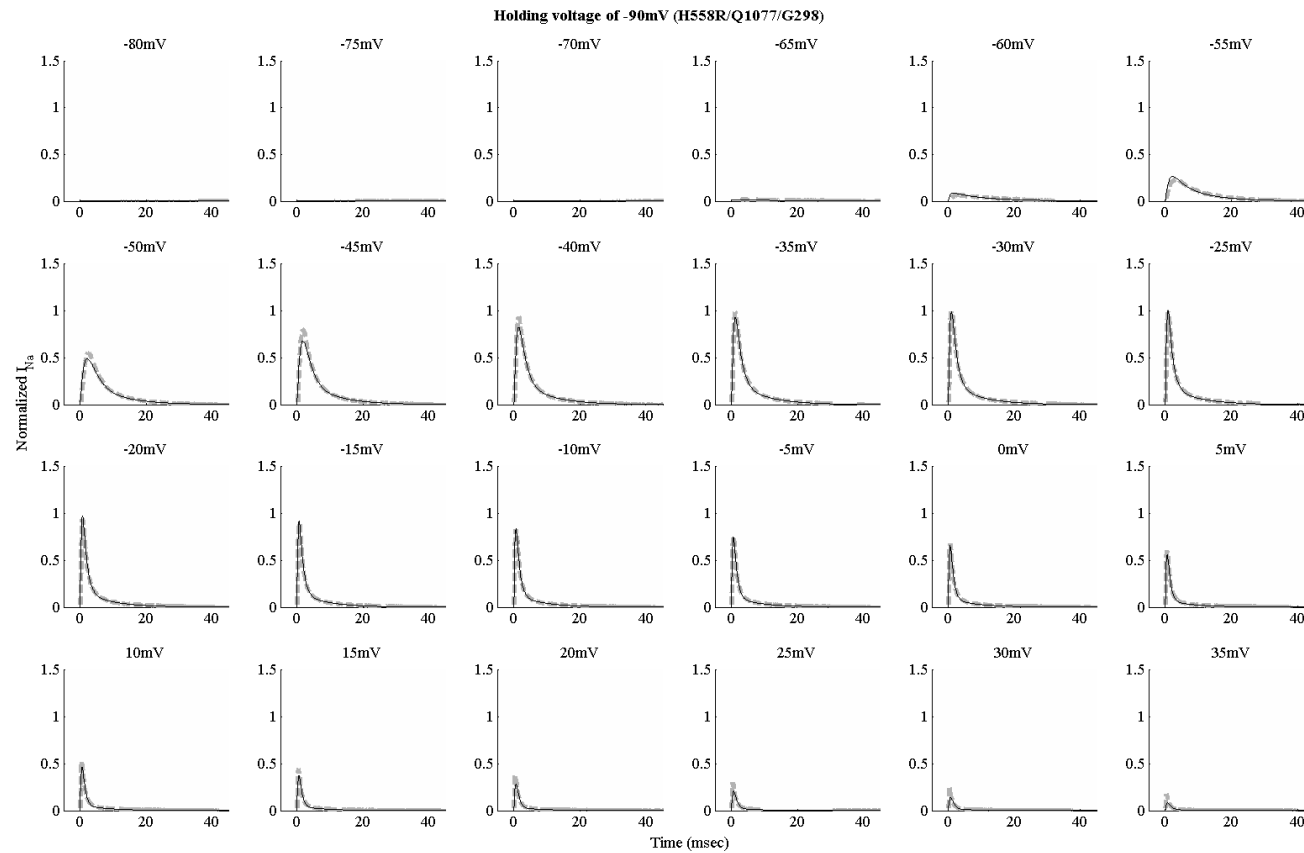
Figure A6.4. Results for the H558R/Q1077/G298 model. Each subplot represents the normalized sodium current versus time trace under a clamping voltage. A total of 24 clamping voltages were used, from -80 mV to 35 mV. Solid line represents model predicted data while dashed lines are for average experimental data.

Appendix 7. Complete sodium current results for G298S models at -90 mV

The complete results for the verification of the G298S sodium channel models for all four backgrounds at -90 mV are provided here, a subset of the results was shown in Chapter 3.
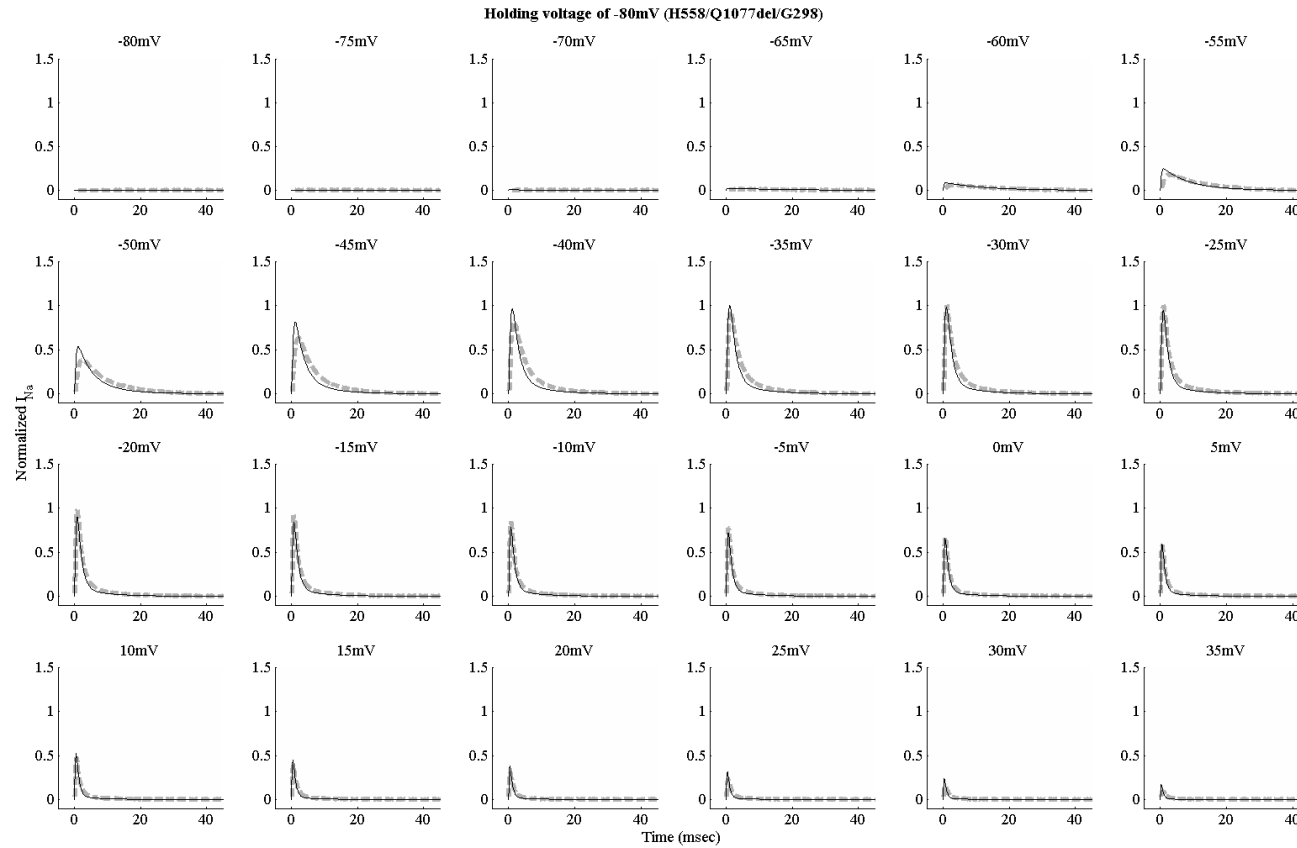
Figure A7.1. Results for the H558/Q1077del/G298S model. Each subplot represents the normalized sodium current versus time trace under a clamping voltage. A total of 24 clamping voltages were used, from -80 mV to 35 mV. Solid line represents model predicted data while dashed lines are for average experimental data.

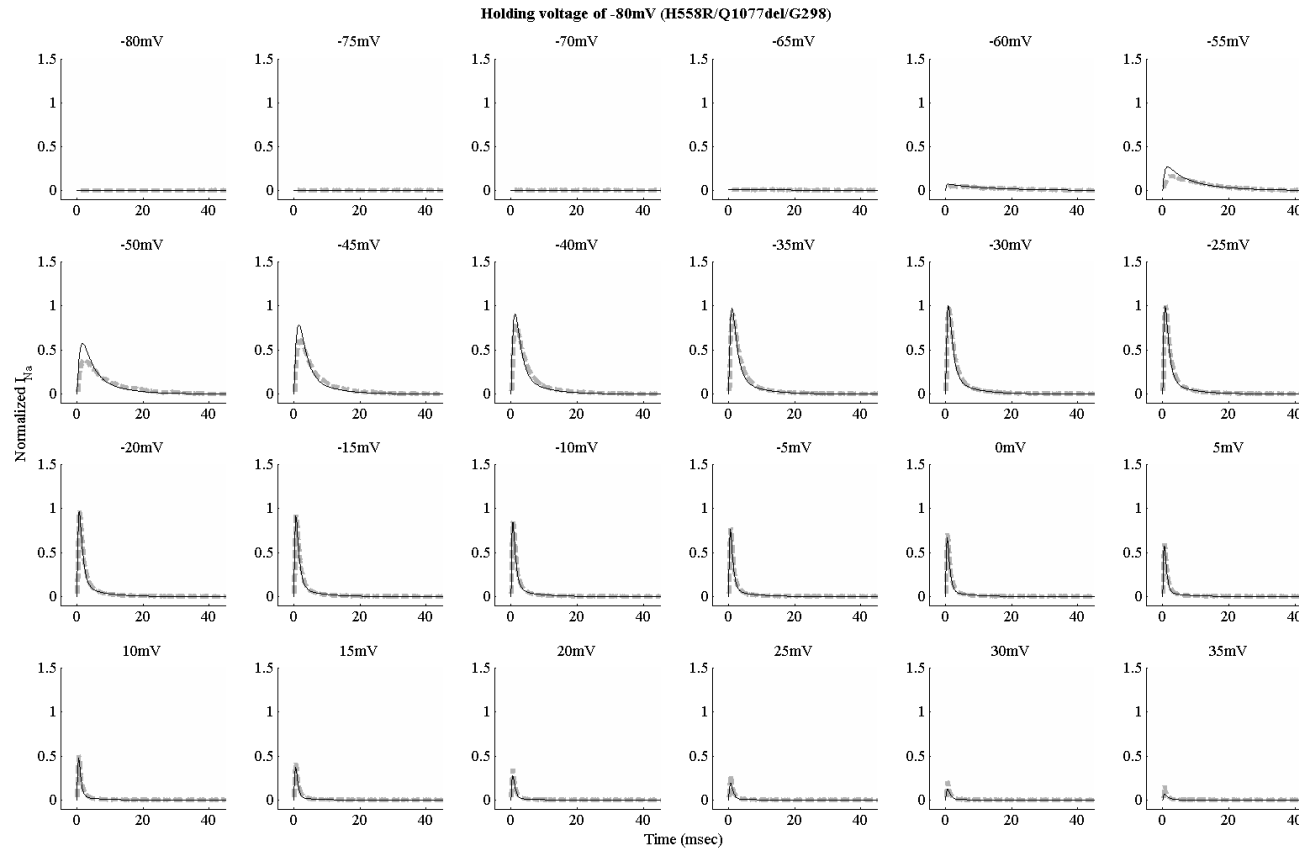**Holding voltage of -90mV (H558R/Q1077del/G298S)**

Figure A7.2. Results for the H558R/Q1077del/G298S model. Each subplot represents the normalized sodium current versus time trace under a clamping voltage. A total of 24 clamping voltages were used, from -80 mV to 35 mV. Solid line represents model predicted data while dashed lines are for average experimental data.
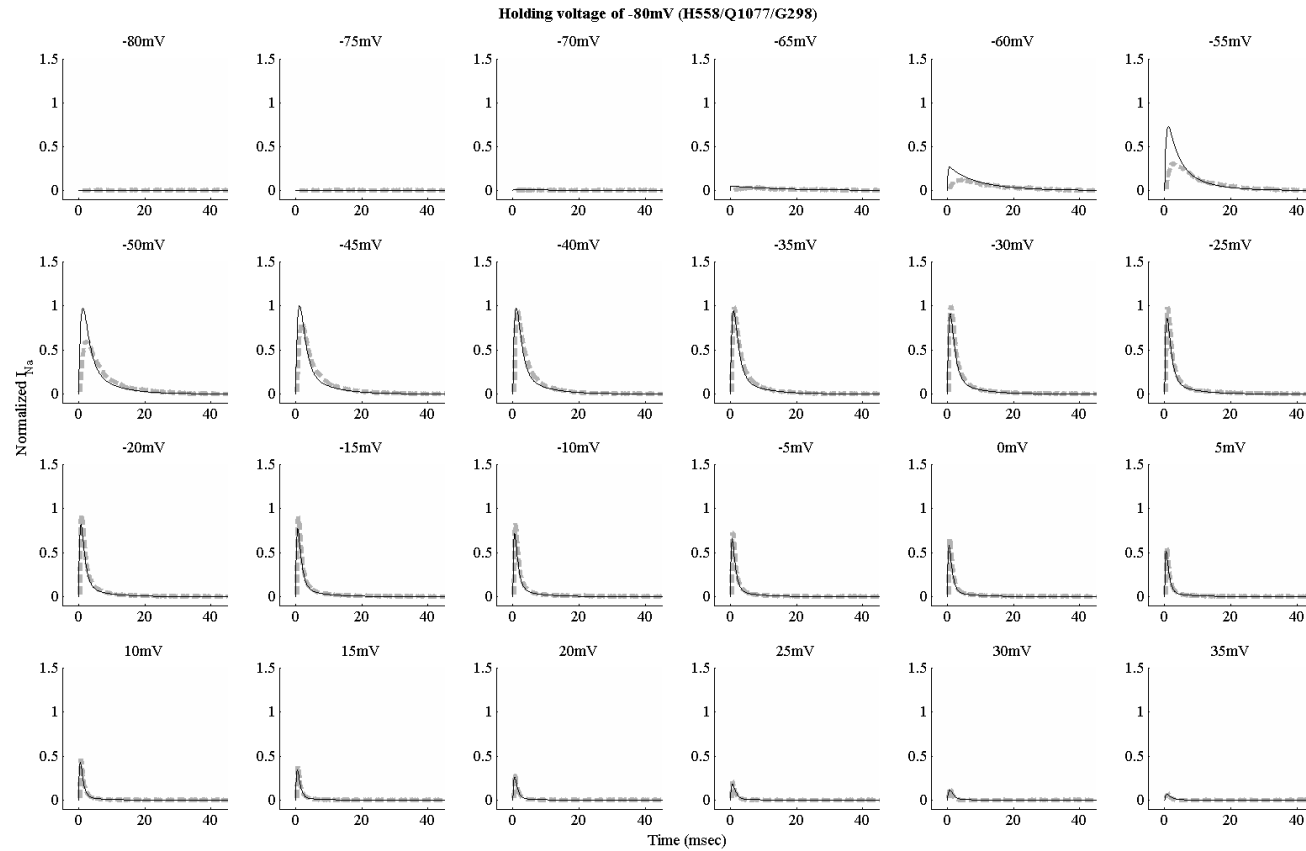
Figure A7.3. Results for the H558/Q1077/G298S model. Each subplot represents the normalized sodium current versus time trace under a clamping voltage. A total of 24 clamping voltages were used, from -80 mV to 35 mV. Solid line represents model predicted data while dashed lines are for average experimental data.

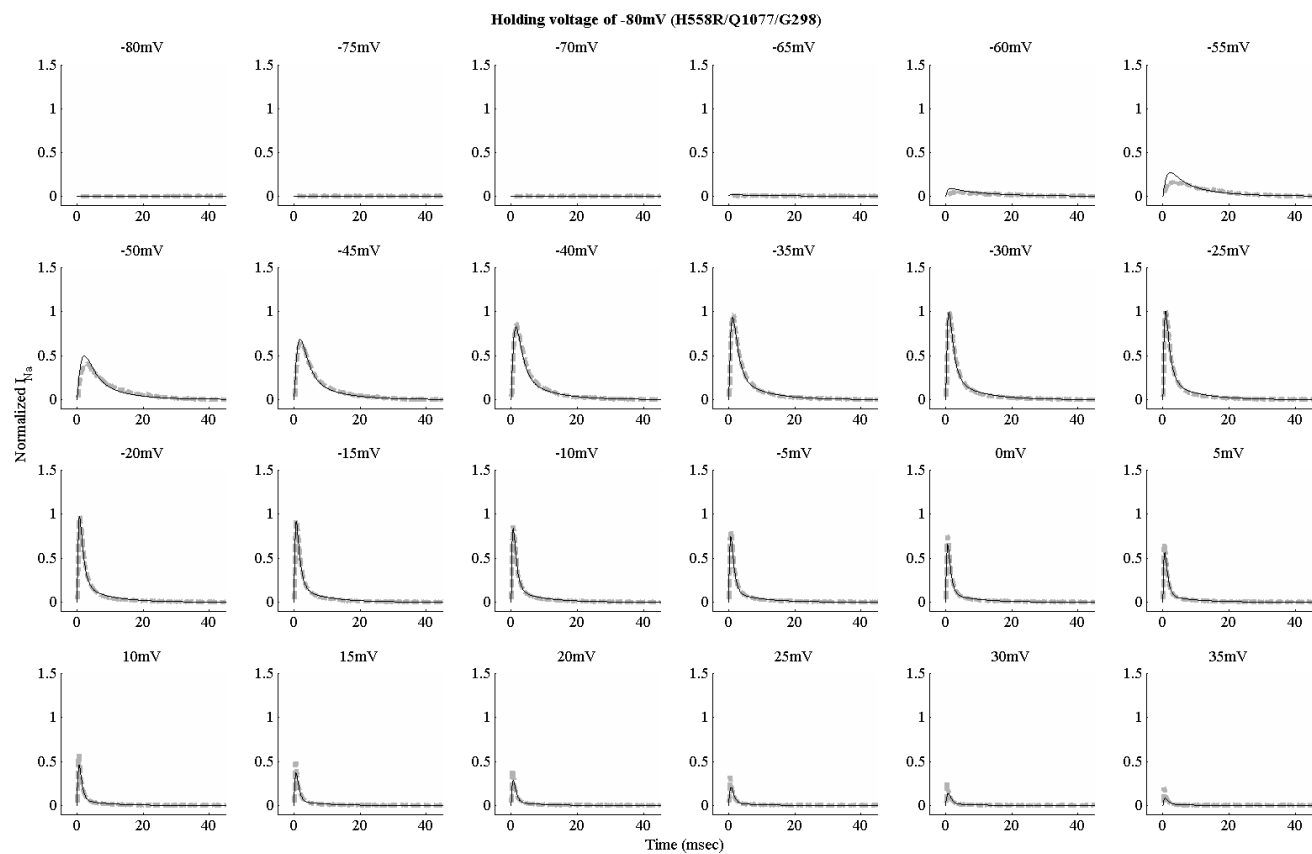**Holding voltage of -90mV (H558R/Q1077/G298S)**

Figure A7.4. Results for the H558R/Q1077/G298S model. Each subplot represents the normalized sodium current versus time trace under a clamping voltage. A total of 24 clamping voltages were used, from -80 mV to 35 mV. Solid line represents model predicted data while dashed lines are for average experimental data.

Appendix 8. Complete sodium current results for G298 models at -80 mV

The complete results for the verification of the G298 sodium channel models for all four backgrounds at -80 mV are provided here, a subset of the results was shown in Chapter 3.

Figure A8.1. Results for the H558/Q1077del/G298 model. Each subplot represents the normalized sodium current versus time trace under a clamping voltage. A total of 24 clamping voltages were used, from -80 mV to 35 mV. Solid line represents model predicted data while dashed lines are for average experimental data.

Figure A8.2. Results for the H558R/Q1077del/G298 model. Each subplot represents the normalized sodium current versus time trace under a clamping voltage. A total of 24 clamping voltages were used, from -80 mV to 35 mV. Solid line represents model predicted data while dashed lines are for average experimental data.

Figure A8.3. Results for the H558/Q1077/G298 model. Each subplot represents the normalized sodium current versus time trace under a clamping voltage. A total of 24 clamping voltages were used, from -80 mV to 35 mV. Solid line represents model predicted data while dashed lines are for average experimental data.

Figure A8.4. Results for the H558R/Q1077/G298 model. Each subplot represents the normalized sodium current versus time trace under a clamping voltage. A total of 24 clamping voltages were used, from -80 mV to 35 mV. Solid line represents model predicted data while dashed lines are for average experimental data.

Appendix 9.   Tables of parameter values for the G298S models

The original form of the rate equation, which is thermodynamically based, is given by $k = A\,exp(B + CV_m)$ and has three parameters of A, B, and C. In the event where the explicit representation of the three parameters does not matter, the simplified alternative form of $k = A'\,exp(CV_m)$ may be considered for implementation to improve computational efficiency such as for the parameterization procedure or in higher spatial scale investigations. For convenience, the parameter values of the simplified alternative form of the rate equations for the G298S models (corresponding to Tables 3.16 to 3.19 in the main text) are provided here.

Table A9.1. Parameter values of the simplified rate equations for the V1_WT (H558/Q1077del/G298) and V1_MT (H558/Q1077del/G298S) models.

Model	V1_WT		V1_MT	
Equation	$k_{i,j}=A'\,exp(CV)$			
State transition	A' (ms^{-1})	C (mV^{-1})	A' (ms^{-1})	C (mV^{-1})
O→I1	1.1288136	0.014105	1.271245	0.013251
I1→I2	31.355084	-0.00147	0.2492341	8.25E-05
C3→C2	0.12675	1.35E-05	0.0999266	6.71E-07
C2→C1	5.3501175	0.009075	2.3923261	0.012529
C1→O	5.8574569	0.027162	1106.6103	0.15577
I2→I1	5.655E-08	-0.19518	3.505E-06	-0.07881
C2→C3	0.0038589	-0.03231	0.0098547	-0.00944
C1→C2	0.0012514	-0.12304	0.0028778	-0.09343
O→C1	0.000214	-0.1887	6.133E-05	-0.15874
I1→C1	0.7437463	-0.00232	0.0632175	0.002923
C1→I1	0.1491684	-0.00217	0.1635209	-0.00109
I1→O	9.655E-09	0.21914	4.277E-08	-0.10859

Table A9.2. Parameter values of the simplified rate equations for the V2_WT (H558R/Q1077del/G298) and V2_MT (H558R/Q1077del/G298S) models.

Model	V2_WT		V2_MT	
Equation	$k_{i,j}$=A'exp(CV)			
State transition	A' (ms^{-1})	C (mV^{-1})	A' (ms^{-1})	C (mV^{-1})
O→I1	1.3768921	0.019379	1.2344659	0.013426
I1→I2	0.1705975	-0.00024	0.199538	0.005872
C3→C2	28.865128	-0.00029	87669.143	-0.05534
C2→C1	14.916817	0.038026	15.041164	0.059176
C1→O	6.0903065	0.014891	4.3592174	0.00391
I2→I1	5.65E-08	-0.10784	5.667E-05	0.041269
C2→C3	35.009859	0.10401	97551.111	0.056623
C1→C2	0.1739364	-0.08117	0.0097085	-0.05566
O→C1	1.563E-06	-0.24795	3.804E-05	-0.22839
I1→C1	0.0564746	0.000115	0.0499112	0.001762
C1→I1	0.1474728	-0.03967	0.0144284	-0.04812
I1→O	3.719E-08	0.000219	4.717E-08	-0.00099

Table A9.3. Parameter values of the simplified rate equations for the V3_WT (H558/Q1077/G298) and V3_MT (H558/Q1077/G298S) models.

Model	V3_WT		V3_MT	
Equation	$k_{i,j}$=A'exp(CV)			
State transition	A' (ms^{-1})	C (mV^{-1})	A' (ms^{-1})	C (mV^{-1})
O→I1	1.0489262	0.013052	1.0301866	0.003512
I1→I2	0.1601424	7.28E-05	15.029949	0.0751
C3→C2	2.829E-05	0.011129	46855899	0.018823
C2→C1	889.12019	0.00193	3.8861105	-0.00096
C1→O	3.8868259	0.029006	9.0677443	0.037862
I2→I1	0.0001701	0.001704	0.0171244	0.076449
C2→C3	3.6691816	-0.08035	0.1106734	0.008181
C1→C2	228.55863	0.11515	0.0887268	-0.10116
O→C1	3.489E-09	-0.3522	2.922E-07	-0.26534
I1→C1	0.0645877	-0.00267	0.5972008	-0.00184
C1→I1	1.919E-89	0.003774	0.0168065	-0.09776
I1→O	1.616E-48	-0.04346	0.0127835	0.088102

Table A9.4. Parameter values of the simplified rate equations for the V4_WT (H558R/Q1077/G298) and V4_MT (H558R/Q1077/G298S) models.

Model	V4_WT		V4_MT	
Equation	$k_{i,j}=A'exp(CV)$			
State transition	A' (ms^{-1})	C (mV^{-1})	A' (ms^{-1})	C (mV^{-1})
O→I1	1.0718779	0.016644	0.9711668	0.010451
I1→I2	0.1302365	-0.00027	47.442056	0.07498
C3→C2	9.228596	-0.00028	0.1343483	1.37E-05
C2→C1	31.428084	0.073074	5.8792268	0.02748
C1→O	4.8703404	0.005846	19.291147	0.079874
I2→I1	9.345E-07	-0.09772	4.205E-05	-0.05031
C2→C3	32.308408	0.12543	0.0030772	-0.03935
C1→C2	0.0703902	-0.08102	0.4535345	0.000154
O→C1	1.402E-06	-0.23442	2.723E-06	-0.23273
I1→C1	0.0639947	5.52E-05	0.0006996	0.20869
C1→I1	0.0688094	-0.07212	0.1220208	0.000195
I1→O	8.385E-08	7.24E-05	3.012E-05	-0.1016

Appendix 10. Complete sodium current results for G298S models at -80 mV

The complete results for the verification of the G298S sodium channel models for all four backgrounds at -80 mV are provided here, a subset of the results was shown in Chapter 3.
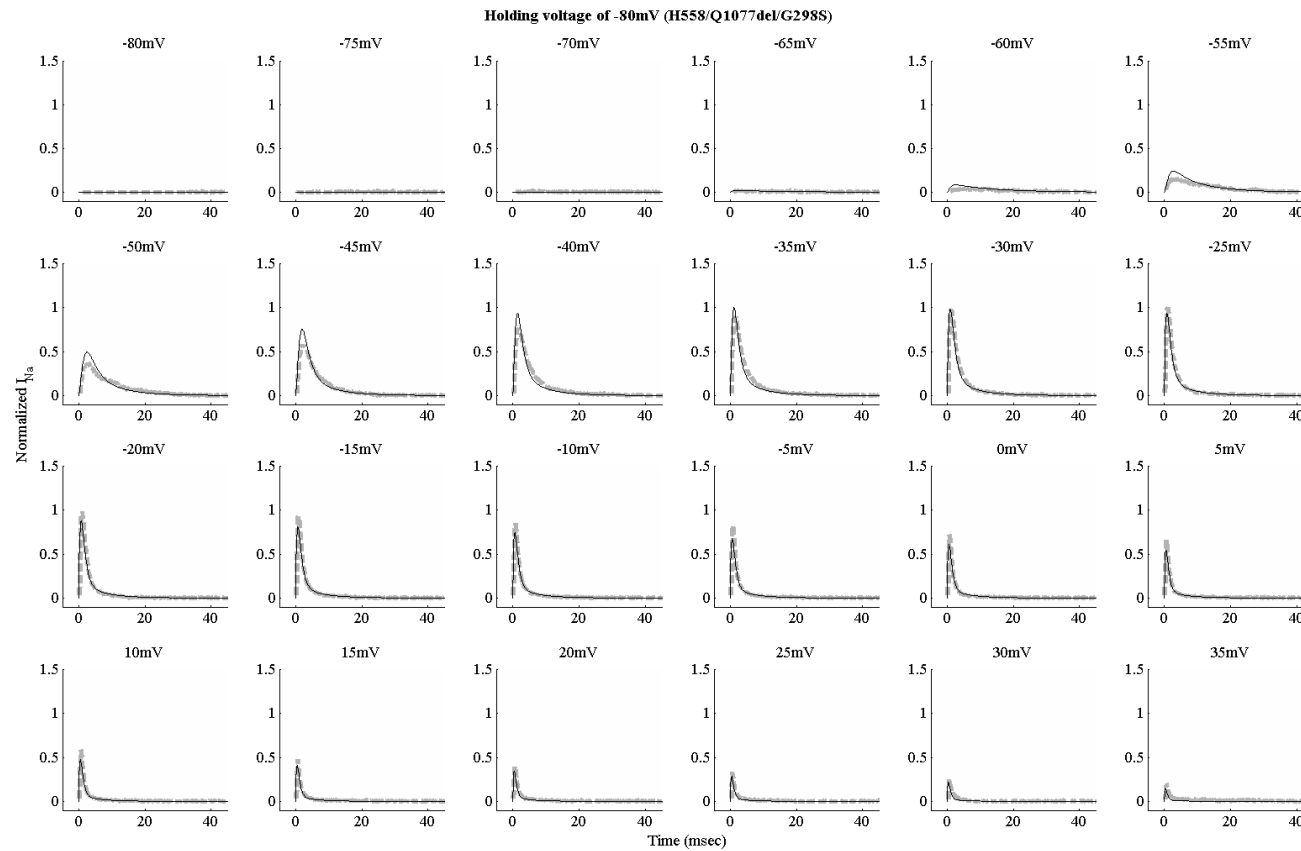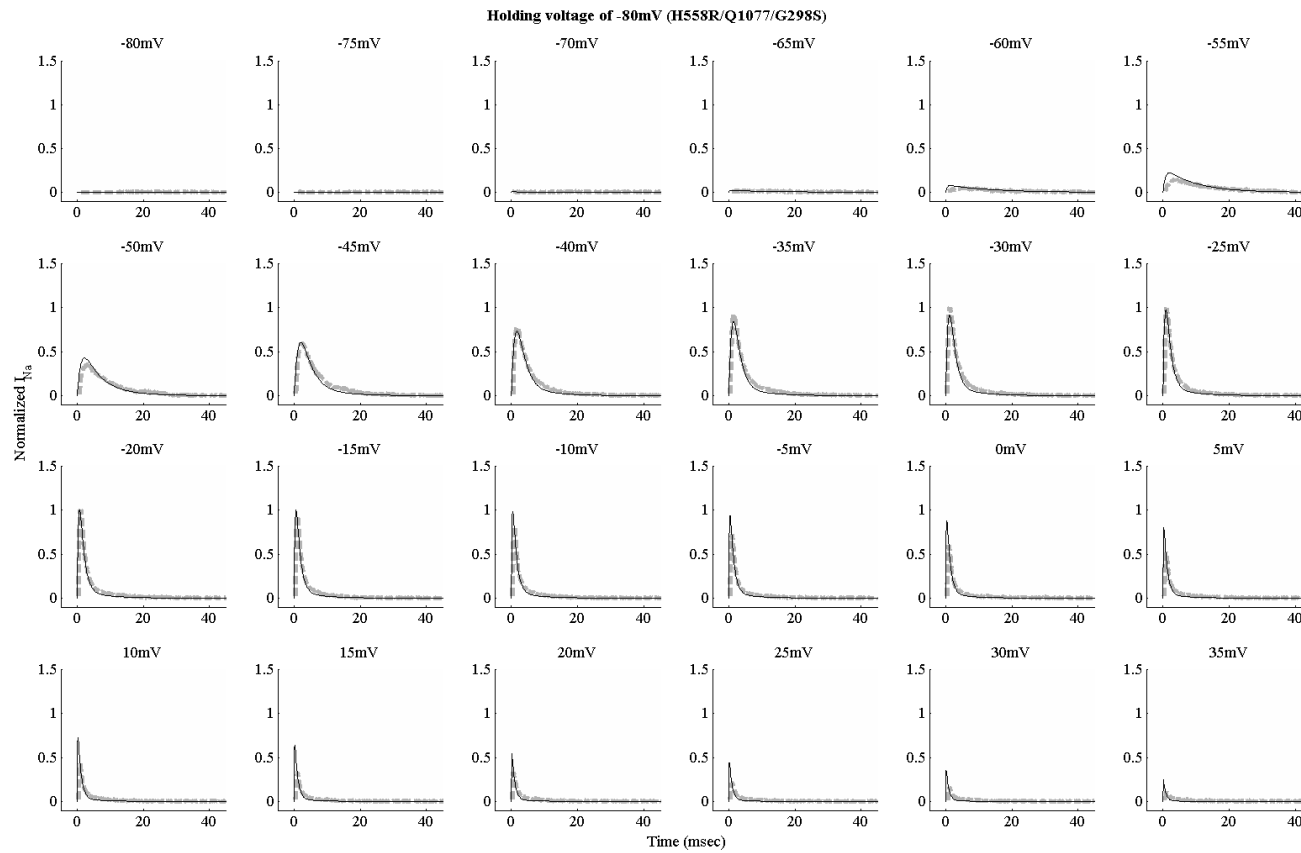
Figure A10.1. Results for the H558/Q1077del/G298S model. Each subplot represents the normalized sodium current versus time trace under a clamping voltage. A total of 24 clamping voltages were used, from -80 mV to 35 mV. Solid line represents model predicted data while dashed lines are for average experimental data.
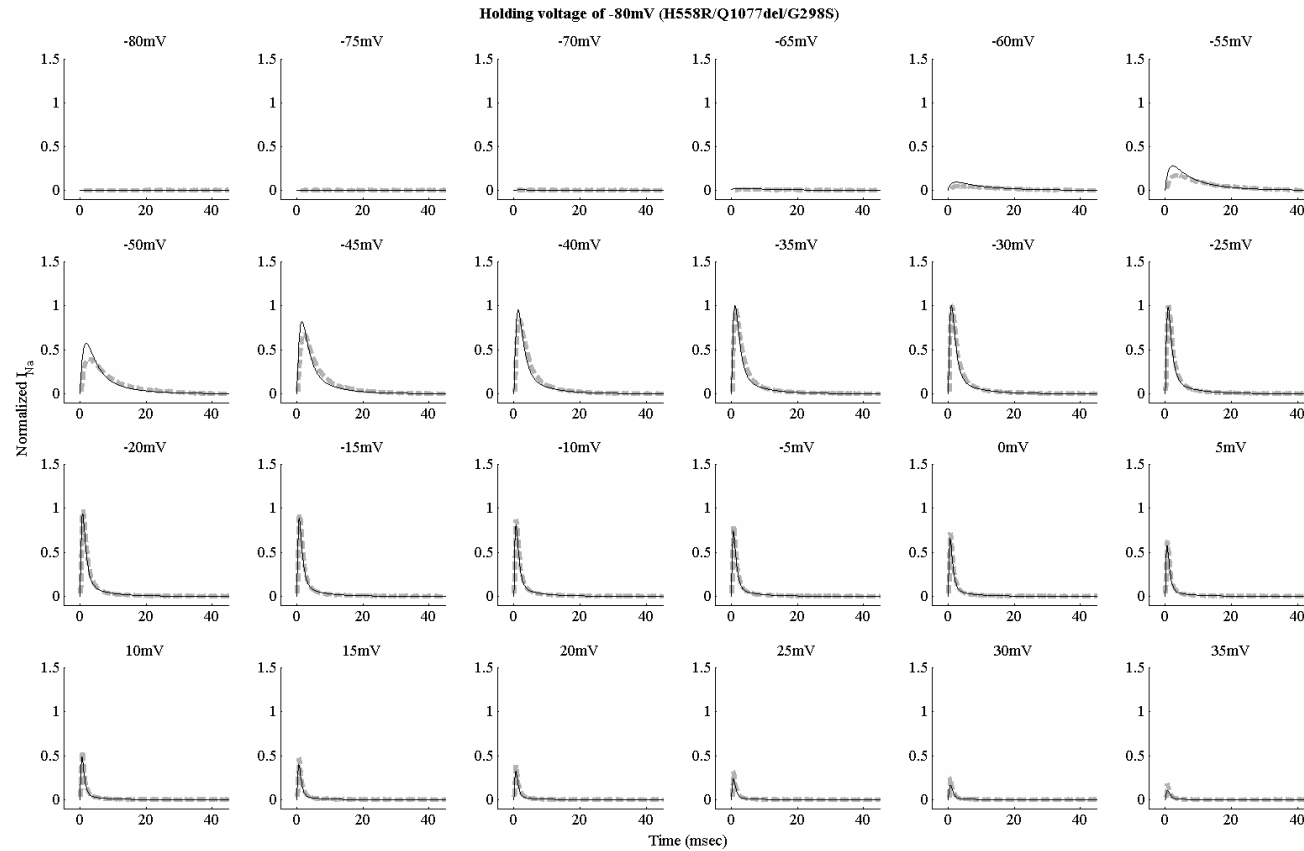
Figure A10.2. Results for the H558R/Q1077del/G298S model. Each subplot represents the normalized sodium current versus time trace under a clamping voltage. A total of 24 clamping voltages were used, from -80 mV to 35 mV. Solid line represents model predicted data while dashed lines are for average experimental data.

Holding voltage of -80mV (H558/Q1077/G298S)
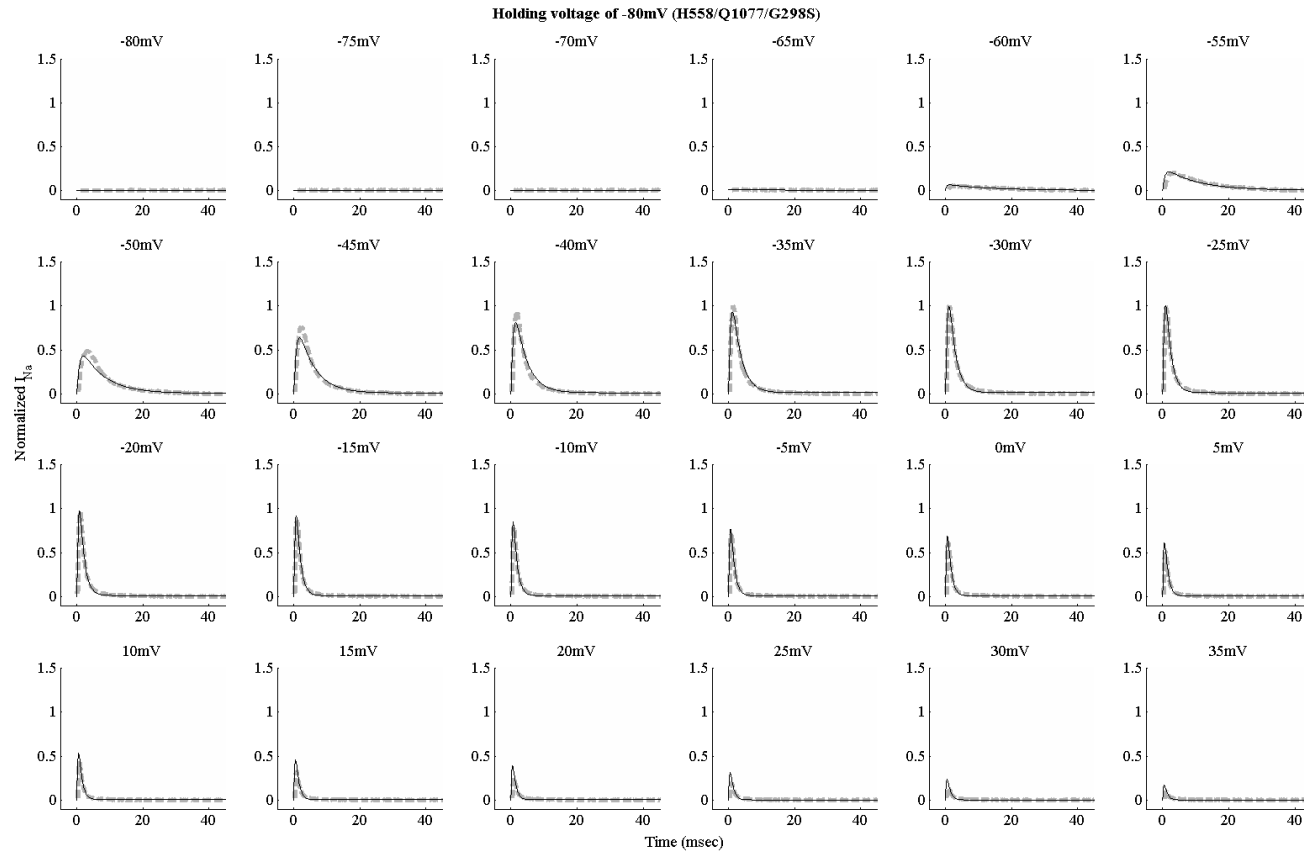
Figure A10.3. Results for the H558/Q1077/G298S model. Each subplot represents the normalized sodium current versus time trace under a clamping voltage. A total of 24 clamping voltages were used, from -80 mV to 35 mV. Solid line represents model predicted data while dashed lines are for average experimental data.

Figure A10.4. Results for the H558R/Q1077/G298S model. Each subplot represents the normalized sodium current versus time trace under a clamping voltage. A total of 24 clamping voltages were used, from -80 mV to 35 mV. Solid line represents model predicted data while dashed lines are for average experimental data.

Appendix 11. Comparison of the steady-state values of the G298/G298S models

Each figure shows a comparison of the steady-state values for the G298 and G298S sodium channel models from the same background.
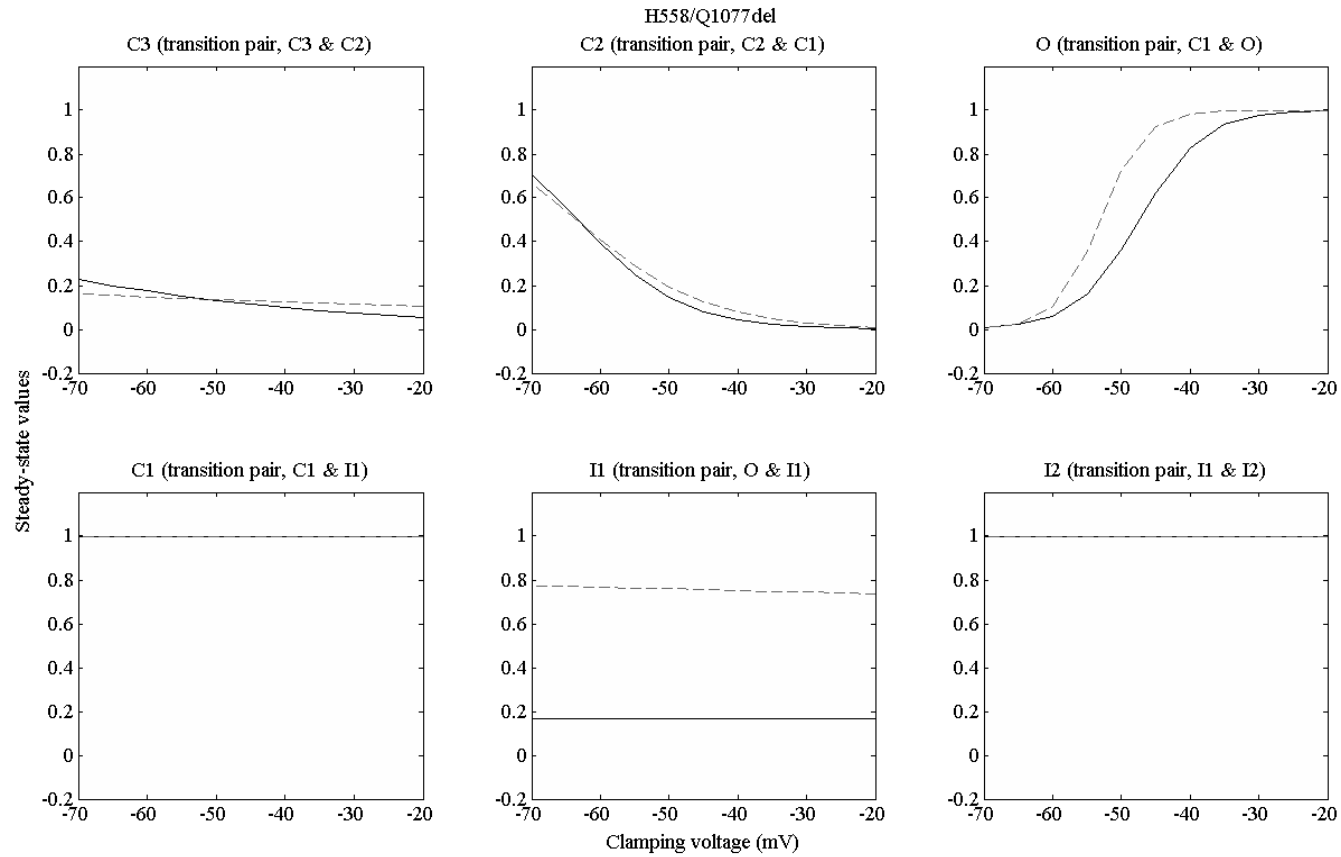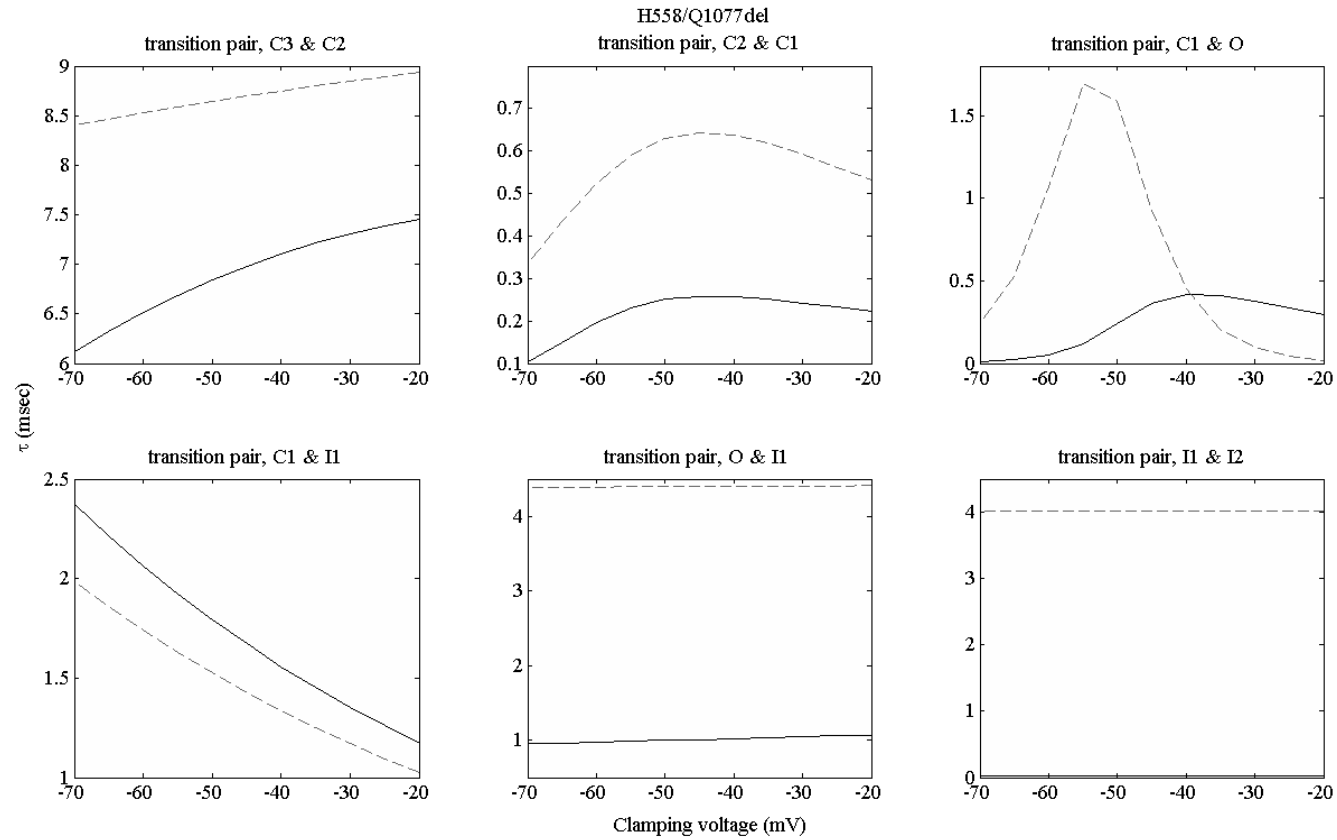
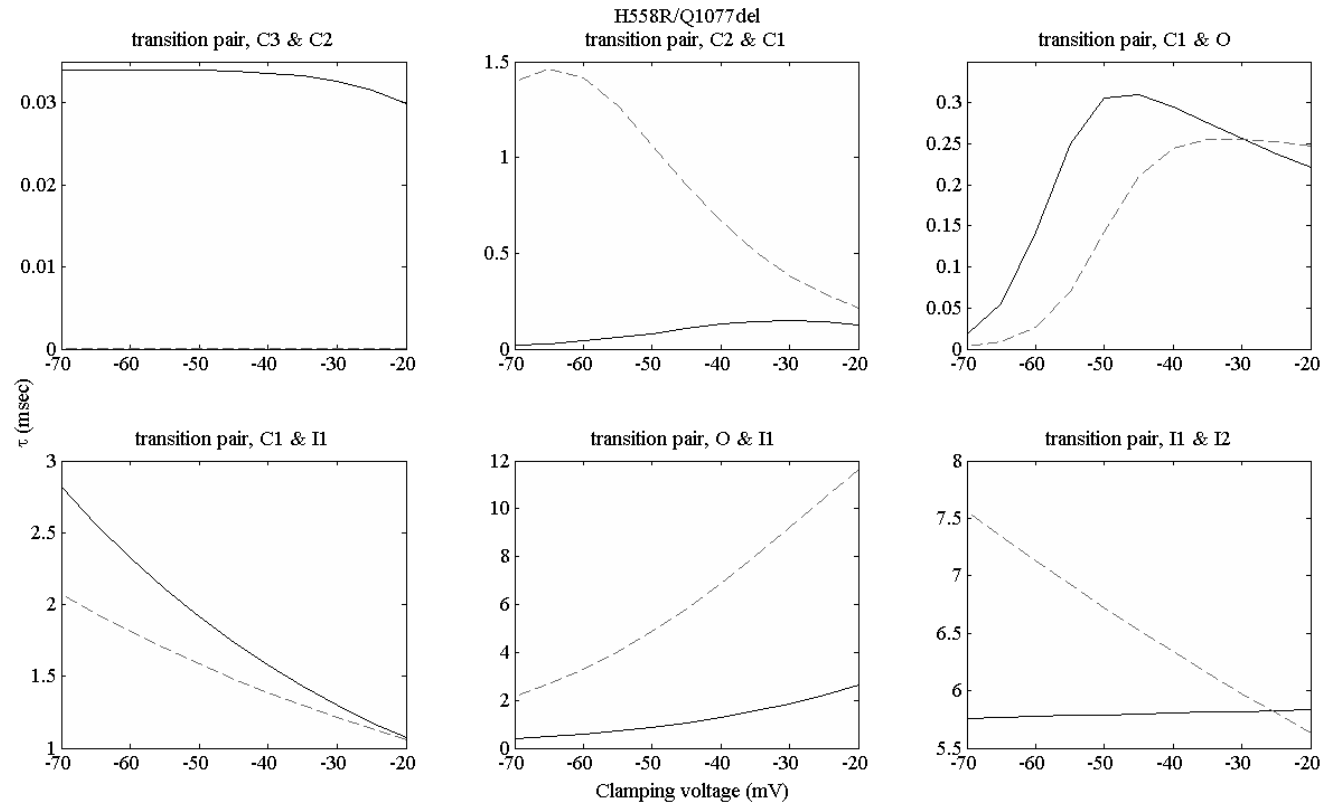Figure A11.1. The steady-state values for the H558/Q1077del background. G298 results in solid line, G298S results in dashed line.
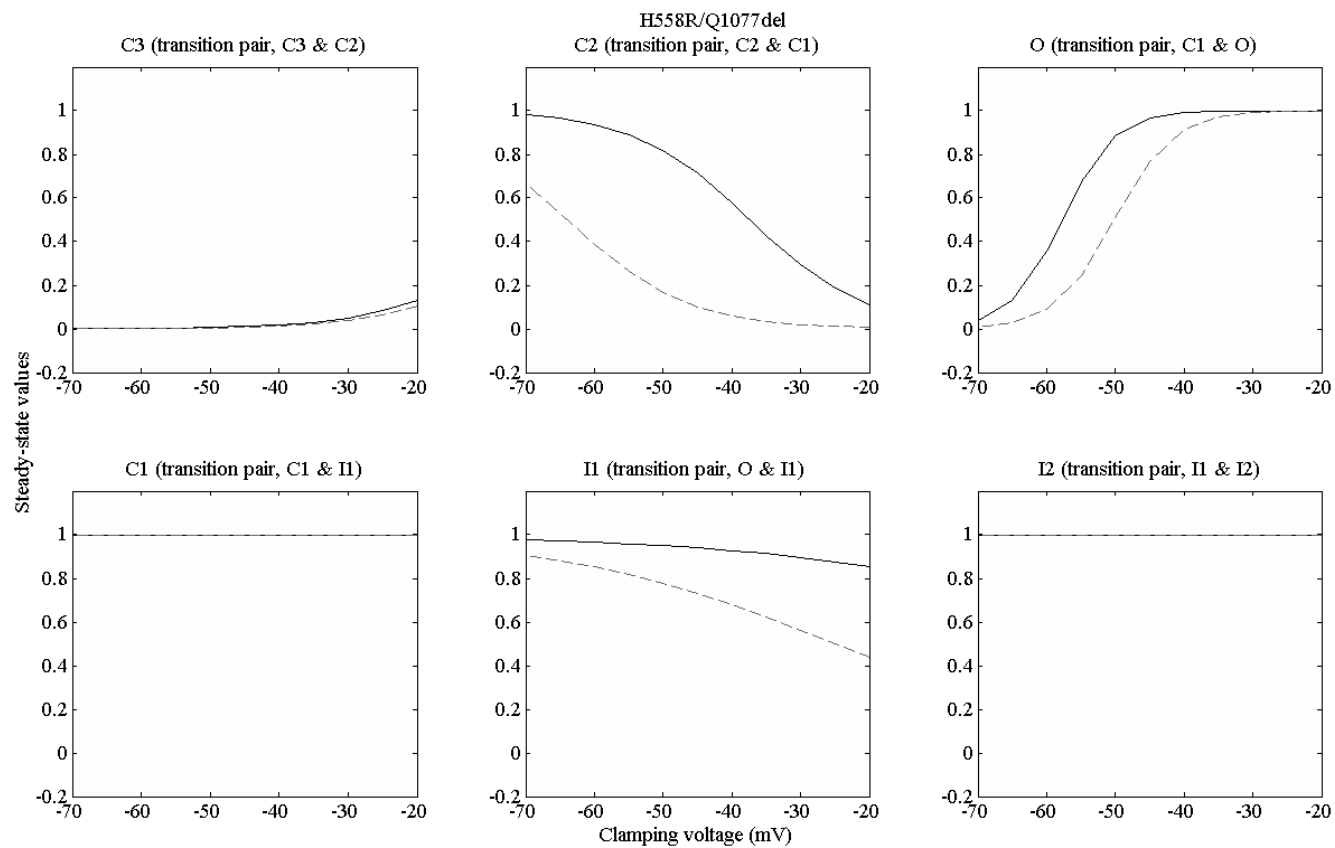
Figure A11.2. The steady-state values for the H558R/Q1077del background. G298 results in solid line, G298S results in dashed line.
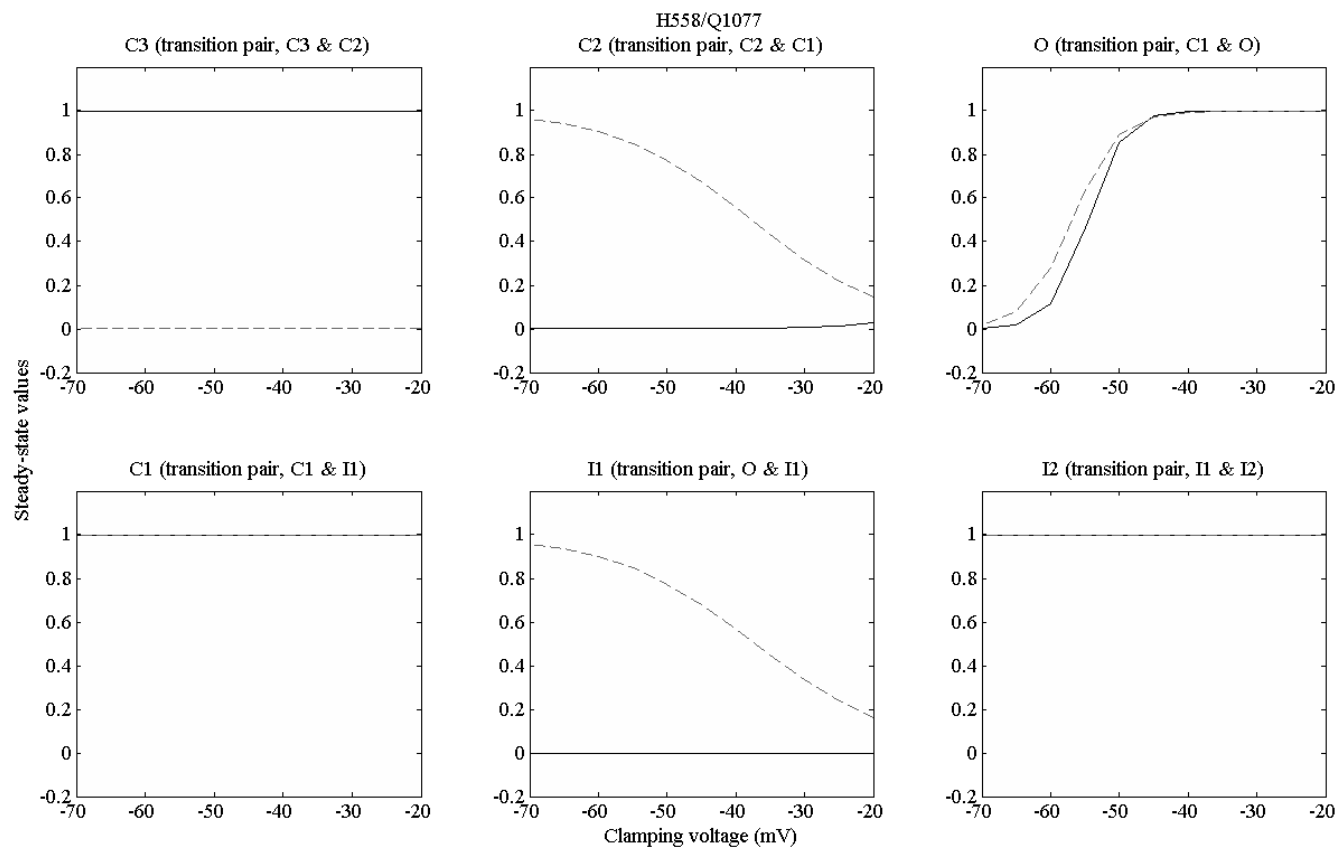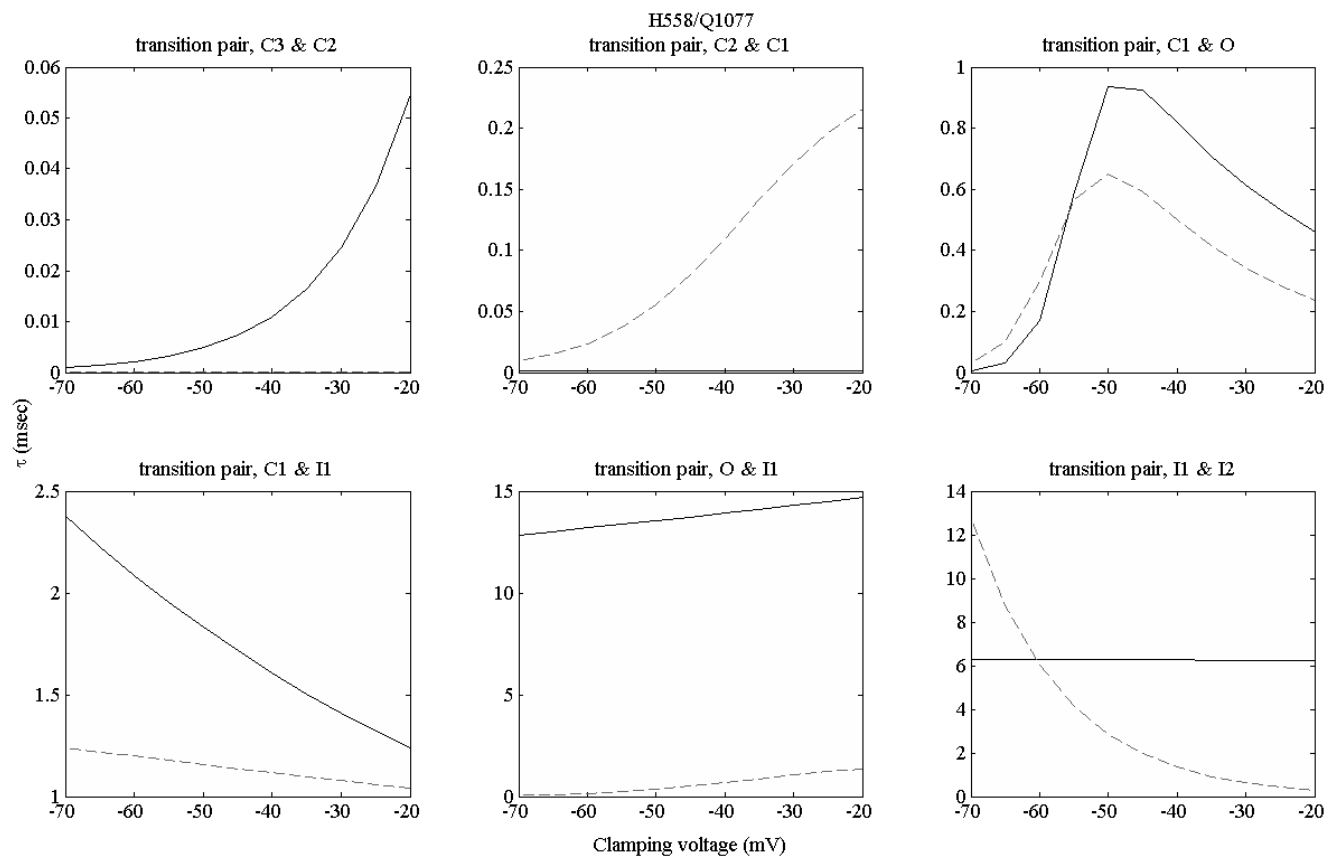
Figure A11.3. The steady-state values for the H558/Q1077 background. G298 results in solid line, G298S results in dashed line.
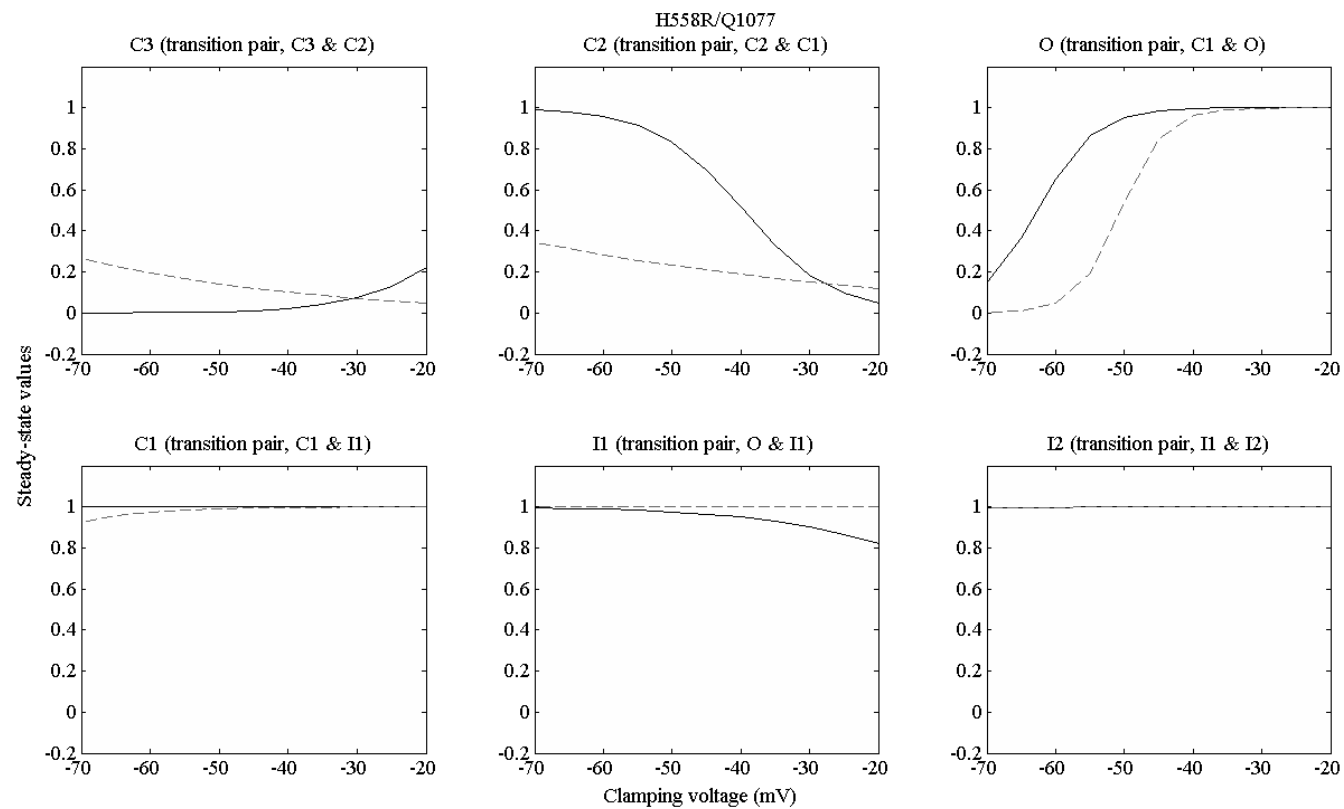
Figure A11.4. The steady-state values for the H558R/Q1077 background. G298 results in solid line, G298S results in dashed line.

Appendix 12. Comparison of the time constants of the G298/G298S models

Each figure shows a comparison of the time constant values for the G298 and G298S sodium channel models from the same background.

Figure A12.1. The time constant, τ, values for the H558/Q1077del background. G298 results in solid line, G298S results in dashed line.
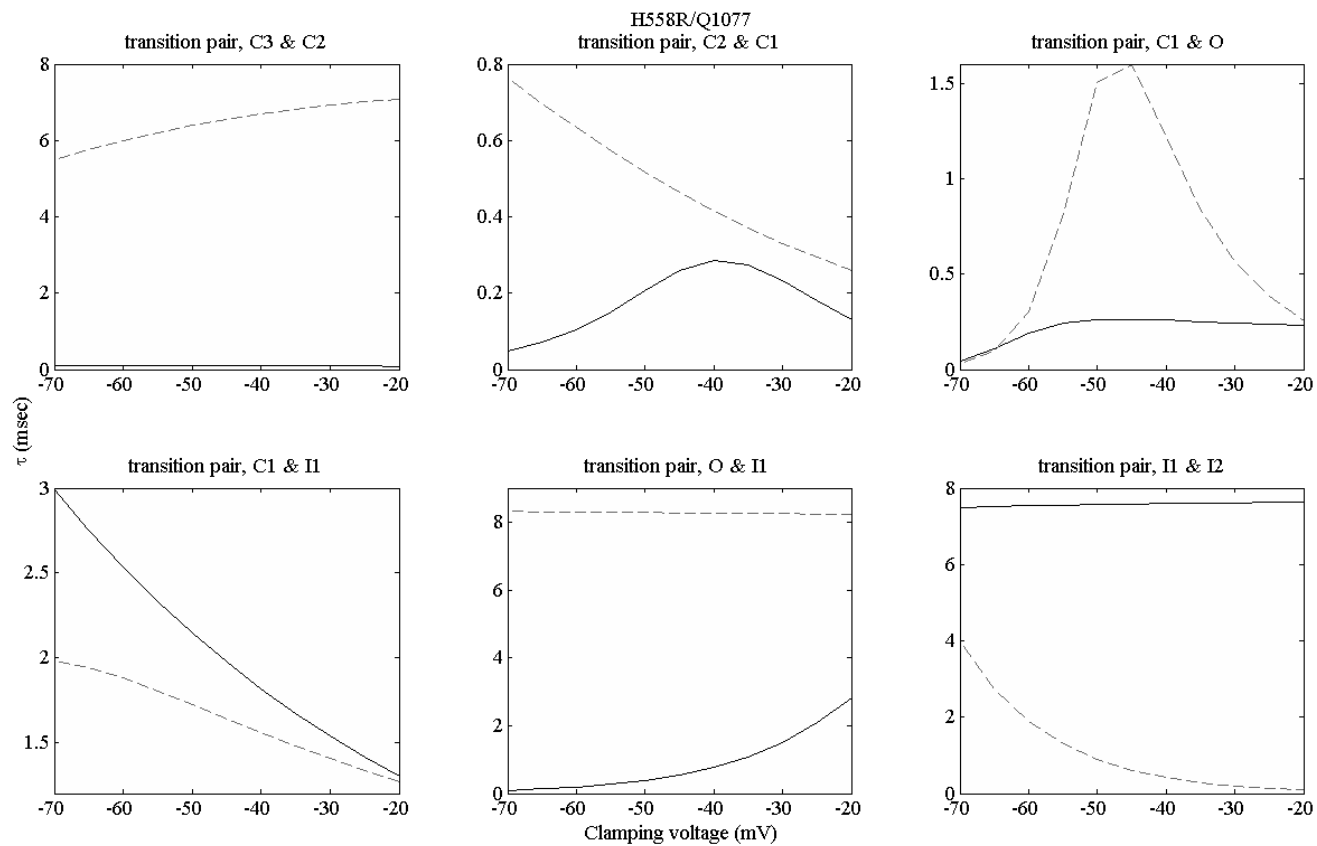
Figure A12.2. The time constant, τ, values for the H558R/Q1077del background. G298 results in solid line, G298S results in dashed line.

Figure A12.3. The time constant, τ, values for the H558/Q1077 background. G298 results in solid line, G298S results in dashed line.

Figure A12.4. The time constant, τ, values for the H558R/Q1077 background. G298 results in solid line, G298S results in dashed line.

Appendix 13. Non-stationary fluctuation analysis

Ion channel open probability, single channel conductance and ion channel density are relatively important biophysical values for the modelling of ion channels. This section shows the mathematical derivation of an equation that is useful to obtain these biophysical values from experimental data measured from repeated voltage-clamp recordings of the same sample, i.e., a non-stationary fluctuation analysis. Firstly, consider the average open probability of a population of N identical and independent ion channels at a point in time, say in a biological cell:

$$< P_O > = P_O. \tag{A13.1}$$

The probability of K of these channels being open is given by:

$$P(K\ channels\ open) = \frac{N!}{K!(N-K)!} P_O{}^K (1 - P_O)^{N-K}. \tag{A13.2}$$

The average open probability can in turn be expressed by:

$$< P_O > = \sum_{K=0}^{N} \frac{K}{N} P(K\ channels\ open)$$

$$= \sum_{K=0}^{N} \frac{K}{N} \frac{N!}{K!(N-K)!} P_O{}^K (1 - P_O)^{N-K}. \tag{A13.3}$$

Or equivalently,

$$N P_O = \sum_{K=0}^{N} K \frac{N!}{K!(N-K)!} P_O{}^K (1 - P_O)^{N-K}. \tag{A13.4}$$

An alternative way to derive average open probability in a population of N identical and independent ion channels is demonstrated below. Begin with the binomial expansion:

$$(\alpha P_o + (1 - P_O))^N = \sum_{K=0}^{N} \frac{N!}{K!(N-K)!} (\alpha P_o)^K (1 - P_O)^{N-K}. \tag{A13.5}$$

Differentiate Eq. A13.5 with respect to α:

$$N(\alpha P_o + (1 - P_o))^{N-1} P_o = \sum_{K=0}^{N} K \frac{N!}{K!(N-K)!} \alpha^{K-1} P_o{}^{K} (1 - P_O)^{N-K}. \tag{A13.6}$$

If $\alpha = 1$, the expression is reduced to the average open probability identical to the earlier equation of Eq. A13.4:

$$NP_o = \sum_{K=0}^{N} K \frac{N!}{K!(N-K)!} P_o{}^{K} (1 - P_O)^{N-K}, \tag{A13.7}$$

$$< P_o > = \sum_{K=0}^{N} \frac{K}{N} \frac{N!}{K!(N-K)!} P_o{}^{K} (1 - P_O)^{N-K}. \tag{A13.8}$$

With Eq. A13.8 as a basis, the following shows the second moment of the distribution:

$$< P_O^2 > = \sum_{K=0}^{N} \left(\frac{K}{N}\right)^2 \frac{N!}{K!(N-K)!} P_o{}^{K} (1 - P_O)^{N-K}. \tag{A13.9}$$

Now perform another round of differentiation of Eq. A13.5 with respect to α:

$$N(N-1)(\alpha P_o + (1 - P_o))^{N-2} P_o{}^2 = \sum_{K=0}^{N} K(K-1) \frac{N!}{K!(N-K)!} \alpha^{K-2} P_o{}^{K} (1 - P_O)^{N-K}. \tag{A13.10}$$

Again, let $\alpha = 1$ in Eq. A13.9:

$$N(N-1) P_o{}^2 = \sum_{K=0}^{N} K(K-1) \frac{N!}{K!(N-K)!} P_o{}^{K} (1 - P_O)^{N-K}. \tag{A13.11}$$

Simplifying Eq. A13.11 gives:

$$N(N-1) P_o{}^2 = \sum_{K=0}^{N} K^2 \frac{N!}{K!(N-K)!} P_o{}^{K} (1 - P_O)^{N-K} - \sum_{K=0}^{N} K \frac{N!}{K!(N-K)!} P_o{}^{K} (1 - P_O)^{N-K}$$

$$= N^2 \sum_{K=0}^{N} \frac{K^2}{N^2} \frac{N!}{K!(N-K)!} P_o{}^{K} (1 - P_O)^{N-K} - N \sum_{K=0}^{N} \frac{K}{N} \frac{N!}{K!(N-K)!} P_o{}^{K} (1 - P_O)^{N-K}. \tag{A13.12}$$

Substitute Eq. A13.8 and Eq. A13.9 into Eq. A13.12 to get:

$$N(N-1) < P_o >^2 = N^2 < P_O^2 > - N < P_o >. \tag{A13.13}$$

Rearrange Eq. A13.13 to get:

$$N < P_O > - N < P_o >^2 = N^2 < P_O^2 > - N^2 < P_o >^2,$$

$$\frac{<P_O>(1 - <P_o>)}{N} = < P_O^2 > - < P_o >^2. \tag{A13.14}$$

The right term of Eq. A13.14 gives the variance of P_O, therefore:

$$\sigma_{Po} = \frac{<P_O>(1-<P_o>)}{N}.$$

(A13.15)

The above can be adapted to a more useful form by multiplying single channel current, i (assumed constant) to Eq. A13.12:

$$i^2N(N-1)P_o{}^2 = N^2 \sum_{K=0}^{N} \frac{K^2}{N^2} \frac{N!}{K!(N-K)!} i^2 P_o{}^K (1-P_O)^{N-K} - N \sum_{K=0}^{N} \frac{K}{N} i^2 \frac{N!}{K!(N-K)!} P_o{}^K (1-P_O)^{N-K}.$$

(A13.16)

Simplifying Eq. A13.16 gives:

$$N^2 i^2 <P_o>^2 - Ni^2 <P_o>^2 = N^2 <(iP_O)^2> - Ni^2 <P_O>.$$

(A13.17)

Rearrangement of Eq. A13.17 gives:

$$Ni^2 <P_O> - Ni^2 <P_o>^2 = N^2 <(iP_O)^2> - N^2 i^2 <P_o>^2.$$

(A13.18)

With a population of N channels with single current, i, and an open probability of P_O, the macroscopic current of this system, I, is given by:

$$I = NiP_O.$$

(A13.19)

Using Eq. A13.19, Eq. A13.18 can be simplified:

$$i(Ni<P_O>)(1-<P_O>) = <(NiP_O)^2> - (Ni<P_O>)^2,$$

$$i<I>(1-<P_o>) = <I^2> - <I>^2.$$

(A13.20)

The right hand term of Eq. A13.20 gives the variance, and therefore the following is obtained:

$$\sigma_I = i<I>(1-<P_o>),$$

$$\sigma_I(t) = i<I(t)>(1-<P_o(t)>).$$

(A13.21)

Eq. A13.21 is useful when the appropriate experimental data of *I(t)* is available; specifically, *I(t)* measured over a voltage clamp protocol from the same cell several times allows the variance, $\sigma_I(t)$, and mean values, *I(t)*, to be computed. In turn, the single channel current, i, and the open probability, $P_o(t)$, can be parameterized by fitting against the experimental data of $\sigma_I(t)$

and *I(t)*. The number of channels, *N*, can also be derived. The parameter

values of i, $P_o(t)$ and N are useful for ion channel modelling.

Appendix 14. Complete equations of the human jejunal smooth muscle cell model

Table A14.1. Model parameters.

Parameter name	Description	Value	Units
R	Ideal gas constant	8.314	J/(molK)
F	The Faraday constant	96.48534	C/mmol
T	Temperature	310	K
C_m	Cell membrane capacitance	50	pF
V_{cell}	Cell volume	3.5e-12	l
$[Ca^{2+}]_o$	Extracellular calcium concentration	2	mM
$[K^+]_o$	Extracellular potassium concentration	5.4	mM
$[Na^+]_o$	Extracellular sodium concentration	140	mM
$[Ca^{2+}]_i^{total}$	Initial value of total intracellular calcium concentration	0.004914	mM
$[Ca^{2+}]_i^{free}$	Initial value of free intracellular calcium concentration	1.26e-4	mM
$[K^+]_i$	Intracellular potassium concentration	150	mM
$[Na^+]_i$	Intracellular sodium concentration	10.5	mM
Q_{10}^{Ca}	Q_{10} for calcium channels	2.1	-
Q_{10}^{K}	Q_{10} for potassium channels	3.1	-
Q_{10}^{Na}	Q_{10} for sodium channels	2.45	-
G_{couple}	Coupling conductance between ICC and SMC	2.6	nS
V_{rest}^{ICC}	Resting membrane potential of ICC	-57	mV
V_{peak}^{ICC}	Peak membrane potential of ICC	-23.5	mV
V_{amp}^{ICC}	Amplitude of ICC membrane potential (given by $V_{peak}^{ICC} - V_{rest}^{ICC}$)	33.5	mV
t_{period}	Period of single ICC slow wave	10000	ms
t_{peak}^{ICC}	Duration of ICC slow wave upstroke to reach V_{peak}^{ICC}	300	ms
$t_{plateau}^{ICC}$	Duration of ICC slow wave from start to plateau phase	9700	ms
t_{slope}	Slope factor in V_m^{ICC} equation	600	ms
f_1	ICC conditioning factor 1	12000	ms
f_2	ICC conditioning factor 2	300	ms
$[CRT]_{total}$	Total calreticulin concentration	0.034	mM
n_{CRT}	Hill coefficient for calreticulin	1	-

K_D^{CRT}	Dissociation constant for calreticulin	0.0009	mM
$[CaM]_{total}$	Total calmodulin concentration	0.012	mM
n_{CaM}	Hill coefficient for calmodulin	4	-
K_D^{CaM}	Dissociation constant for calmodulin	0.0001	mM^4
G_{CaL}	Maximum conductance of I_{CaL}	1.44	nS
G_{CaT}	Maximum conductance of I_{CaT}	0.0425	nS
G_{Kv}	Maximum conductance of I_{Kv}	1.0217	nS
$\tau_{x_{Kv}}$	Time constant for x_{Kv} of I_{Kv}	4.7803	ms
$\tau_{y_{Kv}}$	Time constant for y_{Kv} of I_{Kv}	763.7564	ms
G_{BK}	Maximum conductance of I_{BK}	80	nS
G_{Na}	Maximum conductance of I_{Na}	25.1	nS
P_{NCX}	Maximum I_{NCX}	39.8437	pA/pF
K_{mCa}	$[Ca^{2+}]_i$ half saturation constant of I_{NCX}	1.38	mM
K_{mNai}	$[Na^+]_i$ half saturation constant of I_{NCX}	87.5	mM
k_{sat}	Saturation factor for I_{NCX}	0.1	-
γ	Voltage dependence parameter of I_{NCX}	0.35	-
P_{NaK}	Maximum I_{NaK}	0.1852	pA/pF
K_{mK}	$[K^+]_o$ half saturation constant of I_{NaK}	1	mM
K_{mNa}	$[Na^+]_i$ half saturation constant of I_{NaK}	40	mM
G_{NS_Na}	Maximum conductance of non-selective current carrying sodium ions, I_{NS_Na}	0.022488	nS
G_{NS_K}	Maximum conductance of non-selective current carrying potassium ions, I_{NS_K}	0.017512	nS

Complete equations of the hJSMC model
1. Governing equation for single hJSMC electrophysiology

Voltages in mV, ionic currents in pA

$$\frac{dV_m}{dt} = -\frac{I_{ion} + I_{Stim}}{C_m} \qquad (A14.1)$$

2. Ionic currents, I_{ion}

$$I_{ion} = I_{CaL} + I_{CaT} + I_{Kv} + I_{BK} + I_{Na} + I_{NCX} + I_{NaK} + I_{NS} \qquad (A14.2)$$

3. I_{Stim} equations

$$I_{Stim} = G_{couple}(V_m - V_m^{ICC}) \tag{A14.3}$$

Mathematical profile of the prescribed V_m^{ICC} that describes a single slow wave:

$$V_m^{ICC} = \begin{cases} V_{rest}^{ICC} + V_{amp}^{ICC}\left(\dfrac{t}{f_2}\right) & for \quad 0 \le t < t_{peak}^{ICC} \\[4mm] V_{rest}^{ICC} + V_{amp}^{ICC}\left(1 + \exp\left(\dfrac{-f_1}{2t_{slope}}\right)\right)\left(\dfrac{1}{1 + \exp\left(\dfrac{t - f_2 - 0.5f_1}{t_{slope}}\right)}\right) & for \quad t_{peak}^{ICC} \le t < t_{plateau}^{ICC} \end{cases}$$

$$\tag{A14.4}$$

4. Equations for tracking the intracellular ionic concentrations

Ion concentration should be tracked in mM

$$\frac{d[Ca^{2+}]_i^{total}}{dt} = -\left(I_{CaL} + I_{CaT} - 2I_{NCX}\right)\frac{1}{2FV_{cell}} \tag{A14.5}$$

$$\frac{d[K^+]_i}{dt} = -\left(I_{Kv} + I_{BK} + I_{stim} - 2I_{NaK} + I_{NS\_K}\right)\frac{1}{FV_{cell}} \tag{A14.6}$$

$$\frac{d[Na^+]_i}{dt} = -\left(I_{Na} + 3I_{NaK} + 3I_{NCX} + I_{NS\_Na}\right)\frac{1}{FV_{cell}} \tag{A14.7}$$

5. Nernst potential

Nernst potential unit is mV

$$E_{Ca} = \frac{RT}{2F}\ln\frac{[Ca^{2+}]_o}{[Ca^{2+}]_i} \tag{A14.8}$$

$$E_K = \frac{RT}{F}\ln\frac{[K^+]_o}{[K^+]_i} \tag{A14.9}$$

$$E_{Na} = \frac{RT}{F}\ln\frac{[Na^+]_o}{[Na^+]_i} \tag{A14.10}$$

6. Calcium buffering

Calcium concentration in mM

$$\frac{d[Ca^{2+}]_i^{free}}{dt} = \frac{d[Ca^{2+}]_i^{total}}{dt} \div \left(1 + \frac{n_{CRT}[CRT]_{total} K_D^{CRT} \left([Ca^{2+}]_i^{free} \right)^{n_{CRT}-1}}{\left(\left([Ca^{2+}]_i^{free} \right)^{n_{CRT}} + K_D^{CRT} \right)^2} + \right.$$

$$\left. \frac{n_{CaM}[CaM]_{total} K_D^{CaM} \left([Ca^{2+}]_i^{free} \right)^{n_{CaM}-1}}{\left(\left([Ca^{2+}]_i^{free} \right)^{n_{CaM}} + K_D^{CaM} \right)^2} \right)$$

(A14.11)

7. L-type calcium current, I_{CaL}
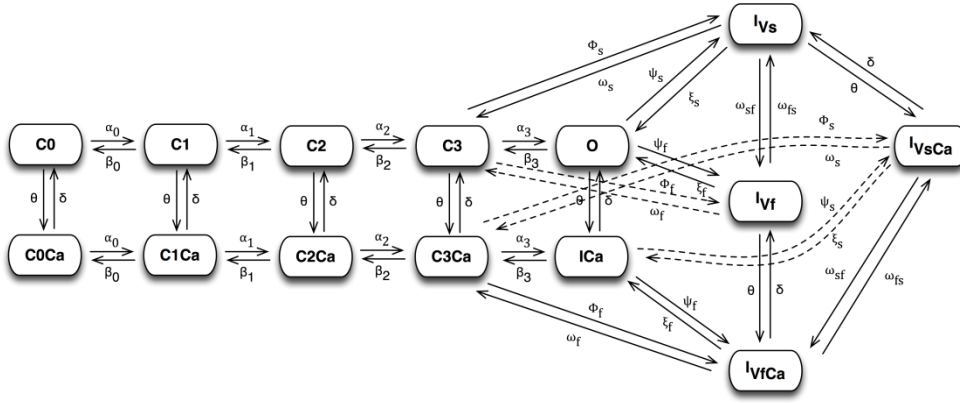
Figure A14.1. L-type Ca^{2+} channel Markov model topology. Prefixes *C, I,* O denote closed, inactivated and open states respectively; suffixes *Ca, V_m, f,* s found in some of the states refer to calcium-bound, voltage-dependent, fast, and slow properties of these states respectively. The topology was designed to best describe observed characteristics of the L-type Ca^{2+} channels. O is the state that conducts Ca^{2+} ions across the channels.

$$I_{CaL} = G_{CaL} P_O (V_m - E_{Ca})$$

(A14.12)

Common rate equations:

$$a = 0.7310 \exp(\frac{V_m}{30.0})$$

(A14.13)

$$b = 0.2149 \exp(\frac{-V_m}{40.0})$$

(A14.14)

Rate equations for horizontal activation transitions:

$$a_0 = 4a$$

(A14.15)

$$a_1 = 3a \tag{A14.16}$$

$$a_2 = 2a \tag{A14.17}$$

$$a_3 = a \tag{A14.18}$$

Rate equations for horizontal deactivation transitions (ms^{-1}):

$$b_0 = b \tag{A14.19}$$

$$b_1 = 2b \tag{A14.20}$$

$$b_2 = 3b \tag{A14.21}$$

$$b_3 = 4b \tag{A14.22}$$

Rate equations for fast and slow inactivation transitions (ms^{-1}):

$$\phi_f = 0.4742 \exp(\frac{V_m}{10.0}) \tag{A14.23}$$

$$\phi_s = 0.05956 \exp(\frac{-V_m}{40.0}) \tag{A14.24}$$

$$\xi_f = 0.01407 \exp(\frac{-V_m}{300.0}) \tag{A14.25}$$

$$\xi_s = 0.01213 \exp(\frac{V_m}{500.0}) \tag{A14.26}$$

$$\psi_f = 0.02197 \exp(\frac{V_m}{500.0}) \tag{A14.27}$$

$$\psi_s = 0.00232 \exp(\frac{-V_m}{280.0}) \tag{A14.28}$$

$$\omega_f = \frac{b_3 \xi_f \phi_f}{a_3 \psi_f} \tag{A14.29}$$

$$\omega_s = \frac{b_3 \xi_s \phi_s}{a_3 \psi_s} \tag{A14.30}$$

$$\omega_{sf} = \frac{\xi_s \psi_f}{\xi_f} \tag{A14.31}$$

$$\omega_{fs} = \psi_s \tag{A14.32}$$

Rate equations for calcium dependent transitions (ms⁻¹):

$$\theta = \frac{4}{1 + \dfrac{1}{[Ca^{2+}]_i^{free}}} \tag{A14.33}$$

$$\delta = 0.01 \tag{A14.34}$$

8. T-type calcium current, I_{CaT}

$$I_{CaT} = G_{CaT} d_{CaT} f_{CaT} (V_m - E_{Ca}) \tag{A14.35}$$

Equations for gating variables (ms⁻¹):

$$\frac{dd_{CaT}}{dt} = \frac{d_{CaT}^{\infty} - d_{CaT}}{\tau_{d_{CaT}}} \tag{A14.36}$$

$$\frac{df_{CaT}}{dt} = \frac{f_{CaT}^{\infty} - f_{CaT}}{\tau_{f_{CaT}}} \tag{A14.37}$$

Equations for steady-state values of the gating variables:

$$d_{CaT}^{\infty} = \frac{1}{1 + \exp\left(-\dfrac{V_m + 60.5}{5.3}\right)} \tag{A14.38}$$

$$f_{CaT}^{\infty} = \frac{1}{1 + \exp\left(\dfrac{V_m + 75.5}{4.0}\right)} \tag{A14.39}$$

Equations for the time constant variables:

$$\tau_{d_{CaT}} = 1.9058 \qquad (A14.40)$$

$$\tau_{f_{CaT}} = 0.38117\left(8.6 + 14.7\exp\left(-\frac{(V_m + 50)^2}{900}\right)\right) \qquad (A14.41)$$

9. Voltage dependent potassium current, I_{Kv}

$$I_{Kv} = G_{Kv}x_{Kv}y_{Kv}(V_m - E_K) \qquad (A14.42)$$

Rate equations for the gating variables (ms^{-1}):

$$\frac{dx_{Kv}}{dt} = \frac{x_{Kv}^{\infty} - x_{Kv}}{\tau_{x_{Kv}}} \qquad (A14.43)$$

$$\frac{dy_{Kv}}{dt} = \frac{y_{Kv}^{\infty} - y_{Kv}}{\tau_{y_{Kv}}} \qquad (A14.44)$$

Equations for the steady-state values of the gating variables:

$$x_{Kv}^{\infty} = \frac{1}{1 + \exp\left(-\dfrac{V_m + 43.0}{17.36}\right)} \qquad (A14.45)$$

$$y_{Kv}^{\infty} = \frac{1}{1 + \exp\left(\dfrac{V_m - 44.9}{12.0096}\right)} \qquad (A14.46)$$

10. Calcium & voltage activated potassium current, I_{BK}
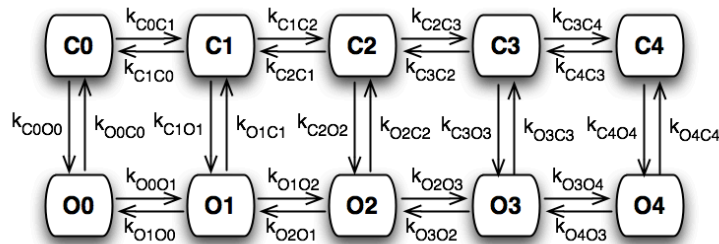
Figure A14.2. A10-state Markov model of homotetrameric BK channel. Upper tier states are various closed conformation states (with prefix *C*) while lower tier states are various open-

oriented conformation states (with prefix O). In each tier, the horizontal transitions depend on $[Ca^{2+}]_i^{free}$, that reflects cooperative Ca^{2+} binding to each of the four alpha subunits of the BK homotetramer. The membrane voltage dependency is found in the vertical transitions between states. O4 is the conformation state that conducts ions across BK channels under a voltage driving force.

$$I_{BK} = G_{BK} P_O (V_m - E_K) \qquad (A14.47)$$

Common rate equations:

$$a = \exp(\frac{8.47188 V_m}{T}) \qquad (A14.48)$$

$$b = \exp(\frac{-7.77556 V_m}{T}) \qquad (A14.49)$$

$$k_{on} = 40633 \qquad (A14.50)$$

$$k_{off}^C = 11 \qquad (A14.51)$$

$$k_{off}^O = 1.1 \qquad (A14.52)$$

Rate equations for voltage dependent transitions (ms^{-1}):

$$k_{C0O0} = 0.02162a \qquad (A14.53)$$

$$k_{C1O1} = 0.000869a \qquad (A14.54)$$

$$k_{C2O2} = 0.0000281a \qquad (A14.55)$$

$$k_{C3O3} = 0.000781a \qquad (A14.56)$$

$$k_{C4O4} = 0.044324a \qquad (A14.57)$$

$$k_{O0C0} = 318.1084b \qquad (A14.58)$$

$$k_{O1C1} = 144.1736b \qquad (A14.59)$$

$$k_{O2C2} = 32.6594b \qquad (A14.60)$$

$$k_{O3C3} = 0.095312b \qquad (A14.61)$$

$$k_{O4C4} = 0.000106b \tag{A14.62}$$

Rate equations for calcium dependent transitions (ms⁻¹):

$$k_{C0C1} = 4k_{on}[Ca^{2+}]_i^{free} \tag{A14.63}$$

$$k_{C1C2} = 3k_{on}[Ca^{2+}]_i^{free} \tag{A14.64}$$

$$k_{C2C3} = 2k_{on}[Ca^{2+}]_i^{free} \tag{A14.65}$$

$$k_{C3C4} = k_{on}[Ca^{2+}]_i^{free} \tag{A14.66}$$

$$k_{C4C3} = 4k_{off}^C[Ca^{2+}]_i^{free} \tag{A14.67}$$

$$k_{C3C2} = 3k_{off}^C[Ca^{2+}]_i^{free} \tag{A14.68}$$

$$k_{C2C1} = 2k_{off}^C[Ca^{2+}]_i^{free} \tag{A14.69}$$

$$k_{C1CO} = k_{off}^C[Ca^{2+}]_i^{free} \tag{A14.70}$$

$$k_{O0O1} = 4k_{on}[Ca^{2+}]_i^{free} \tag{A14.71}$$

$$k_{O1O2} = 3k_{on}[Ca^{2+}]_i^{free} \tag{A14.72}$$

$$k_{O2O3} = 2k_{on}[Ca^{2+}]_i^{free} \tag{A14.73}$$

$$k_{O3O4} = k_{on}[Ca^{2+}]_i^{free} \tag{A14.74}$$

$$k_{O4O3} = 4k_{off}^O[Ca^{2+}]_i^{free} \tag{A14.75}$$

$$k_{O3O2} = 3k_{off}^O[Ca^{2+}]_i^{free} \tag{A14.76}$$

$$k_{O2O1} = 2k_{off}^O[Ca^{2+}]_i^{free} \tag{A14.77}$$

$$k_{O1O0} = k_{off}^O[Ca^{2+}]_i^{free}$$

11. Voltage dependent sodium current, I_{Na}
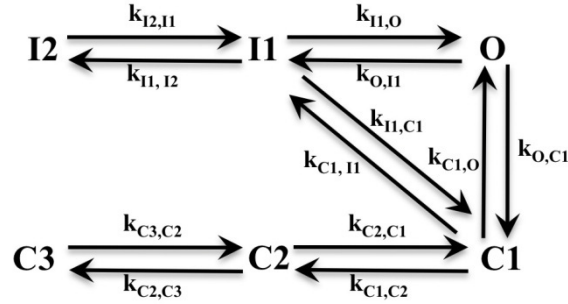
Figure A14.3. Six-state Markov model of Na$_v$1.5. *C* refers to closed state, *I* refers to inactivated state, and *O* refers to open state where Na$^+$ ions are conducted across the channels.

$$I_{Na} = G_{Na} P_O (V_m - E_{Na}) \tag{A14.78}$$

Rate equations (ms^{-1}):

$$k_{O,I1} = 1.6164 \exp(0.30763 + 0.0060535 V_m) \tag{A14.79}$$

$$k_{I1,I2} = 0.027735 \exp(0.051490 - 0.046865 V_m) \tag{A14.80}$$

$$k_{C3,C2} = 0.000526 \exp(-0.069102 + 0.0031945 V_m) \tag{A14.81}$$

$$k_{C2,C1} = 1.4496 \exp(-0.15660 + 0.058353 V_m) \tag{A14.82}$$

$$k_{C1,O} = 1.5329 \exp(0.0093193 + 0.041075 V_m) \tag{A14.83}$$

$$k_{I2,I1} = 0.0039239 \exp(2.6793 + 0.0061468 V_m) \tag{A14.84}$$

$$k_{C2,C3} = 0.55432 \exp(-0.099074 + 0.036441 V_m) \tag{A14.85}$$

$$k_{C1,C2} = 3.1566 \exp(0.36352 + 0.077193 V_m) \tag{A14.86}$$

$$k_{O,C1} = 2.3915 \exp(-13.335 - 0.25289 V_m) \tag{A14.87}$$

$$k_{I1,C1} = 1.9046 \exp(-2.4840 + 0.020406 V_m) \tag{A14.88}$$

$$k_{C1,I1} = 0.00021688 \exp(-0.063438 + 0.0046683 V_m) \tag{A14.89}$$

$$k_{I1,O} = 0.12052 \exp(-9.6028 + 0.083025 V_m) \qquad (A14.90)$$

12. Sodium-calcium exchanger, I_{NCX}

$$I_{NCX} = P_{NCX} \frac{\exp\left(\frac{\gamma V_m F}{RT}\right)[Na^+]_i^3[Ca^{2+}]_o - 2.5 \exp\left(\frac{(\gamma - 1.0)V_m F}{RT}\right)[Na^+]_o^3[Ca^{2+}]_i^{free}}{\left(K_{mNai}^3 + [Na^+]_o^3\right)\left(K_{mCa} + [Ca^{2+}]_o\right)\left(1 + k_{sat} \exp\left(\frac{(\gamma - 1.0)V_m F}{RT}\right)\right)}$$

$$(A14.91)$$

13. Sodium Potassium Pump, I_{NaK}

$$I_{NaK} = P_{NaK} \frac{K_o[Na^+]_i}{([K^+]_o + K_{mK})([Na^+]_i + K_{mNa})\left(1 + 0.1245 \exp\left(-\frac{0.1 V_m F}{RT}\right) + 0.0353 \exp\left(-\frac{V_m F}{RT}\right)\right)}$$

$$(A14.92)$$

14. Non selective leak current, I_{NS}

$$I_{NS} = I_{NS\_Na} + I_{NS\_K} \qquad (A14.93)$$

$$I_{NS\_Na} = g_{NS\_Na}(V_m - E_{Na}) \qquad (A14.94)$$

$$I_{NS\_K} = g_{NS\_K}(V_m - E_K) \qquad (A14.95)$$

Appendix 15. Calcium buffering for equilibrium reactions

Free intracellular calcium is buffered by a number of proteins. This buffering affects the concentration of free calcium ions that would exert regulatory effects on cellular mechanisms. This section provides the derivation of the calcium buffering equations for two buffering proteins.

Consider the reaction between n molar of calcium ions and a buffering protein, BP:

$$nCa + BP \longleftrightarrow Ca_nBP$$
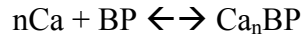
The dissociation constant, K_D, is given by a ratio of the respective concentrations:

$$K_D = \frac{[Ca]^n[BP]}{[Ca_nBP]}. \tag{A15.1}$$

By conservation of mass, the sum of buffered calcium and buffering protein/calcium concentrations gives the total buffering protein/calcium concentration:

$$[BP]_{total}=[Ca_nBP]+[BP], \tag{A15.2}$$

$$[Ca]_{total}=[Ca_nBP]+[Ca]. \tag{A15.3}$$

Rearrange Eq. A15.2 and Eq. A15.3 to get:

$$[BP]=[BP]_{total}-[Ca_nBP], \tag{A15.4}$$

$$[Ca_nBP]=[Ca]_{total}-[Ca]. \tag{A15.5}$$

Substitution of the Eq. A15.4 and Eq. A15.5 into equation of K_D in Eq. A15.1 and with rearrangement gives:

$$[Ca]_{total} = [Ca] + \frac{[BP]_{total}}{1 + \frac{K_D}{[Ca]^n}}. \tag{A15.6}$$

Using chain rule differentiation on total intracellular concentration, i.e., Eq.

A15.6, the following time derivative was obtained:

$$\frac{d[Ca]_{total}}{dt} = \frac{d[Ca]_{total}}{d[Ca]}\frac{d[Ca]}{dt}.$$
(A15.7)

Eq. A15.6 is differentiated with respect to [Ca] and substituted into Eq. A15.7

to get the following:

$$\frac{d[Ca]_{total}}{dt} = \frac{d[Ca]}{dt}\left(1 + \frac{nk_D[Ca]^{n-1}[BP]_{total}}{([Ca]^n + K_D)^2}\right).$$
(A15.8)

Re-expression of Eq. A15.8 gives the desired equation to solve for free

calcium concentration:

$$\frac{d[Ca]}{dt} = \frac{\frac{d[Ca]_{total}}{dt}}{\left(1 + \frac{nk_D[Ca]^{n-1}[BP]_{total}}{([Ca]^n + K_D)^2}\right)}.$$
(A15.9)

The above steps can be extended for the case of two types of buffering

proteins, BP1 and BP2:

$$nCa + BP1 \longleftrightarrow Ca_nBP1$$
(A15.10)

$$mCa + BP2 \longleftrightarrow Ca_mBP2$$
(A15.11)
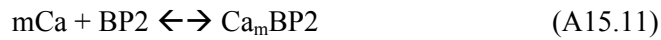
Here are the respective dissociation constants, K_{D1} and K_{D2}:

$$K_{D1} = \frac{[Ca]^n[BP1]}{[Ca_nBP1]},$$
(A15.12)

$$K_{D2} = \frac{[Ca]^m[BP2]}{[Ca_mBP2]}.$$
(A15.13)

The following relationships were established through conservation of mass:

$$[BP1]_{total}=[Ca_nBP1]+[BP1],$$
(A15.14)

$$[BP2]_{total}=[Ca_mBP2]+[BP2],$$
(A15.15)

$$[Ca]_{total}=[Ca_nBP1]+ [Ca_mBP2]+[Ca].$$
(A15.16)

Rearrange Eq. A15.14 and Eq. A15.15 to get:

$$[BP1]= [BP1]_{total} -[Ca_nBP1],$$
(A15.17)

$$[BP2]= [BP2]_{total} -[Ca_mBP2]. \tag{A15.18}$$

Substitute Eq. A15.17 into Eq. A15.12 and rearrange to get:

$$\frac{K_{D1}}{[Ca]^n} = \frac{[BP1]_{total} - [Ca_nBP1]}{[Ca_nBP1]}$$

$$= \frac{[BP1]_{total}}{[Ca_nBP1]} - 1, \tag{A15.19}$$

$$[Ca_nBP1] = \frac{[BP1]_{total}}{1+\frac{K_{D1}}{[Ca]^n}}. \tag{A15.20}$$

Similarly, substitute Eq. A15.16 into Eq. A15.13 and rearrange to get:

$$[Ca_mBP2] = \frac{[BP2]_{total}}{1 + \frac{K_{D2}}{[Ca]^m}}. \tag{A15.21}$$

Next, substitute Eq. A15.20 and Eq. A15.21 into Eq. A15.16 to get:

$$[Ca]_{total} = [Ca] + \frac{[BP1]_{total}}{1+\frac{K_{D1}}{[Ca]^n}} + \frac{[BP2]_{total}}{1+\frac{K_{D2}}{[Ca]^m}}. \tag{A15.22}$$

Apply chain rule differentiation to Eq. A15.22 to obtain the following:

$$\frac{d[Ca]_{total}}{dt} = \frac{d[Ca]_{total}}{d[Ca]}\frac{d[Ca]}{dt}$$

$$= \frac{d[Ca]}{dt}\left(1 + \frac{nK_{D1}[Ca]^{n-1}[BP1]_{total}}{([Ca]^n+K_{D1})^2} + \frac{mK_{D2}[Ca]^{m-1}[BP2]_{total}}{([Ca]^m+K_{D2})^2}\right). \tag{A15.23}$$

Finally, re-expression of Eq. A15.23 gives the desired equation to solve for

free calcium concentration in the presence of two types of buffering proteins:

$$\frac{d[Ca]}{dt} = \frac{\frac{d[Ca]_{total}}{dt}}{\left(1 + \frac{nK_{D1}[Ca]^{n-1}[BP1]_{total}}{([Ca]^n+K_{D1})^2} + \frac{mK_{D2}[Ca]^{m-1}[BP2]_{total}}{([Ca]^m+K_{D2})^2}\right)}. \tag{A15.24}$$

Appendix 16. FTCS discretization of the extended bidomain equations

To solve the extended bidomain problem using the finite time central space (FTCS) method, Eqs. 5.32, 5.33 and 5.35 from Chapter 5 were discretized to the form shown here, in Eqs. A16.1 to A16.3.

$$
\begin{aligned}
& \frac{V_m^{ICC}|_x^{t+\Delta t} - V_m^{ICC}|_x^t}{\Delta t} \\
& = \frac{1}{C_m^{ICC}} \left(\frac{\sigma_i^{ICC}}{A_m^{ICC}} \left(\frac{\varphi_i^{ICC}|_{x+\Delta x}^t - 2\varphi_i^{ICC}|_x^t + \varphi_i^{ICC}|_{x-\Delta x}^t}{(\Delta x)^2} \right) \right. \\
& \left. - \frac{A_m^{gap}}{A_m^{ICC}} I_{gap}|_x^t - \sum I_{ion}^{ICC}|_x^t + I_{stim}^{ICC} \right)
\end{aligned}
\tag{A16.1}
$$

$$
\begin{aligned}
& \frac{V_m^{SMC}|_x^{t+\Delta t} - V_m^{SMC}|_x^t}{\Delta t} \\
& = \frac{1}{C_m^{SMC}} \left(\frac{\sigma_i^{SMC}}{A_m^{SMC}} \left(\frac{\varphi_i^{SMC}|_{x+\Delta x}^t - 2\varphi_i^{SMC}|_x^t + \varphi_i^{SMC}|_{x-\Delta x}^t}{(\Delta x)^2} \right) \right. \\
& \left. + \frac{A_m^{gap}}{A_m^{SMC}} I_{gap}|_x^t - \sum I_{ion}^{SMC}|_x^t + I_{stim}^{SMC} \right)
\end{aligned}
\tag{A16.2}
$$

$$
\begin{aligned}
& \varphi_e|_{x+\Delta x}^{t+\Delta t} - 2\varphi_e|_x^{t+\Delta t} + \varphi_e|_{x-\Delta x}^{t+\Delta t} \\
& \qquad = \frac{(\Delta x)^2}{\sigma_e + \sigma_i^{ICC} + \sigma_i^{SMC}} \left(I_{stim}^{EXT} \right. \\
& \qquad - \sigma_i^{ICC} \left(\frac{V_m^{ICC}|_x^{t+\Delta t} - V_m^{ICC}|_x^t}{\Delta t} \right) \\
& \qquad \left. + \sigma_i^{SMC} \left(\frac{V_m^{SMC}|_x^{t+\Delta t} - V_m^{SMC}|_x^t}{\Delta t} \right) \right)
\end{aligned}
\tag{A16.3}
$$

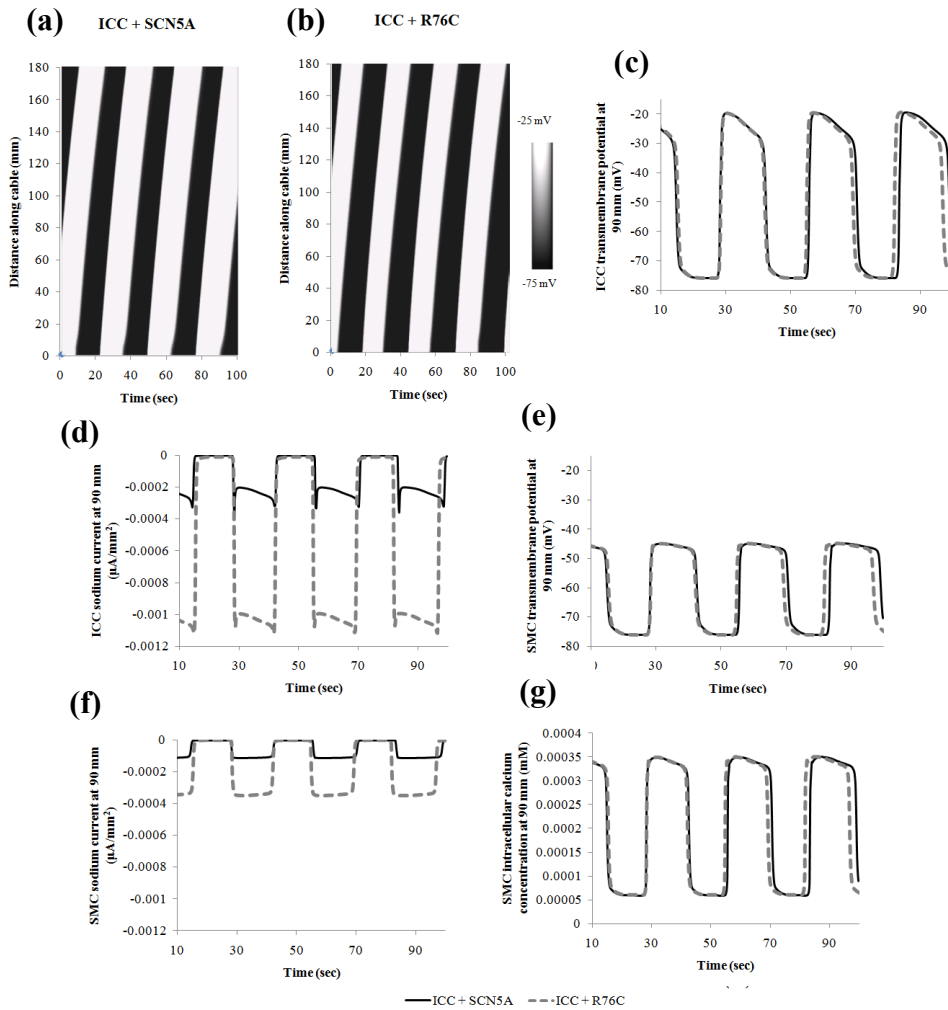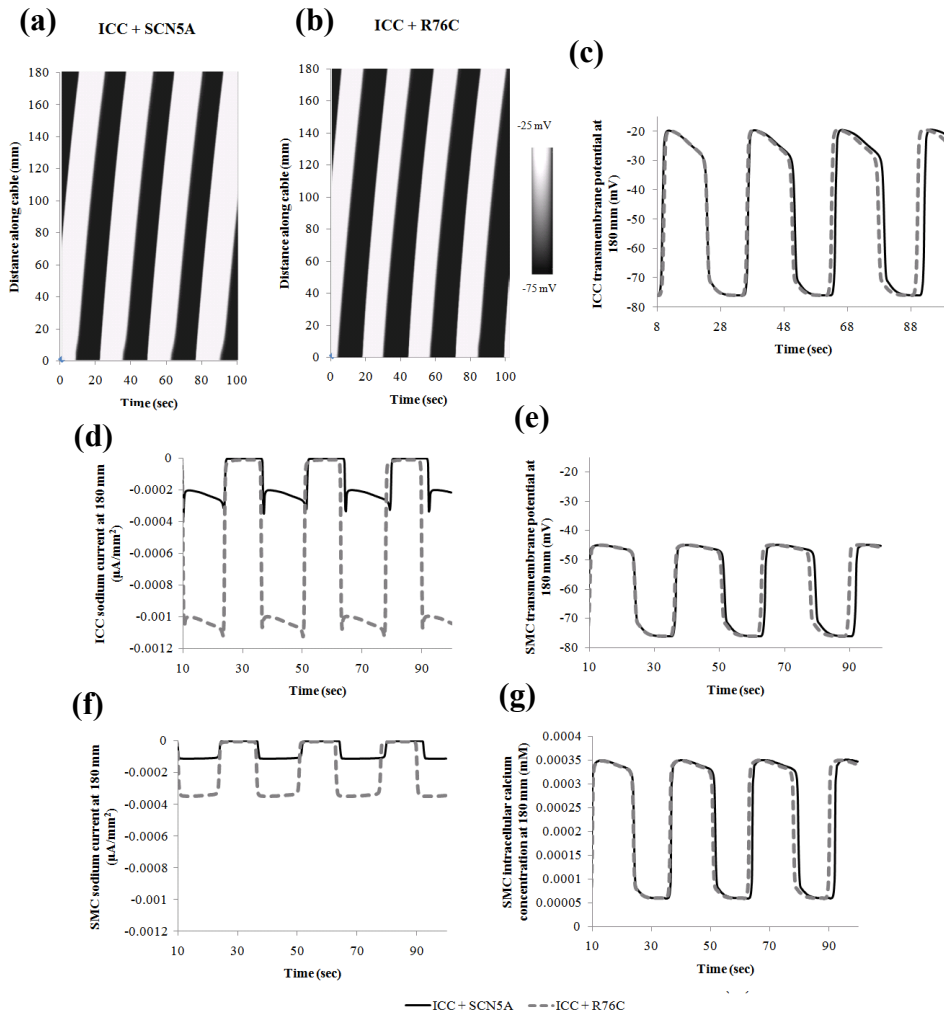## Appendix 17. Cable model results at 90 mm and 180 mm (SCN5A/R76C)

Figure A17.1. SCN5A versus R76C slow wave results for the position of 90 mm from the proximal end of the cable model. (a) and (b) are the spatiotemporal plots for ICC with wild-type sodium channels and ICC with R76C mutation respectively. (c) and (e) are the ICC and SMC slow wave potentials respectively. (d) and (f) are the ICC and SMC sodium currents respectively. (g) is the SMC intracellular calcium concentration. Solid lines for wild-type results and dashed lines for R76C mutation results.

Figure A17.2. SCN5A versus R76C slow wave results for the position of 180 mm from the proximal end of the cable model. (a) and (b) are the spatiotemporal plots for ICC with wild-type sodium channels and ICC with R76C mutation respectively. (c) and (e) are the ICC and SMC slow wave potentials respectively. (d) and (f) are the ICC and SMC sodium currents respectively. (g) is the SMC intracellular calcium concentration. Solid lines for wild-type results and dashed lines for R76C mutation results.

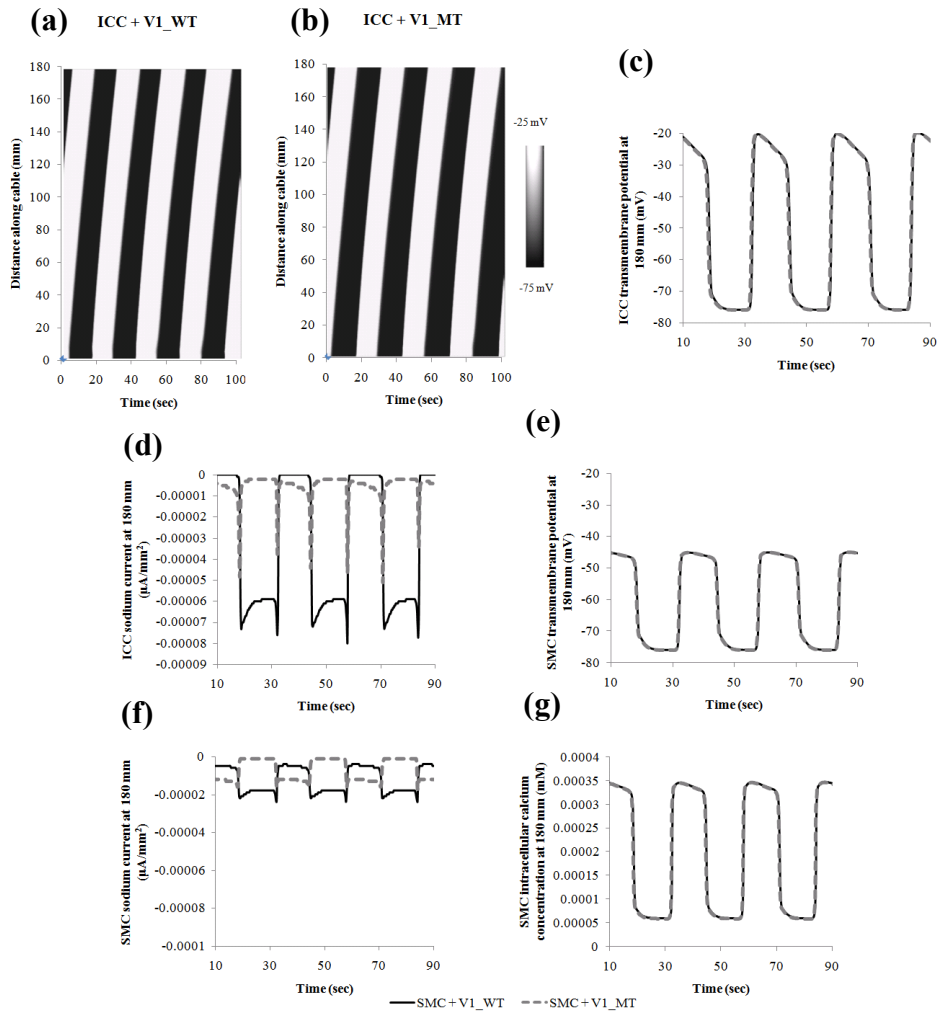## Appendix 18. Cable model results at 90 mm and 180 mm (H558/Q1077del)
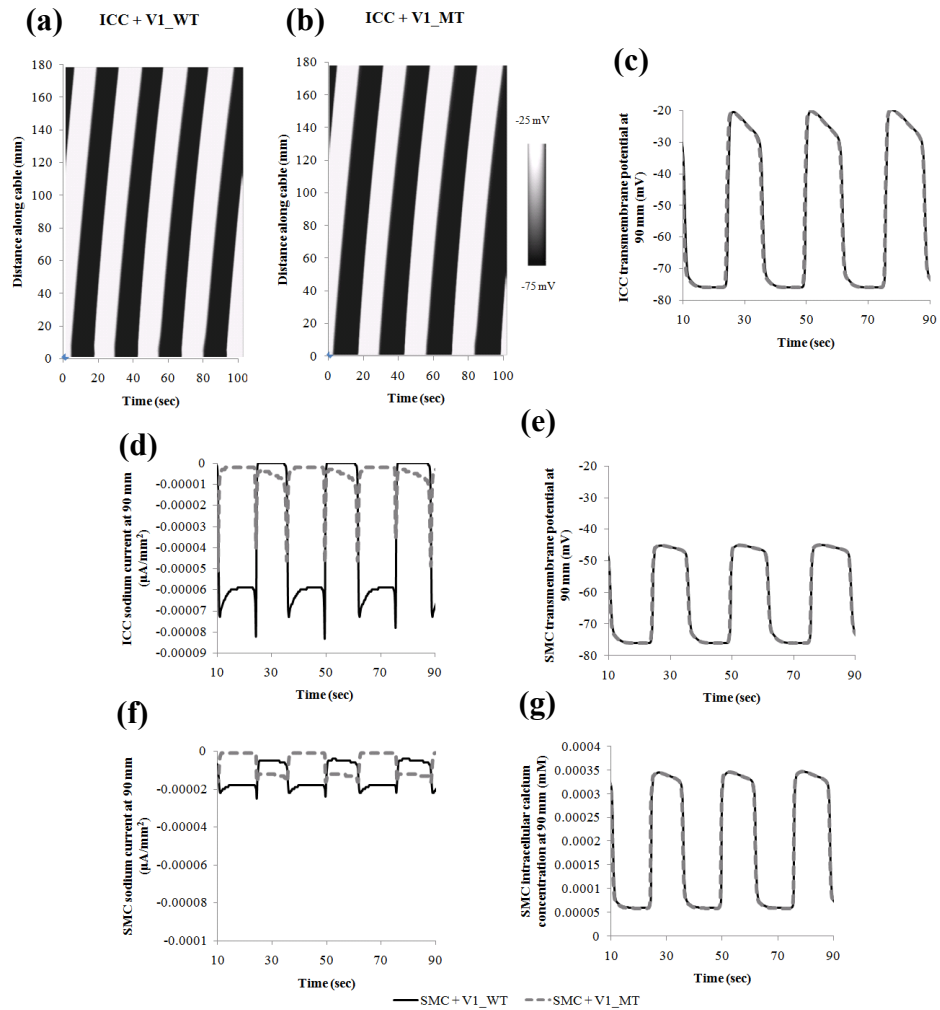
Figure A18.1. H558/Q1077del/G298 versus H558/Q1077del/G298S slow wave results for the position of 90 mm from the proximal end of the cable model. (a) and (b) are the spatiotemporal plots for ICC with wild-type sodium channels and ICC with G298S sodium channels respectively. (c) and (e) are the ICC and SMC slow wave potentials respectively. (d) and (f) are the ICC and SMC sodium currents respectively. (g) is the SMC intracellular calcium concentration. Solid lines for wild-type results and dashed lines for G298S mutation results.
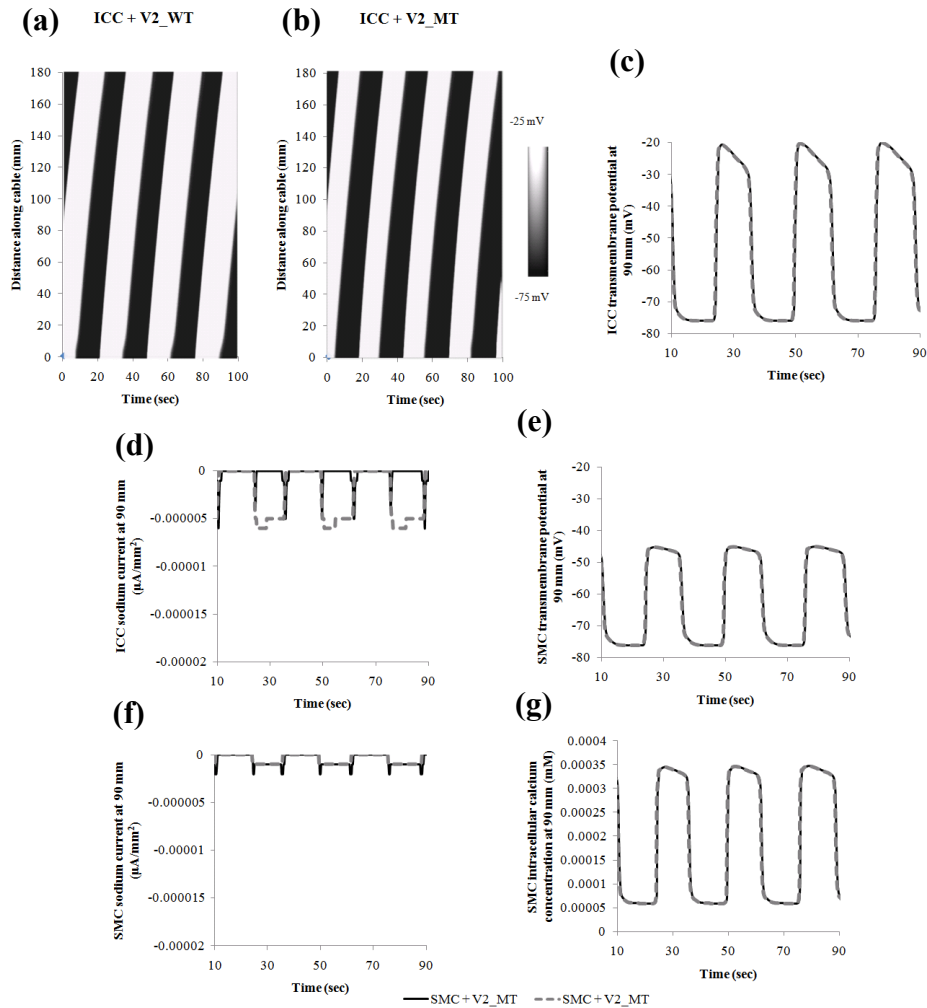
Figure A18.2. H558/Q1077del/G298 versus H558/Q1077del/G298S slow wave results for the position of 180 mm from the proximal end of the cable model. (a) and (b) are the spatiotemporal plots for ICC with wild-type sodium channels and ICC with G298S sodium channels respectively. (c) and (e) are the ICC and SMC slow wave potentials respectively. (d) and (f) are the ICC and SMC sodium currents respectively. (g) is the SMC intracellular calcium concentration. Solid lines for wild-type results and dashed lines for G298S mutation results.

Appendix 19. Cable model results at 90 mm and 180 mm (H558R/Q1077del)

(a) ICC + V2_WT

(b) ICC + V2_MT

(c)

(d)

(e)

(f)

(g)

SMC + V2_MT   SMC + V2_MT

Figure A19.1. H558R/Q1077del/G298 versus H558R/Q1077del/G298S slow wave results for the position of 90 mm from the proximal end of the cable model. (a) and (b) are the spatiotemporal plots for ICC with wild-type sodium channels and ICC with G298S sodium channels respectively. (c) and (e) are the ICC and SMC slow wave potentials respectively. (d) and (f) are the ICC and SMC sodium currents respectively. (g) is the SMC intracellular calcium concentration. Solid lines for wild-type results and dashed lines for G298S mutation results.
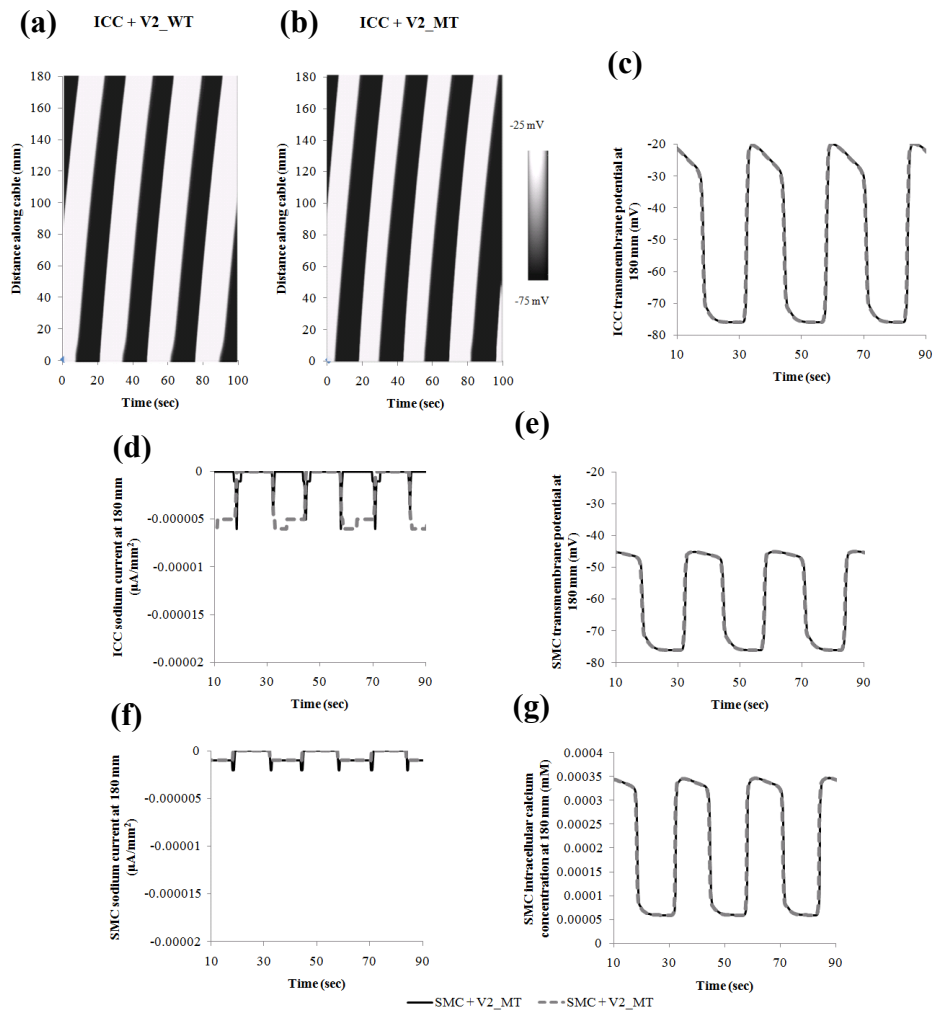
Figure A19.2. H558R/Q1077del/G298 versus H558R/Q1077del/G298S slow wave results for the position of 180 mm from the proximal end of the cable model. (a) and (b) are the spatiotemporal plots for ICC with wild-type sodium channels and ICC with G298S sodium channels respectively. (c) and (e) are the ICC and SMC slow wave potentials respectively. (d) and (f) are the ICC and SMC sodium currents respectively. (g) is the SMC intracellular calcium concentration. Solid lines for wild-type results and dashed lines for G298S mutation results.

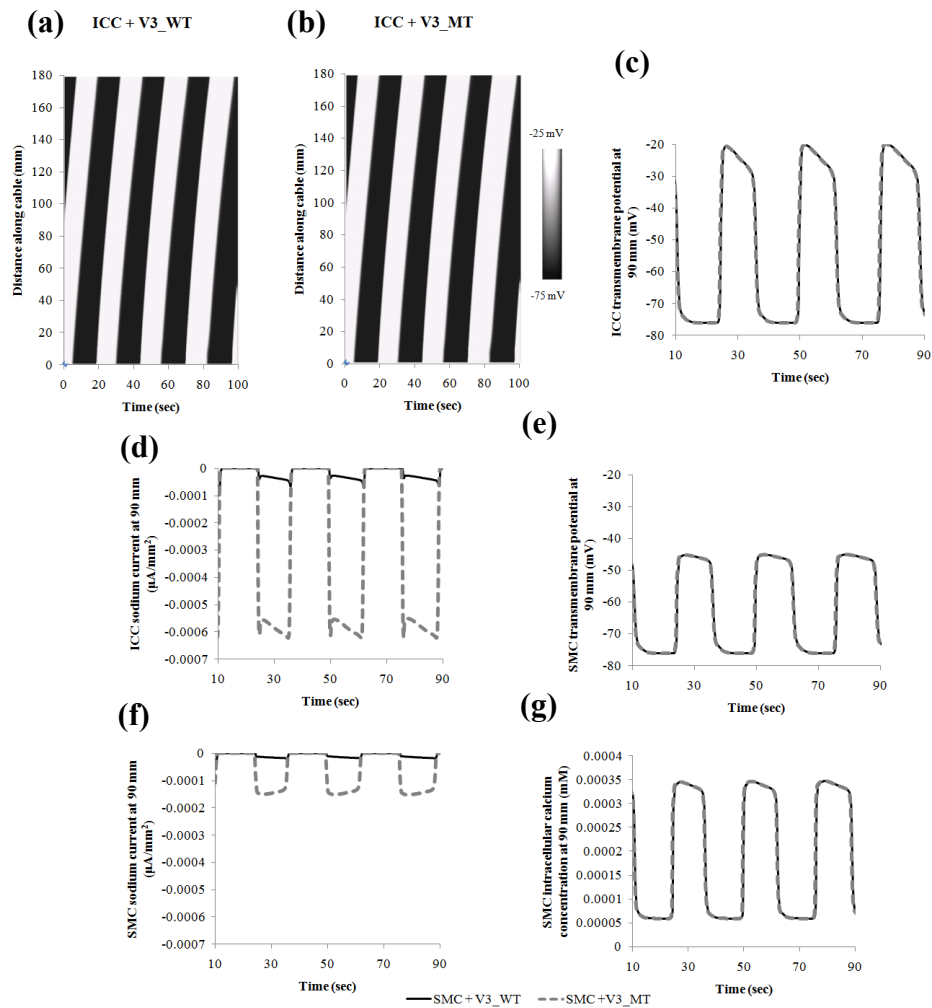## Appendix 20. Cable model results at 90 mm and 180 mm (H558/Q1077)

Figure A20.1. H558/Q1077/G298 versus H558/Q1077/G298S slow wave results for the position of 90 mm from the proximal end of the cable model. (a) and (b) are the spatiotemporal plots for ICC with wild-type sodium channels and ICC with G298S sodium channels respectively. (c) and (e) are the ICC and SMC slow wave potentials respectively. (d) and (f) are the ICC and SMC sodium currents respectively. (g) is the SMC intracellular calcium concentration. Solid lines for wild-type results and dashed lines for G298S mutation results.
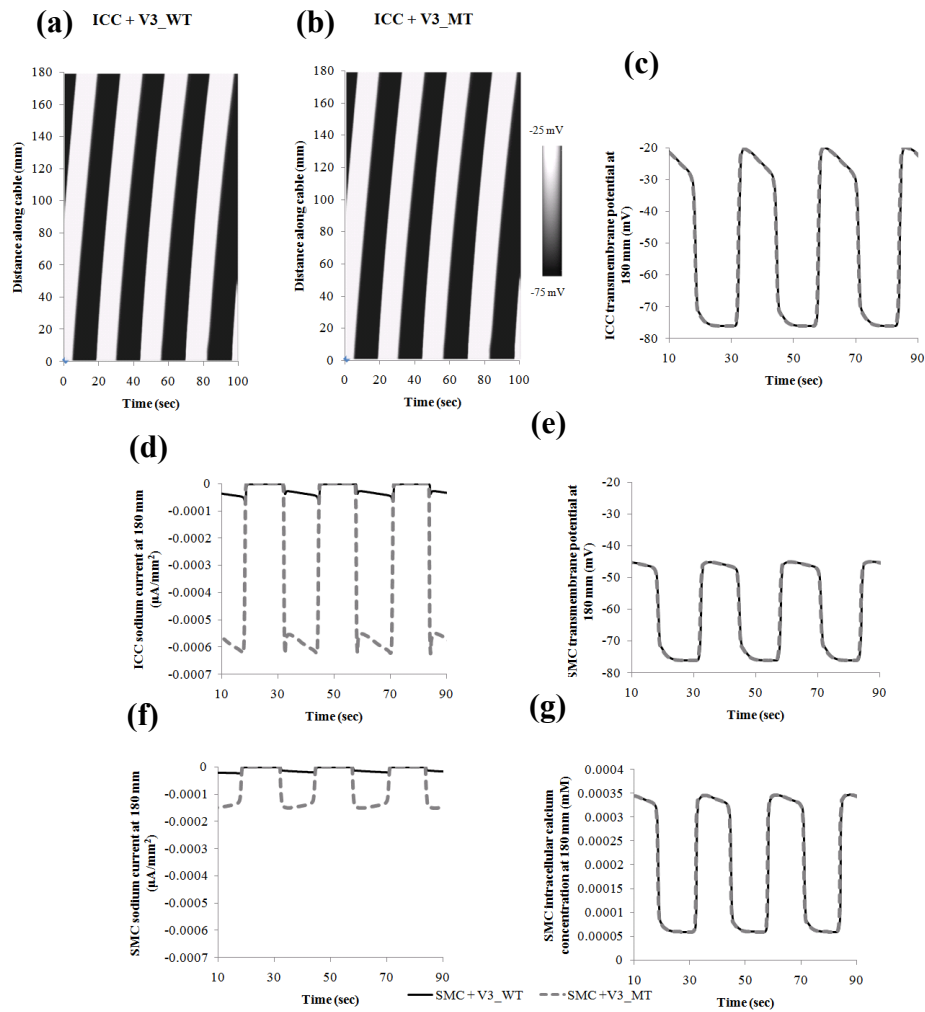
Figure A20.2. H558/Q1077/G298 versus H558/Q1077/G298S slow wave results for the position of 180 mm from the proximal end of the cable model. (a) and (b) are the spatiotemporal plots for ICC with wild-type sodium channels and ICC with G298S sodium channels respectively. (c) and (e) are the ICC and SMC slow wave potentials respectively. (d) and (f) are the ICC and SMC sodium currents respectively. (g) is the SMC intracellular calcium concentration. Solid lines for wild-type results and dashed lines for G298S mutation results.

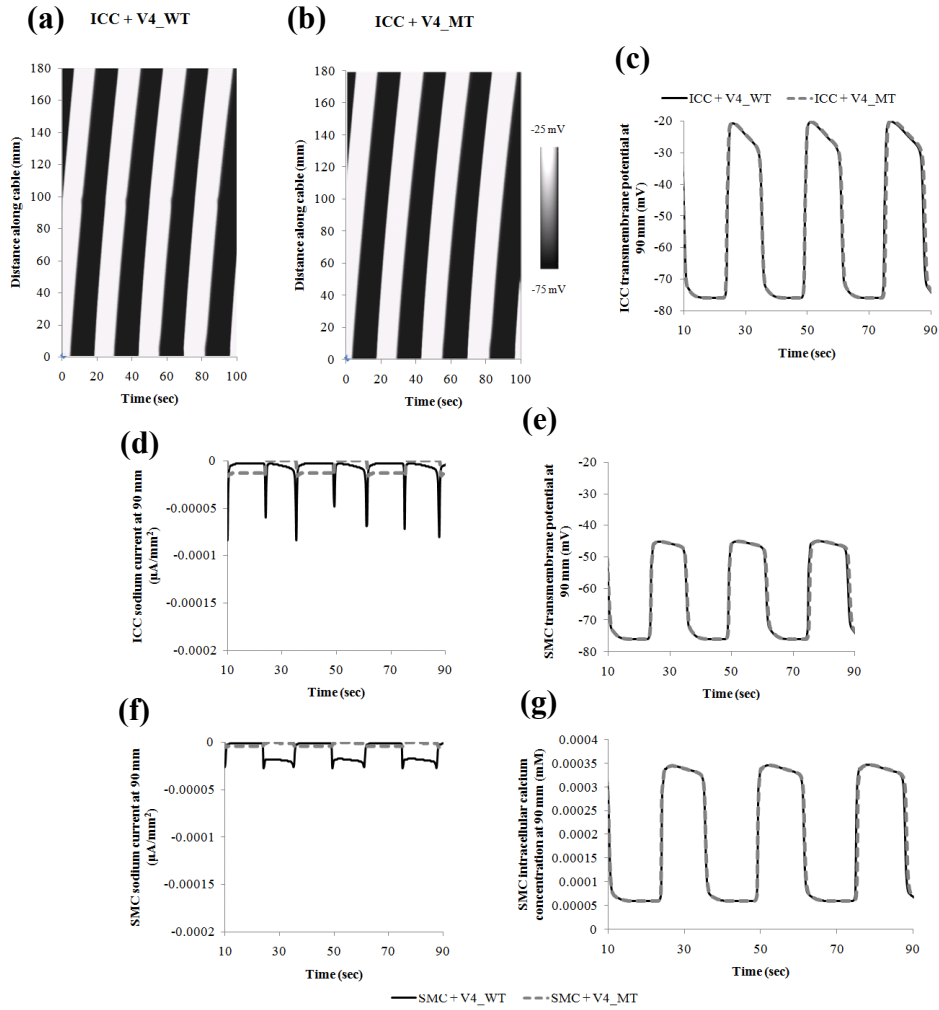**Appendix 21. Cable model results at 90 mm and 180 mm (H558R/Q1077)**

Figure A21.1. H558R/Q1077/G298 versus H558R/Q1077/G298S slow wave results for the position of 90 mm from the proximal end of the cable model. (a) and (b) are the spatiotemporal plots for ICC with wild-type sodium channels and ICC with G298S sodium channels respectively. (c) and (e) are the ICC and SMC slow wave potentials respectively. (d) and (f) are the ICC and SMC sodium currents respectively. (g) is the SMC intracellular calcium concentration. Solid lines for wild-type results and dashed lines for G298S mutation results.
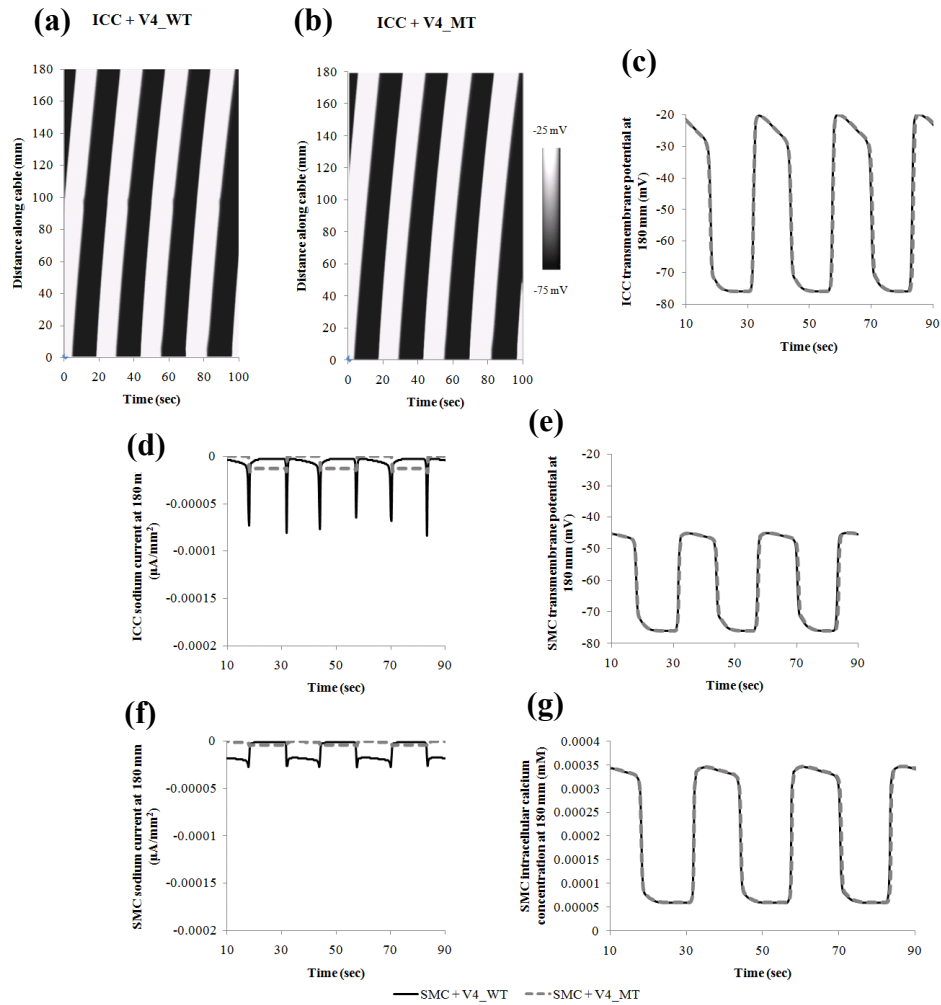
Figure A21.2. H558R/Q1077/G298 versus H558R/Q1077/G298S slow wave results for the position of 180 mm from the proximal end of the cable model. (a) and (b) are the spatiotemporal plots for ICC with wild-type sodium channels and ICC with G298S sodium channels respectively. (c) and (e) are the ICC and SMC slow wave potentials respectively. (d) and (f) are the ICC and SMC sodium currents respectively. (g) is the SMC intracellular calcium concentration. Solid lines for wild-type results and dashed lines for G298S mutation results.

Appendix 22. Computer languages, programs and tools

Operating systems
Linux (Fedora, Ubuntu)
Mac
Windows

Integrated development environments
Eclipse
Code::Blocks
OpenWatcom

Languages
C
C++
CellML
Matlab
Perl

Computation & visualization programs
CHASTE
CMISS cm
CMISS cmgui
CMISS unemap
OpenMP

Other programs
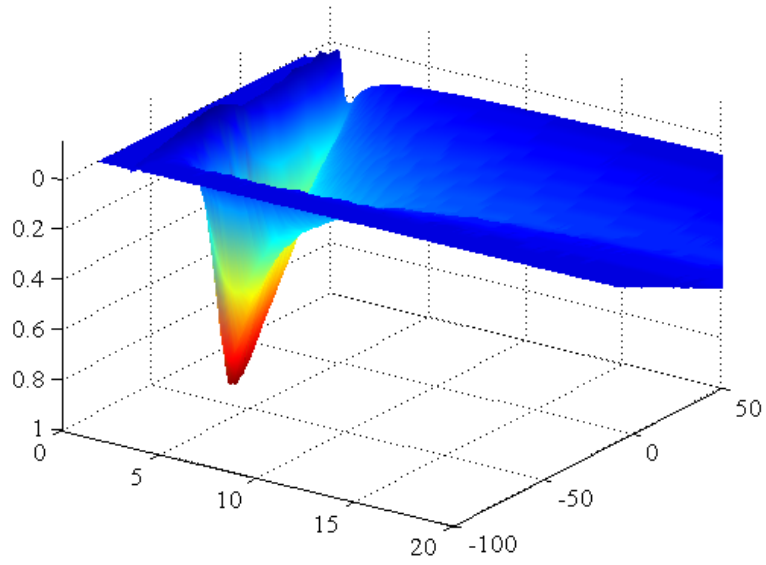Copasi
GIMP
GNUplot
Inkscape
QuB
Octave
Scilab
OpenCell
Stimfit

/**********
The End
**********/